Static and Blast Performance of Reinforced Concrete Beams Built with High-Strength Steel and Stainless Steel Reinforcement

by

Yang Li

Thesis submitted to the University of Ottawa

in partial fulfilment of the requirements for the degree of

Doctor of Philosophy

in Civil Engineering

uOttawa

Department of Civil Engineering

Faculty of Engineering

University of Ottawa

Abstract

High-strength steel (HSS) conforming to ASTM A1035 is becoming increasingly used in various structural applications, including in high-rise buildings and bridges. Due to their chemistry and manufacturing process, ASTM A1035 steel bars result in a combination of high tensile strength to yield ratio and varying levels of corrosion resistance. One potential application of ASTM A1035 bars is in the blast-resistant design of concrete structures, where their use can allow for reduced steel congestion, and increased blast resistance. Despite their high initial cost, stainless steel (SS) reinforcing bars are also seeing increased use in concrete construction. Solid stainless steel bars are referenced in ASTM A955, which is applicable to various stainless steel alloys. In addition to their inherent corrosion resistance, most stainless steel bars possess greater tensile strength, and importantly, exceptional ductility, when compared to ordinary steel reinforcement. This unique combination of strength and ductility makes SS bars well-suited for blast design applications.

The overarching aim of this thesis is to gain better understanding of the blast behavior of RC flexural members designed with high-strength (HSS) and stainless steel (SS) reinforcement. This objective is achieved through a combined experimental and numerical research program. As part of the experimental research, a large set of beams, subdivided into three series, are tested under either quasi-static bending or simulated blast loads using the University of Ottawa shock-tube. Series 1 (HSC-HSS) and Series 2 (HSC-SS) aim at examining the effects of blast detailing (as recommended in modern blast codes,) on the quasi-static, blast and post-blast behaviour of high-strength concrete (HSC) beams reinforced with either ASTM A1035 high-strength bars (8 beams) or ASTM A955 stainless steel bars (16 beams). In addition to the influence of detailing, the effects of steel grade/type, steel ratio and steel fibers are also studied. Series 3 further studies the benefits of combining higher grade or higher ductility reinforcement, with more advanced ultra-high performance concrete (UHPC). This series includes 20 UHPC beams built with either ordinary, HSS or SS reinforcing bars (UHPC-NSS, UHPC-HSS and UHPC-SS). In addition to the effect of steel grade/type, concrete type, steel ratio and steel detailing are also studied.

The results from Series 1 and 2 demonstrate the benefits of implementing high-strength and stainless steel reinforcement in HSC beams subjected to blast loads, where their use leads to increased blast capacity, reduced support rotations, and higher damage tolerance. The results further demonstrate the benefits of “blast detailing” on the ductility and resilience of such beams, under both static and blast loads. The results also show that the use of steel fibers can

be used to relax blast detailing in the beams with high-strength or stainless steel by increasing the required tie spacing from d/4 to d/2. The results from Series 3 confirm that the use of UHPC in beams enhances flexural response (in terms of strength and stiffness), which in turn results in superior blast resistance. Conversely, the high bond capacity of UHPC makes such beams more vulnerable to bar fracture. Increasing the steel ratio is found to effectively increase the failure displacement and ductility of the UHPC beams. The use of high-strength steel is found to increase load capacity and blast resistance, while the use of stainless steel results in remarkable ductility, which further enhances beam response under blast loading.

As part of the numerical research program, the static and blast responses of the test beams are simulated using either 2D or 3D finite element (FE) modelling, using software *VecTor2* and *LS-DYNA*. The numerical results show that the 2D FE modelling using software *VecTor2* can provide reliable predictions of the static and blast responses of the HSS or SS reinforced HSC beams built with varying detailing, in terms of load-deflection response, cracking patterns, failure mode, displacement time histories and dynamic reactions. Likewise, the 3D FE modelling using software *LS-DYNA* with appropriate modelling of UHPC (using the *Winfrith Concrete* or *CSCM* models) can well predict the blast responses of UHPC beams with ordinary, high-strength and stainless steel, in terms of displacement/load-time histories, damage and failure modes.

Acknowledgments

Foremost, I would like to express my deepest and sincere appreciation and gratitude to my supervisor Dr. Hassan Aoude. I still remember nine years ago how nervous I was in front of Dr. Aoude's office door because I can speak little English. Without his endless help, patience, motivation and guidance, I cannot be here.

The financial supports from the China Scholarship Council (CSC) and the University of Ottawa are greatly appreciated.

Also, I would like to express my appreciation to Dr. Muslim Majeed and Dr. Gamal Elnabelsya for their continuous help in the structural lab.

I would like to thank my colleagues Roukaya Bastami, Charlemagne Charles, Dr. Junbo Yan, Dr. Xiangyong Ni, Chuanjing Li, Hyunchul Jung, Jordan Gandia, and co-op students Felix Li, Boukary Timi Kaoura and Fawwaz Ibrahim for their help during the construction, testing and the analysis.

I would like to extend my appreciation to my friends Dr. Wenjun Chen, Shuang Hu, Dr. Peng Lin, and Dr. Bochun Zhang. Special thanks to Dr. Junqiang Zhao, who took a walk with me almost everyday during the pandemic.

Finally, I would like to thank my mother, my father, and my wife for giving me the strength to complete this thesis and for their support and encouragement during my study.

Notations

Symbol	Definition
ε_y	Steel reinforcement yield strain
ε_r	Steel reinforcement rupture strain
ε_u	Steel reinforcement ultimate strain
ρ	Longitudinal tension reinforcement ratio
ρ'	Longitudinal compression reinforcement ratio
ρ_b	Balanced reinforcement ratio
Δ	Displacement in static test
Δ_y	Yield displacement in static test
Δ_{max}	Failure displacement in static test
Δ_{max}/Δ_y	Ductility in static test
Δ_{peak}	Displacement at P_{max}
Δ_{test}^{R}	Tested residual displacement during residual static test
Δ_{max}^{R}	Maximum residual displacement
Δ_{peak}^{num}	Predicted displacement at P_{max}^{num}
Δ_{max}^{num}	Predicted failure displacement
θ_{max}	Maximum support rotation in blast test
ξ	Damping ratio
A	Area impacted by the blast pressure
A_b	Bar area
A_u	Overall toughness in static test
A_u^{num}	Predicted toughness
d	Effective beam depth
d_b	Steel reinforcement bar diameter
d_f	Fiber diameter
D	Repeat blast loading
Dx1	Singly blast loading
DIF_c	Dynamic increase factor for concrete in compression
DIF_t	Dynamic increase factor for concrete in tension
DIF_s	Dynamic increase factor for steel in tension
D_{max}	Maximum mid-span displacement in blast test
D_{res}	Residual mid-span displacement in blast test
$D_{cycle\ 2}$	Displacement amplitude @ second peak

D_{max}^{num}	Predicted maximum displacement
$D_{cycle\ 2}^{num}$	Predicted displacement @ second peak
E	Elastic modulus
f_c'	Compressive concrete strength
f_u	Steel ultimate stress
f_y	Steel yield stress
h	Beam depth
I_r	Peak reflected impulse in blast test
k_s	Secant stiffness in static test
k_s^R	Residual secant stiffness
L_f	Fiber length
P_d	Driver pressure
P_r	Peak reflected pressure in blast test
P_y	Yield load in static test
P_v	Predicted shear load capacity
P_{fl}	Predicted flexural load capacity
P_{max}	Maximum load in static test
P_{max}^R	Peak residual load
P_{max}^D	Peak dynamic load
P_{max}^{num}	Predicted peak load
$P_{max}^{D-\mathrm{num}}$	Predicted peak dynamic load
s	Stirrup spacing
S	Static loading
t_d	Positive phase duration in blast test
V_c	Shear resistance of concrete
V_{fib}	Shear resistance of fiber
V_{r0}	Shear resistance of a reinforced concrete beam
V_s	Shear resistance of transverse steel
V_f	Fiber content
Z	Scaled distances

Abbreviation	Definition
DTT	Direct tension test
DIF	Dynamic increase factor
LTD	Load transfer device
HSC	High-strength concrete
HSFRC	High-strength fiber reinforced concrete
NSS	Normal-strength steel
HSS	High-strength steel
SS	Stainless steel
S1	Austenitic XM-28 stainless steel
S2	Duplex 2304 stainless steel
U1	Ultra-high performance concrete with 1% fiber
U2	Ultra-high performance concrete with 2% fiber
U3	Ultra-high performance concrete with 3% fiber
UHPC	Ultra-high performance concrete
RRI	Residual resistance index
RSI	Residual stiffness index
RDI	Residual displacement index
IEI	Impact Energy Index
REI	Residual Energy Index
TEI	Total Energy Index

Table of content

Lists of Figures

Lists of Tables

Chapter 1 Introduction

1.1 Background

Interest in the use of high-strength reinforcing steel in concrete construction has seen rapid growth. High-strength steel (HSS) is typically defined as steel with a yield strength (f_y) which exceeds 500 MPa. Examples of worldwide applications of HSS bars, include: USD 685 (f_y = 690 MPa) in Japan, SD 685 (f_y = 690 MPa) in Taiwan, China, HRB 600 (f_y = 600 MPa) in China and KS SD600 (f_y = 600 MPa) in Korea. In North America, Grade 550 MPa reinforcement is referenced in the ASTM A615 and A706 specifications, while guidelines have also been developed for SAS670 steel, a German-produced high-strength reinforcing bar with a yield strength of 670 MPa (NEHRP, 2014). High-strength steel conforming to ASTM A0135 is also gaining wider acceptance in the US and Canada (ASTM, 2011). Due to their chemistry and manufacturing process, ASTM A0135 steel bars result in a combination of high tensile strength to yield ratio, and varying levels of corrosion resistance, which makes them well-adapted for high-rise buildings, bridges and marine structures (CSRI, 2017). Another promising application of ASTM A1035 bars is in the design of blast-resistant concrete structures, where their use can allow for reduced steel congestion, and increased blast resistance.

Despite their high initial cost, stainless steel (SS) reinforcing bars are also seeing increased use in concrete construction. Solid stainless steel bars are referenced in ASTM A955, which is applicable to various stainless alloys (ASTM, 2020a). In addition to their inherent corrosion resistance, most stainless steel bars possess greater tensile strength, and importantly, exceptional ductility, when compared to ordinary and high-strength steel reinforcement. This unique combination of strength and ductility make SS bars well-adapted for blast design applications.

Ultra-high performance concrete (UHPC) is another novel material which has gained increased interest in research and design due its high strength properties and remarkable toughness. These properties also make UHPC an ideal material for blast and impact applications. However, the high bond capacity and toughness of UHPC also makes flexural members vulnerable to brittle bar fracture failures, especially when using moderate amounts of ordinary steel reinforcement. The combined use of UHPC and higher strength HSS or higher ductility SS reinforcement presents a potential solution to this problem, which can also allow for the design of truly high performance and blast-resilient structures.

1.2 Research needs

1.2.1.General need for blast research on higher grade reinforcement:

The unique properties of high-strength and stainless steel make them well-suited for blast-resistant design applications. However, research on the impact and blast response of reinforced concrete structures with ASTM A1035 or ASTM A955 reinforcement is scarce. Indeed, most existing research on higher grade steel comes from early impact studies, on steel types that are now longer used in practice. As current blast design provisions are intended for concrete structures with ordinary steel reinforcement, there is an important need for data on the blast behaviour of structures built with high strength steel and stainless steel reinforcement conforming to the ASTM A1035 or ASTM A955 specifications.

1.2.2. Influence of detailing in flexural members with higher grade steel:

The use of higher grade reinforcement is advantageous in flexural members as it can reduce steel requirements and allow for more efficient design sections. On the other hand, the high yield strength of such reinforcement can make flexural members more susceptible to brittle failures, where concrete fails in compression prior to steel yielding. This same effect and brittle failure mode has been observed in beams tested under blast loading. The use of improved detailing as specified in the CSA S850 standard (i.e., provision of top continuity bars and closely spaced ties) is a potential solution to this problem. Thus, there is a need to study the influence of improved detailing on the ductility of such beams, under both static and blast loads.

1.2.3. Influence of HSS and SS on the ductility of UHPC flexural members:

As noted in the introduction, UHPC is a material which is ideal for blast applications due to its high strength properties and remarkable toughness. However, the high bond capacity and toughness of UHPC also make flexural members vulnerable to brittle bar fracture failures, especially when using low amounts of ordinary steel reinforcement. The use of higher strength or higher ductility reinforcement, presents a potential solution to this problem. Data is therefore needed to examine the benefits of implementing higher strength HSS or higher ductility SS reinforcement in UHPC beams tested under both static and blast conditions.

1.3 Thesis objectives and scope

1.3.1.Objectives

The primary objective of the research program is to increase understanding of the performance of RC structures built high strength and stainless steel reinforcing bars under both static and blast conditions. The thesis further aims to study the benefits of combining such high-performance reinforcement with high-strength or ultra-high performance concrete. These effects are investigated in fundamental reinforced concrete beam elements subjected to shear and flexure. These objectives are achieved through a combined experimental and numerical research program. The experimental research program includes three series of tests which aim at studying the following aspects:

1. The effects of detailing on the quasi-static and blast performance of HSC beams built with Grade 690 MPa ASTM A0135 high-strength steel reinforcement;
2. The effects of detailing on the quasi-static and blast performance of HSC beams built with Grade 520 MPa ASTM A955 stainless steel reinforcement;
3. The effects of higher grade HSS bars and higher ductility SS bars on the quasi-static and blast performance of UHPC beams.

The numerical research program aims at demonstrating the ability of 2D and 3D finite-element modelling to reliably predict the static and blast responses of HSC/UHPC members reinforced with higher grade HSS or higher ductility SS reinforcing bars.

1.3.2.Scope

The scope of the experimental research includes quasi-static, blast and post-blast residual static tests on three series of large–scale beams, as follows:

1. Series 1(HSC-HSS): Tests on eight (8) beams designed with HSC and Grade 690 MPa ASTM A1035 high-strength reinforcing bars. In addition to studying the effect of steel detailing, the tests examine the effects of steel type (HSS vs ordinary steel), tension steel ratio, and the influence of steel fibers;
2. Series 2 (HSC-SS): Tests on sixteen (16) beams designed with HSC and Grade 520 MPa ASTM A955 stainless steel reinforcing bars. In addition to the effect of steel detailing, the tests examine the influence of stainless steel alloy/type (Austenitic vs. Duplex), tension steel ratio and the influence of steel fibers;

3. Series 3 (UHPC-NSS, HSS and SS): Tests on twenty (20) UHPC beams designed with either Grade 400 MPa ordinary steel, Grade 690 MPa high-strength steel, or Grade 520 MPa stainless steel reinforcement. In addition to the effects of steel grade/type, the tests examine the effects of concrete type (i.e., UHPC vs HSC), tension steel ratio, detailing level and fiber content in the UHPC.

The numerical research program includes the following scope:

1. Two-dimensional (2D) FE modelling of the HSC-HSS and HSC-SS beams tested in the experimental program are predicted using software VecTor2;
2. Three-dimensional (3D) FE modelling of the ordinary, HSS and SS reinforced UHPC beams tested in the experimental program are predicted using software LS-DYNA.

1.4 Thesis Breakdown

This thesis consists of ten chapters which are divided as follows:

Chapter 1 - Introduction: Provides an introduction to the thesis, and clarifies the objectives and scope of the proposed research;

Chapter 2 - Literature Review: Summarizes previous studies on the static and impact/blast behaviours of RC and UHPC beams with high-strength and stainless steel;

Chapter 3 - Experimental Program: Describes the experimental research program and provides information on the test matrix, specimen designs, test setups and testing procedures;

Chapter 4 - Discussion of test results (Series 1): Presents a discussion on the results from Series 1 (HSC-HSS), examining the effects of steel detailing, steel grade, steel ratio and fibers on the static, blast and post-blast response of the high-strength steel reinforced concrete beams. The content in this chapter is extracted from a published paper in the journal Engineering Structures (Paper 1);

Chapter 5 - Discussion of test results (Series 2A): Presents a discussion on the results of singly-reinforced beams built with nominal detailing from Series 2A (HSC-SS), examining the effects of steel type (stainless vs. ordinary steel), and steel fibers in HSC beams built with and without transverse reinforcement. This chapter forms the content of Paper 2 (to be submitted);

Chapter 6 - Discussion of test results (Series 2B): Presents a discussion on the results of doubly-reinforced beams built with blast detailing from Series 2B (HSC-SS), examining the effects of steel detailing, steel grade, stainless steel types, steel ratio and fibers on the static,

blast and post-blast response of the stainless steel reinforced concrete beams. This chapter forms the content of Paper 3 (to be submitted);

Chapter 7 - Discussion of static test results (Series 3): Presents a discussion on the static results from Series 3 (UHPC-NSS, UHPC-HSS and UHPC-SS), examining the effects of UHPC on flexural and shear response, and the influence of steel ratio, steel type (HSS/SS vs. ordinary steel), detailing and fiber content. The content in this chapter is extracted from a published paper in an ACI Special Publication (Paper 4);

Chapter 8 - Discussion of blast test results (Series 3): Presents a discussion on the blast and post-blast results from Series 3 (UHPC-NSS, UHPC-HSS and UHPC-SS), examining the effects of UHPC on flexural and shear response, and the influence of steel ratio, steel type (HSS/SS vs. ordinary steel), detailing and repeated blast loading. This chapter forms the content of Paper 5 (to be submitted);

Chapter 9 - Finite element analysis results: Presents the numerical research program, which aims to predict the static and blast response of the HSC beams using 2D FE modelling (VecTor2), and the blast response of the UHPC beams using 3D FE modelling (LS-DYNA). The chapter presents comparisons between the experimental and analytical load-displacement responses and damage modes (for the static simulations), and a comparison of the experimental and analytical displacement/load–time history responses and damage modes (for the blast simulations).

Chapter 10 - Conclusions: Summarizes the conclusions from the experimental and numerical research programs, and provides recommendations for future research.

Appendix A - Detailed Experimental results: Presents the individual experimental results for the beams in this PhD program.

Chapter 2 Literature review

2.1 Introduction

This chapter provides a literature review related to this thesis. The first section reviews previous research on RC elements with high strength steel (HSS) bars under impact/blast. The next section reviews previous research which has examined the effect of stainless steel reinforcement under impact loading. The next section reviews previous research on ultra-high performance concrete (UHPC) under impact/blast loading. The final section reviews FEM research on UHPC elements under impact/blast loading.

2.2 Previous impact/blast research on RC elements with high strength steel reinforcement

Experimental studies on the dynamic behaviour of beams built with high-strength bars are scarce (Mylrea, 1940; Simms, 1945; Mavis & Richards, 1955; Mavis & Greaves, 1957; Mavis & Stewart, 1959; Cernica & Charignon, 1963; Miyamoto et al., 1989). As shown in **Table 2.1**, a review of previous studies indicates most available data comes from early impact tests on members built with reinforcing bar types that are no longer used in practice (see **Table 2.2**) (CRSI, 2001). Likewise, there exists no data on the dynamic performance of beams built with Grade 690 MPa ASTM A1035 reinforcement. Moreover, there is limited data on the dynamic performance of beams built with high-strength concrete ($f_c' \geq 55\ MPa$) and high-strength bars. Nonetheless, most of these early impact studies demonstrate that the use of higher strength bars improves the performance of beams under dynamic loading.

Mylrea (1940) conducted an early study investigating the effect of reinforcement grade on the drop-hammer impact response of beams having varying longitudinal reinforcement ratios (0.03-0.2%) and yield strengths ranging from 320 MPa to 790 MPa corresponding to "structural/rail/extra high-grade" steel. The experiments only examined the drop-height required to rupture the steel reinforcement in the beam specimens. The falling height needed to rupture the steel reinforcement was found to increase with the increase in the amount and yield strength of the steel reinforcement.

Mavis and Stewart (1959) studied the dynamic behavior of 27 reinforced concrete beams having varying tensile reinforcement ratios (0.6-1.2%) and yield strengths ranging from 240 to 450 MPa, corresponding to "structural/intermediate/hard grade" steel. The specimens

were tested using spring-loaded actuated impulsive loads applied at third-points over a 2.44 m simply supported span. Static tests were conducted to evaluate the residual resistance of the beams after dynamic testing. The majority of beams having hard-grade reinforcement showed higher residual capacity when compared to companions with structural or intermediate type bars. Furthermore, beams reinforced with one hard grade bar matched the performance of beams with two structural grade bars. Similarly beams having higher reinforcement ratios had higher residual capacities, with the best performance obtained for the beam with two hard grade bars, followed by two intermediate grade bars and finally two structural grade bars.

Cernica and Charignon (1963) studied the behaviour of beams with varying tensile and compressive reinforcement ratios, and steel grades ("structural": 290 MPa, "intermediate": 335 MPa, "high strength grade": 475 MPa) using a spring-loaded test setup. Beams tested under impulsive and static loads behaved differently in terms of load capacity, reactions, type of failure and stress distribution due to the effect of loading rate, with higher ultimate load capacities recorded under dynamic loading when compared to static loading. Beams reinforced with high-strength reinforcement showed equal or better performance when compared to those with structural or intermediate grade bars when evaluated in terms of ultimate and residual strength capacity.

Miyamoto et al. (1989) presented a numerical study examining the effect of loading rate, beam depth, concrete strength, fibers and high-yield strength steel (referred to as HT steel) on the impact behaviour of beams. The FEM simulations showed that at higher loading-rates, the failure load capacity of the beams increased as high-yield strength steel was introduced. While the beams with conventional reinforcement showed a decrease in deformation capacity with an increase in loading-rate, the opposite trend was observed in the case of the HT beam (that is deflection at failure became larger with increased loading-rate). Moreover, the deformation capacity was greater for the HT beam when compared to beams with conventional reinforcement at loading-rates $\geq$ 20 kN/ms, demonstrating the effectiveness of the high-yield strength steel in impact applications. Total energy (amount of energy required to cause beam failure) increased for all beams with an increase in loading-rate. Total energy for the high-yield strength beam was lower than that of conventional RC beam at loading rates below 15 kN/ms, however the HT beam showed improved performance at larger loading-rates. The numerical simulation was also used to evaluate the damage in the beams. The analysis showed that the failure region was smaller (indicating greater damage) in the HT beam at loading-rates below 10 kN/ms, although the failure condition improved at higher loading-rates.

Data on the blast behavior of beams built with high-strength bars is very scarce, however Keenan (1963) conducted an early analytical & experimental study on this topic. The blast tests included sixteen beams reinforced with high-strength bars having a specified yield stress of 620 MPa. The study concluded that greater blast resistance can be gained with high-grade steel when compared to lower grade steel, however the author noted that the limited strain-capacity of high-strength steel may restrict its use in blast-resistant design.

More recently, Liao et al. (2019) examined blast behavior of concrete beams with normal-strength and high-strength steel under various blast loading using a blast pressure simulator. Three sets of beams including one beam with high-strength rebar and one companion beam with normal-strength steel in each set were tested under low, medium and high blast loading. Under lower blast load, the beam with high-strength steel had similar deformation when compared to the companion beam with normal-strength reinforcement. While under higher blast load, the use of high-strength reinforcement significantly improved the blast performance of RC beams in terms of reducing deformations and reducing crack length & width.

Li and Aoude (2019) investigated blast response of beams built with high-strength concrete and high-strength Grade 690 MPa ASTM A1035 reinforcement using a shock-tube. The study found the use of high-strength reinforcement in HSC beams improved performance by increasing blast capacity and better controlling peak displacements. Increasing the high-strength steel ratio further improved blast performance within balanced conditions. However, beams tested under blast loads were susceptible to sudden cover spalling and more severe crushing failures (see **Figure 2.1**a). To mitigate this brittle behaviour, Li and Aoude (2020) further investigated the effect of steel fibers on blast response of beams built with high-strength concrete and high-strength reinforcement. The use of fibers was effective in improving the blast behaviour by increasing blast capacity, reducing maximum displacements/support rotations and better controlling damage (crushing and spalling). The use of high-strength bars in HSFRC beams significantly increased the capacity under both static and dynamic loads as long as the tension steel ratio stayed below the balanced steel conditions.

A limited number of blast studies in this research area have also been conducted on slabs. Among them, Thiagarajan et al. (2015) examined the effect of concrete type and reinforcement grade on the blast response of slabs tested using a shock-tube. The tests included four slab specimens with different combinations of normal-strength concrete (NSC), high-strength concrete (HSC), normal strength reinforcement (NSR) and high-strength low-alloy

vanadium reinforcement (HSLA-V). When compared to the control slab with conventional materials (NSC & NSR), substitution with either HSC concrete or HSLA-V bars led to enhanced blast performance with reductions in peak deflections and less damage (see **Figure 2.1b**). Optimal results were obtained when both high-strength concrete and steel were used.

Li et al. (2015a) reported another study examining the effect of high-strength materials on the blast response of slabs. As part of the study, a series of ultra-high-performance concrete (UHPC) panels reinforced with three different steel types having yield strengths of 300, 600 and 1750 MPa were tested under close-in live explosives. A companion slab with normal-strength concrete and 600 MPa steel was also tested. The authors noted that the UHPC panel with high-strength steel had the best behavior in terms of displacement control and overall damage tolerance, with the introduction of ultra-high-strength steel in UHPC leading to a 40% reduction in maximum displacement when compared to mild steel. While the NSC slab with conventional reinforcement suffered a brittle collapse, no damage was observed in the UHPC slab with ultra-high-strength reinforcement.

Table 2.1 Previous impact and blast studies investigating the effect of steel reinforcement grade in beams and one-way slabs

Study/Authors	Dynamic testing method	Specimen type	No. of specimens	Beam dimensions			Concrete strength (MPa)	Tension steel yield strength (MPa)	Steel designation [Specified Grade in ksi]	Primary conclusions
				B (mm)	H (mm)	L (mm)				
1940 Mylrea	Impact: FM	RC Beams	8	254	406	2438	20	310- 772	ASTM A15 Structural [33] ASTM A16 Rail [40] ASTM A15 Hard [50]	▪ Falling height needed to rupture the steel reinforcement was found to increase with the increase in the amount and yield strength of the steel reinforcement.
1945 Simms	Impact: FM	RC Beams RC Slabs	Not reported	100 508	200 150	2133 1828	20 26	124-310	ASTM A15 Intermediate [40] ASTM A431 Hard [75]	▪ While beam static strength increased when the high-strength steel was substituted for mild steel, beams reinforced with mild steel were better able to withstand severe impact forces. In general, beams with high-strength steel showed poor performance under impact when compared to beams with equal amounts of mild steel.
1955 Mavis & Richards	Impact: DF	RC Beams	8	127	127	1981	25-44	274-522	ASTM A15 Structural [33] ASTM A15 Intermediate [40] ASTM A15 Hard [50]	▪ The majority of beams having hard-grade bars showed higher residual capacity when compared to companions with structural or intermediate type bars. ▪ Beams reinforced with one hard grade bar matched the performance of beams with two structural grade bars. ▪ Beams having higher reinforcement ratios had higher residual capacities, with the best performance obtained for the beam with two hard grade bars, followed by two intermediate grade bars and finally two structural grade bars.
1957 Mavis & Greaves	Impact: SL	RC Beams	4	104	150	1981	45	327-464		
1959 Mavis & Stewart	Impact: SL	RC Beams	27	147	279	2590	39-43	285-464		
1963 Cernica & Charignon	Impact: SL	RC Beams	42	127	191	2743	53	285-464	ASTM A15 Structural [33] ASTM A15 Intermediate [40] ASTM A432 Hard [60]	▪ Beams reinforced with high-strength reinforcement showed equal or better performance when compared to those with structural or intermediate grade bars when evaluated in terms of ultimate and residual strength capacity.
1989 Miyamoto et al.	FEM	RC Beams	19	150	160-180	1300	38-84	353-685	SD30/685 [40,100]	▪ Beams with high-strength bars showed an increase in deformation capacity with an increase in loading-rate (opposite trend observed for beam with conventional reinforcement). ▪ Total energy required to cause failure was lower for beam with high-strength bars when compared to beam with conventional bars at lower loading-rates, however better performance was observed at high loading-rates. ▪ Failure region was smaller (greater damage) in the beam with high-strength bars at low loading-rates, although the failure condition improved at higher loading-rates.
1963 Keenan	Blast: PBS	PS/RC Beams	16	200	305	4572	42-56	620	ASTM A15 Intermediate [40] ASTM A432 Hard [60] ASTM A431 Hard [75] Other [90]	▪ More resistance can be gained with a larger amount of high-grade steel than lower grades of steel. ▪ Excessive deflections may be better controlled by prestressing the tensile steel.
2019 Liao et al.	Blast: PBS	RC beams	6	Haunched T-shaped 150 x 300		1700	40	433-756	HTB700 [100]	▪ Under small peak overpressure blast loading, the deformation of high-strength RC beams are similar to ordinary RC beams. ▪ With the increase of blast loads, high strength reinforcement significantly reduced component deformation and crack length and width.
2019 Li & Aoude	Blast: ST	RC beams	10	125	250	2440	50-100	400-690	ASTM 1035 [100]	▪ The use of high-strength reinforcement in HSC beams improved blast performance by increasing blast capacity and better controlling peak displacements. ▪ Increasing the high-strength steel ratio further improved blast performance. ▪ The use of higher strength concrete is better suited for beams designed with high-strength bars
2020 Li & Aoude	Blast: ST	RC beams	6	125	250	2440	100	400-690	ASTM 1035 [100]	▪ The use of fibers was effective in improving the blast behaviour of the HSS-RC beams by increasing blast capacity, reducing maximum displacements/support rotations and better controlling damage. ▪ The results show that the use of high-strength bars in place of normal-strength bars increases the capacity of HSFRC beams tested under both static and dynamic loads.
2015 Thiagarajan et al.	Blast: ST	RC Slabs	4	Slab length x width x thickness 1652 x 876 x 102			28-107	400-572	HSLA-V [80]	▪ When compared to the control slab with convention materials (NSC & NR), substitution with either HSC concrete or HSLA-V bars led to enhanced blast performance. Optimal results when combining HSC and high-strength reinf.
2015 Li et al.	Blast: LE	RC slabs	5	Slab length x width x thickness 2000 x 1000 x 100			57-129	300-1750	Not reported [43, 87, 250]	▪ UHPC beam with high-strength steel had the best behavior in terms of displacement control and overall damage tolerance. Introduction of ultra-high-strength steel in UHPC led to a 40% reduction in maximum displacement when compared to mild steel. While the NSC slab with conventional reinforcement suffered a brittle collapse, no damage was observed in the UHPC slab with ultra-high-strength reinforcement.

Note: FM: Falling mass, SL: Spring-loaded, DC: Deformation controlled, PBS: pneumatic blast simulator, ST: shock-tube, LE – Live explosive testing, PS: prestressed concrete beam

Table 2.2 Reference standards and properties of older and currently used high-strength steels in North America (1911 to current)

ASTM Spec	Year		Notes on Steel Type	Grade 33 (Structural)		Grade 40 (Intermediate)		Grade 50 (Hard)		Grade 60		Grade 75		Grade 80		Grade 100		Grade 120	
	Start	End		Min. yield	Min. Tensile	Min. yield	Min. Tensile	Min. yield	Min. Tensile	Min. yield	Min. Tensile	Min. yield	Min. Tensile	Min. yield	Min. Tensile	Min. yield	Min. Tensile	Min. yield	Min. Tensile
A15	1911	1966	Billet	33	55	40	70	50	80										
A408	1957	1966	Billet	33	55	40	70	50	80										
A432	1959	1966	Billet							60	90								
A431	1959	1966	Billet									75	100						
A615	1968	1972	Billet			40	70			60	90	75	100						
A615	1974	1986	Billet			40	70			60	90								
A16	1913	1966	Rail					50	80										
A61	1963	1966	Rail							60	90								
A616	1968	1999	Rail					50	80	60	90								
A160	1936	1964	Axle	33	55	40	70	50	80										
A160	1965	1966	Axle	33	55	40	70	50	80	60	90								
A617	1968	1999	Axle			40	70			60	90								
A615	1987[a]	Present	Carbon			40	70			60	90	75	100	80	105	100	115		
A706	1974[b]	Present	Low-Alloy							60	80			80	100				
A955M	1996	Present	Stainless							60	90	75	100						
A1035	2003	Present	Low-Carbon Chromium													100	150	120	150
SAS670[c]	1999	Present	---													97	116		

Note: Grades are indicated in ksi (1 ksi = 6.9 MPa).

Note: Source of data: CRSI Report 48: Evaluation of reinforcing bars in old reinforced concrete structures (see reference CRSI, 2001).

[a] Grade 75 steel in ASTM A615 steel was re-instated in 1987. Grades 80 and 100 were added in 2008 and 2012, respectively.

[b] Grade 80 steel in ASTM A706 was added in 2008.

[c] SAS670 steel is a German-produced high-strength steel available for use in North America.

Beam C100-No.4HS | Beam C100-No.5HS | Beam C100-No.6HS

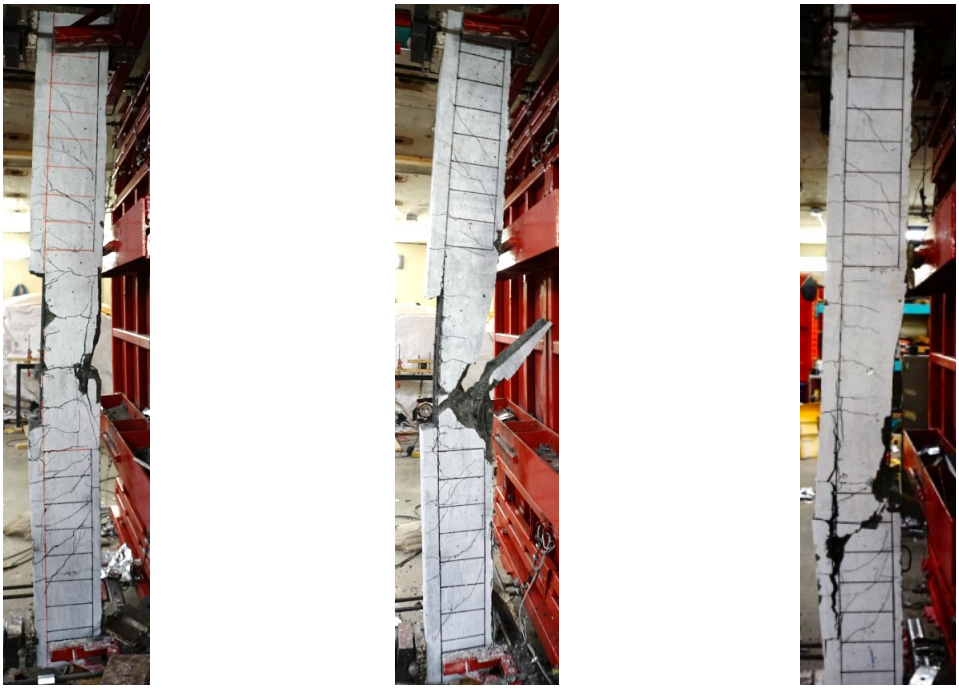

(a) Previous research on beams with HSS reinforcement (Li & Aoude, 2019)

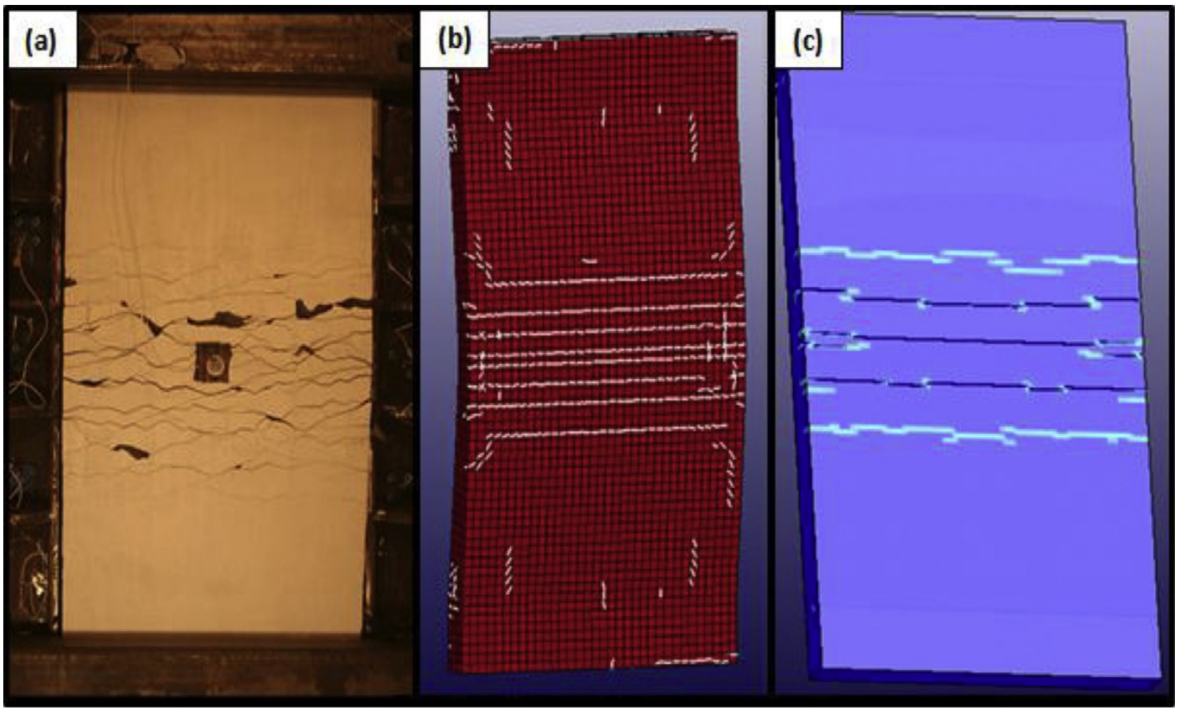

(b) Previous research on slabs with HSS reinforcement (Thiagarajan et al., 2015)

Figure 2.1 Some of the previous research on beams and slabs with HSS reinforcement

2.3 Previous impact/blast research on RC elements with stainless steel reinforcement

Research on the impact and blast performance of reinforced concrete elements with stainless steel reinforcing bars is scarce or non-existent. However, a series of studies examining the impact performance of RC columns reinforced with duplex stainless steel (Type 2304) under lateral impacts has been conducted by researchers in China (see **Table 2.3**). As shown in **Figure 2.2**, all columns in these tests had the same dimension with a diameter of 340 mm and a length (overall height) of 2200 mm, with testing conducted using a "multi-function super-high heavy hammer impact test system".

In the first series of tests, Zhang et al. (2017a) examined the effects of stainless steel (conventional vs. stainless) and reinforcement ratios (1.2%, 2.2%) under single-impact loads. The maximum displacement of the column with stainless steel was around 13% lower than the companion column reinforced with conventional steel.

The same experimental parameters (steel type & reinforcement ratio (1.8%, 2.2%) were investigated by Wu et al. (2019a) and Wu and Xu (2020) under repeat-impact loading. Similar to columns tested under single-impacts, columns with stainless reinforcement had less maximum impact force and peak displacement when compared to columns with conventional bars. Increasing the steel reinforcement ratio resulted in a reduction in peak values of acceleration, top displacement, and reinforcement strain at equivalent impact velocity. In addition, the authors proposed a damage factor $D = 1 - \frac{v^2}{v_0^2}$, where v is the wave velocity after damage and v_0 is the initial wave velocity. The damage degree of the columns with stainless steel was lower than the companion column with conventional steel.

Zhou et al. (2019) further investigated the impact performance of columns with stainless steel rebar using an equal-strength replacement concept. Under the same impact energy, the columns with conventional steel and equal-replacement stainless steel had similar impact force and peak displacement with differences within 10%.

Zhou et al. (2020) further studied the influence of closed-cell aluminum foam on columns with equal-strength stainless steel reinforcement under impact loading. The failure modes, crack number & distribution and concrete damage were observed to be consistent for columns before and after the equal-strength replacement of stainless steel. However, the use of stainless steel reinforcement improved overall stiffness and reduced maximum lateral displacements owing to its higher strength and toughness.

Table 2.3 Previous impact studies investigating the effect of stainless steel reinforcement

Study	Type of element	No. of Specimens	Beam dimensions			Concrete strength (MPa)	Tension steel			Parameters investigated										
			B (mm)	H (mm)	L (mm)		Yield strength (MPa)	Reinf. ratio (%)	Type	Concrete strength	Tension steel type	Beam depth	a/d ratio	Tension reinf. ratio	Comp. reinf. ratio	Shear reinf. ratio	Stirrups in constant moment	Fiber reinforcement	Cyclic loading	Axial load
2017 Zhang et al.	Column	4	Diameter 340 mm		2200	40	368, 748	1.2%, 2.2%	S2		x			x						x
2019 Wu et al.		2	Diameter 340 mm		2200	40	368, 748	2.2%	S2		x									x
2019 Wu et al.		2	Diameter 340 mm		2200	40	748	1.2%, 2.2%	S2					x						x
2019 Zhou et al.		4	Diameter 340 mm		2200	40	368, 729	2.1-4.2%	S2		x			x						x
2020 Zhou et al.		4	Diameter 340 mm		2200	40	440-720	2.2%-5.4%	S2		x			x						x

Note: S2=2304 duplex stainless steel;

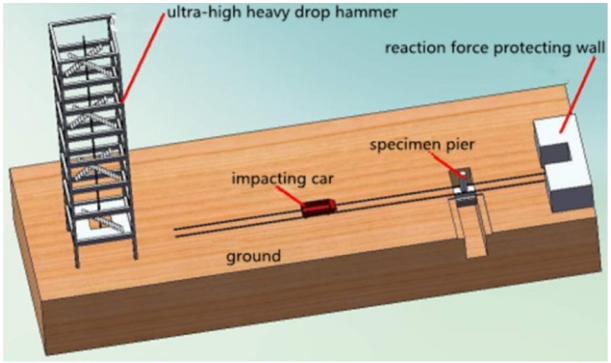

(a) Multi-function super-high heavy hammer impact test system

(b) Impact test machine & column specimen

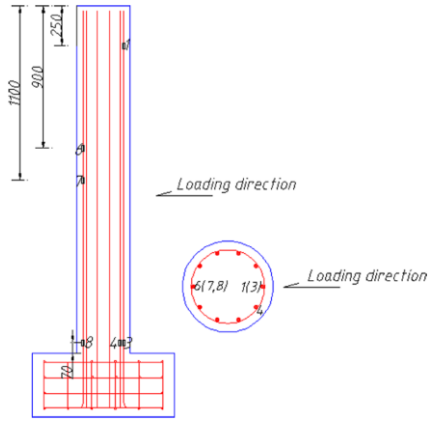

(c) Design details of the columns

Figure 2.2 Impact tester and column design setup (Zhang et al., 2017)

2.4 Previous impact/blast research on RC elements with UHPC

A number of studies have investigated the behaviour of ultra-high performance concrete (UHPC) beams (Fujikake, 2014; Yoo et al., 2015; Yoo et al., 2017a), columns (Huynh et al., 2015; Wei et al., 2019), and slabs (Othman & Marzouk, 2016) under impact loading (see **Table 2.4**). It is noted that in practice UHPC is nearly always reinforced with fibers; therefore, in this thesis, the term UHPC also refers to ultra-high performance fiber reinforced concrete (UHPFRC).

Fujikake (2014) examined impact performance of UHPC beams using a drop hammer setup. Four I-shape UHPC beams with identical properties were tested under varied drop heights (0.8-1.6 m). The results showed that the use of UHPC prevents shear failure and reduced maximum displacement when compared to conventional RC beams.

Yoo et al. (2015) studied the dynamic behavior of four reinforced concrete beams with varied with tensile reinforcement ratios (0-1.71%) under repeat impact loading. Increasing the reinforcement ratio was found to reduce maximum and residual displacements and crack widths. The authors noted that the beam with 1.06% reinforcement ratio failed in shear while the companion static beam failed in flexure, indicating UHPC beams were more vulnerable to shear failure under impact loading.

Yoo et al. (2017a) further investigated the influence of fiber contents and fiber types on impact performance of UHPC beams. Eight beams varied with fiber content (0-2%), fiber types (smooth or twisted) and fiber length (13-19.5 mm) were tested under drop hammer. The results showed that the use of steel fibers significantly reduced maximum and residual displacements under impact loading, and also improved post-impact residual capacity. The beams with longer fibers had better performance in terms of displacement and residual capacities when compared to shorter fibers. The authors also indicated that moment capacities were enhanced under impact loading, while no noticeable differences in moment ratios were observed when comparing beams with different fiber contents, types and lengths.

Huynh et al. (2015) investigate the potential use of RPC (one type of UHPC) as a replacement for HSC for columns under impact loading. The testing parameters for 16 specimens were composition of concrete (HSC, RPC, and HSC core with RPC shell) and magnitude & eccentricity of axial force. The results showed that RPC specimens had a higher impact resistance and energy absorption ability compared to HSC specimens. Wei et al. (2019) experimentally investigated UHPC column under impact loading. Six beams were varied with

cross-section shape (circular or square), concrete types (NSC or UHPC) and drop height. The authors found that the use of UHPC increased impact resistance, decreased mid-span displacements and changed failure mode from brittle shear to flexure.

Othman and Marzouk (2016) tested six slabs varied in concrete type (HSC or UHPC), fiber content (1-3%) and reinforcement ratio (0.47-1%) using a drop hammer apparatus. The UHPC specimens had superior performance in terms of damage modes and displacement and changed failure modes from brittle shear to flexure when compared to HSC specimens. Increasing fiber content enhanced impact behaviour of UHPC slabs by reducing maximum and residual displacement. Steel reinforcement ratio also had significant effects by reducing displacement response and preventing sudden punching shear modes.

Table 2.5 presents some of the previous research on UHPC elements tested under blast loading. Among previous investigations, most studies examined behavior on slabs (Cavill et al., 2006; Wu et al., 2009; Yi et al., 2012; Mao et al., 2014; Stolz et al., 2014; Li et al., 2015a; Li et al., 2015b; Li et al., 2016; Foglar et al., 2017) and other studies focused on columns (Burrell et al., 2013; Roller et al., 2013; Aoude et al., 2015; Li et al., 2015c; Xu et al., 2016; De Carufel & Aoude). However, there is no study examining the blast performance of UHPC beams.

In general, these studies demonstrate that the use of UHPC leads to improvements in blast resistance, deflection control and damage tolerance. For example, Wu et al. (2009) found UHPC slabs suffered less damage than NRC (normal reinforced concrete) slabs and had reduced peak displacements. Likewise, Li et al. (2015b); Li et al. (2016) evaluated spallation and cratering of specimens quantitatively after blast testing and reported that UHPC had significantly reduced concrete punching and spall damage as compared with the NRC slab. Similarly, Yi et al. (2012) noted that UHSC and RPC panel specimens had higher blast-resistant capacities when compared to NSC slabs. The use of rebar and steel fibers used in the UHSC and RPC specimens led to sufficient ductility, and outstanding energy absorption and crack controlling capacities. Stolz et al. (2014) studied the effects of slab thickness and reinforcement ratios on blast behaviour of UHPC slabs. The slab with larger thickness and higher reinforcement ratios led to better peak & residual displacements and less damage though damage modes were similar. Li et al. (2015a) examined the combined use of UHPC and high-strength reinforcement and the results demonstrated superior behaviour when compared to the companion NSC slab with conventional reinforcement. Cavill et al. (2006) tested five slabs

with high-strength pre-stressed reinforcement. Panels with the pre-stressed steel showed high energy absorption and an ability to sustain deflections up to span/28 without fracture. Foglar et al. (2017) investigated the effects of fiber content, fiber types and the use of basalt mesh in UHPC beams under blast loading. The specimen with 80 kg/m^3 of 30 mm fibers and 80 kg/m^3 of 13 mm fibers had almost no damage when compared to the specimen with 80 kg/m^3 of 30 mm fibers. The use of basalt mesh improved the blast performance in terms of reducing the area of spalling and the volume of debris but had a greater extent of internal damage when compared to the regular UHPC specimen.

Previous research also indicates that the use of UHPC improves the blast performance of columns in terms of improved control of displacement and damage. Burrell et al. (2013) tested six columns under blast loading. The results showed that the use of UHPC reduced mid-span displacements when compared to companion NSC columns. However, the high-bond capacity and toughness of the UHPC concrete eventually led to reinforcement steel rupture failure modes. Roller et al. (2013) tested 10 RC columns and found that the use of UHPC improved post-blast residual capacity up to 70%. Aoude et al. (2015) investigated the effect of fiber content, fiber properties (aspect ratio) and seismic detailing in UHPC columns under blast loading. Increasing fiber content from 2% to 4% led to enhancement in blast performance, while Increasing the fiber content beyond 4% did not result in further improvements in blast behavior. It was further noted that the use of fibers with an increased aspect ratio resulted in enhanced blast performance. Moreover, the combined use of UHPC and seismic detailing resulted in reduced displacements and an ability to sustain larger blast loads before failure. Li et al. (2015c) found that increasing axial load from 0 to 1000 kN in UHPC columns resulted in a reduction in mid-span displacement due to the initial compression stress on the tension side of the lateral blast. Xu et al. (2016) further explained this effect as the axial load modified boundary conditions and limited end rotation which out-weigh the P-delta effects. De Carufel and Aoude (2020) showed that the use of high-strength (HS) or stainless steel (SS) bars in the UHPC columns enhanced blast performance, with better control of maximum and residual displacements at equivalent blasts, when compared to ordinary steel bars. Increasing the HS or SS steel ratio was found to further enhance blast capacity and prevent brittle bar rupture failure.

Table 2.4 Previous impact studies on UHPC components

Study	Test Method [1]	Specimen Type [2]	Concrete type	Concrete strength (MPa)	Fiber type [3]	Parameters investigated												Primary Conclusions
						Concrete strength	FRC type	Fiber content	Fiber type	Fiber length	Fiber yield strength	Hybrid fibers	Long. reinf. ratio	Shear reinf. ratio	Reinf. Detailing / type	Specimen dimensions	Axial load	
Fujikake, 2014	FM	Beam	UHPC	215	SF: SP	x												▪ UHPC prevents shear failure in all the beams. All specimens exhibit ductile flexural tension failures with numerous fine cracks (multiple cracking).
Yoo et al., 2015	FM	Beam	UHPC	200	SF: SP								x					▪ UHPC beams show lower maximum deflections, improved deflection recovery and reduced crack width/spacing, as the reinforcement ratio increased.
Yoo et al., 2017	FM	Beam	UHPC	202-212	SF: SP			x	x	x								▪ The use of fibers significantly improves impact performance of UHPC and improves post-impact residual capacity. Longer fibers were found to better control displacements and increase residual capacity. ▪ Effect of reinforcement ratio was investigated by FEM, it is noted that even with less longitudinal reinforcement, the UHPC columns preserve a good impact resistance. ▪ Increasing axial loads could increase mass and velocity asymptotes in P-I diagram.
Huynh et al., 2015	FM	Column	UHPC	160	SF: SP	x											x	▪ Fiber-reinforced UHPC improves impact performance of columns when compared to HSC.
Wei et al., 2019	FM	Column	UHPC	136	SF	x							x			x	x	▪ Square and circular normal-strength RC columns experienced brittle shear failure with a large part of concrete fragmentation; while square and circular UHPC columns only showed minor flexural damage.
Othman & Marzouk 2016	FM	R/2x//Plate	UHPC	162	SF: SP	x		x							x			▪ UHPC shows superior performance under multiple impacts when compared to HSC, with improved control of maximum and residual displacements, the ability to resist greater impact forces. ▪ Fiber content and steel arrangement found to affect performance of UHPC plates

[1]Impact method: FM: falling mass;

[2]Specimen type: R = reinforced, 2x = two-way slabs/plates;

[3]Fiber type: SF = steel fiber; SP = short prismatic.

Table 2.5 Previous blast studies on UHPC panels and slabs

Study	Test Method [1]	Type of Blast	Specimen Type	Concrete type	Concrete strength (MPa)	Fiber type [2]	Parameters investigated												Primary Conclusions
							Concrete strength	FRC type	Fiber content	Fiber type	Fiber length	Fiber yield strength	Hybrid fibers	Long. reinf. ratio	Shear reinf. ratio	Reinf. detailing / type	Specimen dimensions	Axial load	
Cavill et al. 2006	LE	Close-in	R/2x Slab	UHPC	160-200	SF								x					▪ The use of UHPC provides an effective solution for blast and impact resistance. ▪ The UHPC slab panels displayed high ductility and no signs of fragmentation, with the pre-stressed panels showing an even higher energy absorption with an ability to sustain deflections up to span/28 without fracture.
Wu et al., 2009	LE	Close-in	R/UR Slab	UHPC	40-152	SF	x												▪ UHPFC slab suffered less damage than the NRC slabs when subjected to similar blast loads. ▪ Adhesive bonding externally bonded FRP material to the compressive face of the NRC slab improved its blast resistance but the percentage improvement could not be quantified
Yi et al. 2011	LE	Close-in	R/2x Slab	UHPC RPC	26-200	SF	x												▪ UHSC and RPC panel specimens have higher blast-resistant capacities than NSC specimens. ▪ Rebar and short steel fibers used in the UHSC and RPC specimens, provide sufficient ductility, and outstanding energy absorption and crack controlling capacities.
Mao et al. 2014	LE	Near-field; Far-field	R/ Slab	UHPC	170-190	SF							x	x					▪ Under far field blast loading, steel bar reinforcement and steel fibres are of similar effect in providing extra resistance to the UHPC panel; near field blast loading, the resistance of UHPC panels can be increased significantly with steel reinforcement bar.
Stoltz et al. 2014	ST	N.A.	R/2x Slab	UHPC	100-130	SF								x		x	x		▪ The slab with 10 cm thickness has a higher yield and ultimate strength than the slab with 6 cm thickness. ▪ Plates with a higher reinforcement ratio showed a reasonably higher dynamic bending strength than the less reinforced plates.
Li et al., 2015	LE	Close-in	R/Slab	UHPC	57-129	SF	x							x		x			▪ UHPC beam with high-strength steel had the best behavior in terms of displacement control and overall damage tolerance. Introduction of ultra-high-strength steel in UHPC led to a 40% reduction in maximum displacement when compared to mild steel. ▪ The NSC slab with conventional reinforcement suffered a brittle collapse, no damage was observed in the UHPC slab with ultra-high-strength reinforcement.
Li et al. 2015	LE	Close-in	UR/R Slab	UHPC	57-129	SF	x												▪ UHPC has significantly reduced concrete punching and spall damage as compared with the NRC slab.
Li et al. 2016	LE	Close-in	R/Slab	UHPC	40-145	SF	x							x			x		▪ Spallation and cratering of specimens were evaluated quantitatively. UHPC slabs significantly improved blast resistance capacity when compared to NSC slabs.
Foglar et al., 2017	LE	Close-in	Slab	HPFRC UHPC	69-130	SF	x	x	x				x						▪ Increasing the fiber content and the compressive strength of fiber concrete up to ultrahigh-performance fiber concrete further enhances its blast performance. ▪ The UHPC specimens have less damage than HPFRC slab. ▪ A basalt mesh inserted into the concrete cover at the soffit of the UHPC specimen improves its blast performance, as expressed by the area of spalling and by the volume of debris.

Study	Test Method [1]	Type of Blast	Specimen Type	Concrete type	Concrete strength (MPa)	Fiber type [2]	Parameters investigated											Primary Conclusions
							Concrete strength	FRC type	Fiber content	Fiber type	Fiber length	Fiber yield strength	Hybrid fibers	Long. reinf. ratio	Shear reinf. ratio	Reinf. detailing / type	Specimen dimensions	Axial load	
Burrell et al. 2013	ST	Far-field	Column	UHPC	165	SF	x								x			x	▪ The use of UHPC drastically reduced the mid-span displacements and blast capacity when compared to normal strength concrete columns. ▪ The high strength and toughness of the UHPC concrete eventually led to reinforcement steel rupture failure modes. ▪ The additional transverse reinforcement provided both enhanced ductility and confinement. Columns designed with seismic detailing experienced a smaller maximum displacement of approximately 27%.
Roller et al. 2013	LE	Close-in	Column	UHPC	160-200	SF								x				x	▪ Results show that implementing UHPC significantly increases column post-blast residual capacity (up to 70%). ▪ Adding a thin layer of energy absorbing material to an existing column considerably increases the residual capacity of the structural member.
Aoude et al. 2015	ST	Far-field	Column	UHPC	128-165	SF: SP	x		x	x				x	x	x		x	▪ CRC columns show increased blast capacity, damage tolerance and improved control of displacements when compared to NSC. ▪ Increasing the fiber content from 2% to 4% resulted in reduced displacements and higher blast capacity. Increasing the fiber content beyond 4% did not result in further improvements in blast behavior. ▪ The use of fibers with increased aspect ratio improved the blast performance. ▪ The combined use of UHPC and seismic detailing resulted in reduced displacements and an ability to sustain larger blast loads before failure
Li et al. 2015	LE	Close-in	Column	UHPC	150	SF: SP, T				x	x							x	▪ UHPC reinforced with different fiber types and with Nano-materials is developed. ▪ UHPC columns show enhanced blast performance when compared to conventional concrete columns. Application of axial load further reduces displacements in UHPC columns
Xu et al. 2016	LE	Close-in	Column	UHPC	150	SF	x											x	▪ UHPC columns show enhanced blast resistance when compared to HSC columns in terms of blast capacity, damage tolerance and failure mode ▪ Axial load reduces displacements in UHPC columns under blast loads.
Decarufel & Aoude 2020	ST	Far-field	Column	UHPC	150	SF								x				x	▪ The use of UHPC increased blast resistance and reduced maximum and residual displacements at an equivalent blast. ▪ The use of high-strength (HS) or stainless steel (SS) bars in the UHPC columns further enhanced blast performance, with better control of maximum and residual displacements at equivalent blasts. ▪ Increasing the HS or SS ratio prevents brittle failure (bar rupture).

[1]Blast method: ST: shock-tube, LE: Live explosive testing; [2]Specimen type: UR = unreinforced, R = reinforced; 2x = two-way slab;

[2]Fiber type: SF = steel fiber, SP = short prismatic, T = twisted.

2.5 Previous FEM research on UHPC elements under impact/blast loading

Due to the difficulties of experimental blast testing, previous studies have used commercial software such as LS-DYNA to study the impact and blast behaviour of reinforced concrete components. Simulating UHPC material response is a challenge owing to its high compressive and tensile strength, and high energy absorption capacity. In LS-DYNA, several numerical constitutive models have been developed for UHPC. Among those models, the CONCRETE_DAMAGE_REL3 (MAT_072), Winfrith_Concrete (MAT_084) and CSCM (MAT_159) are commonly used. **Table 2.6** presents a number of FEM studies examining the impact and blast performance of UHPC components using the CONCRETE_DAMAGE_REL3 mode (Mao et al., 2014; Liu et al., 2017b; Liu et al., 2018a; Li & Wu, 2018; Chen et al., 2019; Xu et al., 2020; Oppong et al., 2021; Zhang et al., 2021; Liu et al., 2022a; Su et al., 2022; Liao et al., 2022), Winfrith_Concrete model (Thai & Kim, 2015; Zhang et al., 2017b; Zhang et al., 2017c; Lee et al., 2020; Yan et al., 2022), and CSCM model (Guo et al., 2018; Fan et al., 2018a; Fan et al., 2018b; Fan et al., 2019; Fan et al., 2020a; Fan et al., 2020b; Wang et al., 2019a; Wang et al., 2019b; Wei et al., 2019; Li et al., 2020; Saini et al., 2021; Wei et al., 2021; Xu et al., 2021; Jia et al., 2021; Gholipour & Billah, 2022a, 2022b). For the CONCRETE_DAMAGE_REL3 (MAT_072) model, most studies used this model to simulate UHPC member under close-in explosion and high-velocity impact (projectile & vehicle). Mao et al. (2014) first noted that the use of the equation of state 8 (EOS 8) in LS-DYNA to define the relationship between pressure and volumetric strain can well predict displacement response and damage pattern. The following studies have confirmed that implementation of the equation of state 8 (EOS 8) can well predict behaviour of UHPC members under projectile impact (Liu et al., 2017b; Liu et al., 2018a), vehicle impact (Oppong et al., 2021) and close-in blast loading (Chen et al., 2019). Xu et al. (2020) further calibrated the equation of state (EOS) by deriving the combination of hydro-static compression test, "p-alpha equation" and Mie–Grueneisen equation of state. The calibrated MAT_072 can accurately predict behaviour of UHPC members under low-velocity impact loading. Zhang et al. (2021) further calibrated failure surfaces and dynamic increase factors for UHPC members subjected to high-velocity projectile impact. The failure surface parameters were expressed as a function of concrete strength (f_c'). Following a similar approach, Liu et al. (2022a) considered element size effects for key model parameters. In addition, EOS parameters were further calibrated to evaluate local damage mode under contact explosions. Su et al. (2022) systematically calibrated the failure surface, EOS,

damage evolution and strain rate effect parameters and validated them through sets of experiments under drop hammer impact and close-in explosion.

For the CSCM model (MAT_159), most studies used this model for simulating UHPC members under low-velocity impact. Guo et al. (2018) carefully calibrated the model parameters for UHPC, including the bulk and shear moduli, failure surface parameters, cap and hardening parameters as well as strain-rate parameters. A number of studies (Fan et al., 2018a; Fan et al., 2018b; Fan et al., 2019; Fan et al., 2020a; Fan et al., 2020b; Wang et al., 2019a; Wang et al., 2019b; Wei et al., 2019; Li et al., 2020; Gholipour & Billah, 2022a, 2022b) have confirmed that the use of the calibration proposed by Guo et al. (2018) can well predict UHPC beams/columns under low-velocity lateral impact loading. In addition, Saini et al. (2021), Wei et al. (2021), Xu et al. (2021) also calibrated and verified those parameters under the low-velocity drop hammer test. Finally, Jia et al. (2021) calibrated the fracture energy hardening parameters and validated the model by accurately predicting the impact response of UHPC components from other studies. The Winfrith_Concrete model (Thai & Kim, 2015; Zhang et al., 2017b; Zhang et al., 2017c; Lee et al., 2020; Yan et al., 2022) has also been used for simulating behaviour of UHPC under impact or blast loading. Yan et al. (2022) concluded that the numerical model can accurately simulate displacement response and damage modes of UHPC beams under blast loading.

For steel reinforcement models, both PLASTIC_KINEMATIC (MAT_003) and PIECEWISE_LINEAR_PLASTICITY (MAT_024) have been used in the literature to simulate behaviour of reinforcement in concrete structures (see **Table 2.6**). The advantages of MAT_024 are that the model allows users to define realistic non-linear stress-strain behaviour using up to eight plastic strains and corresponding yield stress points. In addition, MAT_024 allows users to define strain rate curves in table LCSS with logarithmic interpolation (Hallquist, 2007). In comparison, MAT_003 uses the Cowper-Symonds model to implement DIF effects.

Research shows that application of blast and impact leads to an increase in member strength and stiffness when compared to quasi-static loading. The increases in member strength and stiffness are affected by the strain rate, and result from the apparent increase in concrete and steel material strength properties under dynamic loading. Over the years, researchers have also proposed strain-rate dependent models for predicting the DIF of concrete and steel materials. **Table 2.6** presents the DIF models for concrete and steel reinforcement used in LS-DYNA analysis. The Winfrith Concrete Model (MAT_084) includes the strain rate

enhancement by adopting the CEB model (CEB, 1991), as shown in **Equation 2-1**. Previous studies have demonstrated that the UHPC is less sensitive to rate effects when compared to conventional concrete, as a result, the CEB model overestimates the DIF values (Zhang et al., 2021; Liu et al., 2022b). In comparison, the Fujikake et al. model (Fujikake et al., 2006a) shown in **Equation 2-2** can well estimate the DIF for UHPC in both compression and tension. Therefore, Guo et al. (2018), Saini et al. (2021), Wei et al. (2021), and Xu et al. (2021) calibrated the DIF parameters in the CSCM model using the Fujikake et al. model. For the steel model, the Cowper-Symonds model (Hallquist, 2007) is commonly used to consider strain rate effects (see **Equation 2-3**). While the Hunan University team (Guo et al., 2018; Fan et al., 2018a; Fan et al., 2020a; Fan et al., 2019; Fan et al., 2020b) also found the JSCE model (JSCE, 1993) (see **Equation 2-4**) can well predict DIF for steel in tension. Finally, Li and Wu (2018) ignored the rate effects for high-strength steel due to a lack of reliable DIF data.

CEB model (1991):

$$DIF_c = \begin{cases} \left(\frac{\dot{\varepsilon}}{\dot{\varepsilon}_{oc}}\right)^{1.026\alpha} & \text{for } \dot{\varepsilon} \le 30s^{-1} \\ \gamma\left(\frac{\dot{\varepsilon}}{\dot{\varepsilon}_{oc}}\right)^{1/3} & \text{for } \dot{\varepsilon} > 30s^{-1} \end{cases}; DIF_t = \begin{cases} \left(\frac{\dot{\varepsilon}}{\dot{\varepsilon}_{ot}}\right)^{\delta} & \text{for } \dot{\varepsilon} \le 1s^{-1} \\ \beta^*\left(\frac{\dot{\varepsilon}}{\dot{\varepsilon}_{ot}}\right)^{1/3} & \text{for } \dot{\varepsilon} > 1s^{-1} \end{cases} \quad \text{2-1}$$

$$\log\gamma = 6.156\alpha - 2,\ \ \alpha = 1/(5 + 9f_c'/10),\ \ \dot{\varepsilon}_{oc} = 30 \cdot 10^{-6}s^{-1}$$

$$\delta = 1/(5 + 8 \cdot f_c'/f_{c0}'),\ \ \log\beta^* = 6\delta - 2,\ \ f_{c0}' = 10\ \text{MPa},\ \ \dot{\varepsilon}_{ot} = 10^{-6}s^{-1}$$

Fujikake et al. (2006a)

$$DIF_c = \begin{cases} 1 & \text{for } \dot{\varepsilon} \le \dot{\varepsilon}_{sc} \\ \left(\frac{\dot{\varepsilon}}{\dot{\varepsilon}_{sc}}\right)^{0.0055\left[\log\left(\frac{\dot{\varepsilon}}{\dot{\varepsilon}_{sc}}\right)\right]^{0.951}} & \text{for } \dot{\varepsilon} > \dot{\varepsilon}_{sc} \end{cases}; DIF_t = \begin{cases} 1 & \text{for } \dot{\varepsilon} \le \dot{\varepsilon}_{st} \\ \left(\frac{\dot{\varepsilon}}{\dot{\varepsilon}_{st}}\right)^{0.0013\left[\log\left(\frac{\dot{\varepsilon}}{\dot{\varepsilon}_{st}}\right)\right]^{1.95}} & \text{for } \dot{\varepsilon} > \dot{\varepsilon}_{st} \end{cases} \quad \text{2-2}$$

$$\dot{\varepsilon}_{sc} = 10^{-6}/s;\ \dot{\varepsilon}_{st} = 1.2 \times 10^{-5}/s$$

Cowper-Symonds model (2007):

$$DIF_s = 1 + \left(\frac{\dot{\varepsilon}}{C}\right)^{1/p} \quad \text{2-3}$$

JSCE (1993)

$$DIF_s = 1.202 + 0.040 \times \log_{10}\dot{\varepsilon} \quad \text{2-4}$$

Where, DIF_c, DIF_t, DIF_s = dynamic increase factor for concrete in compression, concrete in tension and steel in tension; $\dot{\varepsilon}$ = strain rate.

Table 2.6 Previous FEM studies on UHPC components

Study	Loading type [a]	Elements	Concrete (UHPC)			Reinforcement	
			Concrete model	Rate effect	Calibration	Reinf. model	Rate effect
Mao et al. (2014)	Blast (Far field)	Slab	MAT_072	Proposed	-	MAT_003	Ignored
Liu et al. (2017b) Liu et al. (2018a)	Impact (Projectile)	Slab		Proposed	-	MAT_003	Cowper-Symonds
Li and Wu (2018)	Blast	Column		Proposed	-	MAT_024	Ignored
Chen et al. (2019)	Blast (Close-in)	Column		CEB model	-	MAT_003	Cowper-Symonds
Xu et al. (2020)	Impact	Beam & Column		Fujikake et al.	Proposed	Not mentioned	
Oppong et al. (2021)	Impact (Vehicle)	Beam		Not mention	-	Not mentioned	
Zhang et al. (2021)	Impact (projectile)	Varied		Proposed	Proposed	Not mentioned	
Liu et al. (2022a)	Blast (Close-in)	Slab		Fujikake et al.	Proposed	MAT_003	Cowper-Symonds
Su et al. (2022)	Impact & Blast (Close-in)	Varied		Proposed	Proposed	MAT_003	Cowper-Symonds
Liao et al. (2022)	Blast (Close-in)	Slab		CEB model	-	MAT_003	Cowper-Symonds
Thai and Kim (2015)	Impact	Slab	MAT_084	CEB model	-	MAT_024	Cowper-Symonds
Zhang et al. (2017b) Zhang et al. (2017c)	Impact	Slab		CEB model	-	-	-
Lee et al. (2020)	Impact & Blast (Far field)	Column		CEB model	-	MAT_003	Cowper-Symonds
Yan et al. (2022)	Blast (Close-in)	Beam		CEB model	-	MAT_024	Malvar
Guo et al. (2018)	Impact	Beam	MAT_159	Fujikake et al.	Proposed	MAT_024	JSCE
Fan et al. (2018a)	Impact	Column		Fujikake et al.	Guo et al.	MAT_024	JSCE
Fan et al. (2018b)	Impact	Column		Fujikake et al.	Guo et al.	MAT_003	Cowper-Symonds
Fan et al. (2019)	Impact	Column		Fujikake et al.	Guo et al.	MAT_024	JSCE
Fan et al. (2020a)	Impact	Column		Fujikake et al.	Guo et al.	MAT_003	JSCE
Fan et al. (2020b)	Impact	Column		Fujikake et al.	Guo et al.	MAT_024	JSCE
Wang et al. (2019a); Wang et al. (2019b)	Impact	UHPC filled steel tube		Fujikake et al.	Guo et al.	No steel rebar	
Wei et al. (2019)	Impact	Column		Fujikake et al.	Guo et al.	MAT_024	Malvar
Li et al. (2020)	Impact	Beam		Fujikake et al.	Guo et al.	MAT_003	Cowper-Symonds
Saini et al. (2021)	Impact	Beam		Fujikake et al.	Proposed	Not mention	
Wei et al. (2021)	Impact	Beam		Fujikake et al.	Proposed	MAT_024	Malvar
Xu et al. (2021)	Impact	UHPCFTWST columns		Ignored	Proposed	No steel rebar	
Jia et al. (2021)	Impact	Varied		Proposed	Proposed	MAT_003	Cowper-Symonds
Gholipour and Billah (2022a)	Impact	Column		Fujikake et al.	Guo et al.	MAT_024	Cowper-Symonds
Gholipour and Billah (2022b)	Impact	Beam		Fujikake et al.	Guo et al.	MAT_024	Cowper-Symonds

[a] Far filed: scaled distance (Z) > 1.2 m/kg$^{1/3}$; Close-in: scaled distance (Z) ≤ 1.2 m/kg$^{1/3}$

2.6 Summary

This chapter presented a literature review on the impact and blast behaviour of RC components constructed with high-strength reinforcement, stainless steel reinforcement or UHPC. Based on these studies, the following conclusions can be summarized:

- Research on the impact and blast performance of RC beams with high-strength bars is limited and is mostly from early impact studies on beams built with steel types that are no longer used in practice. Research conducted by Li and Aoude (2019) at the University of Ottawa indicates that the use of Grade 690 MPa high-strength reinforcement conforming to ASTM A1035 in HSC beams can improve blast performance by increasing blast capacity and better controlling peak displacements. On the other hand, the research indicates that the high yield strength of ASTM A1035 reinforcement can make flexural members more vulnerable to brittle compression failures, where concrete fails prior to steel yielding;
- Research on the impact and blast performance of RC elements built with stainless steel bars is scarce or non-existent. Previous impact testing on columns indicates that the use of stainless steel reinforcement can improve overall stiffness, reduce maximum lateral displacements and increase damage tolerance. The high toughness and ductility of stainless steel reinforcement make it an ideal material to resist blast loading; however, no research exists on the blast response of RC elements with stainless steel reinforcement. Moreover, previous impact research has been limited to a single type of stainless steel alloy (S2304 Duplex stainless steel); therefore further research is needed to study the impact and blast response of RC elements reinforced with other stainless steel types;
- There exists important research which demonstrates the superior impact and blast performance of UHPC, however most previous blast research has focussed on slabs or columns. Thus research is needed to investigate the extreme load behaviour of UHPC beams under blast loads. Most previous studies have focussed on UHPC components built with ordinary steel reinforcement, while only a few studies have examined the combined use of UHPC and high performance steel. As noted by Burrell et al. (2013), the high-bond capacity of UHPC can eventually lead to bar fracture failures. Similarly, Aghdasi and Ostertag (2020) recommended a minimal reinforcement ratio of 4% for Grade 400 MPa reinforcement to prevent brittle failure modes (bar rupture) in UHPC elements. Thus further research is needed to gain knowledge on the influence of increased steel ratios and high performance steel reinforcing materials on the blast response of UHPC.

In this PhD research, Series 1 (HSC-HSS) and Series 2 (HSC-SS) aim at filling the above-mentioned research gaps by increasing understanding of the influence of steel detailing on the blast behavior of beams with higher grade HSS steel and higher ductility stainless steel reinforcement. The UHPC beams with ordinary steel from Series 3 aim at studying the effect of increased steel ratios on the blast behavior of UHPC. In addition, the UHPC beams with high-strength or stainless steel from Series 3 are intended to provide a greater understanding on the influence of higher grade HSS bars and higher ductility stainless steel bars on the blast behavior of UHPC beams.

Chapter 3 Experimental program

3.1 Chapter Overview

The experimental research program includes beams constructed with various combinations of high-strength concrete (HSC), ultra-high performance concrete (UHPC), normal-strength steel (NSS), high-strength steel (HSS) and stainless steel (SS) reinforcement. Parameters investigated include the effects of reinforcement detailing, steel type, concrete type, tension steel ratio and fibers. This chapter summarizes the details of the beam designs, material properties, specimen construction, experimental setups and testing procedures.

3.2 Specimen Specifications

A total of forty-four beams are included in this study. The beams are organized in three series based on their concrete and steel reinforcement combination as follows:

- **Series 1**: Eight (8) beams constructed with high-strength concrete & Grade 690 MPa ASTM A1035 high-strength steel reinforcing bars (HSC-HSS);
- **Series 2**: Sixteen (16) beams constructed with high-strength concrete & Grade 520 MPa ASTM A955 stainless steel reinforcing bars (HSC-SS);
- **Series 3**: Twenty (20) beams constructed with ultra-high performance concrete (UHPC) and either (a) normal-strength (ordinary) steel (NSS), (b) high-strength steel (HSS) or (c) higher-ductility stainless steel (SS).

All the beams in this study have the same dimensions of 125 mm × 250 mm × 2440 mm (b × h × L), and are tested under four-point loading, with a clear span of 2232 mm and two equal shear spans of 741 mm (a/d ratio = 3.7). Tension reinforcement consists of either 15M/20M Canadian size bars (for the normal-strength steel), or 2-No.4 or 2-No.5 U.S. size bars (for the high-strength or stainless steel), while transverse reinforcement consists of closed ties or open-stirrups made from 6.3 mm steel wire.

Four different beam designs are considered in the research, each corresponding to different detailing levels (see **Figure 3.1**):

- ***Type A*** (*blast* detailing): These beams are designed following the stringent detailing requirements of the CSA S850 blast standard, with provision of top continuity bars (compression bars) and closed ties spaced at s = 50 mm (d/4) throughout their span;
- ***Type B*** (*intermediate* detailing): These beams are designed with more relaxed detailing, with top continuity bars and closed ties spaced at s = 100 mm (d/2) throughout their spans;
- ***Type C*** (*nominal* detailing): These beams are singly-reinforced and provided with U-shaped (open) stirrups, spaced at s = 100 mm (d/2) in their shear spans only;
- ***Type D*** (no stirrups): These beams are singly reinforced and lack transverse reinforcement.

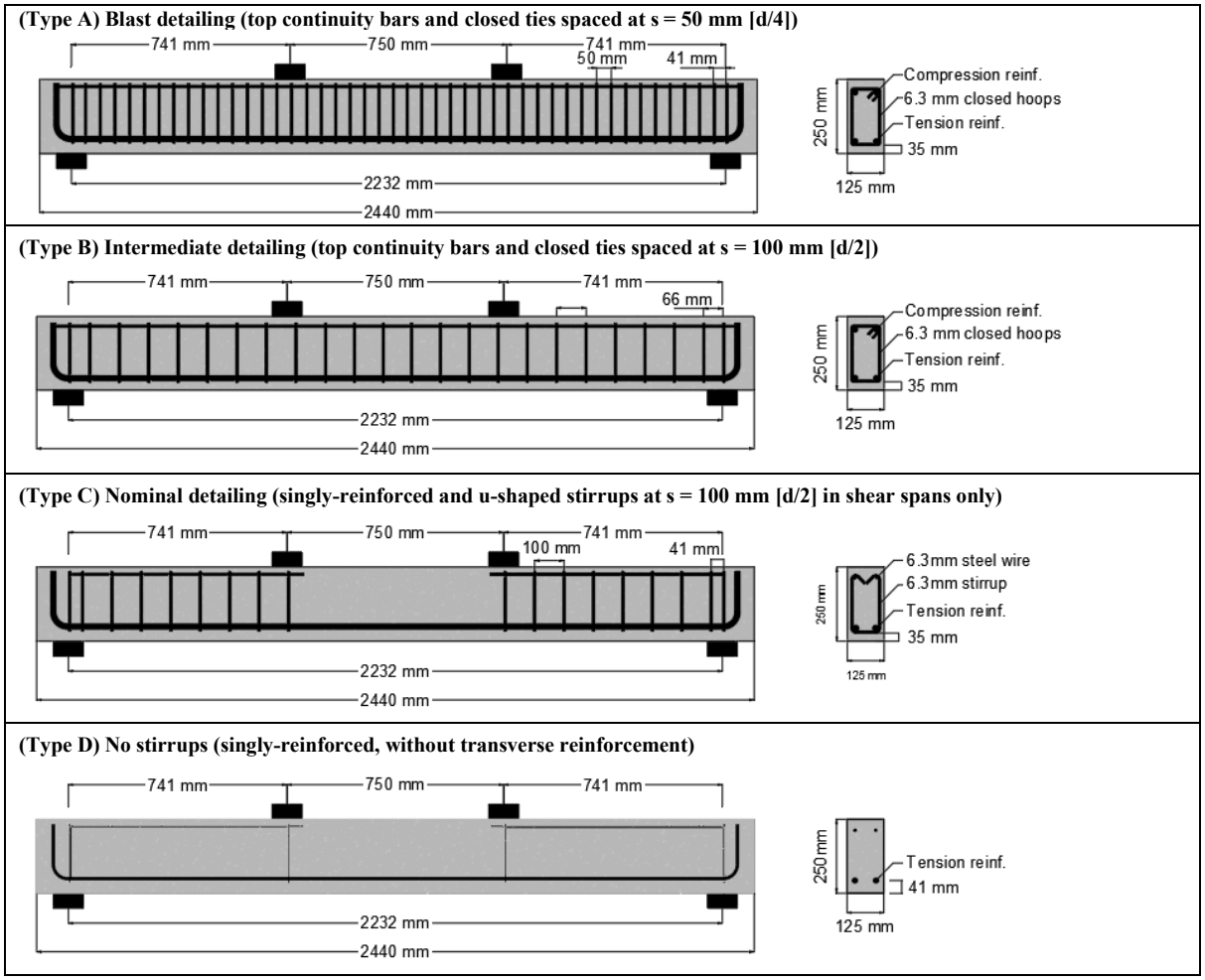

Figure 3.1 Beam designs (types) and reinforcement details

3.2.1. Series 1 (HSC-HSS)

All beams in Series 1 are built with HSC and Grade 690 MPa ASTM A1035 high-strength steel reinforcement. Longitudinal steel in tension consists of either 2-No.4 or 2-No.5 high-strength bars (ρ = 1% or 1.5%), while transverse reinforcement consists of closed ties made from 6.3 mm steel wire arranged at various spacing (s). **Table 3.1** summarizes the details of the eight specimens from the current study, and six companions "control beams" tested in a previous study (Li & Aoude, 2019). *Group A* beams (6 specimens) are built with plain HSC and are designed in accordance with the CSA S850 "blast detailing" requirements, with provision of top continuity bars (either 2 - No.3 or 2 - No.4 bars, ρ'= 0.6% and 1.0%) and closely spaced ties at s = 50 mm (d/4) throughout their span (see **Figure 3.1a**). Two of the beams are tested under static loads, two under repeated blast loads and two under singly-applied blast loads. *Group B* beams (2 specimens) are constructed with high-strength fiber reinforced concrete (HSFRC) containing 0.75% of hooked-end steel fibers, and relaxed detailing, with ties spaced at s = 100 mm (d/2), when compared to *Group A* (see **Figure 3.1b**). This set includes one beam tested under static loads and one beam tested under repeated blast loads. *Group C* consists of a control set of beams (6 specimens) built with HSC or HSFRC, high-strength bars and "nominal detailing"; these beams were singly-reinforced, with open-stirrups provided in the shear spans only (see **Figure 3.1c**) and were tested previously by Li and Aoude (2019, 2020). Within this set, three beams were tested under static loads, with three replicate beams tested under blast conditions.

Table 3.1 Beam properties in series 1 (HSC-HSS)

Group [a]	Beam ID	No. of beams tested	Concrete Type	Fiber content V_f [c]	Longitudinal Reinf.			Transverse Reinf.		Loading type [d]
					Type	Tension steel (ρ)	Comp. steel (ρ')	Type	Tie/stirrup Spacing	
A	C100-No.4HS-DR-d/4	2	HSC	-	Grade 690 MPa ASTM A1035	2-No.4 (1.0%)	2-No.3 (0.6%)	Closed ties (full span)	50 mm (d/4)	S, D
	C100-No.5HS-DR-d/4	2		-		2-No.5 (1.5%)	2-No.4 (1.0%)		50 mm (d/4)	S, D
	C100-No.4HS-DR-d/4 [x1]	1		-		2-No.4 (1.0%)	2-No.3 (0.6%)		50 mm (d/4)	Dx1
	C100-No.5HS-DR-d/4 [x1]	1		-		2-No.5 (1.5%)	2-No.4 (1.0%)		50 mm (d/4)	Dx1
B	CF100-No.5HS-DR-d/2	2	HSFRC	0.75 %		2-No.5 (1.5%)	2-No.4 (1.0%)	Closed ties (full span)	100 mm (d/2)	S, D
C [b]	C100-No.4HS-S	2	HSC	-	Grade 690 MPa ASTM A1035	2-No.4 (1.0%)	-	Stirrups (shear spans only)	100 mm (d/2)	S, D
	C100-No.5HS-S	2		-		2-No.5 (1.5%)	-		100 mm (d/2)	S, D
	CF100-No.5HS-S	2	HSFRC	1.0 %		2-No.5 (1.5%)	-		100 mm (d/2)	S, D

[a] Group A: HSC beams with blast detailing; Group B: HSFRC beams with intermediate detailing; Group C: beams with nominal detailing.
[b] Beams in Group C were tested by Li and Aoude (2019, 2020).
[c] Hooked-end steel fibers (length = 30 mm).
[d] S, D, Dx1: specimens tested under static, repeated dynamic and single dynamic loading, respectively.

3.2.2. Series 2 (HSC-SS)

This series includes a total of fourteen beams built with HSC and Grade 520 MPa stainless steel (SS) reinforcement. A total of sixteen beams were included in Series 2.

Series 2A includes seven singly-reinforced HSC-SS beams built with nominal detailing or without stirrups (Type C or D detailing). Tension steel consists of 2-No.5 XM-28 (S1) stainless bars (ρ = 1.5%), while transverse reinforcement consists of U-shaped stirrups made from 6.3 mm steel wire. As shown in **Table 3.2** the beams are subdivided into two groups. *Group C* consists of a set of four HSC or HSFRC beams with Type C "nominal detailing" consisting of open-stirrups in the shear-spans (see **Figure 3.1c**), with two beams tested under static loads and two beams tested under repeated blasts. *Group D* (3 specimens) includes three HSC or HSFRC beams built without stirrups (Type D detailing) (**Figure 3.1d**), with two beams tested under static loads and one replicate HSFRC beam tested under repeated blasts. The HSFRC in these tests contains 1% of hooked-end steel fibers. The main parameters investigated include the effects of steel type (stainless vs. ordinary steel), and the effects of fibers.

Series 2B includes nine doubly-reinforced beams HSC-SS beams built with blast or intermediate detailing (Type A or B detailing). Tension steel consists of either 2-No.4 or 2-No.5 SS bars (ρ = 1% or 1.5%), while transverse reinforcement consists of closed ties made from 6.3 mm steel wire spaced at either 50 or 100 mm. As shown in **Table 3.3**, the beams are subdivided into two groups. *Group A* beams (7 specimens) are built with plain HSC and are designed in accordance with the CSA S850 "blast detailing" requirements, with provision of top continuity bars (either 2 - No.3 or 2 - No.4 SS bars) and ties at s = 50 mm (d/4) throughout their span (see **Figure 3.1a**). To examine the effect of alloy type, five beams are built with XM-28 austenitic bars (S1), with two beams built with 2304 duplex bars (S2). Three of the beams are tested under static loads, three under repeated blast loads and one under singly-applied blast loads. *Group B* beams (2 specimens) are constructed with HSFRC containing 0.75% of hybrid steel fibers, and relaxed detailing, with ties spaced at s = 100 mm (d/2), when compared to *Group A* (see **Figure 3.1b**). This group includes one beam tested under static loads and one beam tested under repeated blast loads. The main parameters investigated include the effects of detailing (blast vs. nominal), steel type (stainless vs. ordinary steel), and the ability of fibers to improve blast performance and relax detailing (from d/4 to d/2).

Table 3.2 Beam properties in Series 2A (Singly-reinforced)

Type [a]	Beam ID	No. of beams tested	Concrete Type	Fiber content V_f	Longitudinal Reinf.		Transverse Reinf.		Loading type [b]
					Type	Tension steel (ρ)	Type	Tie/stirrup Spacing	
C	C100-No.5S1-S	2	HSC	-	XM-28 (S1)	2-No.5 (1.5%)	Stirrups (shear spans only)	100 mm (d/2)	S, D
	CF100-No.5S1-S	2	HSFRC	1.0 % [c]		2-No.5 (1.5%)		100 mm (d/2)	S, D
D	C100-No.5S1	1	HSC	-		2-No.5 (1.5%)	No stirrups	-	D
	CF100-No.5S1	2	HSFRC	1.0 % [c]		2-No.5 (1.5%)	No stirrups	-	S, D

[a] Group C: beams with nominal detailing. Group D: no transverse reinforcement.
[b] S, D: specimens tested under static and repeated dynamic.
[c] Hooked-end steel fibers (length = 30 mm).

Table 3.3 Beam properties in Series 2B (Doubly-reinforced)

Type [a]	Beam ID	No. of beams tested	Concrete Type	Fiber content V_f	Longitudinal Reinf.			Transverse Reinf.		Loading type [b]
					Type	Tension steel (ρ)	Comp. steel (ρ')	Type	Tie/stirrup Spacing	
A	C100-No.4S1-DR-d/4	2	HSC	-	XM-28 (S1)	2-No.4 (1.0%)	2-No.3 (0.6%)	Closed ties (full span)	50 mm (d/4)	S, D
	C100-No.5S1-DR-d/4	2		-		2-No.5 (1.5%)	2-No.4 (1.0%)		50 mm (d/4)	S, D
	C100-No.5S1-DR-d/4 [x1]	1		-		2-No.5 (1.5%)	2-No.4 (1.0%)		50 mm (d/4)	Dx1
	C100-No.5S2-DR-d/4	2		-	2304 (S2)	2-No.5 (1.5%)	2-No.4 (1.0%)		50 mm (d/4)	S, D
B	CF100-No.5S1-DR-d/2	2	HSFRC	0.75 % [c]	XM-28 (S1)	2-No.5 (1.5%)	2-No.4 (1.0%)	Closed ties (full span)	100 mm (d/2)	S, D

[a] Group A: HSC beams with blast detailing; Group B: HSFRC beams with intermediate detailing.
[b] S, D, Dx1: specimens tested under static, repeated dynamic and single dynamic loading, respectively.
[c] Hybrid steel fibers: 0.25% micro-fibers (length =13 mm) and 0.5% of macro hooked-end fibers (length =30 mm).

3.2.3. Series 3 (UHPC with NSS, HSS and SS bars)

The third series of tests studies the static and blast performance of ultra-high performance concrete (UHPC) beams designed with varying steel types (ordinary, high-strength or stainless steel bars: UHPC-NSS, UHPC-HSS and UHPC-SS). A total of twenty beams were included in Series 3, which are further subdivided in two groups.

Group 1 includes six UHPC beams cast with 3% fibers (designated as U3) (see **Table 3.4**). The beams in this group are singly-reinforced, and were built without stirrups (Type D detailing) (see **Figure 3.1d**). Longitudinal steel consists of either 2-15M ordinary bars, or 2-No.5 high-strength or stainless steel bars (ρ = 1.5%). Within this group, 3 beams are tested under static loads and 3 are tested under blast loads. To examine the effect of concrete type, the results are compared to a control set of high-strength concrete beams with identical properties, and built either without or with stirrups (made from 6.3 mm wire) spaced at 100 mm (d/2) in the shear spans (Type C, "nominal" detailing) (see **Figure 3.1c**). The reference beams (Type C & D) in **Table 3.6** are tested by Li et al. (2018); Li and Aoude (2019) and in Series 2A from the current project.

Group 2 includes 14 UHPC beams cast with 2% fibers (designated as U2) (see **Table 3.5**). The beams in this group are doubly-reinforced, and transverse reinforcement consists of closed ties made from 6.3 mm steel wire which are spaced at 100 mm (s = d/2) along the entire beam span (Type B, "intermediate" detailing) (**Figure 3.1b**). In the HSS set, one beam is also built with UHPC containing 1% fibers (U1) and ties at 50 mm (s = d/2) (**Figure 3.1a**). Longitudinal steel consists of either 2-15M or 2-20M bars (ρ = 1.5% or 2.4%) in tension, and 2-10M bars (ρ' = 0.8%) in compression for the beams with ordinary steel. The beams with HSS or SS are reinforced with either 2-No.4 or 2-No.5 bars (ρ = 1.0% or 1.5%) in tension, and 2-No.3 or 2-No.4 bars (ρ' = 0.6% - 1.0%) in compression. Within this group, 6 beams are tested under static loads and 8 are tested under blast loads. To examine the effect of concrete type, the results are compared to a control set of high-strength concrete beams with identical properties, but with ties spaced at 50 mm (d/4) over their full span (Type A, "blast" detailing) (**Figure 3.1a**). The reference beams (Type A) in **Table 3.6** are tested by Charles (2019); and in Series 1 and Series 2B from the current project.

Table 3.4 Beam properties in Group 1

Type [a]	Beam ID	No. of beams tested	Concrete Type	Fiber content V_f [b]	Longitudinal Reinf.			Transverse Reinf.		Loading type [c]
					Type	Tension steel (ρ)	Comp. steel (ρ')	Type	Tie/stirrup Spacing	
D	U3-15M	2	UHPC	3.0%	Ordinary	2-15M (1.5%)	-	No stirrups	-	S, Dx1
	U3-No.5HS	2	UHPC	3.0 %	ASTM A1035	2-No.5 (1.5%)	-	No stirrups	-	S, Dx1
	U3-No.5S1	2	UHPC	3.0 %	XM-28	2-No.5 (1.5%)	-	No stirrups	-	S, Dx1

[a] Group B: 2% fibers and intermediate detailing; Group D: 3% fibers and no stirrups.
[b] Smooth steel fibers (length = 13 mm).
[c] S, D, Dx1: specimens tested under static, repeated dynamic and single dynamic loading.

Table 3.5 Beam properties in Group 2

Type [a]	Beam ID	No. of beams tested	Concrete Type	Fiber content V_f [b]	Longitudinal Reinf.			Transverse Reinf.		Loading type [c]
					Type	Tension steel (ρ)	Comp. steel (ρ')	Type	Tie/stirrup Spacing	
B	U2-15M-DR-d/2	2	UHPC	2.0 %	Ordinary	2-15M (1.5%)	2-10M (0.8%)	Closed ties (full span)	100 mm (d/2)	S, Dx1
	U2-20M-DR-d/2	2				2-20M (2.4%)	2-10M (0.8%)		100 mm (d/2)	S, Dx1
	U2-20M-DR-d/2 (R)	1				2-20M (2.4%)	2-10M (0.8%)		100 mm (d/2)	D
A	U1-No.5HS-DR-d/4	1	UHPC	1.0 %	ASTM A1035	2-No.5 (1.5%)	2-No.4 (1.0%)	Closed ties (full span)	50 mm (d/4)	Dx1
B	U2-No.4HS-DR-d/2 (R)	2		2.0 %		2-No.4 (1.0%)	2-No.3 (0.6%)		100 mm (d/2)	S, D
	U2-No.5HS-DR-d/2	2				2-No.5 (1.5%)	2-No.4 (1.0%)		100 mm (d/2)	S, Dx1
B	U2-No.4S1-DR-d/2 (R)	2	UHPC	2.0 %	XM-28 (S1)	2-No.4 (1.0%)	2-No.3 (0.6%)	Closed ties (full span)	100 mm (d/2)	S, D
	U2-No.5S1-DR-d/2	2		2.0 %		2-No.5 (1.5%)	2-No.4 (1.0%)		100 mm (d/2)	S, Dx1

[a] Group A: 1% fibers and blast detailing; Group B: 2% fibers and intermediate detailing.
[b] Smooth steel fibers (length = 13 mm).
[c] S, D, Dx1: specimens tested under static, repeated dynamic and single dynamic loading.

Table 3.6 Beam properties in companion (control) beams of Series 3

Type [a]	Beam ID	No. of beams tested	Concrete Type	Fiber content V_f	Longitudinal Reinf.			Transverse Reinf.		Loading type [b]
					Type	Tension steel (ρ)	Comp. steel (ρ')	Type	Tie/stirrup Spacing	
A	C100-15M-DR-d/4 [c]	2	HSC	-	Ordinary	2-15M (1.5%)	2-10M (0.8%)	Closed ties (full span)	50 mm (d/4)	S, Dx1
	C100-20M-DR-d/4 [c]	2				2-20M (2.4%)	2-10M (0.8%)		50 mm (d/4)	S, D
	C100-No.4HS-DR-d/4 [d]	1			ASTM A1035	2-No.4 (1.0%)	2-No.3 (0.6%)		50 mm (d/4)	D
	C100-No.5HS-DR-d/4 [d]	2				2-No.5 (1.5%)	2-No.4 (1.0%)		50 mm (d/4)	S, Dx1
	C100-No.4S1-DR-d/4 [e]	1			XM-28	2-No.4 (1.0%)	2-No.3 (0.6%)		50 mm (d/4)	D
	C100-No.5S1-DR-d/4 [e]	2				2-No.5 (1.5%)	2-No.4 (1.0%)		50 mm (d/4)	S, Dx1
C	C100-15M-S [f]	2	HSC	-	Ordinary	2-15M (1.5%)	-	Stirrups (shear spans only)	100 (d/2)	S, D
	C100-No.5HS-S [g]	2			ASTM A1035	2-No.5 (1.5%)	-		100 (d/2)	S, D
	C100-No.5S1-S [e]	2			XM-28	2-No.5 (1.5%)	-		100 (d/2)	S, D
D	C100-15M	2	HSC	-	Ordinary	2-15M (1.5%)	-	No stirrups	-	S, D
	C100-No.5HS	2			ASTM A1035	2-No.5 (1.5%)	-	No stirrups	-	S, D
	C100-No.5S1	1			XM-28	2-No.5 (1.5%)	-	No stirrups	-	D

[a] Group A: HSC beams with blast detailing; Group C: beams with nominal detailing. Group D: no transverse reinforcement.
[b] S, D, Dx1: specimens tested under static, repeated dynamic and single dynamic loading.
[c, f, g] Tested by Charles (2019), Li et al. (2018) & Li and Aoude (2019).
[d, e] From Series 1 and 2B

3.2.4.Specimen Nomenclature

The specimen IDs in **Table 3.1** to **Table 3.6** provide an indication of the design details described in the previous sections, including the concrete type (C100 or CF100 for plain HSC and HSFRC; U1, U2, U3 for UHPC with 1%, 2% and 3% steel fibers, respectively), tension steel bar size (15M, 20M, No.4 or No.5), steel grade (with HS, S1/S2 indicating use of high-strength and stainless bars respectively). and "DR-d/4" or "DR-d/2" indicating the use of *Type A* and *Type B* detailing: top continuity bars and ties spaced at s = d/4 or d/2). **Figure 3.2** and **Figure 3.3** further explain the nomenclature used in the HSC & UHPC beam designs.

For example, Series 1 beam: C100-No.5HS-DR-d/4 is designed with plain HSC, No.5 high-strength bars and "blast detailing" (top continuity bars ties and ties spaced at d/4). Likewise, CF100-No.5HS-DR-d/2 is the companion beam with 0.75% fibers and "intermediate detailing" (increased tie spacing of d/2). On the other hand, C100-No.5HS is the control HSC beam with "nominal detailing" (singly-reinforced, with stirrups spaced at s = d/2 in the shear spans only). The [x1] in the nomenclature of beams C100-No.4HS-DR-d/4 [x1] and C100-No.5HS-DR-d/4 [x1] indicates the beams are tested under single, rather than repeated blast loads. A similar logic is used in the UHPC beam nomenclature. In **Series 3**, most beams are tested under singly-applied blast loading, therefore the [R] in the nomenclature indicates the beam is tested under repeated blasts.

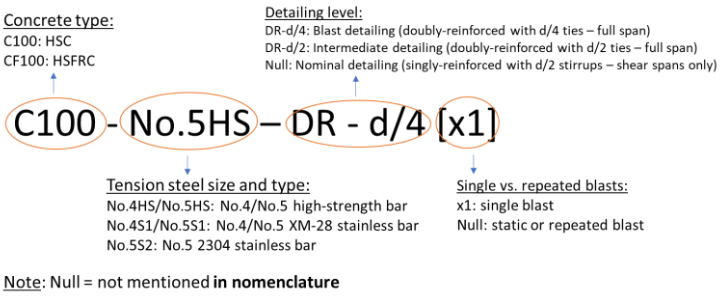

Figure 3.2 Nomenclature in HSC beam designs (Series 1 & 2)

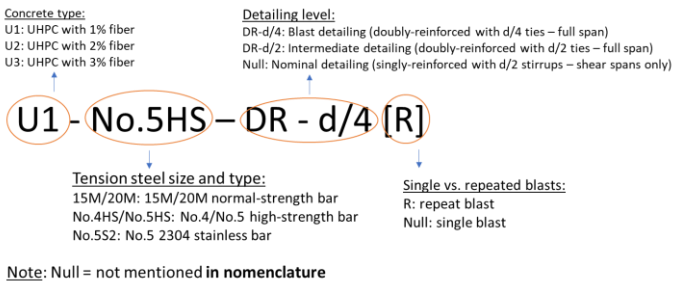

Figure 3.3 Nomenclature in UHPC beam designs (Series 3)

3.3 Materials

3.3.1. Concrete

Two types of concrete were used in this study: high-strength concrete (HSC) was used in **Series 1 & 2** and ultra-high performance concrete (UHPC) was used in **Series 3**. In all cases, the concrete materials were mixed using a large pan-mixer at the University of Ottawa.

The C100 high-strength concrete mix has a target strength of 100 MPa. **Table 3.7** lists the quantities of Portland cement, slag, silica fume, sand, coarse aggregate (10 mm & 20 mm) and liquid admixtures (super-plasticizer & set retarder) used in this concrete (see **Figure 3.4**). The CF100 mix had the same properties as the base HSC mix, but was reinforced with 0.75% or 1.0% (60 or 78 kg/m^3) of hooked-end steel macro fibers (L_f = 30 mm).

The ultra-high performance concrete mix in this research is provided by Sika, and has a target strength of 140 MPa at 28 days. **Table 3.8** presents the properties of the mix in terms of pre-blended & pre-packaged material (see **Figure 3.5**), water, types A/B/C admixtures, and steel fibers. The U1 and U2 mixes were manufactured using the same pre-blended material but were reinforced with 1% or 2% (78 or 156 kg/m^3) of straight steel micro fibers (L_f = 13 mm). The U3 mix used a different pre-blended mix, with 3% (234 kg/m^3) of the same fiber.

Table 3.7 HSC mix properties

Cement (kg/m^3)	Slag (kg/m^3)	Silica fume (kg/m^3)	Sand (kg/m^3)	Aggregate 10 mm [3/8"] (kg/m^3)	Aggregate 19 mm [3/4"] (kg/m^3)	Water (kg/m^3)	SP (L/m^3)	Retarder (L/m^3)
373	164	48	734	560	560	157	13.1	3.3

Table 3.8 UHPC mix properties

	Premix (kg/m^3)	Water (kg/m^3)	Admixture A (kg/m^3)	Admixture B (kg/m^3)	Admixture C (kg/m^3)	Steel fibers (kg/m^3)
UHPC-1%	1929.41	185.40	24.19	25.35	38.33	78
UHPC-2%						156
UHPC-3%	1902.40	184.93	24.91	25.35	38.32	234

Cement

Aggregate 1 (19 mm)

Aggregate 2 (9.5 mm)

Sand

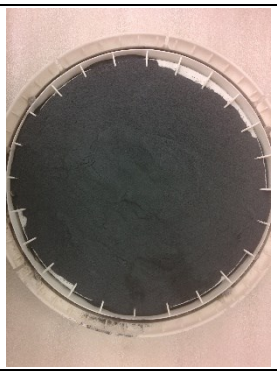

Silica fume

Slag

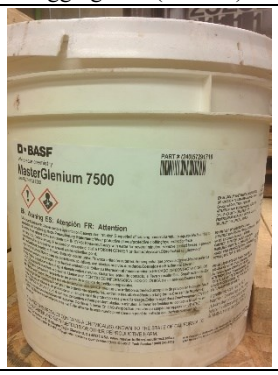

Super-plasticizer

Retarder

Figure 3.4 Materials used in the base HSC mix

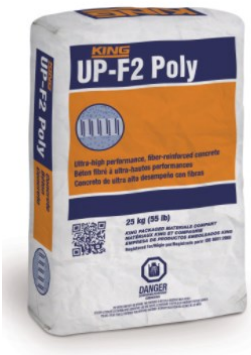

(a) Pre-blended material for U1 and U2

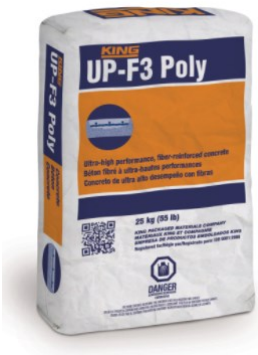

(b) Pre-blended material bag for U3

Figure 3.5 Pre-blended, pre-packaged material for UHPC

3.3.2. Steel reinforcement

Five types of steel reinforcement were used for this research, including one type of transverse reinforcement and four types of longitudinal steel. Steel properties were determined by testing three coupons of each steel type in tension using a GALDABINI SUN 60 Universal Floor Standing Testing Machine. **Table 3.9** summarizes the properties of the various steels used in this research, including steel ID, bar diameter and area, yield strain and strength, ultimate strain and strength and strain at rupture. **Figure 3.6** shows typical stress-strain curves for each steel type. While **Figure 3.7** shows stress-strain curves for all the steel reinforcement.

The smooth non-deformed wire used for the transverse reinforcement had a diameter of d_b = 6.3 mm and a cross-section of A_b = 32 mm^2, with an average yield stress of 540 MPa and ultimate stress of 645 MPa. The average yield strengths (f_y) of the 10M, 15M and 20M normal-strength longitudinal reinforcing bars were 455, 472 and 433 MPa, respectively, and sample stress-strain curves are shown in **Figure 3.6a.** The No.3, No.4 and No.5 high-strength ASTM A1035 bars had average yield strengths (f_y) of 952, 904 and 929 MPa (determined using the 0.2% offset method); sample stress-strain curves are shown in **Figure 3.6b.** Two types of stainless steel alloys were considered in this study, including XM-28 (austenitic) and 2304 (duplex) SS bars. **Table 3.10** presents the heat chemistry of the two types of stainless steel. The XM-28 (S1) stainless steel shows higher strength when compared to the regular grade steel, with higher ductility when compared to the other steel types. Two batches of XM-28 steel were used for the No.5 bars. The batch 2 bars (with higher yield strength) were only used in CF100 beams in Series 2A. The average yield strengths of the No.3, No.4, No.5 (batch 1) and No.5 (batch 2) XM-28 stainless steel reinforcement were 660 MPa, 628 MPa, 600 MPa and 648 MPa. Typical stress-strain curves for XM-28 stainless steel are shown in **Figure 3.6c**. The 2304 (S2 type) stainless steel shows behaviour which is intermediate between those of the HS and S1 types. The average yield strengths of the No.4 and No.5 2304 bars were 596 MPa and 620 MPa, and sample stress-strain curves are shown in **Figure 3.6d**.

Table 3.9 Steel reinforcement mechanical properties

Reinf. Type	ID	Bar Diameter d_b(mm)	Bar Area A_b (mm^2)	Yield		Ultimate		Rupture
				Strain ε_y (mm/mm)	Strength f_y (MPa)	Strain ε_u (mm/mm)	Strength f_u (MPa)	Strain ε_r (mm/mm)
Smooth non-deformed wire	6.3NS	6.35	32	0.0027	540	0.070	645	0.151
Grade 400	10M	11.3	100	0.0021	455	0.201	584	0.216
	15M	16.0	200	0.0026	472	0.142	576	0.198
	20M	19.5	300	0.0022	433	0.149	601	0.161
Grade 690 ASTM A1035	No.3	9.5	71	0.0070	952	0.052	1276	0.059
	No.4	12.7	129	0.0067	904	0.056	1277	0.061
	No.5	15.9	200	0.0070	929	0.049	1217	0.058
XM-28 Stainless	No.3	9.5	71	0.0057	660	0.244	982	0.292
	No.4	12.7	129	0.0056	628	0.216	979	0.289
	No.5 (batch 1)	15.9	200	0.0054	600	0.34	862	0.34
	No.5 (batch 2)	15.9	200	0.0054	648	0.40	903	0.40
2304 Stainless	No.4	12.7	129	0.0049	596	0.187	809	0.217
	No.5	15.9	200	0.0058	620	0.164	848	0.231

Table 3.10 Heat chemistry of stainless steel

Steel type	Bar size	C	Mn	Cr	Ni	Mo	N	Other elements					
								Si	P	S	Cu	Co	B
XM-28	No.3/No.4	0.083	12.84	17.94	0.93	-	0.265	0.98	0.036	0.0009	-	-	-
	No.5 (B1)	0.05	11.9	17.4	0.8	0.34	0.24	0.42	0.018	0.002	0.13	0.04	0.0024
	No.5 (B2)	0.05	12.0	17.5	0.86	0.47	0.29	0.32	0.021	0.001	0.1	0.03	0.0024
2304	No.4	0.02	1.68	22.55	4.45	0.194	0.129	0.52	0.03	0.0011	0.26	0.11	-
	No.5	0.017	1.62	22.59	4.3	0.192	0.174	0.47	0.033	0.0009	0.26	0.07	-

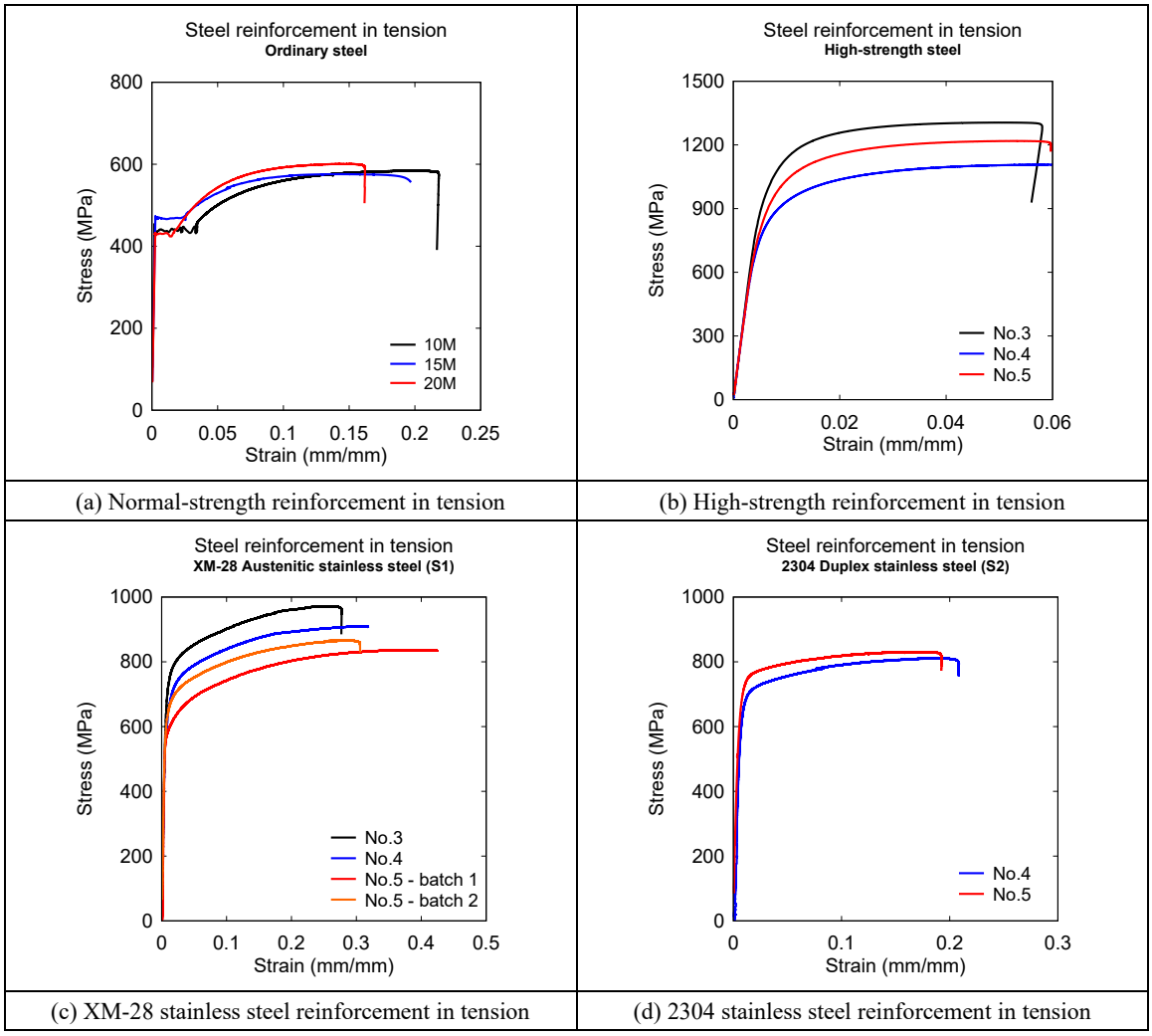

(a) Normal-strength reinforcement in tension

(b) High-strength reinforcement in tension

(c) XM-28 stainless steel reinforcement in tension

(d) 2304 stainless steel reinforcement in tension

Figure 3.6 Steel reinforcement in tension

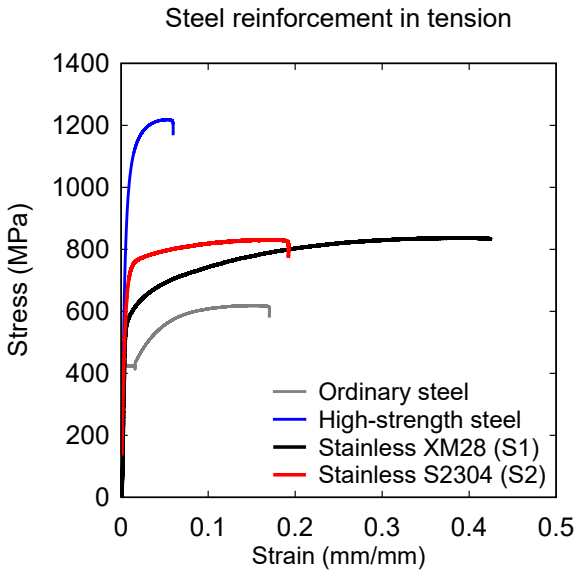

Figure 3.7 Steel reinforcement in tension (all types)

3.3.3. Fibers

Two types of steel fibers were used in this research. **Table 3.11** summarizes the properties of both fibers, while **Figure 3.8** shows sample photos. The hooked-end steel fiber (ZP 305) was used in the HSFRC in **Series 1** and **Series 2**, at volumetric ratios of 0.75% or 1%. These fibers had a length (L_f) of 30 mm, diameter (d_f) of 0.55 mm, aspect ratio (L_f/d_f) of 55 and tensile strength of 1350 MPa. Smooth straight steel fibers (OL13/0.2) were used in the UHPC mix (beams in **Series 3**) with varied volumetric ratios of 1%, 2% or 3% (in U1, U2 and U3). These fibers had a length of 13 mm, diameter of 0.2 mm, aspect-ratio of 65, and a tensile strength of 2750 MPa. A hybrid mix (0.25% of OL and 0.5% of ZP fibers) was used in one beam in Series 2B to allow for direct comparison with the beams tested by Charles (2019).

Table 3.11 Fiber properties

Fiber ID	Fiber Name	Length L_f (mm)	Diameter d_f (mm)	Aspect Ratio (mm/mm)	Tensile Strength (MPa)
ZP	ZP 305 (3D)	30	0.55	55	1350
OL	OL 13/0.2	13	0.21	62	2750

(a) Hooked-end ZP fibers (L_f = 30 mm)

(b) Straight OL fibers (L_f = 13 mm)

Figure 3.8 Photographs of fibers

3.3.4. Concrete Properties

This section summarizes the hardened state properties of the different concretes used in this research. These data include compressive strength, flexural strength/toughness and tension results from tests on standard cylinders, prisms and direct tension specimens.

3.3.4.1.Compression tests

Concrete properties in compression were determined by testing standard cylinders of each concrete type in compression using a 1000 kN PILOT CONTROL machine which was connected to a StrainSmart data acquisition system to record the data. Three 100 × 200 mm cylinders were tested in accordance with the ASTM C39 "Standard Test Method for Compressive Strength of Cylindrical Concrete Specimens" (ASTM, 2018) to determine the average compressive strength of the high-strength concrete in the Series 1-2 HSC beams. Similarly, the compressive strength of the UHPC in Series 3 was determined as per ASTM 1856 "Standard Practice for Fabricating and Testing Specimens of Ultra-High Performance Concrete" (ASTM, 2017) by testing three 75 × 150 mm cylinders. In all cases, cylinder tests were conducted on the day of the beam tests. **Table 3.12** summarizes the results from these tests. Additional sample cylinders were instrumented with LVDTs to determine the full stress-strain response of the concrete (HSC and HSFRC only). **Figure 3.10a** shows typical stress-strain curves for these concrete types.

Table 3.12 Concrete compressive strength summary

Series	Beam ID	Concrete Type	Fiber (V_f)	Cylinder Size	Cylinder Test compression strength (MPa)				Loading type [1]
					Cylinder 1	Cylinder 2	Cylinder 3	Avg.	
Series 1	C100-No.4HS-DR-d/4	HSC	-	100 × 200 mm	97.1	92.6	97.7	96	S, D
	C100-No.5HS-DR-d/4		-		91.3	93.2	98.4	94	S, D
	C100-No.4HS-DR-d/4 [x1]		-		97.1	92.6	97.7	96	Dx1
	C100-No.5HS-DR-d/4 [x1]		-		91.3	93.2	98.4	94	Dx1
	CF100-No.5HS-DR-d/2	HSFRC	Hook-end (0.75%)		101.3	100.8	97.6	100	S, D
Series 2A	C100-No.5S1-S	HSC	-	100 × 200 mm	94.8	101.8	95.5	97	S
			-		100.1	97.6	105.6	101	D
	C100-No.5S1		-		96.7	105.2	100.5	101	S
	CF100-No.5S1-S	HSFRC	Hook-end (1%)		97.6	100.5	108.2	102	S
					95.2	97.6	98.3	97	D
	CF100-No.5S1		Hook-end (1%)		112.3	110.6	105.9	110	S
					102.6	110.6	103.1	105	D
Series 2B	C100-No.4S1-DR-d/4	HSC	-	100 × 200 mm	94.6	105.2	96.5	99	S
			-		95.1	103.2	96.1	98	D
	C100-No.5S1-DR-d/4		-		98.7	105.3	104.2	103	S
			-		100.3	100.8	108.6	103	D
	C100-No.5S1-DR-d/4 [x1]		-		93.6	103.2	106.4	101	Dx1
	C100-No.5S2-DR-d/4		-		105.4	96.4	103.5	102	S
			-		97.6	100.5	103.2	100	D
	CF100-No.5S1-DR-d/2	HSFRC	Hybrid: Straight (0.25%) & Hook-end (0.5%)		106.2	109.2	107.5	108	S
					109.5	110.6	112.3	111	D
Series 3 Group 1	U3-15M	UHPC	Straight (3%)	75 × 150 mm	153.7	150.9	143.7	149	S, Dx1
	U3-No.5HS				141.6	140.7	137.8	140	S, Dx1
	U3-No.5S1				142.3	158.2	143.6	148	S, Dx1
Series 3 Group 2 (NSS)	U2-15M-DR-d/2		Straight (2%)	75 × 150 mm	152.7	136.4	131.8	140	S, Dx1
	U2-20M-DR-d/2		Straight (2%)		141.6	140.7	137.8	140	S, Dx1
	U2-20M-DR-d/2 (R)		Straight (2%)		142.5	143.2	135.5	140	S, D
Series 3 Group 2 (HSS)	U2-No.4HS-DR-d/2 (R)	UHPC	Straight (2%)	75 × 150 mm	146.3	142.5	150.6	146	S, D
	U1-No.5HS-DR-d/4		Straight (1%)		128.1	137.0	118.7	128	Dx1
	U2-No.5HS-DR-d/2		Straight (2%)		141.5	133.9	137.2	137	S, Dx1
Series 3 Group 2 (SS)	U2-No.4S1-DR-d/2 (R)	UHPC	Straight (2%)	75 × 150 mm	151.0	154.7	147.6	151	S, D
	U2-No.5S1-DR-d/2		Straight (2%)		145.2	168.6	145.6	153	S, Dx1

Note: [1] S, D, Dx1: specimens tested under static, dynamic, single dynamic loading.

3.3.4.2.Flexural tests

The flexural properties were determined by testing standard prisms in flexure. Samples were tested using a GALDIBINI SUN 60 Universal Floor Standing Testing Machine, with deflections captured using a pair of LVDTs as shown in **Figure 3.9**. For the HSC in Series 1-2, 100 mm × 100 mm × 400 mm prisms were tested over a span of 300 mm in accordance with the ASTM C1609 standard (ASTM, 2019). For the UHPC beams in Series 3, 75 mm × 75 mm × 280 mm prisms were tested over a span of 225 mm in accordance with the ASTM 1856 (ASTM, 2017) standard. **Table 3.13** reports average flexural strength and toughness properties obtained from these tests. Sample load-deflection curves are shown in **Figure 3.10(b,c)**.

Table 3.13 Results from the ASTM C1609 toughness tests

Concrete Mix	ASTM C1609										
	P_1	δ_1	P_p	δ_p	f_1	f_p	P_{600}	f_{600}	P_{150}	f_{150}	T_{150}
C100	-	-	28.4	0.09	-	8.52	-	-	-	-	-
CF100	30.3	0.06	30.3	0.06	9.09	9.09	20.83	6.2	2.0	0.6	19.14
U2	55.7	0.53	55.7	0.53	29.7	29.7	-	-	33.5	17.9	62.6
U3	65.2	0.72	66.9	0.90	34.8	35.7	-	-	58.0	30.9	85.6

L = Span Length
P_1= First-Peak Load (kN)
δ_1= Net Deflection at First-Peak Load (mm)
P_p= Peak Load (kN)
δ_p= Net Deflection at Peak Load (mm)
f_1= First-Peak Strength (MPa)
f_p= Peak Strength (MPa)
P_{600}= Residual Load at net deflection of L/600 (kN)
f_{600}= Residual Strength at net deflection of L/600 (MPa)
P_{150}= Residual Load at net deflection of L/150 (kN)
F_{150}= Residual Strength at net deflection of L/150 (MPa)
T_{150}= Area under load vs. net deflection curve (0 to L/150), (kN·mm)
FT = Flexural Toughness Factor = $(T_{150}\cdot L)/(L/150\cdot b\cdot d^2)$

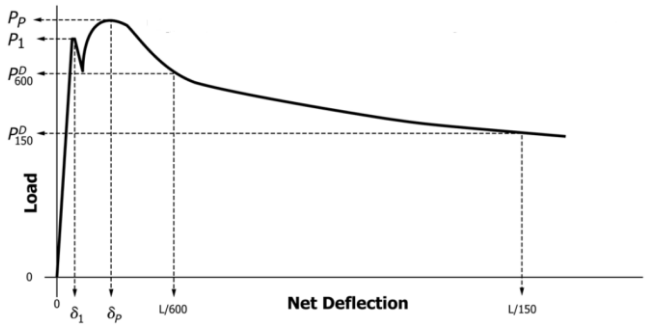

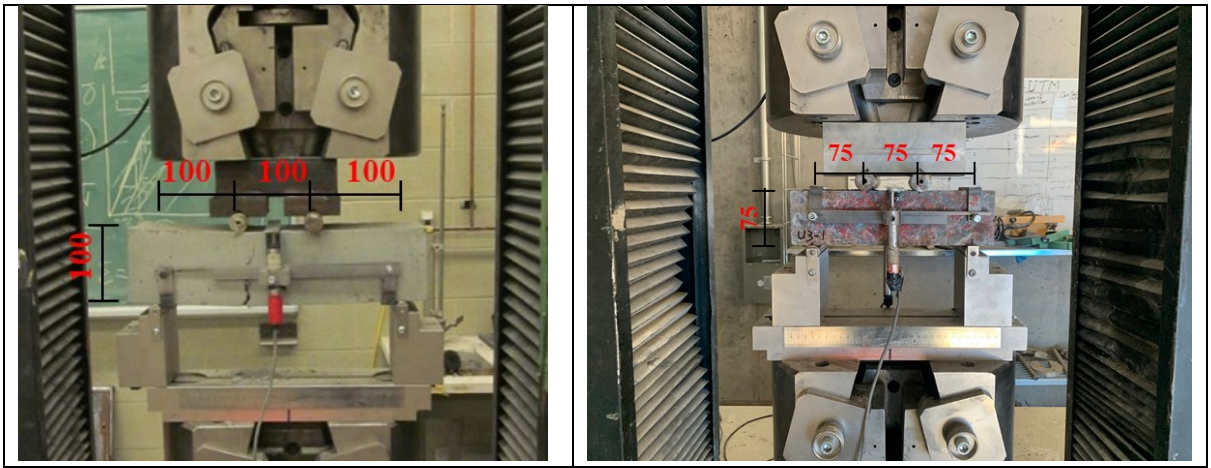

(a) Setup for HSC (b) Setup for UHPC

Figure 3.9 Flexural prism testing setup

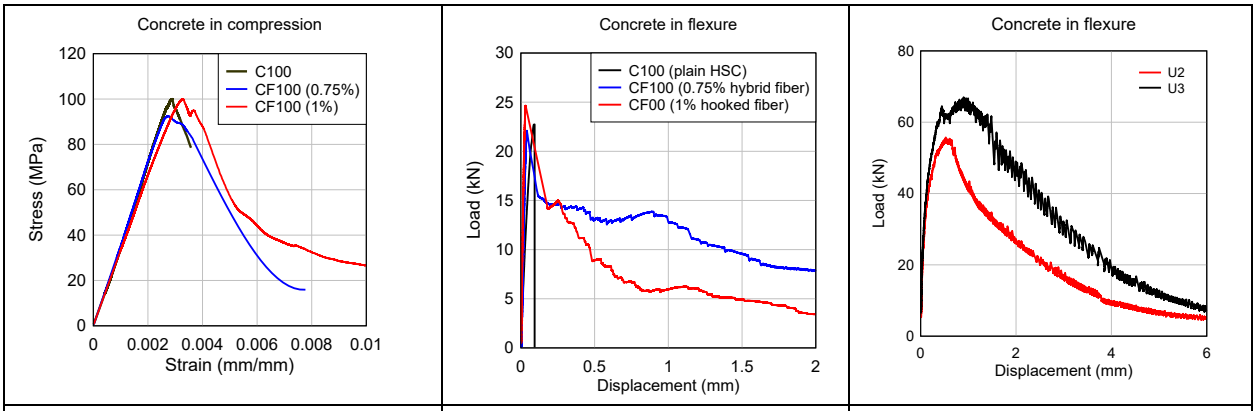

(a) Concrete in compression (HSC series)	(b) Concrete in flexure (HSC series)	(c) Concrete in flexure (UHPC series)

Figure 3.10 Material test results

3.3.4.3.Direct tension test

UHPC properties were also studied by conducting direct tension tests on UHPC prisms in accordance with the FHWA recommendations (Graybeal & Baby, 2019; Graybeal & Baby, 2013). **Figure 3.11** shows the direct tension test configuration and grip plate details for the 432-mm (17-inch)-long specimens. Graybeal and Baby (2013) suggested the use of 51 × 51 × 432 mm (2’’× 2’’ × 17’’) specimens since longer specimens can reduce the magnitude of bending stresses imparted during the initial gripping procedure. The specimens were tested under uniaxial tension test over a gauge length of 102 mm using the GALDIBINI SUN 60 Universal Floor Standing Testing Machine, with displacements captured using a pair of LVDTs. The specimen was loaded in displacement control with a loading rate of 0.025 mm/s (0.0010 inches/s) until either (1) the average displacement along the gauge length is at least 5 mm (0.2 inches) or (2) strain localization has occurred (Graybeal & Baby, 2019). Sample load-deflection curves are shown in **Figure 3.12**. The average peak tensile stress of UHPC with 2% and 3% fibers were determined as 9.82 MPa and 10.78 MPa with corresponding strains of 2.4 mm/m and 2.59 mm/m, respectively.

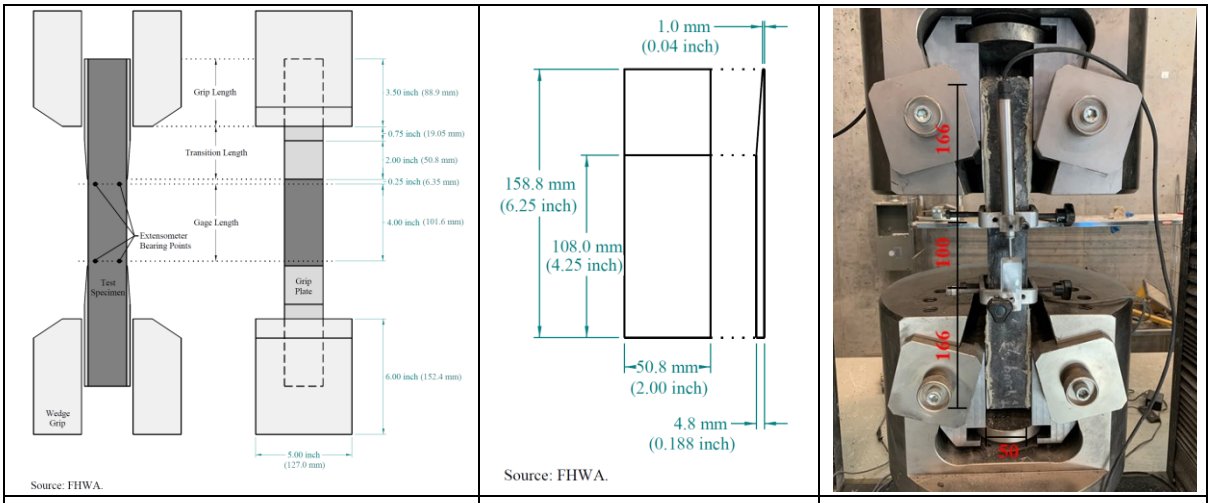

(a) Side view (left) and front view (right) (Adopted from Graybeal & Baby (2013, 2019))

(b) Grip plate (Adopted from Graybeal & Baby (2013, 2019))

(c) Test setup

Figure 3.11 Direct tension test setup and specimen dimensions

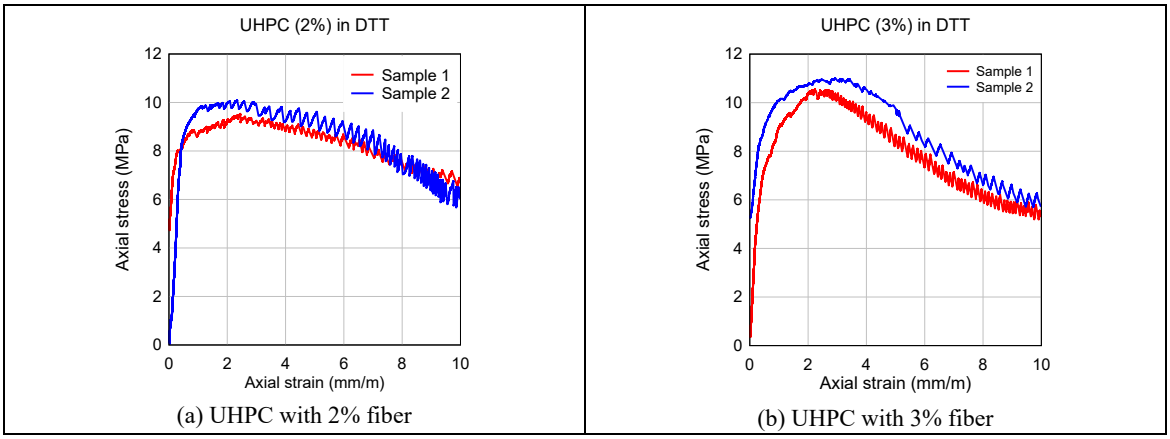

(a) UHPC with 2% fiber

(b) UHPC with 3% fiber

Figure 3.12 Direct tension test results

3.4 Test setup and procedure

3.4.1.Quasi-static tests

The static response of the beams was studied using the setup shown in **Figure 3.13a**. In all cases, the beams were tested under four-point bending over a simply-supported span of 2232 mm, with two equal shear spans of 741 mm, and a constant moment region of 750 mm. The setup included a hydraulic jack, load cells (below the load point and at the supports) and a displacement gage at mid-span. In addition, as shown in **Figure 3.14a**, strains in the tension and compression reinforcing bars were monitored using strain gages applied on the steel at midspan (SG-T and SG-C). Additional surface strain-gages were placed on the concrete in the

compression zone at midspan at depths of 20 mm, 50 mm and 80 mm from the top beam surface (SG1, SG2 and SG3) as shown in **Figure 3.14b**.

3.4.2.Blast test setup

Blast testing was conducted using the University of Ottawa shock-tube which can simulate the shockwaves caused by the far-field detonation of high explosives. **Figure 3.15a** shows the main components of this equipment which include: 1) a variable length driver (which generates the shockwave energy through the rapid release of compressed air), 2) a double diaphragm spool section (which triggers the tests), 3) an expansion section and 4) an end-frame with 2 m x 2 m opening.

Figure 3.15b shows the setup for a typical beam. The setup includes two piezoelectric pressure gages (to capture pressure-time histories), LVDTs placed at mid-span and 1/3-span (to capture displacements) and load-cells at the member supports (to capture dynamic reactions), with the beams connected to the shock-tube using simple supports (see **Figure 3.15c**). A steel load-transfer device (LTD) with two loading beams is used to collect and transfer the blast pressure onto the specimens, resulting in the same loading pattern used in the static tests. Additional instrumentation includes strain-gages to capture strains in the tension and compression bars at midspan, and a pair of high-speed cameras which record videos of the tests at a frame-rate of 500 frames/second. All data was captured using a data acquisition system at a sampling rate of 100 kHz.

3.4.3.Blast test sequence

The beams in the blast testing phase of the test program were subjected to single or gradually increasing blast pressures (repeated blasts) until failure. **Figure 3.15d** shows sample shockwaves corresponding to *Blasts-30psi* to *90psi* in the HSC series tests. Similarly, **Figure 3.15e** shows sample shockwaves corresponding to *Blasts-30psi* to *100psi* for the UHPC series tests. These blasts were obtained by varying the input driver pressure from 30-100 psi (207-690 kPa), with the driver length fixed at 9 ft (2743 mm).

Table 3.14 presents the average shockwave data corresponding to these blasts, including peak reflected pressure (P_r), peak reflected impulse (I_r), and positive phase duration (t_d) based on the data collected from all completed blast tests. Various blast and response parameters are defined in **Figure 3.15f**. To correlate the shockwaves to actual blast conditions, estimates of the corresponding scaled distances (Z) and equivalent TNT charge weights, as determined from the CSA S850 standard (CSA, 2012) are also reported in **Table 3.14**.

Table 3.14: Driver length/pressure and average reflected shockwave data

Blast ID	Driver Pressure kPa (psi)	Driver Length mm (ft)	Average Peak Reflected Pressure, P_r (kPa)	Average Peak Reflected Impulse, I_r (kPa·msec)	Average Positive Phase Duration, (msec)	Scaled distance Z (m/kg$^{1/3}$)	Equivalent Charge weight (kg)*
Blast-30psi	207 (30)	2743 (9)	44.4	360.2	20.4	7.96	248
Blast-50psi	345 (50)	2743 (9)	61.3	545.2	20.7	6.54	447
Blast-70psi	483 (70)	2743 (9)	81.3	728.0	21.3	5.59	716
Blast-90psi	620 (90)	2743 (9)	92.4	882.4	21.9	5.22	879
Blast-100psi	690 (100)	2743 (9)	104.0	978.5	23.1	4.92	1050

[a] Note: Assumed stand-off distance = 50 meters.

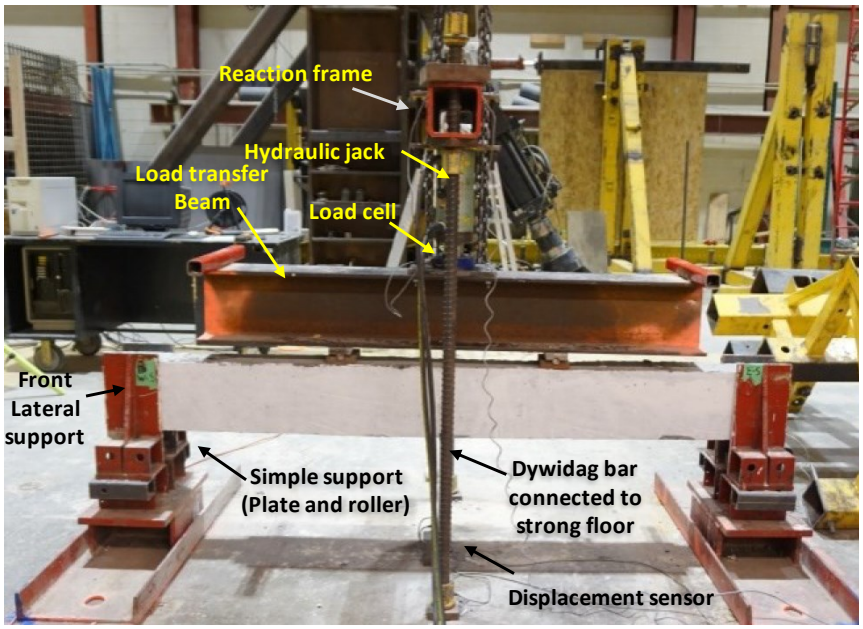

Figure 3.13 static test setup

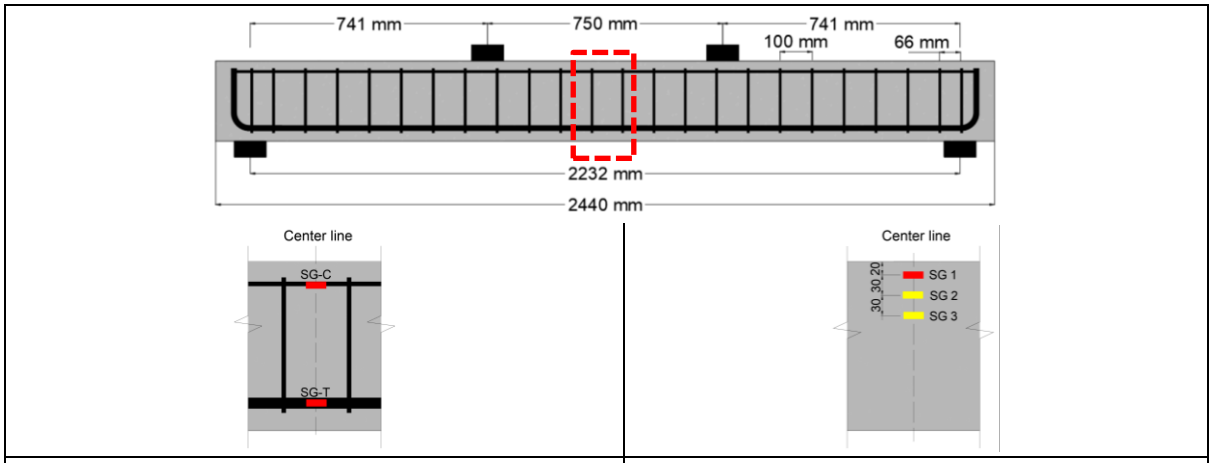

(a) Strain gauges on longitudinal reinf. (b) Strain gauges on surface concrete

Figure 3.14 Locations of steel/concrete strain gauges

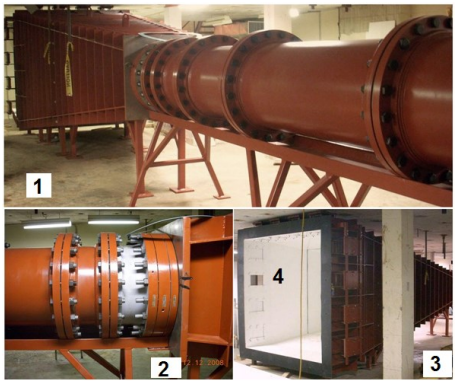

(a) Shock-tube components

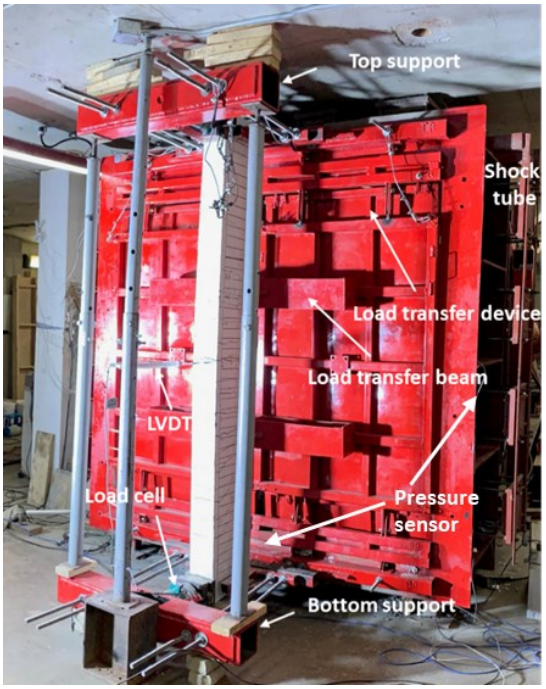

(b) Dynamic test setup

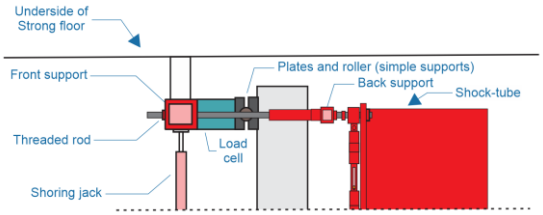

(c) Top support detail

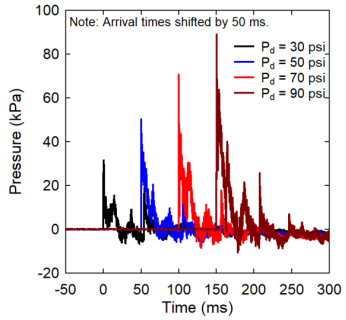

(d) Sample shockwave time histories (HSC series)

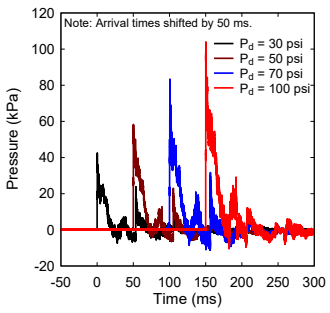

(e) Sample shockwave time histories (UHPC series)

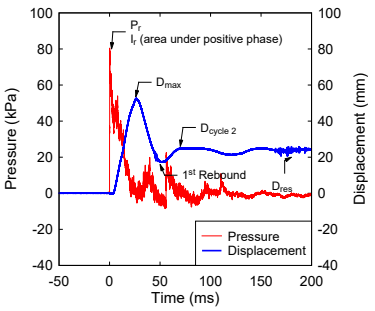

(f) Definition of key parameters

Figure 3.15 Dynamic test setup and test sequence

3.5 References (Chapters 1-3)

Aghdasi, P., & Ostertag, C. P. (2020). Tensile fracture characteristics of Green Ultra-High Performance Fiber-Reinforced Concrete (G-UHP-FRC) with longitudinal steel reinforcement. *Cement and Concrete Composites, 114*, 103749. doi:https://doi.org/10.1016/j.cemconcomp.2020.103749

Aoude, H., Dagenais, F. P., Burrell, R. P., & Saatcioglu, M. (2015). Behavior of ultra-high performance fiber reinforced concrete columns under blast loading. *International Journal of Impact Engineering, 80*, 185-202. doi:https://doi.org/10.1016/j.ijimpeng.2015.02.006

ASTM A1035/A1035M-11 (2011). Standard Specification for Deformed and Plain, Low-Carbon, Chromium, Steel Bars for Concrete Reinforcement. ASTM International, West Conshohocken, PA, pp. 5.

ASTM C1856/C1856M-17 (2017). Standard Practice for Fabricating and Testing Specimens of Ultra-High Performance Concrete. ASTM International, West Conshohocken, PA, pp. 4.

ASTM C39 / C39M-18 (2018). Standard Test Method for Compressive Strength of Cylindrical Concrete Specimens. ASTM International, West Conshohocken, PA, pp. 8.

ASTM C1609 / C1609M-19 (2019). Standard Test Method for Flexural Performance of Fiber-Reinforced Concrete (Using Beam With Third-Point Loading). ASTM International, West Conshohocken, PA, pp. 9.

ASTM A955/A955M − 20c (2020). Standard Specification for Deformed and Plain Stainless Steel Bars for Concrete Reinforcement. ASTM International, West Conshohocken, PA, pp. 16.

Burrell, R. P., Aoude, H., & Saatcioglu, M. (2013). Blast Behaviour of Ultra High Strength CRC Columns. *ACI Special Publication, 293*, 1-18.

Cavill, B., Rebentrost, M., & Perry, V. (2006). *Ductal®-An ultra-high performance material for resistance to blasts and impacts.* Paper presented at the 1st Specialty Conference on Disaster Mitigation, Calgary, Alberta, Canada.

CEB-FIP (1991). Model Code 1990. Comite Euro-International Du Beton, Paris, pp. 87-109.

Cernica, J., & Charignon, M. (1963). Ultimate static and impulse loading of reinforced concrete beams. *ACI Journal Proceedings, 60*(9), 1219-1298.

Charles, C. J. (2019). *Effect of detailing and fibers on the static and blast behaviour of high-strength concrete beams.* (MASc. thesis). University of Ottawa, Ottawa, ON, Canada.

Chen, L., Hu, Y., Ren, H., Xiang, H., Zhai, C., & Fang, Q. (2019). Performances of the RC column under close-in explosion induced by the double-end-initiation explosive cylinder. *International Journal of Impact Engineering, 132*, 103326. doi:https://doi.org/10.1016/j.ijimpeng.2019.103326

Concrete Reinforcing Steel Institute (2001). *Evaluation of reinforcing bars in old reinforced concrete structures*. Engineering Data Rep. 48.

Canadian Standards Association (CSA) (2012). Design and assessment of buildings subjected to blast loads. CSA S850-12, Mississauga, ON, Canada, pp. 126.

Concrete Reinforcing Steel Institute (2017). *FAQs About Low-Carbon, Chromium ASTM A1035 Types CS, CM and CL Steel Reinforcing Bar (ETN-M-11-17)*. http://resources.crsi.org/index.cfm/_api/render/file/?method=inline&fileID=119C15CA-A667-FBFE-FC13E2CE25B8DD93.

De Carufel, S., & Aoude, H. (2020). Combined use of UHPC and High-Performance Steel to Improve the Blast Performance of Columns with Square Cross-section. *ACI Symposium Publication, 341*, 27-47.

Fan, W., Guo, W., Sun, Y., Chen, B., & Shao, X. (2018a). Experimental and numerical investigations of a novel steel-UHPFRC composite fender for bridge protection in vessel collisions. *Ocean Engineering, 165*, 1-21. doi:https://doi.org/10.1016/j.oceaneng.2018.07.028

Fan, W., Shen, D., Huang, X., & Sun, Y. (2020a). Reinforced concrete bridge structures under barge impacts: FE modeling, dynamic behaviors, and UHPFRC-based strengthening. *Ocean Engineering, 216*, 108116. doi:https://doi.org/10.1016/j.oceaneng.2020.108116

Fan, W., Shen, D., Yang, T., & Shao, X. (2019). Experimental and numerical study on low-velocity lateral impact behaviors of RC, UHPFRC and UHPFRC-strengthened columns. *Engineering Structures, 191*, 509-525. doi:https://doi.org/10.1016/j.engstruct.2019.04.086

Fan, W., Shen, D., Zhang, Z., Huang, X., & Shao, X. (2020b). A novel UHPFRC-based protective structure for bridge columns against vehicle collisions: Experiment, simulation, and optimization. *Engineering Structures, 207*, 110247. doi:https://doi.org/10.1016/j.engstruct.2020.110247

Fan, W., Xu, X., Zhang, Z., & Shao, X. (2018b). Performance and sensitivity analysis of UHPFRC-strengthened bridge columns subjected to vehicle collisions. *Engineering Structures, 173*, 251-268. doi:https://doi.org/10.1016/j.engstruct.2018.06.113

Foglar, M., Hajek, R., Fladr, J., Pachman, J., & Stoller, J. (2017). Full-scale experimental testing of the blast resistance of HPFRC and UHPFRC bridge decks. *Construction and Building Materials, 145*, 588-601. doi:https://doi.org/10.1016/j.conbuildmat.2017.04.054

Fujikake, K. (2014). Impact performance of ultra-high performance fiber reinforced concrete beam and its analytical evaluation. *International Journal of Protective Structures, 5*(2), 167-186. doi:https://doi.org/10.1260/2041-4196.5.2.167

Fujikake, K., Senga, T., Ueda, N., Ohno, T., & Katagiri, M. (2006). Effects of Strain Rate on Tensile Behavior of Reactive Powder Concrete. *Journal of Advanced Concrete Technology, 4*(1), 79-84. doi:https://doi.org/10.3151/jact.4.79

Gholipour, G., & Billah, A. H. M. M. (2022a). Dynamic behavior of bridge columns reinforced with shape memory alloy rebar and UHPFRC under lateral impact loads. *International Journal of Impact Engineering, 168*, 104297. doi:https://doi.org/10.1016/j.ijimpeng.2022.104297

Gholipour, G., & Billah, A. H. M. M. (2022b). Nonlinear Analysis of Shear-Deficient Beams Strengthened Using UHPFRC under Combined Impact and Blast Loads. *Journal of Structural Engineering, 148*(6), 04022056. doi:https://doi.org/10.1061/(asce)st.1943-541x.0003368

Graybeal, B. A., & Baby, F. (2013). Development of Direct Tension Test Method for Ultra-High-Performance Fiber-Reinforced Concrete. *ACI Materials Journal, 110*(2), 177-186. doi:https://doi.org/10.14359/51685532

Graybeal, B. A., & Baby, F. (2019). Tension Testing of Ultra-High Performance Concrete. *No. FHWA-HRT-17-053*: U.S. Federal Highway Administration, pp. 206

Guo, W., Fan, W., Shao, X., Shen, D., & Chen, B. (2018). Constitutive model of ultra-high-performance fiber-reinforced concrete for low-velocity impact simulations. *Composite Structures, 185*, 307-326. doi:https://doi.org/10.1016/j.compstruct.2017.11.022

Hallquist, J. O. (2007). LS-DYNA keyword user's manual. *Livermore Software Technology Corporation*, pp. 2937

Huynh, L., Foster, S., Valipour, H., & Randall, R. (2015). High strength and reactive powder concrete columns subjected to impact: experimental investigation. *Construction and Building Materials, 78*, 153-171. doi:https://doi.org/10.1016/j.conbuildmat.2015.01.026

Jia, P. C., Wu, H., Wang, R., & Fang, Q. (2021). Dynamic responses of reinforced ultra-high performance concrete members under low-velocity lateral impact. *International Journal of Impact Engineering, 150*, 103818. doi:https://doi.org/10.1016/j.ijimpeng.2021.103818

Japan Society of Civil Engineers (1993). Impact behavior and design of structures. Structural Engineering Series 6 (in Japanese). Japan Society of Civil Engineers, Tokyo, pp.

Keenan, W. A. (1963). Blast Loading of Concrete Beams Reinforced with High-Strength Deformed Bars. *Technical Report R226*: U.S. Naval Civil Engineering Laboratory,

Lee, J.-Y., Aoude, H., Yoon, Y.-S., & Mitchell, D. (2020). Impact and blast behavior of seismically-detailed RC and UHPFRC-Strengthened columns. *International Journal of Impact Engineering, 143*, 103628. doi:https://doi.org/10.1016/j.ijimpeng.2020.103628

Li, J., & Wu, C. (2018). Damage evaluation of ultra-high performance concrete columns after blast loads. *International Journal of Protective Structures, 9*(1), 44-64. doi:https://doi.org/10.1177/2041419617743986

Li, J., Wu, C., & Hao, H. (2015a). An experimental and numerical study of reinforced ultra-high performance concrete slabs under blast loads. *Materials and Design, 82*, 64-76. doi:https://doi.org/10.1016/j.matdes.2015.05.045

Li, J., Wu, C., & Hao, H. (2015b). Investigation of ultra-high performance concrete slab and normal strength concrete slab under contact explosion. *Engineering Structures, 102*, 395-408. doi:https://doi.org/10.1016/j.engstruct.2015.08.032

Li, J., Wu, C., Hao, H., & Su, Y. (2015c). Investigation of ultra-high performance concrete under static and blast loads. *International Journal of Protective Structures, 6*(2), 217-235. doi:https://doi.org/10.1260/2041-4196.6.2.217

Li, J., Wu, C., Hao, H., Wang, Z., & Su, Y. (2016). Experimental investigation of ultra-high performance concrete slabs under contact explosions. *International Journal of Impact Engineering, 93*, 62-75. doi:https://doi.org/10.1016/j.ijimpeng.2016.02.007

Li, R. W., Zhou, D. Y., & Wu, H. (2020). Experimental and numerical study on impact resistance of RC bridge piers under lateral impact loading. *Engineering Failure Analysis, 109*, 104319. doi:https://doi.org/10.1016/j.engfailanal.2019.104319

Li, Y., Algassem, O., & Aoude, H. (2018). Response of high-strength reinforced concrete beams under shock-tube induced blast loading. *Construction and Building Materials, 189*, 420-437. doi:https://doi.org/10.1016/j.conbuildmat.2018.09.005

Li, Y., & Aoude, H. (2019). Blast response of beams built with high-strength concrete and high-strength ASTM A1035 bars. *International Journal of Impact Engineering, 130*, 41-67. doi:https://doi.org/10.1016/j.ijimpeng.2019.02.007

Li, Y., & Aoude, H. (2020). Influence of steel fibers on the static and blast response of beams built with high-strength concrete and high-strength reinforcement. *Engineering Structures, 221*, 111031. doi:https://doi.org/10.1016/j.engstruct.2020.111031

Liao, Q., Xie, X., & Yu, J. (2022). Numerical investigation on dynamic performance of reinforced ultra‐high ductile concrete‐ultra‐high performance concrete panel under explosion. *Structural Concrete*, 1-15. doi:https://doi.org/10.1002/suco.202100919

Liao, Z., Tang, D., Li, Z., Xue, Y., & Shao, L. (2019). Study on explosion resistance performance experiment and damage assessment model of high-strength reinforcement concrete beams. *International Journal of Impact Engineering, 133*, 103362. doi:https://doi.org/10.1016/j.ijimpeng.2019.103362

Liu, J., Li, J., Fang, J., Liu, K., Su, Y., & Wu, C. (2022a). Investigation of ultra-high performance concrete slabs under contact explosions with a calibrated K&C model. *Engineering Structures, 255*, 113958. doi:https://doi.org/10.1016/j.engstruct.2022.113958

Liu, J., Li, J., Fang, J., Su, Y., & Wu, C. (2022b). Ultra-high performance concrete targets against high velocity projectile impact – a-state-of-the-art review. *International Journal of Impact Engineering, 160*. doi:10.1016/j.ijimpeng.2021.104080

Liu, J., Wu, C., Li, J., Su, Y., & Chen, X. (2018). Numerical investigation of reactive powder concrete reinforced with steel wire mesh against high-velocity projectile penetration. *Construction and Building Materials, 166*, 855-872. doi:https://doi.org/10.1016/j.conbuildmat.2018.02.001

Liu, J., Wu, C., Li, J., Su, Y., Shao, R., Liu, Z., & Chen, G. (2017). Experimental and numerical study of reactive powder concrete reinforced with steel wire mesh against projectile penetration. *International Journal of Impact Engineering, 109*, 131-149. doi:https://doi.org/10.1016/j.ijimpeng.2017.06.006

Mao, L., Barnett, S., Begg, D., Schleyer, G., & Wight, G. (2014). Numerical simulation of ultra high performance fibre reinforced concrete panel subjected to blast loading. *International Journal of Impact Engineering, 64*, 91-100. doi:https://doi.org/10.1016/j.ijimpeng.2013.10.003

Mavis, F., & Greaves, M. (1957). Destructive impulse loading of reinforced concrete beams. *ACI Journal Proceedings, 54*(9), 233-252.

Mavis, F., & Richards, F. (1955). Impulse testing of concrete beams. *ACI Journal Proceedings, 52*(9), 93-102.

Mavis, F., & Stewart, J. (1959). Further tests of dynamically loaded beams. *ACI Journal Proceedings, 55*(5), 1215-1223.

Miyamoto, A., King, M. W., & Fujii, M. (1989). Non-linear dynamic analysis and design concepts for RC beams under impulsive loads. *Bulletin of the New Zealand national society for earthquake engineering, 22*(2), 98-111.

Mylrea, T. (1940). Effect of impact on reinforced concrete beams. *ACI Journal Proceedings, 36*(6), 581-594.

NEHRP Consultants Joint Venture (2014). *Use of High-Strength Reinforcement in Earthquake-Resistant Concrete Structures*. Washington, DC.

Oppong, K., Saini, D., & Shafei, B. (2021). Ultra high-Performance Concrete for Improving Impact Resistance of Bridge Superstructures to Overheight Collision. *Journal of Bridge Engineering, 26*(9), 04021060. doi:https://doi.org/10.1061/(asce)be.1943-5592.0001736

Othman, H., & Marzouk, H. (2016). Impact response of ultra-high-performance reinforced concrete plates. *ACI Structural Journal, 113*(6), 1325-1334. doi:https://doi.org/10.14359/51689157

Roller, C., Mayrhofer, C., Riedel, W., & Thoma, K. (2013). Residual load capacity of exposed and hardened concrete columns under explosion loads. *Engineering Structures, 55*, 66-72. doi:https://doi.org/10.1016/j.engstruct.2011.12.004

Saini, D., Oppong, K., & Shafei, B. (2021). Investigation of Concrete Constitutive Models for Ultra-High Performance Fiber-Reinforced Concrete under Low-Velocity Impact. *International Journal of Impact Engineering, 157*, 103969. doi:https://doi.org/10.1016/j.ijimpeng.2021.103969

Simms, L. (1945). Actual and estimated impact resistance of some reinforced-concrete units failing in bending. *Journal of the Institution of Civil Engineers, 23*(4), 163-179.

Stolz, A., Fischer, K., Roller, C., & Hauser, S. (2014). Dynamic bearing capacity of ductile concrete plates under blast loading. *International Journal of Impact Engineering, 69*, 25-38. doi:https://doi.org/10.1016/j.ijimpeng.2014.02.008

Su, Q., Wu, H., & Fang, Q. (2022). Calibration of KCC model for UHPC under impact and blast loadings. *Cement and Concrete Composites, 127*, 104401. doi:https://doi.org/10.1016/j.cemconcomp.2021.104401

Thai, D. K., & Kim, S. E. (2015). Failure analysis of UHPFRC panels subjected to aircraft engine model impact. *Engineering Failure Analysis, 57*, 88-104. doi:https://doi.org/10.1016/j.engfailanal.2015.07.005

Thiagarajan, G., Kadambi, A. V., Robert, S., & Johnson, C. F. (2015). Experimental and finite element analysis of doubly reinforced concrete slabs subjected to blast loads. *International Journal of Impact Engineering, 75*, 162-173. doi:https://doi.org/10.1016/j.ijimpeng.2014.07.018

Wang, W., Wu, C., Li, J., Liu, Z., & Lv, Y. (2019a). Behavior of ultra-high performance fiber-reinforced concrete (UHPFRC) filled steel tubular members under lateral impact loading. *International Journal of Impact Engineering, 132*, 103314. doi:https://doi.org/10.1016/j.ijimpeng.2019.103314

Wang, W., Wu, C., Li, J., Liu, Z., & Zhi, X. (2019b). Lateral impact behavior of double-skin steel tubular (DST) members with ultra-high performance fiber-reinforced concrete (UHPFRC). *Thin-Walled Structures, 144*, 106351. doi:https://doi.org/10.1016/j.tws.2019.106351

Wei, J., Li, J., & Wu, C. (2019). An experimental and numerical study of reinforced conventional concrete and ultra-high performance concrete columns under lateral impact loads. *Engineering Structures, 201*, 109822. doi:https://doi.org/10.1016/j.engstruct.2019.109822

Wei, J., Li, J., Wu, C., Liu, Z.-x., & Fang, J. (2021). Impact resistance of ultra-high performance concrete strengthened reinforced concrete beams. *International Journal of Impact Engineering, 158*, 104023. doi:https://doi.org/10.1016/j.ijimpeng.2021.104023

Wu, B., & Xu, S. (2020). Experimental study on damage evaluation of stainless steel–reinforced concrete piers under lateral impact. *Advances in Mechanical Engineering, 12*(5), 168781402092488. doi:https://doi.org/10.1177/1687814020924886

Wu, B., Xu, S., & Zhang, G. (2019). Study on Cumulative Damage Law of Stainless Steel-Reinforced Concrete Columns under Step Impact Loading. *Advances in Materials Science and Engineering, 2019*, 1-8. doi:https://doi.org/10.1155/2019/4076145

Wu, C., Oehlers, D. J., Rebentrost, M., Leach, J., & Whittaker, A. S. (2009). Blast testing of ultra-high performance fibre and FRP-retrofitted concrete slabs. *Engineering Structures, 31*(9), 2060-2069. doi:https://doi.org/10.1016/j.engstruct.2009.03.020

Xu, J., Wu, C., Xiang, H., Su, Y., Li, Z.-X., Fang, Q., . . . Li, J. (2016). Behaviour of ultra high performance fibre reinforced concrete columns subjected to blast loading. *Engineering Structures, 118*, 97-107. doi:https://doi.org/10.1016/j.engstruct.2016.03.048

Xu, S., Wu, P., Liu, Z., & Wu, C. (2021). Calibration of CSCM model for numerical modeling of UHPCFTWST columns against monotonic lateral loading. *Engineering Structures, 240*, 112396. doi:https://doi.org/10.1016/j.engstruct.2021.112396

Xu, S., Wu, P., & Wu, C. (2020). Calibration of KCC concrete model for UHPC against low-velocity impact. *International Journal of Impact Engineering, 144*, 103648. doi:https://doi.org/10.1016/j.ijimpeng.2020.103648

Yan, J., Liu, Y., Bai, F., Ni, X., Xu, Y., Yan, Z., & Huang, F. (2022). Dynamic response of GFRP-reinforced UHPC beams under close-in blast loading. *Materials & Design*, 111140. doi:https://doi.org/10.1016/j.matdes.2022.111140

Yi, N.-H., Kim, J.-H. J., Han, T.-S., Cho, Y.-G., & Lee, J. H. (2012). Blast-resistant characteristics of ultra-high strength concrete and reactive powder concrete. *Construction and Building Materials, 28*(1), 694-707. doi:https://doi.org/10.1016/j.conbuildmat.2011.09.014

Yoo, D.-Y., Banthia, N., Kim, S.-W., & Yoon, Y.-S. (2015). Response of ultra-high-performance fiber-reinforced concrete beams with continuous steel reinforcement subjected to low-velocity impact loading. *Composite Structures, 126*, 233-245. doi:https://doi.org/10.1016/j.compstruct.2015.02.058

Yoo, D.-Y., Banthia, N., & Yoon, Y.-S. (2017). Impact Resistance of Reinforced Ultra-High-Performance Concrete Beams with Different Steel Fibers. *ACI Structural Journal, 114*(1), 113-124. doi:https://doi.org/10.14359/51689430

Zhang, F., Shedbale, A. S., Zhong, R., Poh, L. H., & Zhang, M.-H. (2021). Ultra-high performance concrete subjected to high-velocity projectile impact: implementation of K&C model with consideration of failure surfaces and dynamic increase factors. *International Journal of Impact Engineering, 155*. doi:https://doi.org/10.1016/j.ijimpeng.2021.103907

Zhang, G., Xu, S., Xie, H., Zhou, X., & Wang, Y. (2017a). Behavior of stainless steel–reinforced concrete piers under lateral impact loading. *Advances in Mechanical Engineering, 9*(5), 168781401770993. doi:https://doi.org/10.1177/1687814017709936

Zhang, T., Wu, H., Fang, Q., Huang, T., Gong, Z. M., & Peng, Y. (2017b). UHP-SFRC panels subjected to aircraft engine impact: Experiment and numerical simulation. *International Journal of Impact Engineering, 109*, 276-292. doi:https://doi.org/10.1016/j.ijimpeng.2017.07.012

Zhang, T., Wu, H., Zhang, F. J., Fang, Q., & Huang, T. (2017c). Ballistic limit of aircraft engine missile impact on ultra-high-performance steel-fiber-reinforced concrete panels. *International Journal of Protective Structures, 8*(4), 503-523. doi:https://doi.org/10.1177/2041419617716498

Zhou, X., Zhang, H., Zhang, W., & Zhang, G. (2020). Study on the Influence of Closed-Cell Aluminum Foam on the Impact Performance of Concrete Pier after Equal Replacement with Stainless Steel Reinforcement. *Advances in Materials Science and Engineering, 2020*, 1-17. doi:https://doi.org/10.1155/2020/8356319

Zhou, X., Zhang, W., Gao, Y., Zhang, G., & Xiong, R. (2019). A Comparative Test Study of the Impact Performances of Stainless-Steel Rebar Equal-Strength Replacement Piers. *International Journal of Steel Structures, 20*(1), 67-79. doi:https://doi.org/10.1007/s13296-019-00269-5

Chapter 4 Test results from Series 1 (HSC-HSS)

Paper 1: Effects of detailing on the blast and post-blast resilience of high-strength steel reinforced concrete beams

4.1 Introduction

This chapter discusses the results from Series 1 (HSC-HSS) of the research program. The tests aimed at examining the effects of detailing and steel fibers on the static, blast and post-blast performance of high-strength concrete beams built with higher grade steel reinforcement conforming to ASTM A1035. Beams built with HSC, Grade 690 MPa high-strength bars, and detailed according to the CSA S850 standard (CSA, 2012), were tested under static and blast loads. Beams with steel fibers and relaxed detailing were also tested. Test variables included the effects of reinforcement detailing, steel type (high-strength vs. ordinary steel), and steel fibers.

4.2 Research contribution

The content in this chapter is included in the following published paper:

Li, Y., & Aoude, H. (2020). Effects of detailing on the blast and post-blast resilience of high-strength steel reinforced concrete (HSS-RC) beams. Engineering Structures, 219, 110869. doi:https://doi.org/10.1016/j.engstruct.2020.110869

4.3 Experimental program

The details of the experimental program were provided in **Chapter 3** (see *Series 1*). All beams had dimensions of 125 mm × 250 mm × 2440 mm (b × h × L), and were built with HSC and Grade 690 MPa ASTM A1035 reinforcement. Longitudinal reinforcement in tension consisted of either 2-No.4 or 2-No.5 high-strength bars (ρ = 1% or 1.5%), while transverse steel consisted of closed ties or open-stirrups made from 6 mm wire arranged at various spacing (s). As summarized in **Table 4.1** and **Figure 4.1**, the specimens can be subdivided into three groups: *Group A* beams (6 specimens) were designed according to modern blast standards, with top continuity bars and closely spaced ties at s = 50 mm (d/4) throughout the beam span; *Group B* beams (2 specimens) were designed with high-strength fiber-reinforced concrete (HSFRC) and a larger tie spacing of s = 100 mm (d/2); *Group C* includes a control set of singly-reinforced beams with "nominal detailing" with open-stirrups spaced at s = 100 mm (d/2) in the shear spans only, which were tested in a previous study by Li and Aoude (2019, 2020).

The beam nomenclature in **Table 4.1** and **Figure 4.1** indicates the design parameters of the test and control beams,, including the concrete type (C100 or CF100 for plain HSC and HSFRC, respectively), tension steel bar size (No.4 or No.5), steel grade (with "HS" indicating use of high-strength bars), and detailing level (with "DR-d/4" or "DR-d/2" indicating the use of top continuity bars and closed ties spaced at d/4 or d/2). For example, C100-No.5HS-DR-d/4 is a doubly-reinforced beam made with plain HSC, No.5 high-strength bars and "blast detailing" (ties spaced at d/4 throughout the span). Likewise, CF100-No.5HS-DR-d/2 is the companion beam with 0.75% fibers and "intermediate detailing" (increased tie spacing of d/2). On the other hand, C100-No.4HS-S and CF100-No.5HS-S are singly-reinforced HSC and HSFRC beams with "nominal detailing" (open stirrups at d/2 in the shear spans only) tested by Li and Aoude (2019, 2020). Finally, the [x1] in the nomenclature of beams C100-No.4HS-DR-d/4 [x1] and C100-No.5HS-DR-d/4 [x1] indicates the beams were tested under single, rather than repeated, blast loads.

Blast tests were conducted using the University of Ottawa shock-tube with companion beams tested under quasi-static four-point bending. Details on the test setups and testing protocols were provided in see **Section 3.4**. **Figure 4.2** shows sample shockwaves corresponding to *Blasts-30psi* to *90psi*. These blasts were obtained by varying the input driver pressure from 30 to 90 psi (207–620 kPa), with the driver length fixed at 9 ft (2743 mm). A summary of key blast parameters is presented in **Table 4.2**: including, the reflected pressures (P_r), reflected impulses (I_r) and positive shockwave duration (t_d).

Table 4.1 Beam properties and average concrete properties

Group [a]	Beam ID	Concrete		Reinforcement details				Loading type
		f'_c (MPa)	V_f (%)	Tension steel ρ	Comp. steel ρ'	Transverse steel		
						Type	Spacing	
A	C100-No.4HS-DR-d/4	95.8	-	2-No.4 (1.0%)	2-No.3 (0.6%)	Closed hoops (full span)	50 mm (d/4)	S, D
	C100-No.5HS-DR-d/4	94.3	-	2-No.5 (1.5%)	2-No.4 (1.0%)		50 mm (d/4)	S, D
	C100-No.4HS-DR-d/4 [x1]	95.8	-	2-No.4 (1.0%)	2-No.3 (0.6%)		50 mm (d/4)	Dx1
	C100-No.5HS-DR-d/4 [x1]	94.3	-	2-No.5 (1.5%)	2-No.4 (1.0%)		50 mm (d/4)	Dx1
B	CF100-No.5HS-DR-d/2	99.9	0.75%	2-No.5 (1.5%)	2-No.4 (1.0%)		100 mm (d/2)	S, D
C	C100-No.4HS-S [b]	96.4	-	2-No.4 (1.0%)	-	U-shaped Stirrups (shear span)	100 mm (d/2)	S, D
	C100-No.5HS-S [b]	95.0	-	2-No.5 (1.5%)			100 mm (d/2)	S, D
	CF100-No.5HS-S [c]	104.0	1%	2-No.5 (1.5%)			100 mm (d/2)	S, D

[a] Group A: HSC beams with blast detailing; Group B: HSFRC beams with intermediate detailing; Group C: beams with nominal detailing
[b, c] Beams in Group C were tested by Li and Aoude (2019, 2020)

(a) **Group A**: HSC beams with Blast detailing (top continuity bars and closed ties @ d/4): 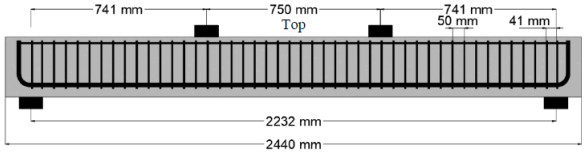	Specimens: C100-No.4HS-DR-d/4 C100-No.5HS-DR-d/4 C100-No.4HS-DR-d/4 [x1] C100-No.5HS-DR-d/4 [x1]	Test S, D S, D Dx1 Dx1
(b) **Group B**: HSFRC beam with Intermediate detailing (top continuity bars and closed ties @ d/2): 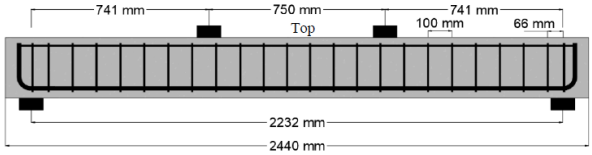	Specimens: CF100-No.5HS-DR-d/2	Test S, D
(c) **Group C**: HSC beams with Nominal detailing (singly-reinforced and stirrups @ d/2): 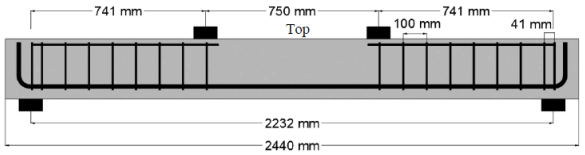	Control specimens: C100-No.4HS-S C100-No.5HS-S CF100-No.5HS-S	Test S, D S, D S, D

Figure 4.1 Specimen Designs

Note: S = static test, D = dynamic blast test

Table 4.2 Driver length/pressure and average reflected shockwave data

Blast ID	Driver Pressure kPa (psi)	Driver Length mm (ft)	Average Peak Reflected Pressure, P_r (kPa)	Average Peak Reflected Impulse, I_r (kPa·ms)	Average Positive Phase Duration, t_d (ms)
Blast-30psi	207 (30)	2743 (9)	44.4	360.2	20.4
Blast-50psi	345 (50)	2743 (9)	61.3	545.2	20.7
Blast-70psi	483 (70)	2743 (9)	81.3	728.0	21.3
Blast-90psi	620 (90)	2743 (9)	92.4	882.4	21.9

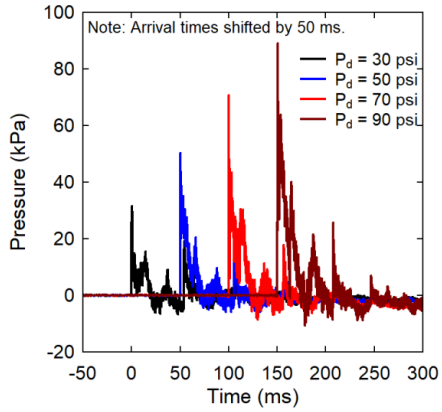	Specimens: C100-No.4HS-DR-d/4 C100-No.5HS-DR-d/4 C100-No.4HS-DR-d/4 [x1] C100-No.5HS-DR-d/4 [x1] CF100-No.5HS-DR-d/2	Test sequence: Blast-30, 50, 70 psi Blast-30, 50, 70, 90 psi Blast-70 psi Blast-90 psi Blast-30, 50, 70, 90 psi
	Control specimens: C100-No.4HS-S C100-No.5HS-S CF100-No.5HS-S	Test sequence: * Blast-30, 40, 50 psi Blast-30, 50, 70 psi Blast-30, 50, 70, 90, 100 psi

Figure 4.2 Sample shockwaves and testing protocols

* Note: an additional elastic shot using 17 psi driver pressure was applied to the control specimens prior to *Blast-30psi*.

4.4 Static test results

The static load-deflection and load-strain curves are shown in **Figure 4.3**, while key parameters from these curves are summarized in **Table 4.3**, including: maximum load (P_{max}), secant stiffness (k_s), yield displacement (Δ_y), maximum (failure) displacement (Δ_{max}), ductility (Δ_{max}/Δ_y) and toughness (A_u), defined as the area under the curves up to Δ_{max}. Post-blast residual static test results are presented in **Table 4.5**. The following sections review the effects of steel detailing, fibers and steel type on the static response of the beams.

Table 4.3 Results from static tests

Beam	Load		Displacement		Secant Stiffness k_s (N/mm)	Ductility Δ_{max}/Δ_y	Toughness A_u (J)
	Yield P_y (kN)	Peak P_{max} (kN)	Yield Δ_y (mm)	Failure Δ_{max} (mm)			
C100-No.4HS-DR-d/4	140.6	160.5	25.2	79.9	7079	3.2	9673
C100-No.5HS-DR-d/4	184.1	207.9	28.4	96.3	7960	3.4	18028
CF100-No.5HS-DR-d/2	213.5	244.5	26.1	116.0	10049	4.4	23658
C100-No.4HS-S	118.4	126.7	29.2	35.2	4741	1.2	2655
C100-No.5HS-S	185.4	194.7	31.4	34.0	6152	1.1	3686
CF100-No.5HS-S	214.8	244.6	26.0	65.5	10084	2.5	12264

Note: P_y = yield strength; P_{max} = peak static strength; Δ_y = yield displacement; Δ_{max} = maximum displacement; k_s = secant stiffness; A_u = area under the load deflection curve up to Δ_{max}.

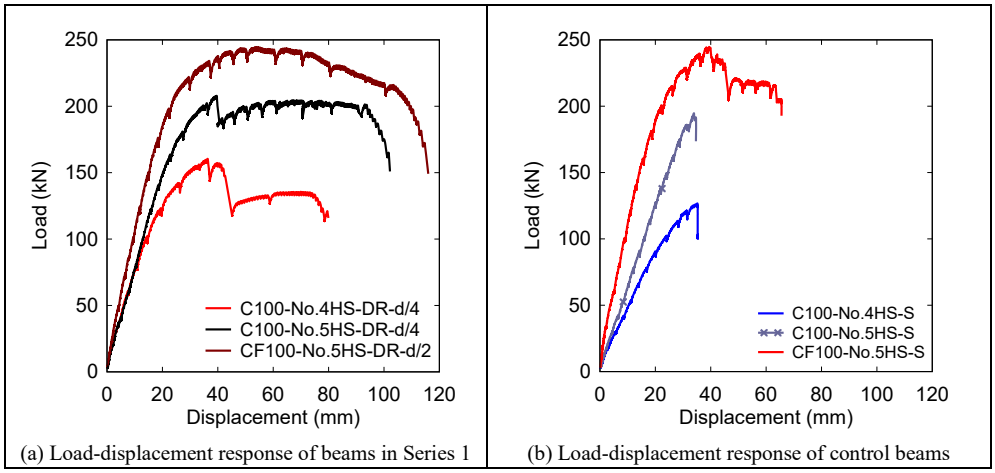

(a) Load-displacement response of beams in Series 1 (b) Load-displacement response of control beams

Figure 4.3 Summary of static test results (load-deflection curves)

4.4.1. Effects of reinforcement detailing

The effect of blast detailing in the high-strength steel HSC beams can be examined in **Figure 4.4a** which compares the responses of beams C100-No.4HS-DR-d/4 and C100-

No.5HS-DR-d/4, with the nominally-detailed beams tested by Li and Aoude (2019) (C100-No.4HS-S and C100-No.5HS-S). Photos illustrating the beam failures are shown in **Figure 4.5**.

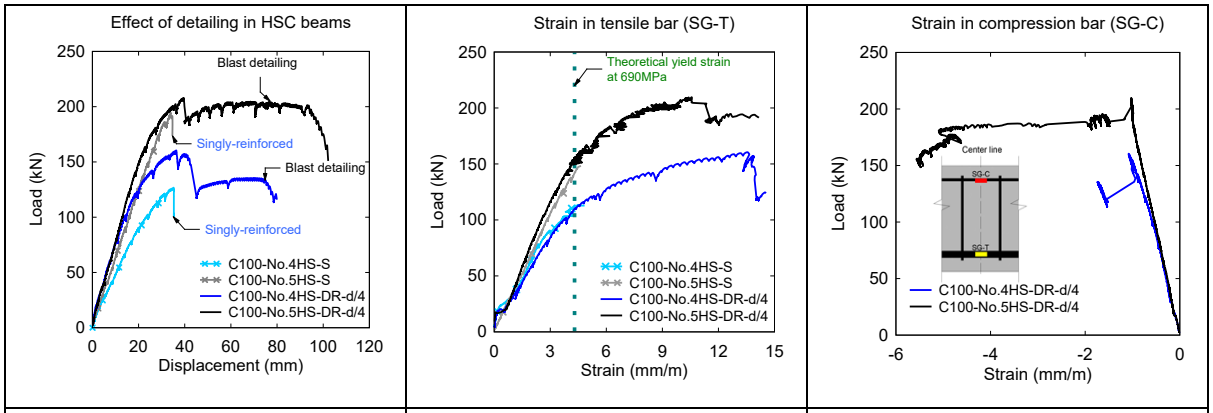

(a) load-deflection curves | (b) Strains in tension HS bars | (c) Strain in compression bar

Figure 4.4 Static results: effects of reinforcement detailing

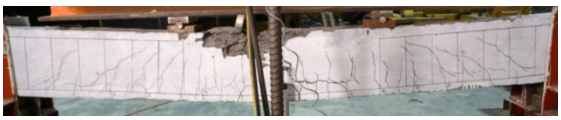

Sudden concrete crushing: $\Delta = 35\ mm$

(a) C100-No.4HS-S (Nominal detailing)

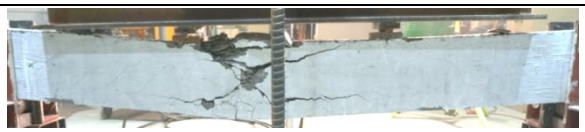

Sudden concrete crushing: $\Delta = 34\ mm$

(b) C100-No.5HS-S (Nominal detailing)

$\Delta = 36\ mm$

Bar rupture: $\Delta_{max} = 80\ mm$

(c) C100-No.4HS-DR-d/4 (Blast detailing)

$\Delta = 70\ mm$

Bar rupture: $\Delta_{max} = 96\ mm$

(d) C100- No.5HS-DR-d/4 (Blast detailing)

(e) C100-No.4HS-DR-d/4
(At bar rupture)

(f) C100-No.5HS-DR-d/4
(Just before bar rupture)

Figure 4.5 Damage/failure modes under static loading: effects of detailing

It can be observed that the improved steel detailing enhanced all aspects of structural response including strength, stiffness and ductility. In the No.4 series, beam C100-No.4HS-DR-d/4 shows increases of 21% and 49% in strength (P_{max}) and stiffness (k_s) when compared to beam C100-No.4HS-S. Likewise, beam C100-No.5HS-DR-d/4 shows improvements of 7% and 29% in strength/stiffness when compared to C100-No.5HS-S. More impressive is the enhancement in post-peak ductility. While the control beams fail suddenly by crushing of concrete soon after peak, the blast-detailed beams show sustained post-peak response prior to failure. It is noted that the drop in load-carrying capacity at a displacement of ~40 mm occurred due to the sudden crushing of the top cover concrete. Nonetheless, a clear post-peak response was developed in the specimens with blast detailing. As a result, beams C100-No.4HS-DR-d/4 and C100-No.5HS-DR-d/4 show important increases in maximum displacement (Δ_{max}), ductility (Δ_{max}/Δ_y) and overall toughness (A_u) when compared to the companion beams with nominal detailing (see **Table 4.3**). The improvement can be explained by the ability of the compression bars and closely spaced ties to confine and strengthen the midspan concrete compression zone, which in turn allowed for better engagement (higher strain development) in the HS steel bars in tension (see **Figure 4.4b**). Indeed, beams C100-No.4HS-DR-d/4 and C100-No.5HS-DR-d/4 failed at maximum displacements of 80 mm (L/28) and 96 mm (L/23), not by crushing of concrete, but by rupture of the high-strength reinforcing bars which underwent large inelastic strains before failure. The results clearly demonstrate the substantial increases in ductility that can be gained through careful detailing in ASTM A1035-reinforced HSC beams, even when using relatively high tension steel ratios.

Figure 4.4a can also be used to examine the effect of tension steel ratio in the doubly-reinforced beams with No.4/No.5 high-strength bars. In addition to the increase in strength and stiffness, it can be observed that increasing the tension steel ratio from 1% to 1.5% increases the failure displacement due to the ability of the increased bar size to delay tension bar rupture. Indeed, when concrete is well confined, failure in beams with high-strength bars can be governed by tension bar rupture (Ousalem et al., 2009; Rautenberg et al., 2013; Cheng & Giduquio, 2014; Trejo et al., 2016; Bandelt & Billington, 2016; Su et al., 2019). The blast-detailed beams in the current study showed high deformation capacity, despite the bar fractures. However, since such failure results in a total loss of member strength, this failure mode should be considered when designing lightly-reinforced HSS-RC beams (i.e., a minimum area of longitudinal reinforcement should be required to prevent premature bar fracture). This is especially important due to the relatively low strain capacity of the high-strength ASTM A1035

reinforcement. Further research on beams having varying geometries, span-to-depth ratios, concrete strengths/types is required to develop such minimum limits.

In addition to providing confinement, the spacing of transverse reinforcement is a critical parameter that affects the stability of compression steel in doubly-reinforced beams. Giduquio et al. (2015) previously recommended a maximum spacing of $8d_b$ for the transverse steel in ASTM A1035-reinforced beams to prevent against premature bar buckling. Similarly, Park and Paulay (1975) and Rashid and Mansur (2005) recommended reducing the tie spacing in the plastic hinge zone in conventional RC beams to d/4 to ensure ductility. Examining the photos in **Figure 4.5**, it can be observed that the use of d/4 tie spacing ensured excellent control of concrete damage and prevented bar buckling in the tested beams. This is especially evident in beam C100-No.5HS-DR-d/4, where the top cover concrete is lost, but the core concrete remained well-confined, with bar buckling prevented until very late stages of loading. The results confirm the improved response characteristics that can be gained from the use of blast detailing in HSS-RC beams, even under quasi-static loads.

4.4.2. Ability of fibers to relax detailing

The effect of steel fibers and their ability to relax detailing can be examined in **Figure 4.6a** which compare the responses of beams C100-No.5HS-DR-d/4 and CF100-No.5HS-DR-d/2, which were built with plain HSC vs. HSFRC, and ties spaced at 50 mm (d/4) vs. 100 mm (d/2), reflecting blast and intermediate detailing, respectively. For comparison, the responses of the companion singly-reinforced C100-No.5HS (plain HSC) and CF100-No.5HS-S (HSFRC having 1% fibers) tested by Li and Aoude (2019, 2020), are also shown in the Figure.

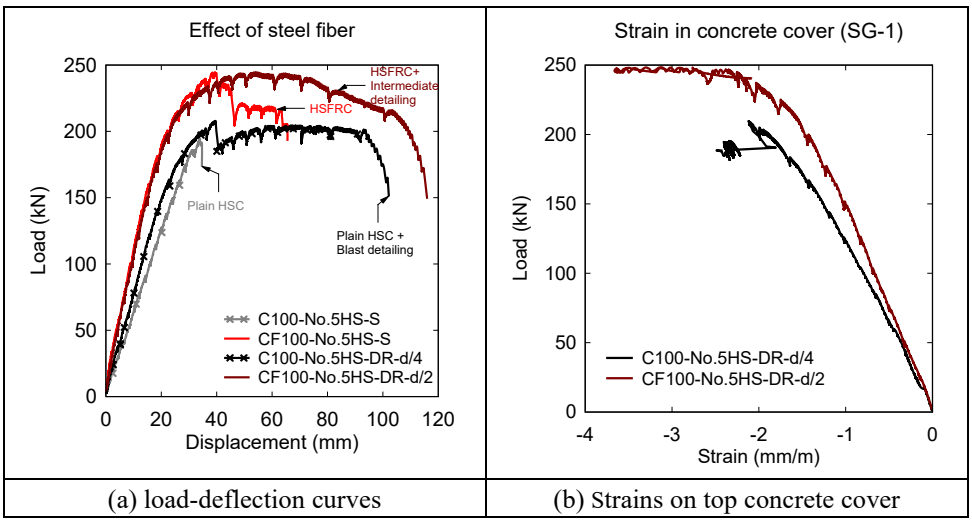

(a) load-deflection curves (b) Strains on top concrete cover

Figure 4.6 Static results: effects of reinforcement detailing

The results from the singly-reinforced beams (which did not have compression bars or ties in the midspan zone) clearly demonstrate the benefits of introducing fibers in HS steel RC beams. In addition to increasing strength (P_{max}) and stiffness (k_s), provision of 1% steel fibers leads to important increases in maximum displacement (Δ_{max}), ductility (Δ_{max}/Δ_y) and overall toughness (A_u) (see **Figure 4.6a** and **Table 4.3**). The enhanced behavior can be explained by the ability of fibers to improve the toughness of the high-strength concrete in compression (Mansur et al. (1997)).

$\Delta = 65\ mm$

Concrete compression failure: $\Delta_{max} = 65\ mm$

(a) CF100-No.5HS-S
(Nominal detailing + fibers)

$\Delta = 100\ mm$

Bar rupture: $\Delta_{max} = 116\ mm$

(b) CF100-No.5HS-DR-d/2
(Intermediate detailing + fibers)

(c) C100-No.5HS-DR-d/4
(Just before bar rupture)

(d) CF100-No.5HS-DR-d/2
(Just before bar rupture)

Figure 4.7 Damage/failure modes under static loading: effect of fibers

The result from beam CF100-No.5HS-DR-d/2 shows that the use of moderate amounts of steel fibers (0.75%) combined with compression bars and intermediate ties allows for a synergy effect which allows for impressive structural performance. Indeed, the results show that fibers can be used to relax detailing (from d/4 to d/2), with a response that not only matched, but out-performed that of beam C100-No.5HS-DR-d/4, with increased strength, stiffness and overall toughness (area under the load-deflection curve) when compared to its companion. The flexural resistance enhancement results from the improve tensile response of HSFRC which is related to the fiber pullout resistance across cracks as reported by Ashour and Wafa (1993) and Imam et al. (1995), and also recognized in the flexural capacity equations

recommended in ACI-544.4R (ACI, 1988). Examining the failure photos, it can be seen that crushing of the top cover concrete is well controlled in the beam with fibers (see **Figure 4.7d**). Indeed, **Figure 4.6b** shows the development of higher strains in strain gage SC1 in the beam containing fibers (well above the 0.003 crushing strain that is generally assumed for plain concrete). Similarly, while both beams show high ductility, a larger maximum displacement is experienced by the fiber-reinforced specimen (Δ_{max}^{S} = 116 vs. 96 mm). The result can be explained by the ability of the fibers to contribute to tension resistance, which in turn reduces strains and delays rupture in the high-strength bars. On the other hand, previous research indicates that fibers can result in crack localization in HSC beams which can lead to bar rupture failures, especially as the steel ratio is reduced (Yoo et al., 2017b; Dancygier & Karinski, 2019). In the current study Beam CF100-No.5HS-DR-d/2 showed high deformation capacity and ductility of $\Delta_{max}/\Delta_y > 4$, despite the bar fracture, due to the relatively high tension steel ratio. However, the issue of premature bar fracture should be considered when using fibers in lightly-reinforced HSS-RC beams due to the limited strain capacity of the high-strength reinforcement.

4.4.3. Effects of steel type and ability of HS steel to reduce reinforcement

The effect of steel type (Grade 690 MPa vs Grade 400 MPa) on the static response of beams with blast detailing can be examined in **Figure 4.8** which compares the responses of beam C100-No.5HS-DR-d/4 (ρ = 1.5%) from the current study, and beams C100-15M-DR-d/4 (ρ = 1.5%) & C100-20M-DR-d/4 (ρ = 2.4%) tested by Charles (2019). The companion beams contained 2-15M and 2-20M normal-strength tension bars. All four beams were doubly-reinforced and provided with closed ties spaced at 50 mm (d/4) throughout their spans.

Comparing beams C100-No.5HS-DR-d/4 and C100-15M-DR-d/4 (equal tension steel ratios of 1.5%), it can be seen that the high-strength bars significantly increased load-carrying capacity (P_{max}= 245 and 108 kN) and stiffness (k_s = 8180 and 6562 N/mm). On the other hand, the use of high-strength bars resulted in a relative loss in ductility (Δ_{max}= 4.4 vs. 10), with failure transitioning to bar rupture in the beam with No.5HS bars (see **Figure 4.9**). The main reason for this observation in the reduced tension strain capacity of the high-strength reinforcement (fracture strain, ε_u = 6%) when compared to that of the normal-strength reinforcement (ε_u = 20%). Next, the responses of beams C100-No.5HS-DR-d/4 (ρ = 1.5%) and C100-20M-DR-d/4 (ρ = 2.4%), which had similar ρf_y ratios of 10.4 and 9.6 MPa, can be compared. It can be observed that the beam with reduced amounts of high-strength bars shows a higher load resistance when compared to the more heavily reinforced beam with 20M normal-

strength bars. The results confirm that reducing the steel area in HSS-RC beams (in proportion to the yield strength) results in comparable performance when compared to conventionally-reinforced HSC beams. On the other hand, high-strength steel shows reduced strain capacity which can result in earlier bar rupture failures when compared to normal-strength reinforcement, and this effect should be considered in design.

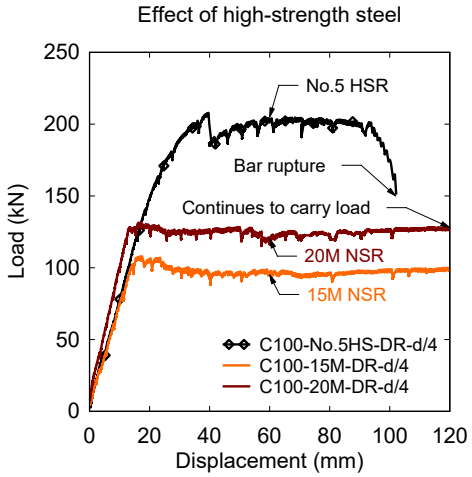

Figure 4.8 Static results: effects of steel type

Cover concrete crushing: Δ_{max}= 150 mm

$\Delta = 100\ mm$

Bar rupture: Δ_{max}= 116 mm

(a) C100-15M-DR-d/4 (normal-strength steel)

(b) C100-No.5HS-DR-d/4 (high-strength steel)

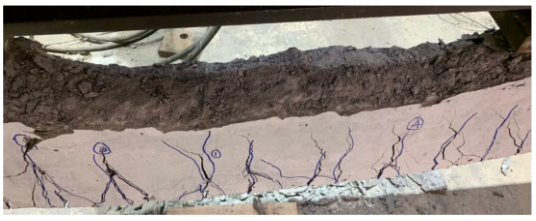

(c) C100-15M-DR-d/4 (normal-strength steel)

(d) C100-No.5HS-DR-d/4 (high-strength steel)

Figure 4.9 Damage/failure modes under static loading: effects of steel type

4.5 Blast test results

The results from the blast tests are summarized in **Table 4.4**, which reports the shockwave data (P_r , I_r and t_d = peak reflected pressure, impulse, and positive phase duration) as well as specimen response after each test (D_{max} , D_{res} and θ_{max} = maximum displacement,

residual displacement and support rotation) for all tested beams. Photos showing the damage in the beams are presented in **Figure 4.10** and **Figure 4.11**, while displacement comparisons are shown in **Figure 4.12** to **Figure 4.16**.

Table 4.4 also compares the results with the response limits in the CSA S850 blast standard (CSA, 2012). These response limits (B1-B4) correspond to specific values of support rotation (θ_{max}) or ductility ratio (μ_{max}). In the case of singly-reinforced and doubly-reinforced beams, B1, B2, B3 and B4 correspond to $\mu_{max} = 1$, $\theta_{max} = 1°$ and 4°, $\theta_{max} = 4°$ and 6°, and $\theta_{max} = 10°$, respectively. These limits in turn define component damage levels: "Blowout" (greater than B4), "Hazardous failure" (between B4 and B3); "Heavy" (between B3 and B2); "Moderate" (between B2 and B1) and "Superficial" (less than B1). The following sections review the effects of detailing, fibers and steel type on the blast response of the beams.

Table 4.4 Results from the blast tests

Beams	Blast ID (psi)	Shockwave Properties [1]			Specimen Response [2]					CSA S850 Response limits and Component damage	
		P_r (kPa)	I_r (kPa·ms)	t_d (ms)	D_{max} (mm)	D_{res} (mm)	θ_{max} (°)	$D_{\sum res}$ (mm)	Observed Damage [Max. Crack width]	Response limit	Expected Damage level
C100-No.4HS-DR-d/4	30	45.0	367.2	20.9	20.4	5.4	1.0	5.4	Minor F cracking [HL]	<B1	Superficial
	50	57.5	531.5	20.8	35.6	9.2	1.8	14.6	Moderate F cracking [0.5]	B1-B2	Moderate
	70	80.5	722.5	20.9	52.6	24.7	2.7	39.3	Cover crushing & Moderate F cracking [3.0]	B1-B2	Moderate
C100-No.4HS-DR-d/4 (x1)	70	80.6	723.8	21.3	53.9	26.7	2.8	26.7	Moderate F cracking [2.0]	B1-B2	Moderate
C100-No.5HS-DR-d/4	30	44.2	362.9	20.1	15.2	1.3	0.8	1.3	Minor F cracking [HL]	<B1	Superficial
	50	63.4	574.1	20.7	26.8	4.3	1.4	5.6	Minor F cracking [0.3]	B1-B2	Moderate
	70	85.7	739.6	21.3	41.4	8.8	2.1	14.4	Moderate F cracking [1.0]	B1-B2	Moderate
	90	90.4	876.5	21.6	56.4	17.8	2.9	32.2	Cover crushing & Moderate F cracking [2.5]	B1-B2	Moderate
C100-No.5HS-DR-d/4 (x1)	90	82.7	824.4	21.7	51.7	21.0	2.7	21	Cover crushing & Moderate F cracking [1.5]	B1-B2	Moderate
CF100-No.5HS-DR-d/2	30	44.1	350.6	20.3	15.6	2.3	0.8	2.3	Minor F cracking [HL]	<B1	Superficial
	50	62.9	530.0	20.6	25.0	0.9	1.3	3.2	Minor F cracking [HL]	B1-B2	Moderate
	70	78.3	725.9	21.6	32.6	7.7	1.7	10.9	Minor F cracking [0.4]	B1-B2	Moderate
	90	94.4	920.8	22.2	40.9	15.6	2.1	26.5	Moderate F cracking [1.25]	B1-B2	Moderate

[1]: P_r = Reflected pressure; I_r = Reflected impulse; t_d = positive phase duration;
[2]: D_{max}= maximum displacement;D_{res}= residual displacement; θ_{max}= maximum support rotation; $D_{\sum res}$ = cumulative residual displacement.

	(a) C100-No.5HS-S *@ Blast-70psi* **(singly-reinforced)**	(b) C100-No.5HS-DR-d/4 *@ Blast-90psi* **(blast-detailed)**	(c) CF100-No.5HS-DR-d/2 *@ Blast-90psi* **(fiber-reinforced)**
Video still	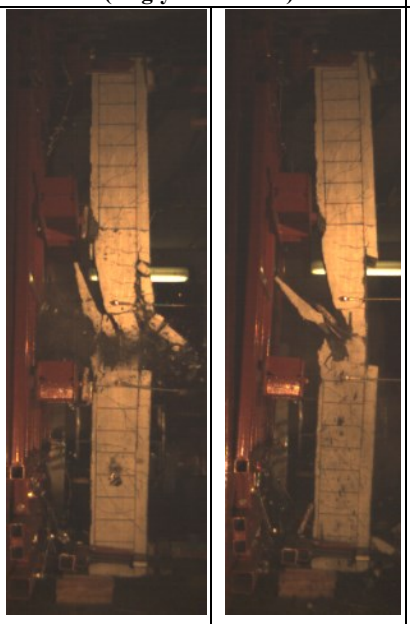	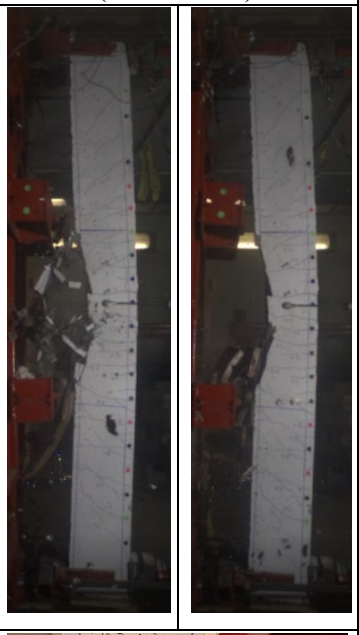	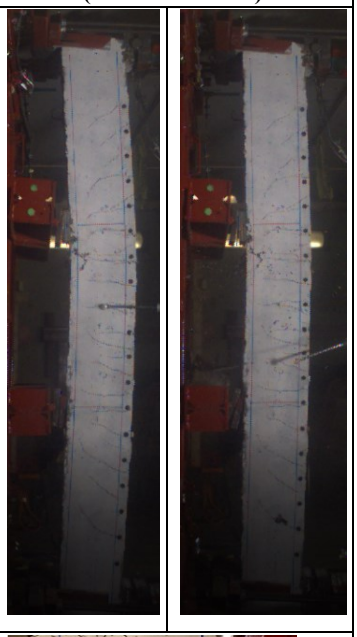
Close-in damage	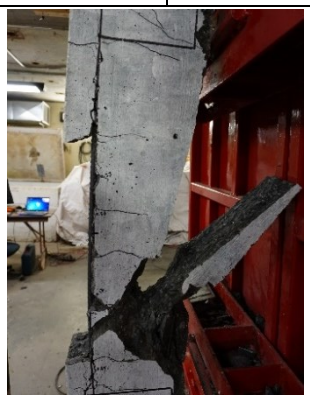		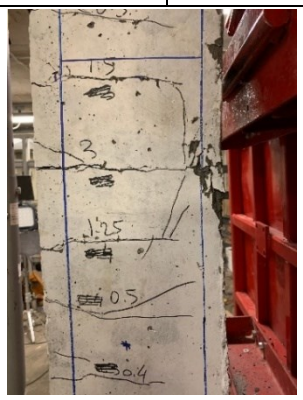

Figure 4.10 High-speed stills and close-up photos showing failure process and damage in beams.

(a) Control (No.4)	(b) Blast detailing (No.4)		(c) Control (No.5)	(d) Blast detailing (No.5)	
C100-No.4HS-S	**C100-No.4HS-DR-d/4**		**C100-No.5HS-S**	**C100-No.5HS-DR-d/4**	
Blast-50psi	*Blast-50psi*	*Blast-70psi*	*Blast-70psi*	*Blast-70psi*	*Blast-90psi*
		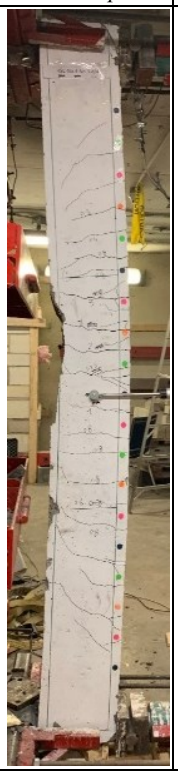		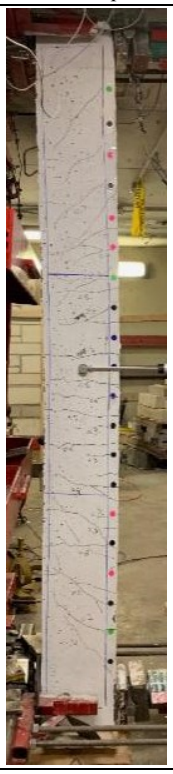	
(e) Control FRC (1% fibers)		**(f) Intermediate detailing (0.75% fibers)**		**(g) Companion beams tested under single blasts**	
CF100-No.5HS-S		**CF100-No.5HS-DR-d/2**		**C100-No.4HS-DR-d/4 [x 1]**	**C100-No.5HS-DR-d/4 [x 1]**
Blast-70psi	*Blast-90psi*	*Blast-70psi*	*Blast-90psi*	*Blast-70psi*	*Blast-90psi*
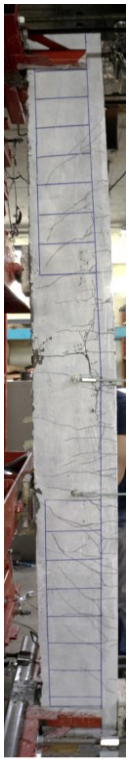		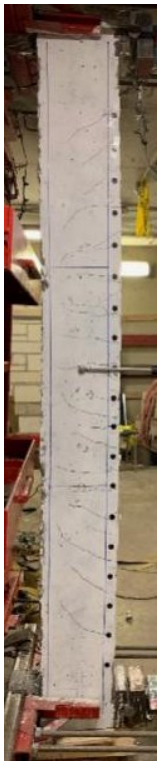	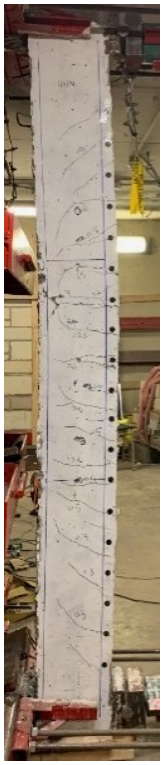	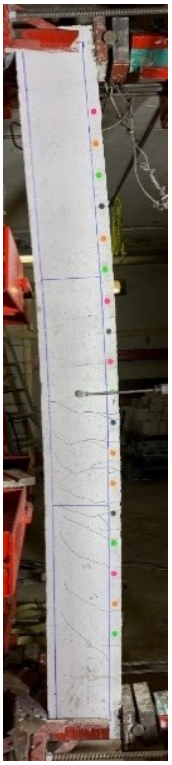	

Figure 4.11 Blast damage at Blasts 50psi, 70psi and 90psi

4.5.1.Effects of reinforcement detailing

The previous sections demonstrated the benefits of improved steel detailing on the static response of the HSS-RC beams. As demonstrated in this section, the use of blast detailing also improves all aspects of blast response in such beams. **Figure 4.12** compares the displacements in the companion blast-detailed and nominally-detailed beams from the current study and Li and Aoude (2019). Beginning with the No.4 series, it can be observed that beam C100-No.4HS-DR-d/4 shows important reductions of 9% (20.4 mm vs 22.4 mm) and 32% (35.6 mm vs 52.7 mm) in maximum displacements when compared to C100-No.4HS-S at *Blasts-30psi* and *50psi* (see **Figure 4.12a**). No clear trend emerges for the residual displacements; however, the use of compression bars results in significant reductions in rebound displacements. Importantly, blast detailing prevents failure at *Blast*-50psi (I_r = 540 kPa·ms) which resulted in a support rotation of θ_{max}= 2.4º ("Heavy" damage) and severe concrete failure in the HSC beam with nominal detailing (see **Figure 4.12a**). In comparison, beam C100-No.4HS-DR-d/4 survives *Blast*-50psi, and a further test at *Blast*-70psi, with support rotations of 1.8º and 2.7º ("moderate" damage). As shown in **Figure 4.11b** the beam shows high damage tolerance, with damage limited to loss of the top concrete cover in the midspan region. Moreover, this beam showed significant post-blast residual capacity in next sub-section.

Figure 4.12b compares the results for the beams in the No.5 series. Similar to the previous set, beam C100-No.5HS-DR-d/4 shows decrease of 14% (15.2 mm vs. 17.7 mm) and 36% (41.4 mm vs. 64.7 mm) in maximum deformations at *Blast-30psi* and *Blast-70psi* when compared to C100-No.5HS-S. Failure in beam C100-No.5HS-S occurred at *Blast-70psi* (I_r = 750 kPa·ms) which resulted in a support rotation of θ_{max} = 3º ("heavy" damage), with complete disintegration of the HSC compression zone and significant blast fragments (see **Figure 4.11c** and **Figure 4.10a**). In comparison damage remained well controlled in the beam with blast detailing at *Blast-70psi*, and subsequent testing at *Blast-90psi* (I_r = 877 kPa-ms), with support rotations of θ_{max}= 2.1º and 2.9º ("moderate" damage). Similar to the previous series, damage in the blast-detailed beam was limited to top cover concrete crushing, with the use of closely spaced ties ensuring integrity of core concrete and preventing bar buckling (see **Figure 4.11d**). Similarly, the C100-No.5HS-DR-d/4 beam showed significant post-blast residual capacity, as shown in **Figure 4.17b**. In summary, the results demonstrate the significant increases in blast resistance and ductility that can be gained from the use of blast detailing in high-strength steel reinforced concrete beams designed using the guidelines in the CSA S850 blast standard.

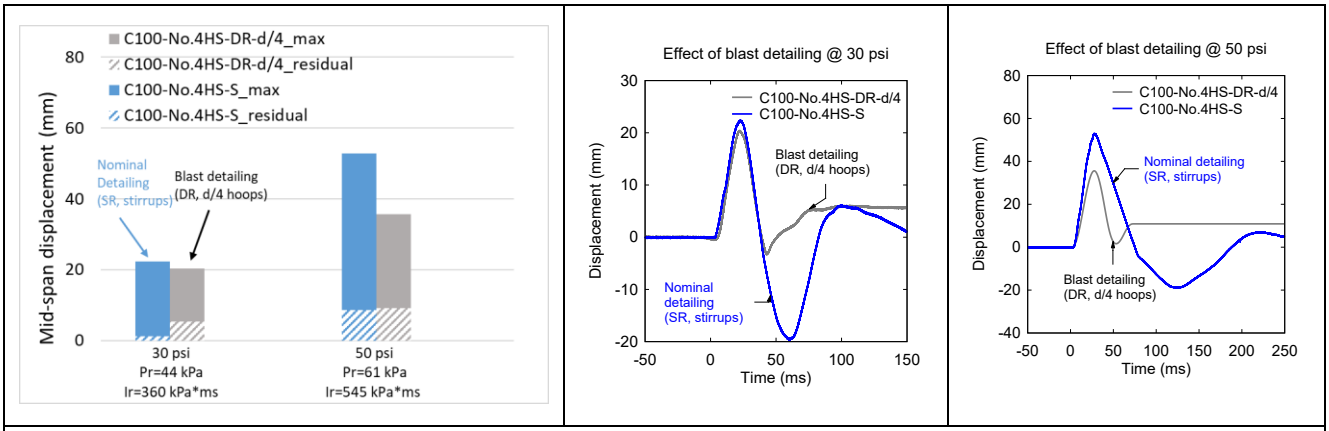

(a) Effect of blast detailing in No.4 series

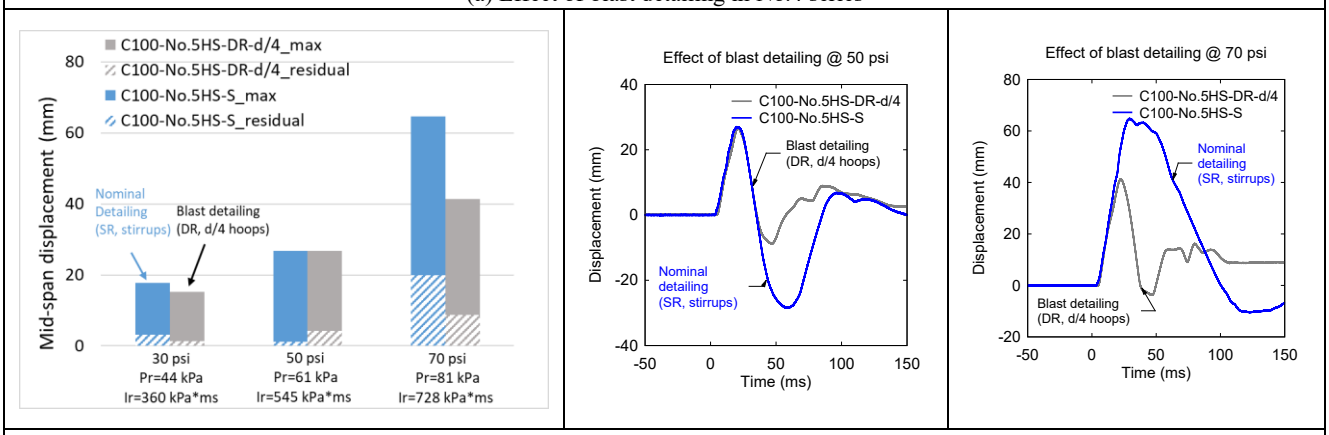

(b) Effect of blast detailing in No.5 series

Figure 4.12 Displacement comparisons: effect of blast detailing and fibers

4.5.2. Ability of fibers to relax detailing

The ability of fibers to relax blast detailing and improve blast behaviour in the doubly-reinforced high-strength steel reinforced concrete beams can be examined in **Figure 4.13** which compares the blast responses of beams C100-No.5HS-DR-d/4 (plain HSC and ties at d/4) and CF100-No.5HS-DR-d/2 (HSFRC containing 0.75% fibers and ties at d/2). Examining the results, it can be seen that the displacement responses are similar (within ±5%) under the first two shots (*Blasts-30psi* and *50psi*) which tested the beams within the elastic range. The benefit of the fibers becomes more clear at *Blasts-70psi* and *90psi* which brought the tension steel into the inelastic range, with reductions of 21% (32.6 mm vs. 41.4 mm) and 28% (40.9 mm vs. 56.4 mm) in maximum deformations for the beam with fibers. While both beams survive these blasts, damage in the plain HSC beam is associated with crushing of the top cover concrete, which results in the generation of blast fragments as shown in **Figure 4.10b** and **Figure 4.11d**. Previous research has shown that fibers are effective in increasing the spalling resistance and damage tolerance of high-strength concrete exposed to blast loads (Luccioni et al., 2017; Magnusson et al., 2010). As shown in **Figure 4.10c** and **Figure 4.11f**, damage remains well

controlled in the fiber-reinforced concrete beam, with no crushing, spalling or secondary fragments, even after intense blast testing.

As shown in **Figure 4.17(b,c)**, both beams show significant residual post-blast static capacity, with P_{max}^{R} = 244.3 vs. 205.4 kN for beams CF100-No.5HS-DR-d/2 and C100-No.5HS-DR-d/4. However increased stiffness k_s^R (8749 vs 6401 N/mm), peak residual capacity P_{max}^{R} (244.3 vs. 205.4 kN) and residual maximum displacement Δ_{max}^{R} (100.5 vs 88.6 mm) are observed in the fiber-reinforced concrete specimen (increases of 37%, 19% and 13%, when compared to the plain HSC beam). In summary, the results demonstrate that the use of moderate amounts of fibers and intermediate ties results in excellent blast performance. Thus, fibers can potentially be used to relax detailing and simplify construction of HSS-RC beams designed for blast resistance.

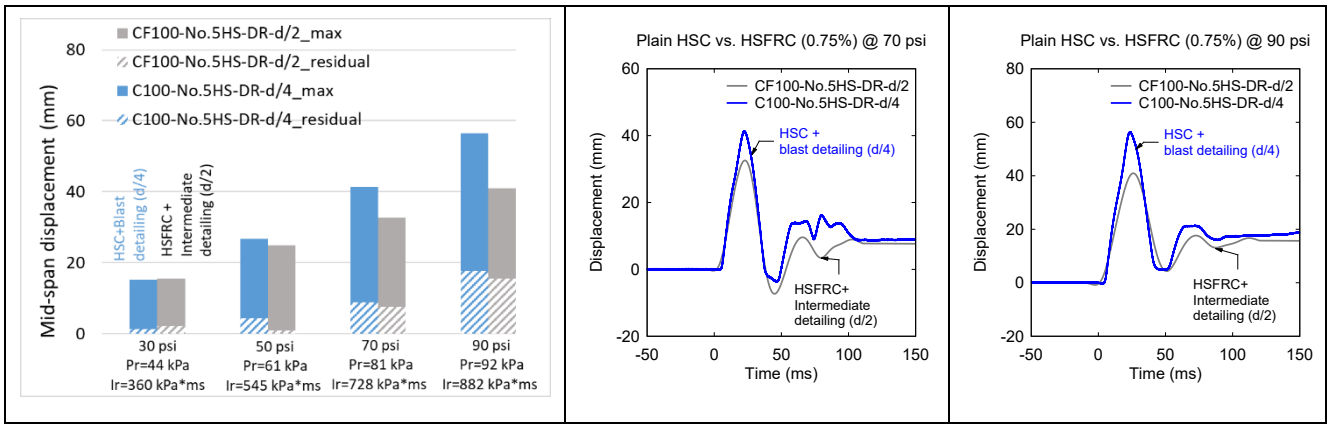

Figure 4.13 Displacement comparisons: effect of fibers (ability to relax detailing from d/4 to d/2)

4.5.3.Effects of steel type and ability of HS steel to reduce tension steel

The effect of steel type and ability of high-strength steel to reduce reinforcement in the blast tested beams is examined by comparing the responses of C100-No.5HS-DR-d/4 from the current study (Grade 690 MPa bars, ρ = 1.5%), and beams C100-15M-DR-d/4 & C100-20M-DR-d/4 from (Charles, 2019) (Grade 400 MPa bars, with ρ = 1.5% & 2.4%). The displacement results for these beams are shown in **Figure 4.14.**

Examining the effect of steel type in beams C100-No.5HS-DR-d/4 and C100-15M-DR-d/4 (equal steel areas) it can be seen that the use of high-strength bars results in reductions of 19% (26.8 mm vs. 33.1 mm) and 35% (41.4 mm vs. 63.4 mm) in maximum deformations, and decreases of 76% (18 mm vs. 4.3 mm) and 80% (8.8 mm vs. 45 mm) in residual displacements at *Blast-50psi* and *70psi* (see **Figure 4.14**). Both beams show important post-blast residual

capacity, demonstrating the benefits of blast detailing in both conventionally-reinforced and ASTM A1035-reinforced HSC beams.

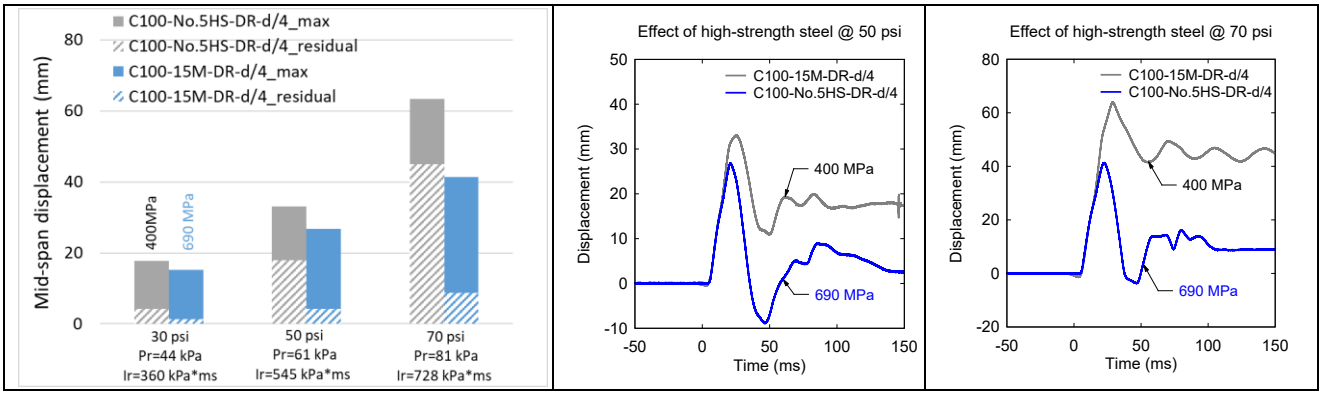

Figure 4.14 Displacement comparisons: effect of steel type (equal areas of steel)

Next the ability of high-strength reinforcement to reduce steel reinforcement is examined in **Figure 4.15** which compares the responses of C100-No.5HS-DR-d/4 and C100-20M-DR-d/4 which were built with plain HSC and steel ties at d/4, but No.5 high-strength and 20M normal-strength tension bars, respectively. As noted before, both beams had similar ρf_y ratios of 10.4 and 9.6 MPa, respectively. The response of beam CF100-No.5HS-DR-d/2 which was built with HSFRC, No.5 bars, and relaxed tie spacing of d/2 (100 mm) is also included in the comparison. Beginning with the plain HSC companions it can observed that beams C100-No.5HS-DR-d/4 and C100-20M-DR-d/4 show similar responses under *Blasts-30psi* and *70psi*, though the beam with increased steel area shows reduced maximum deformations. However, as the beams are pushed further into the inelastic range at *Blast*-90psi, beam C100-No.5HS-DR-d/4 shows reductions of 43% (56.4 mm vs. 71.6 mm) and 68% (17.8 mm vs. 48.2 mm) in maximum and residual deformations when compared to the more heavily-reinforced C100-20M-DR-d/4 specimen. Adding fibers to the HSC in beam CF100-No.5HS-DR-d/2 results in performance that not only matched, but outperformed that of beam C100-20M-DR-d/4. Indeed, previous research by Lepage et al. (2012) has shown that the combined use of fibers, increased tie spacing and reduced amounts of longitudinal reinforcement (in proportion to the increase in yield stress; i.e. similar $\rho \cdot f_y$) can be used to achieve similar deformation capacities when compared to conventionally-reinforced concrete members with seismic detailing, which is similar to the observation in the current study in beams tested under blast loading.

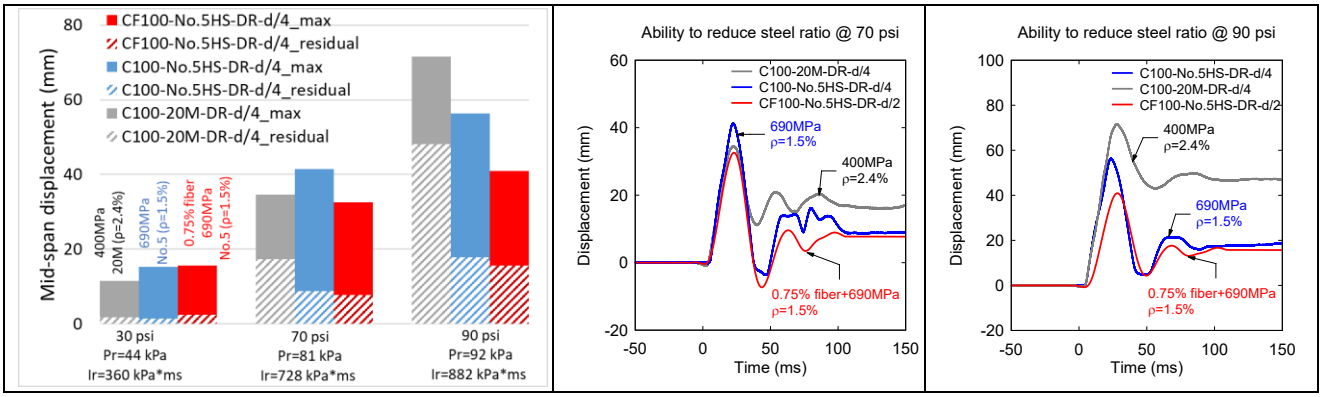

Figure 4.15 Displacement comparisons: effect of steel type (ability to reduce longitudinal steel)

4.5.4. Effects of repeated blast testing

The majority of beams in this study were tested under repeated blast loading to allow for comparison with the previous tests conducted by Li and Aoude (2019). To study the influence of repeated testing, the responses of beams C100-No.4HS-DR-d/4[x1] and C100-No.5HS-DR-d/4[x1], which were tested under single shots corresponding to *Blasts-70psi* and *90psi*, are compared to their companions (C100-No.4HS-DR-d/4 and C100-No.5HS-DR-d/4) which were tested under repeated blasts.

Comparing the results in **Figure 4.16,** it can be seen that the companion beams in each set show similar displacement histories due to the excellent damage tolerance provided by the blast detailing. For example, in the No.4 set beams C100-No.4HS-DR-d/4[x1] and C100-No.4HS-DR-d/4 show similar maximum and residual displacements of 53/54 mm and 25/27 mm under *Blast-70psi*. In the No.5 set, the beams tested under single and repeated blasts show maximum displacements of 56/52 mm, representing an 8% increase for the beam tested under repeated loads, though both beams show similar residual deformations (18/21 mm). The slight increase in maximum displacement can be explained by the more intense testing applied on the beam with No.5 bars (i.e., *Blast-70psi*) prior to the final shot, which resulted in greater accumulation of damage at *Blast-90psi*. Nonetheless, it can be concluded that the repeated tests did not significantly affect the blast displacement responses of the blast-detailed HSC beams.

Conversely, examination of the failure photos shows that the beams tested under repeated tests showed loss of top cover concrete (see **Figure 4.11(b,d)**), whereas the midspan cover damage was prevented or reduced in the companions tested under single blasts (see **Figure 4.11g**). **Figure 4.17(a, b)** compare the residual capacity test results of the companion beams tested under single and repeated blasts. In the No.4 series, the beam tested under

repeated blasts shows lower peak residual strength owing to the lack of top cover concrete which spalled during the blast tests. On the other hand, after the initial drop in load, both beams show remarkably similar residual deformation capacity, with failure associated with bar rupture in both specimens.

In the No.5 set, both beams show similar post-blast residual capacities, however failure in beam C100-No.5HS-DR-d/4 occurs earlier due to compression bar buckling (see close up damage in **Figure 4.18c**). This result can be explained by the high residual strains which had built up in the compression bars during the repeated blast tests, combined with the damaged cover region which was no longer able to restrain bar buckling. In comparison, bar buckling is delayed, with failure occurring due to bar rupture in beam C100-No.5HS-DR-d/4[x1]. It is interesting to note that even in this case, bar buckling does eventually occur between the ties. Indeed, as shown in **Figure 4.4c**, high strain demands were imposed in the compression bars, even in the case of the undamaged C100-No.5HS-DR-d/4 beam tested under static loads only; this situation was intensified in the case of the beams tested under blast loads. In the current study, the blast-detailed beams had a tie spacing of s = 50 mm which corresponds to s = $4d_b$ and s = d/4 as recommended in (Giduquio et al., 2015; Park & Paulay, 1975; Rashid & Mansur, 2005), therefore bar buckling only occurred at very large deformations during the post-blast residual test, with no major effects on static or blast response. However, high strain demands in the compression bars could lead to premature bar buckling if a large tie spacing is used; therefore, transverse reinforcement spacing should carefully be considered when designing such beams.

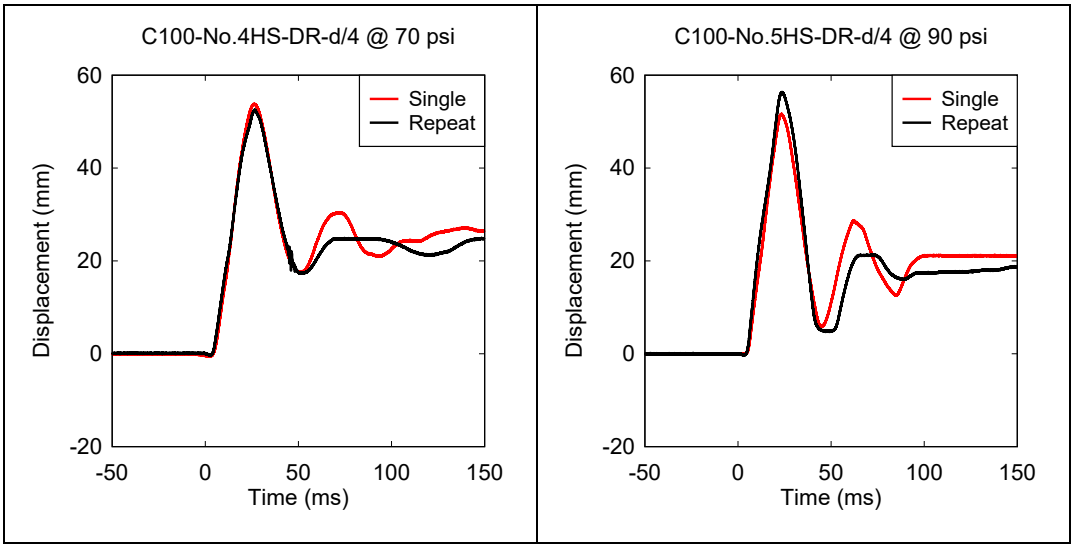

Figure 4.16 Displacement comparisons: effect of single versus repeated blasts

4.6 Post-blast residual static test results

This test program included companion beams with identical properties tested under static and blast conditions. The blast-tested beams were subsequently tested under static four-point bending to assess their post-blast residual capacity. The results of these tests, along with the results from the original undamaged beams are shown in **Figure 4.17,** while **Figure 4.18** shows photos of the beams after residual testing. The maximum residual capacity (P_{max}^{R}), residual secant stiffness (k_s^R) and maximum post-blast residual displacement Δ_{max}^{R} are reported in **Table 4.5**. It is noted that P_{max}^{R} refers to the maximum load reached by the blast-damaged beams during the residual static test.

Table 4.5 Results from the post-blast residual static tests

Beam	Dynamic loading type	Load		Stiffness		Displacement			Energy-absorption		
		P_{max}^{R} (kN)	RRI	k_s^R (N/mm)	RSI	Δ_{test}^{R} (mm)	Δ_{max}^{R} (mm)	RDI	IEI	REI	TEI
C100-No.4HS-DR-d/4	Repeated	143.2	0.89	5529	78%	53.9	85.7	107%	0.477	0.498	0.975
C100-No.4HS-DR-d/4 [x1]	Single	161.5	1.01	6629	94%	57.4	84.1	105%	0.411	0.631	1.042
C100-No.5HS-DR-d/4	Repeated	205.4	0.99	6401	80%	48.6	88.6	92%	0.372	0.385	0.757
C100-No.5HS-DR-d/4 [x1]	Single	209.3	1.01	7918	99%	90.8	111.8	116%	0.275	0.771	1.046
CF100-No.5HS-DR-d/2	Repeated	244.3	1.00	8749	87%	74.0	100.5	87%	0.333	0.548	0.880

Note: P_{max}^{R} =Peak residual load; k_s^R=Residual secant stiffness; Δ_{test}^{R} = test residual displacement; Δ_{max}^{R}= Max. residual displacement (where = cumulative displacement after blast testing); RRI=residual resistance index; RSI=residual stiffness index; RDI=residual displacement index; IEI=Impact Energy Index; REI=Residual Energy Index; TEI=Total Energy Index

Adhikary et al. (2014) proposed a residual resistance index defined as $RRI = \frac{P_{max}^{R}}{P_{max}}$ and damage index, $D = 1 - RRI$, to assess the post-blast resistance of impact-damaged beams. According to this study (Adhikary et al., 2014), the degree of damage caused by dynamic loading can be classified as "low", "medium", "high" and "severe" if the damage index is: D < 0.2, D = 0.2-0.5, D = 0.5-0.8 and D = 0.8-1.0, respectively. As shown in **Figure 4.17(a,b)**, all blast-detailed HSC beams showed significant residual capacities, with an ability to sustain significant load even after intense blast testing. Examining **Table 4.5**, all blast tested beams show RRI above 0.89, with damage indices < 0.2, which confirms the low damage in the beams tested under both single and repeated blast loads. The highest damage index of 0.11 (RRI = 0.89) is observed in beam C100-No.4HS-DR-d/4; as noted before, this beam suffered loss of cover concrete during blast testing and therefore has a relative loss in residual strength when

compared to its undamaged companion. The near perfect RRI results for the remaining beams, including beam CF100-No.5HS-DR-d/2 (see **Figure 4.17c**), demonstrate the high resilience of the blast-detailed and fiber-reinforced HSC beams. Adhikary et al. (2014) also proposed a "Residual stiffness index" (RSI) defined as the ratio of secant stiffness of impact-damaged to undamaged specimens ($RSI = \frac{k_s^R}{k_s}$) and noted higher RSI indices (lower stiffness degradation) in doubly-reinforced beams compared to singly-reinforced specimens. The results from the current tests show that the varied between 0.8 to 0.99 which indicates that all beams show high residual stiffness even after intense blast testing.

A new ratio for displacements, the Residual displacement index ($RDI = \frac{\Delta_{max}^R}{\Delta_{max}}$), is proposed to assess the effect of blast loading on the residual displacement capacity of the beams. As shown in **Figure 4.17(a-c)** all beams reached maximum displacements which were similar to those observed in the static tests, with near-perfect ratios for the No.4 series beams, and beam C100-No.5HS-DR-d/4[x1]. A reduced ratio of 0.92 is observed in C100-No.5HS-DR-d/4 due to the change in failure mode from bar rupture to bar buckling. Similarly, the earlier bar rupture in CF100-No.5HS-DR-d/2, results in *RDI* = 0.87.

Zanuy and Ulzurrun (2018) proposed three additional indices, called the "Impact Energy Index" (IEI), "Residual Energy Index" (REI) and "Total Energy Index" (TEI) to better assess the energy absorbed and failure mode after impact testing. As shown in **Figure 4.17e** the IEI index is calculated using only the undamaged quasi-static response, with $\text{IEI} = \frac{A}{A+B}$, and where A is the energy calculated up to the residual deflection, and A+B equals the total energy-absorption capacity of the undamaged beam. After dynamic testing, the energy absorbed in the residual test, denoted as C in **Figure 4.17e** can be calculated, with $\text{REI} = \frac{C}{A+B}$. In the last step the total energy index can be calculated as $\text{TEI} = \text{IEI} + \text{REI}$. According to Zanuy and Ulzurrun (2018) the IEI and REI "do not provide in itself an easy identification of residual failure mode or ductility". On the other hand, the TEI can provide a better indication of ductility and failure mode, with $\text{TEI} \leq 0.85$ indicating a change from "ductile" to "brittle" failure for undamaged versus damaged specimens, and a TEI of about 1.0 indicating the same failure mode for undamaged and damaged beams. Examining the results in **Table 4.5**, most beams show TEI indices ≥ 0.9, with ratios of ~ 1.0 for beams C100-No.4HS-DR-d/4, C100-No.4HS-DR-d/4[x1] and C100-No.5HS-DR-d/4[x1]. These beams showed similar energy-absorption capacity, ductility and failure mode when compared to their undamaged

companions. On the other hand, beam C100-No.5HS-DR-d/4 which was tested under repeated blasts shows a lower TEI = 0.76, with a change in failure mode (premature bar buckling) when compared to the undamaged beam (bar rupture). Similarly, beam CF100-No.5HS-DR-d/2 shows a relatively high TEI = 0.88, but suffered earlier bar rupture when compared to its undamaged companion. In general, the results show that the TEI index can be used to accurately assess the residual energy absorption capacity and failure mode of blast-damaged beams.

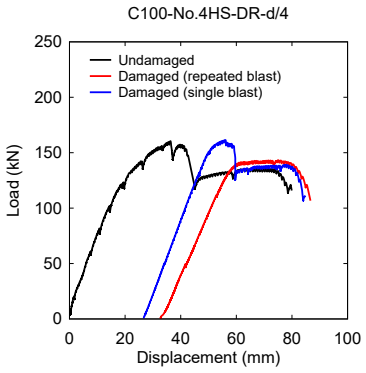

(a) C100-No.4HS-DR-d/4

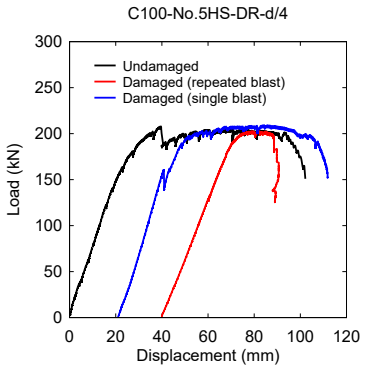

(b) C100-No.5HS-DR-d/4

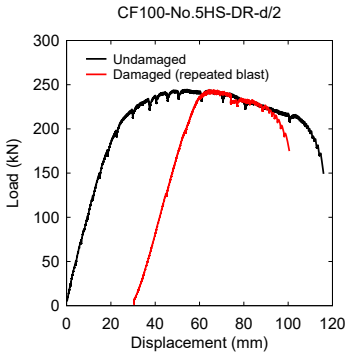

(c) CF100-No.5HS-DR-d/2

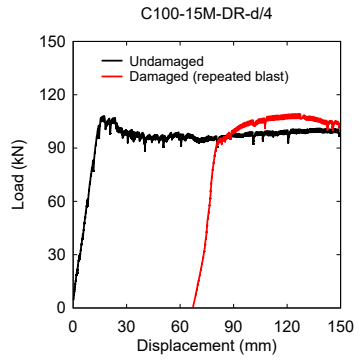

(d) C100-15M-DR-d/4

Undamaged = undamaged beam tested under static loading only;
Damaged (repeated blast) = damaged beam tested under residual static loads after repeated blast tests
Damaged (single blast) = damaged beam tested under residual static loads after single blast application

Impact Energy Index (IEI) $\mathrm{IEI} = \frac{A}{A+B}$

Residual Energy Index (REI) $\mathrm{REI} = \frac{C}{A+B}$

Total Energy Index (TEI) $\mathrm{TEI} = \mathrm{IEI} + \mathrm{REI}$

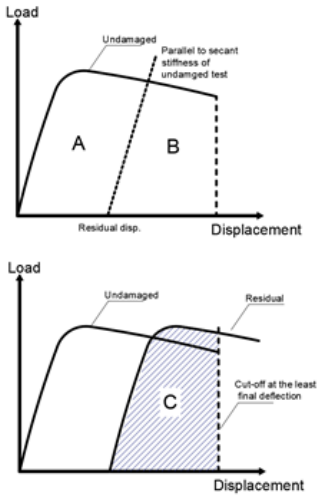

(e) Definition of areas used for calculating the residual damage indices (IEI, REI, TEI)

Figure 4.17 Comparison of undamaged and post-blast residual static test results for beams

(a) C100-No.4HS-DR-d/4
(repeated blasts)

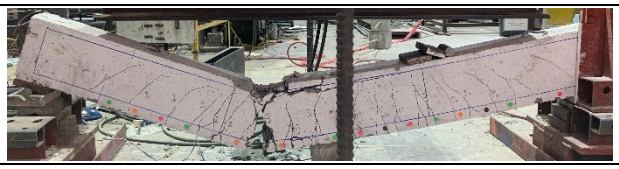

(b) CF100-No.4HS-DR-d/4 [x1]
(single blast)

Close up of damage

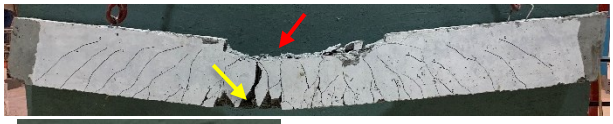

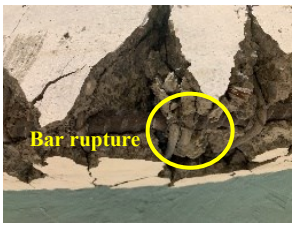

Close-up of damage

(c) C100-No.5HS-DR-d/4
(repeated blasts)

(d) C100-No.5HS-DR-d/4 [x1]
(single blast)

(e) CF100-No.5HS-DR-d/2

Figure 4.18 Failure modes of beams after the post-blast residual static tests

4.7 Conclusions

This chapter presented the results from **Series 1** of the PhD program, and examined the influence of blast detailing on the static and blast behavior of high-strength steel reinforced concrete (HSS-RC) beams. The effects of detailing, fibers and steel type were investigated. The following conclusions can be drawn from this study:

1 The use of blast detailing significantly enhanced the response of the HSS-RC beams under both static and blast loads. Under static loading, the use of top continuity (compression) bars and closely-spaced ties increased load-carrying capacity, stiffness and ductility due to the ability of the improved detailing to enhance the toughness of the concrete compression zone. Likewise, blast detailing significantly enhanced blast response by reducing displacements, increasing blast capacity and allowing for significant post-blast residual resistance;

2 The use of moderate amounts of steel fibers (as low as 0.75%) can be used to relax blast detailing in HSS-RC beams by increasing tie spacing from d/4 to d/2. In this study, fibers and intermediate detailing allowed for significantly high static, blast and post-blast resistance, with better control of damage when compared to the companion HSC beam designed with blast detailing;

3 The results show that substitution of normal-strength bars with high-strength bars increased the capacity of the beams under both static and blast loads. Similarly, fibers and reduced amounts of high-strength bars allowed for similar performance when compared to beams with larger amounts of normal-strength reinforcement. On the other hand, it is important to consider the possibility of bar fracture when designing well-detailed HSS-RC beams, especially when using low steel ratios and/or fibers;

4 All beams showed significant residual post-blast capacity which closely matched the responses and failure modes of the undamaged beams tested under static loads only. All beams showed high RRI (low damage), high RSI (low stiffness degradation) and significant TEI (high residual energy absorption capacity) due to the positive influence of the blast detailing. In addition, the TEI index was able to indicate the change in failure mode in the beams tested under repeated blast loads.

4.8 References (Chapter 4)

ACI Committee 544 (1988). Design considerations for steel-fiber reinforced concrete. ACI 544.4R-188, American Concrete Institution, Detroit, Mich., pp. 18.

Adhikary, S. D., Li, B., & Fujikake, K. (2014). Residual resistance of impact-damaged reinforced concrete beams. *Magazine of Concrete Research, 67*(7), 364-378. doi:https://doi.org/10.1680/macr.14.00312

Ashour, S. A., & Wafa, F. F. (1993). Flexural behavior of high-strength fiber reinforced concrete beams. *ACI Structural Journal, 90*(3), 279-287. doi:https://doi.org/10.14359/4186

Bandelt, M. J., & Billington, S. L. (2016). Impact of Reinforcement Ratio and Loading Type on the Deformation Capacity of High-Performance Fiber-Reinforced Cementitious Composites Reinforced with Mild Steel. *Journal of Structural Engineering, 142*(10), 04016084. doi:https://doi.org/10.1061/(asce)st.1943-541x.0001562

Charles, C. J. (2019). *Effect of detailing and fibers on the static and blast behaviour of high-strength concrete beams.* (MASc. thesis). University of Ottawa, Ottawa, ON, Canada.

Cheng, M. Y., & Giduquio, M. B. (2014). Cyclic behavior of reinforced concrete flexural members using high-strength flexural reinforcement. *ACI Structural Journal, 111*(4), 893-902. doi:https://doi.org/10.14359/51686632

Canadian Standards Association (CSA) (2012). Design and assessment of buildings subjected to blast loads. CSA S850-12, Mississauga, ON, Canada, pp. 126.

Dancygier, A. N., & Karinski, Y. S. (2019). Effect of cracking localization on the structural ductility of normal strength and high strength reinforced concrete beams with steel fibers. *International Journal of Protective Structures, 10*(4), 457–469. doi:https://doi.org/10.1177/2041419618824609

Giduquio, M. B., Cheng, M.-Y., & Wibowo, L. S. (2015). High-Strength Flexural Reinforcement in Reinforced Concrete Flexural Members under Monotonic Loading. *ACI Structural Journal, 112*(6), 793-803. doi:https://doi.org/10.14359/51688057

Imam, M., Vandewalle, L., & Mortelmans, F. (1995). Shear–moment analysis of reinforced high strength concrete beams containing steel fibres. *Canadian Journal of Civil Engineering, 22*(3), 462-470. doi:https://doi.org/10.1139/l95-054

Lepage, A., Tavallali, H., Pujol, S., & Rautenberg, J. M. (2012). High-performance steel bars and fibers as concrete reinforcement for seismic-resistant frames. *Advances in Civil Engineering, 2012*, 450981. doi:https://doi.org/10.1155/2012/450981

Li, Y., & Aoude, H. (2019). Blast response of beams built with high-strength concrete and high-strength ASTM A1035 bars. *International Journal of Impact Engineering, 130*, 41-67. doi:https://doi.org/10.1016/j.ijimpeng.2019.02.007

Li, Y., & Aoude, H. (2020). Influence of steel fibers on the static and blast response of beams built with high-strength concrete and high-strength reinforcement. *Engineering Structures, 221*, 111031. doi:https://doi.org/10.1016/j.engstruct.2020.111031

Luccioni, B., Isla, F., Codina, R., Ambrosini, D., Zerbino, R., Giaccio, G., & Torrijos, M. C. (2017). Effect of steel fibers on static and blast response of high strength concrete. *International Journal of Impact Engineering, 107*, 23-37. doi:https://doi.org/10.1016/j.ijimpeng.2017.04.027

Magnusson, J., Hallgren, M., & Ansell, A. (2010). Air-blast-loaded, high-strength concrete beams. Part I: Experimental investigation. *Magazine of Concrete Research, 62*(2), 127-136. doi:https://doi.org/10.1680/macr.2008.62.2.127

Mansur, M. A., Chin, M. S., & Wee, T. H. (1997). Flexural behavior of high-strength concrete beams. *ACI Structural Journal, 94*(6), 663-674. doi:https://doi.org/10.14359/9726

Ousalem, H., Takatsu, H., Ishikawa, Y., & Kimura, H. (2009). Use of high-strength bars for the seismic performance of high-strength concrete columns. *Journal of Advanced Concrete Technology, 7*(1), 123-134. doi:https://doi.org/10.3151/jact.7.123

Park, R., & Paulay, T. (1975). *Reinforced concrete structures*. New York: John Wiley & Sons.

Rashid, M., & Mansur, M. (2005). Reinforced high-strength concrete beams in flexure. *ACI Structural Journal, 102*(3), 462-471. doi:https://doi.org/10.14359/14418

Rautenberg, J. M., Pujol, S., Tavallali, H., & Lepage, A. (2013). Drift capacity of concrete columns reinforced with high-strength steel. *ACI Structural Journal, 110*(2), 307-317. doi:https://doi.org/10.14359/51684410

Su, J., Wang, J., Li, Z., & Liang, X. (2019). Effect of reinforcement grade and concrete strength on seismic performance of reinforced concrete bridge piers. *Engineering Structures, 198*, 109512. doi:https://doi.org/10.1016/j.engstruct.2019.109512

Trejo, D., Link, T. B., & Barbosa, A. R. (2016). Effect of Reinforcement Grade and Ratio on Seismic Performance of Reinforced Concrete Columns. *ACI Structural Journal, 113*(5), 907-916. doi:https://doi.org/10.14359/51689015

Yoo, D.-Y., Yuan, T., Yang, J.-M., & Yoon, Y.-S. (2017). Feasibility of replacing minimum shear reinforcement with steel fibers for sustainable high-strength concrete beams. *Engineering Structures, 147*, 207-222. doi:https://doi.org/10.1016/j.engstruct.2017.06.004

Zanuy, C., & Ulzurrun, G. S. D. (2018). Residual behavior of reinforced steel fiber‐reinforced concrete beams damaged by impact. *Structural Concrete, 20*(2), 597-613. doi:https://doi.org/10.1002/suco.201800253

Chapter 5 Test results from Series 2A (HSC-SS)

Paper 2: Influence of Stainless Steel and Fibers on the Behaviour of HSC Beams under Static and Blast Loading

5.1 Introduction

This chapter presents the results of Series 2A of the research program, and investigates the effects of stainless steel (SS) reinforcement and fibers on the blast behaviour of high-strength concrete (HSC) beams. As part of the study, a series of HSC beams built with Grade 520 MPa stainless steel bars conforming to ASTM A955 were tested under blast loads using a shock-tube. Companion beams were also tested under quasi-static conditions. Test variables included the effects of steel type (stainless vs. ordinary steel), and steel fibers, in beams built with and without transverse reinforcement.

5.2 Research contribution

The content of this chapter is included in the paper titled "Influence of Stainless Steel and Fibers on the Behaviour of HSC Beams under Static and Blast Loading" (to be submitted).

5.3 Experimental program

The details of the testing program were provided in **Chapter 3** (see *Series 2A*). **Table 5.1** and **Figure 5.1** provide the details of the seven beams included in this series. Three beams were tested under static loads, with four specimens tested under blast loads using the University of Ottawa shock-tube. All beams had dimensions of 125 mm × 250 mm × 2440 mm (b × h × L), and were cast using either plain or fiber-reinforced high-strength concrete (HSC or HSFRC). *Group 1* included beams cast with plain HSC concrete (designated as *C100*), while *Group 2* were cast with HSFRC concrete (*CF100*) having 1% of steel fibers in the mix (80 kg/m^3). All beams were reinforced with 2-No.5, Grade 520 MPa, XM-28 stainless-steel bars conforming to ASTM A955, resulting in a longitudinal steel ratio of ρ = 1.5%. Each group included specimens with and without stirrups to examine flexural and shear behaviour. For the beams with stirrups (flexural specimens), transverse reinforcement consisted of U-shaped stirrups made from 6.3 mm steel wire, spaced at s = 100 mm in the shear spans. The shear specimens were built without stirrups. To examine the effect of steel type, the performance of the test beams is compared to a control set of HSC beams with similar designs, but built with ordinary (Grade 400 MPa) steel (Li et al., 2018; Algassem et al., 2019). The control set included

10 beams (5 static and 5 blast), built with either C100 or CF100 concrete, with and without stirrups, and reinforced with either 2-15M or 2-20M bars (ρ = 1.5% or 2.4%).

The beam nomenclature in **Table 5.1** and **Figure 5.1** indicates the design parameters of the test and control beams, including the concrete type (C100 vs. CF100), tension bar size (No.5, 15M, 20M) and steel type (S1: stainless steel), and whether the beam contains stirrups (where "S" indicates the beam has stirrups). For example, C100-No.5S1-S is constructed with plain C100 concrete, 2-No.5 stainless bars and stirrups in the shear span, while CF100-No.5S1-S is the beam built with fibers. The companion beams without stirrups are C100-No.5S1 and CF100-No.5S1 (no "-S" in the nomenclature). In the control set, C100-15M-S and C100-20M-S are the beams built with C100 concrete, ordinary 15M and 20M steel bars, and stirrups. C100-15M and CF100-15M were built without stirrups, and cast with C100 or CF100 concrete, respectively. It is noted, no stirrups were provided in CF100-15M since the fibers were sufficient to ensure the beam would fail in flexure.

Blast tests were conducted using the University of Ottawa shock-tube with companion beams tested under quasi-static four-point bending. Details on the test setups and testing protocols were provided in see **Section 3.4**. **Figure 5.2** shows sample shockwaves corresponding to *Blasts 30-90psi* which were used in this series. These blasts were obtained by varying the input driver pressure from 30 to 90 psi (207–620 kPa), with the driver length fixed at 9 ft (2743 mm). A summary of key blast parameters is presented in **Table 5.2**: including, the reflected pressures (P_r), reflected impulses (I_r) and positive shockwave duration (t_d).

Table 5.1 Beam Design details

Series	Beam ID	Concrete strength f'_c (MPa)	Fiber content V_f (%)	Longitudinal reinforcement			Transverse steel (Yes/No)	Test Type
				Type (Grade)	Number and size [c]	ρ (%) [ρ/ρb]		
Stainless steel (SS)	C100-No.5S1-S	97, 101	-	SS steel XM-28 (520)	2-No.5 (Batch B1)	1.5 [0.45]	Yes	S & D
	C100-No.5S1	101	-				No	D
	CF100-No.5S1-S	97, 102	1%		2-No.5 (Batch B2)		Yes	S & D
	CF100-No.5S1	110, 105	1%				No	S & D
Ordinary steel (Control)	C100-15M-S [a]	107	-	Ordinary (400)	2-15M	1.5 [0.31]	Yes	S & D
	C100-15M [a]	101	-				No	S & D
	CF100-15M [b]	106	1%				No	S & D
	C100-20M-S [a]	106	-		2-20M	2.4% [0.44]	Yes	S & D
	CF100-20M-S [b]	105	1%				Yes	S & D

Note: f'_c = average concrete compressive strength; ρ = longitudinal steel ratio; ρ_b = balanced steel ratio

[a] Companion beams with plain HSC and ordinary steel tested by Li et al. (2018)

[b] Companion beams with HSFRC and ordinary steel tested by Algassem et al. (2019)

[c] B1: stainless steel from batch 1, f_y = 600 MPa and f_u = 862 MPa; B2: stainless steel from batch 2, f_y = 648 MPa and f_u = 903 MPa.

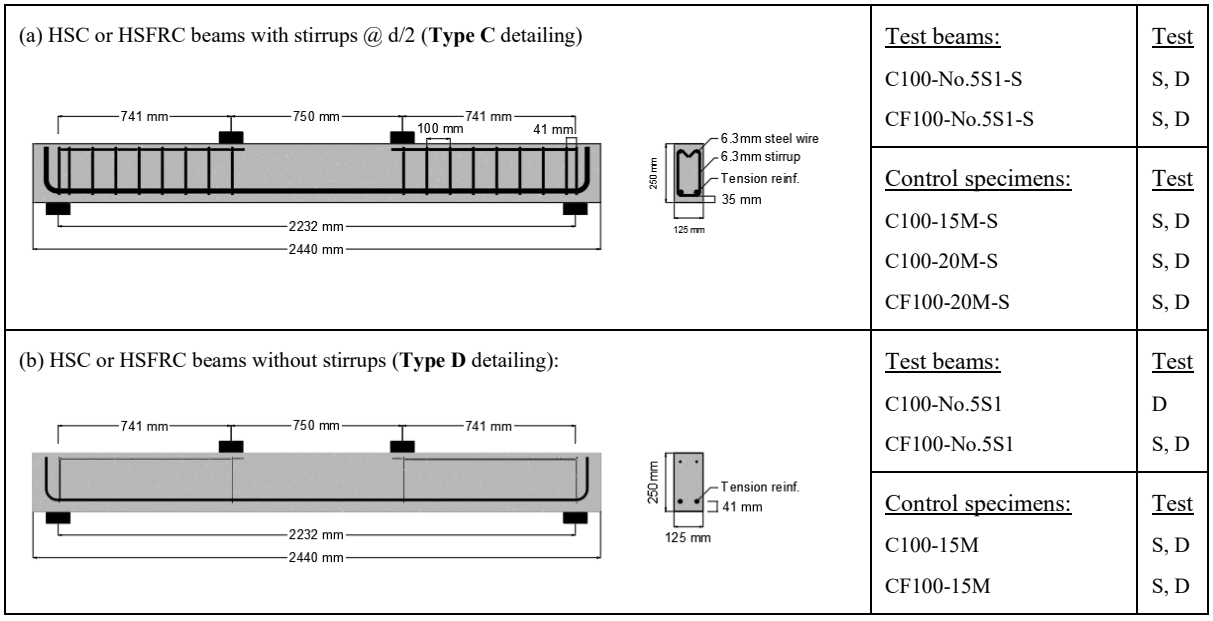

Figure 5.1 Specimen Designs

Note: S = static test, D = dynamic blast test

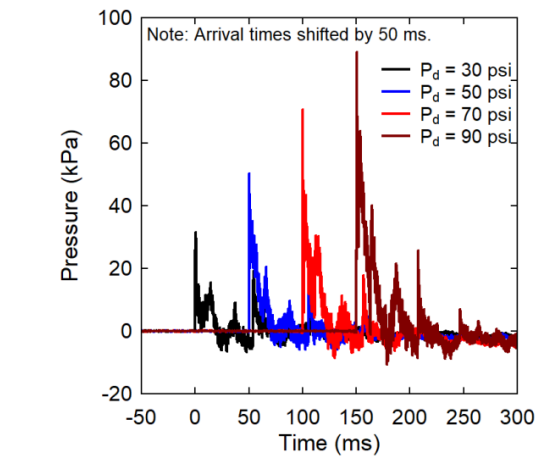

Specimens:	Test sequence:
C100-No.5S1-S	Blast-30, 50, 70 psi
CF100-No.5S1-S	Blast-30, 50, 70, 90 psi
C100-No.5S1	Blast-30 psi
CF100-No.5S1	Blast-30, 50, 70 psi
Control Specimens:	**Test sequence:** *
C100-15M-S	Blast-30, 50 psi
C100-15M	Blast-30 psi
CF100-15M	Blast-30, 50, 70 psi
C100-20M-S	Blast-30, 50, 70 psi
CF100-20M-S	Blast-30, 50, 70, 90 psi

Figure 5.2 Sample shockwaves and testing protocols

* Note: an additional elastic shot using 17 psi driver pressure was applied to the control specimens prior to *Blast-30psi*.

Table 5.2 Average blast properties for beams tested in Series 2A

Blast Load	**Driver Pressure kPa (psi)**	**Driver Length mm (ft)**	**Average Reflected Pressure, P_r (kPa)**	**Average Reflected Impulse, I_r (kPa·ms)**	**Average Positive Phase Duration, t_d (ms)**
Blast-30 psi	207 (30)	2743 (9)	42.7	366	21.3
Blast-50 psi	345 (50)		57.3	524	22.4
Blast-70 psi	483 (70)		77.4	728	23.4
Blast-90 psi	621 (90)		89.4	842	24.7

5.4 Summary of results

5.4.1.Static test results

The results from the static tests are plotted in **Figure 5.3**, while **Table 5.3** summarizes key parameters from the tests, including: maximum and yield load (P_{max}, P_y), secant stiffness (k_s), displacements at yield and failure (Δ_y, Δ_{max}), as well as ductility (Δ_{max}/Δ_y) and toughness (A_u), representing the area under the load-deflection curves up to Δ_{max}.

Table 5.3 Experimental results from the static tests

Series	Beam	Load		Displacement		Secant Stiffness k_s (N/mm)	Ductility Δ_{max}/Δ_y	Toughness A_u (J)
		Yield P_y (kN)	Peak P_{max} (kN)	Yield Δ_y (mm)	Failure Δ_{max} (mm)			
SS	C100-No.5S1-S	105.2	121.6	15.6	42.6	6744	2.73	4061
	CF100-No.5S1-S	146.9	157.8	17.1	115.5	8591	6.75	12886
	CF100-No.5S1	-	139.3	-	15.8	8807	-	1333
NS	C100-15M-S	94.5	104.6	14.6	40.7	6342	2.74	3272
	C100-15M	-	90	-	15.3	5882	-	726
	CF100-15M	111.6	115.9	14.5	124.0	7697	8.55	8711
	C100-20M-S	118.2	137.5	15.0	31.0	7880	2.1	2998
	CF100-20M-S	145.5	148.4	16.9	126.0	8600	3.1	13682

Note: P_y = yield strength; P_{max} = peak static strength; Δ_y = yield displacement; Δ_{max} = maximum displacement; k_s = secant stiffness; A_u = area under the load deflection curve up to Δ_{max}.

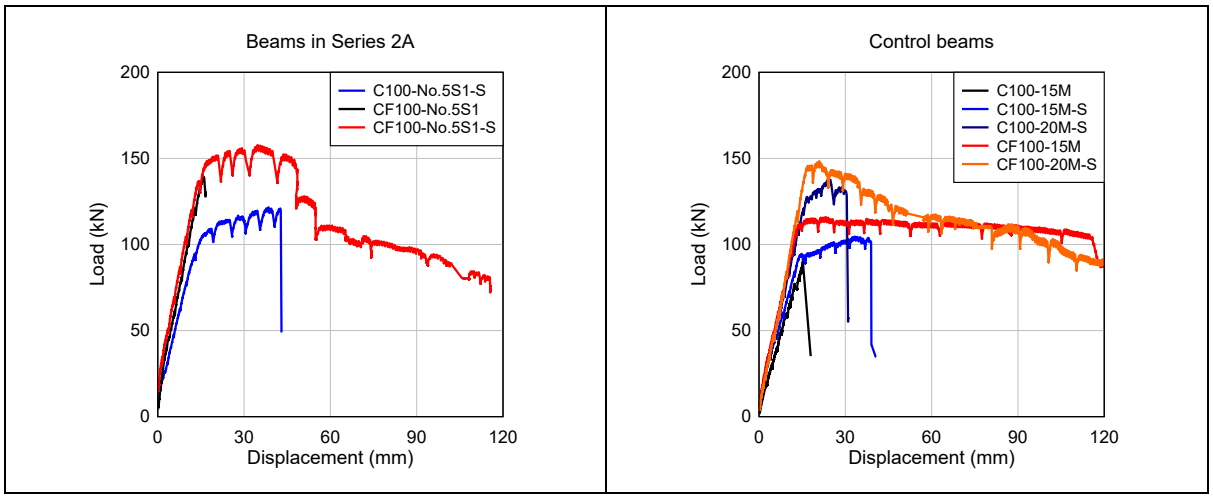

Figure 5.3 Summary of static test results (load-deflection curves)

5.4.2.Blast test results

The results from the blast tests are reported in **Table 5.4** in terms of peak reflected pressure, positive reflected impulse and positive phase duration (P_r , I_r and t_d). The table also reports the response of the beams after each test in terms of maximum and residual displacements (D_{max} , D_{res}) and corresponding maximum support rotation (θ_{max}), with an indication of the expected damage in the CSA S850 blast standard (CSA, 2012).

Table 5.4 Experimental results from the blast tests

	Beams	Blast ID (psi)	Shockwave Properties[1]			Beam response[2]				CSA S850 Response limits and Component damage[3]	
			P_r (kPa)	I_r (kPa·ms)	t_d (ms)	D_{max} (mm)	D_{res} (mm)	θ_{max} (°)	Observed Damage	Response Limit	Damage level
SS	C100-No.5S1-S	30	46.7	371.6	21.5	16.6	2.0	0.9	Minor cracking	<B1	Superficial
		50	57.6	539.0	23.1	30.5	5.6	1.6	Moderate cracking	B1-B2	Moderate
		70	76.1	707.3	24.4	134	87	6.9	Severe concrete crushing & spalling	B3-B4	Hazardous
	CF100-No.5S1-S	30	43.0	376.7	21.9	14.5	0	0.7	Minor cracking	<B1	Superficial
		50	56.8	481.8	22.9	21.8	0.5	1.1	Moderate cracking	B1-B2	Moderate
		70	75.3	764.6	24.4	50.2	15.7	2.6	Moderate cracking	B2-B3	Heavy
		90	89.4	841.5	24.7	93.8 *	43.6 *	4.8	Fiber pullout	B2-B3	Heavy
	C100-No.5S1	30	39.1	365.6	20.7	18.9	2.4	1.0	Shear failure	-	-
	CF100-No.5S1	30	41.9	350.3	21.1	13.8	2.7	0.7	Minor cracking	<B1	Superficial
		50	57.6	551.6	21.3	24.0	2.5	1.2	Moderate cracking	B1-B2	Moderate
		70	80.8	713.0	22.8	117.8	81.1	6.1	Shear failure	-	-
NSS (Controls)	C100-15M-S	30	42.9	341	15.9	21.4	4.7	1.1	Moderate F cracks	B1-B2	Moderate
		50	58.6	516	17.6	79.6	22.1	6.4	Severe crushing	B3-B4	Hazardous
	C100-15M	30	35.9	323.6	19.4	16.08	5.49	0.8	Shear failure	-	-
	CF100-15M	30	40.3	348	25.8	15.0	2.7	0.8	Hairline F cracks	<B1	Superficial
		50	56.5	512	25.6	33.3	10.1	1.7	Crack localization	B1-B2	Moderate
		70	69.5	657	20.7	78.9	54.7	4.1	Fiber pullout	B2-B3	Heavy
	C100-20M-S	30	39.2	360	18.4	15.1	0.2	0.8	Minor F cracking	<B1	Superficial
		50	57.4	538	18.8	32.9	12.4	1.7	Moderate F cracking	B1-B2	Moderate
		70	68.8	703	20.4	118.1	71.7	6.1	Severe crushing	B3-B4	Hazardous
	CF100-20M-S	30	41.4	358	24.1	14.9	2.2	0.8	Hairline F cracks	<B1	Superficial
		50	57.4	552	21.8	27.6	4.0	1.4	Further crack opening	B1-B2	Moderate
		70	71.1	733	22.7	67.0	41.8	3.4	Further crack opening & onset of crushing	B2-B3	Heavy
		90	79.1	774	24.8	153.0	79.2	7.9	Fiber pullout & Concrete crushing	B3-B4	Hazardous

[1]: P_r = Reflected pressure; I_r = Reflected impulse; t_d = positive phase duration; Z = scaled distance.
[2]: D_{max} = maximum mid-span displacement; D_{res} = residual mid-span displacement; θ_{max} = maximum support rotations.
[3]: CSA component damage and response limits: "Blowout" (Component is overwhelmed by blast load causing debris with significant velocities) = response greater than B4; "Hazardous failure" (component has failed with no significant velocities) = response in between B4 and B3; "Heavy damage" (Component has not failed but has significant permanent deflections causing it to be unrepairable) = response in between B3 and B2; "Moderate damage" (Component has permanent deflections but is repairable) = response in between B2 and B1; "Superficial damage" (component has no visible permanent damage) = response less than B1.
* Data captured from the camera.

5.5 Discussion of Results

5.5.1.Effect of stainless steel in plain HSC beams

This section compares the responses of beam C100-No.5S1-S, built with stainless steel, with that of beam C100-15M-S, built with ordinary 15M bars, under static and blast loading.

Figure 5.4 compares the static load-deflection responses of the specimens. The results show that the increased tensile strength of the stainless-steel reinforcement increased the beam load carrying capacity under static loading. In the plain HSC beams, C100-No.5S1-S shows a 16% increase in capacity (P_{max}) when compared to C100-15M-S, which was built with equal amounts of ordinary steel. Beams C100-No.5S1-S and C100-15M-S showed similar failure displacements (Δ_{max} = 43 vs. 41 mm) and ductility (Δ_{max}/Δ_y = 2.73 vs. 2.74), with both beams failing by concrete crushing after steel yielding (see **Figure 5.5**). Due to the increased load-capacity, higher toughness is observed for the beam with SS bars (A_u = 4061 vs. 3272 J). In general, it can be concluded that use of moderate stainless steel ratio (ρ = 1.5%), combined with high-strength concrete, allowed for sufficient ductility in beam C100-No.5S1-S.

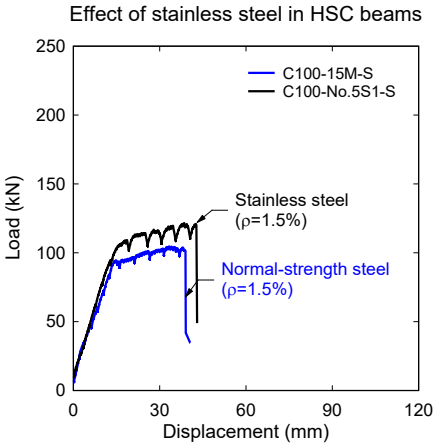

Figure 5.4 Static test results: effect of stainless steel in HSC beams

Stainless steel	Ordinary steel
Δ_{max}= 43 mm Concrete crushing zone 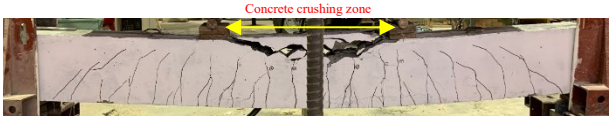	Δ_{max}= 41 mm 
(a) C100-No.5S1-S (crushing failure)	**(b) C100-15M-S (crushing failure)**

Figure 5.5 Beam photos and failure modes at end of static testing

The use of stainless bars also allowed for improved performance under blast loading, by reducing displacements at equivalent blasts and increasing blast capacity. **Figure 5.6** compares the displacement-histories at *Blasts-30psi* and *50psi*, and shows that the use of SS bars reduced maximum displacements by 22% and 62%. Likewise, residual displacements were reduced by 57% and 75% under the same two blasts. Importantly, while beam C100-15M-S failed at *Blast-50psi* (I_r = 516 kPa-ms), failure was delayed to *Blast-70psi* in beam C100-No.5S1-S (I_r = 707 kPa-ms). The results correspond to the findings reported in previous impact tests, where the use of stainless bars in SS-RC columns increased impact resistance and reduced maximum displacements when compared to specimens with ordinary steel reinforcement (Zhang et al., 2017a; Wu et al., 2019a; Wu & Xu, 2020). However, owing to the increased blast intensity, the failure was relatively more severe in the beam with SS reinforcement, and consisted of severe concrete crushing and significant spalling in the midspan region (see **Figure 5.7** & **Figure 5.8**). Indeed, the high-speed video stills show that the concrete damage and spalling in C100-No.5S1-S resulted in significant flying debris at failure. The next section explores the ability of steel fibers to improve blast performance and reduce fragmentation in the SS-reinforced concrete beams.

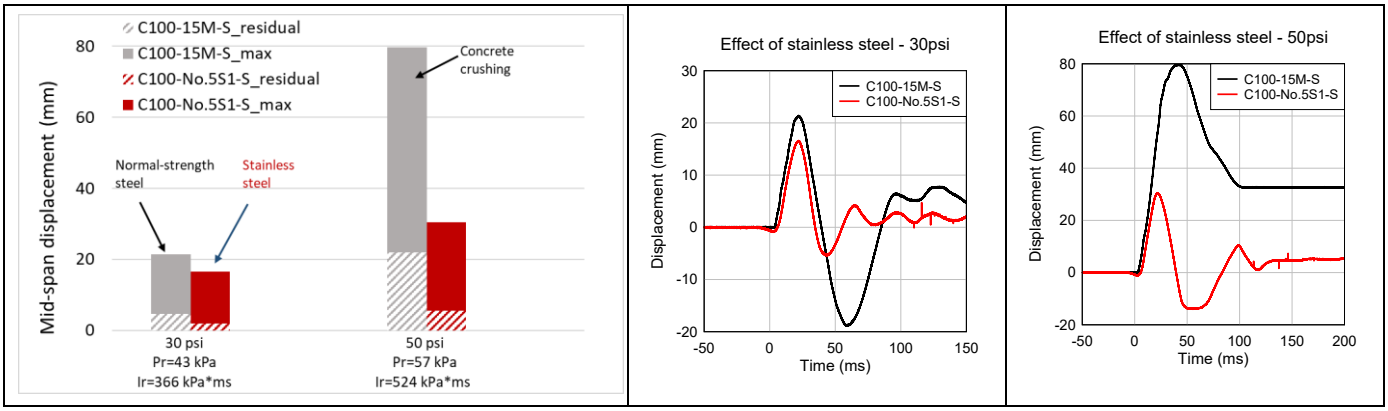

Figure 5.6 Blast test results: effect of stainless steel in HSC beams

Plain HSC and SS bars		Plain HSC and ordinary bars
(a) C100-No.5S1-S		(b) C100-15M-S
Blast-50psi	*Blast-70psi*	*Blast-50psi*
		

Figure 5.7 Comparison of blast damage: effect of stainless steel in HSC beams

	Ordinary bars	Stainless bars
Plain HSC	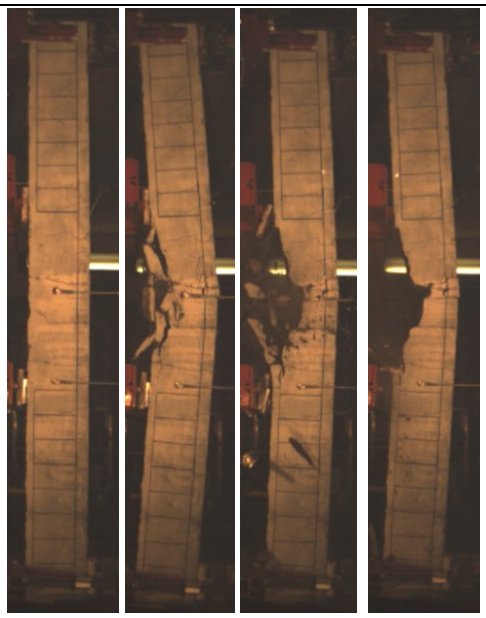	
	(a) C100-15M-S @ *Blast-50psi*	(b) C100-No.5S1-S @ *Blast-70psi*

Figure 5.8 High-speed video stills showing failure process

5.5.2. Ability of fibers to improve flexural response in beams with SS bars

This section compares the static and blast responses of beams CF100-No.5S1-S and C100-No.5S1-S, built with stainless steel, but cast with plain and fiber-reinforced HSC, respectively. It is noted, both beams were designed with stirrups to promote flexural failure.

As shown in **Figure 5.9a,** the provision of fibers improved all aspects of structural response under static loading. Keeping in mind the larger yield strength of the bars in batch *B2* (f_y = 648 vs 600 MPa), beam CF100-No.5S1-S shows increases of 30% in P_{max} , and 27% in stiffness (k_s), when compared C100-No.5S1-S. The increase in P_{max} is 30% when the results are normalized with respect to f_y, which confirms the beneficial effects of the fibers on flexural resistance. The results correspond to the previous findings of Ashour and Wafa (1993) and Imam et al. (1995) for HSC beams with ordinary steel reinforcement, and can be explained by the ability of fibers to improve the concrete tensile response as the fibers gradually pullout across the cracks. Importantly, the use of fibers was also effective in increasing ductility and overall toughness (area under the load-deflection curve); with increases of 147% in Δ_{max}/Δ_y (6.75 vs. 2.73), and 217% in A_u (12866 vs. 4061 J). Indeed, beam C100-No.5S1-S failed suddenly by crushing of concrete at Δ = 43 mm; in comparison crushing was delayed to Δ = 50 mm, and was much more gradual in beam CF100-No.5S1-S (see **Figure 5.10**). The results can be explained by the ability of the HSFRC concrete to better counter the high strain demands imposed on the HSC compression zone by the higher-strength stainless bars, especially as the tension bars go into the non-linear strain-hardening range (see strain readings in **Figure 5.9b**).

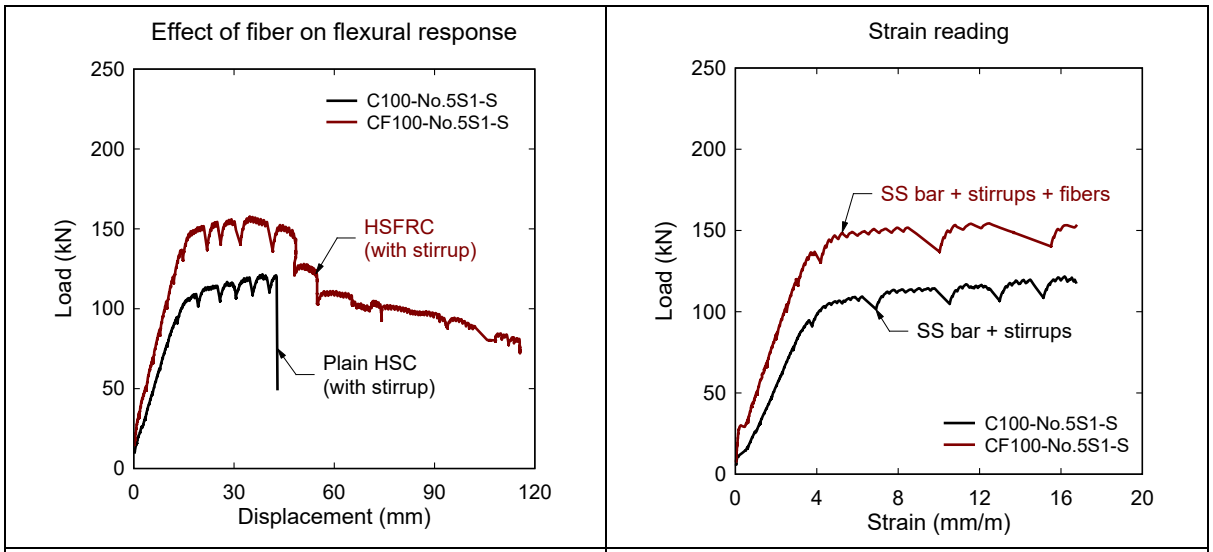

(a) Load-displacement response (b) Strains in stainless steel reinforcement

Figure 5.9 Static test results: effect of fibers on flexural response

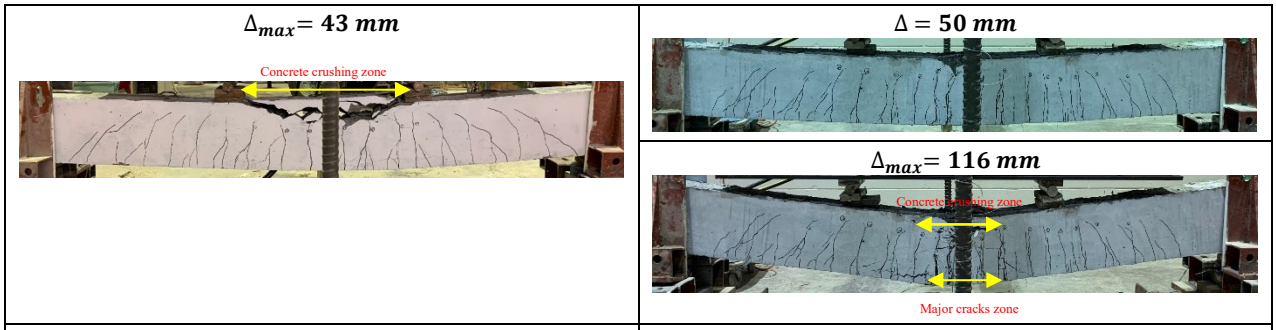

(a) C100-No.5S1-S (crushing failure)	(b) CF100-No.5S1-S (gradual crushing)

Figure 5.10 Beam photos and failure modes at end of static testing

The use of steel fibers also showed beneficial effects on blast behavior. As shown in **Figure 5.11**, adding steel fibers into the HSC mix led to better control of displacements at *Blasts-30, 50, 70psi*, with reductions of 13%, 29% and 63% in maximum displacements, and significant decreases of 100%, 91%, and 82% in residual displacements, when comparing beams CF100-No.5S1-S and C100-No.5S1-S. Importantly, the fibers improved damage tolerance and increased blast capacity. Failure of the plain HSC beam occurred at *Blast-70psi* (I_r = 707 kPa-ms) and was associated with severe crushing, cover spalling, and blast fragments (see **Figure 5.12a**). In contrast, failure was delayed to *Blast-90psi* (I_r = 842 kPa-ms) in the *CF100* specimen, with remarkable control of crushing, spalling and fragments despite the more intense blast (see **Figure 5.12b**). Indeed, the ability of fibers to control blast fragments is clear when examining the high-speed video stills in **Figure 5.13**. In summary, the results confirm the important benefits that can be achieved by coupling the higher-grade stainless-steel reinforcement with high-performance concrete and fibers in blast-applications.

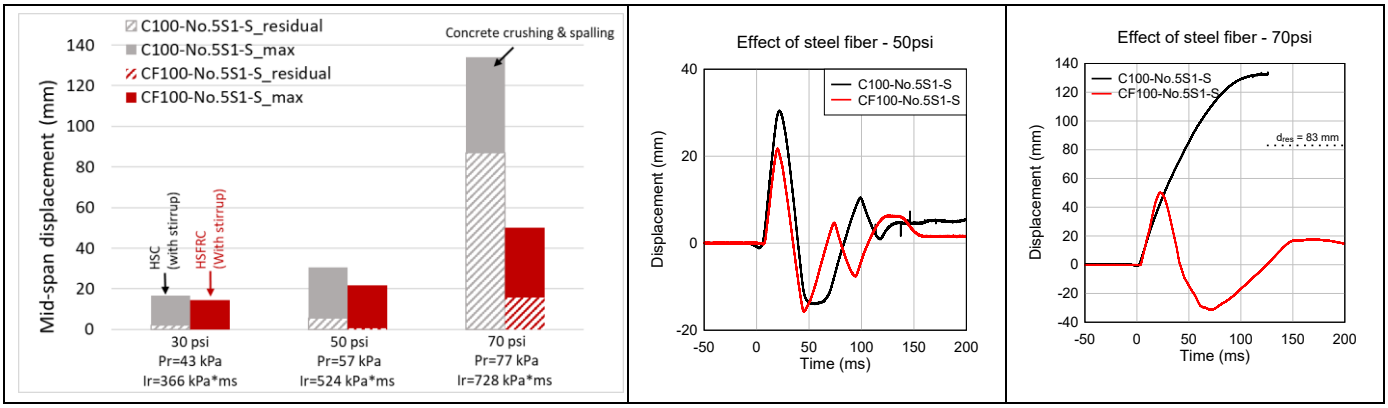

Figure 5.11 Blast test results: effect of fibers on flexural response

Plain HSC and SS bars		HSFRC and SS bars	
(a) C100-No.5S1-S		(b) CF100-No.5S1-S	
Blast-50psi	*Blast-70psi*	*Blast-50psi*	*Blast-70psi*
		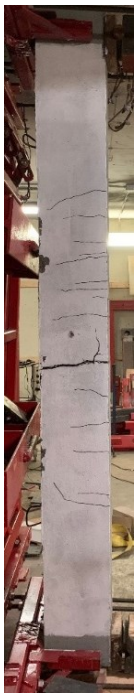	

Figure 5.12 Comparison of blast damage: effect of fibers on flexural response

Plain HSC and SS bars	HSFRC and SS bars
	
(a) C100-No.5S1-S @ *Blast-70psi*	(b) CF100-No.5S1-S @ *Blast-90psi*

Figure 5.13 High-speed video stills showing failure process

5.5.3. Effect of stainless steel in HSC beams with fibers

The previous sections confirm the ability of stainless steel and fibers to improve beam response under static and blast conditions. In this section, the effect of stainless-steel in beams built with fibers is investigated by comparing beam CF100-No.5S1-S, built with stainless steel, and beam CF100-15M built with ordinary 15M bars. It is noted that beam CF100-15M was built without stirrups in the shear spans since the fibers were sufficient to prevent shear failure.

Comparing to the *C100* set (see **Section 5.5.1**), a larger increase of 36% in P_{max} is observed in the *CF100* set (CF100-No.5S1-S vs. CF100-15M) owing to the larger yield stress of the batch *B2* stainless steel bars when compared to the Grade 400 MPa bars (f_y = 648 vs 472 MPa). As shown in **Figure 5.14a**, the provision of fibers allows both *CF100* beams to show remarkable ductility, however the ductile behaviour is more obvious in the case of the beam with ordinary steel bars which shows almost no drop in capacity even at very large displacements. Indeed, the beam with SS bars shows a steady decrease in capacity after peak, with a relatively sudden drop in strength (of ~ 20%) at Δ = 50 mm due to crushing of the high-strength concrete in the mid-span zone (see **Figure 5.15**). This can be explained by the increased strain demands imposed on the compression concrete as the tension stainless bars are pushed into the strain-hardening range (as also confirmed in the strain readings in **Figure 5.14b**), resulting in more noticeable concrete crushing, despite the provision of fibers.

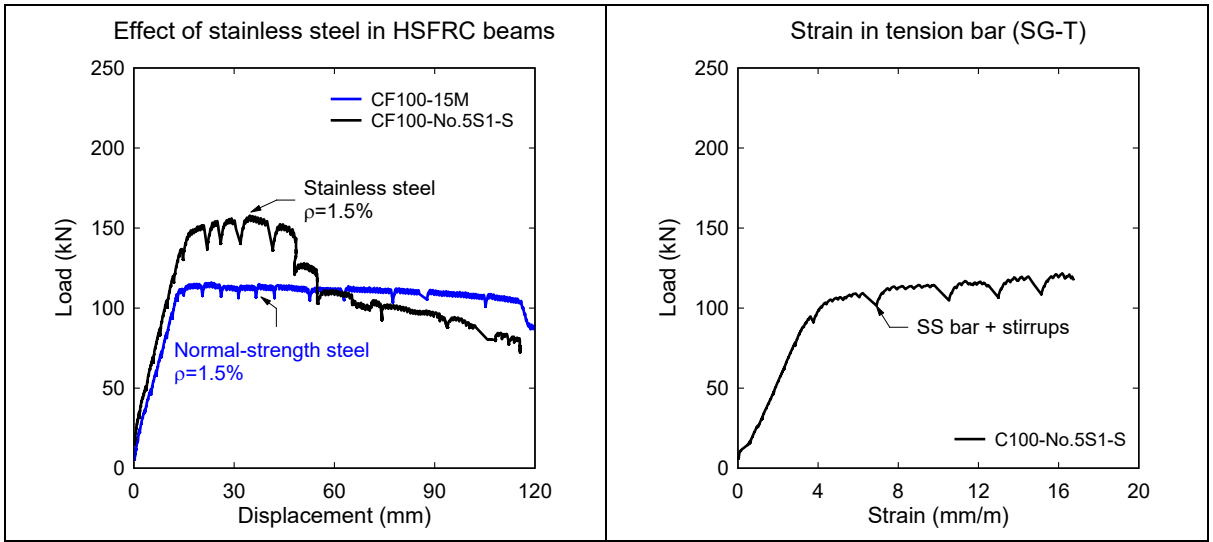

(a) Load-displacement response (b) Strains in stainless steel reinforcement

Figure 5.14 Beam static test results: effect of stainless steel in HSFRC beams

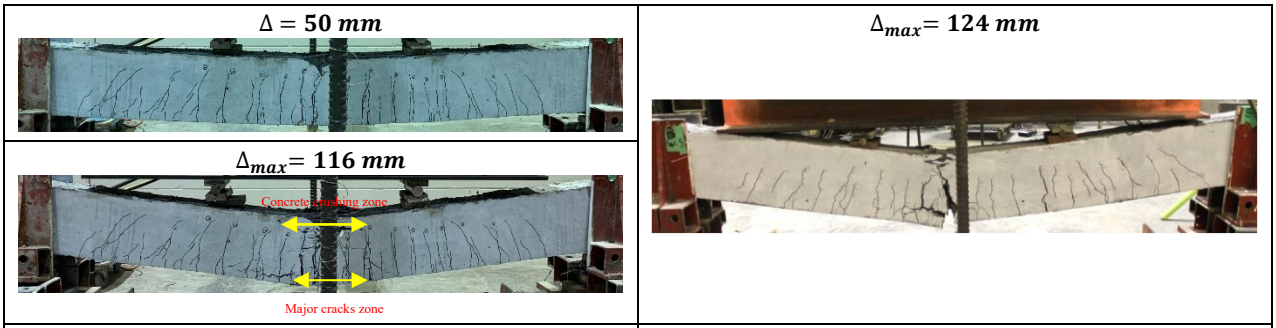

(a) CF100-No.5S1-S (gradual crushing) (b) CF100-15M (fiber pullout)

Figure 5.15 Beam photos and failure modes at end of static testing

Under blast loading, **Figure 5.16** shows that use of SS reinforcement in the *CF100* set led to reductions of 35% and 36% in maximum displacements at *Blast-50psi* and *Blast-70psi*, along with significant reductions in residual displacements (71% at *Blast-70psi*, and a nearly elastic response at *Blast-50psi*). The beam with SS bars was further able to withstand one additional shot corresponding to *Blast-90psi* loading (I_r = 842 kPa·ms). Failure in both beams was well controlled and associated with fiber pullout at the critical crack location at midspan (**Figure 5.17 & Figure 5.18**). The high-speed video further demonstrates the controlled failure process and limited debris in both fiber-reinforced specimens. The results in these tests, along with those previously reported by Algassem et al. (2019) and Li and Aoude (2020), confirm the beneficial effects of fibers on improving blast response and damage tolerance in HSC beams with varied types of steel reinforcement (ordinary, stainless and high-strength steel).

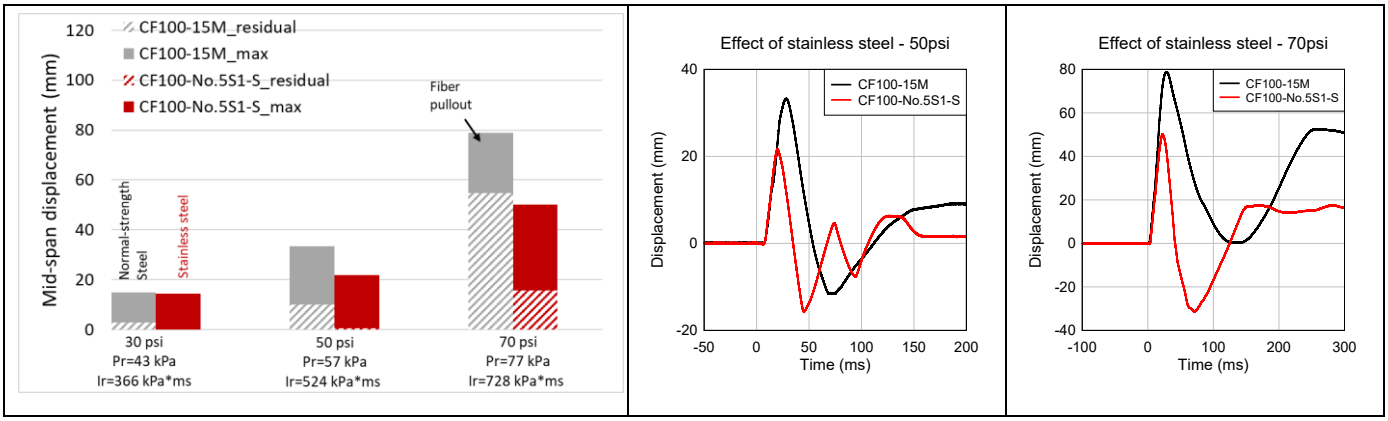

Figure 5.16 Blast test results: effect of stainless steel in HSFRC beams

HSFRC and SS bars		HSFRC and Ordinary bars	
(a) CF100-No.5S1-S		(b) CF100-15M	
Blast-50psi	*Blast-70psi*	*Blast-50psi*	*Blast-70psi*
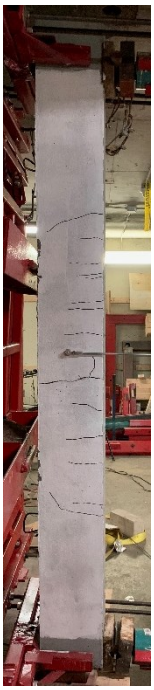			

Figure 5.17 Comparison of blast damage: Effects of stainless steel in HSFRC beams

	Stainless bars	Ordinary bars
HSFRC (with fibers)		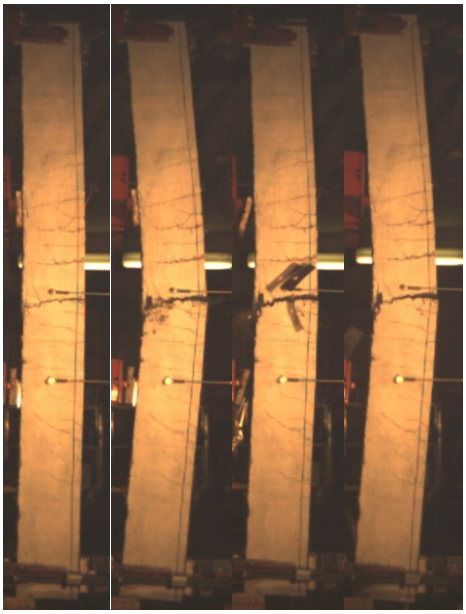
	(a) CF100-15M @ *Blast-70psi*	(b) CF100-No.5S1-S @ *Blast-90psi*

Figure 5.18 High-speed video stills showing failure process

5.5.4. Ability of fibers to improve shear response in beams with SS bars

In addition to the benefits on flexural response, previous research indicates the ability of steel fibers to improve shear response in HSC beams (Algassem et al., 2019; Li & Aoude, 2020). This section examines this effect in beams built with stainless steel reinforcement. In the static group, beam CF100-No.5S1 was built with No. 5 stainless bars (ρ=1.5%), and without stirrups to examine shear response. No companion SS beam without fibers was tested, however considering the minor effects of longitudinal steel type on shear resistance (Rabi et al., 2022), its response can be compared to that of beam C100-15M which was built with plain HSC and 15M ordinary reinforcing bars (ρ=1.5%). As shown in **Figure 5.19a**, both beams failed in shear, however the use of 1% steel fibers in CF100-No.5S1 increased shear capacity by 55% (P_{max} = 139 kN vs. 90 kN) owing to the ability of the fibers to increase the diagonal tension capacity of the high-strength concrete. It is interesting to note that the fibers allowed the tension steel bars to just reach yielding prior to the shear failure (see strain readings in **Figure 5.19b**). However, the increased flexural demands imposed by the SS reinforcement did not allow the fibers to prevent shear collapse (see **Figure 5.20**), indicating that fibers should be combined with at least minimum stirrups in beams with higher grade SS bars.

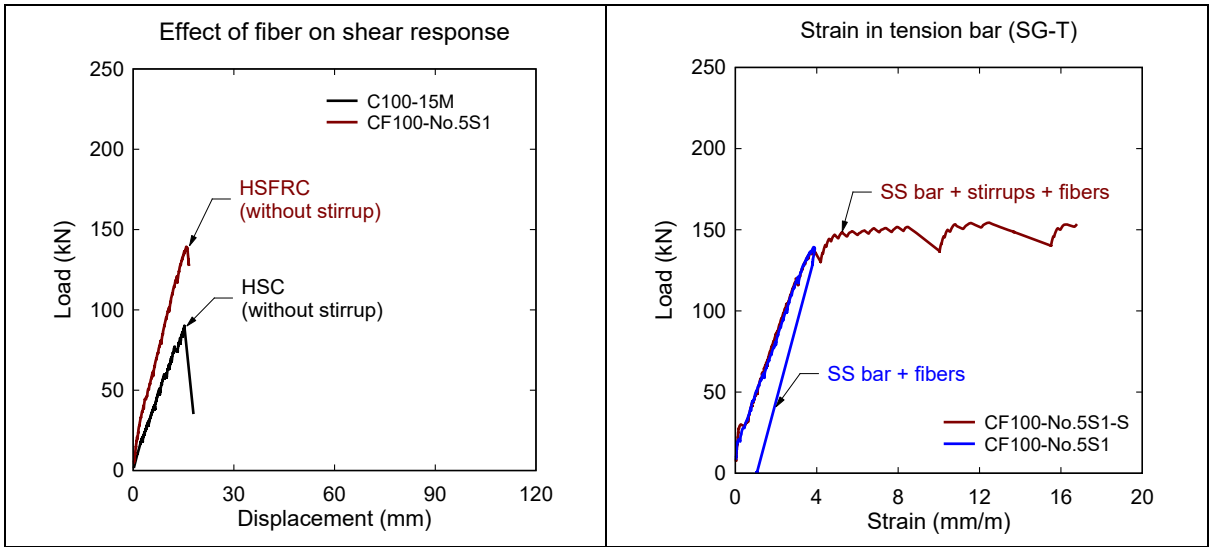

(a) Load-displacement response | (b) Strains in stainless steel reinforcement

Figure 5.19 Static test results: effect of fibers on shear response

Stainless steel and fibers	**Ordinary steel**
Δ_{max}= **16** mm	Δ_{max}= **15** mm
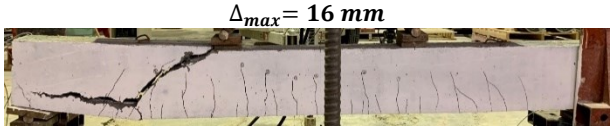	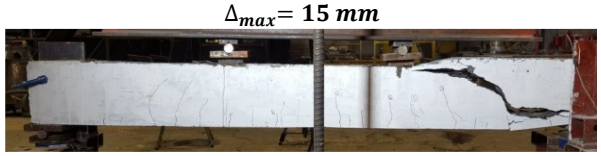
(a) CF100-No.5S1 (shear failure)	(b) C100-15M (shear failure)

Figure 5.20 Beam photos and failure modes at end of static testing

The same trends are observed under blast loading. Beams C100-No.5S1 and C100-15M, built with plain HSC, no stirrups, but with SS and ordinary steel bars, failed at relatively load blast pressures under *Blast-30psi* (**Figure 5.22(a,b)**). The results confirm the limited effects of longitudinal steel type on shear resistance, even under blast loading. In comparison, the provision of 1% steel fibers allowed beam CF100-No.5S1 to survive *Blasts-30psi* and *50psi*, with failure delayed to *Blast-70psi* (**Figure 5.21** & **Figure 5.22c**), representing a 95% increase in failure impulse. However, the beam ultimately failed in shear indicating that fibers were insufficient to completely replace transverse reinforcement in the beam with SS bars.

To further examine the results, the shear capacities of beams C100-No.5S1 and CF100-No.5S1 are predicted using the equations in the CSA A23.3 standard and Aoude et al. (2012). According to the CSA A23.3 approach (CSA, 2014), the shear resistance of a reinforced concrete beam is given by $V_{r0} = V_c + V_s$, where $V_c = \beta\sqrt{f_c'}b_w d_v$ (from concrete), and $V_s = \frac{A_v f_y}{s} d_v \cot\theta$ (from the transverse steel), and where, β = aggregate interlock factor, f_c' = concrete strength, b_w = beam width, d_v = shear depth, f_y and s = stirrup yield strength and spacing; θ = shear crack angle. In the Aoude et al. (2012) model, the shear resistance of a beam with fibers is $V_{rf} = V_{r0} + V_{fib}$, where V_{r0} is the beam's shear capacity without fibers (calculated according to the general method in the CSA A23.3 standard) and V_{fib} is the added shear capacity provided by the fibers (see **Figure 5.23)**. In this model, $V_{fib} = N_{fib} 0.83 f_p\, b_w d_v \cot\theta$, where N_{fib} = number of fibers pre unit area and f_p = pullout strength of the fibers (Aoude et al., 2012). Using these models, the predicted shear capacities of beams C100-No.5S1 and CF100-No.5S1 are found to be 40.6 kN and 100.8 kN, respectively. At *Blast-30psi*, the peak reflect pressure (P_r) was approximately 41 kPa for both beams. Multiplying this pressure by the area of the load transfer device ($A = 3.4\ m^2$) results in a maximum applied shear force of $V_{fBlast\,1} = 0.5 \cdot P_r A \approx 70$ kN, which can explain the shear failure observed in beam C100-No.5S1. Conversely, the use of fibers in beam CF100-No.5S1 results in shear resistance ($V_{rf} = 101$ kN) which just exceeds the applied shear force under *Blast-30psi* and *Blast-50psi* loads ($V_{fBlast\,1} \approx 70$ kN and $V_{fBlast\,2} \approx 98$ kN), although the shear resistance was insufficient at *Blast-70psi* ($V_{fBlast\,3} \approx 131.6$ kN).

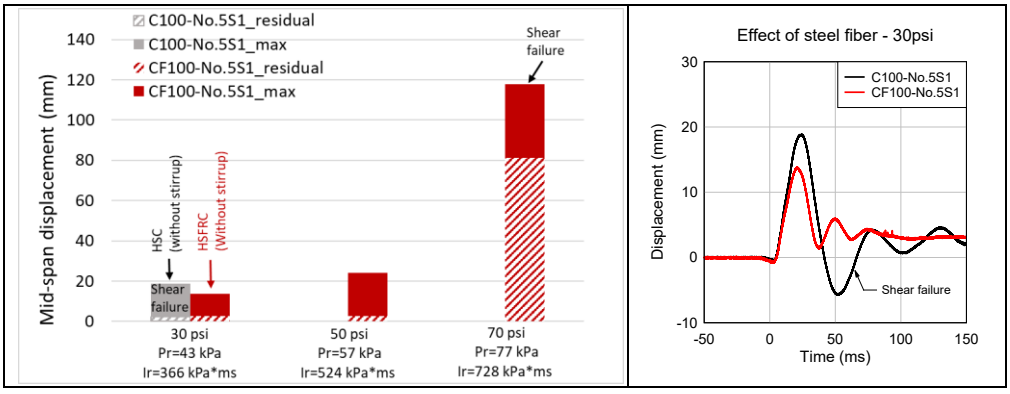

Figure 5.21 Blast displacements: effect of fibers on shear response

Plain HSC and ordinary bars	Plain HSC and SS bars	HSFRC and SS bars		
(a) C100-15M	(b) C100-No.5S1	(c) CF100-No.5S1		
Blast-30psi	*Blast-30psi*	*Blast-30psi*	*Blast-50psi*	*Blast-70psi*
				

Figure 5.22 Comparison of blast damage: effect of fibers on shear response

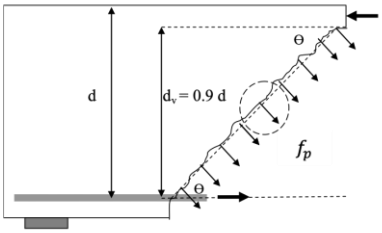

$$V_{fib} = N_{fib} 0.83 f_p\, b_w d_v \cot\theta$$

$$N_{fib} = \frac{v_f}{A_f} \times \alpha \times \eta_l$$

$$f_p = \left(\tau_{bond} \times \pi \times d_f \times \frac{L_{f,straight}}{2}\right) + \Delta P'$$

$$\Delta P' = \frac{3.05}{\cos(45^\circ \times \frac{\pi}{180^\circ})} \left(f_{fy} \times \frac{\pi (d_f/2)^2}{6}\right)$$

A_f = cross-sectional area of the fiber

α = orientation factor, use 3/8

η_l = embedment length factor, use 0.5

τ_{bond}=5-6 Mpa (high-strength concrete)

$L_{f,straight}$= straight portion of the fiber

f_{fy}= fiber yield strength

Figure 5.23 Fiber pullout at critical shear crack according to Aoude model (Aoude et al., 2012)

5.5.5. Effect of equal-strength replacement stainless steel reinforcement

One of the benefits of the stainless-steel reinforcement is its increased yield and ultimate strength. This section compares the static and blast responses of beam C100-No.5S1-S and CF100-No.5S1-S, which had a reinforcement ratio of ρ=1.5%, with that of beams C100-20M-S and CF100-20M-S, which had 2-20M ordinary steel bars, resulting in ρ = 2.4%.

Figure 5.24a compares the static responses of the beams in the HSC set. It can be observed that beam C100-No.5S1-S shows slightly lower load capacity (12% reduction in P_{max}) when compared to C100-20M-S which had increased amounts of ordinary bars. The result is expected considering the ordinary and stainless beams had ρf_y values of 10.4 MPa vs. 9.0 MPa, representing a ρf_y ratio (ordinary vs. stainless) of 1.15. Nonetheless, the beam with SS bars shows more ductile behaviour with increases of ~ 30% in Δ_{max}/Δ_y, and A_u toughness, when compared to the beam with 20M ordinary bars. Similar trends are observed under blast loading, with both beams showing similar maximum displacements under *Blast-30, 50 ,70psi* loading, with differences of +10%, -7% and +13% (see **Figure 5.25a**). Both beams fail at *Blast-70psi* with severe concrete crushing in the compression zone, while spalling is observed in the beam with stainless steel (see **Figure 5.26(a,b)**). The findings are consistent with those in Zhou et al. (2019); Zhou et al. (2020) & Zhou et al. (2020), where columns built with conventional steel (10-Φ22 or 8-Φ22) and equal-strength replacement stainless steel (8-Φ20 or 6-Φ20) had similar impact force and peak displacements, with differences within ± 10%.

Figure 5.24b compares the static responses of the beams in the fiber-reinforced concrete set. Owing to the higher yield strength of the SS bars in batch B2 (f_y = 648 MPa), beam CF100-No.5S1-S, with ρ = 1.5%, shows similar yield capacity (P_y), but higher ultimate strength (P_{max}), when compared to beam CF100-20M-S which had ρ = 2.4%. The ordinary and stainless beams had ρf_y values of 10.4 MPa vs. 9.7 MPa, representing a ρf_y ratio of 1.07. However, as shown in **Figure 5.24c**, the steel fibers in beam CF100-No.5S1-S allowed the stainless-steel to go well into the strain-hardening stage, resulting in an increased load capacity after yielding. The results demonstrate the synergetic effects that can be gained from the combined use of fibers and stainless-steel reinforcement. Improved performance is further observed under blast loading; where beam CF100-No.5S1-S shows reductions of 21%, 25% and 39% in maximum displacements, and 88%, 62% and 45% in residual displacements, when compared to the more heavily-reinforced CF100-20M-S specimen at *Blast-50, 70, 90psi* (see **Figure 5.25b**). Both beams fail at *Blast-90psi*, however slightly more obvious crushing is

observed in the beam with fibers and ordinary steel bars (see **Figure 5.26(c,d)**). The differences in terms of displacement control and damage tolerance are still more significant when comparing beams CF100-No.5S1-S (ρ = 1.5%, and fibers) and C100-20M-S (ρ = 2.4%, no fibers), further confirming the benefits of combining fibers and stainless-steel reinforcement.

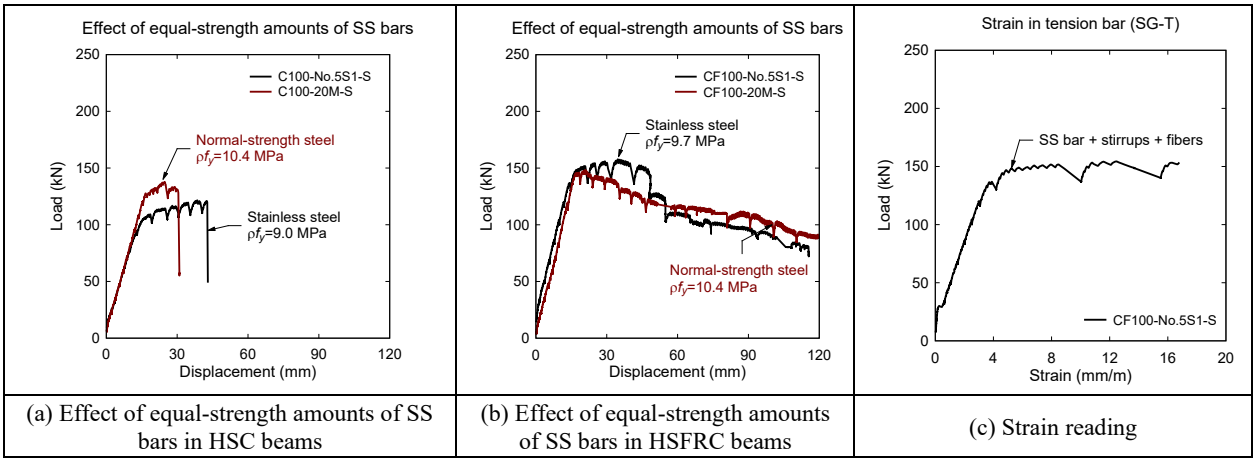

(a) Effect of equal-strength amounts of SS bars in HSC beams | (b) Effect of equal-strength amounts of SS bars in HSFRC beams | (c) Strain reading

Figure 5.24 Beam static test results: effect of equal-strength amounts of SS bars

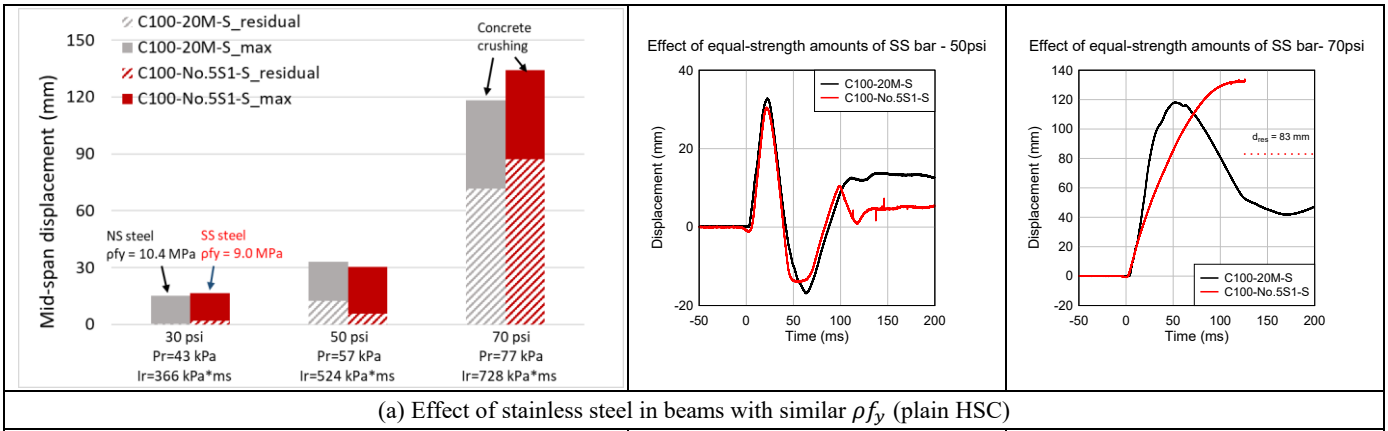

(a) Effect of stainless steel in beams with similar ρf_y (plain HSC)

(b) Effect of stainless steel in beams with similar ρf_y (with fibers)

Figure 5.25 Effects of stainless steel on displacements under blast loads (similar ρf_y)

Plain HSC and No.5 SS bars ρf_y = 9.0 MPa	**Plain HSC and 20M ordinary bars ρf_y = 10.4 MPa**	**HSFRC and No.5 SS bars ρf_y = 9.7 MPa**	**HSFRC and 20M ordinary bars ρf_y = 10.4 MPa**
(a) C100-No.5S1-S	(b) C100-20M-S	(c) CF100-No.5S1-S	(d) CF100-20M-S
Blast-70psi	*Blast-70psi*	*Blast-90psi*	*Blast-90psi*
			

Figure 5.26 Comparison of blast damage in beams with equal-strength amounts of bars

5.6 Conclusions

This chapter presented the results from **Series 2A** of the PhD program, and examined the flexural behaviour of HSC beams built stainless steel bars under static and blast conditions. The test variables included the effects of steel type and fibers in beams designed to fail in shear and flexure. The following conclusions can be drawn from this study:

1. The use of stainless steel increased the load-carrying capacity of the plain and fiber-reinforced HSC beams built with stirrups under static loading. The use of stainless bars also improved blast performance by reducing displacements and increasing blast capacity. In general, the use of moderate stainless steel ratio (ρ =1.5%) combined with high-strength concrete allowed for relatively ductile response under static and blast loads;
2. The use of steel fibers further improved the blast response of the beams with stainless bars. In the beams with stirrups, the use of 1% fibers reduced displacements at equivalent blasts, and increased blast capacity. Importantly, the provision of fibers enhanced damage tolerance, and reduced the amount of spalling and secondary blast fragments;
3. In the beams without stirrups, the use of 1% steel fibers increased shear capacity allowing for a near-doubling in failure impulse. However, the use of fibers was insufficient to prevent shear failure and fully replace stirrups owing to the increased shear demands imposed by the higher-strength and strain-hardening stainless steel bars. Thus, fibers should be combined with transverse reinforcement to prevent shear failures in SS-RC beams;
4. Replacing ordinary steel bars with near equal-strength amounts of stainless steel bars (i.e., similar ρf_y ratios) allowed for similar beam responses under static and blast loading. The coupled use of reduced amounts of stainless bars and fibers was particularly effective under blast loading. The differences in terms of displacement control and damage tolerance were still more significant when comparing beams CF100-No.5S1-S (ρ = 1.5%, and fibers) and C100-20M-S (ρ = 2.4%, no fibers), confirming the benefits of combining fibers and stainless steel reinforcement.

5.7 References (Chapter 5)

Algassem, O., Li, Y., & Aoude, H. (2019). Ability of steel fibers to enhance the shear and flexural behavior of high-strength concrete beams subjected to blast loads. *Engineering Structures, 199*, 109611. doi:https://doi.org/10.1016/j.engstruct.2019.109611

Aoude, H., Belghiti, M., Cook, W. D., & Mitchell, D. (2012). Response of Steel Fiber-Reinforced Concrete Beams with and without Stirrups. *ACI Structural Journal, 109*(3), 359-367. doi:https://doi.org/10.14359/51683749

Ashour, S. A., & Wafa, F. F. (1993). Flexural behavior of high-strength fiber reinforced concrete beams. *ACI Structural Journal, 90*(3), 279-287. doi:https://doi.org/10.14359/4186

Canadian Standards Association (CSA) (2012). Design and assessment of buildings subjected to blast loads. CSA S850-12, Mississauga, ON, Canada, pp. 126.

Canadian Standards Association (CSA) (2014). Design of concrete structures. CAN/CSA A23.3-14, Mississauga, ON, pp. 295.

Imam, M., Vandewalle, L., & Mortelmans, F. (1995). Shear–moment analysis of reinforced high strength concrete beams containing steel fibres. *Canadian Journal of Civil Engineering, 22*(3), 462-470. doi:https://doi.org/10.1139/l95-054

Li, Y., & Aoude, H. (2020). Influence of steel fibers on the static and blast response of beams built with high-strength concrete and high-strength reinforcement. *Engineering Structures, 221*, 111031. doi:https://doi.org/10.1016/j.engstruct.2020.111031

Rabi, M., Shamass, R., & Cashell, K. A. (2022). Structural performance of stainless steel reinforced concrete members: A review. *Construction and Building Materials, 325*, 126673. doi:https://doi.org/10.1016/j.conbuildmat.2022.126673

Wu, B., & Xu, S. (2020). Experimental study on damage evaluation of stainless steel–reinforced concrete piers under lateral impact. *Advances in Mechanical Engineering, 12*(5), 168781402092488. doi:https://doi.org/10.1177/1687814020924886

Wu, B., Xu, S., & Zhang, G. (2019). Study on Cumulative Damage Law of Stainless Steel-Reinforced Concrete Columns under Step Impact Loading. *Advances in Materials Science and Engineering, 2019*, 1-8. doi:https://doi.org/10.1155/2019/4076145

Zhang, G., Xu, S., Xie, H., Zhou, X., & Wang, Y. (2017). Behavior of stainless steel–reinforced concrete piers under lateral impact loading. *Advances in Mechanical Engineering, 9*(5), 168781401770993. doi:https://doi.org/10.1177/1687814017709936

Zhou, X., Zhang, H., Zhang, W., & Zhang, G. (2020). Study on the Influence of Closed-Cell Aluminum Foam on the Impact Performance of Concrete Pier after Equal Replacement with Stainless Steel Reinforcement. *Advances in Materials Science and Engineering, 2020*, 1-17. doi:https://doi.org/10.1155/2020/8356319

Zhou, X., Zhang, W., Gao, Y., Zhang, G., & Xiong, R. (2019). A Comparative Test Study of the Impact Performances of Stainless-Steel Rebar Equal-Strength Replacement Piers. *International Journal of Steel Structures, 20*(1), 67-79. doi:https://doi.org/10.1007/s13296-019-00269-5

Chapter 6 Test results from Series 2B (HSC-SS)

Paper 3: Effects of detailing on the behaviour of high-strength concrete beams built with stainless steel reinforcement under static and blast load conditions

6.1 Introduction

This chapter discusses the results from Series 2B (HSC-SS) of the research program, and examines the effects of detailing on the static, blast and post-blast performance of high-strength concrete (HSC) beams built with stainless steel (SS) reinforcement conforming to ASTM A955. As part of the study, a series of HSC beams built with Grade 520 MPa stainless steel bars, and detailed according to the CSA S850 standard (CSA, 2012), were tested under static and blast loads using a shock-tube. Beams with steel fibers and relaxed detailing were also tested. The results are compared to a companion set of beams which were built with nominal detailing, as well as a control set of blast-detailed beams built with ordinary steel bars. Test variables included the effects of detailing (blast vs. nominal), steel type (stainless vs. ordinary steel), stainless steel alloy (austenitic vs duplex), and the influence of steel fibers.

6.2 Research contribution

The content of this chapter is included in the paper titled "Effects of detailing on the behaviour of high-strength concrete beams built with and stainless steel reinforcement under static and blast load conditions" (to be submitted).

6.3 Experimental program

The details of the experimental program were provided in **Chapter 3** (see Series 2B). **Table 6.1** and **Figure 6.1** provide the details of the nine beams included in this series, and the four companion beams from Series 2A. All beams had dimensions of 125 mm × 250 mm × 2440 mm (b × h × L), and were built with high-strength concrete (HSC) and Grade 520 MPa ASTM A955 reinforcement. Longitudinal reinforcement in tension consisted of either 2-No.4 or 2-No.5 stainless steel bars (ρ = 1% or 1.5%), while transverse steel consisted of closed ties or open stirrups made from 6 mm wire arranged at various spacing (s). Two types of stainless steel alloys were tested, including XM-28 and S2304 (designated as S1 and S2). As shown in **Table 6.1** and **Figure 6.1**, the specimens can be subdivided into three groups: *Group A* beams (7 specimens) were designed according to modern blast standards, with top continuity bars and closely spaced ties at s = 50 mm (d/4) throughout the beam span; *Group B* beams (2 specimens)

were designed with high-strength fiber-reinforced concrete (HSFRC) and a larger tie spacing of s = 100 mm (d/2); *Group C* includes a companion set of singly-reinforced beams with "nominal detailing" with open-stirrups spaced at s = 100 mm (d/2) in the shear spans only from Series 2A. To examine the effects of steel type, the Group A and B beams are also compared to a control set of beams with identical properties but built with ordinary 15M or 20M steel reinforcement, tested by Charles (2019).

The beam nomenclature in **Table 6.1** and **Figure 6.1** indicates the design parameters of the test and control beams, including the concrete type (C100 or CF100), tension bar size (No.4, No.5, 15M, or 20M), stainless steel type (S1 or S2), and detailing level ("DR-d/4", "DR-d/2" and "S" for Type A, B and C detailing). For example, C100-No.5S1-DR-d/4 is constructed with plain C100 high-strength concrete, No.5 S1 stainless bars and Type A blast detailing, while C100-No.5S1-S is the companion beam built with Type C nominal detailing. In the control set, C100-15M-DR-d/4 is the HSC beam built ordinary 15M steel bars, and Type A blast detailing.

Blast tests were conducted using the University of Ottawa shock-tube with companion beams tested under quasi-static four-point bending. Details on the test setups and testing protocols were provided in see **Section 3.4**. **Figure 6.2** shows sample shockwaves corresponding to *Blasts-30, 50, 70, 90psi* used in this series. These blasts were obtained by varying the input driver pressure from 30 to 90 psi (207–620 kPa), with the driver length fixed at 9 ft (2743 mm). A summary of key blast parameters is presented in **Table 6.2**, including, the reflected pressures (P_r), reflected impulses (I_r) and positive shockwave duration (t_d).

Table 6.1 Beam Design details

Group	Beam ID	Concrete Type	Fiber content V_f [c] (%)	Longitudinal Reinf.			Transverse Reinf.		Loading type [e]
				Type [d] (Grade)	Tension steel (ρ)	Comp. steel (ρ')	Type	Tie/stirrup Spacing	
A	C100-No.4S1-DR-d/4	HSC	-	XM-28 (520 MPa)	2-No.4 (1.0%)	2-No.3 (0.6%)	Closed ties (full span)	50 mm (d/4)	S, D
	C100-No.5S1-DR-d/4				2-No.5 (1.5%)	2-No.4 (1.0%)		50 mm (d/4)	S, D
	C100-No.5S1-DR-d/4 [x1]							50 mm (d/4)	Dx1
	C100-No.5S2-DR-d/4			2304 (520 MPa)				50 mm (d/4)	S, D
B	CF100-No.5S1-DR-d/2	HSFRC	0.75 %	XM-28 (520 MPa)	2-No.5 (1.5%)	2-No.4 (1.0%)		100 mm (d/2)	S, D
C [a]	C100-No.5S1-S	HSC	-	XM-28 (520 MPa)	2-No.5 (1.5%)	-	Stirrups (shear spans only)	100 mm (d/2)	S, D
	CF100-No.5S1-S	HSFRC	1.0 %						S, D
Control [b]	C100-15M-DR-d/4	HSC	-	Ordinary (400 MPa)	2-15M (1.5%)	2-10M (0.8%)	Closed ties (full span)	50 mm (d/4)	S, D
	CF100-15M-DR-d/2	HSFRC	0.75%					100 mm (d/2)	S, D
	C100-20M-DR-d/4	HSC	-		2-20M (2.4%)			50 mm (d/4)	S, D
	CF100-20M-DR-d/2	HSFRC	0.75%					100 mm (d/2)	S, D

Note: ρ = tension steel ratio; ρ' = compression steel ratio

[a] Companion beams with Type C (nominal) detailing and stainless steel tested in Series 2A

[b] Control beams with Type A and B detailing and ordinary steel tested by Charles (2019)

[c] HSFRC mix in Group B and control beams contains 0.75% of hybrid fibers; HSFRC mix in Group C contains 1% of hooked-end steel fibers.

[d] XM-28: austenitic stainless steel designated as S1; 2304: duplex 2304 stainless steel designated as S2.

[e] S, D, Dx1: specimens tested under static, repeated dynamic and single dynamic loading, respectively.

(a) **Group A**: HSC beams with Blast detailing (top continuity bars and closed ties @ d/4):

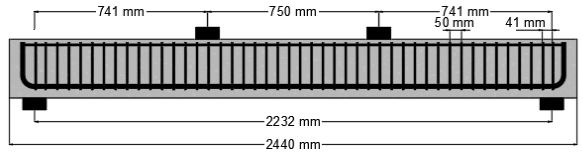

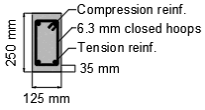

Group A:	Test
C100-No.4S1-DR-d/4	S, D
C100-No.5S1-DR-d/4	S, D
C100-No.5S1-DR-d/4 [x1]	Dx1
C100-No.5S2-DR-d/4	S, D
Control beams:	
C100-15M-DR-d/4	S, D
C100-20M-DR-d/4	S, D

(b) **Group B**: HSFRC beam with Intermediate detailing (top continuity bars and closed ties @ d/2):

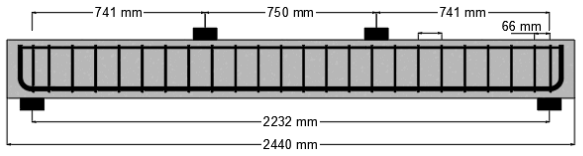

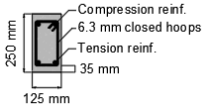

Group B:	Test
CF100-No.5S1-DR-d/2	S, D
Control beams:	
CF100-15M-DR-d/2	S, D
CF100-20M-DR-d/2	S, D

(c) **Group C**: HSC beams with Nominal detailing (singly-reinforced and stirrups @ d/2):

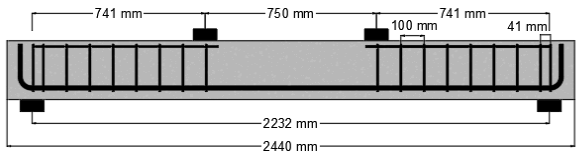

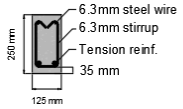

Group C (Series 2A):	Test
C100-No.5S1-S	S, D
CF100-No.5S1-S	S, D

Figure 6.1 Specimen Designs

Note: S = static test, D = repeated blast test, Dx1 = single blast test

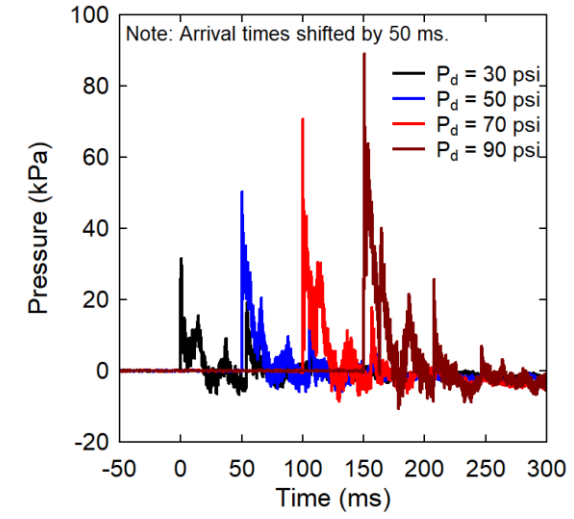

Group A: C100-No.4S1-DR-d/4 C100-No.5S1-DR-d/4 C100-No.5S1-DR-d/4 [x1] C100-No.5S2-DR-d/4	Test sequence: Blast-30, 50, 70, 90 psi Blast-30, 50, 70, 90 psi Blast-90 psi Blast-30, 50, 70, 90 psi
Group B: CF100-No.5S1-DR-d/2	Test sequence: Blast-30, 50, 70, 90 psi
Group C: C100-No.5S1-S CF100-No.5S1-S	Test sequence: Blast-30, 50, 70 psi Blast-30, 50, 70, 90 psi
Control: C100-15M-DR-d/4 C100-20M-DR-d/4 CF100-15M-DR-d/2 CF100-20M-DR-d/2	Test sequence: Blast-30, 50, 70 psi Blast-30, 70, 90 psi Blast-30, 50, 70, 90 psi Blast-30, 70, 90 psi

Figure 6.2 Sample shockwaves and testing protocols

Table 6.2 Average blast properties for beams tested in Series 2B

Blast Load	**Driver Pressure kPa (psi)**	**Driver Length mm (ft)**	**Average Reflected Pressure, P_r (kPa)**	**Average Reflected Impulse, I_r (kPa·ms)**	**Average Positive Phase Duration, t_d (ms)**
Blast-30psi	207 (30)	2743 (9)	42.7	366	21.3
Blast-50psi	345 (50)		57.3	524	22.4
Blast-70psi	483 (70)		77.4	728	23.4
Blast-90psi	621 (90)		89.4	842	24.7

6.4 Summary of results

The results from the static tests are plotted in **Figure 6.3**. **Table 6.3** summarizes key parameters from the tests, including: yield load (P_y), maximum load (P_{max}), secant stiffness (k_s), yield displacement (Δ_y), maximum (failure) displacement (Δ_{max}), ductility (Δ_{max}/Δ_y) and toughness (A_u). representing the area under the load-deflection curves up to Δ_{max}.

Table 6.4 reports a summary of the blast test results, including shockwave data (P_r , I_r and t_d = peak reflected pressure, impulse, and positive phase duration) and specimen response after each test (D_{max} , D_{res} and θ_{max} = maximum displacement, residual displacement and support rotation).

The blast-tested beams were subsequently tested under static four-point bending to assess their post-blast residual capacity. **Table 6.5** summarizes key data from the post-blast residual load-deflection curves, including maximum residual capacity (P_{max}^R), residual secant stiffness (k_s^R) and maximum post-blast residual displacement (Δ_{max}^R). **Figure 6.4** defines various indices used to analyse the post-blast test results**.**

Table 6.3 Experimental results from the static tests

Group	Beam	Load		Displacement		Secant Stiffness k_s (N/mm)	Ductility Δ_{max}/Δ_y	Toughness A_u (J)
		Yield P_y (kN)	Peak P_{max} (kN)	Yield Δ_y (mm)	Failure Δ_{max} (mm)			
A	C100-No.4S1-DR-d/4	91.1	108.5	24.3	150	5303	6.17	13439
	C100-No.5S1-DR-d/4	116.0	135.7	17.5	147	7769	8.57	17033
	C100-No.5S2-DR-d/4	149.1	169.8	23.7	150	7821	6.30	19769
B	CF100-No.5S1-DR-d/2	134.2	153.3	17.8	150	8608	8.43	19250
C	C100-No.5S1-S	105.2	121.6	15.6	42.6	6744	2.73	4061
	CF100-No.5S1-S	146.9	157.8	17.1	115.5	8591	6.75	12886

Note: P_y = yield strength; P_{max} = peak static strength; Δ_y = yield displacement; Δ_{max} = maximum displacement; k_s = secant stiffness; A_u = area under the load deflection curve up to Δ_{max}.

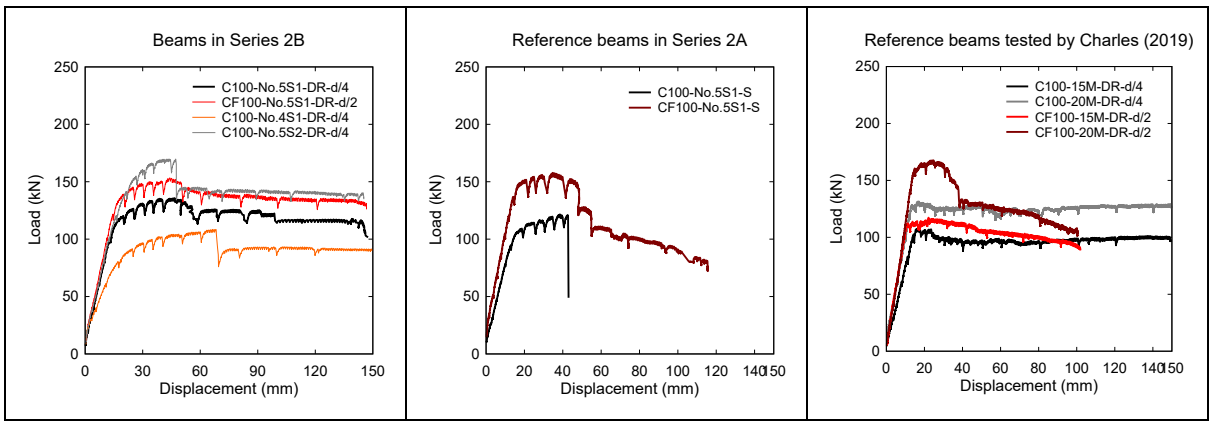

Figure 6.3 Summary of static test results (load-deflection curves)

Table 6.4 Experimental results from the blast tests

	Beams	Blast ID (psi)	Shockwave Properties[1]			Beam response[2]				CSA S850 Response limits and Component damage[3]	
			P_r (kPa)	I_r (kPa·ms)	t_d (ms)	D_{max} (mm)	D_{res} (mm)	θ_{max} (°)	Observed damage	Response limit	Damage level
Group A	C100-No.4S1-DR-d/4	30	45.4	369.4	20.6	19.8	3.5	1.0	Minor F cracking	<B1	Superficial
		50	56.1	503.7	21.2	36.3	12.0	1.9	Moderate F cracking	B1-B2	Moderate
		70	84.1	697.9	22.0	61.4	32.1	3.2	Moderate F cracking	B1-B2	Moderate
		90	94.2	870.8	24.3	108.9	68.4	5.6	Cover crushing & Moderate F cracking	B2-B3	Heavy
	C100-No.5S1-DR-d/4	30	45.4	359.2	20.7	18.9	3.5	1.0	Minor F cracking	<B1	Superficial
		50	62.6	524.9	22.0	27.6	3.8	1.4	Minor F cracking	B1-B2	Moderate
		70	84.3	723.5	24.5	49.1	27.7	2.5	Moderate F cracking	B1-B1	Moderate
		90	92.3	900.4	24.9	74.7	40.9	3.8	Cover crushing & Moderate F cracking	B1-B2	Moderate
	C100-No.5S1-DR-d/4 [x1]	90	84.6	851.6	24.6	65.6	33.8	3.4	Moderate F cracking	B1-B2	Moderate
	C100-No.5S2-DR-d/4	30	46.2	341.1	20.2	16.9	4.4	0.9	Minor F cracking	<B1	Superficial
		50	64.6	523.3	21.2	27.0	3.6	1.4	Minor F cracking	B1-B2	Moderate
		70	74.8	691.8	21.8	45.0	13.5	2.3	Moderate F cracking	B1-B2	Moderate
		90	84.3	897.9	24.0	74.3 *	40.1 *	3.8	Cover crushing & Moderate F cracking	B1-B2	Moderate
Group B	CF100-No.5S1-DR-d/2	30	39.8	379.9	21.1	17.1	3.3	0.9	Minor F cracking	<B1	Superficial
		50	64.7	534.0	21.8	23.8	4.8	1.2	Minor F cracking	B1-B2	Moderate
		70	78.4	713.4	22.1	39.2	14.5	2.0	Moderate F cracking	B1-B2	Moderate
		90	87.2	854.3	23.4	59.3	31.3	3.0	Moderate F cracking	B1-B2	Moderate
Group C	C100-No.5S1	30	46.7	371.6	21.5	16.6	2.0	0.9	Minor cracking	<B1	Superficial
		50	57.6	539.0	23.1	30.5	5.6	1.6	Moderate cracking	B1-B2	Moderate
		70	76.1	707.3	24.4	134	87	6.9	Severe concrete crushing & spalling	B3-B4	Hazardous
	CF100-No.5S1	30	43.0	376.7	21.9	14.5	0	0.7	Minor cracking	<B1	Superficial
		50	56.8	481.8	22.9	21.8	0.5	1.1	Moderate cracking	B1-B2	Moderate
		70	75.3	764.6	24.4	50.2	15.7	2.6	Moderate cracking	B2-B3	Heavy
		90	89.4	841.5	24.7	93.8 *	43.6 *	4.8	Fiber pullout	B2-B3	Heavy

[1]: P_r = Reflected pressure; I_r = Reflected impulse; t_d = positive phase duration;

[2]: D_{max} = maximum mid-span displacement; D_{res} = residual mid-span displacement; θ_{max} = maximum support rotations;

[3]: CSA component damage and response limits: "Blowout" (Component is overwhelmed by blast load causing debris with significant velocities) = response greater than B4; "Hazardous failure" (component has failed with no significant velocities) = response in between B4 and B3; "Heavy damage" (Component has not failed but has significant permanent deflections causing it to be unrepairable) = response in between B3 and B2; "Moderate damage" (Component has permanent deflections but is repairable) = response in between B2 and B1; "Superficial damage" (component has no visible permanent damage) = response less than B1.

* Data captured from the camera.

Table 6.5: Results from the post-blast residual static tests

Beam	Dynamic loading type	Load		Stiffness		Displacement			Energy-absorption		
		P^R_{max} (kN)	RRI	k^R_s (N/mm)	RSI	Δ^R_{test} (mm)	Δ^R_{max} (mm)	RDI	IEI	REI	TEI
C100-No.4S1-DR-d/4	Repeat	91.2	0.841	3264	0.616	90	206	1.373	0.88	0.13	1.01
C100-No.5S1-DR-d/4	Repeat	126.9	0.935	5434	0.699	150	225.9	1.506	0.54	0.53	1.07
C100-No.5S1-DR-d/4 [x1]	Single	140.7	1.037	6999	0.901	137	170.8	1.139	0.32	0.77	1.09
CF100-No.5S1-DR-d/2	Repeat	136.2	0.802	7623	0.886	100	153.9	1.026	0.46	0.60	1.05
C100-No.5S2-DR-d/4	Repeat	141.5	0.923	4755	0.608	145	207.5	1.383	0.55	0.52	1.07

Note: P^R_{max}=Peak residual load; k^R_s =Residual secant stiffness; Δ^R_{test}= final displacement during residual static test; Δ^R_{max}=max. residual displacement = $\Delta^R_{test} + d_{\sum res}$ (where $d_{\sum res}$= cumulative displacement after blast testing); RRI=residual resistance index; RSI=residual stiffness index; RDI=residual displacement index; IEI=Impact Energy Index; REI=Residual Energy Index; TEI=Total Energy Index.

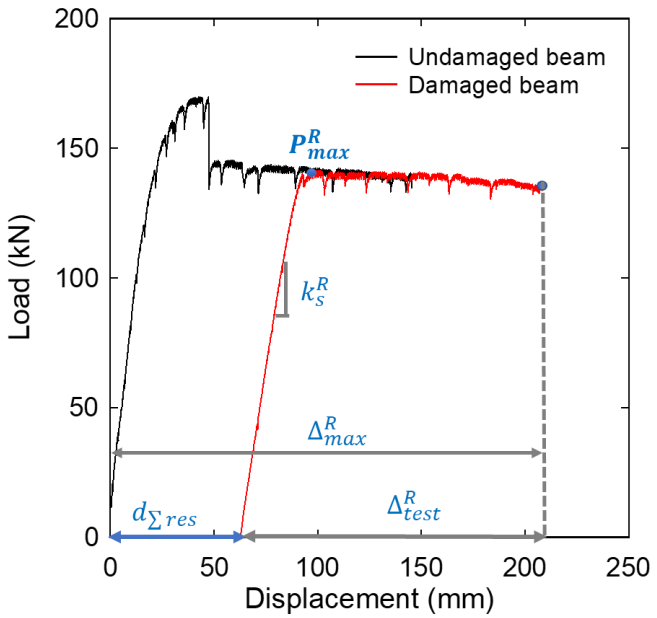

(**a**) Definition of indices from load-displacement curve

Impact Energy Index (IEI) $\quad \mathrm{IEI} = \frac{A}{A+B}$

Residual Energy Index (REI) $\quad \mathrm{REI} = \frac{C}{A+B}$

Total Energy Index (TEI) $\quad \mathrm{TEI} = \mathrm{IEI} + \mathrm{REI}$

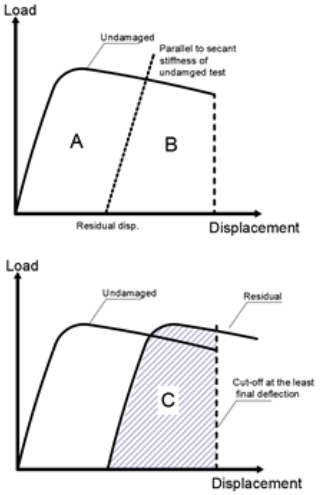

(b) Definition of areas used for calculating the residual damage indices (IEI, REI, TEI)

Figure 6.4 Definition of various indices in post-blast static test

6.5 Discussion of results

6.5.1. Effects of detailing in HSC beams

The effects of detailing in the stainless-steel reinforced HSC beams are examined by comparing beams C100-No.5S1-DR-d/4 and C100-No.5S1-S, which had Type A (Blast) and Type C (nominal) detailing, respectively. As shown in **Figure 6.5**, the blast detailing enhanced all aspects of structural response, including strength (12% increase in P_{max}), stiffness (15% in k_s), ductility (241 % in Δ_{max}/Δ_y) and overall toughness (319% in A_u). Failure in the beam with nominal detailing occurred rather suddenly at Δ = 43 mm due to concrete crushing in the mid-span compression zone (see **Figure 6.6**). In contrast, crushing was limited to the top cover region in beam C100-No.5S1-DR-d/4, which shows a moderate drop in capacity at Δ = 60 mm, but maintains a sustained post-peak response at ~ 80% of P_{max} until the end of testing. The improvement can be explained by the ability of the compression bars and closely spaced ties to confine and strengthen the midspan compression zone, which in turn allows for better engagement of the SS steel bars in tension. Indeed, **Figure 6.5b** shows the development of relatively high compressive strains of 8 mm/m in C100-No.5S1-DR-d/4, compared to 2.5 mm/m in C100-No.5S1-S. The tension steel reaches high strains in both beams (see **Figure 6.5c**), without fracture of the SS bars.

The improved detailing also enhanced all aspects of blast behaviour. As shown in **Figure 6.7**, the use of blast detailing in C100-No.5S1-DR-d/4 reduced maximum and residual displacements by 10% and 32% at *Blast-50psi*, with reductions of 63% and 68% at *Blast-70psi*. Importantly, blast detailing prevents failure at *Blast-70psi* (I_r = 707 kPa·ms), which results in a support rotation of θ_{max} = 6.9º ("Hazardous" damage) in the beam with nominal detailing. Indeed this blast causes important concrete damage in beam C100-No.5S1-S, and the development of significant fragments at failure (see **Figure 6.8** and **Figure 6.9**). In comparison, beam C100-No.5S1-DR-d/4 survived *Blast-70psi*, and an additional test at *Blast-90psi*, with support rotations of 2.5º and 3.8º ("moderate" damage). Damage was better controlled in the beam with blast detailing, and was limited to the top midspan cover region. Moreover, as shown in **Figure 6.10**, beam C100-No.5S1-DR-d/4 shows significant post-blast capacity, with a residual resistance index (RRI) of 0.94, and a remarkable ability to sustain load up to a maximum residual displacement (Δ^R_{max}) of 215 mm, representing an overall ductility of 12. The results confirm the improved response characteristics that can be gained from the use of blast detailing in stainless steel reinforced beams, under both static and blast loads.

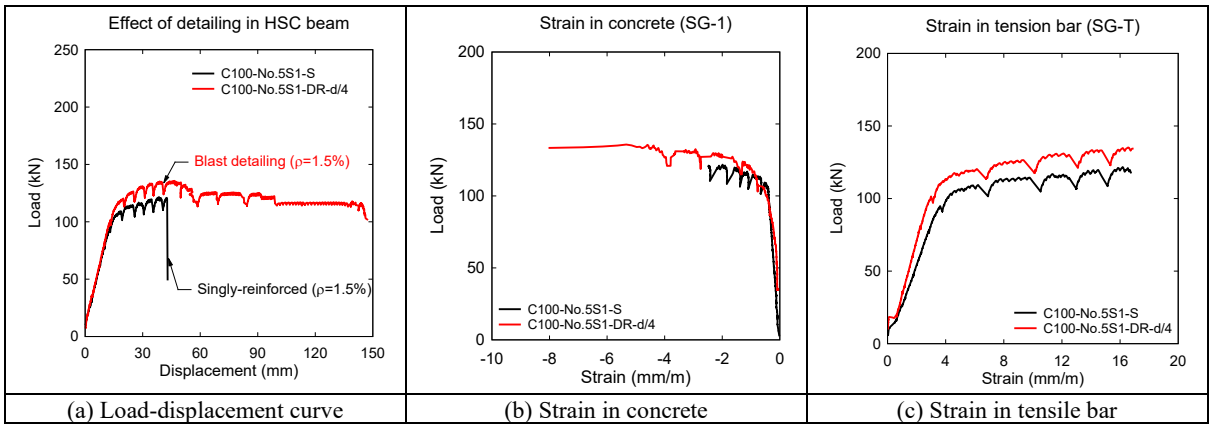

(a) Load-displacement curve | (b) Strain in concrete | (c) Strain in tensile bar

Figure 6.5 Static test result: Effects of detailing in HSC beams

HSC beam with Blast detailing	HSC beam with Nominal detailing
 Cover concrete crushing: $\Delta = 60\ mm$ 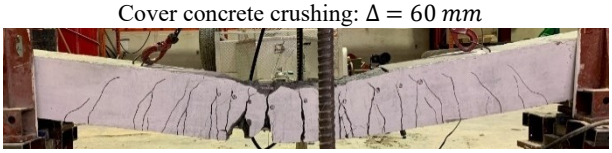 Test terminated: $\Delta_{max} = 150\ mm$ **(a) C100-No.5S1-DR-d/4**	 Concrete crushing: $\Delta_{max} = 43\ mm$ **(b) C100-No.5S1-S**

Figure 6.6 Photos at end of static testing: effect of detailing

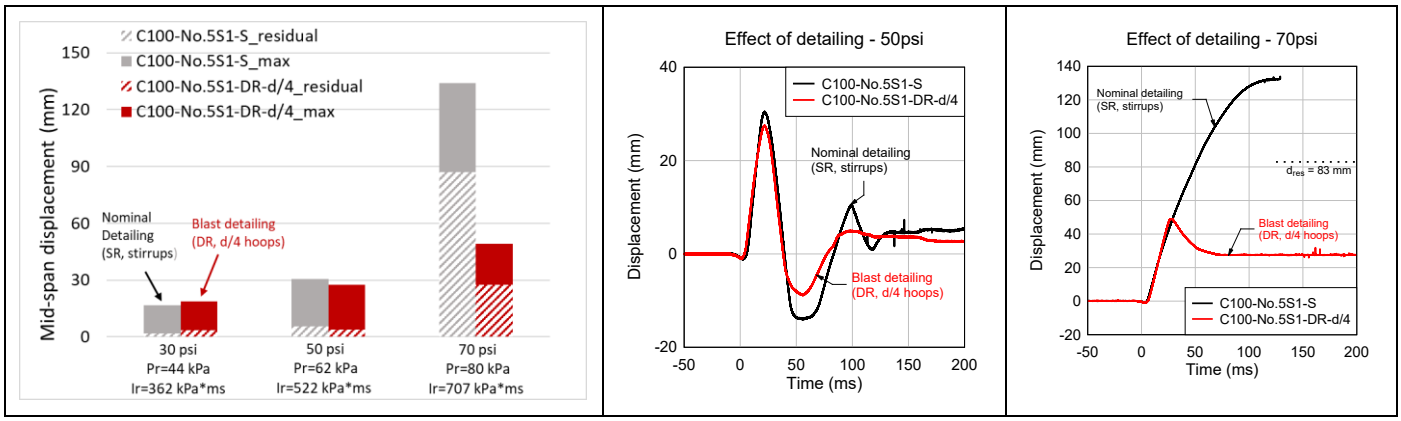

Figure 6.7 Blast test results: effect of detailing

(a) HSC beam with Nominal detailing	(b) HSC beam with Blast detailing	
C100-No.5S1-S	C100-No.5S1-DR-d/4	
Blast-70psi	*Blast-70psi*	*Blast-90psi*
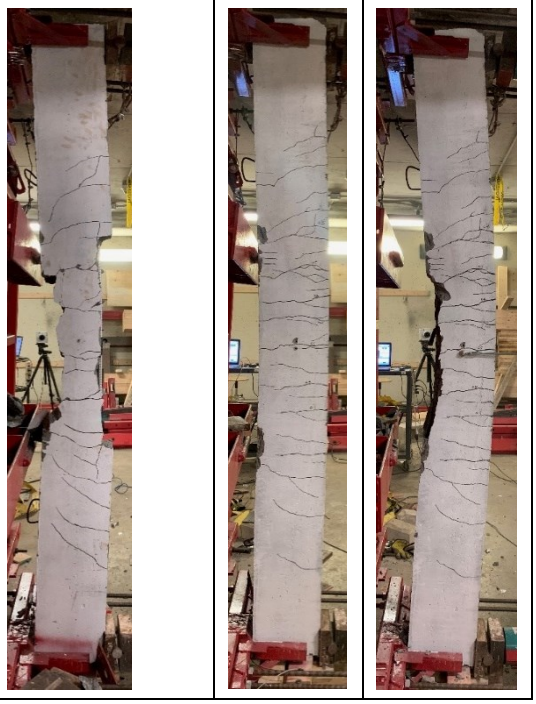		

Figure 6.8 Blast damage photos: effect of detailing

(a) C100-No.5S1-S *@ Blast-70psi* **(singly-reinforced)**	(b) C100-No.5S1-DR-d/2 *@ Blast-90psi* **(blast-detailed)**
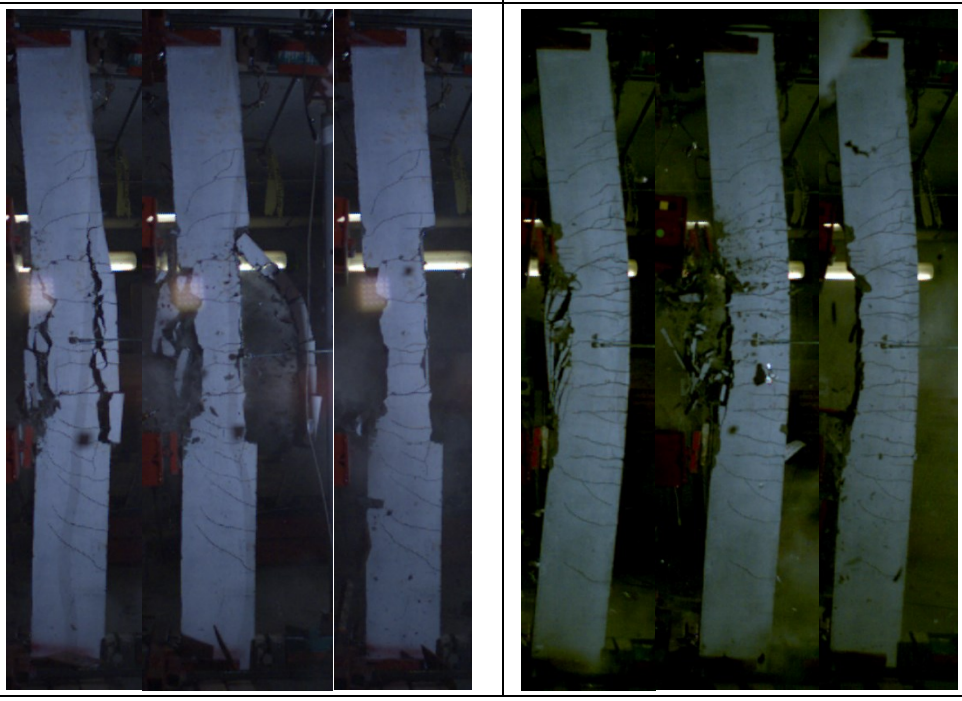	

Figure 6.9 High-speed video stills: effect of detailing

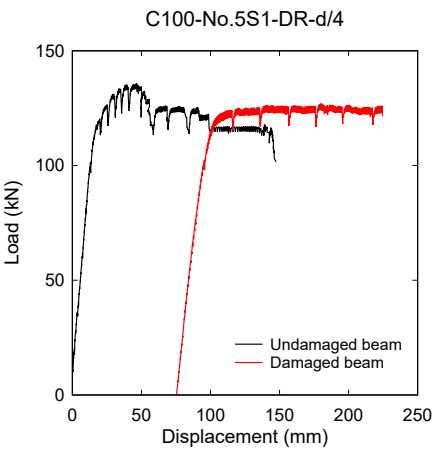

Δ^R_{test}= 150 mm; Δ^R_{max}= 215 mm

Beam: C100-No.5S1-DR-d/4

Figure 6.10 Post-blast residual test: effect of detailing

6.5.2. Effects of steel ratio

The effect of steel ratio can be studied by comparing beams C100-No.4S1-DR-d/4 and C100-No.5S1-DR-d/4, which were built with Type A blast detailing, but had tension steel ratios of ρ = 1.0% and 1.5%, respectively. As shown in **Figure 6.11**, increasing the steel ratio from 1% to 1.5% resulted in increases of 47%, 39% and 27% in stiffness, load capacity and overall toughness under static loads. The blast detailing allows both beams to show impressive ductility, with an ability to sustain significant loads (≥ 0.86 P_{max}) until the end of testing (Δ = 150 mm), resulting in high deformation capacity (Δ_{max}/Δ_y > 6). It is important to note that bar rupture does not occur, even in the case of the lightly-reinforced beam with No.4 bars, due to the high strain capacity of the SS reinforcing bars. Examining the photos in **Figure 6.12,** it can be observed that the use of d/4 tie spacing ensured adequate control of concrete damage and prevented bar buckling. Indeed, while the top cover concrete is lost, the core concrete remained well-confined, with bar buckling prevented until very late stages of loading (see **Figure 6.12**).

As shown in **Figure 6.13**, increasing the stainless steel ratio from 1.0% to 1.5% also enhanced blast performance, by improving control of maximum and residual displacements at equivalent blasts. When compared to the beam with No.4 bars, beam C100-No.5S1-DR-d/4 shows reductions of 24%, 20% and 31% in maximum displacements, as well as decreases of 68%, 14% and 40% in residual deformations, at *Blast-50, 70, 90psi*, respectively. Both beams survived *Blast-90psi* (I_r = 875 kPa·ms), although the support rotation (θ_{max} = 5.6°) for beam C100-No.4S1-DR-d/4 qualifies as "Heavy" according to the CSA S850 standard, compared to "moderate" (θ_{max} = 3.8°) for the beam with No.5 bars. Damage in both beams is associated with the loss of the top concrete cover in the midspan region (see **Figure 6.14**).

Nonetheless, even after the repeated and intense blast tests, both beam shows significant post-blast residual capacity, with RRI indices of 0.84 and 0.94. Both beams show a damage index, $D = 1 - RRI$, which qualifies as a "low" degree of damage ($D \leq 0.2$) (Adhikary et al., 2014). Moreover, both beams show a total energy index (TEI) which exceeds 1.0, which indicates "ductile" failure, and the same failure mode in the damaged and undamaged beams (Zanuy and Ulzurrun (2018)). Indeed, as shown in **Figure 6.15**, both beams were able to reach maximum residual displacements (Δ^R_{max}) which exceed 200 mm, without bar fracture. The results demonstrate the significant energy-absorption capacity and blast resilience that can be gained from the combined use of stainless steel reinforcement and blast detailing in beams designed according to the CSA S850 standard.

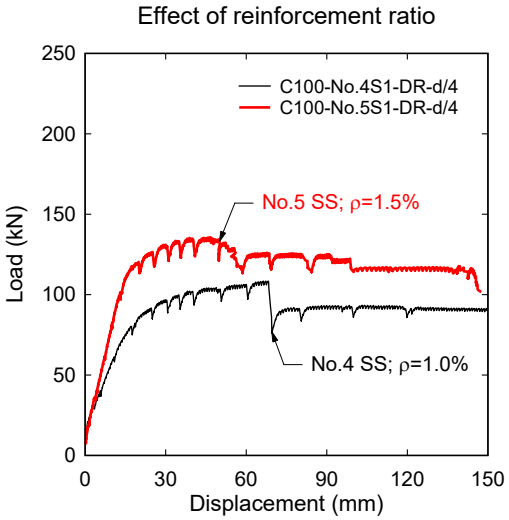

Figure 6.11 Static test results: effect of steel ratio

No.5 S1 bars (ρ =1.5%)	No.4 S1 bars (ρ =1.0%)
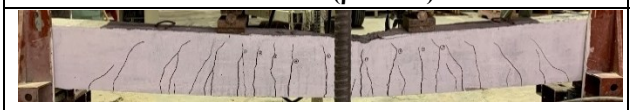	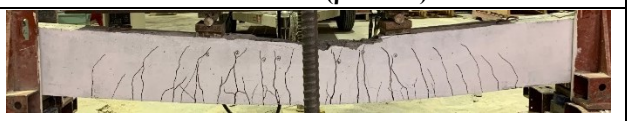
Cover concrete crushing: $\Delta = 60\ mm$	Cover concrete crushing: $\Delta = 70\ mm$
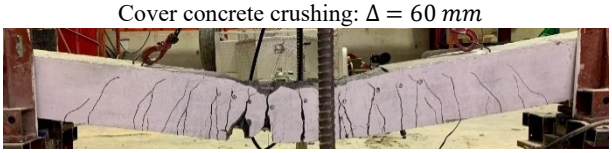	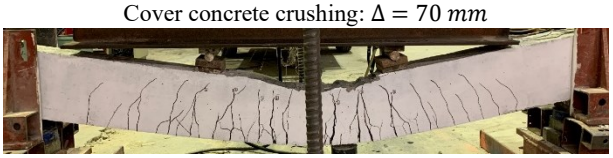
Test terminated: $\Delta_{max} = 150\ mm$	Test terminated: $\Delta_{max} = 150\ mm$
(a) C100-No.5S1-DR-d/4	**(b) C100-No.4S1-DR-d/4**

Figure 6.12 Beam failure photos at end of static testing: effect of steel ratio

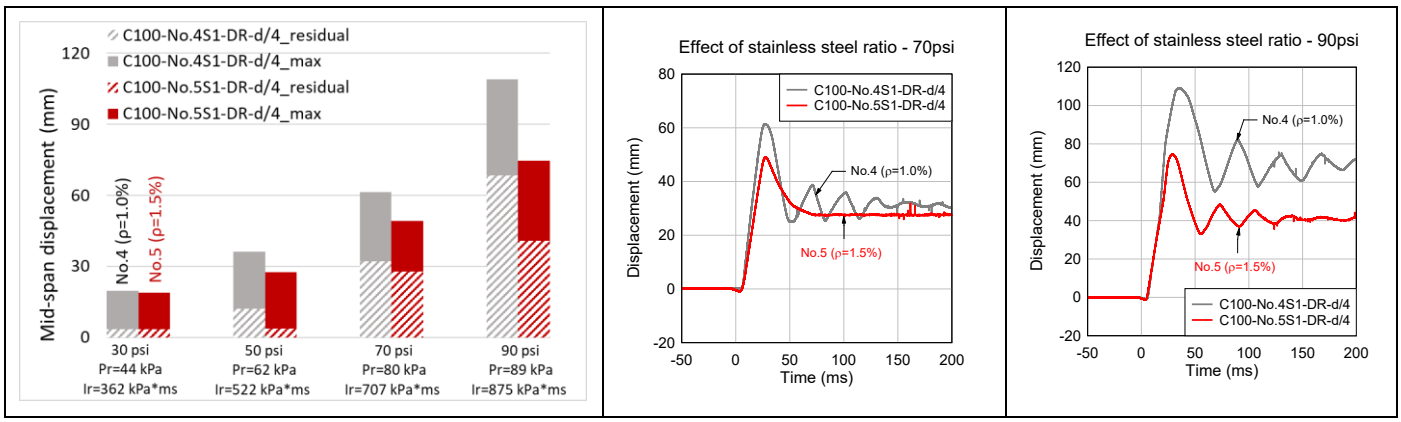

Figure 6.13 Blast test results: effect of steel ratio

(a) Blast detailing (No.4) ρ = 1.0%		(b) Blast detailing (No.5) ρ = 1.5%	
C100-No.4S1-DR-d/4		C100-No.5S1-DR-d/4	
Blast-70psi	*Blast-90psi*	*Blast-70psi*	*Blast-90psi*
		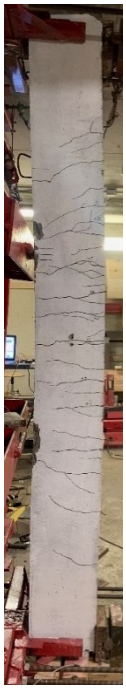	

Figure 6.14 Blast damage photos: effect of steel ratio

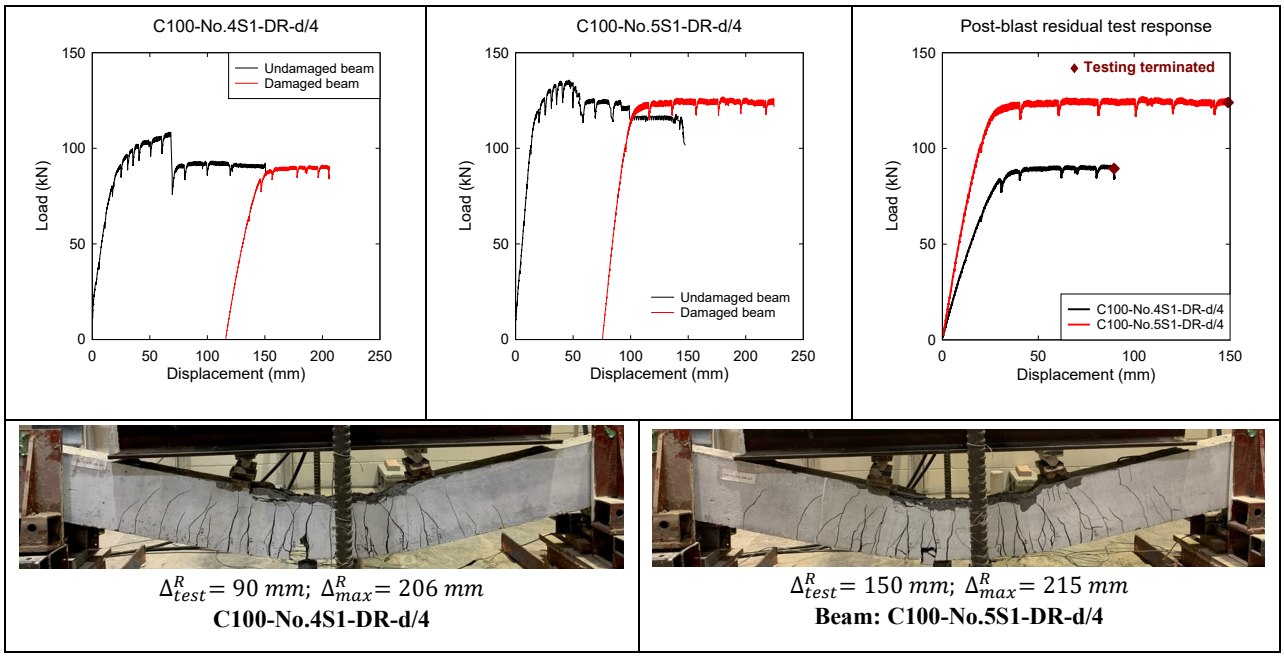

Δ^R_{test}= 90 mm; Δ^R_{max}= 206 mm
C100-No.4S1-DR-d/4

Δ^R_{test}= 150 mm; Δ^R_{max}= 215 mm
Beam: C100-No.5S1-DR-d/4

Figure 6.15 Post-blast residual test: effect of steel ratio

6.5.3. Effects of steel fibers

This section examines the ability of fibers to relax detailing and further improve performance of the test beams under static and blast loads. This effect is studied by comparing beams C100-No.5S1-DR-d/4 and CF100-No.5S1-DR-d/2, which had "blast" and "intermediate" detailing, with ties spaced at d/4 (50 mm) and d/2 (100 mm), respectively.

As shown in **Figure 6.16,** despite the relaxed detailing, beam CF100-No.5S1-DR-d/2 (with fibers) not only matched, but out-performed beam C100-No.5S1-DR-d/4 (plain HSC) under static loading, with noticeable increases in peak strength and overall toughness (area under the curve). This enhancement results from the ability of fibers to improve the HSC tensile response, and better control crushing. Indeed, as shown in **Figure 6.17**, spalling is limited, and crushing is well controlled in the beam with fibers. On the other hand, the use of fibers can result in crack localization in HSC beams, which can lead to bar fracture (Yoo et al., 2017b; Dancygier & Karinski, 2019). It is interesting to note that this phenomenon was negated in the current tests due to the high strain-capacity of the stainless steel bars.

The ability of fibers to improve blast behaviour is further studied in **Figure 6.18**. The CF100 beam with intermediate ties shows reductions of 10%, 14%, 20% and 21% in maximum displacements at *Blasts-30, 50, 70, 90psi* when compared to the C100 specimen. Residual displacements are similar (within ±5%) under *Blasts-30 and 50psi* since the tests were still within the elastic range, however the CF100 beam shows reductions of 48% and 23% in residual displacements at *Blast-70 and 90psi*. Both beams survived *Blast-90psi*, however damage and fragmentation were more significant in the HSC specimen, which shows crushing of top cover concrete, and blast fragments at failure (see **Figure 6.19** and **Figure 6.20**). In comparison, damage was well controlled in the beam with fibers. Both beams show significant post-blast capacity, with RRI and TEI indices which exceed 0.8 and 1.0 ("low damage" and "ductile" behaviour, respectively). Comparing the residual curves, the CF100 beam has a larger post-blast capacity (P_{max}^{R}), stiffness (k_s^R), and RSI, but a lower RRI index (0.8 vs. 0.94), which can be explained by reduced fiber efficiency due to fiber pullout after intense and repeated blasting. Nonetheless, the results demonstrate that moderate amounts of fibers (as low as 0.75%) and intermediate ties result in excellent blast performance, which can be used to simplify the construction of stainless steel reinforced concrete beams.

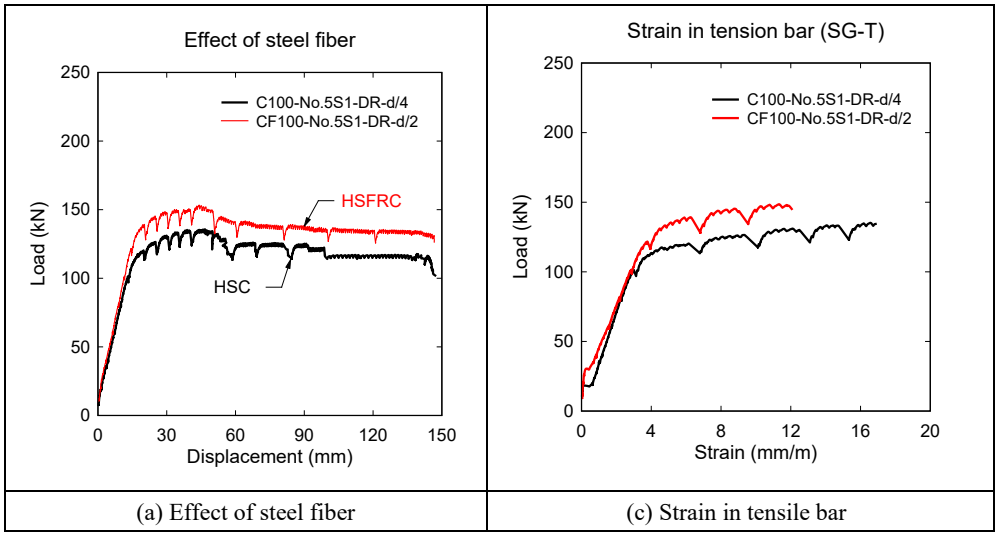

(a) Effect of steel fiber | (c) Strain in tensile bar

Figure 6.16 Static test results: effect of fibers

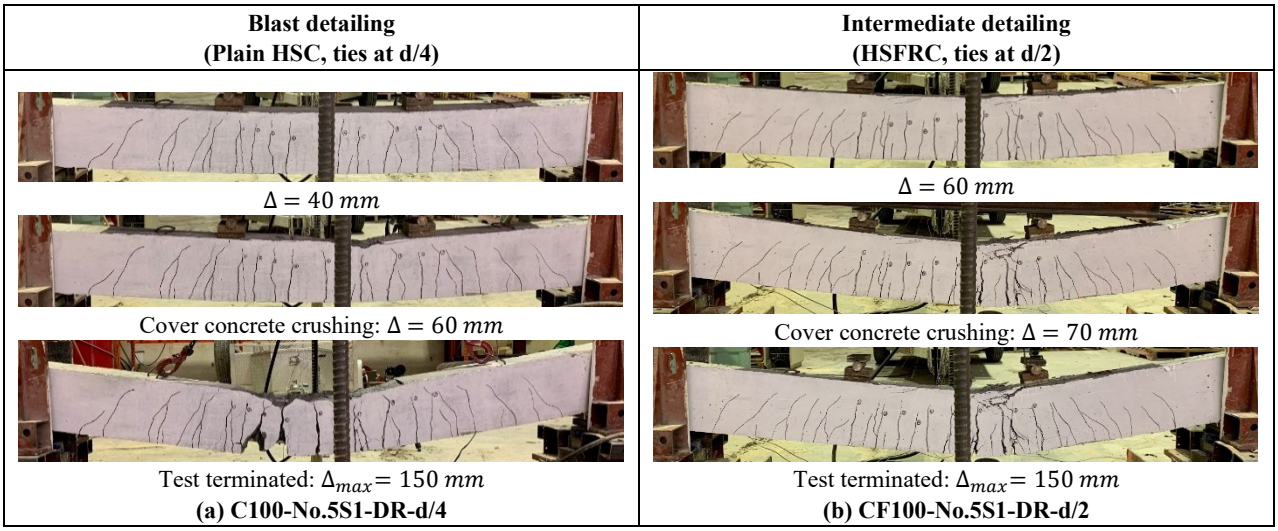

(a) C100-No.5S1-DR-d/4 **(b) CF100-No.5S1-DR-d/2**

Figure 6.17 Beam failure photos at end of static testing: effect of fibers

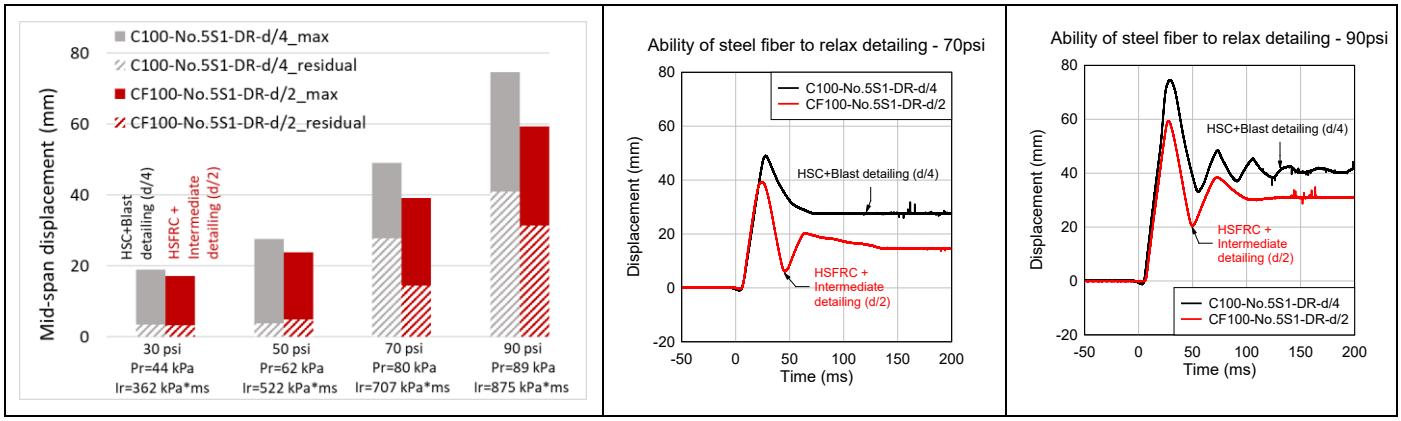

Figure 6.18 Blast test results: effect of fibers

Blast detailing (Plain HSC, ties at d/4)		**Intermediate detailing (HSFRC, ties at d/2)**	
C100-No.5S1-DR-d/4		CF100-No.5S1-DR-d/2	
Blast-70psi	*Blast-90psi*	*Blast-70psi*	*Blast-90psi*
			

Figure 6.19 Blast damage photos: effect of fiber

Blast detailing (Plain HSC, ties at d/4)	**Intermediate detailing (HSFRC, ties at d/2)**
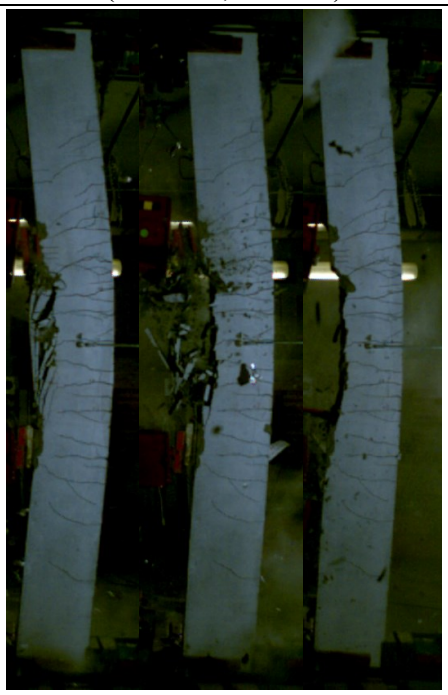	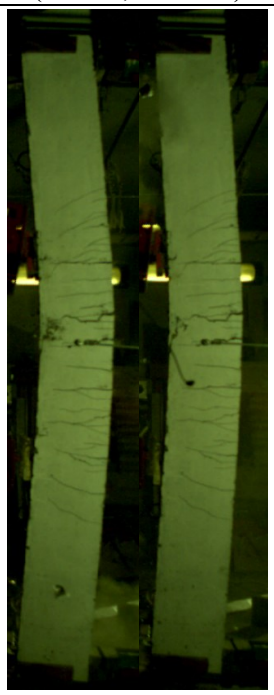
(a) C100-No.5S1-DR-d/2 @ *Blast-90psi*	(b) CF100-No.5S1-DR-d/2 @ *Blast-90psi*

Figure 6.20 High-speed video stills showing: effect of fiber

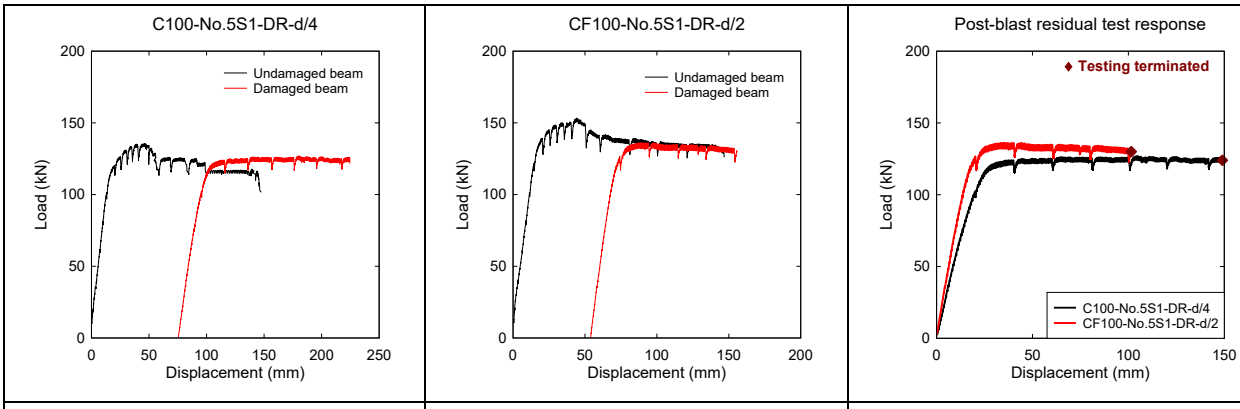

(a) C100-No.5S1-DR-d/4 (b) CF100-No.5S1-DR-d/2 (c) Effect of steel fibers

Δ^{R}_{test}= **150** mm; Δ^{R}_{max}= **215** mm

Beam: C100-No.5S1-DR-d/4

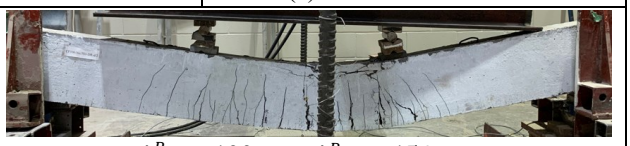

Δ^{R}_{test}= 100 mm; Δ^{R}_{max}= 154 mm

CF100-No.5S1-DR-d/2

Figure 6.21 Post-blast residual test results: effect of fiber

6.5.4.Effects of detailing in HSFRC beams

The effects of detailing in beams built with HSFRC can be studied by comparing the responses of beams CF100-No.5S1-DR-d/2 and CF100-No.5S1-S, which had Type B (intermediate) and Type C (nominal) detailing, respectively.

As shown in **Figure 6.22,** beam CF100-No.5S1-S shows similar peak capacity, and slightly higher stiffness when compared to beam CF100-No.5S1-DR-d/2 owing to its higher fiber content (1% vs. 0.75%). However, the improved detailing in beam CF100-No.5S1-DR-d/2 allows for significant improvements in post-peak response and damage tolerance (**Figure 6.22**). Crushing in beam CF100-No.5S1-S initiates at a displacement of 47 mm, and results in a gradual loss in load capacity with increased displacements, ending with a residual strength of ~ 50% P_{max} at Δ = 116 mm. In comparison, crushing and damage are well-controlled in beam CF100-No.5S1-DR-d/2, with an ability to maintain significant post-peak capacity (85% of P_{max}) until Δ = 150 mm. As a result, the HSFRC beam with intermediate detailing shows enhanced ductility (Δ_{max}/Δ_y) and toughness (A_u) when compared to CF100-No.5S1-S.

The effect of detailing on blast performance is further examined in **Figure 6.23**. Beam CF100-No.5S1-S, which had nominal detailing but increased fiber content, shows reduced maximum and residual displacement at *Blasts-30psi and 50 psi* which tested the beams within the elastic/yield range. However, as the blast intensity is increased into the inelastic range, the provision of top continuity bars and intermediate ties in CF100-No.5S1-DR-d/2 results in improved control of maximum and residual displacements, with decreases of 22% and 8% at *Blast-70psi*, and reductions of 37% and 28% at *Blast-90psi*. The provision of top bars also clearly reduces the rebound displacements under *Blasts-70 and 90psi*. As shown in **Figure 6.24**, damage at the end of blast testing is more significant in beam CF100-No.5S1-S, and is associated with concrete crushing and clear crack localization. In comparison, crushing and crack development are better controlled in beam CF100-No.5S1-DR-d/2. As noted before, the improved detailing also allowed beam CF100-No.5S1-DR-d/2 to maintain significant post-blast residual capacity, with RRI > 0.8 and TEI > 1.0, even after the intense blast testing.

Thus, it can be concluded that improved detailing, consisting of top continuity bars and intermediate ties, enhances the ductility of stainless steel reinforced beams, even when fibers are added.

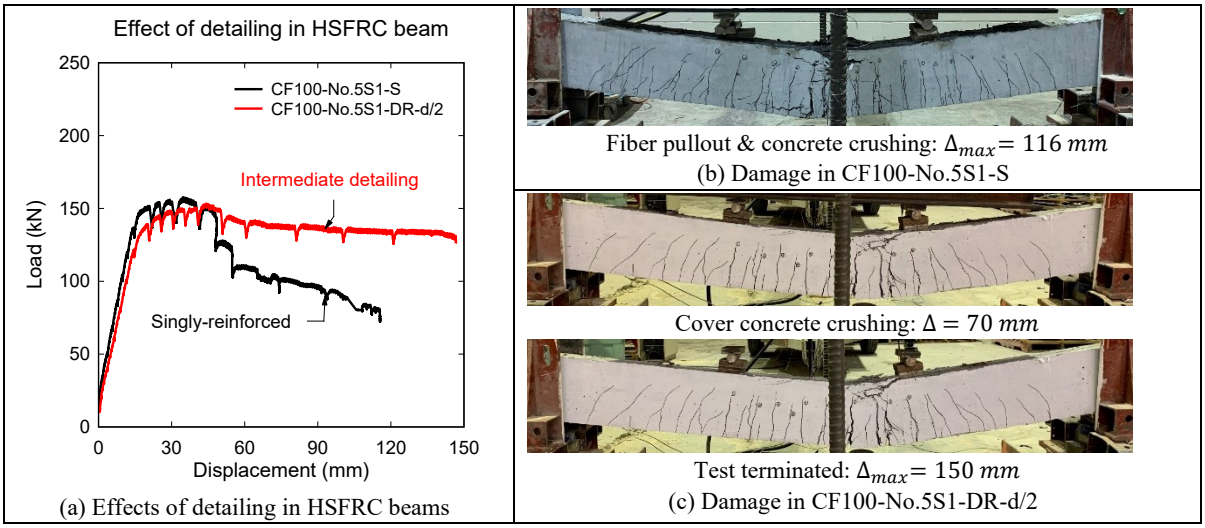

Figure 6.22 Static test results: effect of detailing in beams with fibers

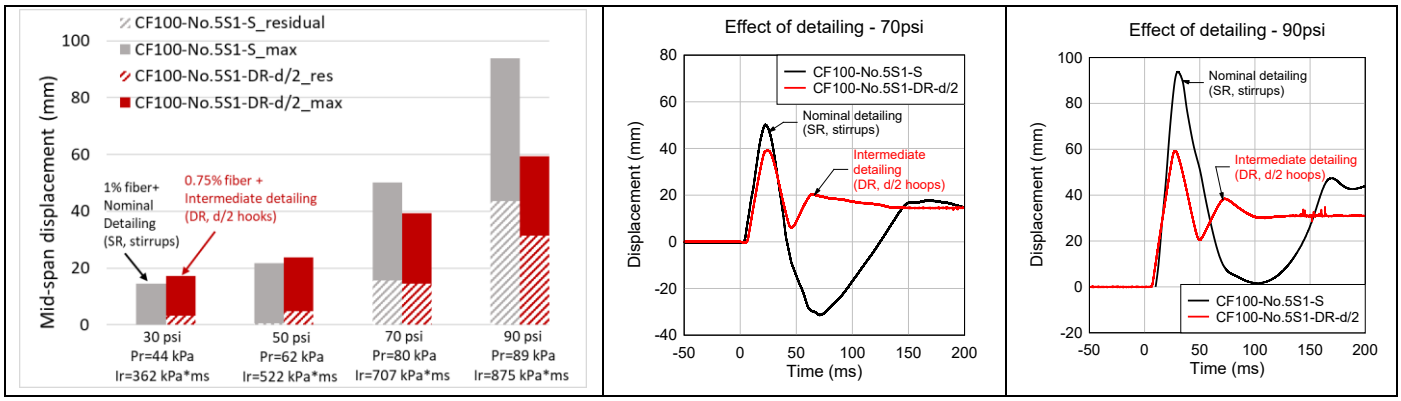

Figure 6.23 Blast test results: effect of detailing in beams with fibers

Nominal detailing (HSFRC, stirrups at d/2)		**Intermediate detailing (HSFRC, ties at d/2)**	
CF100-No.5S1-S		CF100-No.5S1-DR-d/2	
Blast-70psi	*Blast-90psi*	*Blast-70psi*	*Blast-90psi*
		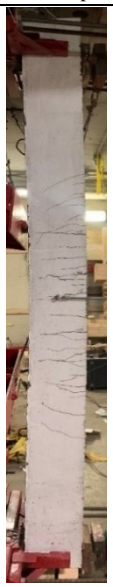	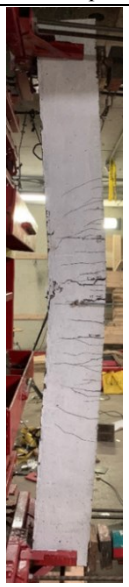

Figure 6.24 Blast damage photos: effect of detailing in beams with fibers

6.5.5. Effects of stainless type

The effect of stainless steel type can be examined by comparing the responses of beams C100-No.5S1-DR-d/4 and C100-No.5S2-DR-d/4, built with austenitic (XM-28) and duplex (2304) stainless steel, designated at types S1 and S2 in the beam nomenclature.

As shown in **Figure 6.25**, beam C100-No.5S2-DR-d/4 shows similar stiffness, but an important increase of 29% in peak load capacity (P_{max}), owing to the higher yield strength of the S2 stainless steel bars (see **Figure 3.7**). The stiffness (k_s) isn't noticeably affected since the two types of stainless steel have similar modulus of elasticity. The blast detailing allows both beams to develop a clear post-peak response, and sustain significant loads up to end testing (Δ =150 mm). A larger drop in capacity due to concrete crushing is observed for the beam with S2 bars at Δ = 53 mm (see **Figure 6.26**), although it maintains a 25% increase in residual capacity at the end of testing. This enhanced load capacity results in greater toughness (16% increase in A_u) when compared to the companion with S1 bars. While crushing initiates at 59 mm in beam C100-No.5S1-DR-d/4, the rate of crushing is more gradual, as also reflected in the shape of the load-deflection response. This behaviour can be explained by the more rounded stress-strain response of the S1 reinforcement, which results in relatively more gradual strain demands on the concrete compression zone.

Figure 6.27 examines the effect of stainless type under blast loading. Though the beam with S2 stainless steel shows higher capacity in the static test, the blast displacements are similar when compared to the beam with S1 reinforcement, except at *Blast-70psi*, where the beam with S2 bars shows reductions of 8% and 51% in maximum and residual displacements. This behaviour is expected since *Blasts-30psi and 50psi* were meant to test the beams within the elastic range, while *Blast-70psi* tested the specimens in the post-peak range. Both beams survive *Blast-90psi* with similar deformations and damage which consisted of the loss of the top concrete cover in the midspan zone (see **Figure 6.28**). It is noted that the maximum displacement which initiates concrete crushing is similar to the that observed in the static tests. Finally, as shown in **Figure 6.29**, the blast detailing allows both beams to show significant residual post-blast capacity. Both beams show an RRI index ≥ 0.9, damage index < 0.1 ("low" damage) and TEI index > 1.0 ("ductile" behaviour), with an ability to sustain significant load up to $\Delta_{max}^{R} \geq 200$ mm. Indeed, despite its reduced ultimate strain capacity, bar fracture is not observed in the beam with S2 bars. As shown in **Figure 6.29**, both beams show similar stiffness and follow the same post-peak trends observed in the undamaged beam tests. While both beams show similar RRI indices (0.92 and 0.94), the beam with S2 bars shows higher residual load

capacity (at P_{max}^{R} and up to the end of residual testing) when compared to the beam with type S1 stainless reinforcement.

In summary, under static load the use of S2 (2304) reinforcement resulted in increased beam strength, with the same ability to sustain load up to the end of testing when compared to S1 (XM-28) steel. The influence of stainless type was more limited under blast loads, although the S2 reinforcement led to an increase in post-blast residual capacity. Despite its reduced ultimate strain (20% vs. 40%), the S2 stainless reinforcement showed adequate ductility during the static and blast tests.

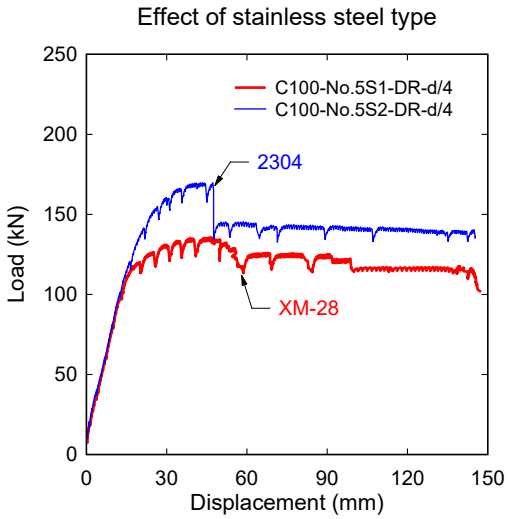

Figure 6.25 Static test results: effect of stainless steel type

Type S1 (XM-28, Austenitic)	**Type S2 (2304, Duplex)**
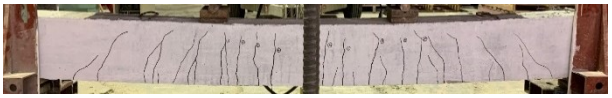	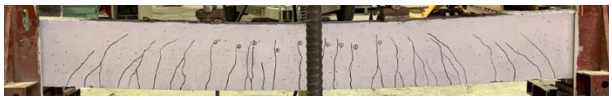
$\Delta = 40\ mm$	$\Delta = 40\ mm$
	
Cover concrete crushing: $\Delta = 60\ mm$	Cover concrete crushing: $\Delta = 53\ mm$
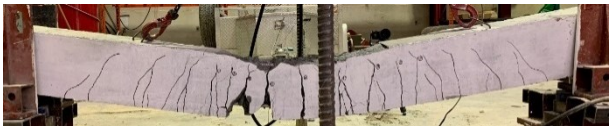	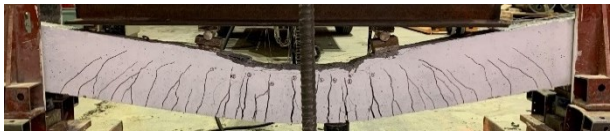
Test terminated: $\Delta_{max} = 150\ mm$	Test terminated: $\Delta_{max} = 150\ mm$
(a) C100-No.5S1-DR-d/4	**(b) C100-No.5S2-DR-d/4**

Figure 6.26 Beam failure photos at end of static testing: effect of stainless steel type

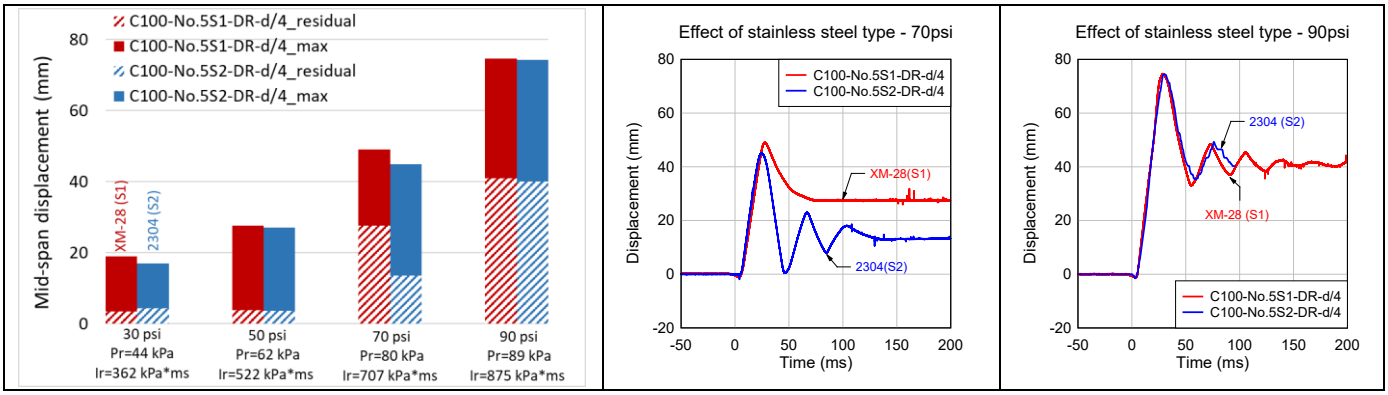

Figure 6.27 Blast test result: effect of stainless steel type

Type S1 (XM-28, Austenitic)		**Type S2 (2304, Duplex)**	
C100-No.5S1-DR-d/4		C100-No.5S2-DR-d/4	
Blast-70psi	*Blast-90psi*	*Blast-70psi*	*Blast-90psi*
	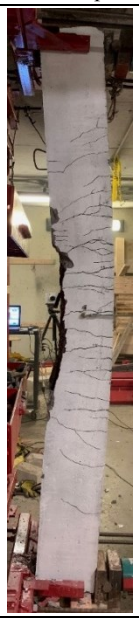		

Figure 6.28 Comparison of blast damage: effect of stainless steel type

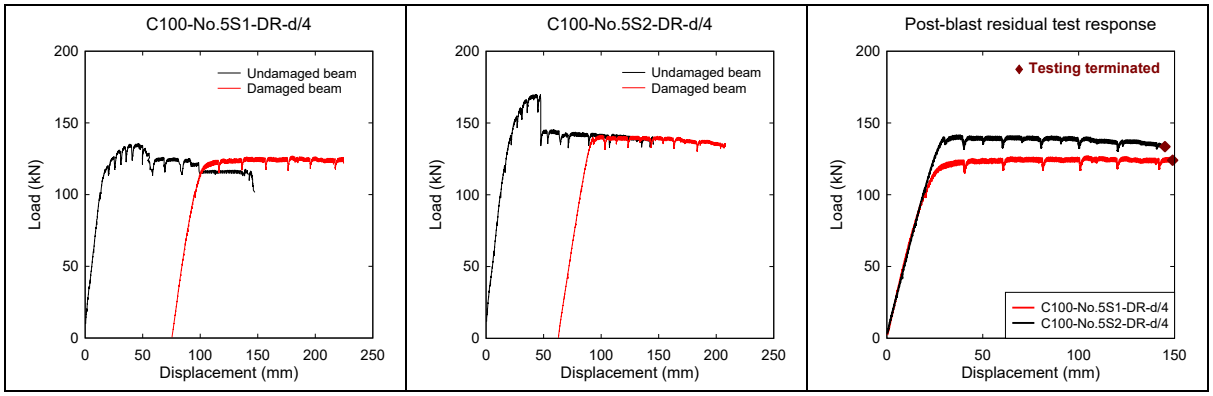

Figure 6.29 Post-blast residual test: effect of stainless steel type

6.5.6. Effects of stainless steel and ability to reduce reinforcement

The effect of stainless steel versus ordinary steel, and its ability to reduce reinforcement, is examined by comparing the test beams with Grade 520 MPa stainless steel in Group A (HSC) and Group B (HSFRC), with the control beams with Grade 400 MPa steel tested by Charles (2019).

Beginning with Group A (plain HSC), the static responses of beams C100-No.5S1-DR-d/4 and C100-15M-DR-d/4, with equal steel ratio, ρ=1.5%, in **Figure 6.30a** shows that the increased yield strength of the stainless steel results in a 26% in peak capacity (P_{max}= 136 vs. 108 kN). While both beams show ductile behaviour and an ability to sustain loads until the end of testing, larger toughness (increase of 22% in A_u) is recorded for the beam with No.5 stainless bars. Under blast loading the use of stainless steel results in reductions of 17% and 23% in maximum deformations, and decreases of 79% and 39% in residual displacements at *Blasts-50 and 70psi* when compared to the beam with ordinary bars (see **Figure 6.31a**). Moreover, the beam with stainless steel survives one more blast at *Blast-90psi*.

Next, the responses of beams C100-No.5S1-DR-d/4 (ρ=1.5%) and C100-20M-DR-d/4 (ρ=2.4%) are compared. Despite the reduced steel ratio and lower ρf_y (7.8 vs. 9.6 MPa), the beam with reduced amounts of stainless steel bars shows comparable performance in terms of peak strength (P_{max}= 136 and 131 kN) and energy absorption capacity (A_u = 17033 vs. 18889 J). As shown in **Figure 6.31a**, the reduced stainless steel ratio was not sufficient to match the displacement responses of C100-20M-DR-d/4 under *Blast-30 and 70psi* loads, although both beams show similar responses at *Blast-90psi*. This can be explained by the higher stiffness of the beam with 20M bars, as also observed under static loading (see **Figure 6.30a**). On the other hand, the strain-hardening behaviour of the stainless steel allows for a better match of post-peak behaviour, which results in similar displacements at *Blast-90psi*. Similar trends are observed in the post-blast tests in **Figure 6.32a**.

The effect of steel type is further investigated in the Group B (HSFRC) beams. **Figure 6.30b** compares the static responses of beams CF100-No.5S1-DR-d/2 and CF100-15M-DR-d/2, which had ρ=1.5%, but were built with SS and ordinary bars, respectively. The use of SS bars enhanced capacity by 31% (P_{max}= 153 and 117 kN), with an important improvement in ductility. While failure of the control beam with 15M ordinary steel bars occurs due to bar fracture, the SS beam shows an ability to sustain significant load (85% of P_{max}) up to the end of testing, without bar fracture. This observation can be explained by the significant strain

capacity of the stainless steel (fracture strain, ε_u = 42%) when compared to the ordinary steel (ε_u = 15%). Under blast loading the use of stainless bars results in reductions of 17%, 33% and 15% in maximum displacements, and decreases of 60%, 58% and 41% in residual displacements at *Blasts-50, 70, 90psi*, respectively (see **Figure 6.31b**), with an increase in post-blast residual capacity (see **Figure 6.32b**).

The ability of the SS to reduce reinforcement is examined by comparing beams CF100-No.5S1-DR-d/2 (ρ=1.5%) and CF100-20M-DR-d/2 (ρ=2.4%) under static (see **Figure 6.30b**) and blast loads (see **Figure 6.31b**). Despite the lower ρf_y ratio (7.8 vs. 9.6 MPa), both beams show similar peak strength under static loading (P_{max} = 153 and 168 kN), with a larger toughness (area under the load-deflection curve) recorded for the beam with reduced amounts of SS bars. While the increased steel ratio (ρ=2.4%) prevents bar rupture, the beam with 20M ordinary steel bars experiences crack localization, concrete crushing, and buckling of the top compression (10M) bars, resulting in an important reduction in capacity to $0.63P_{max}$ at the end of testing. In comparison, the SS beam shows an impressive post-peak response, with an ability to sustain a load of $0.85P_{max}$ until 150 mm. In addition, the stainless steel prevents bar buckling in compression. In the blast tests, the beam with reduced SS bars shows comparable displacements to the beam with ordinary 20M bars under *Blasts-70 and 90psi* loads.

In summary, substitution of ordinary bars with stainless steel bars results in important enhancements in beam response under static and blast loads. In the beams with fibers, the high ductility and strain-capacity of the stainless steel was also effective in preventing bar rupture caused by crack localization.

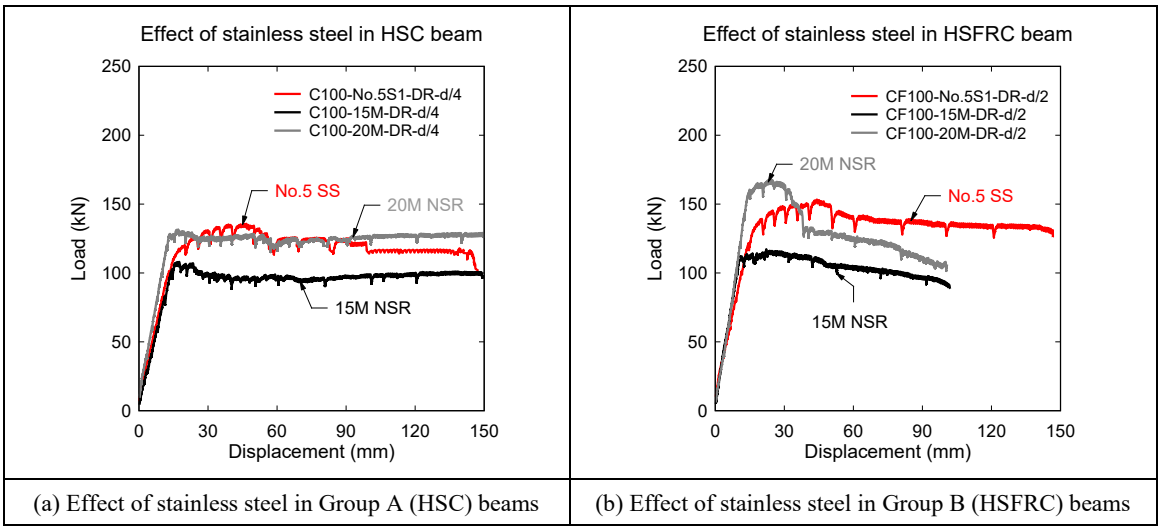

(a) Effect of stainless steel in Group A (HSC) beams

(b) Effect of stainless steel in Group B (HSFRC) beams

Figure 6.30 Beam static test results: stainless vs. ordinary steel

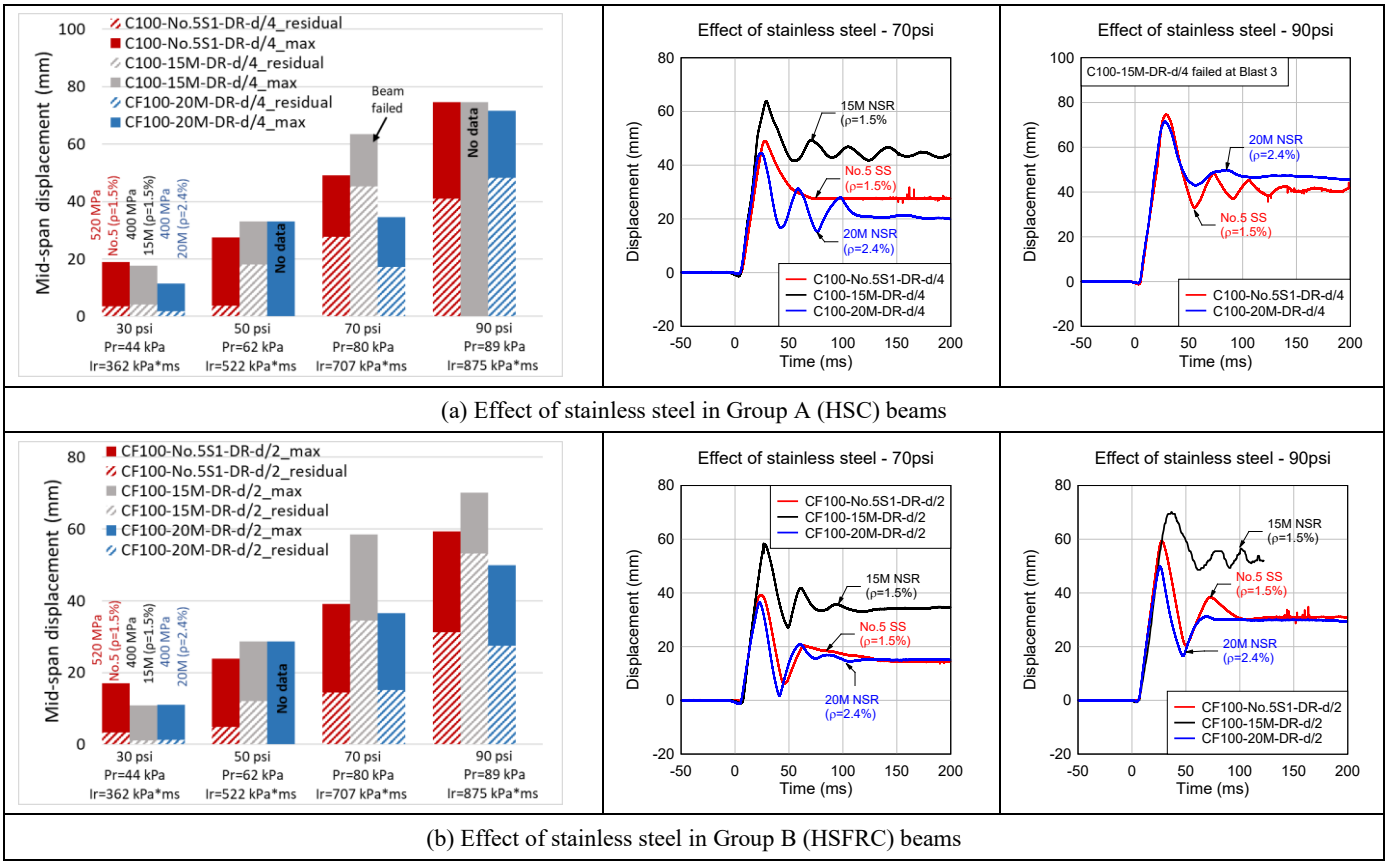

(a) Effect of stainless steel in Group A (HSC) beams

(b) Effect of stainless steel in Group B (HSFRC) beams

Figure 6.31 Blast test results: stainless vs. ordinary steel

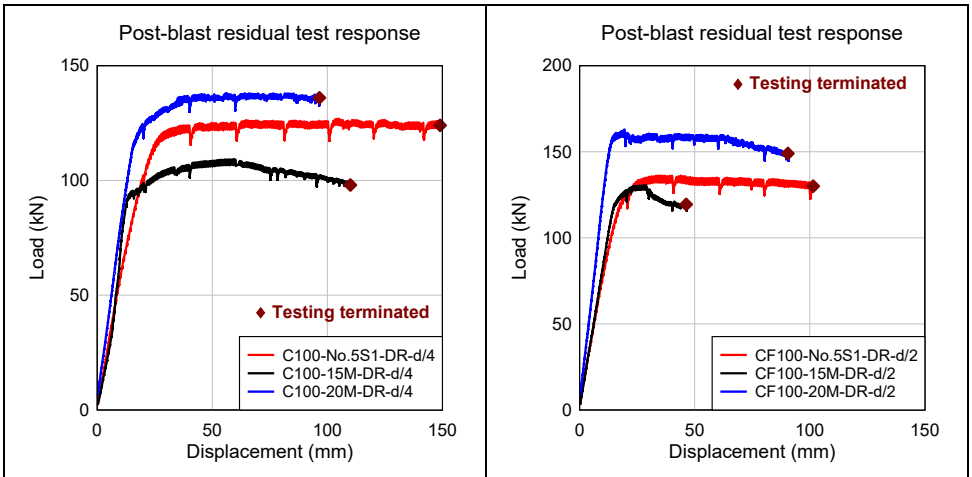

(a) Effect of stainless steel in HSC beams

(b) Effect of stainless steel in HSFRC beams

Figure 6.32 post-blast residual test: stainless vs. ordinary steel

6.5.7. Single vs. repeated blast loading

The majority of the beams in this study were tested under repeated blast loads. The influence of repeated testing can be studied by comparing beams C100-No.5S1-DR-d/4 [x1] and C100-No.5S1-DR-d/4 which were tested under single and repeated blast loads.

As shown in **Figure 6.33**, the beam tested under repeated loads shows increased maximum (75 vs. 66 mm) and residual displacements (41 vs. 34 mm) when compared to the specimen tested under single *Blast-90psi* loading. The increase in maximum and residual displacements can be explained by the increased pressure and impulse applied on beam C100-No.5S1-DR-d/4 (P_r = 92 vs 85 kPa; I_r = 900 vs 852 kPa-ms), and the accumulated damage prior to the final *Blast-90psi* shot. Indeed examining the damage photos in **Figure 6.34**, the beam tested under repeated blasts shows more significant concrete damage, with loss of the top cover concrete, whereas the midspan cover damage is reduced in the companion tested under single blast loading. **Figure 6.35** compares the residual capacity test results of the companion beams tested under single and repeated blasts. The beam tested under repeated blasts shows a lower peak residual strength due to the lack of top cover concrete which spalled during the blast testing. However, after the initial drop in load, both beams show remarkably similar deformation capacity, without bar rupture in both specimens (see **Figure 6.35**).

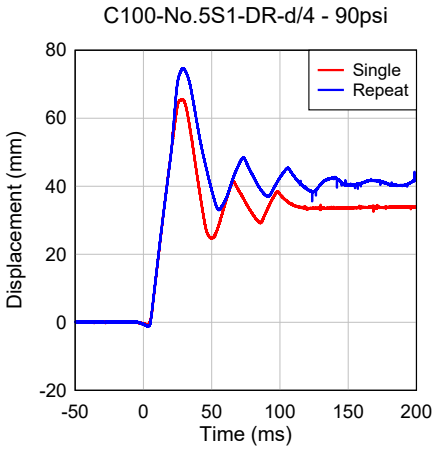

Figure 6.33 Blast test result: effect of repeated loading

(a) Repeated Blasts	(b) Single Blast
C100-No.5S1-DR-d/4	C100-No.5S1-DR-d/4 [x1]
Blast-90psi	*Blast-90psi*
	

Figure 6.34 Comparison of blast damage: effect of repeated loading

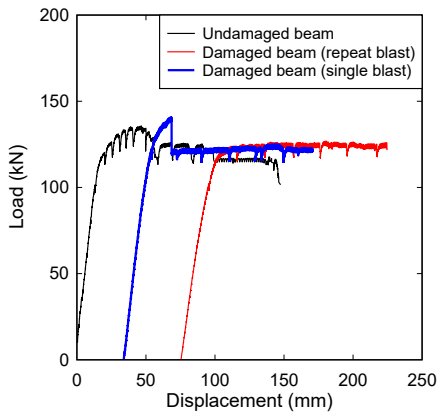

(a) Load-displacement response comparing damaged and undamaged beams

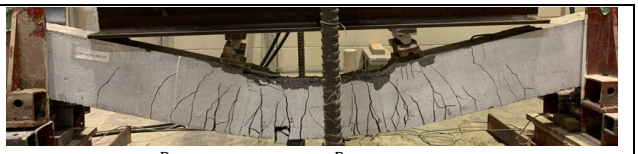

Δ^R_{test}= 150 mm; Δ^R_{max}= 215 mm

(b) Damage after the residual static test C100-No.5S1-DR-d/4 (Repeated blasts)

Δ^R_{test}= 137 mm; Δ^R_{max}= 170.8 mm

(c) Damage after the residual static test: C100-No.5S1-DR-d/4 [x1] (Single blast)

Figure 6.35 post-blast residual static test results: effect of repeated loading

6.6 Conclusions

This chapter presented the results from Series 2B of the PhD program, and examined the influence of blast detailing on the static and blast behavior of stainless steel reinforced concrete beams. The effects of detailing, fibers, steel type (stainless vs. ordinary) and stainless type (austenitic vs. duplex) were also investigated. The following conclusions can be drawn from this study:

1. The use of blast detailing significantly enhanced the response of the stainless steel reinforced HSC beams under both static and blast loads. Under static loading, the use of top continuity (compression) bars and closely-spaced ties (d/4) increased load-carrying capacity, stiffness and ductility due to the ability of the improved detailing to enhance the toughness of the concrete compression zone. Likewise, blast detailing significantly enhanced blast response by reducing displacements, increasing blast capacity and allowing for significant post-blast residual resistance;
2. The use of improved detailing consisting of top continuity bars and intermediate ties (d/2) also enhanced the post-peak response and ductility of stainless steel reinforced HSFRC beams under static loading. Likewise, the blast response was also improved in terms of reducing displacement and the fibers allowed for significant post-blast resistance;
3. The use of moderate amounts of steel fibers (as low as 0.75%) can be used to relax blast detailing in stainless steel reinforced beams by increasing tie spacing from d/4 to d/2. In this research program, fibers and intermediate detailing allowed for significantly high static, blast and post-blast resistance, with better control of damage when compared to the companion HSC beam designed with blast detailing but without fibers;
4. The results showed that substitution of normal-strength bars with stainless steel bars enhanced beam response under static and blast loads. Under static loading, the use of SS bars increased peak load capacity and improved post-peak response with an ability to sustain loads up to very large deformations. Due to the high strain capacity of the SS reinforcing bars, bar rupture did not occur even in the case of the lightly-reinforced beam with No.4 bars (ρ = 1.0%). Similarly, bar rupture was prevented in the HSFRC beam. Likewise, reduced amounts of stainless steel bars allowed for comparable performance when compared to beams with larger amounts of normal-strength reinforcement, under both static and blast loads.

5. Under static loading, the use of 2304 duplex stainless steel reinforcement (S2) resulted in increased beam strength, with the same ability to sustain load up to the end of testing when compared to the XM-28 (S1) reinforcement, despite its reduced ultimate strain capacity. The influence of stainless type was more limited under blast loads, however the S2 reinforcement led to an increase in post-blast residual capacity when compared to the S1 stainless steel bars.
6. All stainless steel reinforced beams with blast detailing showed significant residual post-blast capacity which closely matched the responses and failure modes of the undamaged beams tested under static loads only. All beams showed high RRI (low damage), high RSI (low stiffness degradation) and significant TEI (high residual energy absorption capacity) due to the positive influence of the blast detailing.

6.7 References (Chapter 6)

Adhikary, S. D., Li, B., & Fujikake, K. (2014). Residual resistance of impact-damaged reinforced concrete beams. *Magazine of Concrete Research, 67*(7), 364-378. doi:https://doi.org/10.1680/macr.14.00312

Charles, C. J. (2019). *Effect of detailing and fibers on the static and blast behaviour of high-strength concrete beams.* (MASc. thesis). University of Ottawa, Ottawa, ON, Canada.

Canadian Standards Association (CSA) (2012). Design and assessment of buildings subjected to blast loads. CSA S850-12, Mississauga, ON, Canada, pp. 126.

Dancygier, A. N., & Karinski, Y. S. (2019). Effect of cracking localization on the structural ductility of normal strength and high strength reinforced concrete beams with steel fibers. *International Journal of Protective Structures, 10*(4), 457–469. doi:https://doi.org/10.1177/2041419618824609

Yoo, D.-Y., Yuan, T., Yang, J.-M., & Yoon, Y.-S. (2017). Feasibility of replacing minimum shear reinforcement with steel fibers for sustainable high-strength concrete beams. *Engineering Structures, 147*, 207-222. doi:https://doi.org/10.1016/j.engstruct.2017.06.004

Zanuy, C., & Ulzurrun, G. S. D. (2018). Residual behavior of reinforced steel fiber‐reinforced concrete beams damaged by impact. *Structural Concrete, 20*(2), 597-613. doi:https://doi.org/10.1002/suco.201800253

Chapter 7 Static results from Series 3 (UHPC)

Paper 4: Ductility of Ultra-High Performance Concrete Beams Reinforced with Ordinary, High-strength and Stainless Steel bars

7.1 Introduction

This chapter presents the results of Series 3 of the research program and investigates the influence of reinforcement grade on the flexural behaviour of UHPC beams under static loading. As part of the study, a series of UHPC beams built with either Grade 400 MPa ordinary steel, Grade 690 MPa high-strength steel or Grade 520 MPa stainless steel reinforcement are tested under four-point bending. The first group of beams is built with UHPC having 3% fibers, without transverse reinforcement, while the second group of beams is built with UHPC having 2% fibers and relaxed blast detailing. The results are compared to a control set of beams built with high-strength concrete having nominal and blast detailing, respectively. Test variables included the effects of concrete type, steel type, longitudinal steel ratio and detailing.

7.2 Research contribution

The content of this chapter is included in the following published manuscript:

Li, Y., & Aoude, H. (2022). Ductility of Ultra-High Performance Concrete Beams Reinforced with Ordinary, High-Strength and Stainless Steel Bars. ACI Symposium Publication, 351, 129-150.

7.3 Experimental program

The details of the experimental program were provided in **Chapter 3** (see Series 3 Group 1 and 2). All beams had dimensions of 125 mm × 250 mm × 2440 mm (b × h × L), and were constructed with UHPC having either 2% or 3% steel fibers. The beams were built with three types of longitudinal steel bars: Grade 400 MPa normal-strength steel conforming to CSA G30.18, Grade 690 MPa high-strength steel conforming to ASTM A1035 (ASTM, 2020b), and Grade 520 MPa XM-28 stainless steel conforming to ASTM A955 (ASTM, 2020a).

Group 1 included UHPC beams cast with 3% fibers (designated as U3). The beams in this group were singly-reinforced, and were built without stirrups (Type D detailing). Longitudinal steel consisted of either 2-15M ordinary bars, or 2-No.5 high-strength or stainless steel bars (ρ = 1.5%). To examine the effect of concrete type, the results are compared to a control set of high-strength concrete beams with identical properties, and built either with or

without stirrups made from 6.3 mm steel wire, spaced at 100 mm (d/2) in the shear spans only (Type C or D detailing, respectively).

Group 2 included UHPC beams cast with 2% fibers (designated as U2). The beams in this group were doubly-reinforced, and transverse reinforcement consisted of closed ties made from 6.3 mm steel wire which were spaced at 100 mm (s = d/2) along the entire beam span. (Type B, "intermediate" detailing). Longitudinal steel consisted of either 2-15M or 2-20M bars (ρ = 1.5% or 2.4%) in tension, and 2-10M bars (ρ' = 0.8%) in compression for the beams with normal-strength ordinary steel. The beams with HSS were reinforced with either 2-No.4 or 2-No.5 bars (ρ = 1.0% or 1.5%) in tension, and 2-No.3 or 2-No.4 bars (ρ' = 0.6% - 1.0%) in compression. The beams with SS bars were reinforced with 2-No.5/2-No.4 or 2-No.4/2-No.3 bars in tension/compression. To examine the effect of concrete type, the results are compared to a control set of high-strength concrete beams with identical properties, but with closed ties spaced at 50 mm (d/4) over their full span (Type A, "blast" detailing).

As noted above, each group included specimens reinforced with three different steel types to examine steel type/grade, while the longitudinal steel ratio was varied in Group 2. The effects of concrete type (UHPC vs. HSC), and detailing (Group 1 vs. 2), were also investigated.

The beam nomenclature in **Table 7.1, Table 7.2** and **Figure 7.1** indicates the design parameters, including: the concrete type (C100 vs. U2 or U3), tension bar size (15M, 20M, No.4 or No.5), steel type (HS: high-strength steel, S1: stainless steel, and no indicator for the beams with ordinary steel), and detailing level (DR-d/4: Type A, DR-d/2: Type B, S: Type C, and no indicator for the beams without stirrups). For example, in Group 1, U3-No.5S1 is constructed with U3 concrete (UHPC with 3% fibers), 2-No.5 stainless bars and without stirrups (Type D detailing), while C100-No.5S1 and C100-No.5S1-S are the companion HSC control beams built with and without stirrups (Type C and D), respectively. In Group 2, U2-No.5S1-DR-d/2 is built with U2 concrete (UHPC with 2% fibers), 2-No.5 stainless bars in tension, and intermediate detailing with ties spaced at 100 mm (d/2) throughout the beam span (Type B detailing), while C100-No.5S1-DR-d/4 is the control HSC beam built with ties spaced at 50 mm (d/4) throughout the beam span (Type A detailing).

Table 7.1 Beam design details (Group 1)

Series	Beam ID	Concrete [a]			Longitudinal reinforcement			Transverse reinf.		Detailing
		Type	f'_c MPa	v_f %	Type	Grade MPa	Tension (ρ in %)	Type	Spacing mm	
U3	U3-15M	UHPC	149	3	Ordinary	400	2-15M (1.5%)	-	-	Type D
	U3-No.5HS	UHPC	140	3	High-strength (ASTM A1035)	690	2-No.5 (1.5%)			
	U3-No.5S1	UHPC	148	3	Stainless (XM-28)	520	2-No.5 (1.5%)			
HSC	C100-15M-S [c]	HSC	107	-	Ordinary	400	2-15M (1.5%)	U-shaped [b]	100	Type C
	C100-15M	HSC	101	-				-	-	Type D
	C100-No.5HS-S [d]	HSC	95	-	High-strength (ASTM A1035)	690	2-No.5 (1.5%)	U-shaped [b]	100	Type C
	C100-No.5HS	HSC	96	-				-	-	Type D
	C100-No.5S1-S	HSC	97	-	Stainless (XM-28)	520	2-No.5 (1.5%)	U-shaped [b]	100	Type C

[a] f'_c = average concrete compressive strength; v_f = volumetric fiber content (3% = 234 kg/m^3)

[b] Placed in the shear span only

[c, d] Control beams built with plain HSC tested by Li et al. (2018), Li & Aoude (2019)

Table 7.2 Beam design details (Group 2)

Series	Beam ID	Concrete [a]			Longitudinal reinforcement				Transverse reinf.		Detailing
		Type	f'_c MPa	v_f %	Type	Grade MPa	Tension (ρ in %)	Compression (ρ' in %)	Type	Spacing mm	
U2	U2-15M-DR-d/2	UHPC	140	2	Ordinary	400	2-15M (1.5%)	2-10M (0.8%)	Closed ties (full span)	100	Type B
	U2-20M-DR-d/2	UHPC	140	2			2-20M (2.4%)	2-10M (0.8%)			
	U2-No.4HS-DR-d/2	UHPC	142	2	High-strength (ASTM A1035)	690	2-No.4 (1.0%)	2-No.3 (0.7%)			
	U2-No.5HS-DR-d/2	UHPC	137	2			2-No.5 (1.5%)	2-No.4 (1.0%)			
	U2-No.4S1-DR-d/2	UHPC	151	2	Stainless (XM-28)	520	2-No.4 (1.0%)	2-No.3 (0.7%)			
	U2-No.5S1-DR-d/2	UHPC	153	2			2-No.5 (1.5%)	2-No.4 (1.0%)			
HSC	C100-15M-DR-d/4 [b]	HSC	105	-	Ordinary	400	2-15M (1.5%)	2-10M (0.8%)	Closed ties (full span)	50	Type A
	C100-No.5HS-DR-d/4	HSC	94	-	High-strength (ASTM A1035)	690	2-No.5 (1.5%)	2-No.4 (1.0%)			
	C100-No.5S1-DR-d/4	HSC	103	-	Stainless (XM-28)	520	2-No.5 (1.5%)	2-No.4 (1.0%)			

[a] f'_c = average concrete compressive strength; v_f = volumetric fiber content (2% = 156 kg/m^3)

[b] Control beams built with plain HSC tested by Charles (2019)

Detailing:	Specimens:	Control specimens:
(a) UHPC beam with 3% fiber without stirrup (**Type D** detailing): 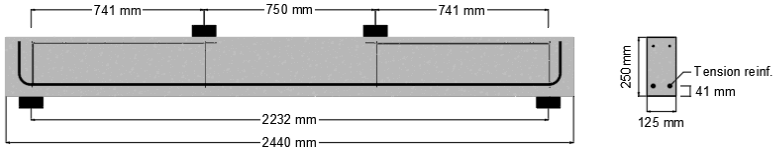	U3-15M U3-No.5HS U3-No.5S1	C100-15M C100-No.5HS
(b) HSC beams with stirrups @ d/2 (**Type C** detailing): 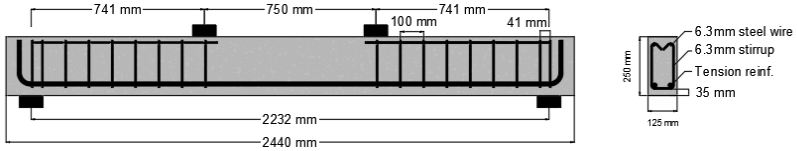		C100-15M-S C100-No.5HS-S C100-No.5S1-S
(c) UHPC beam with 2% fiber and intermediate detailing (**Type B** detailing): 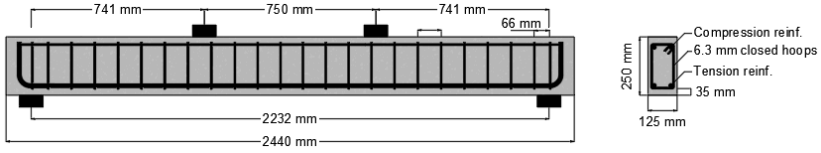	U2-15M-DR-d/2 U2-20M-DR-d/2 U2-No.4HS-DR-d/2 U2-No.5HS-DR-d/2 U2-No.4S1-DR-d/2 U2-No.5S1-DR-d/2	
(d) HSC beams with Blast detailing (**Type A** detailing): 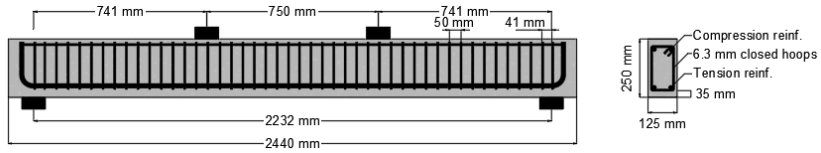		C100-15M-DR-d/4 C100-No.5HS-DR-d/4 C100-No.5S1-DR-d/4

Figure 7.1 Specimen Designs

7.4 Test results

The static load-deflection responses of the Group 1 and Group 2 UHPC specimens are plotted in **Figure 7.3**. **Table 7.3 & Table 7.4** summarize key data extracted from the load-deflection curves, including: yield load (P_y), maximum load (P_{max}), secant stiffness (k_s), yield displacement (Δ_y), maximum (failure) displacement (Δ_{max}), and ductility (Δ_{max}/Δ_y). The beams with high-strength and stainless steel do not show well-defined yield points due to the nature of the steel stress-strain relationship, and therefore yielding in these specimens was estimated using the method shown in **Figure 7.2a** (Pam et al., 2001; Park, 1989). The effects of the variables on post-peak toughness and deformability are evaluated by computing the toughness, defined as the area under the curves up to $3\Delta_y$ ($A_{3\Delta_y}$) and Δ_{max} ($A_{\Delta_{max}}$), as well as comparing the corresponding toughness indices: $I_{3\Delta_y}$ and $I_{\Delta_{max}}$ (Al-Ta'an & Al-Feel, 1990). As shown in **Figure 7.2b**, the toughness indices can be calculated by taking the ratios of the toughness at the critical deflections ($3\Delta_y$ and Δ_{max}) and the area under the load-deflection curve up to yielding (that is, $I_{3\Delta_y} = \frac{Area\ OBDF}{Area\ OAB}$ and $I_{\Delta_{max}} = \frac{Area\ OBEG}{Area\ OAB}$).

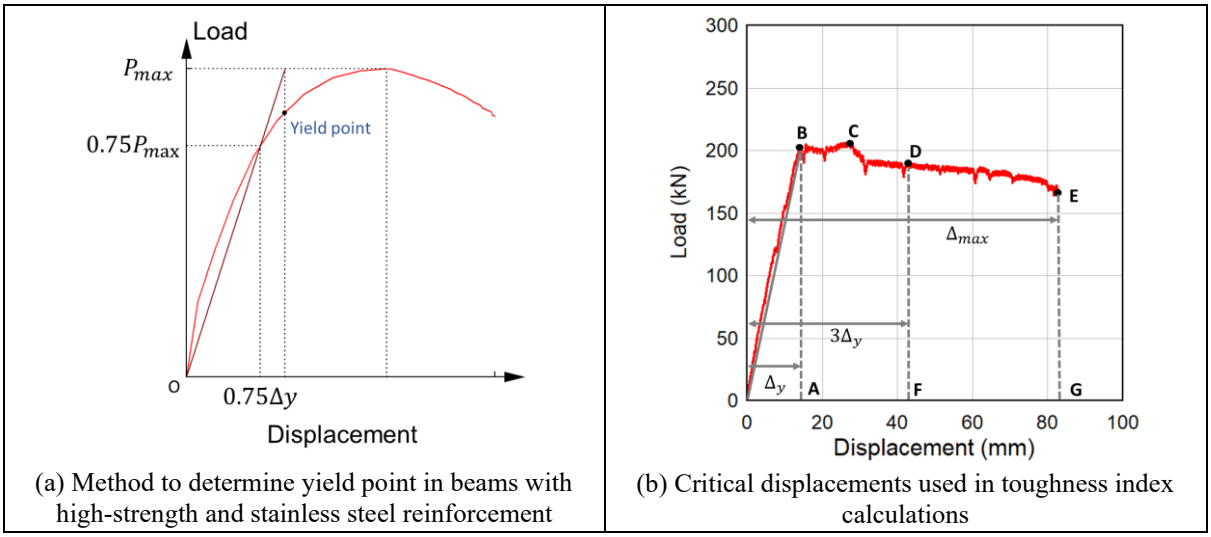

(a) Method to determine yield point in beams with high-strength and stainless steel reinforcement

(b) Critical displacements used in toughness index calculations

Figure 7.2 Definition of yield point and critical displacements for toughness calculations

Table 7.3 Static test results from Group 1

Series	Beam	Load		Displacement		Stiffness k_s N/mm	Ductility Δ_{max}/Δ_y	Toughness (J) [Toughness index]		
		Yield P_y kN	Peak P_{max} kN	Yield Δ_y mm	Failure Δ_{max} mm			A_{Δ_y}	$A_{u,3\Delta_y}$ $[I_{3\Delta_y}]$	$A_{\Delta_{max}}$ $[I_{\Delta_{max}}]$
U3	U3-15M	190.7	190.7	11.6	55.7	16437	4.8	1285	5013 [3.90]	7971 [6.20]
	U3-No.5HS	247.1	280.5	20.3	56.5	15217	2.78	3029	-	11973 [3.95]
	U3-No.5S1	207.8	207.8	14.8	124 *	14040	8.38	1906	6930 [3.64]	18561 [9.74]
HSC	C100-15M-S	94.5	104.6	14.6	40.7	6342	2.74	780	-	3272 [4.19]
	C100-15M	-	90	-	15.3	5882	-	-	-	726
	C100-No.5HS-S	185.4	194.7	31.4	34.0	5904	1.09	3072	-	3686 [1.2]
	C100-No.5HS	-	84.3	-	14.4	5854	-	-	-	643
	C100-No.5S1-S	105.2	121.6	15.6	42.6	6744	2.73	955	-	4061 [4.25]

Note:
P_y = yield strength; P_{max} = peak strength; Δ_y = yield displacement; Δ_{max} = maximum displacement; k_s = secant stiffness; $A_{\Delta_y}, A_{3\Delta_y}, A_{\Delta_{max}}$ = area under the load-deflection curve up to $\Delta_y, 3\Delta_y, \Delta_{max}$; $I_{3\Delta_y}, I_{\Delta_{max}}$ = toughness index at $3\Delta_y, \Delta_{max}$.
* Tested terminated

Table 7.4 Static test results from Group 2

Series	Beam	Load		Displacement		Stiffness k_s N/mm	Ductility Δ_{max}/Δ_y	Toughness J [Toughness index]		
		Yield P_y kN	Peak P_{max} kN	Yield Δ_y mm	Failure Δ_{max} mm			A_{Δ_y}	$A_{u,3\Delta_y}$ $[I_{3\Delta_y}]$	$A_{\Delta_{max}}$ $[I_{\Delta_{max}}]$
U2	U2-15M-DR-d/2	181.2	181.2	12.8	49.1	14156	3.84	1274	5233 [4.11]	6728 [5.28]
	U2-20M-DR-d/2	201.8	207.0	14.2	81.7	14211	5.75	1586	7152 [4.51]	14470 [9.13]
	U2-No.4HS-DR-d/2	151.2	178.4	14.1	39.5	10723	2.8	1369	-	5174 [3.78]
	U2-No.5HS-DR-d/2	249.5	286.6	23.2	55.1	12573	2.38	3407	-	11643 [3.42]
	U2-No.4S1-DR-d/2	107.9	126.2	10.3	124	10476	12.0	700	3188 [4.55]	10295 [14.7]
	U2-No.5S1-DR-d/2	153.1	172.4	12.1	150	12653	12.4	1161	5075 [4.37]	21491 [18.51]
HSC	C100-15M-DR-d/4	105	108	14	150	7516	10.7	738	3546 [4.80]	14018 [18.99]
	C100-No.5HS-DR-d/4	184.1	207.9	28.4	96.3	7960	3.4	2965	14272 [4.81]	18028 [6.08]
	C100-No.5S1-DR-d/4	116.0	135.7	17.5	147	7769	8.57	1211	5723 [4.73]	17033 [14.07]

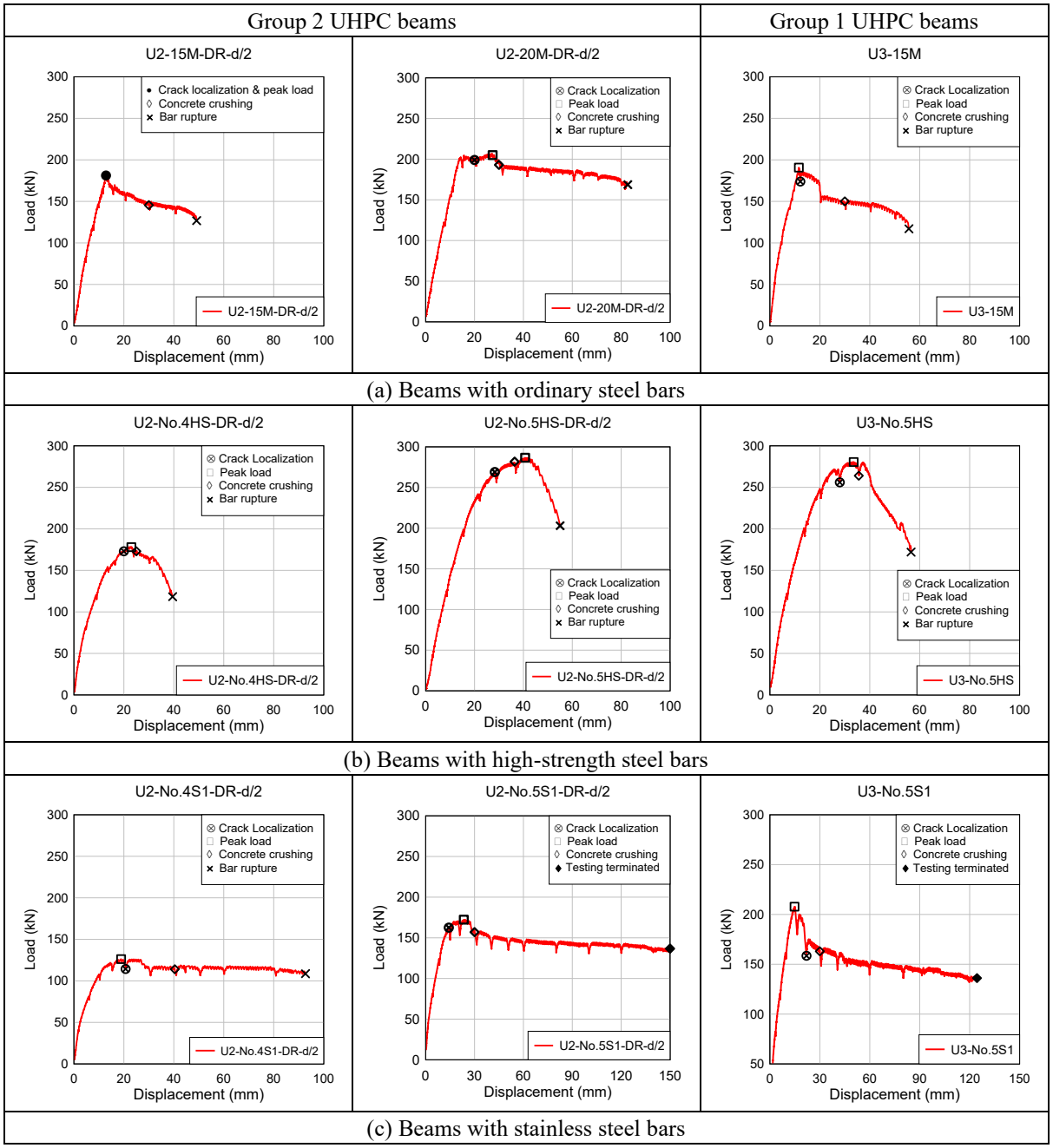

Figure 7.3 Load-deflection curves: stages in response (Group 1 and Group 2 UHPC beams)

7.4.1. Effect of UHPC in Group 1 beams (U3 vs. HSC)

Before examining the effect of steel ratio and type, it is of interest to compare the behaviour of the UHPC beams with that of companion beams built with conventional high-strength concrete (HSC). This effect is first studied in the Group 1 UHPC beams which were singly-reinforced, and built with U3 concrete, varying steel types and Type D detailing (no stirrups). The companion control HSC beams had the same cross-sectional properties and dimensions, but were built with plain high-strength concrete (f_c' = 100 MPa), and included specimens with and without stirrups in the shear spans (Type C and D detailing, respectively).

Comparison of the static response of the specimens is shown in **Figure 7.4**. It can be observed that all HSC beams built without stirrups (C100-15M, C100-No.5HS and C100-No.5S1) fail in shear, regardless of steel type. In comparison, provision of UHPC with 3% fibers, enhances shear capacity and promotes flexural failure in beams U3-15M, U3-No.5HS and U3-No.5S1. Despite the varying shear demands, the UHPC provided sufficient shear resistance in all three beam types. The use of UHPC also resulted in impressive improvements in flexural performance when compared to the companion HSC beams built with stirrups. In the ordinary steel set, beam U3-15M shows enhancements of 159%, 82%, 78% and 144% in terms of stiffness (k_s), peak load capacity (P_{max}), ductility (Δ_{max}/Δ_y) and overall toughness ($A_{\Delta_{max}}$) when compared to beam C100-15M-S. Likewise, the U3 beams with high-strength and stainless steel bars (U3-No.5HS and U3-No.5S1) show enhancements of 158% & 108% in stiffness (k_s), 44% & 71% in load capacity (P_{max}), 155% & 191% in ductility (Δ_{max}/Δ_y) and 225% & 207% in toughness ($A_{\Delta_{max}}$).

The failure mode is also affected by the concrete type. As shown in **Figure 7.5**, the failure in the HSC beams with stirrups is associated with concrete crushing in the midspan compression zone, and is especially sudden in the beams with high-strength bars. In comparison, the high damage tolerance of UHPC in compression, prevents crushing, resulting in increased ductility when compared to the companion beams built with HSC. On the other hand, the high tensile and bond capacity of the UHPC, combined with crack localization, results in bar fracture failures in the beams with normal-strength and high-strength bars. Due to the lack of top reinforcement the failures occur suddenly and result in total beam collapse. Conversely, the use of stainless steel, with its high strain capacity in tension, prevents bar fracture, and results in ductile response without bar fracture until Δ = 150 mm (L/15).

To better understand the influence of the UHPC on improving shear response, the shear resistance of the UHPC beams is predicted using the AFGC design guidelines (AFGC, 2013). According to this model, the shear resistance is contributed by the UHPC concrete, steel fibers and shear reinforcement ($V_r = V_c + V_{fb} + V_s$). The UHPC contribution is determined from $V_c = \frac{0.21}{\gamma_{cf}\gamma_E} k\sqrt{f_c'} b_w d$, where $\gamma_{cf}\gamma_E$ are assumed equal to 1.5; k =*1.0* for non-prestressed beams; f_c', b_w, d are the UHPC concrete strength, beam width and effective depth, respectively. The fiber contribution is $V_{fb} = \frac{0.9 b_w d \sigma_f}{tan\theta}$, where θ equals to 35° as suggested by the CSA A23.3-standard (CSA, 2014) and σ_f is the tensile strength provided by the fibers. The tensile strength was determined using an equation proposed by Voo et al. (2010): $\sigma_f = K_{f,max}\tau_b(\frac{l_f}{d_f}v_f)$, where τ_b is bond stress between the fibers and the concrete matrix ($\tau_b = 0.6\sqrt{f_c'}$ for straight fibers) and $K_{f,max}$ is the maximum value of the global orientation factor ($K_{f,max} = 0.5 - \frac{0.645}{(l_{f/d_f})^{0.45}}$). Using these equations, the predicted shear capacities of the UHPC beams with 2% and 3% fibers are 320.9 kN and 439.9 kN, respectively. Guertin-Normoyle (2017) tested a beam built with UHPC and 2% fibers, type C detailing and the same dimensions used in the current tests. The UHPC beam eventually failed in shear at a load of 318 kN, which confirms that AFGC design guidelines (AFGC, 2013) can well predict the shear capacity of UHPC beams. Using the flexural procedure described in **Section 7.5**, the shear-to-flexure capacity ratios are 2.62, 2.34 and 1.74 for beams U3-15M, U3-No.5S1 and U3-No.5HS; the results confirm that UHPC with 3% steel fibers can substitute for transverse reinforcement and safely avoid shear failure.

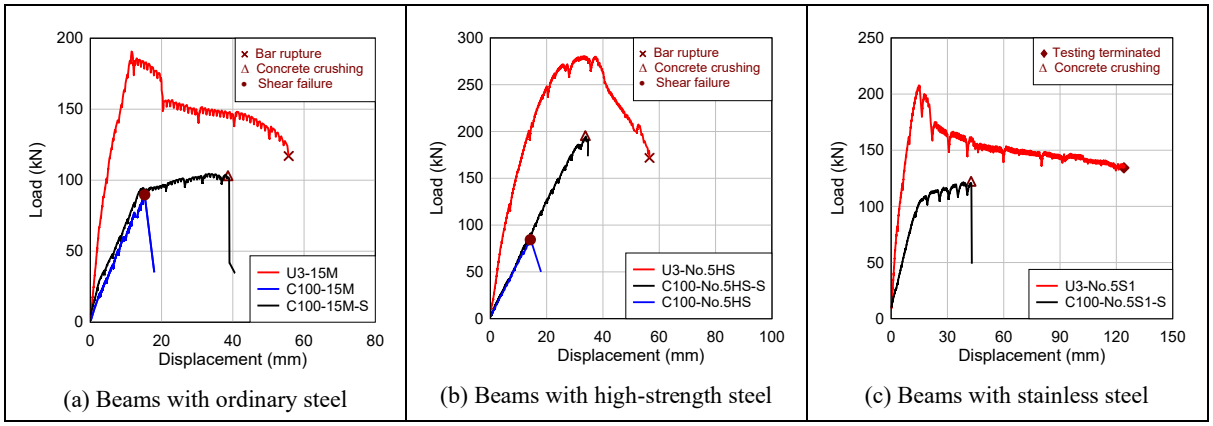

(a) Beams with ordinary steel (b) Beams with high-strength steel (c) Beams with stainless steel

Figure 7.4 Test results: effect of concrete type in Group 1 beams (U3 vs. HSC)

(a) U3-15M	(b) U3-No.5HS	(c) U3-No.5S1
		
Δ = 11.6 mm (Δ_y)	Δ = 20.3 mm (Δ_y)	Δ = 14.8 mm (Δ_y)
		
Δ = 12.5 mm: **Crack localization**	Δ = 28 mm: Crack localization	Δ = 20 mm: Crack localization
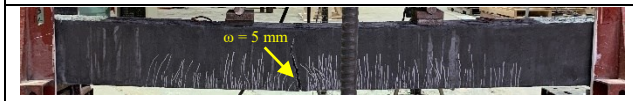		
Δ = 20 mm	Δ = 40 mm	Δ = 30 mm
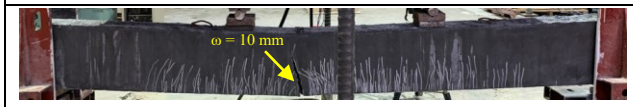	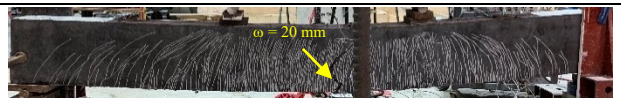	
Δ = 34.8 mm ($3\Delta_y$)	Δ = 50 mm	Δ = 44.4 mm ($3\Delta_y$)
		
Δ_{max} = 55.7 mm: Bar rupture	Δ_{max} = 56.5 mm: Bar rupture	Δ = 124 mm: Testing terminated
		N.A.
Companion HSC beam without stirrups (shear failure)	Companion HSC beam without stirrups (shear failure)	
	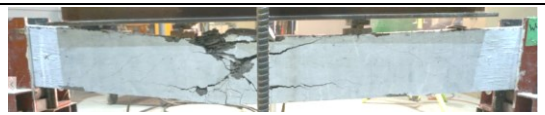	
Companion HSC beam with stirrups (concrete crushing @ Δ_{max} = 40.7 mm)	Companion HSC beam with stirrups (concrete crushing @ Δ_{max} = 34 mm)	Companion HSC beam with stirrups (concrete crushing @ Δ_{max} = 43 mm)

Figure 7.5 Progress of damage and failure mode: U3 beams

7.4.2. Effect of UHPC in Group 2 beams (U2 vs. HSC)

The effect of UHPC is further examined in Group 2, by comparing the responses of the U2 beams with varying steel types and Type B detailing, with that of companion HSC beams with Type A blast detailing. The companion beams had the same properties and dimensions as the UHPC beams, but were built with plain high-strength concrete (f_c' = 100 MPa), and a reduced tie spacing of 50 mm (s = d/4) throughout their span as shown in **Figure 7.1d**.

Figure 7.6a examines the effect of UHPC in the Group 2 beams with ordinary steel. It can be observed that beam U2-15M-DR-d/2 shows significant increases of 116% and 68% in post-cracking stiffness and load capacity due to the increased tensile resistance of the UHPC. On the other hand, the UHPC beam shows a noticeable reduction in ductility due to the change in failure mode. **Figure 7.7a** shows that the cracking patterns and failures are distinct in both beams. Due to the enhanced steel reinforcement detailing, the HSC beam shows a remarkable ability to sustain large post-peak displacements, with damage at the end of testing characterized by concrete crushing in the top mid-span region. The UHPC beam shows many fine and well distributed cracks with no signs of crushing. However, after reaching its peak strength, the damage is characterized by the formation of one dominant crack, which eventually leads to bar fracture. Indeed, as shown in **Figure 7.7a**, the main crack width in the UHPC beam increased from 2 to 18 mm during the test, with the remaining crack widths staying ≤ 0.5 mm. As a result of the high bond capacity of UHPC, the reinforcing bar which bridges the crack develops very large strains over a short length of reinforcement, leading to bar rupture (Dancygier & Karinski, 2019). As a result, despite the increased toughness ($A_{u,3\Delta_y}$) up to $3\Delta_y$, the ductility (Δ_{max}/Δ_y), overall toughness ($A_{\Delta_{max}}$) and toughness index ($I_{\Delta_{max}}$) are decreased by 52%, 64% and 72% in the UHPC specimen.

The same trend is observed in the Group 2 high-strength steel set. As shown in **Figure 7.6b**, beam U2-No.5HS-DR-d/2 shows significant increases of 58% and 38% in post-cracking stiffness and load capacity, but a noticeable reduction in ductility, when compared to beam C100-No.5HS-DR-d/4. As shown in **Figure 7.8b**, failure in the HSC beam is associated with concrete crushing and the formation of several major cracks, and eventual bar fracture. In comparison, the UHPC beam shows limited concrete damage (no signs of crushing), many fine and well-distributed cracks, but fails owing to the formation of one dominant crack, which results in crack localization and bar fracture. While bar fracture occurs in both specimens, it occurs at a much later stage of loading in the HSC companion. As a result, the ductility

(Δ_{max}/Δ_y), overall toughness ($A_{\Delta_{max}}$) and toughness index ($I_{\Delta_{max}}$) are decreased by 30%, 35% and 35% in the UHPC specimen.

The responses of the UHPC and HSC beams in the stainless steel set are compared in **Figure 7.6a**. Unlike the previous two sets, the significant strain capacity of the stainless steel prevents bar fracture in beam U2-No.5S1-DR-d/2, which shows a near perfect load-displacement plateau up to Δ = 150 mm (**Figure 7.6c**). As a result, in addition to the increases in strength and stiffness, the UHPC beam shows improvements of 26%-30% in ductility and toughness. It is interesting to note that while crack localization occurs in the U2-stainless beam, it is associated with two dominant cracks, with the failure mode eventually transitioning from bar fracture to UHPC crushing (**Figure 7.9b**).

The bar fracture failure observed in the current tests result due to the very high bond capacity of UHPC (Khaksefidi et al., 2021) (which results in strain localization), combined with its very high damage tolerance in compression (which delays crushing). As a result, compression failures are less likely to occur in UHPC beams, and bar fracture failures prior to concrete crushing become more likely. This same effect has previously been reported for other high-performance FRCs by Bandelt and Billington (2016), while Pokhrel and Bandelt (2019) note that this effect is even more critical in UHPC, and indicate that: "*the reduction in deformation capacity [is] mainly due to the resistance of the high tensile strength material which prevent[s] multiple dominant cracks from forming … the lower number of cracks and low rebar slip result[s] in strain concentration over a smaller gage length of longitudinal reinforcement, and thereby [leads to] early fracture of the reinforcement*", which corresponds to the observation in the current study. This effect becomes even more critical in beams with high-strength reinforcement, due to their relatively limited strain capacity. The next sections examine the effect of steel ratio on the ductility and failure mode of the UHPC beams.

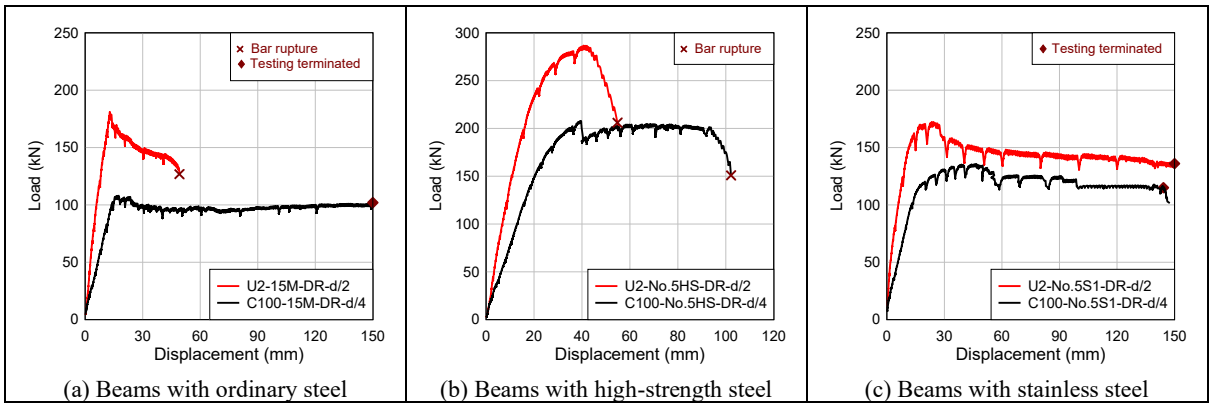

(a) Beams with ordinary steel (b) Beams with high-strength steel (c) Beams with stainless steel

Figure 7.6 Test results: effect of concrete type in Group 2 beams (U2 vs HSC)

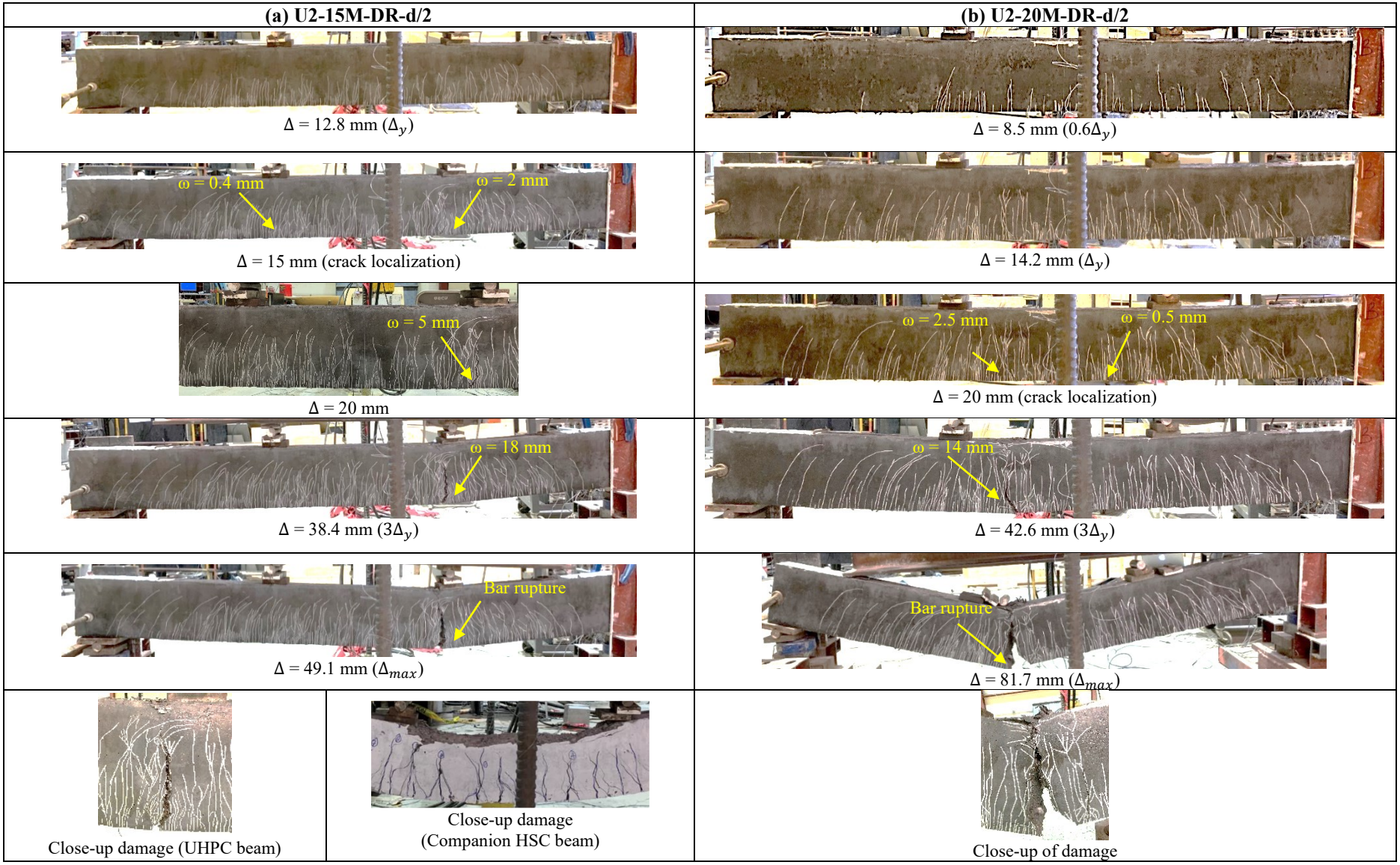

Figure 7.7 Progress of damage and failure mode: U2 beams with ordinary steel (Group 2)

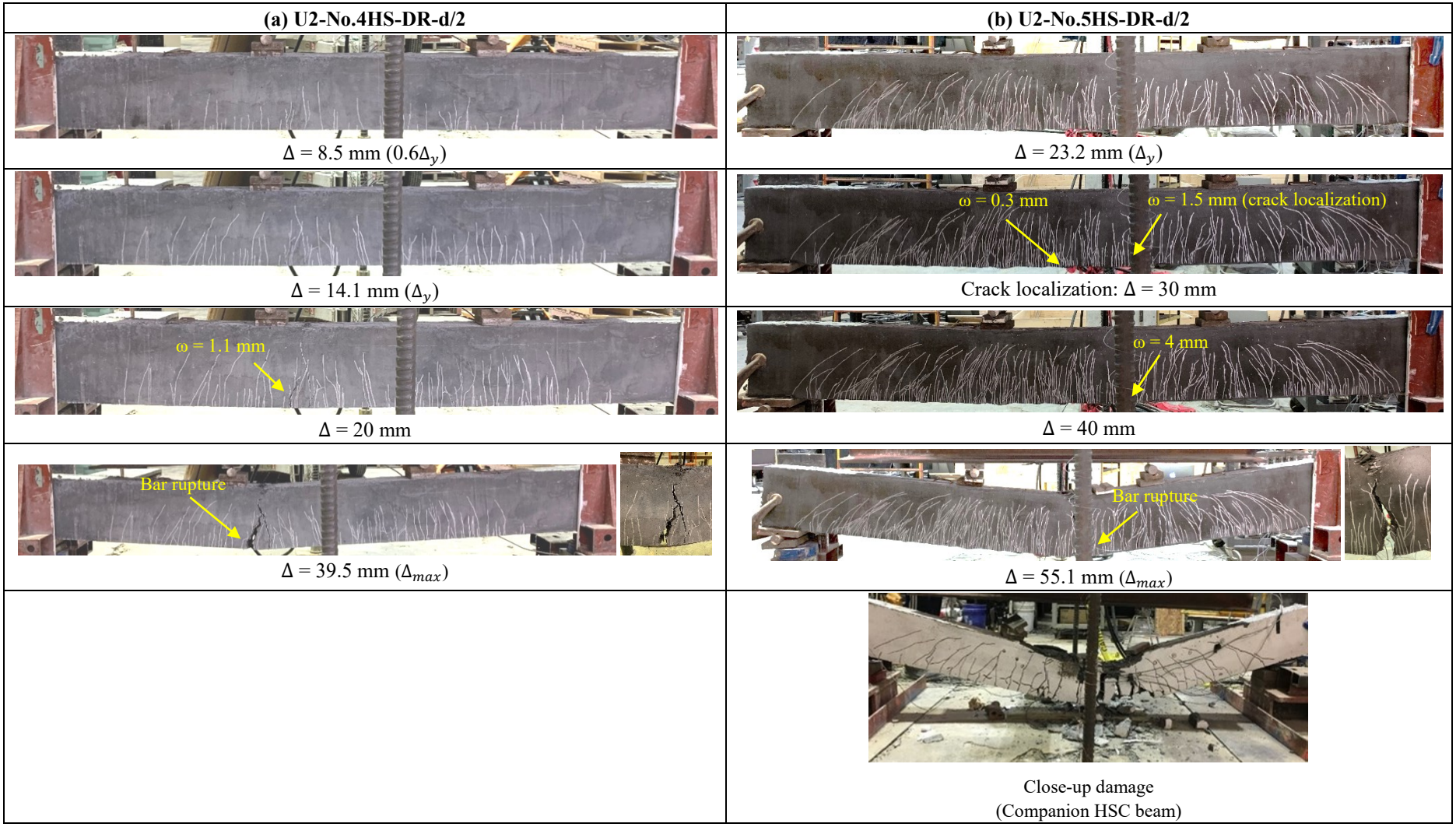

Figure 7.8 Progress of damage and failure mode: U2 beams with high-strength reinforcement (Group 2)

(a) U2-No.4S1-DR-d/2	(b) U2-No.5S1-DR-d/2
	
Δ = 10.3 mm (Δ_y)	Δ = 12.1 mm (Δ_y)
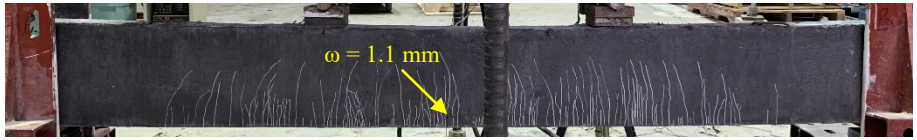	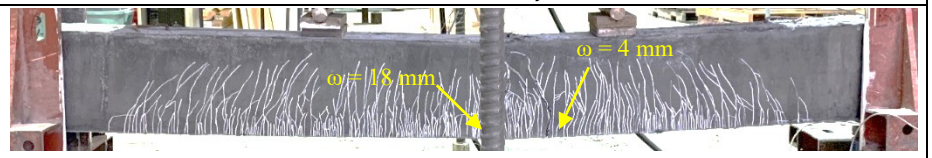
Δ = 20 mm ($3\Delta_y$): Crack localization	Δ = 36.3 mm ($3\Delta_y$)
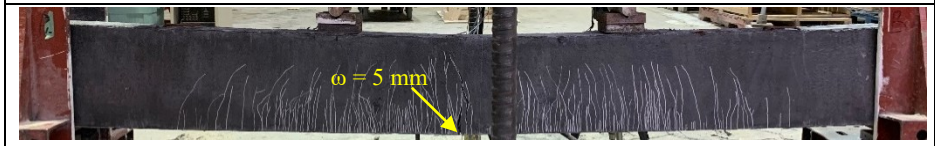	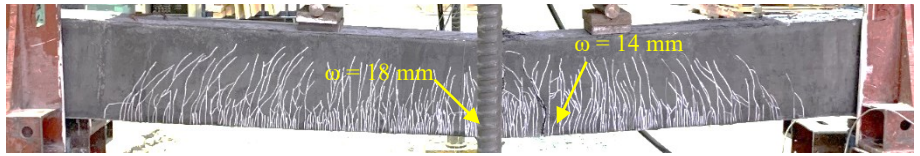
Δ = 30.9 mm ($3\Delta_y$)	Δ = 66.6 mm ($5.5\Delta_y$): **Crack localization: 2 dominant cracks**
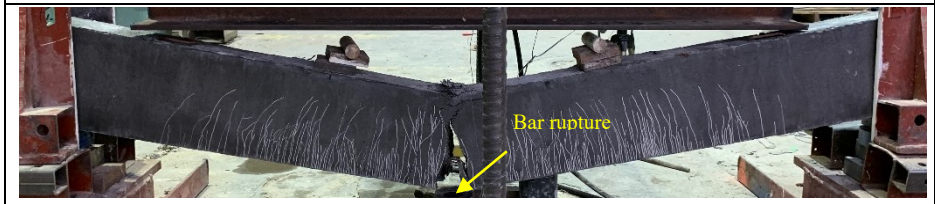	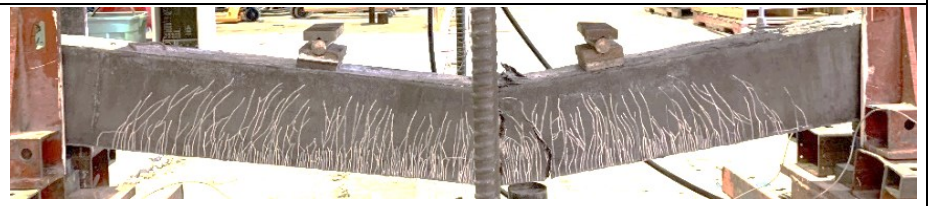
Δ = 124 mm (Δ_{max})	Δ = 150 mm (Δ_{max})**: Concrete crushing**
	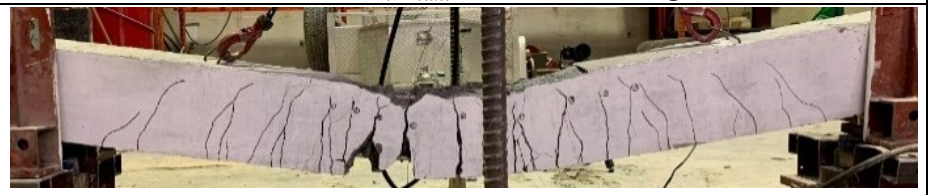
	Companion HSC beam: Δ_{max}**= 150** mm

Figure 7.9 Progress of damage and failure mode: U2 beam with stainless reinforcement (Group 2)

7.4.3.Effect of steel ratio in UHPC beams with NSS bars

The effect of steel ratio is first examined in beams U2-15M-DR-d/2 and U2-20M-DR-d/2 which were built with UHPC, and 2-15M (ρ =1.5%) vs. 2-20M (ρ =2.4%) normal-strength ordinary bars, respectively. Examining **Figure 7.10**, both beams eventually fail by bar fracture, however increasing the steel ratio from ρ = 1.5% to 2.4% improves all aspects of flexural response. Beam U2-20M-DR-d/2 shows a 12% increase in peak capacity, and a 66% increase in failure displacement (Δ_{max} = 82 vs. 49 mm). When taken up to $3\Delta_y$, U2-20M-DR-d/2 shows increases of 37% and 10% in toughness ($A_{u,3\Delta_y}$) and toughness index ($I_{3\Delta_y}$). The ductility (Δ_{max}/Δ_y), overall toughness ($A_{\Delta_{max}}$), and overall toughness index ($I_{\Delta_{max}}$) increase further by 115%, 50% and 73%, due to the delay in bar fracture. The observed trend related to the increase in ductility with steel ratio matches the observations in the tests reported by Yoo et al. (2016), Pokhrel and Bandelt (2019), Hasgul et al. (2018) and Shao and Billington (2021).

It is also interesting to note that the beams show slightly different trends when examining their post-peak responses. The peak capacity in beam U2-15M-DR-d/2 is reached upon yielding, with the beam showing an immediate deflection-softening response (B-F) until bar fracture. Conversely, U2-20M-DR-d/2 shows an initial ascending response (B-C), followed by a gradual descending branch (C-F). The result can be explained by the earlier crack localization in beam with a lower steel ratio (U2-20M-DR-d/2) which results in a loss in fiber bridging capacity and softening in the UHPC response. As the steel ratio is increased, crack localization is delayed (see **Figure 7.7**), which allows U2-20M-DR-d/2 to better maintain its load capacity after yielding. Yoo et al. (2016) also observed a decrease in post-yield capacity at steel ratios of ρ = 0.53% and 1.06%, with a nearly perfect plastic post-peak behavior and much higher ductility at ρ = 1.71%. Shao and Billington (2021) also noted that as the steel ratio is increased, the fiber-bridging capacity is maintained up to the peak load, before crack localization leads to a decrease in capacity.

The purpose of increasing the bar size in the current tests was to delay bar fracture, however the results indicate that larger steel ratios may be needed to promote concrete/UHPC failure after steel yielding without physical bar fracture. Hasgul et al. (2018) reported that a steel ratio of ρ = 4.3% was required to change the failure mode from bar fracture to crushing in UHPC beams, which is similar to the recommendation of ρ = 4% in Aghdasi and Ostertag (2020). Nonetheless, it is important to note that beam U2-20M-DR-d/2 shows a high ductility (Δ_{max}/Δ_y) of 5.75 and drift ratio (Δ_{max}/L_a) of 11% before the bar facture failure. Shao and

Billington (2019) proposed the following limiting steel ratio to ensure a minimum ductility in beams built with HPFRCC materials:

$$A_{s,limit} = \frac{\propto f_t}{(f_{su} - f_y)} \cdot \omega_{limit} \cdot bh \qquad 7\text{-}1$$

Where, f_{su}, f_y = ultimate and yield strength of the steel reinforcement; b, h= beam width and height; $\propto$ = empirical factor that represents the portion of the cross-section that has fiber bridging capacity at peak load (0.5-0.8 (Shao & Billington, 2019)); f_t = tensile strength the HPFRCC material can sustain after cracking; and ω_{limit} is determined based on the desired ductility (0.3 for drift ≥ 2.5% (Shao & Billington, 2019)). Assuming $\propto$ = 0.8, f_t = 8 MPa and using the steel properties in **Table 3.9**, $A_{s,limit}$ results in ρ = 1.4% for U2-20M-DR-d/2, which confirms that the beam had a sufficient amount of steel (ρ = 2.4%) to ensure high deformation capacity. As noted in Shao and Billington (2019), further research is needed to relate the choice of $\propto$ and ω_{limit} to various UHPC tensile testing methods. **Equation 7-1** is also dependent on the assumed steel properties, and a smaller $(f_{su} - f_y)$ would require a greater amount of steel.

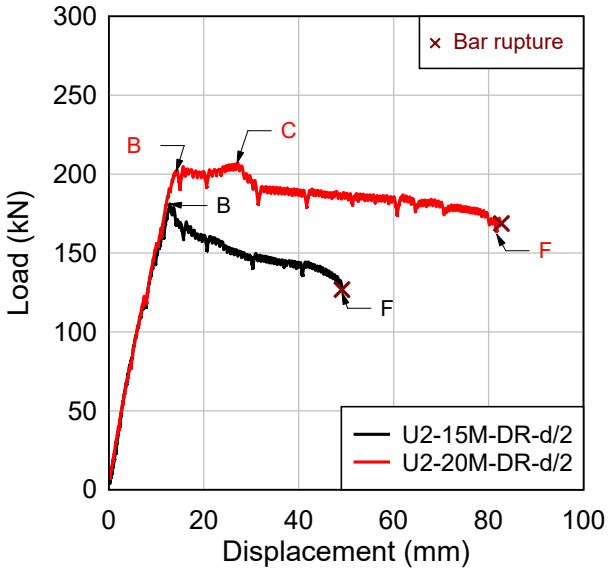

Figure 7.10 Test results: effect of steel ratio in UHPC beams with NSS bars

7.4.4.Effect of steel ratio in UHPC beams with HSS bars

The effect of high-strength steel ratio is studied by comparing the responses of beams U2-No.4HS-DR-d/2 and U2-No.5HS-DR-d/2 which had steel ratios of ρ =1.0% and 1.5%, respectively. As shown in **Figure 7.11**, increasing the steel ratio in U2-No.5HS-DR-d/2 significantly increased its load capacity (P_{max}) by 61% when compared to U2-No.4HS-DR-d/2. Increasing ρ also increases the failure displacement (Δ_{max}) by 40% due to the ability of the increased bar size to delay bar rupture. Owing to the increased load capacity and failure displacement, beam U2-No.5HS-DR-d/2 also shows a significant improvement of 125% in overall toughness ($A_{\Delta_{max}}$). However, increasing the high-strength steel ratio reduced the ductility (Δ_{max}/Δ_y) and toughness index ($I_{\Delta_{max}}$) by 15% and 10%, respectively. This can be explained by the high yield displacement in beam U2-No.5HS-DR-d/2 which results from the nature of the stress-strain response of the ASTM A1035 reinforcement. Nonetheless, the results confirm that increasing the steel ratio delays bar fracture in HSS reinforced UHPC beams, and increases the failure displacement and drift capacity (5.3% to 7.4%). Drift capacity may therefore be a more appropriate indicator of performance when compared to ductility in beams with HSS reinforcement lacking a well-defined yield point.

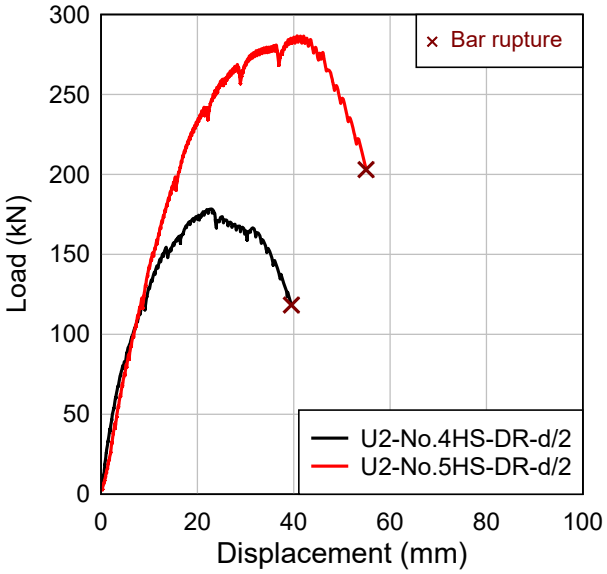

Figure 7.11 Test results: effect of steel ratio in UHPC beams with HSS bars

7.4.5.Effect of steel ratio in UHPC beams with SS bars

The effect of steel ratio is further examined in the SS series by comparing the responses of beams U2-No.4S1-DR-d/2 and U2-No.5S1-DR-d/2. As shown in **Figure 7.12**, increasing the stainless steel ratio from ρ = 1.0% to 1.5% improves all aspects of flexural response. Beam U2-No.5S1-DR-d/2 shows increased stiffness (k_s) and load capacity (P_{max}) by margins of 21% and 37% when compared to beam U2-No.4S1-DR-d/2. More importantly, the results show that increasing the steel ratio prevents bar fracture in the SS reinforced UHPC beams, with the failure transitioning from bar fracture to UHPC crushing at the end of the test (Δ_{max}= 150 mm). Accordingly, beam U2-No.5S1-DR-d/2 shows significant enhancements in ductility (Δ_{max}/Δ_y), overall toughness ($A_{\Delta_{max}}$) and toughness index ($I_{\Delta_{max}}$) by 3%, 109% and 26%.

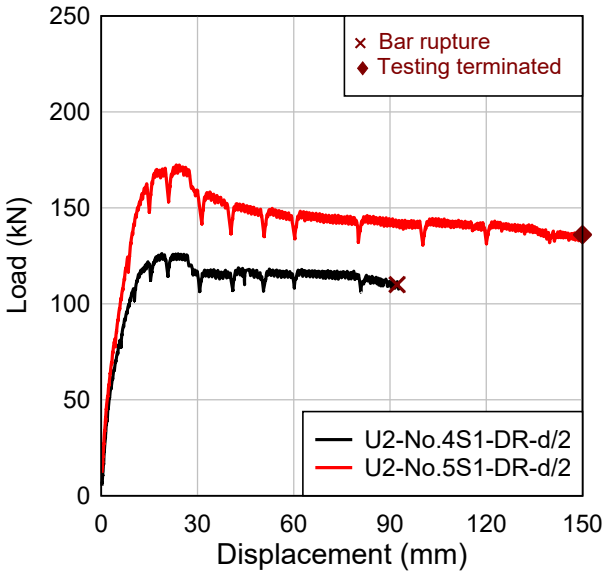

Figure 7.12 Test results: effect of steel ratio in UHPC beams with SS bars

7.4.6. Effect of high-strength steel in UHPC beams

The effect of steel grade (f_y= 690 vs. 400 MPa) can first be investigated by comparing the responses of beams U2-No.5HS-DR-d/2 and U2-15M-DR-d/2 in Group 2. Both beams were built with UHPC and a constant steel ratio of ρ = 1.5%, but contained normal-strength and high-strength bars, respectively.

Examining **Figure 7.13a**, the use of high-strength reinforcement in beam U2-No.5HS-DR-d/2 increased maximum load capacity (P_{max}) by 58%. Although both beams eventually fail due to bar fracture, the beam with high-strength bars delayed failure, with an increase of 12% in maximum displacement (55 mm vs. 49 mm), and an important increase of 73% in overall toughness. As shown in **Figure 7.14**, both beams fail due to bar fracture, however crack localization is delayed in beam U2-No.5HS-DR-d/2. The beam with high-strength bars also shows signs of crushing at failure, which indicates that the HSS bars were better able to engage and utilize the high compression capacity of the UHPC. Owing to the difference in steel stress-strain response, beam U2-No.5HS-DR-d/2 lacks a well-defined yield point whereas clear yielding and a deflection-softening response are observed in beam U2-15M-DR-d/2. The lower strain capacity of the ASTM A1035 bars (rupture strain of ~ 6%) also limits the increase in deformation capacity before bar fracture. As a result, U2-No.5HS-DR-d/2 shows reductions of 38% and 35% in ductility (Δ_{max}/Δ_y) and toughness index ($I_{\Delta_{max}}$). Nonetheless, it should be noted that both beams show acceptable drift ratios ($\Delta_{max}/\mathrm{L}_a$) of 6.6% and 7.4%, with a higher drift ratio for the beam with high-strength reinforcement. A similar observation can be seen in the beams with UHPC and 3% fibers (Group 1). As shown in **Figure 7.13b**, beam U3-No.5HS and U3-15M show similar stiffness and maximum displacements, however the use of high-strength steel results in significant enhancements in peak strength (P_{max}) and overall toughness ($A_{\Delta_{max}}$) by 47% and 50%. Both beams eventually failed by bar fracture, however the beam with high-strength bars shows some signs of crushing at failure.

It is also interesting to compare the responses of beams U2-No.4HS-DR-d/2 (ρ=1.0%) and U2-15M-DR-d/2 (ρ=1.5%), which had similar $\rho \cdot f_y$ ratios of 6.9 and 6.0 MPa. As shown in **Figure 7.13c**, beam U2-No.4HS-DR-d/2 shows similar load resistance (P_{max} = 178 kN vs. 181 kN) and overall toughness ($A_{\Delta_{max}}$ = 5.2 kJ vs. 6.7 kJ) when compared to the beam with increased amounts of normal-strength bars. However, the reduced strain capacity of the ASTM A1035 bars results in reductions of 20% and 27% in failure displacement and overall ductility when comparing beams with HSS and NS bars.

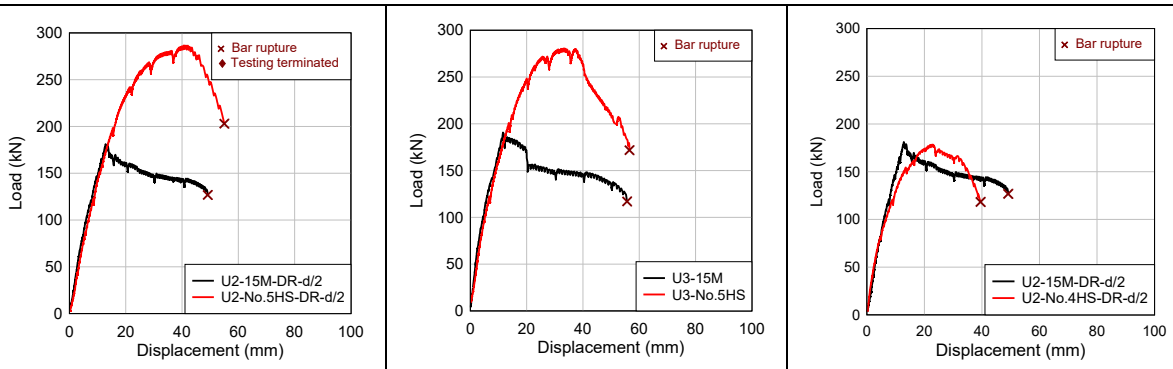

(a) Effect of HSS in U2 beams (same reinf. ratio)	(b) Effect of HSS in U3 beams (same reinf. ratio)	(c) Effect of HSS in U2 beams (similar ρf_y)

Figure 7.13 Test results: effect of high-strength steel

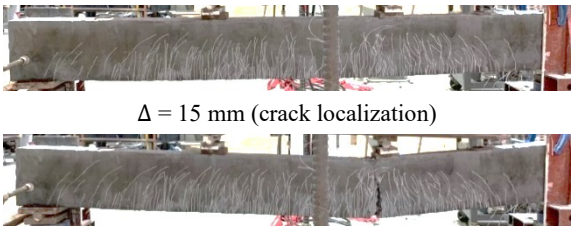

Δ = 15 mm (crack localization)

Δ = 49.1 mm (Δ_{max})

Crack localization: Δ = 30 mm

Δ = 55.1 mm (Δ_{max})

Close-up damage

Close-up damage

(a) U2-15M-DR-d/2	(b) U2-No.5HS-DR-d/2

Figure 7.14 Comparison of damage: effect of high-strength steel

7.4.7. Effect of stainless steel

The effect of stainless steel is first examined by comparing the responses of beams U2-No.5S1-DR-d/2 and U2-15M-DR-d/2, which were built with equal amounts of stainless and normal-strength steel (ρ = 1.5%).

As shown in **Figure 7.15a**, the use of SS bars does not result in an increase in capacity but has a remarkable effect on ductility. The failure displacement (Δ_{max}) is increased by 205% due to the high strain capacity of the stainless steel. Both beams show similar toughness ($A_{u,3\Delta_y}$) and toughness index ($I_{3\Delta_y}$) up to the common deflection $3\Delta_y$, however U2-No.5S1-DR-d/2 shows remarkable increases of 181%, 251% and 219% in overall toughness ($A_{\Delta_{max}}$), toughness index ($I_{\Delta_{max}}$) and ductility (Δ_{max}/Δ_y). Both beams show a softening post-peak response, however the reduction in capacity is more rapid, and failure is more sudden, in beam U2-15M-DR-d/2. In the case of the U2-15M-DR-d/2 specimen, the crack localization leads to the development of high strains over a small gage length of longitudinal reinforcement, thereby leading to bar fracture (Pokhrel & Bandelt, 2019). As shown in **Figure 7.9b**, crack localization is delayed in the beam with stainless steel bars, which allows the plasticity in the steel reinforcement to spread over a longer length, and delays bar fracture. Indeed, crushing of UHPC is clearly visible in U2-No.5S1-DR-d/2 at the end of testing (see **Figure 7.9b**) which indicates that the SS bars allowed for better utilization of UHPC's high compression capacity.

A similar observation can be seen in the Group 1 beams with UHPC and 3% fibers. As shown in **Figure 7.15b**, beam U3-No.5S1 shows similar stiffness, with a modest increase of 9% in peak strength (P_{max}), when compared to the beam U3-15M. Failure in the beam with ordinary steel bars occurs due to bar fracture at Δ = 55 mm, while beam U3-No.5S1 shows a remarkable ability to sustain loads until the end of testing (Δ = 124 mm). As a result, the use of stainless steel significantly enhanced ductility (Δ_{max}/Δ_y) and overall toughness ($A_{\Delta_{max}}$) by 75% and 133%. Both beams in the U3 group experience crack localization at a similar displacement of 20 mm, which results in a drop in load capacity due to the loss of fiber bridging capacity (see **Figure 7.15b**). The strain localization eventually leads to fracture of the ordinary steel bars, while this effect is countered by the high strain capacity of the stainless steel reinforcement. As a result, failure transitions from bar rupture to concrete crushing in the beam with SS bars (see **Figure 7.5c**).

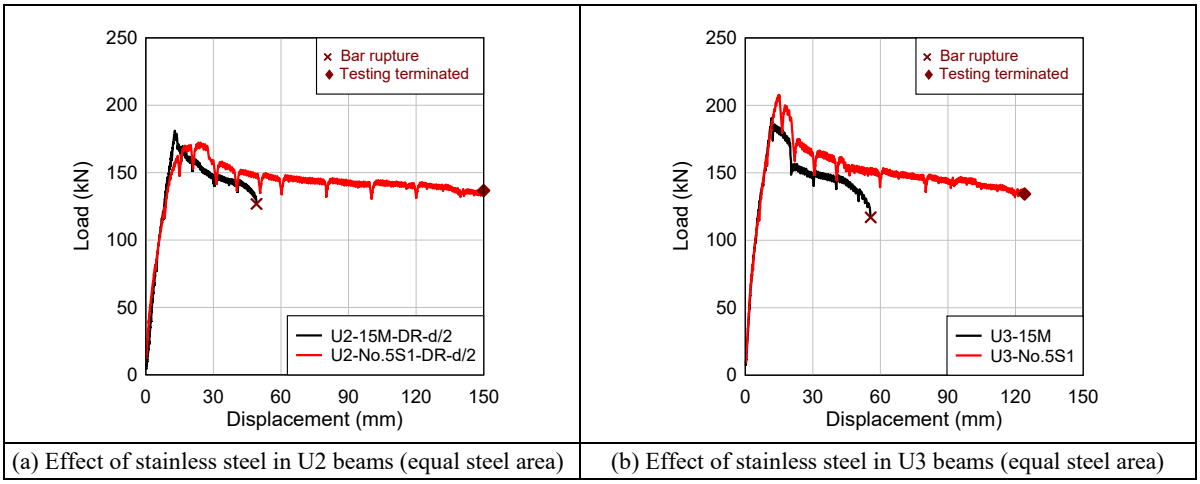

(a) Effect of stainless steel in U2 beams (equal steel area) (b) Effect of stainless steel in U3 beams (equal steel area)

Figure 7.15 Test results: effect of stainless steel

Finally, the effect of high-performance steel type can be studied in **Figure 7.16a** by comparing the responses of beams U2-No.5HS-DR-d/2 and U2-No.5S1-DR-d/2 in Group 2. It is clear that the use of high-strength reinforcement results in a more significant increase in load capacity due to the increased strength of the ASTM A1035 bars, however the SS bars result in important increases of 85%, 353% and 455% in overall toughness ($A_{\Delta_{max}}$ = 21.5 vs. 11.6 kJ), ductility (Δ_{max}/Δ_y = 10.8 vs. 2.4) and toughness index ($I_{\Delta_{max}}$ = 19 vs. 3.4) due to the remarkable strain capacity of the SS reinforcement. Importantly, the SS reinforcement prevents bar rupture (up to Δ_{max} = 150 mm, which is the limitation of the test setup) whereas this effect is not negated in the beam with HSS reinforcement. The same trends are observed when comparing the results of beams U3-No.5HS and U3-No.5S1 in Group 1 (see **Figure 7.16b**). In general, the results point to the excellent compatibility of UHPC and ductile stainless steel.

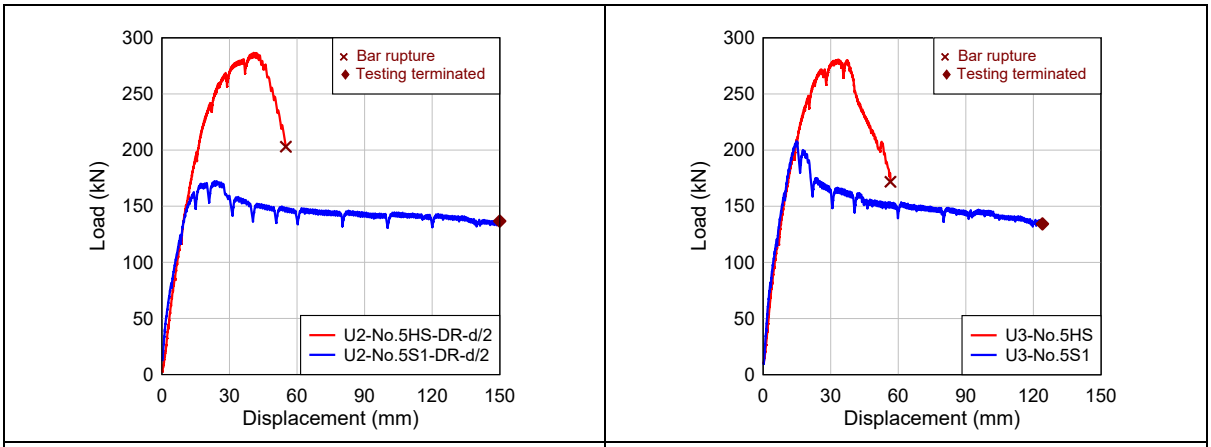

(a) U2 beams (b) U3 beams

Figure 7.16 Test results: effect of stainless steel (HSS vs. SS)

7.4.8. Effect of detailing & fiber content

Before examining the effect of detailing in the UHPC beams, it is interesting to note that significant enhancements in performance owing to the use of improved detailing (Type A blast detailing vs. Type C nominal detailing) in the HSC beams with ordinary, high-strength and stainless steel bars (see **Figure 7.17a**). It is clear that blast detailing improves all aspects of structural response, especially ductility (Δ_{max}/Δ_y), regardless of steel type. The enhancement in performance results from the ability of the top (compression) bars and confinement reinforcement to delay damage in the beam midspan compression zone.

In comparison, the use of improved detailing has limited effects in the UHPC beams. **Figure 7.17(b-d)** compare the responses of the companion UHPC beams built with Type D (no stirrups) and Type B (top continuity bars and ties at d/2) detailing in Groups 1 and 2.

Comparing the beams with ordinary steel (U3-15M vs. U2-15M-DR-d/2**)**, the use of higher fiber content (3%) in the U3 beam results in a modest increase of 5% in maximum capacity (P_{max}), with moderate increases (13-18%) in maximum displacement (Δ_{max}), ductility (Δ_{max}/Δ_y), and toughness ($A_{\Delta_{max}}$) (**Figure 7.17b**). However, the responses of the beam are otherwise quite similar, indicating the limited effects of detailing on beam load-deformation capacity. It is interesting to note that while the U3 beam initially shows higher capacity (due to the effects of higher fiber content on UHPC tensile capacity), the responses show a near-perfect match after a displacement of 20 mm. At this stage the crack width exceeds 5 mm, and the fibers no longer bridges the cracks (Hoang & Fehling, 2017), which can explain the similarity in load-deflection response. Bar fracture occurs in both beams, with a slight delay for the U3 beam.

Similar trends are observed in the high-strength steel set (U3-No.5HS vs. U2-No.5HS-DR-d/2**)**. As shown in **Figure 7.17c**, while the U3 beam shows an increase in initial stiffness, both beams show remarkably similar load-deflection responses, with similar maximum displacement (Δ_{max}), ductility (Δ_{max}/Δ_y) and overall toughness ($A_{\Delta_{max}}$) with differences within ±5%. Failure in both beams was governed by bar fracture, with a slight delay for the U3 beam. As shown in **Figure 7.3b,** crack localization in both beams occurs prior to peak load. As shown in **Figure 7.5b** & **Figure 7.8b**, the major crack width for both beams reaches 4 mm before the peak load. As a result, the fibers have a minor effect on capacity and the strengths at peak load are more governed by the high-strength steel regardless of fiber content. This might explain the similar load capacity in beams U2-No.5HS-DR-d/2 and U3-No.5HS.

Finally, the effects of detailing are examined in the SS set (U3-No.5S1 vs. U2-No.5S1-DR-d/2 vs.). As shown in **Figure 7.17d**, the U3 beam results in a noticeable increase of 21% in maximum capacity (P_{max}), however both beams show remarkably similar responses beyond $\Delta = 20$ mm. Bar rupture was prevented in both specimens until the end of testing (the maximum displacements are slightly different because the U3-No.5S1 test was terminated at Δ = 124 mm). The higher load capacity in the U3 beam can be explained by the high fiber content (3% vs. 2%), which results in higher UHPC tensile capacity. At Δ = 20 mm, the localized crack reaches 5 mm in beam U3-No.5S1 (see **Figure 7.5c**), and results in a loss in fiber bridging capacity (Hoang & Fehling, 2017). As a result, the load capacities were mainly contributed by the stainless steel beyond this stage, and the U2 and U3 beams shows similar load responses until the end of testing.

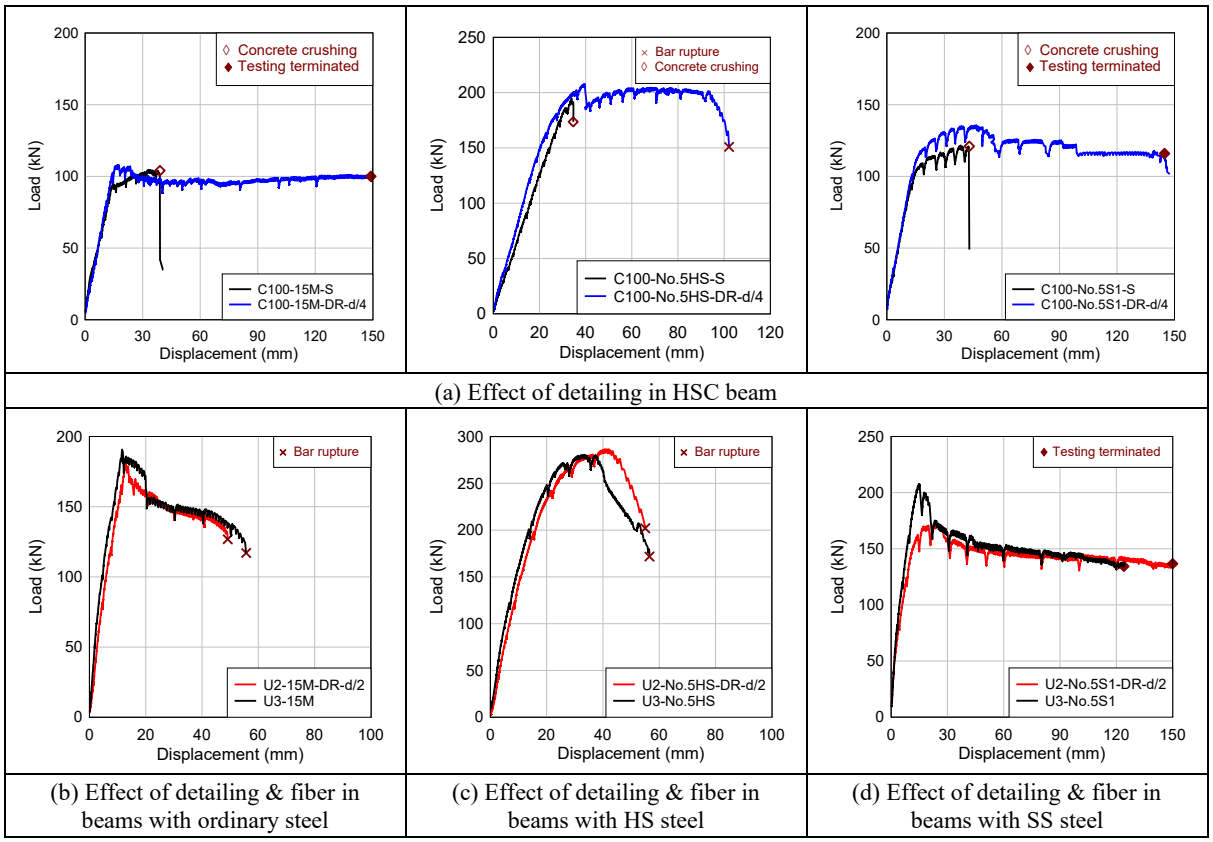

(a) Effect of detailing in HSC beam

(b) Effect of detailing & fiber in beams with ordinary steel

(c) Effect of detailing & fiber in beams with HS steel

(d) Effect of detailing & fiber in beams with SS steel

Figure 7.17 Test results: effect of detailing & fiber content

7.4.9. Effect of fiber content

As noted in the previous section the responses of both beams were quite similar under static loads however failure was delayed in the beam with 3% fibers. A few studies have examined the effect of fiber content on the ductility of UHPC beams under static loading (Kahanji et al., 2017; Qi et al., 2017; Yang et al., 2020; Shao & Billington, 2021; Feng et al., 2021). These studies show that at higher reinforcement ratios ($\rho > 1.5\%$), increasing the fiber content results in a reduction in ductility of UHPC beams, which is counter to the observation in the current tests. For example, Kahanji et al. (2017) found that at a steel ratio of 1.8%, increasing fiber content from 1% to 2% results in similar maximum displacement and slightly reduced ductility, while increasing fiber content from 2% to 4% significantly reduced maximum and ductility. Yang et al. (2020) also found at a steel ratio of 1.58%, increasing fiber content from 1% to 1.5% and 1.5% to 2% results in a reduction in maximum displacement and ductility. Shao and Billington (2021) also observed this trend at a steel ratio of 2.1% when increasing fiber content from 1% to 2%.

However, the opposite trend is observed at lower reinforcement ratios ($\rho \leq 1.5\%$). Qi et al. (2017) found that at a steel ratio of 0.7%, beams had increased ductility when increased fiber content from 1% to 2%. Similarly, Feng et al. (2021) reported at a steel ratio of 1.0% the higher fiber content (3% vs. 2%) resulted in larger maximum displacement. Yang et al. (2020) also found that at steel ratios of 0.79% and 1.18%, increasing the fiber content from 1% to 1.5% increased maximum displacement and ductility, while increasing fiber content from 1.5% to 2% reduced maximum displacement and ductility. In the current tests, increasing fiber content in UHPC beams with ordinary and high-strength steel at a steel ratio of 1.5% resulted in a slight increase in maximum displacement (Δ_{max}), which is similar to the observations in this second group of studies.

7.5 Analytical investigation

In the final section of this chapter, the moment capacities of the UHPC beams with varying steel ratios and steel types are predicted using the sectional analysis procedure in ACI 544 (ACI, 2002). The procedure in ACI 544 was originally developed for conventional fiber-reinforced concrete (FRC). In this paper the modified equations presented in Hasgul et al. (2018) for fiber-reinforced UHPC are used.

According to the ACI 544 model, the moment capacity (M_{fl}) of an FRC beam can be calculated using the following expressions based on the stress distribution shown in **Figure 7.18**:

$$M_{fl} = A_s f_y (d - \frac{a'}{2}) + \sigma_t b(h - e)(\frac{h}{2} + \frac{e}{2} - \frac{a'}{2}) \quad 7\text{-}2$$

$$e = \left(\varepsilon_{s,fiber} + 0.003\right)\left(\frac{c}{0.003}\right) \quad 7\text{-}3$$

$$f_t = 0.772 F_{be}(v_f \frac{l_f}{d_f}) \quad 7\text{-}4$$

Where, A_s = steel cross-sectional area; f_y = steel yield strength; d, h, b = beam effective depth, height and width; c, a' = neutral axis depth and depth of the equivalent compression block; e = distance between the extreme compression fiber and the upper limit of the tensile stress block; σ_t = tensile strength of the fiber reinforced concrete; $\varepsilon_{s,fiber}$ = strain in the fibers; and l_f, d_f, v_f = fiber length, diameter and volume fraction; and F_{be} = fiber efficiency factor. In the original ACI model the tensile strength is derived based on a bond strength of 2.3 MPa. Al-Ta'an and Al-Feel (1990) recommend a higher bond strength of 4.15 MPa for high-strength FRC. Bond is more significant in UHPC, therefore, the tensile strength should be modified (Hasgul et al., 2018; Al-Ta'an & Al-Feel, 1990). Khalil and Tayfur (2013) and Hasgul et al. (2018) noted that **Equation 7-5** can be used to better represent the improved fiber bond capacity and increased tensile resistance of UHPC.

$$f_t = 2\eta_o \eta_b \eta_l v_f \tau_f l_f / d_f \quad 7\text{-}5$$

In the above equation, η_o, η_b, η_l are fiber orientation, shape and length factors taken as 0.41, 1.2 and 0.8, respectively; the UHPC bond strength is taken as $\tau_f = 0.66\sqrt{f_c'}$ (Khalil & Tayfur, 2013). results in $f_t = 8$ MPa, which provides a good estimate of the UHPC's post-cracking tensile capacity up to pullout (Aaleti et al., 2013).

Table 7.5 presents the predicted moment capacities (M_{fl}) and peak load capacities ($P_{fl} = 2 \cdot M_{fl}/a$, where a = shear span length) for the different beams in this study. The actual yield strengths of the steel reinforcement (as presented in **Table 3.9**) are used in the calculations. In general, the analytical results show that the UHPC-modified ACI procedure results in good agreement with the experiments. The experimental-to-predicted load capacity ratios (P_{exp}/P_{fl}) fall in a range of 0.84-1.14 with an average ratio of 1.03 and coefficient of variation (COV) of 10.5%. In comparison, the original ACI equation results in significant under-predictions of moment capacity, with an average P_{exp}/P_{fl} ratio of 1.48. However, **Equation 7-5** does not account for the fiber content, resulting in an underestimate of load capacities of around 10% in the U3 beams from Group 1. Nevertheless, the analysis results indicate that the simplified approach based on the ACI 544, with appropriate modifications for the UHPC tensile capacity, can be used to predict the flexural capacities of UHPC beams reinforced with varying steel types.

It is important to note that the majority of the UHPC beams in this study ultimately failed by rupture of the reinforcement. When rupture occurs, fibers may no longer bridge the cracks, and therefore it may be appropriate to reduce the tensile stress contribution from the UHPC and account for the hardening in the steel reinforcement when predicting the flexural capacity (Shao & Billington, 2019). Shao and Billington (2019) proposed the following parameter (ω) to predict the failure path of beams with high-performance FRC materials:

$$\omega = \frac{(f_{su} - f_y) \cdot A_s}{\alpha b h f_t} \qquad 7\text{-}6$$

Where, f_{su}, f_y A_s = steel cross-sectional area; ∝ = empirical factor that represents the portion of the cross-section that has fiber bridging capacity at peak load (0.5-0.8); *b, h*= beam width and height; f_t = tensile strength the FRC material can sustain after cracking. According to (Shao & Billington, 2021), if ω > 1, hardening of steel compensates for the fiber-bridging loss and the specimen is likely to fail through gradual steel strain hardening (Shao & Billington, 2021). Using ∝ = 0.8, f_t = 8 MPa and the steel properties in **Table 3.9**, the calculated ω ratios range from 0.13 to 0.56 for the beams in the current study, which indicates that strain hardening of the reinforcement likely did not contribute to the peak load after crack localization; further research is recommended.

Table 7.5 Analysis results

Group	Beam	P_{exp} (kN)	ACI - original			ACI – modified UHPC		
			M_{fl} (kN·m)	P_{fl} (kN)	$\frac{P_{exp}}{P_{fl}}$	M_{fl} (kN·m)	P_{fl} (kN)	$\frac{P_{exp}}{P_{fl}}$
Group 1	U3-15M	190.7	40.9	110.4	1.73	62.2	167.9	1.14
	U3-No.5HS	280.5	74.4	200.7	1.40	93.4	252.2	1.11
	U3-No.5S1	207.8	48.7	131.6	1.58	69.5	187.6	1.11
Group 2	U2-15M-DR-d/2	181.2	42.9	115.7	1.57	65.6	177.2	1.02
	U2-20M-DR-d/2	207.0	53.0	143.2	1.45	75.1	202.7	1.02
	U2-No.4HS-DR-d/2	178.4	48.2	130.2	1.37	70.6	190.6	0.94
	U2-No.5HS-DR-d/2	286.6	72.8	196.5	1.46	93.4	252.2	1.14
	U2-No.4S1-DR-d/2	126.2	32.3	87.1	1.45	55.8	150.5	0.84
	U2-No.5S1-DR-d/2	172.4	44.9	121.1	1.42	67.5	182.1	0.95
	Average				1.48			1.03
	COV				8.1%			10.5%

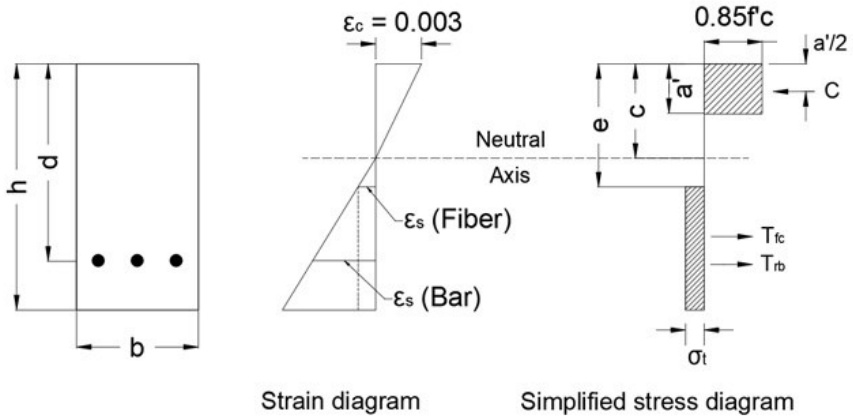

Figure 7.18 ACI-544 flexural capacity model

7.6 Conclusions

This chapter presented the static results from **Series 3** of the PhD program, and examined the influence of steel reinforcement ratio and type, as well as fiber content and detailing on the ductility and failure mode of UHPC flexural members. The following conclusions can be drawn from this study:

1. The results show that failure in the UHPC beams with moderate amounts (ρ = 1.5-2.4%) of normal-strength or high-strength steel was governed by bar fracture. This mode of failure may be linked to the high bond capacity of UHPC and its high damage tolerance in compression. In general, it is recommended that a minimum steel ratio (i.e. similar to the $A_{s,limit}$ equation in reference (Shao & Billington, 2019) be used when designing UHPC beams with mild or high-strength steel reinforcement since premature bar fracture failures may not be acceptable to practitioners;

2. The use of UHPC with 3% fibers prevented shear failure and significantly enhanced all aspects of flexural response when compared to companion HSC beams with nominal detailing. In Group 2, the UHPC beams showed increased strength and stiffness, but reduced ductility when compared to companion HSC beams with blast detailing;

3. Despite the observed failures, increasing the tension steel ratio effectively increased the failure displacement and ductility of the UHPC beams, regardless of steel type;

4. When comparing companion beams with equal amounts of high-strength and normal-strength bars (ρ = 1.5%), the HS reinforcement significantly increased load carrying capacity, with a less prominent effect on failure displacement. Beams with similar ρf_y ratios showed similar peak strengths, but the beam with high-strength bars showed reduced ductility. In general, it can be concluded that the reduced strain capacity of the high-strength reinforcement can negate the possible increase in ductility in UHPC beams;

5. Substitution of normal-strength bars with stainless steel (SS) bars in the UHPC beams did not increase beam capacity but resulted in remarkable enhancements in performance, with increases in failure displacement, ductility, overall toughness, toughness index and drift capacity. The SS bars were able to better utilize the high compressive capacity of the UHPC, with failure occurring due to crushing of concrete rather than fracture of the tension steel reinforcement. Further research examining the effect of steel ratio in SS-reinforced UHPC beams is recommended;

6. UHPC beams with nominal and intermediate detailing showed similar load-deflection responses and failure modes. Increasing fiber content (from 3% to 2%) resulted in moderate increase in peak load (in the NS and SS sets) and a sight delay in failure displacement (in the NS and HS sets). After crack localization and loss of fiber bridging capacity, the U3 and U2 beams showed a near-perfect match in load-displacement response indicating that the response was governed by the steel reinforcement in this later stage of loading.
7. The analytical study showed that the simplified equivalent stress block procedure in ACI 544, with appropriate modifications for the increased UHPC tensile resistance (with f_t as given in **Equation 7-5**, and $\tau_f = 0.66\sqrt{f_c'}$) was able to provide reasonable predictions of the moment capacities of the UHPC beams with varying steel types tested in this study.

7.7 References (Chapter 7)

Aaleti, S., Petersen, B., & Sritharan, S. (2013). Design Guide for Precast UHPC Waffle Deck Panel System, including Connections. *No. FHWA-HIF-13-032*: U.S. Federal Highway Administration, pp. 125

ACI Committee 544 (2002). Report on Fiber Reinforced Concrete. 544.1R-96, American Concrete Institute, Farmington Hills, pp. 66.

AFGC (2013). Ultra high performance fibre-reinforced concretes. AFGC & SETRA Working Group Paris, France, pp. 175.

Aghdasi, P., & Ostertag, C. P. (2020). Tensile fracture characteristics of Green Ultra-High Performance Fiber-Reinforced Concrete (G-UHP-FRC) with longitudinal steel reinforcement. *Cement and Concrete Composites, 114*, 103749. doi:https://doi.org/10.1016/j.cemconcomp.2020.103749

Al-Ta'an, S., & Al-Feel, J. (1990). Evaluation of shear strength of fibre-reinforced concrete beams. *Cement and Concrete Composites, 12*(2), 87-94. doi:https://doi.org/10.1016/0958-9465(90)90045-Y

ASTM A955/A955M − 20c (2020a). Standard Specification for Deformed and Plain Stainless Steel Bars for Concrete Reinforcement. ASTM International, West Conshohocken, PA, pp. 16.

A1035/A1035M − 20 (2020b). Standard Specification for Deformed and Plain, Low-Carbon, Chromium, Steel Bars for Concrete Reinforcement. ASTM International, West Conshohocken, PA, pp. 7.

Bandelt, M. J., & Billington, S. L. (2016). Impact of Reinforcement Ratio and Loading Type on the Deformation Capacity of High-Performance Fiber-Reinforced Cementitious Composites Reinforced with Mild Steel. *Journal of Structural Engineering, 142*(10), 04016084. doi:https://doi.org/10.1061/(asce)st.1943-541x.0001562

Charles, C. J. (2019). *Effect of detailing and fibers on the static and blast behaviour of high-strength concrete beams.* (MASc. thesis). University of Ottawa, Ottawa, ON, Canada.

Canadian Standards Association (CSA) (2014). Design of concrete structures. CAN/CSA A23.3-14, Mississauga, ON, pp. 295.

Dancygier, A. N., & Karinski, Y. S. (2019). Effect of cracking localization on the structural ductility of normal strength and high strength reinforced concrete beams with steel fibers. *International Journal of Protective Structures, 10*(4), 457–469. doi:https://doi.org/10.1177/2041419618824609

Feng, Z., Li, C., Yoo, D.-Y., Pan, R., He, J., & Ke, L. (2021). Flexural and cracking behaviors of reinforced UHPC beams with various reinforcement ratios and fiber contents. *Engineering Structures, 248*, 113266. doi:https://doi.org/10.1016/j.engstruct.2021.113266

Guertin-Normoyle, C. (2017). *Blast Performance of Ultra-High Performance Concrete Beams Tested Under Shock-Tube Induced Loads.* (MASc. thesis). University of Ottawa, Ottawa, ON, Canada.

Hasgul, U., Turker, K., Birol, T., & Yavas, A. (2018). Flexural behavior of ultra‐high‐performance fiber reinforced concrete beams with low and high reinforcement ratios. *Structural Concrete, 19*(6), 1577-1590. doi:https://doi.org/10.1002/suco.201700089

Hoang, A. L., & Fehling, E. (2017). Influence of steel fiber content and aspect ratio on the uniaxial tensile and compressive behavior of ultra high performance concrete. *Construction and Building Materials, 153*, 790-806. doi:https://doi.org/10.1016/j.conbuildmat.2017.07.130

Kahanji, C., Ali, F., & Nadjai, A. (2017). Structural performance of ultra-high-performance fiber-reinforced concrete beams. *Structural Concrete, 18*(2), 249-258. doi:https://doi.org/10.1002/suco.201600006

Khaksefidi, S., Ghalehnovi, M., & de Brito, J. (2021). Bond behaviour of high-strength steel rebars in normal (NSC) and ultra-high performance concrete (UHPC). *Journal of Building Engineering, 33*, 101592. doi:https://doi.org/10.1016/j.jobe.2020.101592

Khalil, W. I., & Tayfur, Y. (2013). Flexural strength of fibrous ultra high performance reinforced concrete beams. *ARPN Journal of Engineering and Applied Sciences, 8*(3), 200-214.

Pam, H., Kwan, A., & Islam, M. (2001). Flexural strength and ductility of reinforced normal-and high-strength concrete beams. *Proceedings of the Institution of Civil Engineers: Structures and Buildings, 146*(4), 381-389. doi:https://doi.org/10.1680/stbu.146.4.381.45454

Park, R. (1989). Evaluation of ductility of structures and structural assemblages from laboratory testing. *Bulletin of the New Zealand national society for earthquake engineering, 22*(3), 155-166.

Pokhrel, M., & Bandelt, M. J. (2019). Material properties and structural characteristics influencing deformation capacity and plasticity in reinforced ductile cement-based composite structural components. *Composite Structures, 224*, 111013. doi:https://doi.org/10.1016/j.compstruct.2019.111013

Qi, J., Wang, J., & Ma, Z. J. (2017). Flexural response of high-strength steel-ultra-high-performance fiber reinforced concrete beams based on a mesoscale constitutive model: Experiment and theory. *Structural Concrete, 19*(3), 719-734. doi:https://doi.org/10.1002/suco.201700043

Shao, Y., & Billington, S. L. (2019). Predicting the two predominant flexural failure paths of longitudinally reinforced high-performance fiber-reinforced cementitious composite structural members. *Engineering Structures, 199*, 109581. doi:https://doi.org/10.1016/j.engstruct.2019.109581

Shao, Y., & Billington, S. L. (2021). Impact of cyclic loading on longitudinally-reinforced UHPC flexural members with different fiber volumes and reinforcing ratios. *Engineering Structures, 241*, 112454. doi:https://doi.org/10.1016/j.engstruct.2021.112454

Voo, Y. L., Poon, W. K., & Foster, S. J. (2010). Shear Strength of Steel Fiber-Reinforced Ultrahigh-Performance Concrete Beams without Stirrups. *Journal of Structural Engineering, 136*(11), 1393-1400. doi:https://doi.org/10.1061/(asce)st.1943-541x.0000234

Yang, I. H., Park, J., Bui, T. Q., Kim, K. C., Joh, C., & Lee, H. (2020). An Experimental Study on the Ductility and Flexural Toughness of Ultrahigh-Performance Concrete Beams Subjected to Bending. *Materials, 13*(10), 2225. doi:https://doi.org/10.3390/ma13102225

Yoo, D.-Y., Banthia, N., & Yoon, Y.-S. (2016). Experimental and numerical study on flexural behavior of ultra-high-performance fiber-reinforced concrete beams with low reinforcement ratios. *Canadian Journal of Civil Engineering, 44*(1), 18-28. doi:https://doi.org/10.1139/cjce-2015-0384

Chapter 8 Blast results from Series 3 (UHPC)

Paper 5: Blast Behaviour of Ultra-High Performance Concrete Beams Reinforced with Ordinary, High-strength and Stainless Steel bars

8.1 Introduction

This chapter presents the results of Series 3 of the research program and investigated the influence of reinforcement grade on the flexural behaviour of UHPC beams under blast loading. As part of the study, a series of UHPC beams built with either Grade 400 MPa ordinary steel, Grade 690 MPa high-strength steel or Grade 520 MPa stainless steel bars are tested under blast loads using a shock-tube. The first group of beams is built with UHPC having 3% fibers, without transverse reinforcement, while the second group of beams is built with UHPC having 2% (or 1%) fibers and intermediate (or blast) detailing. The results are compared to a control set of HSC beams having nominal and blast detailing. Test variables included the effects of concrete type, steel type, longitudinal steel ratio, detailing.

8.2 Research contribution

The content of this chapter is included in the following paper (to be submitted):

Blast Behaviour of Ultra-High Performance Concrete Beams Reinforced with Ordinary, High-strength and Stainless Steel bars.

8.3 Experimental program

The details of the experimental program were provided in **Chapter 3** (see Series 3 - Group 1 and 2). All beams had dimensions of 125 mm × 250 mm × 2440 mm (b × h × L), and were constructed with either 2% or 3% steel fibers. The beams were built with three types of longitudinal steel bars: Grade 400 MPa normal-strength steel conforming to CSA G30.18, Grade 690 MPa high-strength steel conforming to ASTM A1035 (ASTM, 2020b), and Grade 520 MPa XM-28 stainless steel conforming to ASTM A955 (ASTM, 2020a).

Group 1 included beams cast with UHPC with 3% fibers (designated as U3). The beams in this group were singly-reinforced, and were built without stirrups (Type D detailing). Longitudinal steel consisted of either 2-15M ordinary bars, or 2-No.5 high-strength or stainless steel bars (ρ = 1.5%). To examine the effect of concrete type, the results are compared to a control set of high-strength concrete beams with identical properties, and built either without

or with stirrups made from 6.3 mm steel wire, spaced at 100 mm (d/2) in the shear spans only (Type D or C detailing, respectively).

Group 2 included UHPC beams cast with 2% fibers (U2), and one beam cast with 1% fibers (U1). The U2 beams in this group were doubly-reinforced, and transverse reinforcement consisted of closed ties made from 6.3 mm steel wire which were spaced at 100 mm (s = d/2) along the entire beam span (Type B, "intermediate" detailing). The U1 beam had the same details, but had ties spaced at 50 mm (s = d/4) (Type A, "blast" detailing). Longitudinal steel consisted of either 2-15M or 2-20M bars (ρ = 1.5% or 2.4%) in tension, and 2-10M bars (ρ' = 0.8%) in compression for the beams with normal-strength ordinary steel. The beams with HSS or SS were reinforced with either 2-No.4 or 2-No.5 bars (ρ = 1.0% or 1.5%) in tension, and 2-No.3 or 2-No.4 bars (ρ' = 0.6% - 1.0%) in compression. To examine the effect of concrete type, the results are compared to a control set of high-strength concrete beams with identical properties, but with closed ties spaced at 50 mm (d/4) (Type A, "blast" detailing).

As noted above, each group included specimens reinforced with three different steel types to examine steel type/grade, while the longitudinal steel ratio was varied in Group 2. The effects of concrete type (UHPC vs. HSC), and detailing (Group 1 vs. 2), were also investigated. **Table 8.1 & Table 8.2** and **Figure 8.1** indicate the design parameters, including the concrete type (C100 vs. U1, U2 or U3), tension bar size (15/20M, 20M, No.4/5), steel type (HS: high-strength steel, S1: stainless steel, and no indicator for ordinary steel), and detailing level (DR-d/4: Type A, DR-d/2: Type B, S: Type C, and no indicator for Type D). For example, in Group 1, U3-No.5S1 is constructed with U3 concrete (UHPC with 3% fibers), 2-No.5 stainless bars and without stirrups (Type D detailing), while C100-No.5S1 and C100-No.5S1-S are the companion HSC control beams built with and without stirrups (Type C and D), respectively. In Group 2, U2-No.5S1-DR-d/2 is the beam built with U2 concrete (UHPC with 2% fibers), No.5 stainless bars in tension and intermediate detailing with closed ties spaced at 100 mm (d/2) (Type B detailing), while C100-No.5S1-DR-d/4, is the control HSC beam built with closed ties spaced at 50 mm (d/4) throughout the beam span (Type A detailing).

Blast tests were conducted using the University of Ottawa shock-tube (see **Section 3.4)**. **Figure 8.2** shows sample shockwaves corresponding to *Blast-30psi* to *Blast-100psi* used in this series, obtained by varying the driver pressure from 30 to 100 psi (207–690 kPa), with the driver length fixed at 9 ft (2743 mm). Key parameters for each blast are presented in **Table 8.3**.

Table 8.1 Beam design details (Group 1)

Series	Beam ID	Concrete [a]			Longitudinal reinforcement			Transverse reinf.		Detailing
		Type	f'_c MPa	v_f %	Type	Grade MPa	Tension (ρ in %)	Type	Spacing mm	
U3	U3-15M	UHPC	149	3	Ordinary	400	2-15M (1.5%)	-	-	Type D
	U3-No.5HS	UHPC	140	3	High-strength (ASTM A1035)	690	2-No.5 (1.5%)			
	U3-No.5S1	UHPC	148	3	Stainless (XM-28)	520	2-No.5 (1.5%)			
HSC	C100-15M-S [c]	HSC	107	-	Ordinary	400	2-15M (1.5%)	U-shaped [b]	100	Type C
	C100-15M	HSC	101	-				-	-	Type D
	C100-No.5HS-S [d]	HSC	95	-	High-strength (ASTM A1035)	690	2-No.5 (1.5%)	U-shaped [b]	100	Type C
	C100-No.5HS	HSC	96	-				-	-	Type D
	C100-No.5S1-S	HSC	97	-	Stainless (XM-28)	520	2-No.5 (1.5%)	U-shaped [b]	100	Type C
	C100-No.5S1	HSC	101	-				-	-	Type D

[a] f'_c = average concrete compressive strength; v_f = volumetric fiber content (3% = 234 kg/m^3)

[b] Placed in the shear span only

[c, d] Control beams tested by Li et al. (2018), Li & Aoude (2019)

Table 8.2 Beam design details (Group 2)

Series	Beam ID	Concrete [a]			Longitudinal reinforcement				Transverse reinf.		Detailing
		Type	f'_c MPa	v_f %	Type	Grade MPa	Tension (ρ in %)	Comp. (ρ' in %)	Type	Spacing mm	
U2	U2-15M-DR-d/2	UHPC	140	2	Ordinary	400	2-15M (1.5%)	2-10M (0.8%)	Closed ties (full span)	100	Type B
	U2-20M-DR-d/2	UHPC	140	2			2-20M (2.4%)	2-10M (0.8%)			
	U2-No.4HS-DR-d/2	UHPC	142	2	High-strength (ASTM A1035)	690	2-No.4 (1.0%)	2-No.3 (0.7%)			
	U2-No.5HS-DR-d/2	UHPC	137	2			2-No.5 (1.5%)	2-No.4 (1.0%)			
	U2-No.4S1-DR-d/2	UHPC	151	2	Stainless (XM-28)	520	2-No.4 (1.0%)	2-No.3 (0.7%)			
	U2-No.5S1-DR-d/2	UHPC	153	2			2-No.5 (1.5%)	2-No.4 (1.0%)			
U1	U1-No.5HS-DR-d/4	UHPC	128	1	High-strength (ASTM A1035)	690	2-No.5 (1.5%)	2-No.4 (1.0%)	Closed ties (full span)	50	Type A
HSC	C100-15M-DR-d/4 [b]	HSC	105	-	Ordinary	400	2-15M (1.5%)	2-10M (0.8%)	Closed ties (full span)	50	Type A
	C100-No.5HS-DR-d/4	HSC	94	-	High-strength (ASTM A1035)	690	2-No.5 (1.5%)	2-No.4 (1.0%)			
	C100-No.5S1-DR-d/4	HSC	103	-	Stainless (XM-28)	520	2-No.5 (1.5%)	2-No.4 (1.0%)			

[a] f'_c = average concrete compressive strength; v_f = volumetric fiber content (2% = 156 kg/m^3; 1% =78 kg/m^3)

[b] Control beam built with plain HSC tested by Charles (2019)

Table 8.3 Average blast properties for beams

Blast Load	Driver Pressure kPa (psi)	Driver Length mm (ft)	Average Reflected Pressure, P_r (kPa)	Average Reflected Impulse, I_r (kPa·ms)	Average Positive Phase Duration, t_d (ms)
Blast-30psi	207 (30)	2743 (9)	44.4	360.2	20.4
Blast-50psi	345 (50)		61.3	545.2	20.7
Blast-70psi	483 (70)		81.3	728.0	21.3
Blast-90psi	621 (90)		92.4	882.4	21.9
Blast-100psi	690 (100)		104.0	978.5	23.1

(a) UHPC beam with 3% fiber without stirrup (**Type D** detailing): 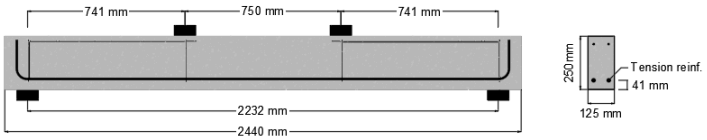	Specimens: U3-15M U3-No.5HS U3-No.5S1 Control specimens: C100-15M C100-No.5HS C100-No.5S1	Test sequence: Blast-100 psi Blast-100 psi Blast-100 psi Test sequence: Blast-30psi Blast-30psi Blast-30psi
(b) HSC beams with stirrups @ d/2 (**Type C** detailing): 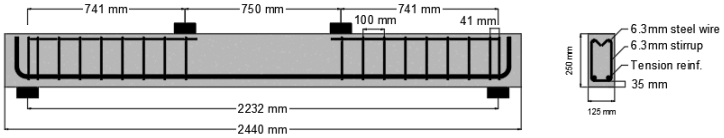	Control specimens: C100-15M-S C100-No.5HS-S C100-No.5S1-S	Test sequence: Blast-30, 50 psi Blast-30, 50, 70 psi Blast-30, 50, 70 psi
(c) UHPC beam with 2% fiber and intermediate detailing (**Type B** detailing): 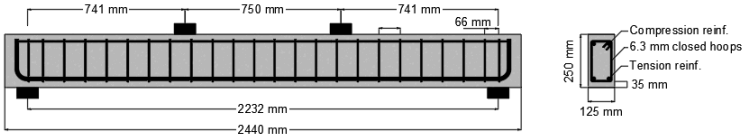	Specimens: U2-15M-DR-d/2 U2-20M-DR-d/2 U2-20M-DR-d/2 (R) U2-No.4HS-DR-d/2 (R) U2-No.5HS-DR-d/2 U2-No.4S1-DR-d/2 (R) U2-No.5S1-DR-d/2	Test sequence: Blast-100 psi Blast-100 psi Blast-30, 70, 100 psi Blast-30, 50, 70, 100 psi Blast-100 psi Blast-30, 50, 70, 100 psi Blast-100 psi
(d) HSC beams with Blast detailing (**Type A** detailing): 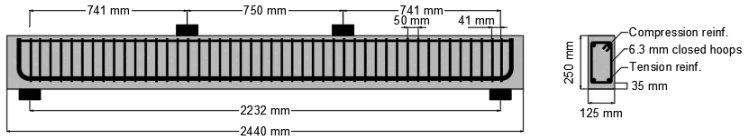	Specimens: U1-No.5HS-DR-d/4 Control specimens: C100-15M-DR-d/4 C100-No.5HS-DR-d/4 C100-No.5S1-DR-d/4	Test sequence: Blast-100 psi Test sequence: Blast-70 psi Blast-90 psi Blast-90 psi

Figure 8.1 Specimen Designs

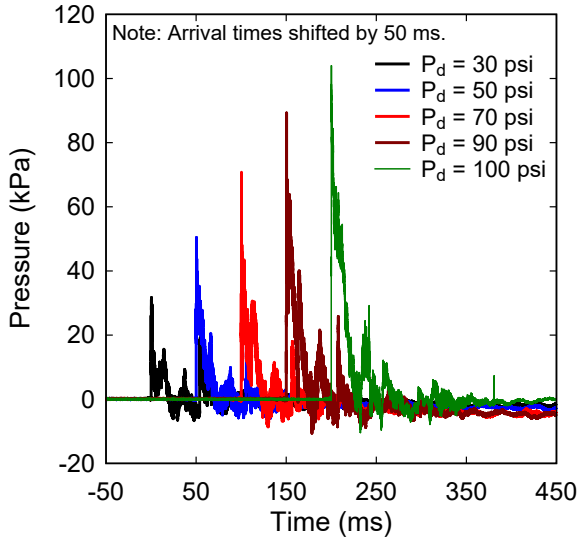

Figure 8.2 Sample shockwaves and testing protocols

8.4 Blast test results and post-blast residual test results

The results from the blast tests for the Group1 and Group 2 beams are summarized in **Table 8.4** and **Table 8.5**, which report the shockwave data (P_r, I_r, and t_d = peak reflected pressure, impulse, and positive phase duration) as well as the specimen response after each test (D_{max}, D_{res} and θ_{max} = maximum displacement, residual displacement and support rotation) for all tested beams. Photos showing the damage in the beams are presented in **Figure 8.3** to **Figure 8.6**, while displacement comparisons are shown in the following sub-sections.

Table 8.4 and **Table 8.5** also compare the results with the response limits in the CSA S850 blast standard (CSA, 2012). These response limits (B1-B4) correspond to specific values of support rotation (θ_{max}) or ductility ratio (μ_{max}). In the case of singly-reinforced and doubly-reinforced beams, B1, B2, B3 and B4 correspond to $\mu_{max} = 1$, $\theta_{max} = 1°$ and 4°, $\theta_{max} = 4°$ and 6°, and $\theta_{max} = 10°$, respectively. These limits in turn define component damage levels: "Blowout" (greater than B4), "Hazardous failure" (between B4 and B3); "Heavy" (between B3 and B2); "Moderate" (between B2 and B1) and "Superficial" (less than B1). The following sections review the effects of concrete type, steel ratio, steel type, detailing and repeated tests on the blast response of the beams.

Table 8.4 Blast test results (Group 1)

Beams	Blast (psi)	Shockwave Properties			Beam response				CSA S850 Response limits and Component damage	
		P_r (kPa)	I_r (kPa·ms)	t_d (ms)	D_{max} (mm)	D_{res} (mm)	θ_{max} (°)	Observed damage [Crack width]	Response Limit	Damage level
U3-15M	100	107.7	1001.4	23.8	-	-	-	Bar rupture	> B4	Blowout
U3-No.5HS	100	93.8	968.1	22.2	34.9	7.0	1.8	Moderate F cracking [0.8 mm]	B1-B2	Moderate
U3-No.5S1	100	90.3	923.5	24.0	54.2	31.5	2.8	Crack localization & fiber pullout [12 mm]	B2-B3	Heavy
C100-15M	30	35.9	323.6	19.4	16.1	5.5	0.8	Shear failure	-	-
C100-15M-S	30	42.9	340.7	15.9	21.40	4.71	1.1	Minor cracking	B1-B2	Moderate
	50	58.6	516.0	17.6	79.64	22.04	6.4	Severe crushing	B3-B4	Hazardous
C100-No.5HS	30	44.7	333.4	20.7	16.9	7.1	0.8	Shear failure	-	-
C100-No.5HS-S (R)	30	43.8	377.6	20.6	17.7	3.1	0.8	Minor F cracking	<B1	Superficial
	50	59.1	547.5	20.5	26.8	1.2	1.2	Moderate F cracking	B1-B2	Moderate
	70	77.6	749.7	24.4	64.7	20.0	3.0	Cover spalling & Severe crushing	B2-B3	Heavy
C100-No.5S1	30	39.1	365.6	20.7	18.9	2.4	1.0	Shear failure	-	-
C100-No.5S1-S (R)	30	46.7	371.6	21.5	16.6	2.0	0.9	Minor cracking [0.25 mm]	<B1	Superficial
	50	57.6	539.0	23.1	30.5	5.6	1.6	Moderate cracking [3.0 mm]	B1-B2	Moderate
	70	76.1	707.3	24.4	134	87	6.9	Severe concrete crushing & spalling	B3-B4	Hazardous

Table 8.5 Blast test results (Group 2)

Beams	Blast (psi)	Shockwave Properties			Beam response				CSA S850 Response limits and Component damage	
		P_r (kPa)	I_r (kPa·ms)	t_d (ms)	D_{max} (mm)	D_{res} (mm)	θ_{max} (°)	Observed damage [Crack width]	Response Limit	Damage level
U2-15M-DR-d/2	100	104.0	978.5	23.1	64.1	52.5	3.3	Fiber pullout [13 mm]	B1-B2	Moderate
U2-20M-DR-d/2	100	94.3	994.5	22.4	48.3	26.8	2.5	Fiber pullout [15 mm]	B1-B2	Moderate
U2-20M-DR-d/2 (R)	30	42.4	346.1	20.2	8.4	0.6	0.4	Minor F cracking [HL]	<B1	Superficial
	70	83.4	708.9	21.8	21.5	1.2	1.0	Minor F cracking [HL]	<B1	Superficial
	100	104	996.1	24.4	46.3	26.8	2.4	Crack localization & fiber pullout [11 mm]	B1-B2	Moderate
U2-No.4HS-DR-d/2 (R)	30	50.2	393.3	20.6	11.3	3.0	0.6	Minor F cracking [HL]	<B1	Superficial
	50	62.3	557.9	22.0	19.8	2.5	1.0	Minor F cracking [HL]	<B1	Superficial
	70	87.4	728.4	22.5	31.2	9.0	1.6	Crack Localization [0.8]	B1-B2	Moderate
	100	98.6	970.2	24.3	42.8 [b]	-	-	Bar rupture	> B4	Blowout
U1-No.5HS-DR-d/4	100	96	941.0	22.1	38.1	10.9	2.0	Moderate F cracking [0.8]	B1-B2	Moderate
U2-No.5HS-DR-d/2	100	106	981.0	22.5	35.9	11.1	1.8	Moderate F cracking [1.5]	B1-B2	Moderate
U2-No.4S1-DR-d/2 (R)	30	43.3	363.1	20.5	12.3	2.8	0.6	Minor F cracking [HL]	<B1	Superficial
	50	58.3	557.6	21.3	28.6	11.6	1.5	Moderate F cracking [2.5]	B1-B2	Moderate
	70	75.2	733.4	22.7	53.9	32.5	2.8	Crack localization & fiber pullout [13]	B1-B2	Moderate
	100	88.7	955.4	24.1	96.5 [b]	-	-	Bar rupture	> B4	Blowout
U2-No.5S1-DR-d/2	100	96.3	966.5	24.2	57.5	36.5	3.0	Crack localization & fiber pullout [10]	B1-B2	Moderate
C100-15M-DR-d/4 [a]	70	69.8	711.9	21.0	61.6	42.4	2.9	Moderate Damage, Cracks opening	B1-B2	Moderate
C100-No.5HS-DR-d/4	90	82.7	824.4	21.7	51.7	21.0	2.7	Cover crushing & Moderate F cracking [1.5]	B1-B2	Moderate
C100-No.5S1-DR-d/4	90	84.6	851.6	24.6	65.6	33.8	3.4	Moderate F cracking [1.5]	B1-B2	Moderate

[a] Companion beam tested by Charles (2019)
[b] Displacement at bar rupture (captured using a high-speed camera)

NSS	HSS	SS
(a) U3-15M @ 100 psi	(b) U3-No.5HS @ 100 psi	(c) U3-No.5S1 @ 100 psi
	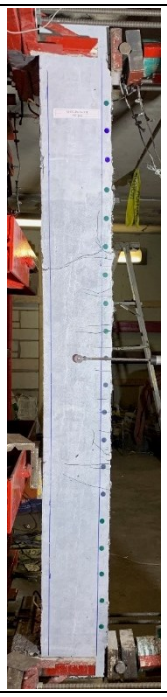	

Figure 8.3 Blast damage photos (Group 1)

UHPC-NSS				
(a) U2-15M-DR-d/2 @ 100 psi	(b) U2-20M-DR-d/2 @ 100 psi	(c-d-e) U2-20M-DR-d/2 (R)		
		@ 30 psi	@ 70 psi	@ 100 psi
			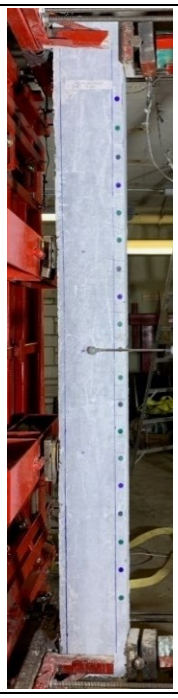	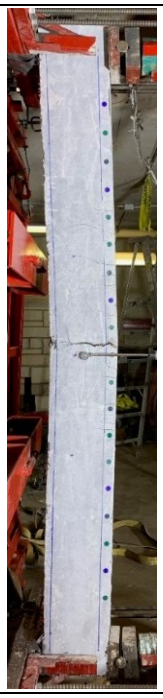

Figure 8.4 Blast damage photos from Group 2 (UHPC-NSS)

UHPC-HSS				
(a-b-c) U2-No.4HS-DR-d/2 (R)			(d) U1-No.5HS-DR-d/4 @ 100 psi	(e) U2-No.5HS-DR-d/2 @ 100 psi
@ 50 psi	@ 70 psi	@ 100 psi		
				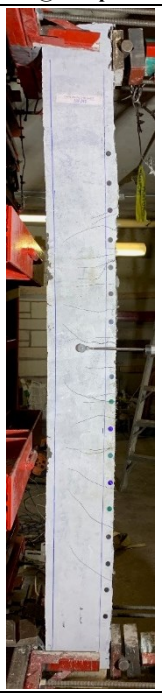

Figure 8.5 Blast damage photos from Group 2 (UHPC-HSS)

UHPC-SS			
(a-b-c) U2-No.4S1-DR-d/2 (R)			(d) U2-No.5S1-DR-d/2 @ 100 psi
@ 50 psi	@ 70 psi	@ 100 psi	
			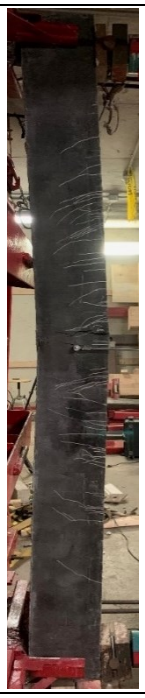

Figure 8.6 Blast damage photos from Group 2 (UHPC-SS)

This test program included companion beams with identical properties tested under static and blast conditions. The blast-tested beams were subsequently tested under static four-point bending to assess their post-blast residual capacity. The results of these tests, along with the results from the original undamaged beams in Group 1 and 2 are shown in **Figure 8.7** and **Figure 8.8,** while **Figure 8.9** and **Figure 8.10** shows photos of the beams after residual testing. The maximum residual capacity (P_{max}^{R}), residual secant stiffness (k_s^R), residual displacement (Δ_{test}^{R}), and maximum post-blast residual displacement (Δ_{max}^{R}) are reported in **Table 8.6**. It is noted that P_{max}^{R} refers to the maximum load reached by the blast-damaged beams during the residual static test. Several indices are also calculated, including: the "Residual Resistance Index" defined as the ratio of the peak load of blast-damaged to undamaged specimens ($RRI = \frac{P_{max}^{R}}{P_{max}}$) and "Residual stiffness index" (RSI) defined as the ratio of stiffness of blast-damaged to undamaged specimens ($RSI = \frac{k_s^R}{k_s}$) (Adhikary et al. (2014)), and "Residual displacement index" ($RDI = \frac{\Delta_{max}^{R}}{\Delta_{max}}$), which assesses displacement capacity of the damaged beams.

Table 8.6 Results from the post-blast residual static tests

Series	Beam	Dynamic loading type	Load		Stiffness		Displacement		
			P_{max}^{R} (kN)	RRI	k_s^R (N/mm)	RSI	Δ_{test}^{R} (mm)	Δ_{max}^{R} (mm)	RDI
Group 1	U3-15M	Single	No residual strength due to bar rupture.						
	U3-No.5HS	Single	291.2	1.04	14549	0.86	43.3	50.3	0.89
	U3-No.5S1	Single	164.2	0.79	11260	0.80	130	161.5	1.30
NSS (Group 2)	U2-15M-DR-d/2	Single	125.9	0.69	13597	0.96	9.3	61.8	1.26
	U2-20M-DR-d/2	Single	205.9	0.99	14190	1.00	86.7	113.5	1.39
	U2-20M-DR-d/2 (R)	Repeated	187.2	0.90	13785	0.97	61.9	90.5	1.17
HSS (Group 2)	U2-No.4HS-DR-d/2	Repeated	No residual strength due to bar rupture.						
	U2-No.5HS-DR-d/2	Single	293.5	1.02	12424	0.98	52.8	63.9	1.16
	U1-No.5HS-DR-d/4 [a]	Single	276.7	-	10613	-	60.3	71.2	-
SS (Group 2)	U2-No.4S1-DR-d/2	Repeated	No residual strength due to bar rupture.						
	U2-No.5S1-DR-d/2	Single	160.7	0.93	11714	0.93	150	186.5	1.24
Control HSC (Group 2)	C100-15M-DR-d/4	Single	102.9	0.95	7987	1.06	106	148.4	1.0
	C100-No.5HS-DR-d/4	Single	209.3	1.01	7918	0.99	90.8	111.8	1.16
	C100-No.5S1-DR-d/4	Single	140.7	1.04	6999	0.90	137	170.8	1.14

[a] No companion beam was tested under static loading.

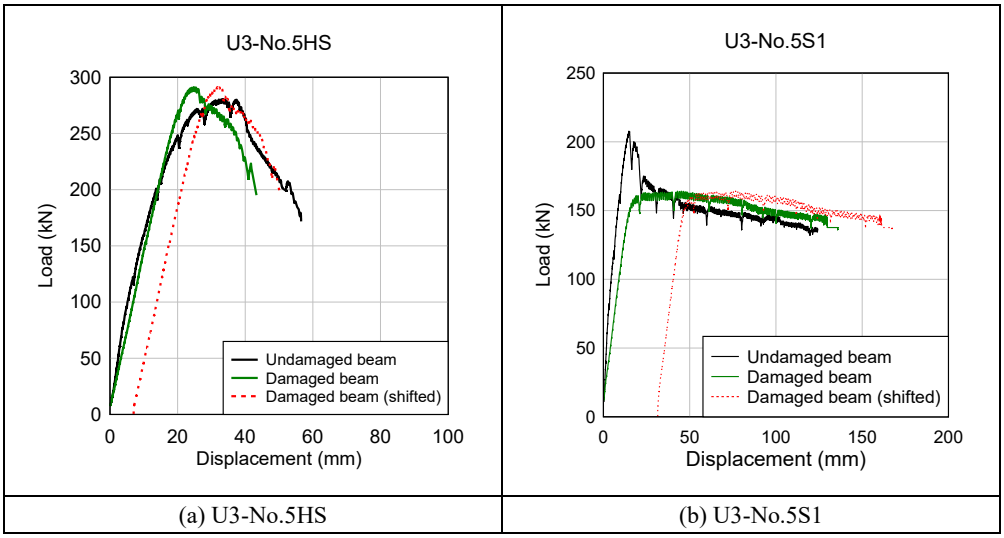

(a) U3-No.5HS (b) U3-No.5S1

Figure 8.7 Post-blast residual static test results (Group 1)

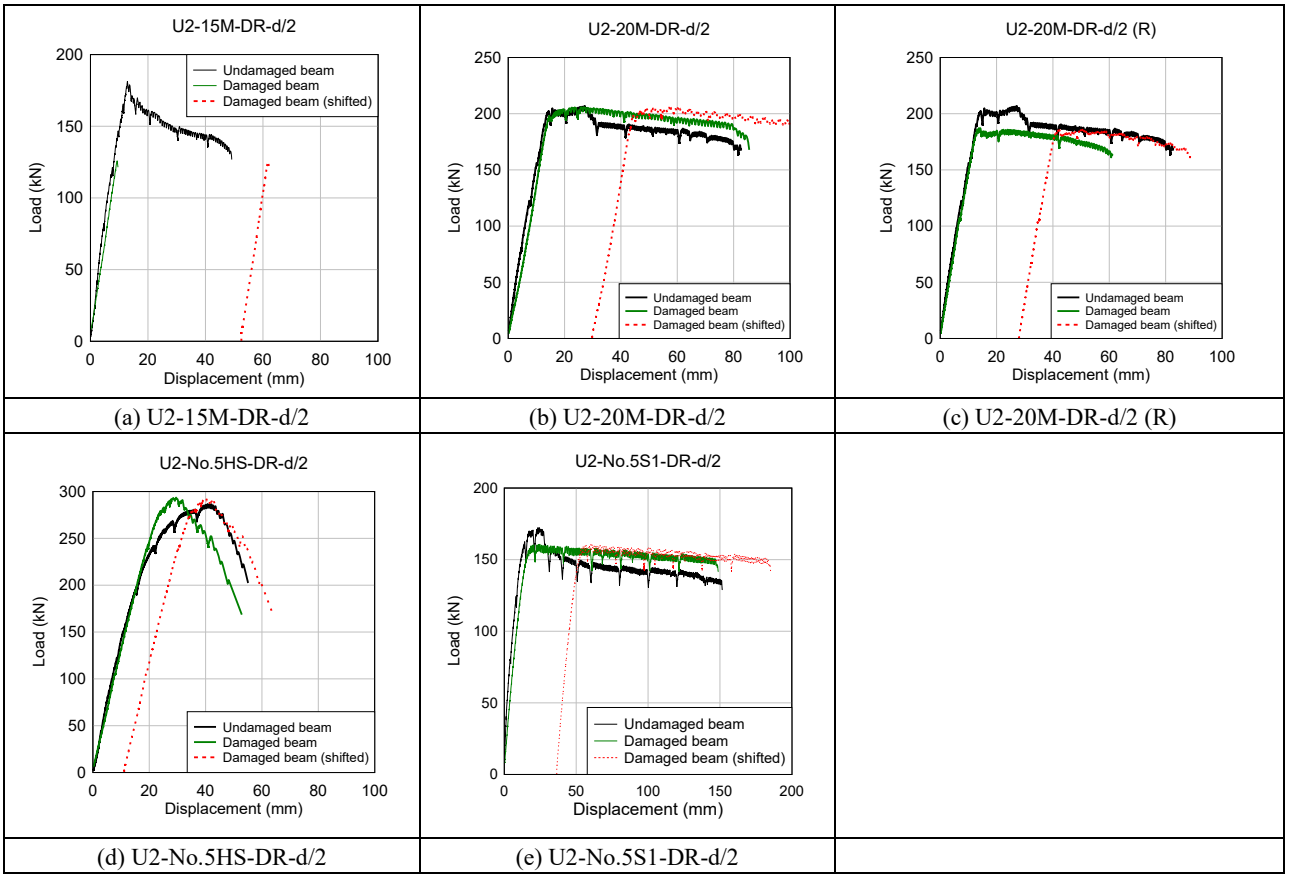

(a) U2-15M-DR-d/2 (b) U2-20M-DR-d/2 (c) U2-20M-DR-d/2 (R)

(d) U2-No.5HS-DR-d/2 (e) U2-No.5S1-DR-d/2

Figure 8.8 Post-blast residual static test results (Group 2)

HSS	(a) U3-No.5HS ($\Delta_{test}^{R} = 43.3\ mm$)	
SS	(b) U3-No.5S1 ($\Delta_{test}^{R} = 130\ mm$)	

Figure 8.9 Failure mode in post-blast residual test (Group 1)

NSS	(a) U2-15M-DR-d/2 ($\Delta_{test}^{R} = 9.3\ mm$)	
	(b) U2-20M-DR-d/2 ($\Delta_{test}^{R} = 86.7\ mm$)	
	(c) U2-20M-DR-d/2 (R) ($\Delta_{test}^{R} = 61.9\ mm$)	
HSS	(d) U1-No.5HS-DR-d/4 ($\Delta_{test}^{R} = 60.3\ mm$)	
	(e) U2-No.5HS-DR-d/2 ($\Delta_{test}^{R} = 52.8\ mm$)	
SS	(f) U2-No.5S1-DR-d/2 ($\Delta_{test}^{R} = 150\ mm$)	

Figure 8.10 Failure mode in post-blast residual test (Group 2)

8.4.1. Effect of UHPC in Group 1 beams (U3 vs. HSC)

This section compares the behaviour of the Group 1 UHPC beams with that of companion beams built with conventional HSC. The Group 1 UHPC beams were singly-reinforced, varying steel types and Type D detailing (no stirrups). The companion beams were built with plain high-strength concrete (f_c' = 100 MPa), and included specimens with and without stirrups in the shear spans (Type C and D detailing, respectively).

As shown in **Figure 8.11**, all HSC beams built without stirrups (C100-15M, C100-No.5HS and C100-No.5S1) failed in shear at *Blast-30psi*, regardless of the steel type. In comparison, all UHPC beams prevented shear failure and showed flexural damage or failure modes at *Blast-100psi*. Beam U3-15M which was built with ordinary steel failed by bar fracture, while beams U3-No.5HS and U3-No.5S1 showed flexural damage and survived the blast test (see **Figure 8.11**). The results correspond to the observations in the static tests, where all UHPC beams shows important increases in shear resistance and failed in flexure.

To better understand the observed failure modes, the shear capacities of the UHPC and companion HSC beams are predicted using the equations in the AFGC guidelines (AFGC, 2013) and the CSA A23.3 standard (CSA, 2014). Using the AFGC equations the shear capacities (P_v) of the UHPC beams with 3% fibers are predicted to be 440 kN. At *Blast-100 psi*, the peak reflected pressures (P_r) were 108, 94 and 90 kPa for beams U3-15M, U3-No.5HS and U3-No.5S1, respectively. Multiplying this pressure by the area of the load transfer device ($A = 3.4\ m^2$) results in a maximum applied shear force ($V_f = 0.5 \cdot P_r A$) of 184 kN, 159 kN and 153 kN. Since the shear capacity-to-applied load ratios are 2.39, 2.77, and 2.88, the results confirm that the UHPC beams had sufficient reserve capacity to avoid shear failure. In comparison, the shear capacities of the plain HSC beams are predicted to be 47 kN using the equations in the CSA A23.3 standard (CSA, 2014). At *Blast-30psi*, the maximum applied shear forces ($V_f = 0.5 \cdot P_r A$) are estimated to be 61 kN, 76 kN and 66.5 kN for beams C100-15M, C100-No.5HS and C100-No.5S1, which can explain the shear failures.

As noted above, the UHPC beams failed in flexure under both static and blast loading. To further study this effect, the static flexural capacities ($P_{fl} = 2 \cdot M_{fl}/a$, where a = shear span) of the UHPC beams are further predicted using the sectional analysis method presented in **Chapter 7.5**. Kishi and Mikami (2012) previously reported that a static flexure-to-shear ratio of 1.5 is required to avoid shear failure and ensure ductile flexure failure in reinforced concrete beams tested under impact. In the current tests the shear-to-flexure capacity ratios

($\alpha = \frac{P_v}{P_{fl}}$) for beams U3-15M, U3-No.5S1 and U3-No.5HS are found to be α =2.62, 2.35 and 1.74, respectively. While these results relate to the beam static capacities, the α ratios confirm that the use of 3% fibers safely allowed the beams to avoid shear failure. The results also show that $\alpha \geq 1.75$ was sufficient to ensure the same flexural mode under both static and blast loads. which is similar to the observation in Kishi and Mikami (2012).

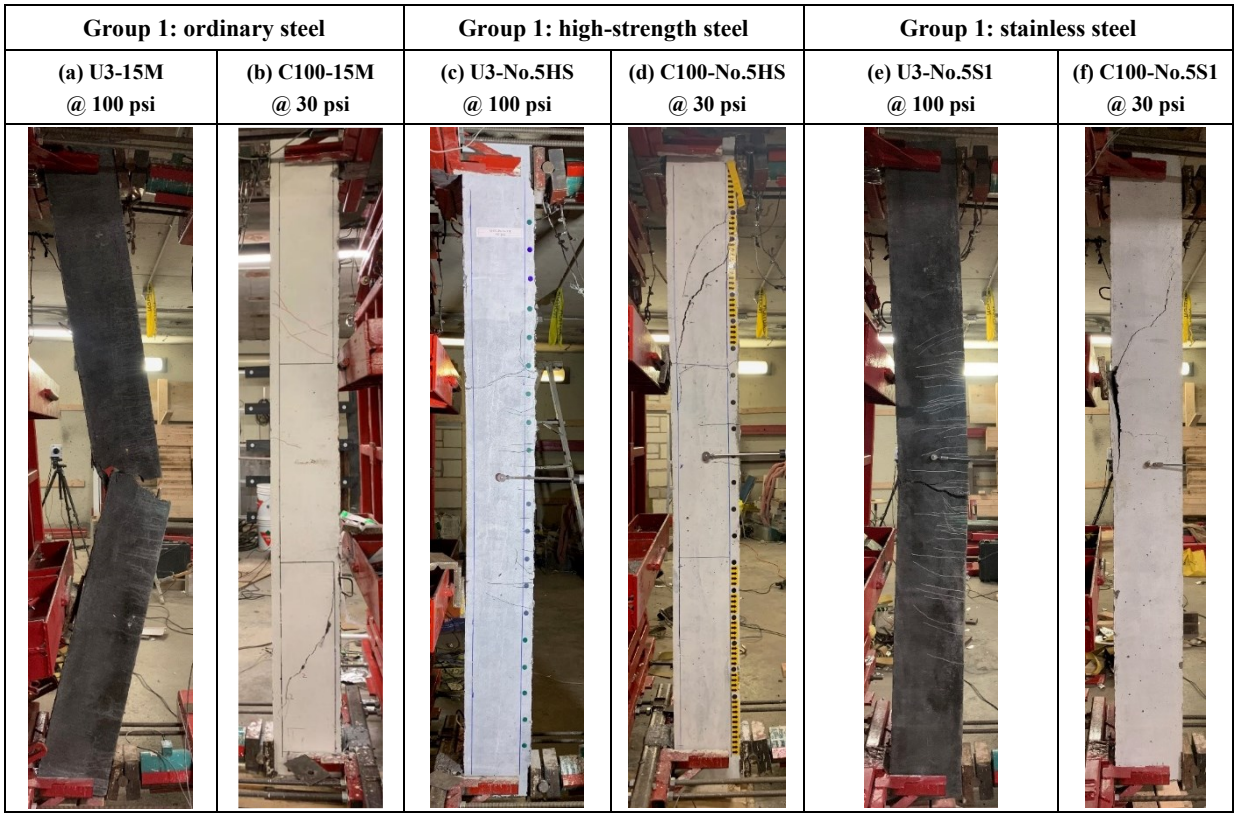

Figure 8.11 : Effect of concrete type on failure mode in Group 1 (U3 vs. HSC beams without stirrups)

The effect of concrete type is further examined by comparing the results of the UHPC beams and the companion HSC beams built with stirrups (Type C detailing). In the ordinary steel set, beams U3-15M-S and C100-15M-S were tested under different blast intensities, but showed distinct failure modes. Failure of the HSC beam was associated with crushing of concrete in the midspan compression zone at *Blast-50psi* (I_r = 545 kPa·ms) (see **Figure 8.13b**). In comparison, Beam U3-15M showed no signs of crushing but suffered a bar rupture failure at the more intense *Blast-100psi* (I_r = 978 kPa·ms) shot (see **Figure 8.13a**), which coincides with the result from static test.

In the high-strength steel set, beam C100-No.5HS-S failed due to concrete crushing and spalling after *Blast-70psi* (I_r = 728 kPa·ms) (see **Figure 8.13d**). In comparison, beam U3-

No.5HS survived *Blast-100psi* (I_r = 978 kPa·ms), with little to no damage, except for the formation of one localized crack near the top loading point (see **Figure 8.13c**). As shown in **Figure 8.14a**, the beam would further show significant post-blast residual capacity (with a near perfect RRI index), but eventually failed by bar fracture during the post-blast test, which once again coincides with the observation in the static test.

Finally, in the SS set, beam C100-No.5S1-S also failed due to concrete crushing and spalling after *Blast-70psi* (I_r = 728 kPa·ms) (see **Figure 8.13f**). In comparison, the U3 beam with SS bars (U3-No.5S1) survives *Blast-100psi* (I_r = 978 kPa·ms), with minor damage consisting of a localized crack at midspan in **Figure 8.13e**. During the subsequent post-blast test the UHPC beam with SS bars shows significant post-blast residual capacity (RRI index = 0.8), with no bar fracture until very large displacements (see **Figure 8.14b**). Once again, the result corresponds to the observation in the static test.

In summary, the results confirm the ability of UHPC to increase shear resistance under blast loading. The ability of UHPC to increase strength and stiffness further allow the UHPC beams to show high blast capacity. On the other hand, UHPC beams with ordinary and high-strength bars are vulnerable to bar fracture failures, while the combined use of UHPC and stainless bars allows for improved ductility.

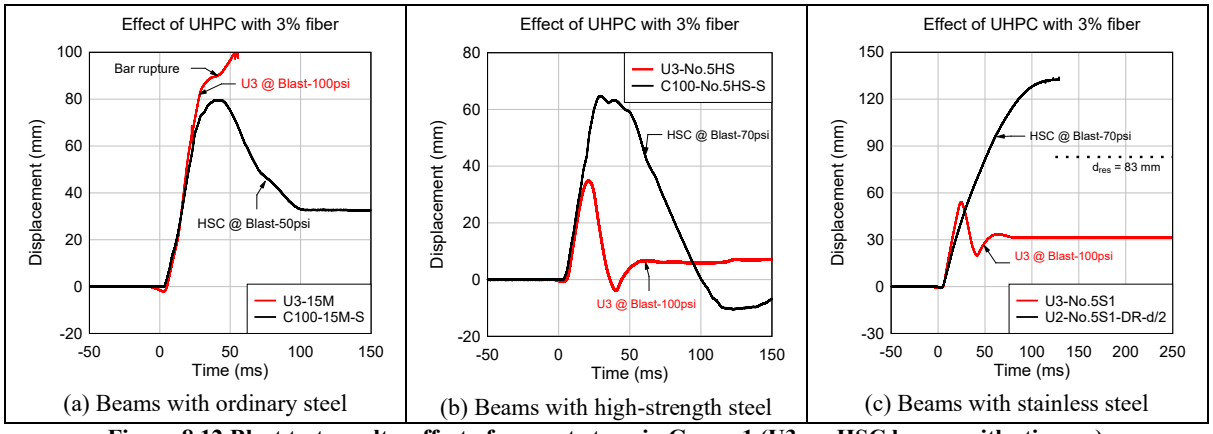

(a) Beams with ordinary steel (b) Beams with high-strength steel (c) Beams with stainless steel

Figure 8.12 Blast test results: effect of concrete type in Group 1 (U3 vs. HSC beams with stirrups)

Group 1: Ordinary steel		Group 1: high-strength steel		Group 1: stainless steel	
(a) U3-15M @ 100 psi	(b) C100-15M-S @ 50 psi	(c) U3-No.5HS @ 100 psi	(d) C100-No.5HS-S @ 70 psi	(e) U3-No.5S1 @ 100 psi	(f) C100-No.5S1-S @ 70 psi
		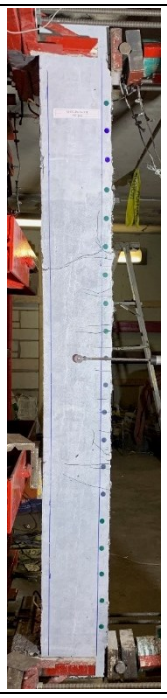			

Figure 8.13 Effect of concrete type on failure mode in Group 1 (U3 vs. HSC beams with stirrups)

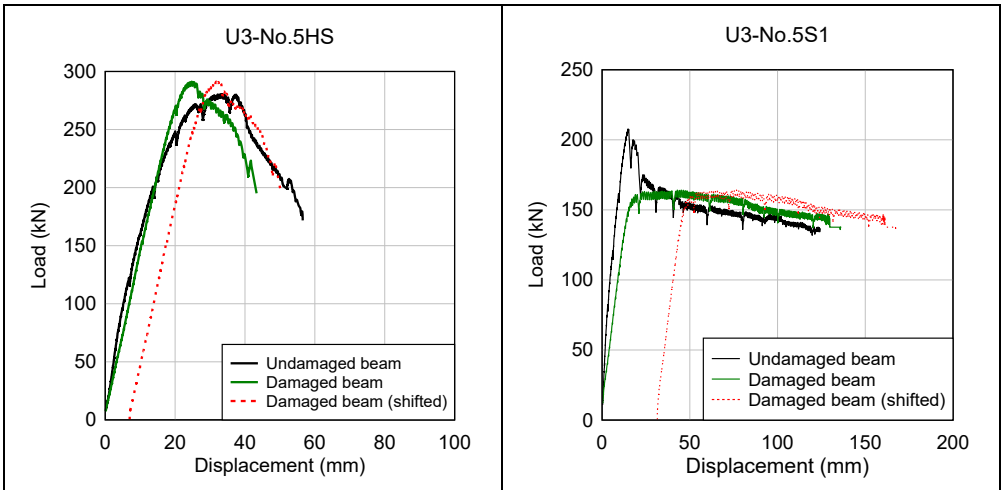

(a) U3-No.5HS (b) U3-No.5S1

Figure 8.14 Post-blast residual static test results (Group 1)

8.4.2. Effect of UHPC in Group 2 beams (U2 vs. HSC)

The effect of UHPC is also examined in Group 2, by comparing the U2 beams with varying steel types and Type B detailing, with companion HSC beams with Type A detailing. The companion beams had the properties and dimensions as the UHPC beams, but were built with plain high-strength concrete (f_c' = 100 MPa), with a reduced tie spacing of 50 mm (s = d/4). The effects are examined in beams with ordinary, high-strength and stainless steel, tested under single or repeated blasts.

8.4.2.1. Beams with ordinary steel

The effect of concrete type is first investigated in beams U2-15M-DR-d/2 vs. HSC-15M-DR-d/4 which were built ordinary steel (ρ = 1.5%) and tested under single blasts. **Figure 8.15a** compares the responses of the beams. The U2 and C100 beams were tested under single blasts corresponding to *Blast-100psi* (I_r = 978 kPa·ms) and *Blast-70psi* (I_r = 712 kPa·ms), respectively. Although the UHPC beam was tested under a more intense blast, it shows similar maximum displacement (64.1 mm vs. 61.6 mm) when compared to the companion HSC beam. Both beams survive the blast, but show distinct damage as shown in **Figure 8.16**. Damage in the UHPC beam is associated with two major localized cracks near the loading points. In comparison, damage in the HSC beam is well controlled, with several well-distributed cracks. During the post-blast test, the UHPC beams fails by bar fracture during the reloading stage (with an RRI = 0.7), indicating that the capacity of the ordinary bars was nearly exhausted during the blast test. In comparison, the HSC beam shows significant post-blast capacity (with RRI = 0.95), and ability to sustain large displacements up to Δ_{test}^{R} =106 mm (Δ_{max}^{R} = 148 mm). The results correspond to the static tests, where the UHPC beam showed increased strength and stiffness, but reduced deformation capacity due to bar fracture.

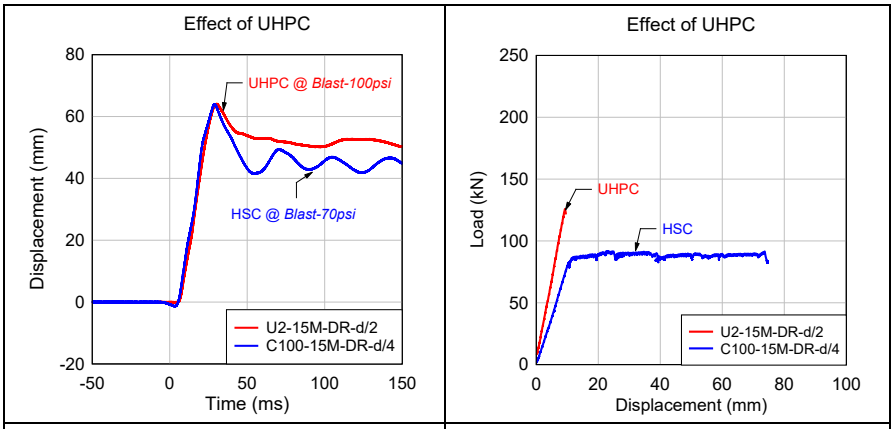

(a) Displacement histories (b) Post-blast residual test

Figure 8.15 Effect of concrete type in Group 2 (ordinary steel)

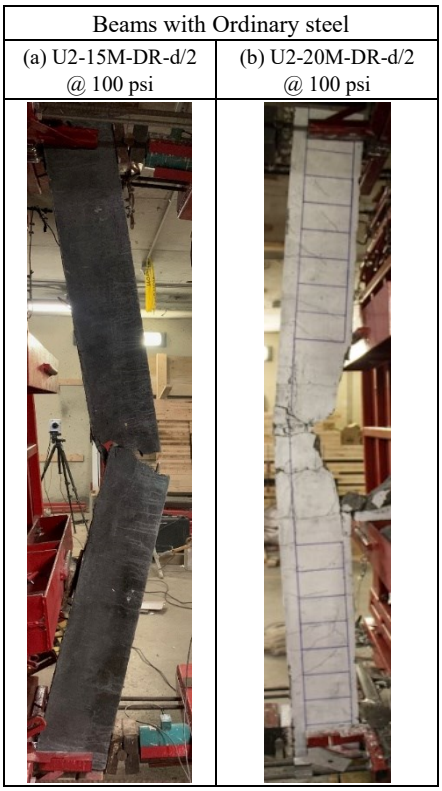

Figure 8.16 Effect of concrete type on failure mode in Group 2 (Ordinary steel)

8.4.2.2. Beams with high-strength steel

The effect of concrete type in the beams with HS steel is studied by comparing beams U2-No.5HS-DR-d/2 vs. HSC-No.5HS-DR-d/4 (ρ = 1.5%) and U2-No.4HS-DR-d/2 vs. C100-No.4HS-DR-d/4 (ρ = 1.0%), under single and repeated blasts, respectively.

The responses of the beams in the No.5HS set are shown in **Figure 8.17a**. Also included is beam U1-No.5HS-DR-d/4 which was built with U1 concrete (1% fibers) and blast detailing. It is noted that the UHPC and C100 beams were tested under single blasts corresponding to *Blast-100psi* (I_r = 979 kPa·ms) and *Blast-90psi* (I_r = 824 kPa·ms), respectively. Comparing the U1 and C100 specimens which had identical Type A detailing, the UHPC beam shows reductions of 26% and 48% in maximum (38.1 mm vs. 51.7 mm) and residual (10.9 mm vs. 21 mm) displacements, despite the larger applied blast. Likewise, the U2 beam with relaxed detailing shows similar reductions of 31% and 47% in maximum (35.9 mm vs. 51.7 mm) and residual (11.1 mm vs. 21 mm) displacements. The results can be explained by the ability of the UHPC to increase strength and stiffness as also observed in the static tests. All beams survive the blast tests, but with distinct damage. As shown in **Figure 8.18c**, damage in the HSC beam was associated with the top cover concrete crushing, while damage in both UHPC beams is

limited to the formation of localized cracks at midspan (see **Figure 8.18(a,b)**). Both UHPC beams show significant post-blast capacity, with an RRI ≥ 1.0, and increases of 40% in P_{max}^{R} and 57% in k_s^R for the U2 beam when compared to beam C100-No.5HS-DR-d/4 (**Figure 8.17b**). The U2 beam also shows important post-blast deformation capacity, with an RDI ≥ 1.0, but eventually fails by bar fracture at Δ_{test}^{R} = 53 mm (Δ_{max}^{R} = 64 mm). Bar fracture also occurs in beam C100-No.5HS-DR-d/4, but occurs at Δ_{test}^{R} = 91 mm (Δ_{max}^{R} = 112 mm), which also corresponds to the observation in the static tests.

The effect of UHPC is further studied in the No.4HS set by comparing beams U2-No.4HS-DR-d/2 (R) and C100-No.4HS-DR-d/4 (R), which were tested under repeated blasts corresponding to *Blast-30, 50, 70 psi*, with an additional *Blast-100 psi* shot applied on the UHPC specimen. As shown in **Figure 8.19a**, the U2 beam shows significant reductions of 45%, 44% and 41% in maximum displacements, with corresponding decreases of 44%, 73% and 64% in residual displacements, during the first three blasts. Examining the damage photos in **Figure 8.18e**, the HSC beam experiences crushing of the top cover concrete at *Blast-70psi*. The UHPC beam shows no signs of cover damage, with one dominant localized crack at mid-span. The formation of the dominant crack eventually leads to bar fracture at *Blast-100psi*. In comparison the companion HSC beam eventually fails by bar fracture during the post-blast residual static test, at Δ_{test}^{R} = 53.9 (Δ_{max}^{R} = 86 mm) (see **Figure 8.19b**).

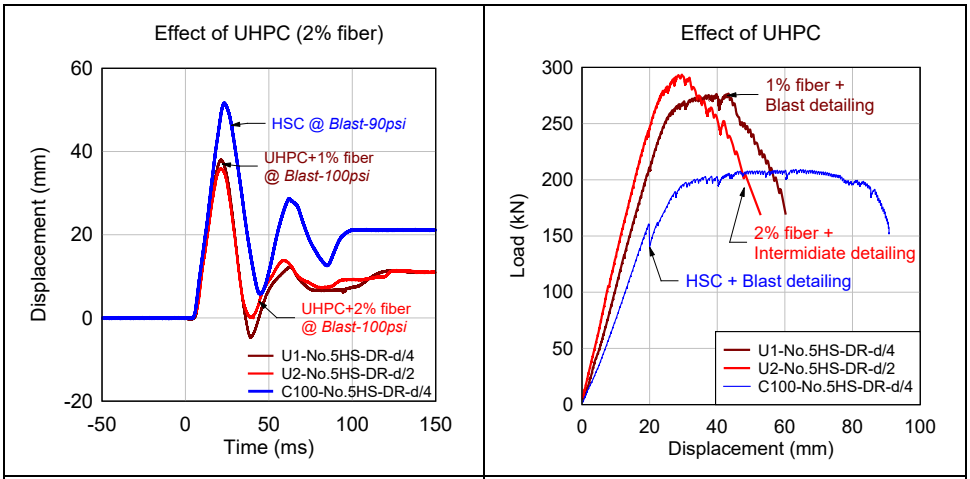

(a) Displacement histories | (b) Post-blast residual test

Figure 8.17 Effect of concrete type in Group 2 (No.5HS set)

Beams with high-strength steel (No.5HS set)			Beams with high-strength steel (No.4HS set)		
(a) U1-No.5HS-DR-d/4 @ 100 psi	(b) U2-No.5HS-DR-d/2 @ 100 psi	(c) C100-No.5HS-DR-d/4 @ 90 psi	(d) U2-No.4HS-DR-d/2 (R) @ 70 psi	(d) U2-No.4HS-DR-d/2 (R) @ 100 psi	(e) C100-No.4HS-DR-d/4 @ 70 psi
	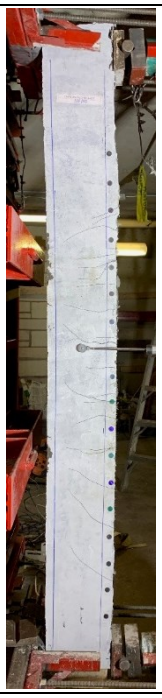				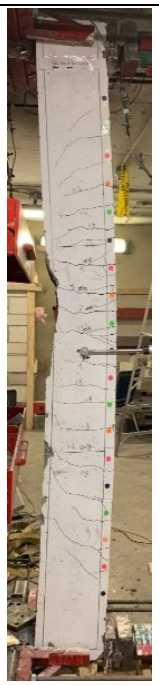

Figure 8.18 Effect of concrete type on failure mode in Group 2 (HSS)

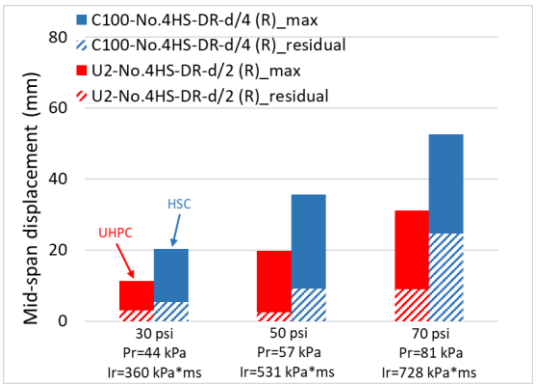

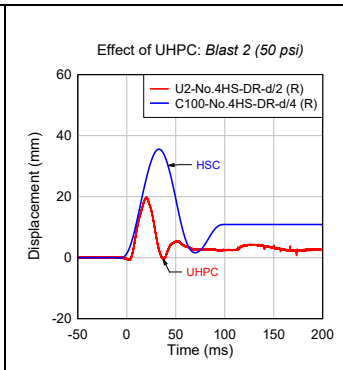

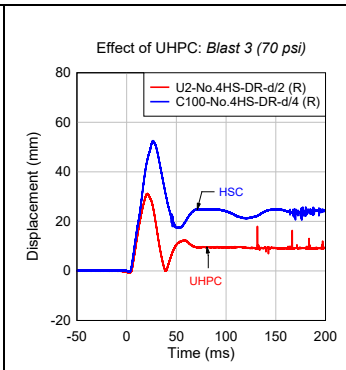

(a) Effect of UHPC (No.4HS)

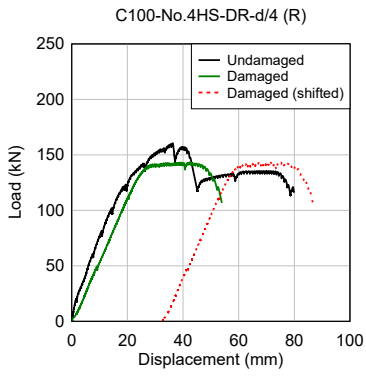

(b) Post-blast residual test: beam C100-No.4HS-DR-d/4

Figure 8.19 Effect of concrete type in Group 2 (No.4HS set)

8.4.2.3.Beams with stainless steel

The effect of concrete type in the SS beams is studied by comparing beams U2-No.5S1-DR-d/2 vs. HSC-No.5S1-DR-d/4 (ρ = 1.5%) and U2-No.4S1-DR-d/2 vs. C100-No.4S1-DR-d/4 (ρ = 1.0%), which were tested under single and repeated blasts, respectively.

The blast responses of the beams in the No.5 stainless set are shown in **Figure 8.20a**. It is noted that the UHPC and C100 beams were tested under single blasts corresponding to *Blast-100psi* (I_r = 967 kPa·ms) and *Blast-90psi* (I_r = 852 kPa·ms), respectively. The U2 beam showed a 12% reduction in maximum displacement (57.5 mm vs. 65.6 mm), but slightly higher residual displacement (36.5 mm vs. 33.8 mm), when compared to the companion C100 beam. Both beams survived blast testing with limited damage, but with distinct cracking patterns (see **Figure 8.21(a,b)**). No concrete crushing was observed in either specimen. Both beams show significant post-blast residual capacity with RRI indices ≥ 0.9, however the UHPC beam shows increases of 14% and 67% in P_{max}^{R} and k_s^R when compared to the beam with C100 concrete (see **Figure 8.20b**). Importantly, the use of SS bars allows both beams to sustained load until very large residual displacements (Δ_{test}^{R} = 150 mm), without bar fracture (see **Figure 8.10f**).

The effect of UHPC in the SS series is further studied in the No.4S1 set by comparing beams U2-No.4S1-DR-d/2 (R) and C100-No.4S1-DR-d/4 (R), which were tested under repeated blasts corresponding to *Blast-30, 50, 70 psi*. The final shot was applied at *Blast-90 psi* for the C100 beam and *Blast-100 psi* for the UHPC specimen. During the first three common blasts, the U2 beam shows reductions of 38%, 21% and 12% in maximum displacements (**Figure 8.22**). The C100 beam survives *Blast-90 psi* (I_r = 882 kPa·ms) but shows a large support rotation of 5.6°, with moderate concrete damage at midspan (**Figure 8.21d**). This beam further shows an ability to sustain loads up to very large displacements in the post-blast residual static test (up to Δ_{test}^{R} = 90 mm; Δ_{max}^{R} = 206 mm). In comparison, the increased intensity of the *Blast-100 psi* (I_r = 978 kPa·ms), led to bar rupture in the UHPC beam. The high speed video indicates bar rupture occurred at 96.5 mm, which is similar to the maximum displacement (Δ_{max} = 92.8 mm) under static loading.

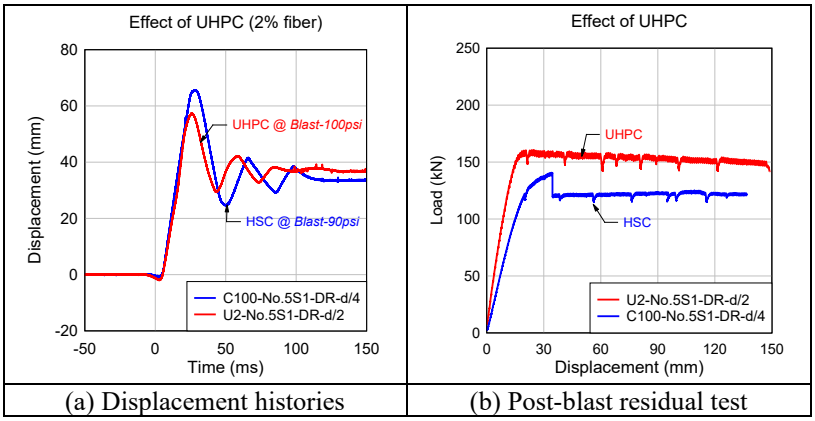

(a) Displacement histories (b) Post-blast residual test

Figure 8.20 Effect of concrete type in Group 2 (No.5S1 set)

Beams with stainless steel (No.5S1 set)		**Beams with stainless steel (No.4S1 set)**	
(a) U2-No.5S1-DR-d/2 @ 100 psi	**(b) C100-No.5S1-DR-d/4 @ 90 psi**	**(c) U2-No.4S1-DR-d/2 (R)**	**(d) C100-No.4S1-DR-d/4 (R)**
		@ 70 psi / **@ 100 psi**	**@ 70 psi** / **@ 100 psi**

Figure 8.21 Effect of concrete type on failure mode in Group 2 (SS beams)

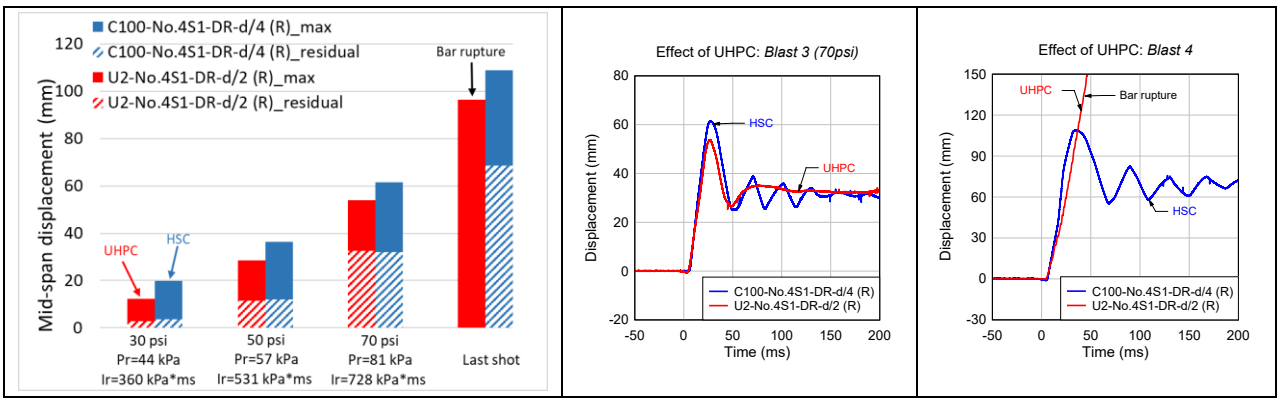

Figure 8.22 Effect of concrete type in Group 2 (No.4S1 set)

8.4.3.Effect of steel ratio in UHPC beams with NSS

The effect of steel ratio is first examined in beams U2-15M-DR-d/2 and U2-20M-DR-d/2 which were built with UHPC, and 2-15M (ρ =1.5%) vs. 2-20M (ρ =2.4%) ordinary steel bars. **Figure 7.10a** examines the effect of reinforcement ratio (ρ) under single *Blast-100psi* loading and shows that increasing the steel ratio led to reductions of 25% and 49% in maximum and residual displacements. Both beams survived the intense blast, however the localized cracking a is more evident in the beam with lower steel ratio (15M bars) (see **Figure 8.26(a,b)**). Both beams were tested for residual capacity after the blast test. As shown in **Figure 7.10b**, the beams show similar residual stiffness (k_s^R), however failure of the beam with 15M bars occurs during the reloading stage. Beam U2-15M-DR-d/2 reaches a residual displacement (Δ_{test}^R) of 9.3 mm before bar rupture indicating the capacity of the bars was nearly exhausted during the blast test. In contrast, beam U2-20M-DR-d/2 shows significant post-blast capacity (P_{max}^R), with a large residual displacement (Δ_{test}^R) of 86.7 mm. The observed trend related to the increase in ductility with the increase in ρ matches the observations in the static test.

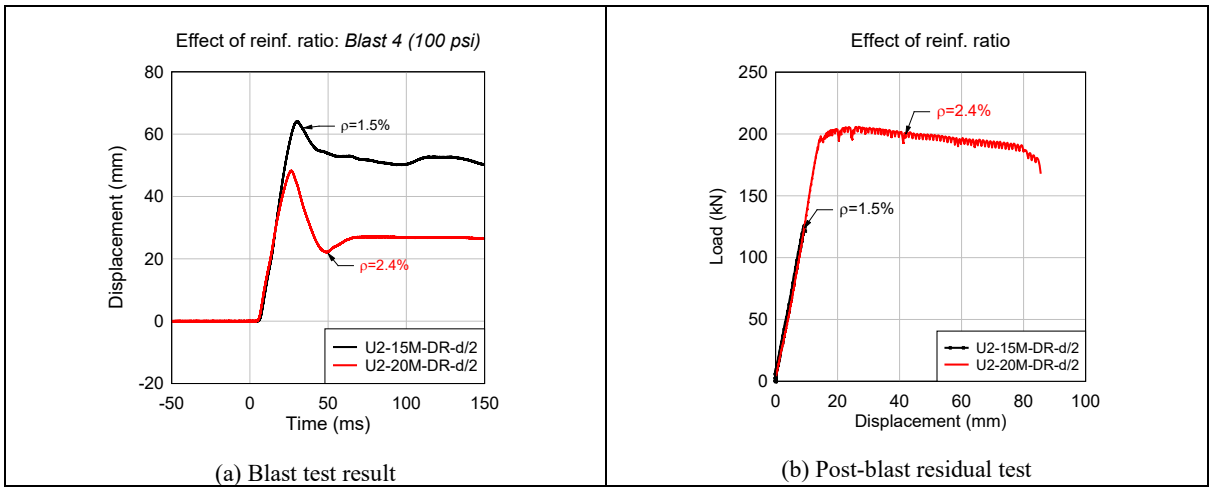

(a) Blast test result (b) Post-blast residual test

Figure 8.23 Effect of steel ratio in UHPC beams with ordinary steel

8.4.4. Effect of steel ratio in UHPC beams with HSS

The effect of steel ratio in the high-strength steel series is studied by comparing the beams U2-No.4HS-DR-d/2 (R) and U2-No.5HS-DR-d/2 which had steel ratios of ρ =1.0% and 1.5%, respectively. It is noted that beam U2-No.4HS-DR-d/2 (R) was tested under repeated blast loading, while beam U2-No.5HS-DR-d/2 was tested under a single application of *Blast-100psi* loading. Examining **Figure 7.11a**, bar rupture failure occurred in beam U2-No.4HS-DR-d/2 (R) at a displacement of 42.8 mm, which was similar to the maximum displacement in the static test (Δ_{max}= 39.5 mm). In comparison, the beam with higher steel ratio (U2-No.5HS-DR-d/2) survived *Blast-100psi*, with a maximum displacement of 35.9 mm and corresponding support rotation (θ_{max}) of 1.8°. Moreover, the beam showed significant post-blast capacity (see **Figure 7.11b**). The beam eventually failed by bar fracture in the post-blast test with a maximum residual displacement of 63.9 mm, which is slightly higher than the maximum displacement in the static test (Δ_{max}= 55.1 mm). The results confirm the ability of increased steel ratio to increase the blast capacity and ductility of HSS-reinforced UHPC beams. The results are also consistent with the static test results, where increasing the HS steel ratio from 1% to 1.5% improved load capacity and increased the failure displacement.

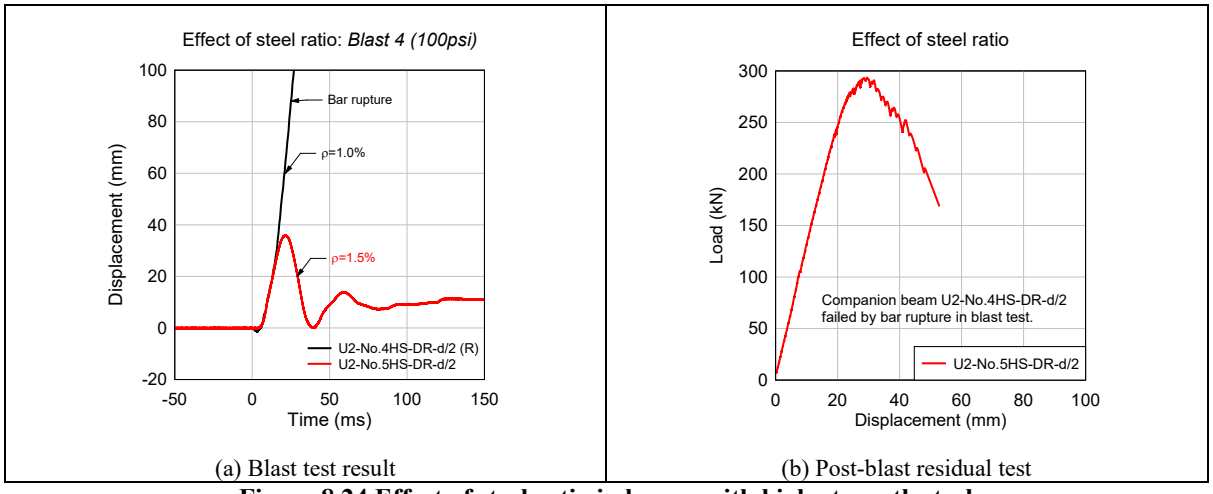

(a) Blast test result (b) Post-blast residual test

Figure 8.24 Effect of steel ratio in beams with high-strength steel

8.4.5.Effect of steel ratio in UHPC beams with SS

The effect of steel ratio is examined in the SS series by comparing beams U2-No.4S1-DR-d/2 and U2-No.5S1-DR-d/2 which had steel ratios of ρ =1.0% and 1.5%, respectively. It is noted that beam U2-No.4S1-DR-d/2 (R) was tested under repeated blasts, while beam U2-No.5S1-DR-d/2 was tested under a single application of *Blast-100psi*. Despite the use of SS reinforcement, beam U2-No.4HS-DR-d/2 (R) suffered a bar fracture failure at *Blast-100psi*. The high-speed camera indicates bar rupture occurred at a displacement of 96.5 mm, which is similar to the maximum displacement in the static test (Δ_{max}= 92.8 mm). In comparison, the beam with higher stainless steel ratio survived *Blast-100psi*, with a maximum displacement of 57.5 mm and a corresponding support rotation (θ_{max}) of 3.0° (**Figure 7.12a)**. Beam U2-No.5S1-DR-d/2 further showed significant post-blast capacity and ductility (see **Figure 7.12b**), with an RRI index ≥ 1.0 and an ability to sustain the load until the end of the post-blast test (Δ^{R}_{test} = 150 mm). The results further confirm the benefits of increasing the tension steel ratio in UHPC beams reinforced with varying steel types.

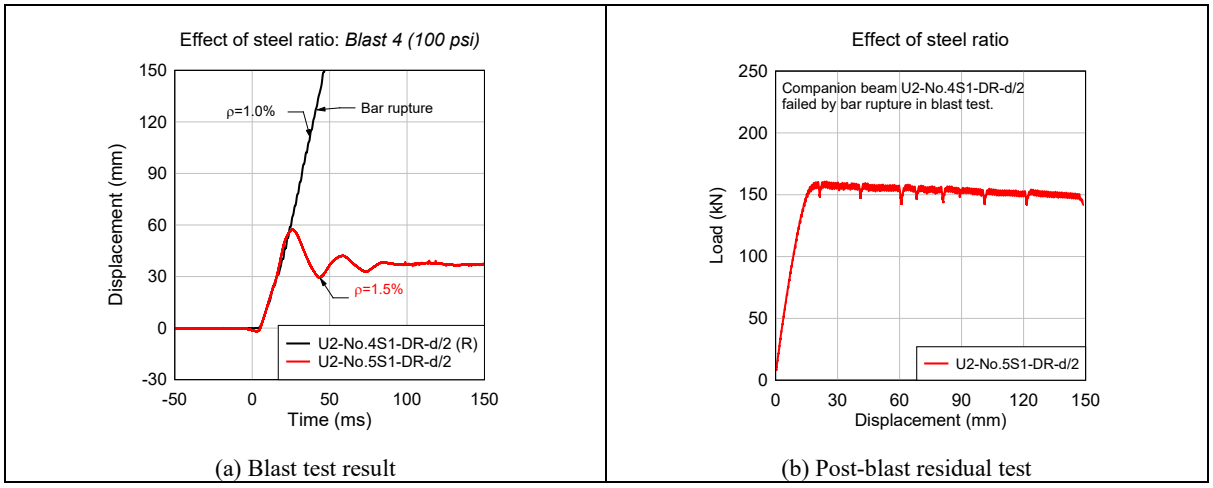

(a) Blast test result (b) Post-blast residual test

Figure 8.25 Effect of steel ratio in beams with SS

Ordinary steel (ρ = 1.5% vs. 2.4%)		High-strength steel (ρ = 1.0% vs. 1.5%)		Stainless steel (ρ = 1.0% vs. 1.5%)	
(a) U2-15M-DR-d/2 @ 100 psi	(b) U2-20M-DR-d/2 @ 100 psi	(c) U2-No.4HS-DR-d/2 @ 100 psi	(d) U2-No.5HS-DR-d/2 @ 100 psi	(e) U2-No.4S1-DR-d/2 @ 100 psi	(f) U2-No.5S1-DR-d/2 @ 100 psi
			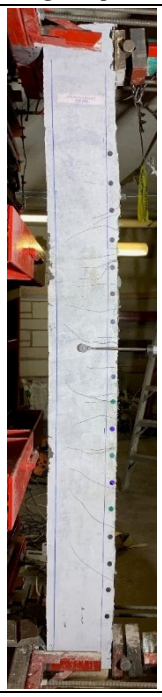		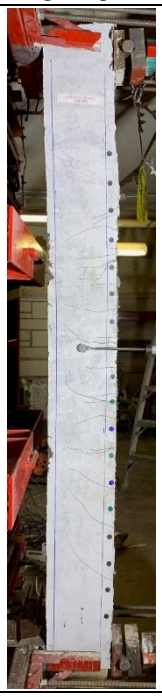

Figure 8.26 Effect of steel ratio on failure mode

8.4.6. Effect of high-strength steel in UHPC beams

The effect of steel grade (f_y= 690 vs. 400 MPa) is first studied by comparing beams U2-No.5HS-DR-d/2 and U2-15M-DR-d/2 in Group 2. Both beams were built with UHPC and a constant steel ratio of ρ = 1.5%, but contained high-strength and normal-strength bars, respectively. Examining **Figure 7.13a**, it can be seen that the use of HSS results in reductions of 44% and 79% in maximum (35.9 mm vs. 64.1 mm) and residual (11.1 mm vs. 52.5 mm) displacements at *Blast-100psi* (I_r = 978 kPa·ms). Both beams survive the blast, however crack localization is more evident in the beam with ordinary steel bars. During the post-blast test the beam with ordinary steel fails during reloading, while the beam with HSS bars shows significant post-blast capacity with an ability to sustain loads up to Δ_{test}^{R} = 52.8 mm (**Figure 7.13c**).

The effect of steel grade is also examined in the Group 1 beams which were built with U3 concrete and without stirrups (**Figure 7.13b**). Under *Blast-100psi*, beam U3-15M suffered bar rupture failure (see **Figure 8.28a**). In comparison the use of high-strength bars in U3-No.5HS prevented failure, and allowed for significant post-blast capacity as shown in **Figure 7.13d**. The results correspond to the observations in the static tests, where substitution of normal-strength bars with higher-strength bars increased strength and overall energy-absorption capacity.

It is also interesting to compare the responses of beams U2-No.5HS-DR-d/2 (ρ=1.5%) and U2-20M-DR-d/2 (ρ=2.4%), which had similar $\rho \cdot f_y$ ratios of 10.4 and 9.6 MPa. As shown in **Figure 7.13a**, at *Blast-100psi*, beam U2-No.5HS-DR-d/2 shows reductions of 26% (35.9 mm vs. 48.3 mm) and 68% (11.1 mm vs. 26.8 mm) in maximum and residual displacements when compared to the more heavily-reinforced U2-20M-DR-d/2 specimen. Both beams survive the blast and show significant post-blast capacity. As shown in **Figure 7.13c**, the beam with high-strength steel shows higher P_{max}^{R} (294 kN VS. 206 kN), but experiences earlier bar fracture when compared to beam U2-20M-DR-d/2, which once again corresponds to the observation in the static tests.

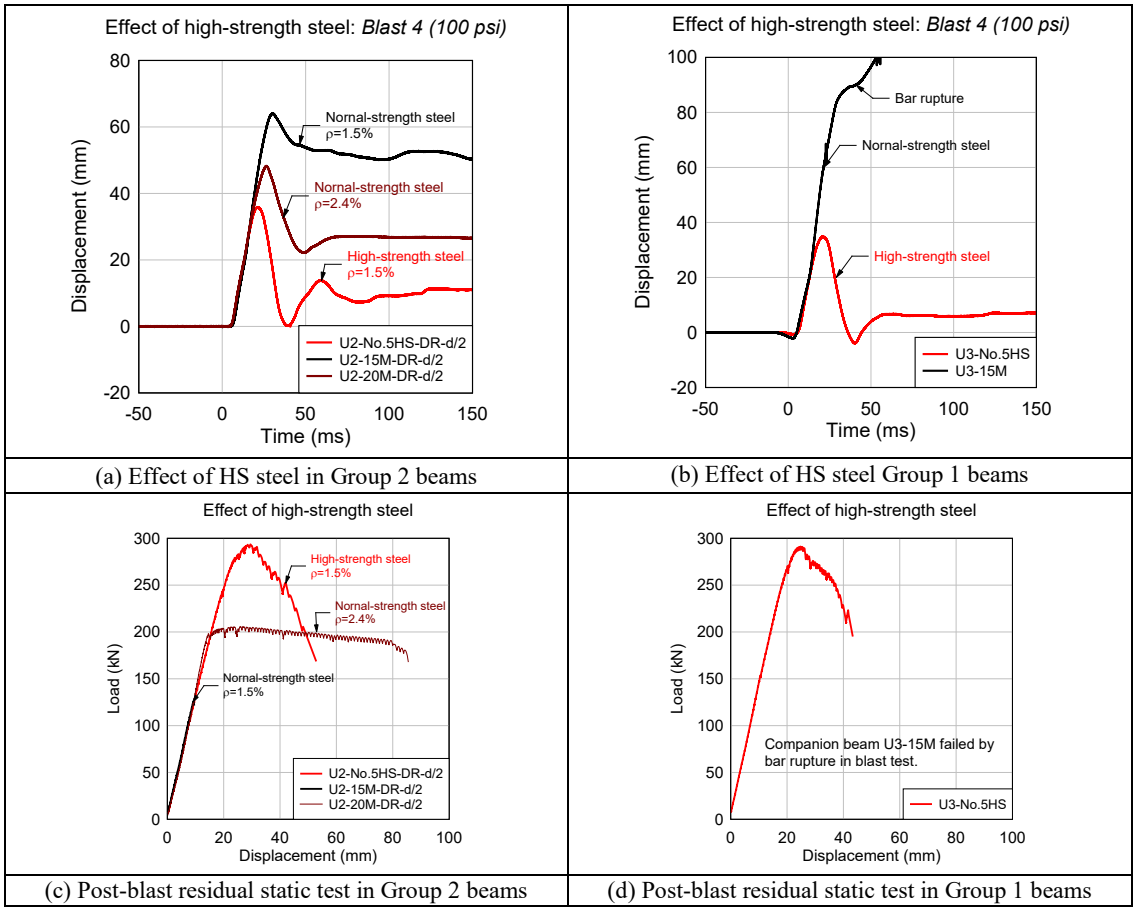

(a) Effect of HS steel in Group 2 beams

(b) Effect of HS steel Group 1 beams

(c) Post-blast residual static test in Group 2 beams

(d) Post-blast residual static test in Group 1 beams

Figure 8.27 Effect of high-strength steel

Group 1 beams		**Group 2 beams**	
(a) U3-15M @ 100 psi	**(b) U3-No.5HS @ 100 psi**	**(c) U2-15M-DR-d/2 @ 100 psi**	**(d) U2-No.5HS-DR-d/2 @ 100 psi**
	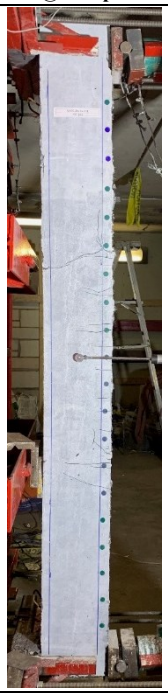		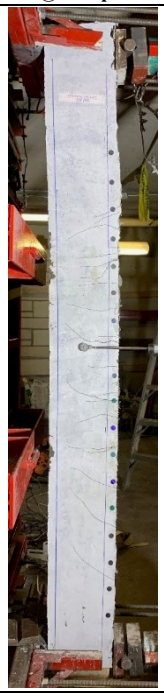

Figure 8.28 Effect of high-strength steel on failure mode

8.4.7. Effect of stainless steel

The effect of stainless steel is first examined by comparing the responses of beams U2-No.5S1-DR-d/2 and U2-15M-DR-d/2 in Group 2. Both beams were built with UHPC and a constant steel ratio of ρ = 1.5%, but contained stainless and normal-strength bars, respectively.

As shown in **Figure 7.15a,** the use of stainless bars led to reductions of 10% and 31% in maximum (57.5 mm vs. 64.1 mm) and residual displacements (36.5 mm vs. 52.5 mm) at *Blast-100psi*. Both beams survived this blast, however the localized cracking is more evident in the beam with ordinary steel bars (**Figure 8.30(c,d)**). As noted before beam U2-15M-DR-d/2 fails by bar fracture upon reloading during the post-blast test. In comparison the beam with SS bars shows significant post-blast capacity, with an ability to sustain loads until very large displacements, without bar fracture (**Figure 7.15c**).

The ability of the SS reinforcement to increase ductility is further confirmed in Group1. As shown in **Figure 7.15b,** beam U3-15M suffers bar rupture failure at *Blast-100psi* (**Figure 8.30a**). In comparison, the use of stainless steel prevents bar rupture, and allows beam U3-No.5S1 to show important post-blast residual capacity up to a displacement of 130 mm, without fracture (**Figure 7.15d**). The results correspond to the observations in the static tests and confirm the excellent compatibility of UHPC and ductile stainless steel under blast loading.

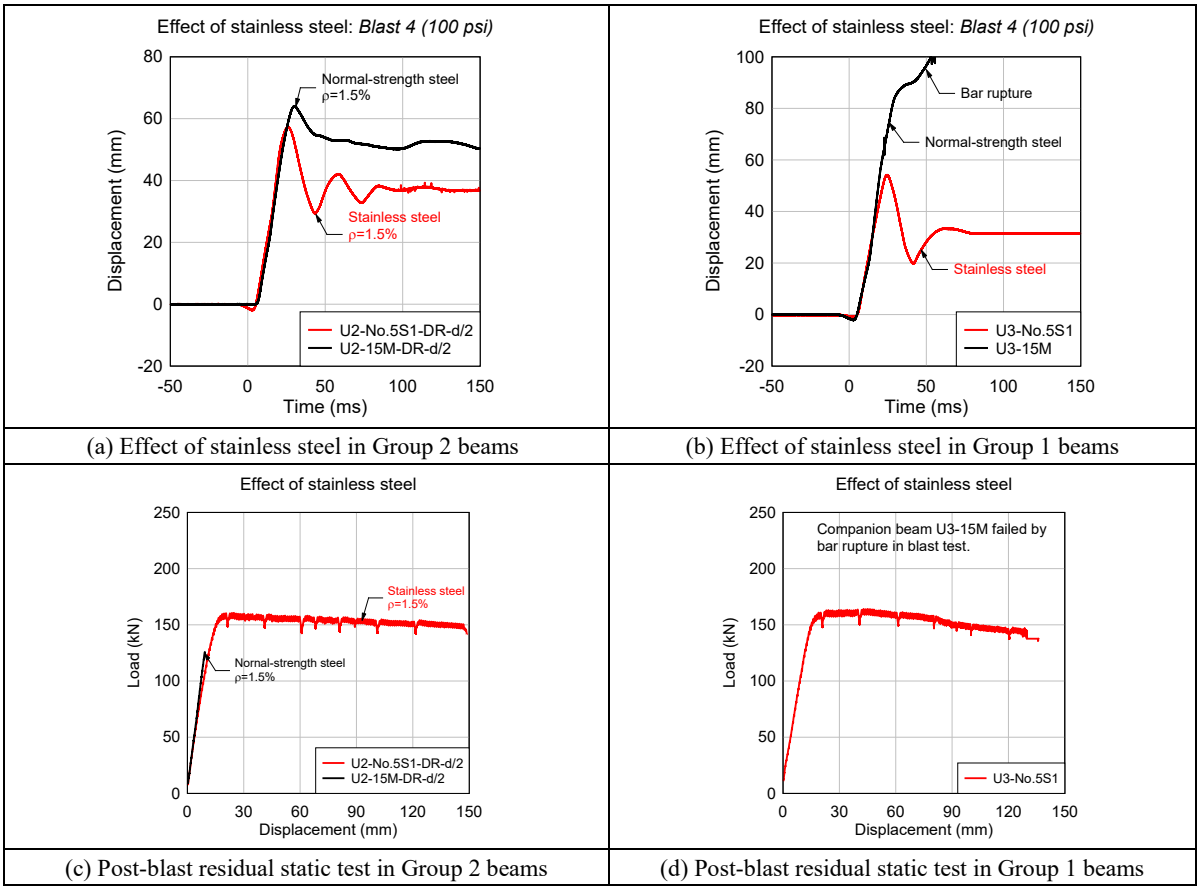

(a) Effect of stainless steel in Group 2 beams

(b) Effect of stainless steel in Group 1 beams

(c) Post-blast residual static test in Group 2 beams

(d) Post-blast residual static test in Group 1 beams

Figure 8.29 Effect of stainless steel

Group 1 beams		**Group 2 beams**	
(a) U3-15M @ 100 psi	**(b) U3-No.5S1 @ 100 psi**	**(c) U2-15M-DR-d/2 @ 100 psi**	**(d) U2-No.5S1-DR-d/2 @ 100 psi**
			

Figure 8.30 Effect of stainless steel on failure mode

8.4.8. Effect of detailing & fiber content

The effects of detailing are examined by comparing the behaviour of companion UHPC beams from Group 1 and 2 with Type D (no stirrups) and Type B (intermediate) detailing. It is noted that the Group 1 beams were built with U3 and U2 concrete, with fiber contents of 3% and 2%, respectively. All the beams were tested under a singly applied *Blast-100psi* loading.

Figure 7.17a compares the blast responses of beams U3-15M & U2-15M-DR-d/2 which were built with ordinary steel and Type D vs. B detailing. The beam responses seem quite different, with bar fracture occurring in beam U3-15M. In comparison, beam U2-15M-DR-D/2 survives the blast, but fails early during the post-blast test indicating that its steel capacity was also nearly exhausted during blast testing. Thus it can be concluded that both beams showed similar performance regardless of detailing level or fiber content.

Figure 7.17b compares the blast responses of beams U3-No.5HS & U2-No.5HS-DR-d/2 which were built with high-strength steel and Type D vs. B detailing. Also included is beam U1-No.5HS-DR-d/4 which contained 1% fibers and Type A detailing. The results show that all three beams survive the intense blast test and show similar maximum displacements with differences within $\pm$ 5%. Examining the damage photos in **Figure 8.33(c,d,e)**, all beams showed many fine and well distributed cracks. All three beams show comparable residual capacities (P_{max}^{R}) and performance during the post-blast tests, although bar fracture failure is slightly delayed for the beam with 1% fibers (U1) (see **Figure 8.32a**).

Figure 7.17c studies the effect of detailing in beams U3-No.5S1 and U2-No5S1-DR-d/2, which were built with stainless steel and Type D vs. B detailing. Both beams show similar responses under the *Blast-100psi* shot, however beam U3-No.5S1 shows decreases of 6% and 13% in maximum and residual displacements. Both beams survive the blast with damage limited to many fine and well distributed cracks. Both beams show comparable responses during the post-blast tests, with no bar fracture in either specimen (see **Figure 8.32b**).

The results confirm the limited effects of detailing on the response of UHPC beams tested under blast loading, which also corresponds to the observation in the static tests.

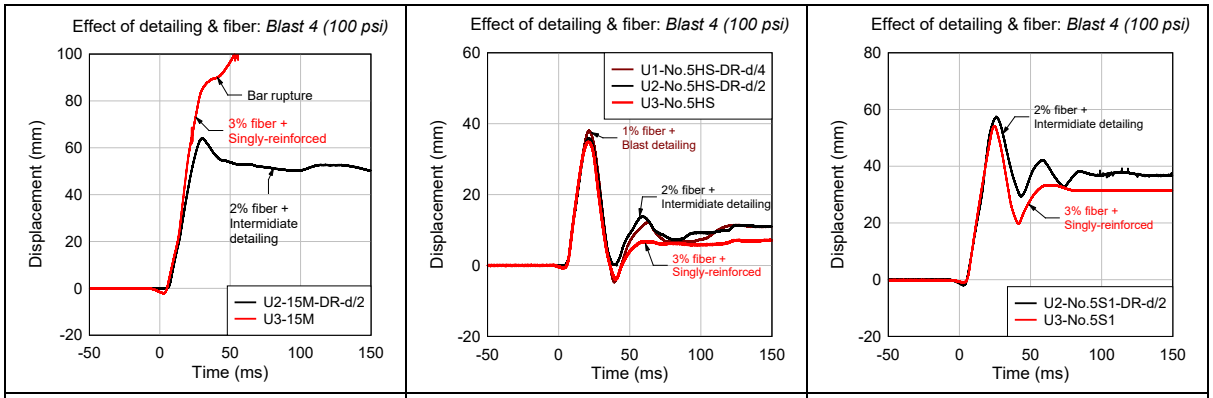

(a) beams with ordinary steel | (b) beams with HS steel | (c) beams with SS steel

Figure 8.31 Blast results: effect of detailing

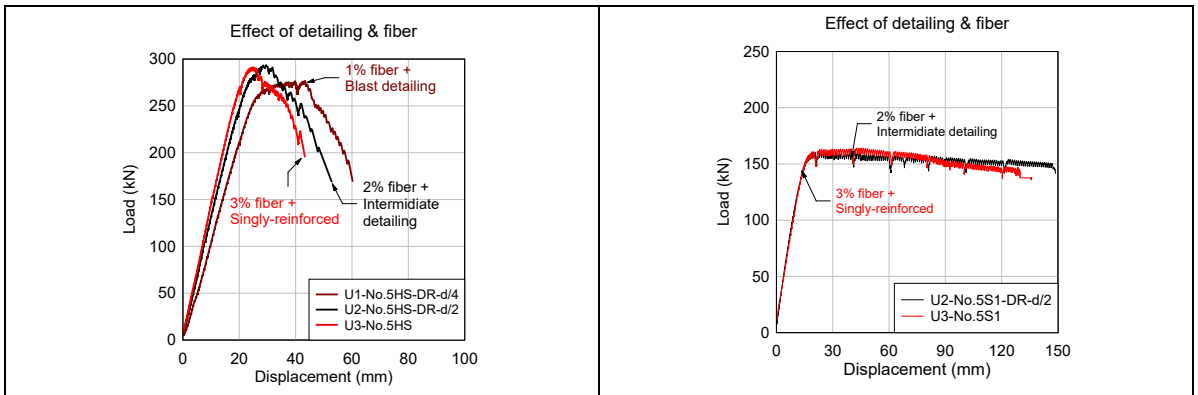

(a) beams with HS steel | (b) beams with SS steel

Figure 8.32 Post-blast residual test: effect of detailing

Ordinary steel		High-strength steel			Stainless steel	
(a) U3-15M @ 100 psi	**(b) U2-15M-DR-d/2 @ 100 psi**	**(c) U3-No.5HS @ 100 psi**	**(d) U2-No.5HS-DR-d/2 @ 100 psi**	**(e) U1-No.5HS-DR-d/4 @ 100 psi**	**(f) U3-No.5S1 @ 100 psi**	**(g) U2-No.5S1-DR-d/2 @ 100 psi**
		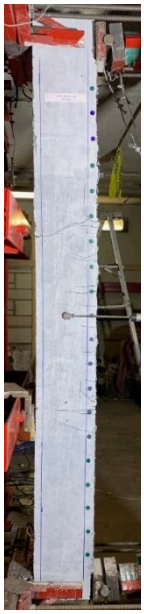	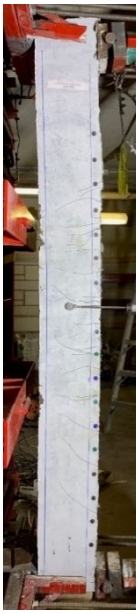			

Figure 8.33 Effect of detailing on failure mode

8.4.9.Effect of repeated loading

The effect of repeated loading can be examined by comparing the responses of the replicate beams U2-20M-DR-d/2 and U2-20M-DR-d/2 (R) which were tested under single and repeated blasts, respectively. **Figure 8.34a** compares the beam responses under *Blast-100psi*. Both beams show remarkably similar maximum displacements (48/46 mm) and residual deformations (27/27 mm). It can therefore be concluded that the repeated tests had very limited effects on displacement response of the UHPC beams under blast loading, which is similar to observation in Section 4.5.4 for conventional HSC beams with blast-detailing. Examining the damage photos in **Figure 8.35**, damage in both beams is limited to a single localized crack in the constant moment area. As shown in **Figure 8.34b** both beams show important post-blast capacity, however a larger residual strength P_{max}^{R} is recorded for the beam tested under single blast loading, which also corresponds to the observation in Section 4.5.4. Both beams eventually fail due to bar fracture, however the repeated blasts result in a greater build-up of residual strains in the steel reinforcement, which causes earlier bar fracture.

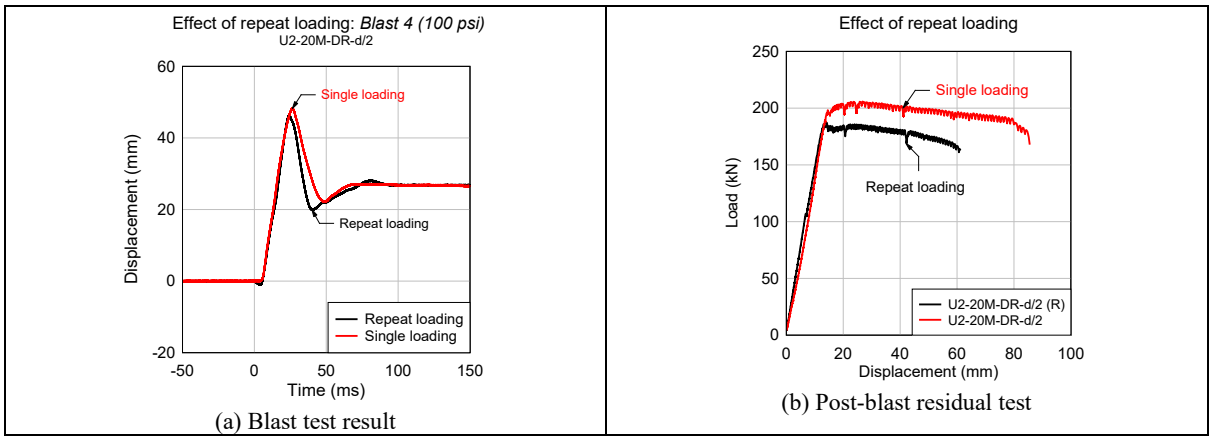

(a) Blast test result

(b) Post-blast residual test

Figure 8.34 Blast and post-blast residual test result: effect of repeated loading

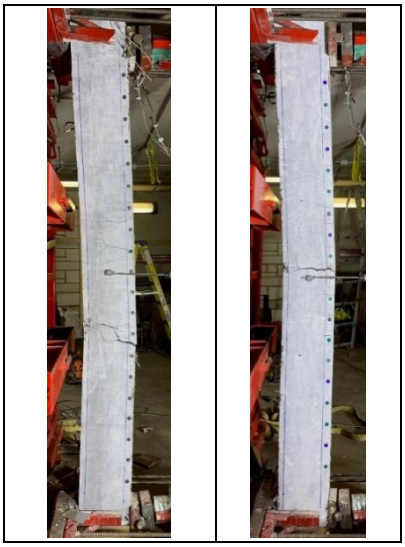

Figure 8.35 Effect of repeated load on damage (single vs repeated loads)

8.5 Conclusions

This chapter presented the results from **Series 3** of the PhD program, and examined the influence of steel reinforcement ratio and type on the blast behavior of UHPC beams. The test variables included the effects of UHPC, steel type and ratio, as well as fiber content and detailing. The following conclusions can be drawn from this study:

1. In Group 1, the use of UHPC with 3% fibers prevented shear failure and showed higher blast capacity when compared to companion HSC beams with nominal detailing. The higher compressive toughness of UHPC prevented damage in compression even under intense blast loading. On the other hand, UHPC beams with ordinary and high-strength bars were vulnerable to bar fracture failures to the high bond capacity of the UHPC, while the combined use of UHPC and stainless bars allowed for improved ductility.

2. In Group 2, the use of UHPC with intermediate detailing showed a better ability to control displacements at equivalent (or larger) blasts when compared to companion HSC beams with blast detailing. However, bar fracture occurred in the beams with low HSS or SS steel ratios (ρ = 1.0%) during the blast tests. For the remaining beams, reduced ductility was also observed in the post-blast tests due to bar fracture failures.

3. Increasing the tension steel ratio in the UHPC beams (from ρ = 1.5% to 2.4% in the beams with ordinary bars, and from ρ = 1.0% to 1.5% in the beams with HSS or SS bars) had a significant effect on blast performance, regardless of the steel type. Under blast loading, increasing the steel ratio resulted in better control of displacements under equivalent blast loading, and delayed bar fracture during the blast or post-blast tests. In addition, the ductility in the post-blast residual test was significantly improved.

4. The use of high-strength steel prevented bar rupture at *Blast-100psi*, and allowed for significant post-blast residual capacity, when compared to the companion beam with equal amounts of ordinary steel in Group1. In Group 2, the use HSS reinforcement (at ρ =1.5%) reduced maximum & residual displacements and further allowed for significant post-blast capacity. In addition, UHPC beams with similar ρf_y (but reduced amounts of HSS bars) showed reductions in maximum & residual displacements, but reduced ductility in the post-blast test, when compared to companion beams with greater amounts of ordinary steel bars.

5. The use of stainless steel significantly increased blast performance by preventing bar rupture in the Group 1 when compared to the companion beam with ordinary steel. The

use of SS reinforcement in Group 2 allowed for better control of displacements under equivalent blasts, and prevented bar rupture during the post-blast test. In both groups, the use of stainless steel allowed for remarkable beam ductility during the post-blast tests, with an ability to sustain the load up to very large deformations ($\Delta > 130$ mm), without bar rupture.

6. Detailing and fiber content had a limited effect on blast response. In the ordinary and SS sets, the U2 and U3 beams with Type B and Type D detailing showed comparable responses in the blast and post-blast tests. Likewise, in the HSS set, the U1, U2 and U3 beams with Type A, Type B and Type D detailing also showed comparable responses.

8.6 References (Chapter 8)

Adhikary, S. D., Li, B., & Fujikake, K. (2014). Residual resistance of impact-damaged reinforced concrete beams. *Magazine of Concrete Research, 67*(7), 364-378. doi:https://doi.org/10.1680/macr.14.00312

AFGC (2013). Ultra high performance fibre-reinforced concretes. AFGC & SETRA Working Group Paris, France, pp. 175.

ASTM A955/A955M − 20c (2020a). Standard Specification for Deformed and Plain Stainless Steel Bars for Concrete Reinforcement. ASTM International, West Conshohocken, PA, pp. 16.

A1035/A1035M − 20 (2020b). Standard Specification for Deformed and Plain, Low-Carbon, Chromium, Steel Bars for Concrete Reinforcement. ASTM International, West Conshohocken, PA, pp. 7.

Canadian Standards Association (CSA) (2012). Design and assessment of buildings subjected to blast loads. CSA S850-12, Mississauga, ON, Canada, pp. 126.

Canadian Standards Association (CSA) (2014). Design of concrete structures. CAN/CSA A23.3-14, Mississauga, ON, pp. 295.

Kishi, N., & Mikami, H. (2012). Empirical formulas for designing reinforced concrete beams under impact loading. *ACI Structural Journal, 109*(4), 509-519. doi:https://doi.org/10.14359/51683870

Chapter 9 Finite Element Modelling

This chapter presents the numerical research program which aims at predicting the static and dynamic responses of the test beams using finite element (FE) modelling. In the first phase, the behaviour of the high-strength concrete (HSC) beams tested in Series 1 and 2 are predicted using the 2D nonlinear finite element software VecTor2. In the second phase, the dynamic responses of the UHPC beams from Series 3 are predicted using the 3D finite-element (FE) software, LS-DYNA. Simulations are conducted for HSC and UHPC beams having varying steel types and detailing. This chapter provides a description of the FE models used in Phase 1 and 2, and presents comparisons between the numerical and experimental results.

9.1 Phase 1 FEM analysis: HSC beams

9.1.1. 2D FEM model

Numerical analyses of the HSC beams in Series 1 and 2 were conducted using software VecTor2 (Wong et al., 2013), a two-dimensional nonlinear finite element (FE) analysis program which can model the response of reinforced concrete structures subjected to static and dynamic loading. The theoretical basis of the finite element procedure in this program are the modified compression field theory (MCFT) (Vecchio & Collins, 1986) and the Disturbed Stress Field Model (DSFM) (Vecchio, 2000, 2001). The DSFM is a smeared rotating crack model which extends the compatibility relationships in the MCFT to include crack shear-slip deformations. Further background on the theoretical basis of the program can be found in the following reference (Wong et al., 2013).

This program was selected for this phase of the research program since it contains an important library of constitutive models for smeared reinforced concrete and discrete steel reinforcement. Extensive studies have demonstrated the ability of the software to provide good response estimates of RC structures under static (Vecchio & Shim, 2004) and cyclic loading (Palermo & Vecchio, 2007; Cortés-Puentes & Palermo, 2012). More recently additional features have been developed in the VecTor suite of software, including impact and blast analysis capabilities (Saatci, 2007; Saatci & Vecchio, 2009; Trommels, 2013; Hrynyk & Vecchio, 2016; Lulec, 2017), and element material modeling of fiber-reinforced concrete materials (Lee et al., 2015; Lee et al., 2013, 2011a, 2011b). The software has been shown to reliably predict the shear, flexure, impact and blast response of reinforced concrete (Saatci &

Vecchio, 2009; Saatci, 2007; Trommels, 2013) and fiber-reinforced concrete (Lee et al., 2016; Susetyo et al., 2013; Isojeh et al., 2019) elements.

Figure 9.1 show schematics of the finite element mesh for the half-span symmetric beams considered in the static and blast analyses. Four-degree-of-freedom rectangular elements having 25 mm × 25 mm mesh size were used for concrete, while two-node truss bar elements were used for the longitudinal reinforcement, with transverse reinforcement smeared within the concrete. In total, 480 rectangular elements and 94 truss elements were used for the concrete and the longitudinal bars. Rectangular elements were assigned to the beams and contained smeared transverse reinforcement.

In the static tests, the numerical analyses were conducted in displacement-control by assigning a monotonically increasing displacement at the node located at a distance "a" (shear span) from the left support (see **Figure 9.1a**). In the case of the blast tests, steel plates and compression-only truss bars were used to simulate the boundary conditions in the shock-tube experiments (see **Figure 9.1b**). The mass of the concrete beam was applied using lumped masses which were applied to all the nodes in the model (Saatci, 2007). The blast load was applied using an idealized five-point curve having the same peak reflected pressure (P_r), and a post-peak response which closely matched the blast wave generated in the experiments (see **Figure 9.1b**). The peak blast load in kN was taken as $P_r \cdot A$, where A = loaded-area of the LTD (load transfer device) = 3.4 m^2. This load was applied to the top steel plate at a distance "a" from the left support. The dynamic analyses were performed using Newmark's constant acceleration method, with a time step of 0.1ms, with Rayleigh damping implemented in the analysis (Saatci, 2007). Trommels (2013) studied the smallest amount of damping that would yield stable results in the blast analysis of reinforced concrete slabs in VecTor2. Ratios of 1% and 5% of critical damping were first selected for the first two vibrational modes, then gradually decreased until the results became unstable. The smallest amount of damping for stable results was found to be 0.5% and 0.75% for the first two modes. Likewise, Saatci and Vecchio (2009) reported damping ratios of 0.5% to 1% assigned to the first two modes were sufficient for stable analysis in the impact modelling of RC beams in VecTor2, with the exception of heavily damaged specimens where a ratio of 5% was required. To study this effect, two cases of damping were considered in the FE simulations of the Series 1 beams: Case 1 with ξ = 0.5% and 0.75% of critical damping for the first two modes, and Case 2 with ξ = 1% and 5% for modes 1 and 2, respectively. For the beams in Series 2, the default case was chosen as ξ = 0.5% and 0.75% of critical damping for the first two modes, respectively.

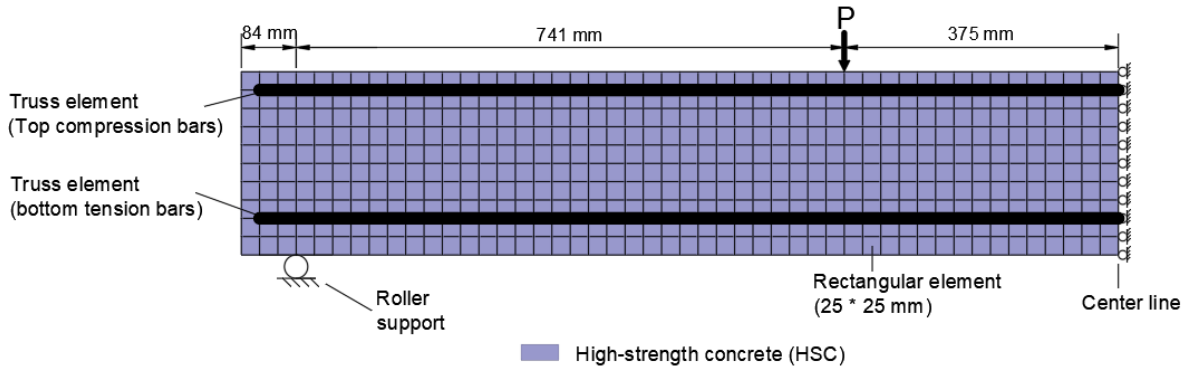

(a) Static FE analysis (Mesh)

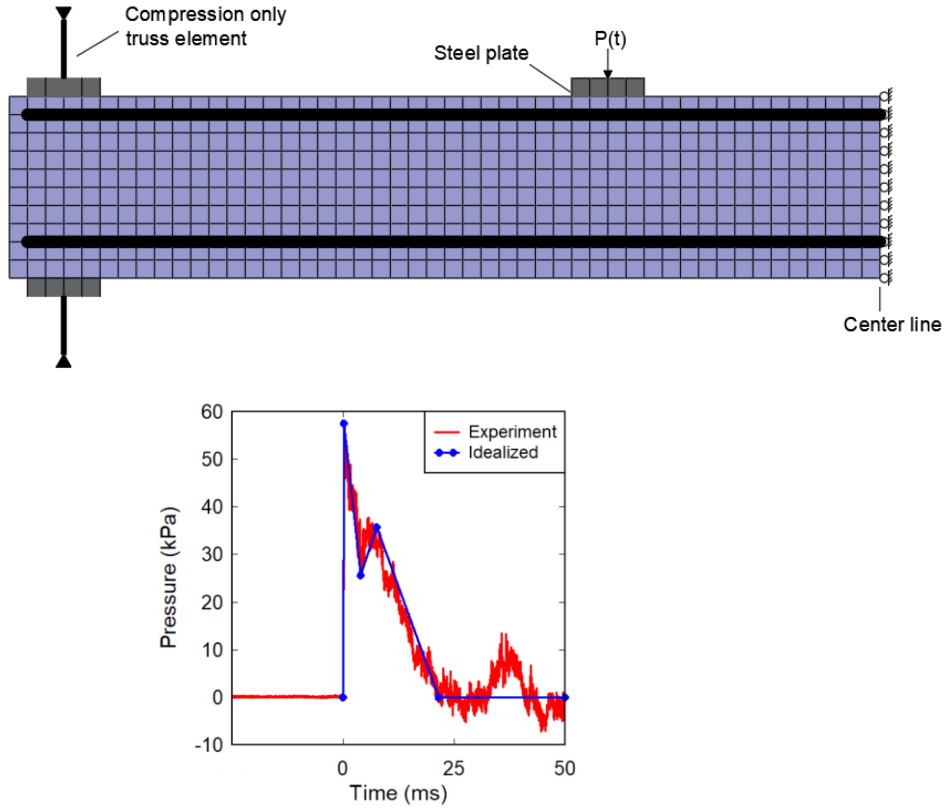

(b) Dynamic FE analysis (Mesh and idealized blast pressure-time history)

Figure 9.1 FEM meshes under static and dynamic loading

9.1.2. Material models

9.1.2.1.Reinforcement model

Table 9.1 lists the material & behaviour models, and fitting curves which were considered for the ordinary, high-strength and stainless steel reinforcement. The tensile response of the ordinary and stainless steel bars was modelled using a curvilinear model (Wong et al., 2013), which consists of three segments: linear-elastic, yield plateau and rounded strain-hardening response. For ordinary steel, yield & ultimate strength, elastic modulus, strain hardening & ultimate strain data were used to define the stress-strain curve. For stainless steel, the strain-hardening strain was set slightly higher than the yield strain, to generate the curvilinear strain hardening response which begins immediately after yielding and continues up to rupture. The properties of the high-strength steel reinforcement were defined using a custom model which closely replicated the actual stress-strain response of the Grade 690 MPa steel reinforcement as obtained from the coupon test data (MMFX model). The hysteresis response of all three types of steel bars was considered using the Seckin model (Seckin, 1981) as recommended in references (Barbachyn et al., 2017; Chan & Mackie, 2018). In the case of the blast tests, dynamic increase factors (DIF) were used to account for strain-rate effects, with the DIF factors for steel applied using the relationships proposed by Malvar-Crawford (Malvar & Crawford, 1998).

Table 9.1 Steel material and behavior models

	Ordinary steel	**High-strength steel**	**Stainless steel**
Base stress-strain curve	Elastic-Hardening (curvilinear)	MMFX (ASTM A1035)	Elastic-Hardening (curvilinear)
Hysteretic Response	Seckin Model	Seckin Model	Seckin Model
Dowel Action	Tassios (crack slip)	Tassios (crack slip)	Tassios (crack slip)
Stress-strain fitting curve	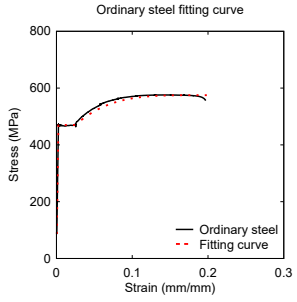	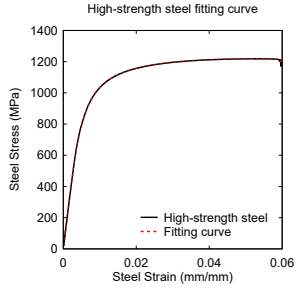	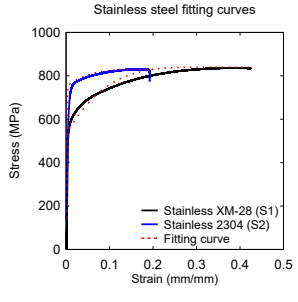

9.1.2.2. Plain HSC models

Table 9.2 lists the concrete constitutive models and behavior models considered in the analyses. For the plain HSC beams, most of the default models were used. However, to better account for the confinement effects in high-strength concrete in the beams with blast and intermediate detailing, the "Popovics" and "Popovics/Mander" models (Popovics, 1973; Mander et al., 1988) were selected for the compression base-curve and post-peak responses, respectively. Since no ties were provided in the beams with nominal detailing, the confinement effects were neglected, and the "Popovics" model (Popovics, 1973) was selected for the entire compression responses. The remaining models are similar to those used in other Vector FE impact studies (Saatci & Vecchio, 2009; Saatci, 2007). Detailed description and discussion of the various models can be found in Wong et al. (2013). In the case of the blast tests, dynamic increase factors (DIF) were used to account for strain-rate effects, with the DIF factor for concrete applied using the relationships proposed by the fib Model Code 2010 (FIB, 2013).

Table 9.2 Concrete material and behavior models

Material property		**HSC beam (Doubly-reinforced)**	**HSC beam (Nominal detailing)**	**HSFRC beams**	**Hybrid HSFRC beams**
Concrete models	*Compression base curve*	Popovics (HSC)	Popovics (HSC)	Lee et at. 2011 (FRC)	Lee et at. 2011 (FRC)
	Compression post-peak	Popovics / Mander	Base curve	Lee et at. 2011 (FRC)	Lee et at. 2011 (FRC)
	Compression softening	Vecchio 1992-A	Vecchio 1992-A	Vecchio 1992-A	Vecchio 1992-A
	Tension stiffening	Modified Bentz 2003	Modified Bentz 2003	Modified Bentz 2003	Modified Bentz 2003
	Tension softening	Linear	Linear	Linear	Custom Input
	FRC tension	Not considered	Not considered	DEM (Lee et al. 2011)	DEM (Lee et al. 2011)
	Confinement strength	Kupfer / Richart	Neglected	Kupfer / Richart	Kupfer / Richart
	Dilatation	Variable – Isotropic	Variable – Isotropic	Variable - Isotropic	Variable – Isotropic
	Cracking criterion	Mohr-Coulomb (Stress)	Mohr-Coulomb (Stress)	Mohr-Coulomb (Stress)	Mohr-Coulomb (Stress)
	Crack Stress Calculation	Basic (MCFT)	Basic (MCFT)	Advanced (Lee 2009)	Advanced (Lee 2009)
	Crack width check	Agg/5.0 Max crack width	Agg/5.0 Max crack width	Agg/5.0 Max crack width	Agg/5.0 Max crack width
	Crack Slip Calculation	Walraven	Walraven	Walraven	Walraven
	Hysteresis	Nonlinear w/ Plastic Offsets	Nonlinear w/ Plastic Offsets	Nonlinear w/ Plastic Offsets	Nonlinear w/ Plastic Offsets
Analysis Options	*Strain history*	Considered			
	Strain rate effects	Fib MC2010/Malvar-Crawford			
	Structural damping	Rayleigh			
	Time stepping integration	Newmark - Constant Average			
	Geometric nonlinearity	Considered			
	Cracking spacing	Uniform: CEB-FIP 1978			

9.1.2.3. HSFRC models

The following models can be considered in VecTor2 to better account for the effects of steel fibers: Lee et al. (2015) (compression model), Lee et al. (2013) (tension stiffening model), Lee et al. (2011a, 2011b) (tension softening model). These models were verified in: Lee et al. (2016), Susetyo et al. (2013), Isojeh et al. (2019) and Hrynyk and Vecchio (2016). **Table 9.2** lists the models that were considered in the numerical simulations of the HSFRC beams. In general, the 'default' constitutive models and analysis parameters were used, with a few exceptions to account for the fibers (see **Table 9.3**). The Lee et al. model (Lee et al., 2015) was chosen for the pre-peak and post-peak response of FRC in compression. The model was derived based on 48 cylinder tests which considered two concrete strengths, and hooked-end steel fibers with three different aspect-ratios and four different volumetric ratios. The model inputs included the concrete cylinder strength (f_c') and fiber properties (V_f, l_f, d_f), where parameters A and B are used to model the pre-peak and post-peak ascending branches of the stress-strain response, ε_c' is the peak strain of FRC, E_c is the elastic modulus of FRC, and f_{c2max} accounts for the compression softening effect (see **Table 9.3**). Compression softening was modelled using Vecchio's 1992-A model (Vecchio, 1992), while the Kupfer/Richart model (Vecchio, 1992) was used for the strength enhancement in concrete due to triaxial stress conditions. The tensile behaviour of FRC was modelled using the diverse embedment model (DEM) (Lee et al., 2011a). In the DEM, the average fiber tensile stress across a crack for a given crack width (f_f) is calculated using a double numerical integration scheme as shown in **Table 9.3**. The model only requires basic user inputs relating to fiber type, geometry, tensile strength and volume fraction. Further details on the DEM can be found in Wong et al. (2013); Lee et al. (2016, 2011a). Tension stiffening ($f_{c.TS}$) was taken into account using the modified Bentz 2003 model which includes a modified formulation for FRC (Lee et al., 2013; Wong et al., 2013). In the equation for $f_{c.TS}$, the coefficient c_f considers the effects of the fibers based on V_f, l_f and d_f. The tensile stresses (f_{c1}) are then evaluated by considering the tension stiffening effect and the stresses transmitted by the steel fibers, while also considering local yielding of the steel reinforcement by applying an upper limit on the tensile stress f_{c1} (see **Table 9.3**) (Lee et al., 2016). The Deluce model (Deluce et al., 2014) was used to account to the crack spacing in FRC. The remaining models in **Table 9.2** correspond to those used in previous FRC studies (Susetyo et al., 2013; Hrynyk & Vecchio, 2016).

Table 9.3 FRC material models in VecTor2.

<table>
<tr><th>FRC in compression [1]</th><th colspan="2">FRC in tension [2]</th></tr>
<tr>
<td rowspan="2">Lee et al. (2015) model : (Lee et al., 2015)

Stress-strain formulation:
$f_{c2}(\varepsilon_{c2}) = f_{c2max}\left[\frac{A(\frac{\varepsilon_{c2}}{\varepsilon_c'})}{A-1+(\frac{\varepsilon_{c2}}{\varepsilon_c'})^B}\right]$
Pre-peak ascending branch parameters:
$A = B = \frac{1}{1-\frac{f_c'}{\varepsilon_c' E_c}}$
Post-peak descending branch parameters:
$A = 1 + 0.723\left(V_f\frac{l_f}{d_f}\right)^{-0.957}$;
$B = \left(\frac{f_c'}{50}\right)^{0.064}\left[1+0.882\left(V_f\frac{l_f}{d_f}\right)^{-0.882}\right]$
Elastic modulus: $E_c = \left(-367V_f\frac{l_f}{d_f}+5520\right)f_c'^{0.41}$;
Peak strain: $\varepsilon_c' = (0.0003V_f\frac{l_f}{d_f}+0.0018)f_c'^{0.12}$
Compression Softening effect: (Vecchio, 1992)
$\frac{f_{c2max}}{f_c'} = \frac{1}{1+0.19(-\varepsilon_{c1}/\varepsilon_{c2}-0.28)^{0.8}}$

where $-\frac{\varepsilon_{c1}}{\varepsilon_{c2}} > 0.28$ and f_{c2max} is the maximum compressive stress considering softening</td>
<td>DEM model: (Lee et al., 2011a)

Tensile stress at crack due to steel fibers:
$f_f = \alpha_f V_f \sigma_{f,cr,avg}$
where:
$\alpha_f = \begin{cases} -0.05\left(\frac{h}{l_f}\right)^{2.8}+0.64 & for\ \frac{h}{l_f}\le 1 \\ 0.087\left(\frac{h}{l_f}\right)^{1.12}+0.5 & for\ \frac{h}{l_f}>1 \end{cases}$
$\sigma_{f,cr,avg} = \frac{2}{l_f}\int_0^{\frac{l_f}{2}}\int_0^{\frac{\pi}{2}}\sigma_{f,cr}(l_a,\theta)sin\theta\ d\theta dl$</td>
<td>Modified Bentz model: (Lee et al., 2013; Wong et al., 2013)

Tension stiffening effect:
$f_{c,TS} = \frac{f_{cr}}{1+\sqrt{3.6c_f M\varepsilon_{c1}}}$
where:
$c_f = 0.6 + \frac{1}{0.034}\frac{l_f}{d_f}\frac{(100V_f)^{1.5}}{M^{0.8}}$
$M = \frac{A_c}{\sum d_b \pi}\ (mm)$</td>
</tr>
<tr>
<td colspan="2">The tensile stress in the concrete matrix is considered by considering both the tension-stiffening effect and the stresses transmitted by steel fibers : (Lee et al., 2016)
$f_{c1} = f_{c,TS} + (1-\alpha_{avg})f_f\cos\theta_f$
$\alpha_{avg} = \frac{2}{5.5}\frac{l_f}{s_{cr}} \le 1.0$
The upper limit of the tensile stress in a concrete matrix which considers local yielding of conventional reinforcement at a crack is given by : (Lee et al., 2016)
$f_{c1} \le \sum_i \rho_i(f_{scr,i}-f_{s,i})cos^2\theta_{n,i} + (1-\alpha_{avg})f_f\cos\theta_f$
Where the average crack spacing is given by: (Deluce et al., 2014)
$s_{cr} = 2\left(c_a+\frac{s_b}{10}\right)k_3 + \frac{k_1k_2}{s_{mi}}$
and where:
$c_a = 1.5a_{gg};\ k_1 = 0.4;\ k_2 = 0.25;\ k_3 = 1-\left[\frac{min(V_f,0.015)}{0.015}\right]\left[1-\frac{1}{k_f}\right];$
$a_{gg} = max.aggregate\ size;\ s_b = \frac{1}{\sqrt{\sum_i \frac{4\rho_{s,i}}{\pi d_{b,i}^2}cos^4\theta_i}};\ s_{mi} = \sum_i \frac{\rho_{s,i}}{d_{b,i}}cos^2\theta_i + k_f\frac{\alpha_f V_f}{d_f};\ k_f = \frac{l_f/d_f}{50} \ge 1.0$
and where the average crack width: $w_{cr} = s_{cr}\varepsilon_{c1}$
which should be not greater than: $w_{cr,max} = (1.7+3.4\frac{V_f l_f}{d_f})w_{cr}$</td>
</tr>
</table>

Note [1] : f_c' = compressive strength of concrete cylinder; f_{c2max} = peak concrete compressive stress in concrete considering softening effect; ε_c' = peak compressive strain of concrete; V_f, l_f, d_f = fiber content; length and diameter; f_{c2} = principal compressive stress in concrete; f_{c2}= average strain in concrete in principal compressive stress direction; ε_{c1} = average strain in concrete in principal tensile stress direction; ε_{c2}= average strain in concrete in principal compressive stress direction;

Note [2] : f_{c1} = principal tensile stress in concrete; f_f = tensile stress at crack due to steel fibers; α_f = fiber orientation factor; $\sigma_{f,cr,avg}$ = average fiber tensile stress at a crack ; h = member thickness; $\sigma_{f,cr}(l_a,\theta)$= fiber tensile stress at a crack for given shorter embedment length l_a and fiber inclination θ; $f_{c,TS}$ = average tensile stress in concrete due to tension stiffening effect; f_{cr} = cracking strength of concrete; M = bond parameter; d_b = diameter of steel reinforcement; A_c = cross-sectional areas of concrete matrix; θ_f = angle between tensile stress direction due to steel fibers and principal tensile stress direction in concrete; α_{avg} = coefficient to relate tensile stress at a crack due to steel fibers with average tensile stress; s_{cr}= average crack spacing in principal tensile stress direction in concrete; f_{scr} = local stress (at crack) in conventional reinforcement; f_s = average stress in conventional reinforcement; ρ_s = reinforcement ratio; a_{gg} = maximum aggregate size; w_{cr} = average crack width.

9.1.2.4. Hybrid HSFRC models

The HSFRC in beam CF100-No.5S1-DR-d/2 from Series 2 contained hybrid steel fibers (micro and macro fibers). In the case of this beam, most of the models presented in the previous section were used, except for tension softening which was modified to better account for the tension behaviour of HSFRC containing hybrid fibers. In this study, the tension softening behaviour is modeled using custom input crack-based model which was used to fit experimental data (see **Figure 9.2**). In the first step, a load-crack width curve was experimentally obtained from a flexural test on a HSFRC prism tested according to ASTM C1609 (ASTM, 2019). To convert the load–crack width curve from the flexural test to a direct tension stress–crack width curve, a simplified equation $f_{DT} = 0.417 f_{ASTM}$ was used to convert the flexural strength obtained in the ASTM C1609 test to a direct tension stress (Amin et al., 2015; Bernard et al., 2020). The remaining concrete constitutive models were the same as those described in the previous section.

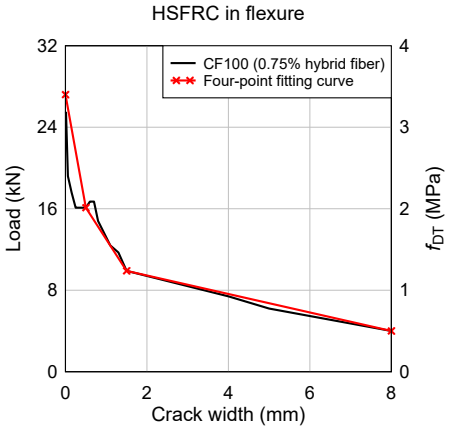

Figure 9.2 Load – crack width curve for HSFRC with hybrid fibers

9.1.3.Mesh sensitivity analysis

The optimal mesh size was selected based on a mesh sensitivity analysis. The accuracy of the FE model was examined by gradually decreasing the mesh size and comparing the ultimate loads in the analysis and experiments. **Figure 9.3** shows the beam FE models with three mesh sizes of 40 mm, 25 mm and 10 mm. The analyses were conducted on two sample beams from Series 1 (C100-No.5HS-DR-d/4) and Series 2 (C100-No.4S1-DR-d/4). **Figure 9.4** shows the normalized load ratio (experimental peak load/predicted peak load) versus number of elements curve and load-displacement curves for the two sample beams. The first mesh (10 mm) resulted in 3186 elements and load ratios of 0.96 & 1.07; the second mesh (25 mm) resulted in 564 elements and load ratios of 0.98 & 1.03, and the final mesh (40 mm) resulted

in 270 elements and an load ratios of 0.83 & 0.9, for beams C100-No.5HS-DR-d/4 & C100-No.4S1-DR-d/4, respectively. The results indicate that the optimal load ratios for both sample specimens were obtained using a mesh size of 25 mm. Moreover, examining the load-displacement curves in **Figure 9.4(b,c)**, the use of a mesh size of 25 mm can well capture the crushing of the cover concrete in both specimens. As a result, the 25 mm mesh size was considered in the subsequent FE analyses.

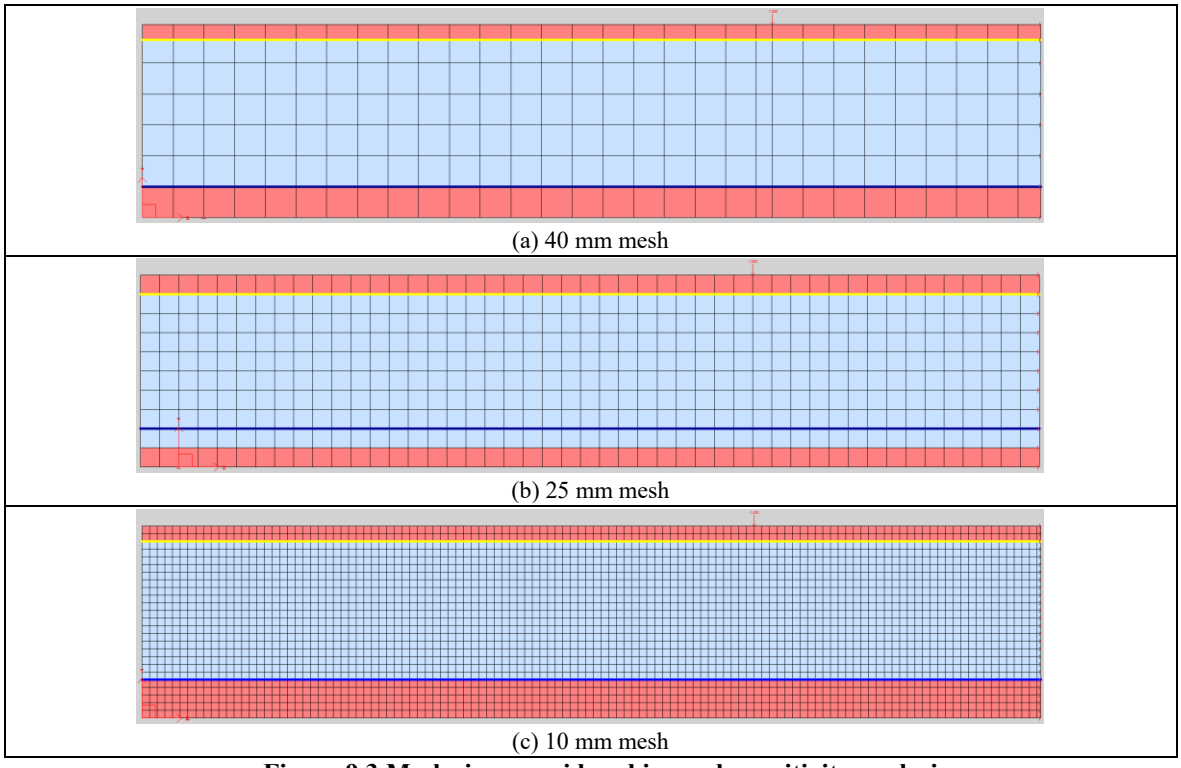

(a) 40 mm mesh

(b) 25 mm mesh

(c) 10 mm mesh

Figure 9.3 Mesh sizes considered in mesh sensitivity analysis

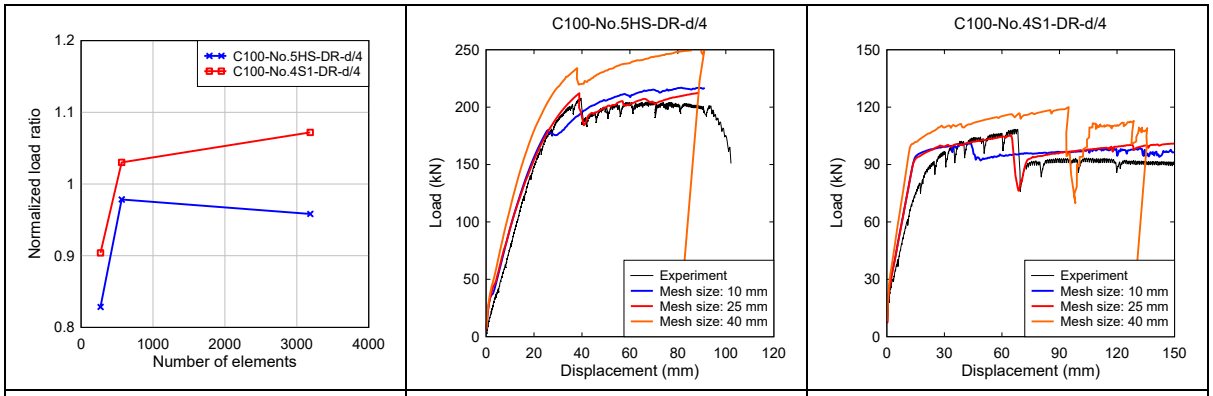

(a) Normalized load ratio vs. No. of elements

(b) Load-displacement of beam C100-No.5HS-DR-d/4

(c) Load-displacement of beam C100-No.4S1-DR-d/4

Figure 9.4 Mesh sensitivity analysis results

9.1.4.Static analysis results

Figure 9.5 - Figure 9.7 show the results of the static FE analyses of the beams in Series 1 (HSC and high-strength steel) and Series 2 (HSC and stainless steel). In general, the numerical results show good agreement with the experimental load-deflection curves, in terms of peak strength, stiffness and general trends of post-peak response (detailed comparison of the results are also presented in **Table 9.4 - Table 9.6**). Considering the beams in Series 1 & 2, the mean experimental-to-predicted ratios for peak load (P_{max}/P_{max}^{num}) and toughness (A_u/A_u^{num}) are found to be 1.04 and 1.10, with coefficient of variation, COVs of 0.053 and 0.231.

Next the static FE analysis results are examined in each series. **Table 9.4** presents the results of the HSC-HSS beams with blast detailing from Series 1. Considering both plain HSC specimens, the mean experimental-to-predicted ratios of peak load (P_{max}/P_{max}^{num}), displacement at peak load ($\Delta_{peak}/\Delta_{peak}^{num}$), failure displacement ($\Delta_{max}/\Delta_{max}^{num}$) and toughness ($A_u/A_u^{num}$) are found to be 1.05, 0.99, 1.08 and 1.15, respectively (see **Table 9.4**). The analysis predicts an ultimate strength of 212 kN at a displacement of 39 mm for beam C100-No.5HS-DR-d/4, which is similar to the experimental result of 208 kN at 40 mm. Similarly, for beam C100-No.4HS-DR-d/4, the analysis showed an ultimate strength of 144 kN at a displacement of 38.4 mm, which is similar to the experimental result of 160.5 kN at 36.3 mm. Importantly, the FE analyses were able to capture the cracking patterns and failure modes of the beams, with bar rupture predicted in both specimens (see **Figure 9.5**).

Table 9.4 Static analysis results (Series 1)

Beam	Experiment				Prediction			
	Peak load (kN)	Displacement (mm)		Toughness (J)	Peak load (kN) [load-ratio]	Displacement (mm) [displacement-ratio]		Toughness (J) [toughness-ratio]
	P_{max}	Peak Δ_{peak}	Failure Δ_{max}	A_u	P_{max}^{a} $[P_{max}/P_{max}^{a}]$	Δ_{peak}^{num} $[\Delta_{peak}/\Delta_{peak}^{num}]$	Failure Δ_{max}^{num} $[\Delta_{max}/\Delta_{max}^{num}]$	A_u^{num} $[A_u/A_u^{num}]$
C100-No.4HS-DR-d/4	160.5	36.3	79.9	9673	144.0 [1.11]	38.4 [0.95]	73.9 [1.08]	8469 [1.14]
C100-No.5HS-DR-d/4	207.9	39.6	96.3	18028	212.2 [0.98]	38.9 [1.02]	88.9 [1.08]	15539 [1.16]
Statistic				Avg.	1.05	0.99	1.08	1.15
				COV	0.088	0.050	0.000	0.012

Note: Δ_{peak} = displacement at P_{max}; P_{max}^{num} = predicted peak load; Δ_{peak}^{num} = predicted displacement at P_{max}^{num}; Δ_{max}^{num} = predicted failure displacement; A_u^{num} = predicted toughness

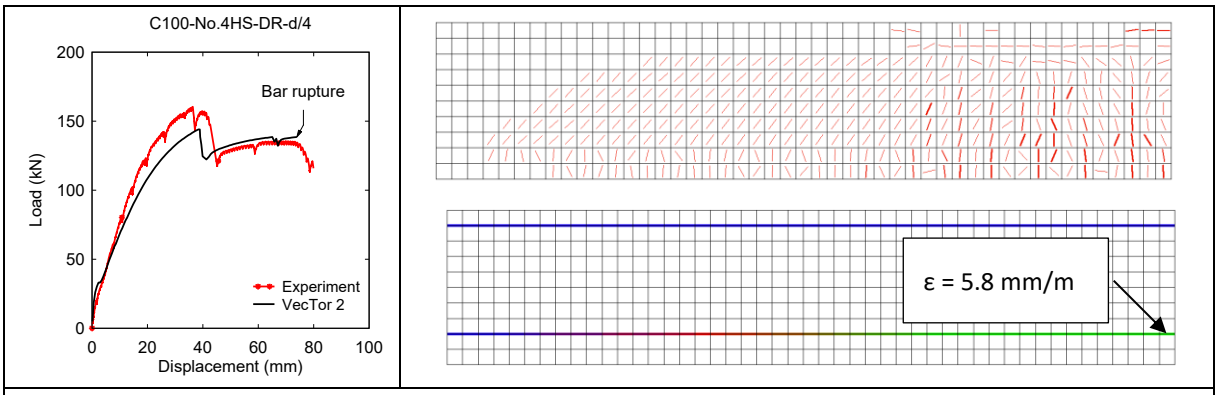

(a) beam C100-No.4HS-DR-d/4

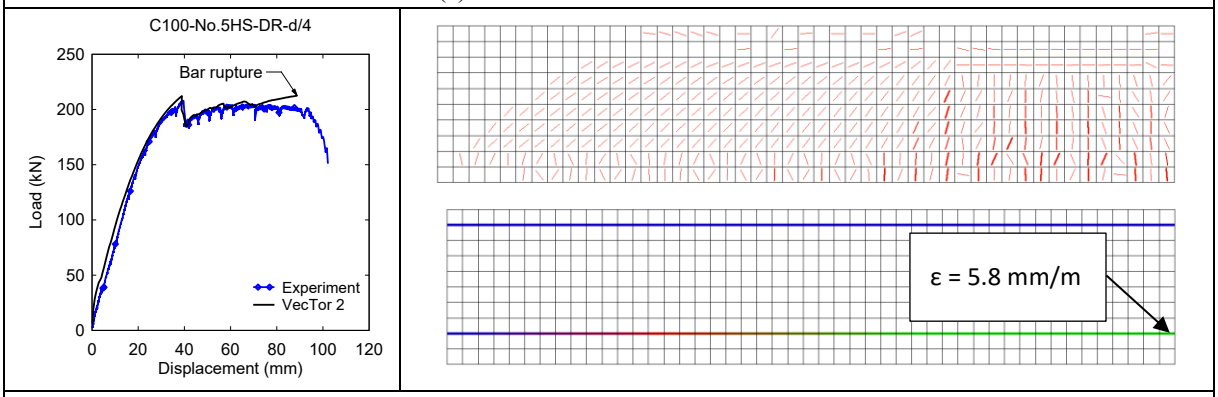

(b) beam C100-No.5HS-DR-d/4

Figure 9.5 Static FE analysis results of Series 1

Next, the static FE analysis results of the HSC-SS beams with nominal detailing from Series 2A are presented in **Table 9.5**. The mean experimental-to-predicted ratios of peak load (P_{max}/P_{max}^{num}), failure displacement ($\Delta_{max}/\Delta_{max}^{num}$) and toughness ($A_u/A_u^{num}$) are found to be 0.99, 1.33 and 1.23, respectively. The FE analysis well predicted the response of beam C100-No.5S1-S with an ultimate strength of 119 kN at a displacement of 43.1 mm, which was similar to the experimental result of 121.6 kN at 42.7 mm. Beam C100-No.5S1-S was predicted to fail in concrete crushing at a displacement of 43.1 mm, which coincided with the experimental observation (see **Figure 9.6**). The FE models were further used to predict the responses of the HSFRC beams built with and without stirrups. In the case of beam CF100-No.5S1-S, which was built with HSFRC and stirrups, the response was well predicted until peak load. In the experiment, the beam sustained a gradual loss in load capacity (50-65% of peak load) until the maximum displacement of 116 mm, however the FE analysis was unable to predict this behaviour. As a result, the beam showed less accurate predictions for maximum displacement and toughness. Nevertheless, the FE analysis was able to capture the cracking patterns and failure modes of the beams (see **Figure 9.6**). For example, the HSFRC beam with stirrups is predicted to fail due to concrete crushing at a predicted maximum displacement (Δ_{max}^{num}) of 56.4 mm, which is similar to the experimental result which consisted of concrete crushing at a displacement of 50 mm (see **Figure 9.6**). Importantly, the shear failure was also captured in beam CF100-No.5S1, which was built without stirrups. Beam CF100-No.5S1 was predicted to fail in shear at a load of 135.9 kN with a corresponding displacement of 16.8 mm, which matched the experimental result of 139.3 kN at 15.8 mm.

Table 9.5 Static analysis results (Series 2A)

Beam	Experiment			Prediction		
	Peak load (kN)	**Displacement (mm)**	**Toughness (J)**	**Peak load (kN) [load-ratio]**	**Displacement (mm) [displacement-ratio]**	**Toughness (J) [toughness-ratio]**
	P_{max}	**Failure** Δ_{max}	A_u	P_{max}^{num} $[P_{max}/P_{max}^{num}]$	**Failure** Δ_{max}^{num} $[\Delta_{max}/\Delta_{max}^{num}]$	A_u^{num} $[A_u/A_u^{num}]$
C100-No.5S1-S	121.6	42.6	4061	119.0 [0.98]	43.1 [0.99]	4068 [1.0]
CF100-No.5S1-S	157.8	115.5	12886	157.6 [1.0]	56.4 [2.05]	7394 [1.74]
CF100-No.5S1	139.3	15.8	1333	135.9 [0.98]	16.8 [0.94]	1419 [0.94]
Statistic			Avg.	0.99	1.33	1.23
			COV	0.012	0.473	0.363

Note: Δ_{peak} = displacement at P_{max}; P_{max}^{num} = predicted peak load; Δ_{peak}^{num} = predicted displacement at P_{max}^{num}; Δ_{max}^{num} = predicted failure displacement; A_u^{num} = predicted toughness

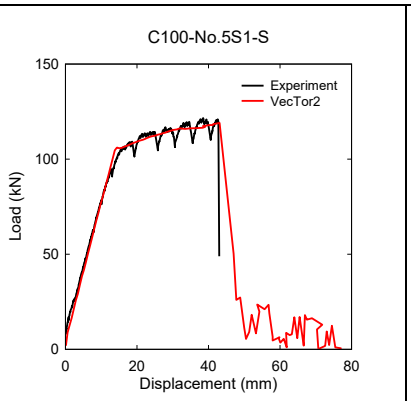

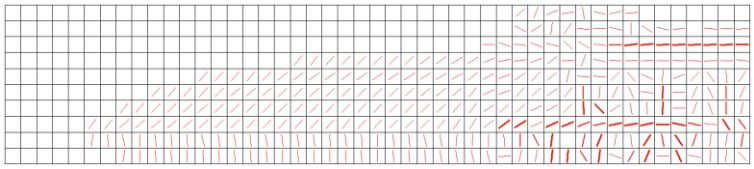

(a) beam C100-No.5S1-S

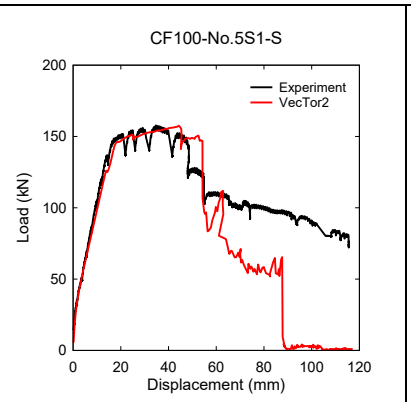

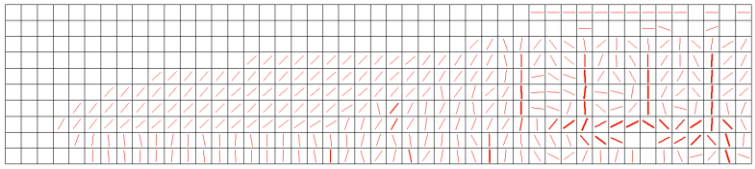

(b) beam CF100-No.5S1-S

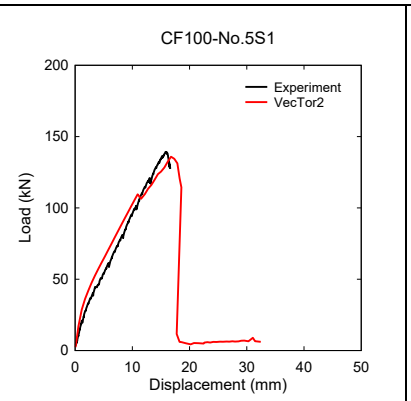

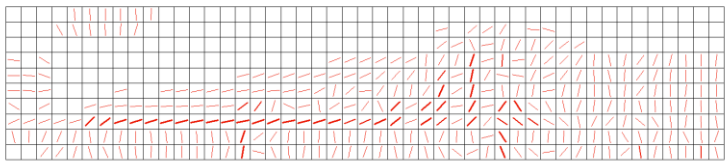

(c) beam CF100-No.5S1

Figure 9.6 Static FE analysis results of Series 2A (nominal detailing)

Finally, **Table 9.6** presents the static FE analysis results of the HSC-SS beams with blast detailing from Series 2B. In general, the numerical results showed good agreement with the experimental load-deflection curves, in terms of peak load, stiffness and general trends of post-peak response. For example, the FE analysis predicts an ultimate strength of 105.3 kN at a displacement of 64.8 mm for beam C100-No.4S1-DR-d/4, which is similar to the experimental result of 108.5 kN at 66.4 mm. In addition, the analysis predicts a load of 101 kN at end of the testing (Δ = 150 mm), which is also reasonable when compared to the experimental result of 90.7 kN. Considering all specimens, the mean experimental-to-predicted ratios of peak load (P_{max}/P_{max}^{num}), load at end of testing (P_{150}/P_{150}^{num}), displacement at peak load ($\Delta_{peak}/\Delta_{peak}^{num}$) and toughness ($A_u/A_u^{num}$) are found to be 1.07, 0.93, 0.93 and 0.98 with corresponding COVs of 0.029, 0.034, 0.175, 0.032, respectively. Importantly, the FE analysis was able to capture the cracking patterns (see **Figure 9.7**), and all the beams are predicted to survive until 150 mm without bar rupture, with concrete crushing occurring in the midspan compression zone.

In conclusion, the results demonstrate that the FE procedure presented in this chapter, with appropriate material models can be used to analyze the shear and flexural behavior of HSC and HSFRC beams reinforced with varying steel types and detailing, under static loads.

Table 9.6 Static analysis results (Series 2B)

Beam	Experiment				Prediction			
	Load (kN)		Displacement (mm)	Toughness (J)	Load (kN) [load-ratio]		Displacement (mm) [displacement-ratio]	Toughness (J)
	P_{max}	@ 150mm P_{150}	Peak Δ_{peak}	A_u	P_{max}^{num} [P_{max}/P_{max}^{num}]	P_{150}^{num} [P_{150}/P_{150}^{num}]	Δ_{peak}^{num} [$\Delta_{peak}/\Delta_{peak}^{num}$]	A_u^{num} [A_u/A_u^{num}]
C100-No.4S1-DR-d/4	108.5	90.7	66.4	13439	105.3 [1.03]	101.0 [0.90]	64.8 [1.02]	14069 [0.96]
C100-No.5S1-DR-d/4	135.7	143.8	46.7	17033	126.7 [1.07]	148.9 [0.97]	68 [0.69]	16748 [1.02]
C100-No.5S2-DR-d/4	169.8	139.6	43.3	19769	155.8 [1.09]	151.5 [0.92]	41.7 [1.04]	20753 [0.95]
CF100-No.5S1-DR-d/2	153.3	129.5	44.2	19250	139.9 [1.10]	142.5 [0.91]	45.6 [0.97]	19797 [0.97]
Statistic				Avg.	1.07	0.93	0.93	0.98
				COV	0.029	0.034	0.175	0.032

Note: P_{max}, P_{max}^{num} = experimental / predicted peak load; P_{150}, P_{150}^{num} = experimental / predicted load at a displacement of 150 mm; Δ_{peak}, Δ_{peak}^{num} = experimental / predicted displacement at P_{max}, A_u, A_u^{num} = predicted toughness.

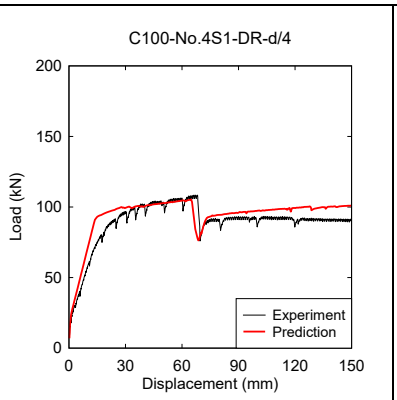

(a) C100-No.4S1-DR-d/4

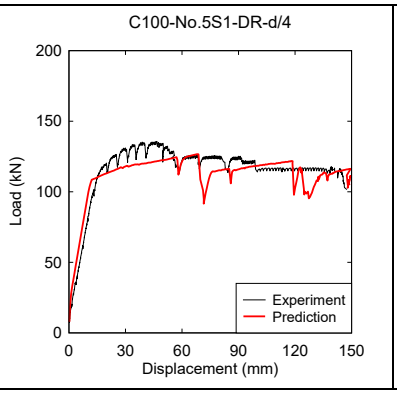

(b) C100-No.5S1-DR-d/4

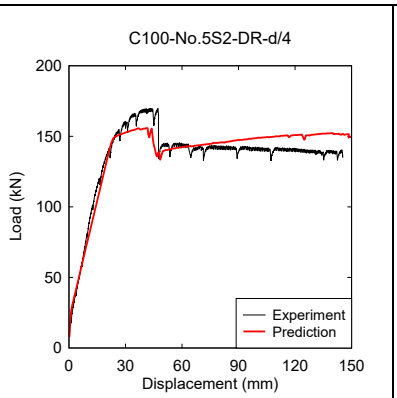

(c) C100-No.5S2-DR-d/4

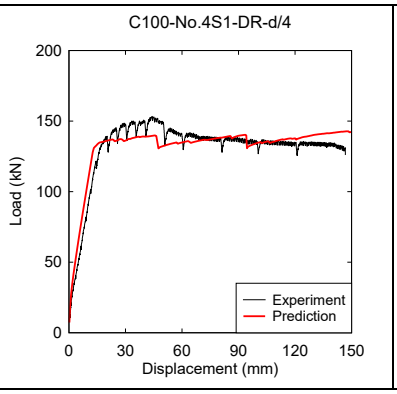

(d) CF100-No.5S1-DR-d/2

Figure 9.7 Static FE analysis results of Series 2B (blast detailing)

9.1.5. Dynamic analysis results

The results of the dynamic FE analyses for the Series 1 and 2 beams are presented in **Table 9.7 - Table 9.9** and **Figure 9.8 - Figure 9.10**, which compare the experimental and analytical maximum mid-span displacements (D_{max} and D_{max}^{num}) and their ratios (D_{max}/D_{max}^{num}). Sample displacement time histories are also shown in **Figure 9.8b**, **Figure 9.9b**, and **Figure 9.10b**. Considering all the beams in Series 1 & 2 and all test shots, the mean D_{max}/D_{max}^{num} ratio using the default damping ratios is found to be 1.04, with a coefficient of variation (COV) of 0.108. Dynamic reaction curves for the beams were also obtained from the analyses and the results for sample beams in each series are shown in **Figure 9.8c, Figure 9.9c**, and **Figure 9.10c**. The mean peak experimental-to-predicted reactions ratios ($P_{max}^{D}/P_{max}^{D-num}$) for all specimens was found to be 1.04 with a COV of 0.137.

Next, the dynamic analysis results are examined in each series. **Table 9.7** examines the blast analysis results of the doubly-reinforced beams with high-strength steel and blast detailing from Series 1. To examine the effect of damping, **Table 9.7** also presents the results for the displacement amplitude during the second positive cycle ($D_{cycle\ 2}$ and ratio $D_{cycle\ 2}/D_{cycle\ 2}^{num}$) under different damping ratios. Considering the four HSC beams in *Group A* and all test shots, the mean D_{max}/D_{max}^{num} ratio using default case (*Case 1)* is found to be 1.03, with a coefficient of variation (COV) of 0.07. Similar results are obtained for *Case 2* with a mean D_{max}/D_{max}^{num} ratio of 1.09 and COV of 0.07. The displacement responses are not as well predicted in the subsequent cycles for Case 1, with a mean $\frac{D_{cycle\ 2}}{D_{cycle\ 2}^{num}}$ ratio of 0.57 for the 2nd cycle amplitude; the response prediction is improved considerably when using the higher damping coefficients in Case 2, with an improved mean ratio of $\frac{D_{cycle\ 2}}{D_{cycle\ 2}^{num}}$ = 0.70. In general, the results indicate that the analysis procedure was able to predict the blast response of the blast-detailed HSC beams with good accuracy up to the first peak, with reduced accuracy at subsequent cycles, with the results sensitive to the choice of damping coefficients. **Table 9.7** presents the results for all beams in terms of peak experimental and predicted reactions, and their ratios ($P_{max}^{D}/P_{max}^{D-num}$). It can be seen that the analytical reaction functions agree reasonably well with the experimental dynamic reactions recorded by the load-cells, with similar results for Case 1 and Case 2.

The FE analysis results of the singly-reinforced beams with stainless steel and nominal detailing from Series 2A are presented in **Table 9.8**. Considering the three HSC and HSFRC beams and all test shots, the mean D_{max}/D_{max}^{num} ratio using the default case is found to be 1.05,

with a coefficient of variation (COV) of 0.084. Similarly, the dynamic reactions were also well predicted with a mean ratio of 1.01 and COV of 0.197. The results showed that the dynamic displacement responses up to peak displacement and dynamic reactions were well predicted.

The FE analysis results of the doubly-reinforced beams with stainless steel and blast detailing from Series 2B are presented in **Table 9.9**. Considering all the beams and all test shots, the average experimental-to-analytical displacement ratio (D_{max}/D_{max}^{num}) and load ratio are found to be 1.03 & 1.07 with a coefficient of variation (COV) of 0.127 & 0.121. In general, the results indicate that the analysis procedure was able to predict the maximum blast response of the stainless steel HSC specimens with good accuracy. The result also confirms blast response of HSFRC beam CF100-No.5S1-DR-d/2 is also reasonably well-predicted.

The foregoing analyses demonstrate that the nonlinear finite element procedure which employed the Disturbed Stress Field Model was able to predict the blast responses of the HSC specimens with adequate accuracy, regardless of steel types. The results however demonstrate the need for further study to examine the effects of damping coefficients when conducting blast analysis. Since tension stiffening response of the concrete might be affected by reinforcement type, further research is also needed to adapt the employed tension stiffening model for the high-strength or stainless reinforcement steel. Further study is also required to better model the fracture response of the high-strength bars due to elevated local stresses at the crack locations.

Table 9.7 Blast analysis results (Series 1)

Beams	Blast ID (psi)	Specimen Response			Predicted Response					
					Case 1			Case 2		
		D_{max} (mm)	$D_{cycle\ 2}$ (mm)	P_{max}^{D} (kN)	D_{max}^{num} $[\frac{D_{max}}{D_{max}^{num}}]$	$D_{cycle\ 2}^{num}$ $[\frac{D_{cycle\ 2}}{D_{cycle\ 2}^{num}}]$	P_{max}^{D-num} $[\frac{P_{max}^{D}}{P_{max}^{D-num}}]$	D_{max}^{num} $[\frac{D_{max}}{D_{max}^{num}}]$	$D_{cycle\ 2}^{num}$ $[\frac{D_{cycle\ 2}}{D_{cycle\ 2}^{num}}]$	P_{max}^{D-num} $[\frac{P_{max}^{D}}{P_{max}^{D-num}}]$
C100-No.4HS-DR-d/4	30	20.4	5.5	97.4	19.6 [1.04]	11.3 [0.49]	116.2 [0.84]	18.8 [1.09]	8.8 [0.63]	111.6 [0.87]
	50	35.6	11.1	147.1	33.4 [1.07]	16.9 [0.66]	147.9 [0.99]	32.0 [1.11]	12.8 [0.87]	145.6 [1.01]
	70	52.6	25.0	193.6	56.4 [0.93]	41.6 [0.6]	164.5 [1.18]	51.7 [1.02]	35.4 [0.71]	171.7 [1.13]
C100-No.4HS-DR-d/4 (x1)	70	53.9	30.4	191	57.2 [0.94]	42.3 [0.72]	164.4 [1.16]	52.5 [1.03]	36.0 [0.84]	173.1 [1.10]
C100-No.5HS-DR-d/4	30	15.2	0.9	111.1	15.5 [0.98]	8.6 [0.1]	138.6 [0.8]	15.2 [1.0]	12.7 [0.07]	133.3 [0.83]
	50	26.8	5.1	188.2	26.1 [1.03]	14.6 [0.35]	191.8 [0.98]	25.3 [1.06]	12.4 [0.41]	187.7 [1.0]
	70	41.4	14.5	247.2	37.0 [1.12]	19.5 [0.74]	219.6 [1.13]	35.4 [1.17]	13.9 [1.04]	218.1 [1.13]
	90	56.4	21.4	277.6	50.2 [1.12]	35.5 [0.60]	239.1 [1.16]	46.7 [1.21]	30.1 [0.71]	238.5 [1.16]
C100-No.5HS-DR-d/4 (x1)	90	51.7	28.7	263.7	48.8 [1.06]	34.5 [0.83]	242.4 [1.09]	45.6 [1.13]	29.3 [0.98]	238.3 [1.11]
				AVG.	1.03	0.57	1.04	1.09	0.70	1.04
				COV	0.07	0.40	0.14	0.07	0.43	0.11

Note: Case 1: damping ratios = 0.5% & 0.75% of critical for mode 1 & 2; Case 2: damping ratios = 1% & 5% of critical for mode 1 & 2; D_{max} = maximum displacement; $D_{cycle\ 2}$ = displacement amplitude @ second peak; P_{max}^{D} = peak dynamic load; D_{max}^{num}= predicted maximum displacement; $D_{cycle\ 2}^{num}$= predicted displacement amplitude @ second peak; P_{max}^{D-num}= predicted peak dynamic load

Table 9.8 Blast analysis results (Series 2A)

Beams	Blast ID	Experiment					Analysis			
		P_r (kPa)	I_r (kPa·ms)	t_d (ms)	D_{max} (mm)	P_{max} (kN)	D_{max}^{num} (mm)	D_{max}/D_{max}^{num}	P_{max}^{D-num} (kN)	P_{max}/P_{max}^{D-num}
C100-No.5S1-S	30	46.7	371.6	21.5	16.6	92	17.1	0.97	121.6	0.76
	50	57.6	539.0	23.1	30.5	132.7	28.8	1.06	131.4	1.01
	70	76.1	707.3	24.4	134	168.4	-*			
CF100-No.5S1-S	30	43.0	376.7	21.9	14.5	99	15.4	0.94	127.1	0.78
	50	56.8	481.8	22.9	21.8	136.3	22.45	0.97	133.1	1.02
	70	75.3	764.6	24.4	50.2	163	47.7	1.05	145.5	1.12
	90	89.4	841.5	24.7	85.0	207.3	73.8	1.15	155.7	1.33
CF100-No.5S1	30	41.9	350.3	21.1	13.8	115.7	11.6	1.19	131.0	0.88
	50	57.6	551.6	21.3	24.0	180	22.8	1.05	153.0	1.18
	70	80.8	713.0	22.8	117.8	216.9	-*			
							Mean	1.05		1.01
							COV	0.084		0.197

*: Specimen failed in analysis.

Table 9.9 Blast analysis results (Series 2B)

Beams	Blast ID	Experiment					Analysis			
		P_r (kPa)	I_r (kPa·ms)	t_d (ms)	D_{max} (mm)	P_{max}^{D} (kN)	D_{max}^{num} (mm)	D_{max}/D_{max}^{num}	P_{max}^{D-num} (kN)	P_{max}/P_{max}^{D-num}
C100-No.4S1-DR-d/4	1	45.4	369.4	20.6	19.8	91.7	18.5	1.07	109.0	0.84
	2	56.1	503.7	21.2	36.3	113.4	32.8	1.11	121.3	0.94
	3	84.1	697.9	22	61.4	139.7	66.7	0.92	129.1	1.08
	4	94.2	870.8	24.3	108.9	141.1	99.7	1.09	128.3	1.10
C100-No.5S1-DR-d/4	1	45.4	359.2	20.7	18.9	115.8	17.7	1.07	134.6	0.86
	2	62.6	524.9	22	27.6	133.4	28.9	0.95	133.4	1.00
	3	84.3	723.5	24.5	49.1	159.6	54.0	0.91	149.3	1.07
	4	92.3	900.4	24.9	74.7	181.7	81.4	0.92	153.5	1.18
C100-No.5S1-DR-d/4 [x1]	4	84.6	851.6	24.6	65.6	201.3	70.5	0.93	152.2	1.32
CF100-No.5S1-DR-d/2	1	39.8	379.9	21.1	17.1	141.2	11.8	1.45	137.2	1.03
	2	64.7	534	21.8	23.8	187.6	23.1	1.03	168.3	1.11
	3	78.4	713.4	22.1	39.2	210.7	41.2	0.95	173.7	1.21
	4	87.2	854.3	23.4	59.3	231	62.3	0.95	202.1	1.14
C100-No.5S2-DR-d/4	1	46.2	341.1	20.2	16.9	113.4	16.1	1.05	119.1	0.95
	2	64.6	523.3	21.2	27.0	172.4	27.2	0.99	170.2	1.01
	3	74.8	691.8	21.8	45.0	215.8	45.6	0.99	177.5	1.22
	4	84.3	897.9	24.0	74.3	207.0	64.5	1.15	184.7	1.12
							Mean	1.03		1.07
							COV	0.127		0.121

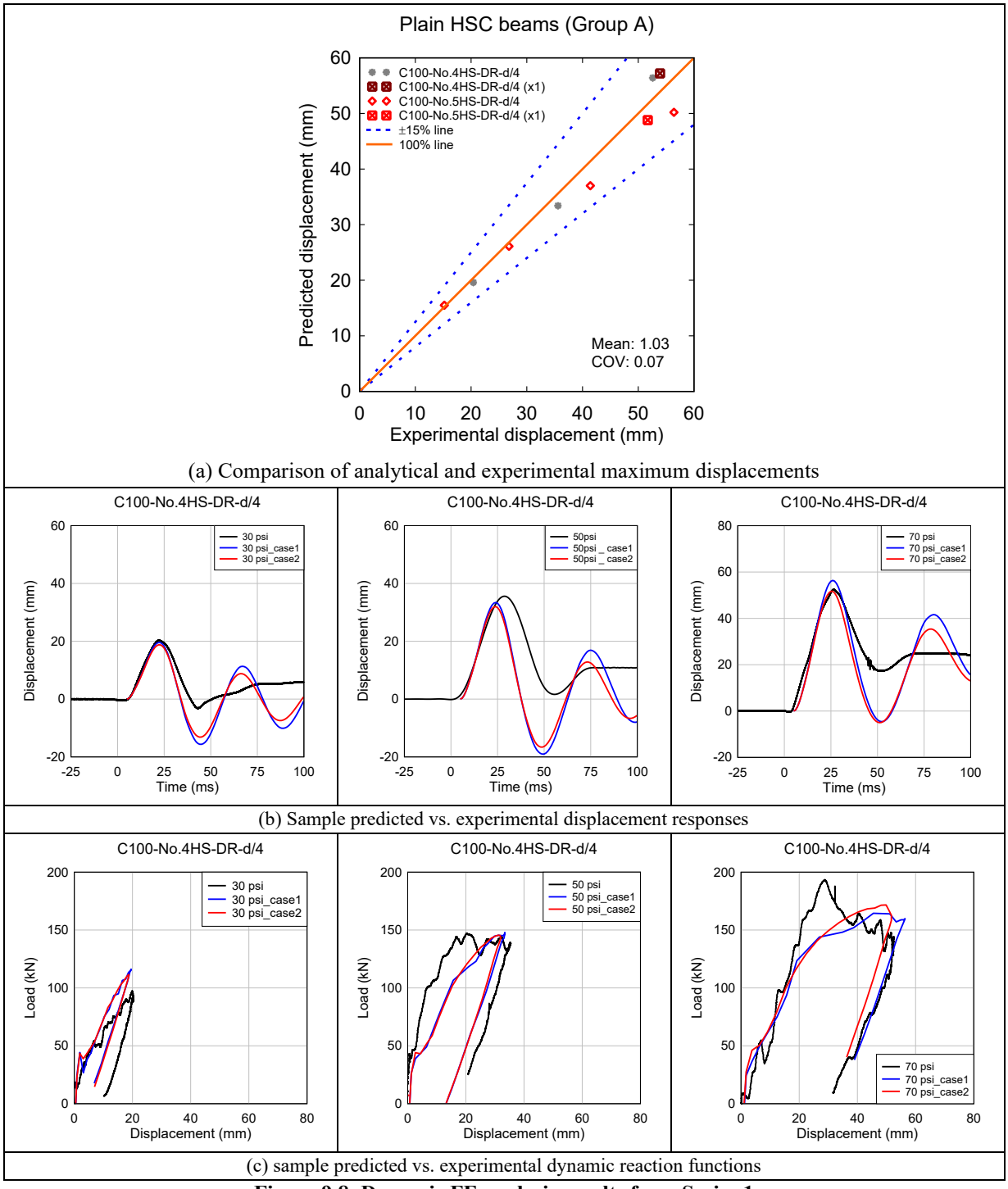

(a) Comparison of analytical and experimental maximum displacements

(b) Sample predicted vs. experimental displacement responses

(c) sample predicted vs. experimental dynamic reaction functions

Figure 9.8 Dynamic FE analysis results from Series 1

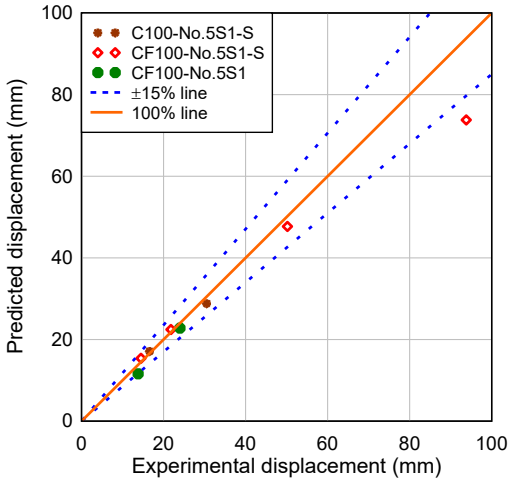

(a) Comparison of analytical and experimental maximum displacements

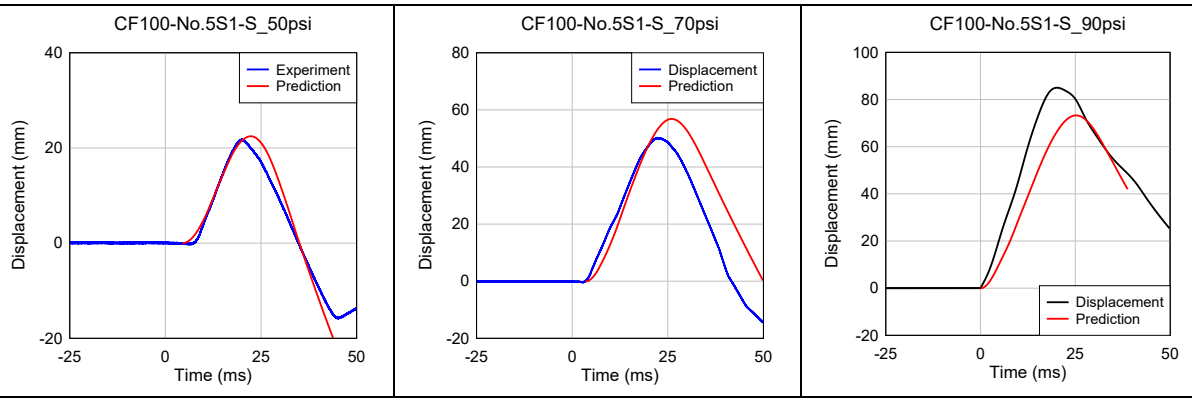

(b) sample predicted vs. experimental displacement response

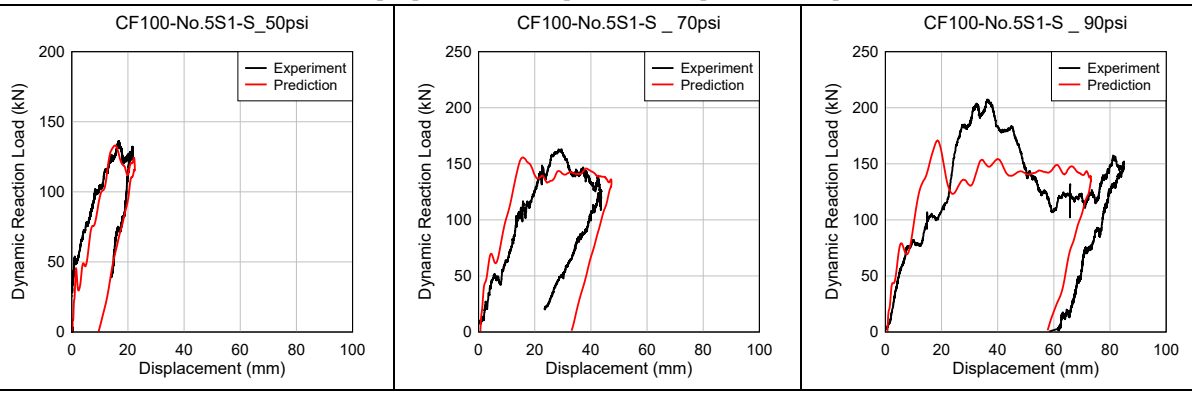

(c) sample predicted vs. experimental dynamic reaction functions

Figure 9.9 Dynamic FE analysis results of Series 2A (nominal detailing)

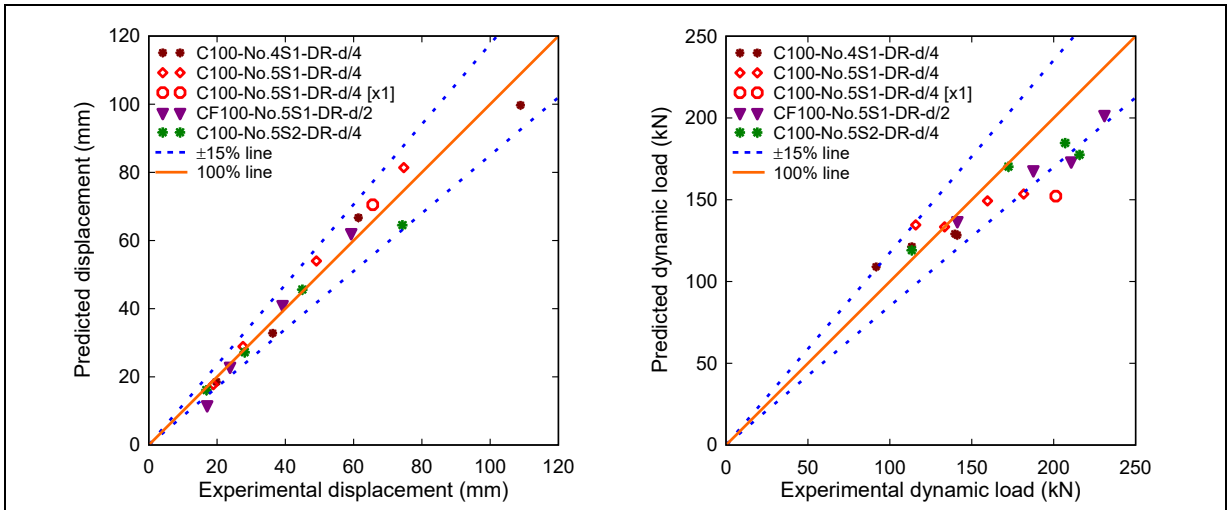

(a) Comparison of analytical and experimental maximum displacements & dynamic peak load

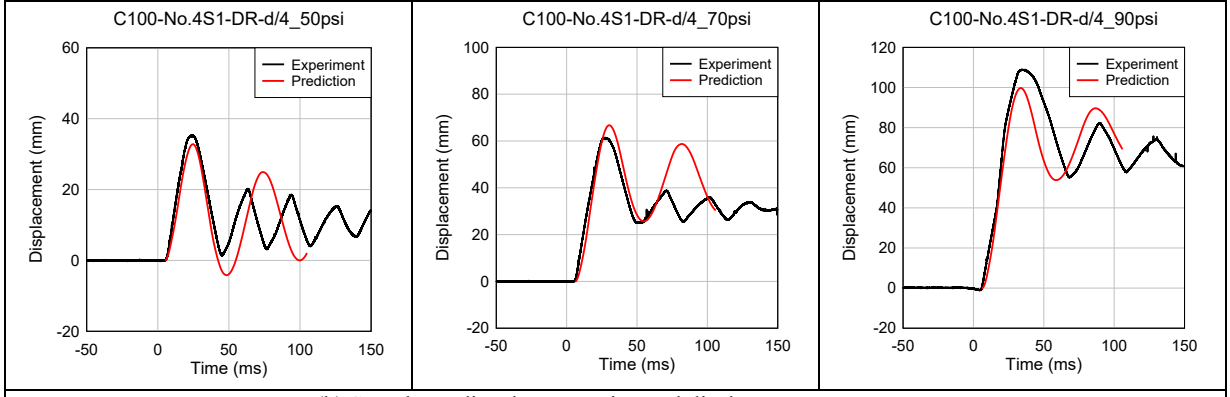

(b) Sample predicted vs. experimental displacement responses

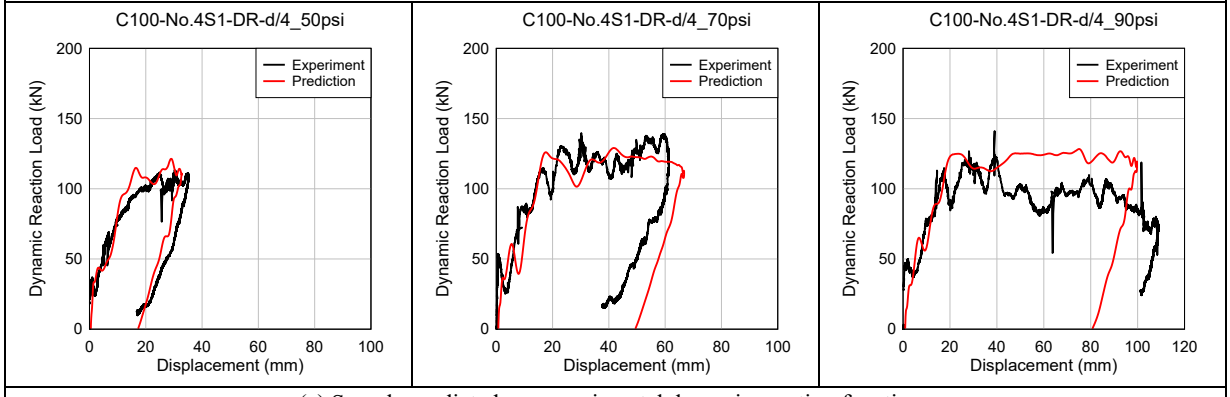

(c) Sample predicted vs. experimental dynamic reaction functions

Figure 9.10 Dynamic FE analysis results from Series 2B (blast detailing)

9.2 Phase 2 FEM analysis: UHPC beams

9.2.1. 3D FEM model

The dynamic response of the UHPC beams was investigated using the explicit dynamic nonlinear finite element software LS-DYNA (Hallquist, 2007). **Figure 9.11a** shows the 3D models used in the simulations. The material parameters for the model are summarized in **Table 9.10**. Eight node solid hexahedron cube elements (*SECTION_SOLID*), with a mesh size of 10 × 10 × 10 mm were used for the UHPC concrete, while two-node Hughes-Liu beam elements (*SECTION_BEAM*), with a size of 10 mm, were used to model the longitudinal and transverse reinforcement in the beams. Perfect bond and strain compatibility between the steel and concrete were assumed by linking the nodes of the concrete and steel bars via the keyword *CONSTRAINED_LAGRANGE_IN_SOLID*. The resulting mesh for a typical beam, consisting of 61000 solid concrete elements and 976 beam elements for the longitudinal reinforcement is shown in **Figure 9.11a**. In addition, as shown in **Figure 9.11b**, the load-transfer device (LTD) of the shock-tube was also modeled using rigid shell elements (*SECTION_SHELL*) including three parts consisting of: two side-by-side rigid steel panels fixed at the top/bottom and a middle portion steel panel. To allow free lateral movement of the middle portion of the LTD, the three parts of the rigid panels are connected using keywords *CONSTRAINED_JOINT_SPHERICAL* at corners. Blast loading on the LTD was simulated by applying idealized triangular pressure time histories on the load transfer device with the *LOAD_SEGMENT_SET* keycard in *LS-DYNA*. The sample idealized pressure-time history for beam U2-No.4HS-DR-d/2 (R) is shown in **Figure 9.11c**. The contact between the LTD and specimens was defined by using the keyword *CONTACT_AUTOMATIC_SURFACE_TO_SURFACE* (Hallquist, 2007). The simply-supported boundary condition was simulated by keyword *SPC_NODES_SET*.

Table 9.10 Material parameters in FE model

Member	Section identifiers	Material model	Main Parameters	Values
Load transfer device	Section_Shell	MAT_RIGID (020)	Density	7800 kg/m^3
			Poisson's ratio	0.3
			Young's modulus	200 GPa
Transverse reinf.	Section_Beam	MAT_PLASTIC_KINEMATIC (003)	Density	7800 kg/m^3
			Poisson's ratio	0.3
			Young's modulus	200 GPa
			Yield stress	550 MPa
			Failure strain	0.15
			Strain rate parameter C	7.274e7
			Strain rate parameter P	11.22
Longitudinal reinforcement	Section_Beam	MAT_PIECEWISE_LINEAR_PLASTICITY (024)	Density	7800 kg/m^3
			Poisson's ratio	0.3
			Young's modulus	200 GPa
			Strain rate parameter C	7.274e7
			Strain rate parameter P	11.22
Concrete	Section_Solid	MAT_WINFRITH_CONCRETE (084)	See **Table 9.11**	
		MAT_CSCM (159)	See **Table 9.12**	

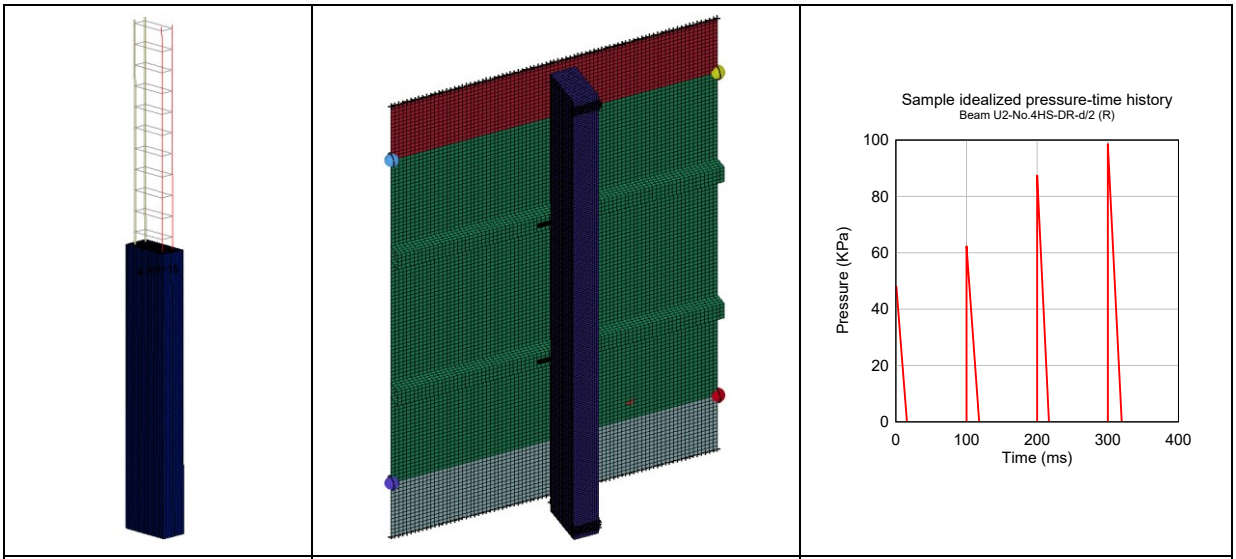

(a) FE model mesh | (b) FE model: beam, boundary conditions and LTD | (c) Sample idealized pressure-time history for beam U2-No.4HS-DR-d/2 (R)

Figure 9.11 Three-dimensional numerical models

9.2.2. 3D FEM material model

LS-DYNA provides many concrete models to predict the dynamic response of RC concrete such as Geologic_Cap_Model (MAT_025), Concrete_Damage_Rel3 (MAT_072R3), Winfrith_Concrete (MAT_084), Brittle_damage (MAT_096), Johnson_Holmquist_Concrete (MAT_111) and CSCM (MAT_159). For normal-strength concrete, Concrete_Damage_Rel3 (MAT_072R3), CSCM_Concrete (MAT_159) and Winfrith_Concrete (MAT_084) only required simple inputs for the uniaxial compression and tension strength. UHPC has different properties due to its higher strength, toughness and tensile strength. As a result, the previous static, impact and blast response of UHPC structural components in previous studies were only predicted by using the four concrete models: 1) Concrete_Damage_Rel3 (MAT_072R3) (Chen et al., 2019; Lai et al., 2018; Li & Wu, 2018; Liu et al., 2022a; Liu et al., 2017a; Liu et al., 2018a; Liu et al., 2017b; Mao et al., 2014; Mao & Barnett, 2017; Oppong et al., 2021; Su et al., 2022; Wu et al., 2019b; Xu et al., 2020; Yin et al., 2019a, 2019b; Zhang et al., 2021; Liao et al., 2022), 2) Winfrith_Concrete (MAT_084) (Thai & Kim, 2015; Thiagarajan et al., 2015; Zhang et al., 2017b; Zhang et al., 2017c; Lee et al., 2020; Yan et al., 2022), 3) Johnson_Holmquist_Concrete (MAT_111) (Tai, 2009; Lai et al., 2015; Ren et al., 2016; Liu et al., 2018b; Cao et al., 2020; Wan et al., 2021; Ren et al., 2022) and 4) CSCM (MAT_159) (Fan et al., 2018a; Fan et al., 2018b; Fan et al., 2019; Fan et al., 2020a; Fan et al., 2020b; Li et al., 2020; Wang et al., 2019b; Wang et al., 2019a; Wei et al., 2019; Yang et al., 2021; Gholipour & Billah, 2022a, 2022b).

Guo et al. (2018) noted that using the K&C model showed low accuracy and over-predicted displacements of UHPC structural components. Guo et al. (2018) calibrated the partial parameters of the CSCM model to well predict the dynamic response of UHPC members. In addition, Saini et al. (2021), Wei et al. (2021), Xu et al. (2021) also calibrated and verified those parameters under the low-velocity drop hammer test. In addition, Jia et al. (2021) further calibrated fracture energy hardening parameters and validated calibration by accurately predicting the impact response of UHPC components from other studies. In this research program, the CSCM model is adopted for analysis. However, the calibration of the CSCM model does not include the effect of fiber content. As a result, the Winfrith_Concrete model is also considered to account for the effect of fiber content.

This section describes the FEM models used in the analysis including steel models for the longitudinal bars & stirrups, and concrete models (Winfrith_Concrete model & CSCM

model) for the UHPC. In addition, simulated material tests and static tests were performed to validate the accuracy of the concrete models.

9.2.2.1. Reinforcement model

The stress-strain response of the longitudinal steel was modelled using Material type 024 (*MAT_PIECEWISE_LINEAR_PLASTICITY*), This model is well suited for elastic-plastic steel materials (Li & Wu, 2018). **Figure 9.12** compares the simulated stress-strain curves of ordinary, high-strength and stainless steel to their corresponding experimental coupon data. The ordinary steel was modelled using a bi-linear elastic-plastic curve (see **Figure 9.12a**) with input values of elastic modulus, yield stress, tangent modulus and failure strain. In addition, MAT_024 also allows users to use a maximum of eight points to define a stress-strain curve. **Figure 9.12(b,c)** compare the simplified eight-point curves with coupon test results, indicating a well-matched non-linear portion for the high-strength and stainless steel reinforcement. The normal-strength 6.3 mm wire used in the stirrups was modelled using a bi-linear, elastic-plastic model (*MAT_PLASTIC_KINEMATIC, MAT_003*). The strain rate effect in all the reinforcement models was taken into account using the Cowper and Symonds Model, which scaled the yield stress with the factor (Hallquist, 2007). The values of parameters C and P were taken as 7.274×10^7 and 11.22 and adopted from previous studies (Yoo et al., 2015; Fujikake et al., 2006b). The detailed inputs for the reinforcement models can be seen in **Table 9.10**.

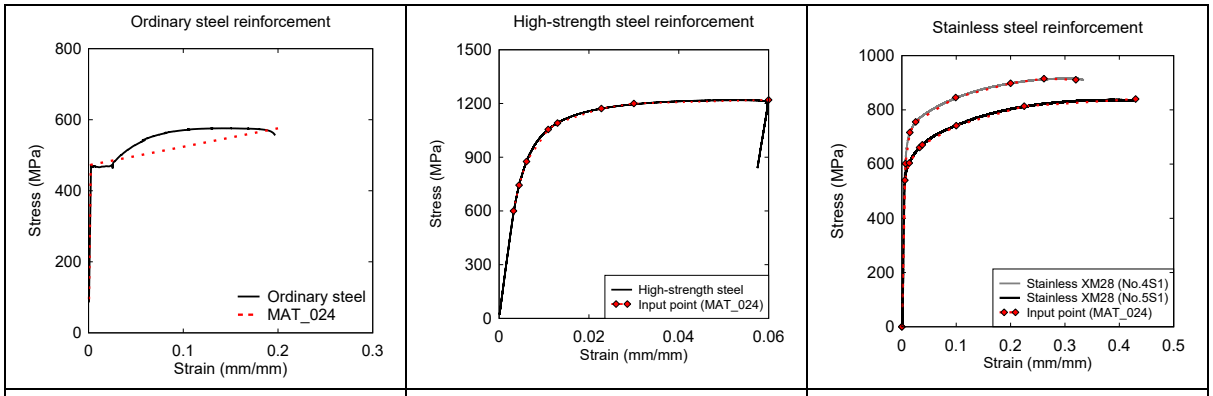

(a) Ordinary steel | (b) High-strength steel model | (c) Stainless steel model

Figure 9.12 Reinforcement steel models

9.2.2.2. Winfrith_Concrete model

The Winfrith concrete model (MAT_084) is based upon a four-parameter (a, b, k_1, k_2) model proposed by Ottosen (Schwer, 2010), described in **Equation 9-1**. Those four parameters are functions of unconfined tensile to compressive strength ratio (f_t/f_c') and can be

experimentally determined from uniaxial compression ($\theta = 60°$), uniaxial tension ($\theta = 0°$), biaxial compression ($\theta = 0°$) and triaxial compression ($\theta = 60°$) tests (Wu et al., 2012).

$$F(I_1, J_2, cos3\theta) = a\frac{J_2}{(f_c')^2} + \lambda\frac{\sqrt{J_2}}{f_c'} + b\frac{I_1}{f_c'} - 1$$

$$\lambda = \begin{cases} k_1\, cos[\frac{1}{3}cos^{-1}(k_2 cos(3\theta))] & cos(3\theta) \geq 0 \\ k_1\, cos[\frac{\pi}{3} - \frac{1}{3}cos^{-1}(-k_2 cos(3\theta))] & cos(3\theta) \leq 0 \end{cases} \qquad 9\text{-}1$$

$$cos(3\theta) = \frac{3\sqrt{3}}{2}\frac{J_3}{J_2^{3/2}}$$

Where, I_1 = First invariant of the stress tensor; J_2 & J_3 = second and third invariant of the deviatoric stress tensor; f_c' = concrete compressive strength.

The Winfrith concrete model is a simple input model, which only requires inputting the mass density, tangent modulus, Poisson's ratio, uniaxial compressive strength, uniaxial tensile strength, aggregate size and rate effects. **Table 9.11** presents the input values for these material properties for the UHPC for the Winfrith concrete model. The elastic modulus of UHPC is determined using **Equation 9-2** as per the FHWA recommendation (Graybeal, 2006; Russell et al., 2013). The Poisson's ratio of UHPC is adopted as 0.2, according to the recommendations by Graybeal (2006). The input value for uniaxial compressive strength is determined from the experiment. The compressive strength (f_c') and tensile strength (f_t') are adopted from the experimental data in **Section 3.3.4**. The Winfrith concrete model also offers a strain rate effects option with distinguishing crack models. For example, the Winfrith concrete model with strain rate effect takes account of the crack model using Griffith's fracture criterion (RATE = 0). In comparison, the model without strain rate effect used a tensile stress-crack width curve to simulate tension behaviour (RATE = 1 or 2) (Schwer, 2011). Sturt (2019) noted that RATE=2 includes an improved crack calculation algorithm to improve material stability when compared to RATE =1. Therefore, RATE=2 with improved material stability and omitting strain rate effects is used in this study. The corresponding crack model using "RATE = 2" is a linear descending curve. The model requires inputting the crack width at which normal tensile stress goes to zero in parameter "FE". Hoang and Fehling (2017) tested 36 prisms under the direct tension test and found that the tensile strength decreased to zero when the crack width reached 5 mm, therefore this value (5 mm) was input for parameter "FE" in the model for UHPC. An

erosion algorithm（MAT_ADD_EROSION) was included in selected beam analyses to delete the failure elements. This keyword included 14 different erosion criteria. However, it is noted that none of them has a direct physical correlation with the concrete damage during impact or blast testing (Sagals et al., 2011). Sagals et al. (2011) chose maximum (governs erosion in tension, positive value) and minimum (governs erosion in compression, negative value) principal stress for erosion criteria. In this study, the maximum principal strain was shown to be the most sensitive erosion criterion (Thai & Kim, 2015). The principal strains from ±7% to ±11% were selected by Thai and Kim (2015). Zhang et al. (2017c) used 0.04 for maximum principal stress by comparing the test data. In this research, values of 0.04 and -0.08 were selected for maximum and minimum principal stress by trial and error.

$$E = 3837\sqrt{f_c'} \qquad 9\text{-}2$$

Table 9.11 Material parameters for the Winfrith_Concrete model (MAT_084)

Parameter	Description	Values		Unit
		UHPC with 2% fiber	UHPC with 3% fiber	
RO	Mass Density	2600	2600	kg/m^3
TM	Tangent modulus	47000	47000	MPa
PR	Poisson's ratio	0.2	0.2	-
UCS	Uniaxial comp. strength	150	150	MPa
UTS	Uniaxial tensile strength	9.82	10.78	MPa
FE	Crack width at which crack-normal tensile stress goes to zero	5	5	mm
ASIZE	Aggregate size	5	5	mm
RATE	Rate effect	2 (without rate effect)		-

9.2.2.3. CSCM model

The other concrete model used to simulate the behaviour of UHPC was the MAT_CSCM (MAT_159) material model. This material model takes into account three meridians (compression, tensile and torsion) for the shear failure surface, including compression state determined from the triaxial compression test (parameters: α, λ, β and θ), torsion state determined from the torsion test (parameters: α_1, λ_1, β_1 and θ_1) and tensile state determined from triaxial extension test (parameters: α_2, λ_2, β_2 and θ_2). Guo et al. (2018) proposed meridian fitting functions to define the parameters of triaxial compression, torsion and tensile surfaces for UHPC material. Jia et al. (2021) further calibrated cap parameters, damage parameters, strain rate parameters, and hardening parameters of the CSCM model. **Table 9.12** lists the detailed input parameters of UHPC material having a concrete strength of

150 MPa as calibrated by Jia et al. (2021). To compare the simulated results of the Winfrith_Concrete model, simulations with/without strain rate effects are considered.

Table 9.12 Material parameters for CSCM model (MAT_159, adopted from Jia et al., 2021)

Card	Parameters	Description	Value	Unit
1	RO	Mass density	2600	kg/m^3
	NPLOT	Controls option for component 7 to the d3plot database	1	-
	INCRE	Maximum strain increment for subincrementation	0	-
	IRATE	Rate effects options	1	-
	ERODE	Elements erode parameter	0	-
	RECOV	The modulus recovered option	1	-
	ITRETRC	Cap retraction option	0	-
2	PRED	Pre-existing damage	0	-
3	G	Shear modulus	1.958×10^4	MPa
	K	Bulk modulus	2.611×10^4	MPa
	α	Tri-axial compression surface constant term	90.02	MPa
	θ	Tri-axial compression surface linear term	0.2257	-
	λ	Tri-axial compression surface nonlinear term	75.67	MPa
	β	Tri-axial compression surface exponent	0.00488	MPa^{-1}
	NH	Hardening initiation	150	-
	CH	Hardening rate	0.98	-
4	α1	Torsion surface constant term	1	-
	θ1	Torsion surface linear term	0	MPa^{-1}
	λ1	Torsion surface nonlinear term	0.4226	-
	β1	Torsion surface exponent	0.00138	MPa^{-1}
	α2	Tri-axial extension surface constant term	1	-
	θ2	Tri-axial extension surface linear term	0	MPa^{-1}
	λ2	Tri-axial extension surface nonlinear term	0.5	-
	β2	Tri-axial extension surface exponent	0.00108	MPa^{-1}
5	R	Cap aspect ratio	3.5664	-
	XD	Cap initial location	458.86	MPa
	W	Maximum plastic volume compaction	0.00522	-
	D1	Linear shape parameter	2.254×10^{-10}	MPa^{-1}
	D2	Quadratic shape parameter	8.461×10^{-6}	MPa^{-2}
6	B	Ductile shape softening parameter	20	-
	GFC	Fracture energy in uniaxial stress	117.7	MPa · mm
	D	Brittle shape softening parameter	500	-
	GFT	Fracture energy in uniaxial tension	5.89	MPa · mm
	GFS	Fracture energy in pure shear stress	5.89	MPa · mm
	PWRC	Shear-to-compression transition parameter	5	-
	PWRT	Shear-to-tension transition parameter	1	-
	PMOD	Modify moderate pressure softening parameter	0	-
7	ETA0C	Rate effects parameter for uniaxial compressive stress	3.043×10^{-5}	-
	NC	Rate effects power for uniaxial compressive stress	0.8703	-
	ETAOT	Rate effects parameter for uniaxial tensile stress	2.155×10^{-4}	-
	NT	Rate effects power for uniaxial tensile stress	0.478	-
	OVERC	Maximum overstress allowed in compression	1000	MPa
	OVERT	Maximum overstress allowed in tension	50	MPa
	SRATE	Ratio of effective shear stress to tensile stress fluidity parameters	1	-
	REP0W	Power which increases fracture energy with rate effects	1	-

9.2.2.4. Model validation (material test)

To validate the UHPC material models, numerical simulations of the uniaxial compression and direct tension tests were conducted. A previous study (Guo et al., 2018) conducted uniaxial tensile and compressive tests using a single solid element simulation approach to get tensile or compressive stress-strain curves of UHPC. Schwer (2011) compared uniaxial compression test results of a unit cube element (a single solid hexahedra element) and a cylinder. The results showed that axial stress-strain responses are nearly identical (Schwer, 2011). However, in this study, to better compare the simulated results to the experimental data, the numerical material tests in LS-DYNA are conducted using the same dimensions used in the experimental material tests. The numerical uniaxial compression test was conducted on a UHPC cylinder with a dimension of Φ75×150 mm. The mesh sizes were chosen as 20 elements in the circumferential direction, 10 elements in the radius direction and 30 elements in the length direction (see **Figure 9.13a**). A numerical simulation of a direct tension test was also conducted using a 50×50×432 mm prism. The element size for the concrete was 5 mm in this test (see **Figure 9.13b**). The keyword **PRESCRIBED_MOTION* was used for the displacement control in the compression and tension test. The loading rates were chosen as 0.15 mm/s and 0.025 mm/s, respectively.

Figure 9.13(c,d) show the simulated stress-strain curves of the Winfrith_Concrete model and CSCM models in uniaxial compression and tension. First, examining the compression behaviour in **Figure 9.13c**, the Winfrith concrete model results in a bi-linear uniaxial compressive stress-strain curve with an elastic modulus defined in the material card. The failure strain was determined by the minimum principal strain at failure in the erosion algorithm (MAT_ADD_EROSION). It is noted that the post-peak strain-softening response is not captured in this simulation (Schwer, 2011). In comparison, the stress-strain curve produced by the CSCM model showed a similar elastic portion but a well-defined post-peak softening response. As noted in previous studies (Guo et al., 2018; Jia et al., 2021), parameters B and D control the ductile softening behavior and can be calibrated by trial and error through single element numerical simulation. Next, the simulated tension stress-strain curves are shown in **Figure 9.13d**. The use of the Winfrith concrete model results in the same peak tensile strength as the experimental direct tension test and similar post-peak response. While the calibration of UHPC material is based on tensile strength of 8 MPa for the CSCM model, which is slightly lower than the experimental data.

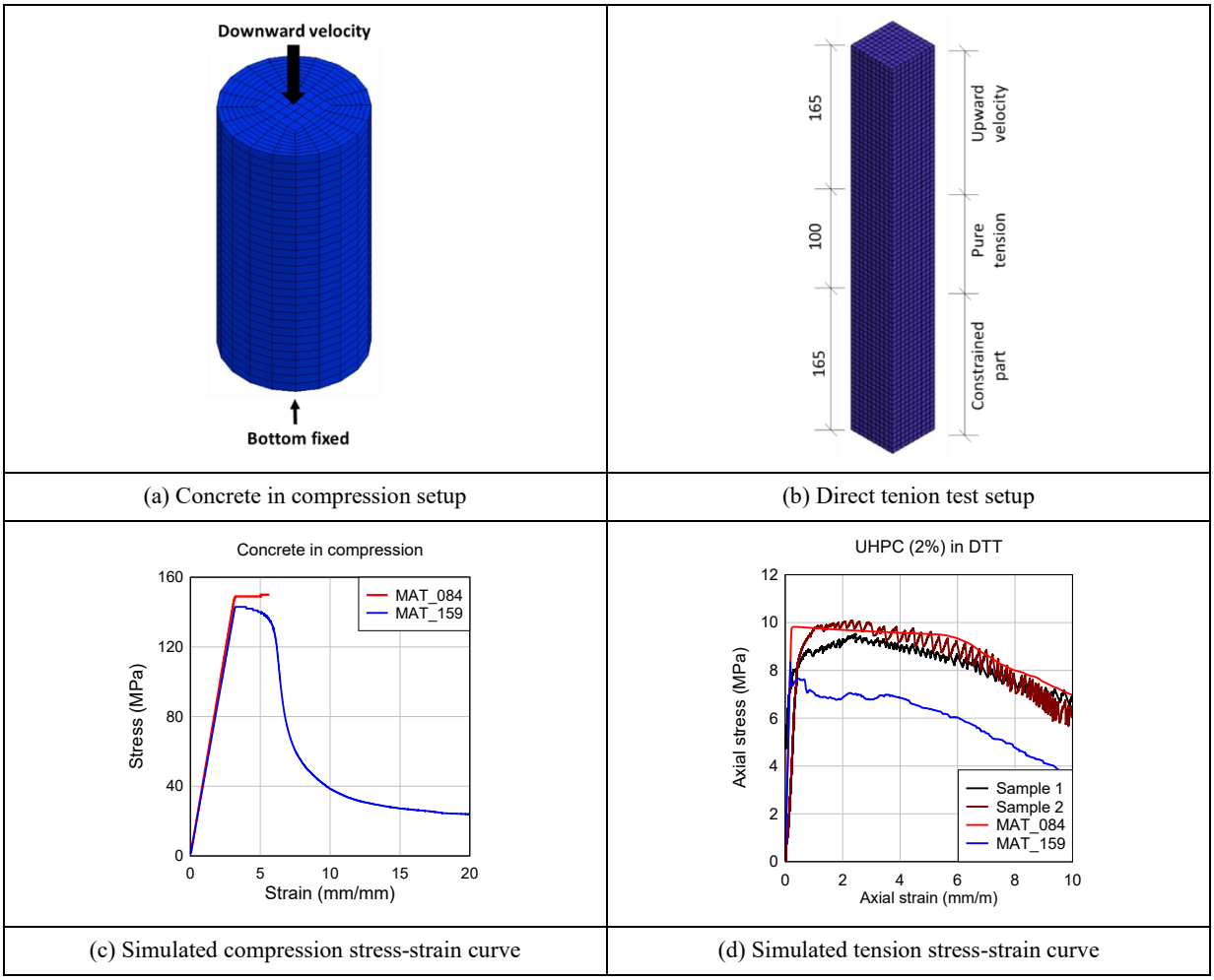

(a) Concrete in compression setup

(b) Direct tenion test setup

(c) Simulated compression stress-strain curve

(d) Simulated tension stress-strain curve

Figure 9.13 Simulation of material test

9.2.2.5. Model validation (static test)

To further validate the concrete and steel reinforcement models, numerical simulations of sample UHPC beams under static loading was performed. The FE model used in the simulations is shown in **Figure 9.14a**. The same concrete and steel models used in the blast simulations were considered in the simulated static tests. The simply-supported boundary condition was simulated by keywords *SPC_NODES_SET*, while the load-transfer beam was modeled using rigid shell elements (*SECTION_SHELL*). Loading was applied under displacement control using the keyword **PRESCRIBED_MOTION* and applied on the load-transfer beam. The loading rate was chosen as 0.1 mm/s. Three sample UHPC beams with various steel types were considered: U2-20M-DR-d/2 (UHPC-NSS), U2-No.5HS-DR-d/2 (UHPC-HSS) and U2-No.5S1-DR-d/2 (UHPC-SS). The Winfrith_Concrete model and CSCM model without rate effects were assigned to the concrete elements and considered to study the differences between the model results.

Figure 9.14(b-d) compares the simulated static test results to the experimental data for each of the sample UHPC beams. In general, the numerical results showed reasonable results when compared to the experimental load-deflection curves regardless of the steel type. Comparing the load-deflection curves, it can be seen that the use of the Winfrith_Concrete model resulted in higher load capacity, but similar post-peak strength when compared to the curves predicted using the CSCM model. This can be explained by the higher concrete tensile strength in the Winfrith_Concrete model, which results in higher load capacity. The next section presents the results of the mesh sensitivity analysis.

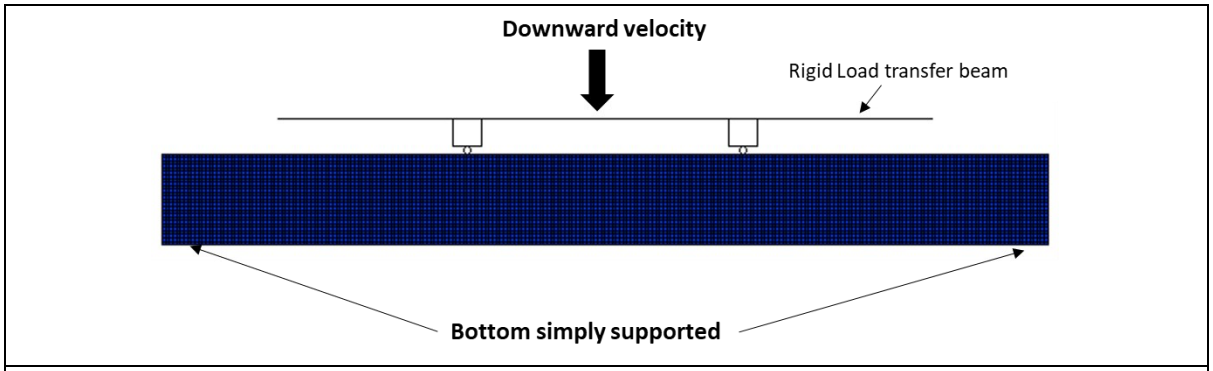

(a) Static test setup

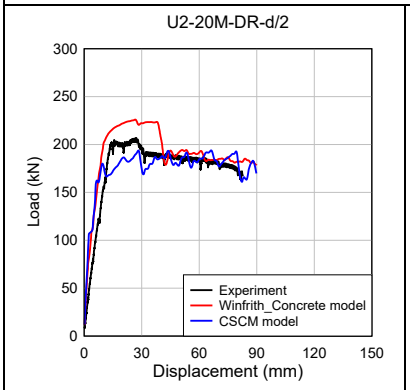

(b) Sample results from Series 3 (UHPC-NSS)

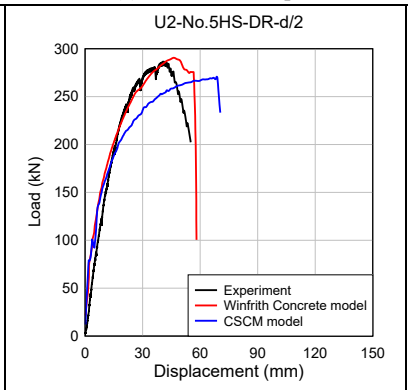

(c) Sample results from Series 3 (UHPC-HSS)

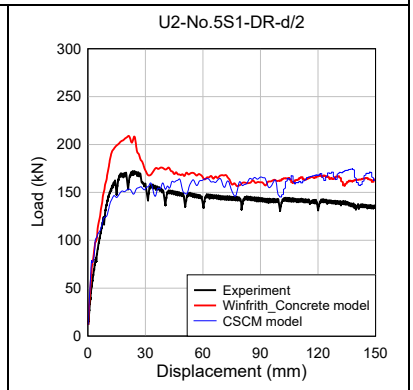

(d) Sample results from Series 3 (UHPC-SS)

Figure 9.14 Simulation of static test

9.2.3. Mesh sensitivity analysis

A mesh sensitivity analysis was performed to determine the optimal mesh size. The FE model accuracy was investigated by gradually decreasing mesh size and comparing the load-displacement response under static loading and comparing the predicted displacement response to the experimental data under blast loading. The analysis time was also a factor to be considered. The numerical computations were conducted with an explicit solver on a desktop (with Intel(R) Core(TM) i7-8700 CPU, 3.20GHz and a memory of 16 GB). Three mesh sizes

of 20 mm, 10 mm and 5 mm were considered in the FE model of a sample beam: U2-No.5S1-DR-d/2. The Winfrith_Concrete model was considered in the simulations. The mesh analysis results and processing times are shown in **Figure 9.15**. Examining the mesh sensitivity analysis results in **Figure 9.15a**, the 20-mm mesh resulted in significantly higher peak load and post-peak capacity when compared to 5-mm mesh and 10-mm mesh. Owing to the over-predicted strength, the 20-mm mesh showed reduced displacements when compared to the experiments under blast loading (see **Figure 9.15b**). The 5-mm mesh showed similar peak load and slightly increased post-peak capacity when compared to 10-mm mesh under static loading (see **Figure 9.15a**). As a result, the differences between the maximum displacements of the beams with 5- and 10-mm mesh sizes under blast loading were within 5%. However, examining the total CPU execution time for the static and blast simulations in **Figure 9.15**, it can be seen that selecting a 5-mm mesh size unreasonably increased the CPU execution time by more than 10 times. Therefore, the 10-mm mesh size was selected as an optimum size for the FE modeling of both the concrete and reinforcement elements.

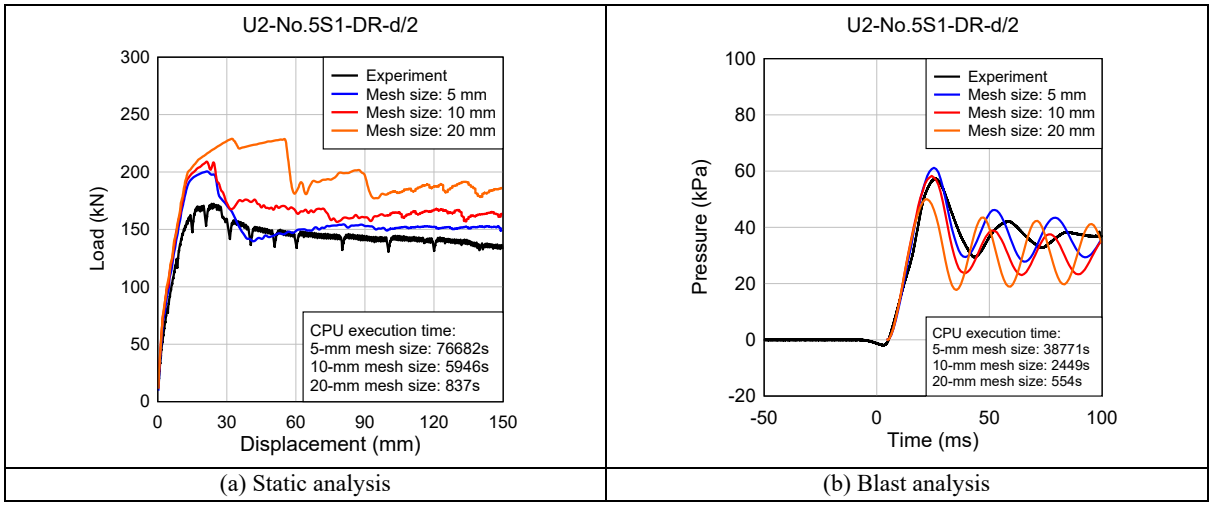

(a) Static analysis (b) Blast analysis

Figure 9.15 Mesh sensitivity analysis

9.2.4. FEM analysis results (Blast loading)

Blast simulations for the UHPC beams in Series 3 were conducted using the 10 mm mesh and previously described FE models. **Table 9.13** presents the experimental & numerical maximum midspan displacements (D_{max} & D_{max}^{num}) and displacement ratios (D_{max}/D_{max}^{num}) using the Winfrith_Concrete model (MAT_084) and CSCM model (MAT_159). The statistical data relating to the accuracy of predicted results (mean and coefficient of variation) are given in **Table 9.13**. The predicted displacement-time and load-time histories for the beams from

Series 3 are shown in **Figure 9.16, Figure 9.19 & Figure 9.22** and **Figure 9.17, Figure 9.20 & Figure 9.23. Figure 9.18, Figure 9.21 & Figure 9.24** also show the crack patterns obtained in the simulations. For the CSCM model, the fringe level was chosen as the effective plastic strain. While the crack modes for the Winfrith_Concrete model are according to the identification of cracked elements using *History variable #3*, indicating the crack opening strain.

First, strain rate effects in the CSCM model are examined in **Table 9.13**. It can be seen that the use of the CSCM model with strain rate effects in concrete slightly reduced maximum displacements. Considering all the beams in Series 3, the mean experimental-to-predicted displacement ratios (D_{max}/D_{max}^{num}) for the CSCM model without or with rate effects are found to be 93.3% and 94.9%, with COVs of 0.159 and 0.153, respectively. However, the concrete strain rate effect had a significant effect on beam U2-15M-DR-d/2, where the beam without rate effect failed in bar rupture, while applying rate effects allowed the beam to survive the blast. It is noted that after the repeated tests and application of Blast-100psi, beam U2-15M-DR-d/2 was indeed near bar rupture during the experiments (this was also clear during the post-blast residual static test). Nevertheless, it still can be concluded that, in general, the strain rate in concrete had a minor impact on UHPC beam displacement response. Similarly, examining the load response in sample beams U2-20M-DR-d/2 (see **Figure 9.17**), U3-No.5HS (**Figure 9.20**) and U2-No.5S1-DR-d/2 (**Figure 9.23**), it can be shown that the results with or without strain rate effects in the CSCM model result in similar load-time history. The results confirm that the rate effects in the UHPC concrete had minor effects on the displacement and load response predictions. As a result, the use of the RATE=2 option (without strain rate effect) in the Winfrith_Concrete model is reasonable.

Next, the prediction results using the Winfrith_Concrete model (MAT_084) and CSCM model (MAT_159) are also compared in **Table 9.13**. In general, both models well predicted beam response under blast loading. Considering all the beams in Series 3 and all test shots, the mean D_{max}/D_{max}^{num} ratios were found to be 99.3% and 94.9%, with coefficient of variations (COVs) of 0.154 and 0.153 for the Winfrith_Concrete model (MAT_084) and CSCM model (MAT_159), respectively. The peak tensile strength in the Winfrith concrete model was defined using the result from the experimental direct tension test, which is higher than the tensile strength of 8 MPa in the CSCM model, which can explain the improved accuracy of the MAT_084 model. More importantly, the higher tensile strength in the Winfrith_Concrete model can better predict the failure in the specimens. For example, the Winfrith_Concrete

model well predicted the maximum displacement of beam U2-15M-DR-d/2 at single *Blast-100 psi*, while the CSCM model predicted almost doubled displacements when compared to the experiments. Similarly, the CSCM model predicted failure in beam U2-No.4HS-DR-d/2 (R) at 70 psi due to bar rupture. In comparison, the Winfrith_Concrete model correctly predicted that the beam survived at 70 psi and captured the bar rupture at 100 psi. However, when examining the displacement ratio (D_{max}/D_{max}^{num}) for each blast separately (**Table 9.13**), it could be noticed that for beams tested under repeated blast loading, early blasts have better ratios when compared to the later ones, especially at *Blast-100 psi*. The repeat testing results in accumulated damage on the concrete, which may not be captured by the Winfrith_Concrete model since the model lacks compression strain-softening. As a result, once the concrete element reached the minimum principal strain at failure in the erosion algorithm, the compressive strength would suddenly decrease to zero. Comparing the load-time histories of those two concrete models in **Figure 9.17, Figure 9.20 & Figure 9.23,** it can be seen that both models showed similar load responses and accurately captured the peak dynamic reactions. Examining the crack patterns and failure modes for specimens from Series 3 in **Figure 9.18, Figure 9.21 & Figure 9.24**, the predicted damage modes generally show good agreement with the experimental results. For example, the CSCM model predicted beam U2-20M-DR-d/2 (R) had minor damage in terms of hairline cracks at *Blast-30psi* and *Blast-50psi*, and eventually suffered crack localized at mid-span at *Blast-100psi*. Similarly, the Winfrith_Concrete model predicted the bar rupture in beam U3-15M, and captured the crack localization in beam U2-No.5S1-DR-d/2.

In conclusion, both the Winfrith_Concrete model (MAT_084) and CSCM model (MAT_159) can predict the blast responses of UHPC beams reinforced with either ordinary, high-strength or stainless steel reinforcement, in terms of maximum displacements, load responses and damage modes. However, there are several limitations when using the Winfrith_Concrete model (MAT_084): 1) the model cannot account for the strain rate effects, therefore it may produce inaccurate results for RC components subjected to high strain rates; 2) the model lacks compression strain-softening behaviour, therefore it may produce inaccurate results for the failure of RC components governed by concrete crushing such as over-reinforced structures.

Table 9.13 FEM results (Series 3)

Series	Beams	Blast ID	Shockwave Properties			Experiment results		Prediction (MAT084) w/o rate effect		Prediction (MAT159) w/o rate effect		Prediction (MAT159) with rate effect	
			P_r (kPa)	I_r (kPa·ms)	t_d (ms)	D_{max} (mm)	D_{res} (mm)	D_{max}^{num}	D_{max}/D_{max}^{num}	D_{max}^{anls}	D_{max}/D_{max}^{num}	D_{max}^{anls}	D_{max}/D_{max}^{num}
UHPC - NSS	U2-15M-DR-d/2	100	104.0	978.5	23.1	64.1	52.5	66.6	96.2%	-*	-	127	50.5%
	U2-20M-DR-d/2	100	94.3	994.5	22.4	48.3	26.8	45.0	107.3%	46.9	103.0%	46.6	103.6%
	U2-20M-DR-d/2 (R)	30	42.4	346.1	20.2	8.4	0.6	8.1	103.7%	7.4	113.5%	7.3	115.1%
		70	83.4	708.9	21.8	21.5	1.2	22.0	97.7%	24.9	86.3%	24.5	87.8%
		100	104	996.1	24.4	46.3	26.8	55.7	83.1%	73.4	63.1%	67.6	68.5%
	U3-15M	100	107.7	1001.4	23.8	- *	-	-*		-*		-*	
UHPC - HSS	U2-No.4HS-DR-d/2 (R)	30	50.2	393.3	20.6	11.3	3.0	12.5	90.4%	13.2	85.6%	13.1	86.3%
		50	62.3	557.9	22.0	19.8	2.5	20.4	97.1%	24.4	81.1%	24.2	81.8%
		70	87.4	728.4	22.5	31.2	9.0	38.1	81.9%	-*		-*	
		100	98.6	970.2	24.3	- *	-	-		-*		-*	
	U2-No.5HS-DR-d/2	100	106	981.0	22.5	35.9	11.1	40.7	88.2%	40.3	89.1%	40.3	89.1%
	U3-No.5HS	100	93.8	968.1	22.2	34.9	7.0	39.3	88.8%	32.6	107.1%	31.8	109.7%
UHPC - SS	U2-No.4S1-DR-d/2 (R)	30	43.3	363.1	20.5	12.3	2.8	11.5	107.0%	10.7	115.0%	10.5	117.1%
		50	58.3	557.6	21.3	28.6	11.6	19.7	145.2%	27	105.9%	26.6	107.5%
		70	75.2	733.4	22.7	53.9	32.5	56.9	94.7%	63.3	85.2%	61.7	87.4%
		100	88.7	955.4	24.1	- *	-	-*		-*		-*	
	U2-No.5S1-DR-d/2	100	96.3	966.5	24.2	57.5	36.5	58.3	98.6%	67.6	85.1%	67.5	85.2%
	U3-No.5S1	100	90.3	923.5	24.0	54.2	31.5	49.6	109.3%	58.1	93.3%	57.3	94.6%
								AVG.	**99.3%**		**93.3%**		**94.9%** **
								COV	**0.154**		**0.159**		**0.153** **

* Bar rupture
** Without U2-15M-DR-d/2

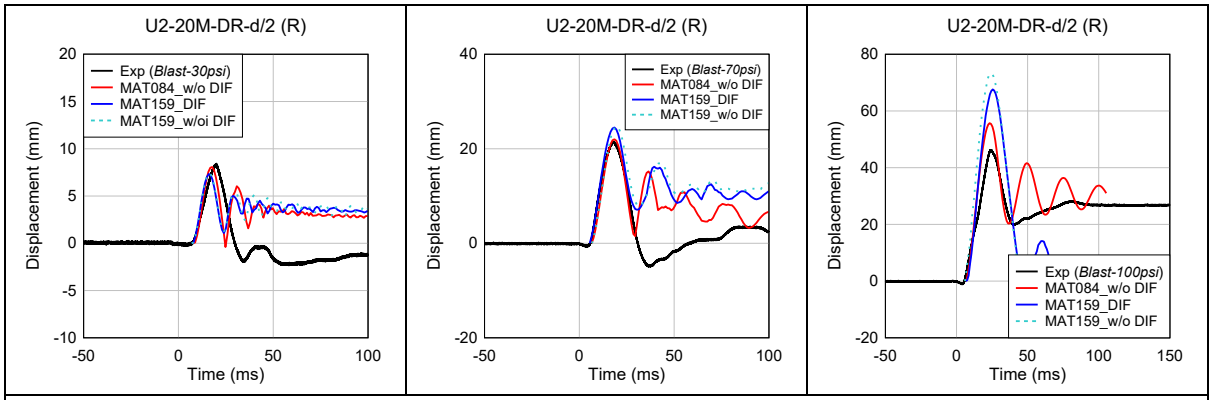

(a) U2-No.20M-DR-d/2 (R)

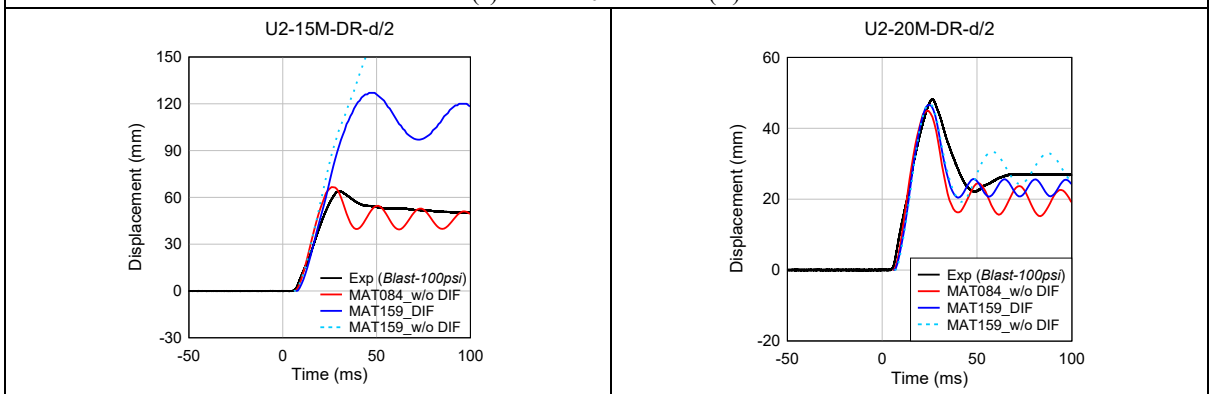

(b) U2-15M-DR-d/2 (c) U2-20M-DR-d/2

Figure 9.16 Predicted displacement response (Series 3: UHPC-NSS)

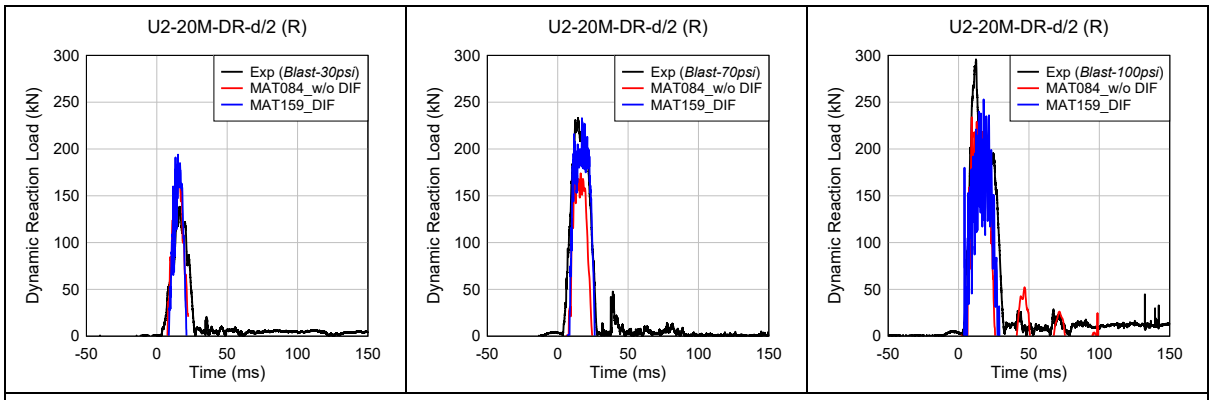

(a) U2-No.20M-DR-d/2 (R)

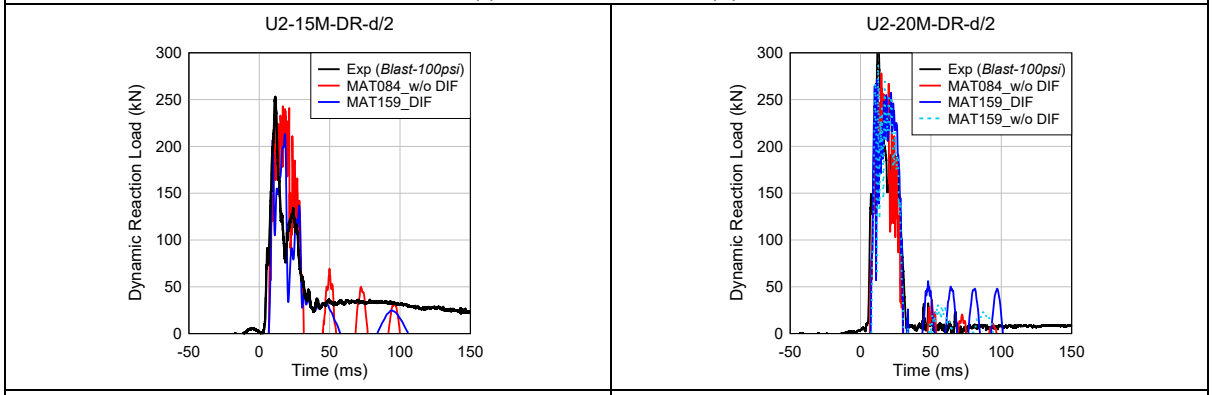

(b) U2-15M-DR-d/2 (c) U2-20M-DR-d/2

Figure 9.17 Predicted load response (Series 3: UHPC-NSS)

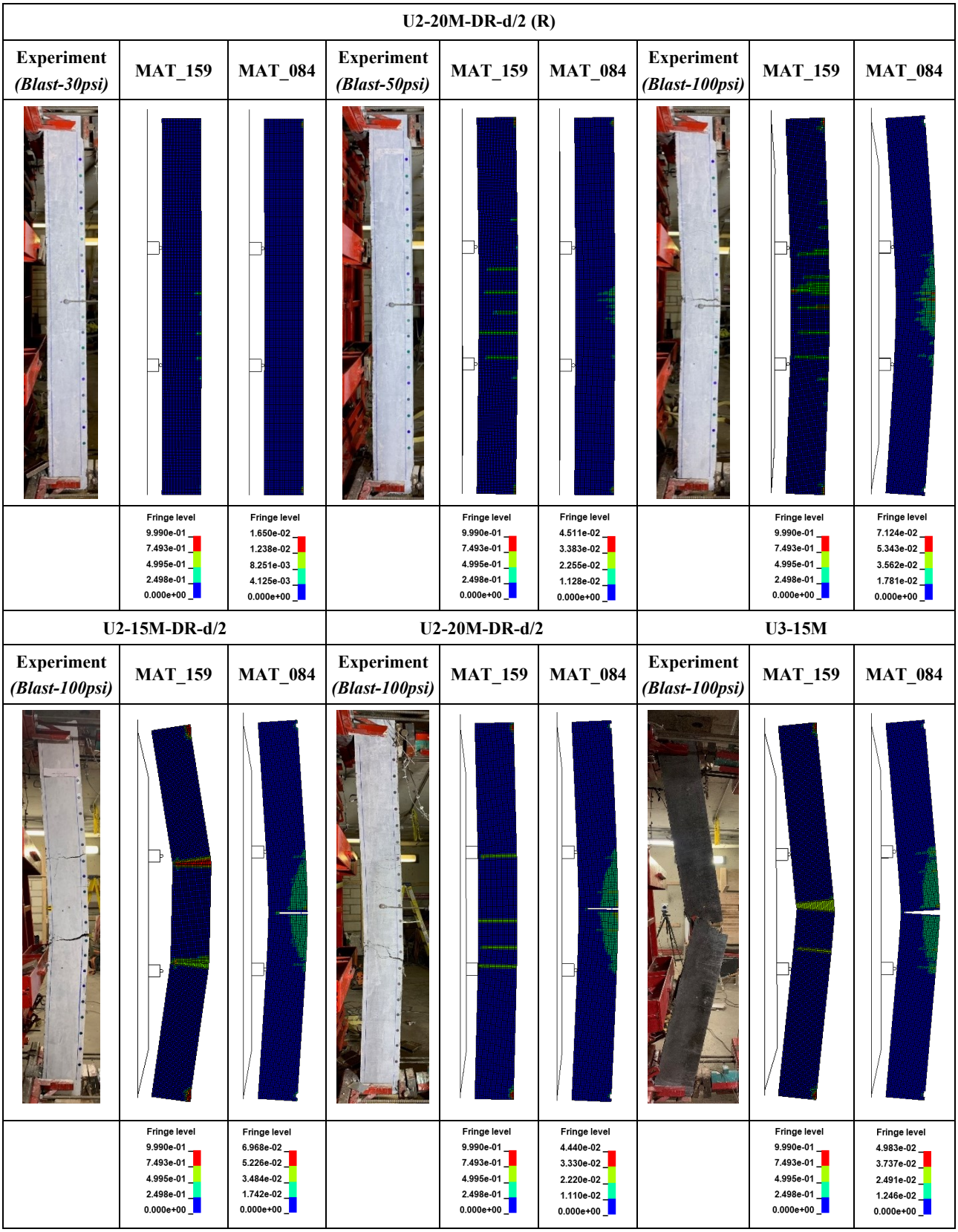

Figure 9.18 Damage mode of specimens (Series 3: UHPC-NSS)

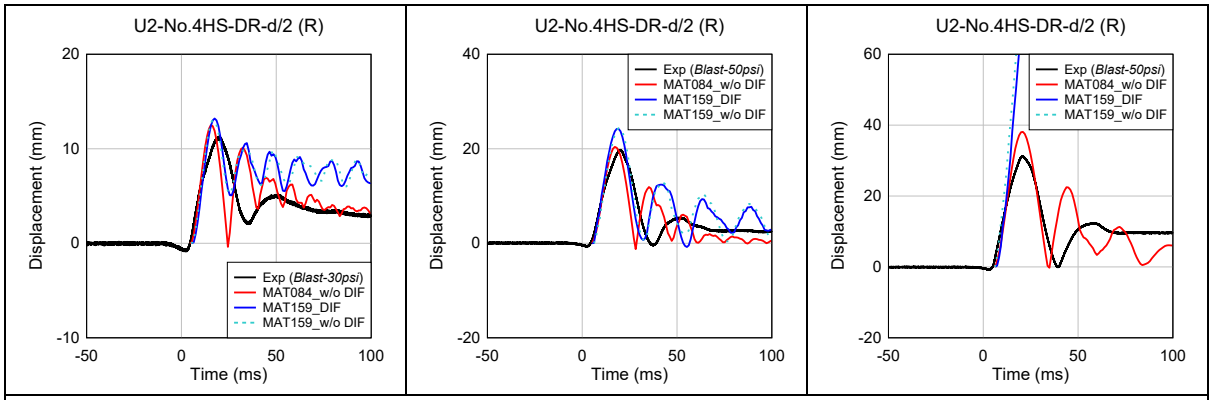

(a) U2-No.4HS-DR-d/2 (R)

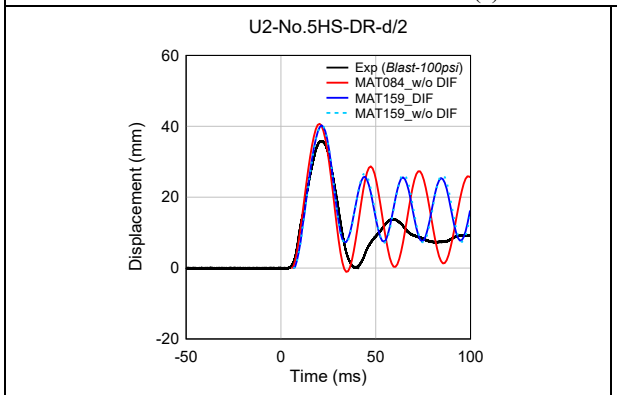

(b) U2-No.5HS-DR-d/2

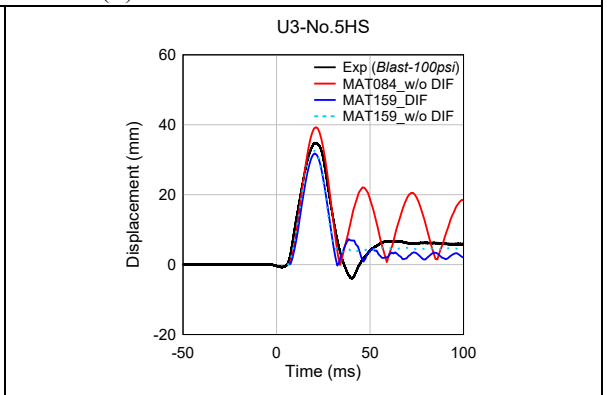

(c) U3-No.5HS

Figure 9.19 Predicted displacement response (Series 3: UHPC-HSS)

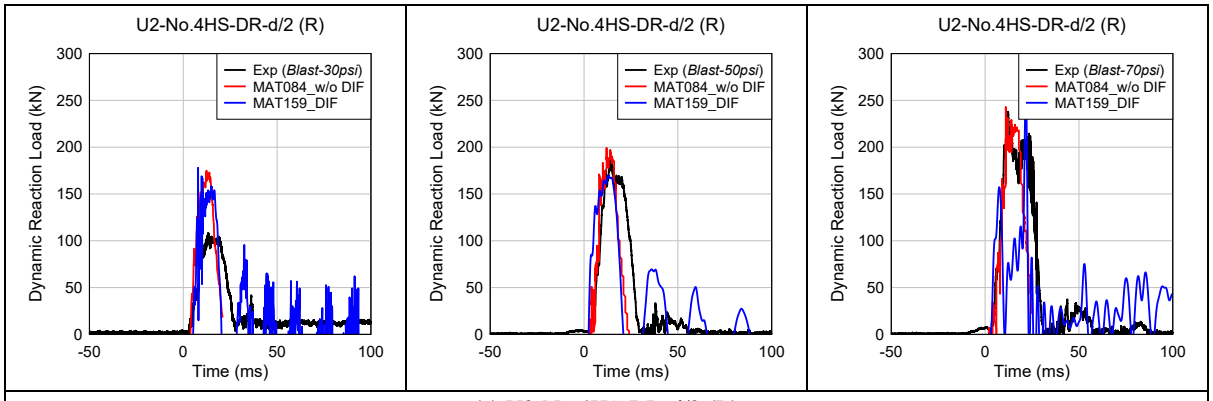

(a) U2-No.4HS-DR-d/2 (R)

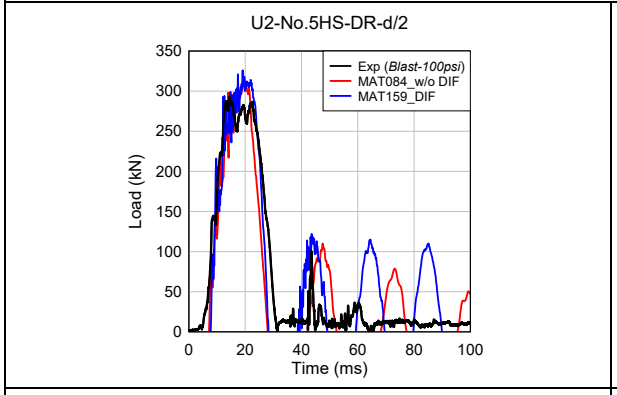

(b) U2-No.5HS-DR-d/2

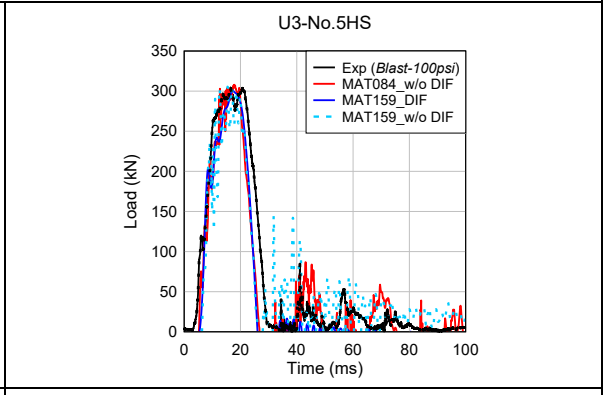

(c) U3-No.5HS

Figure 9.20 Predicted load response (Series 3: UHPC-HSS)

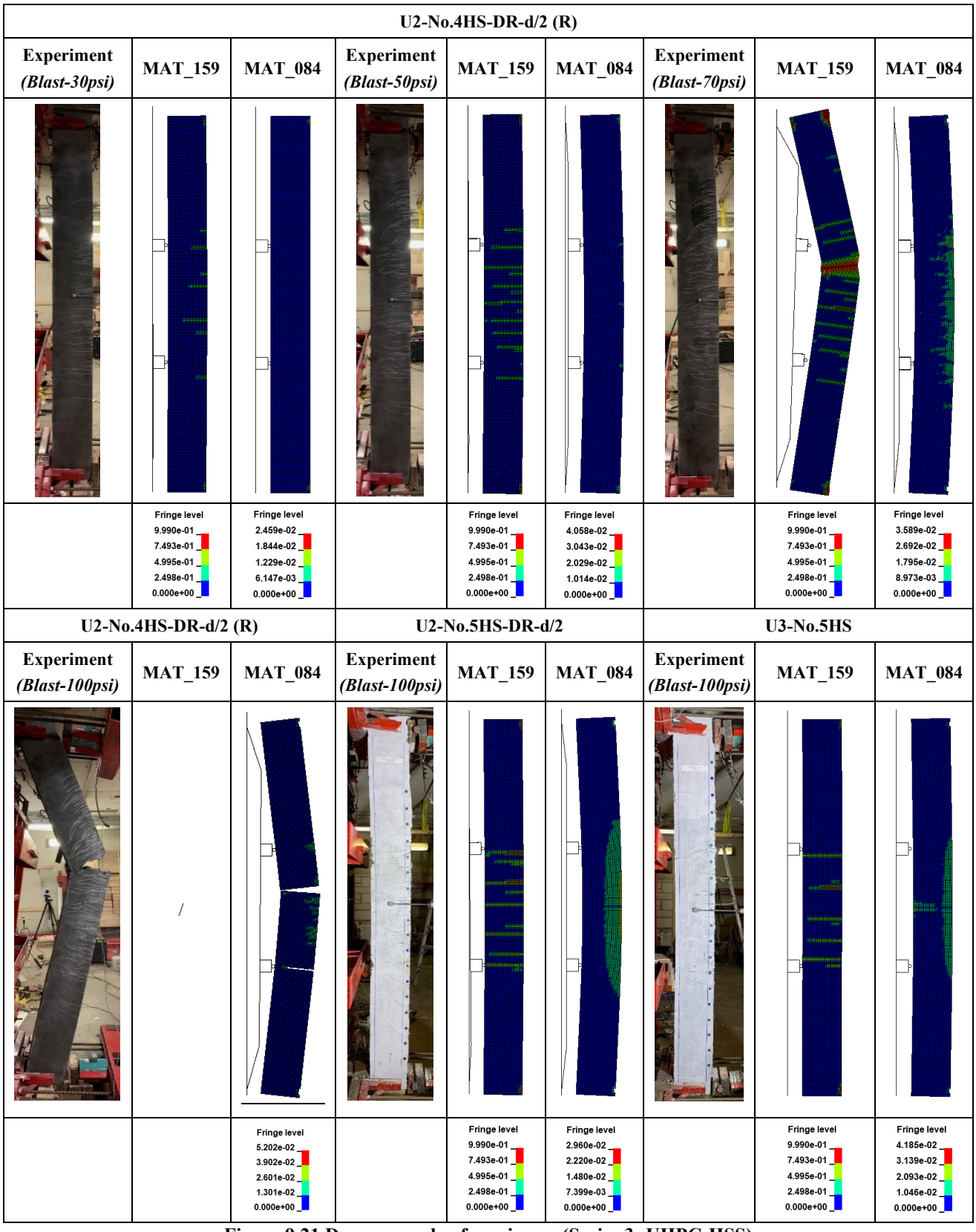

Figure 9.21 Damage mode of specimens (Series 3: UHPC-HSS)

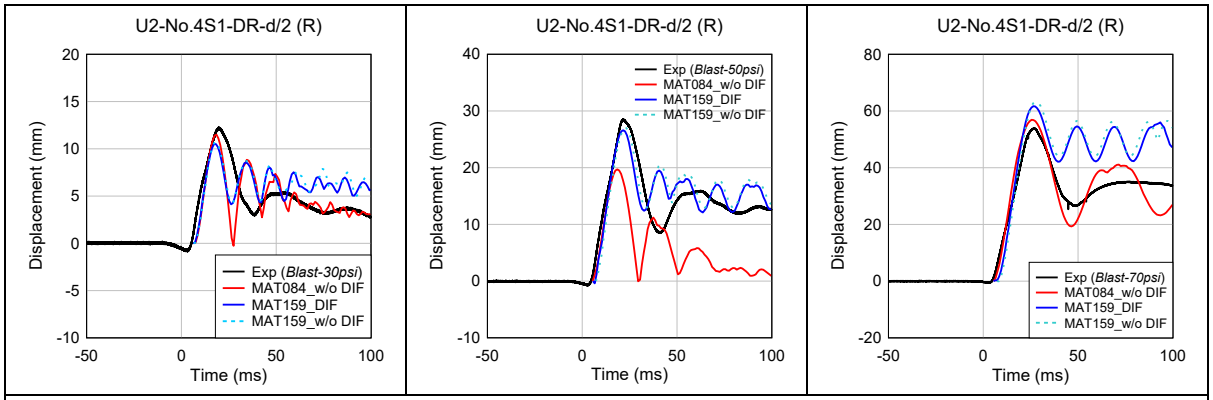

(a) U2-No.4S1-DR-d/2

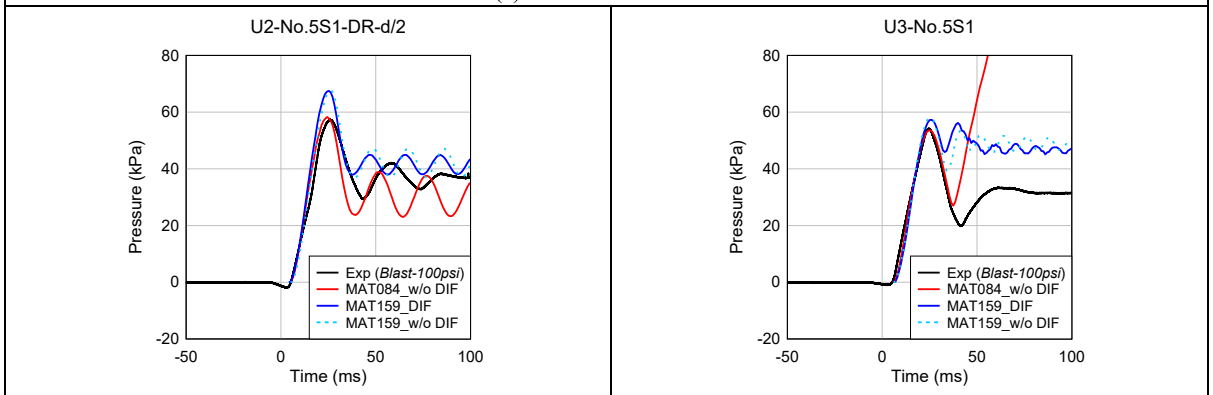

(b) U2-No.5S1-DR-d/2 (c) U3-No.5S1

Figure 9.22 Predicted displacement response (Series 3: UHPC-SS)

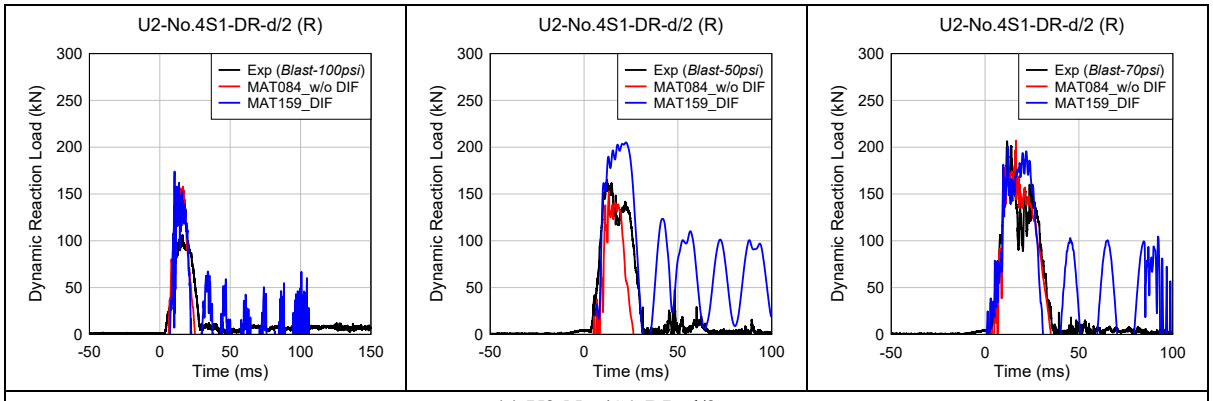

(a) U2-No.4S1-DR-d/2

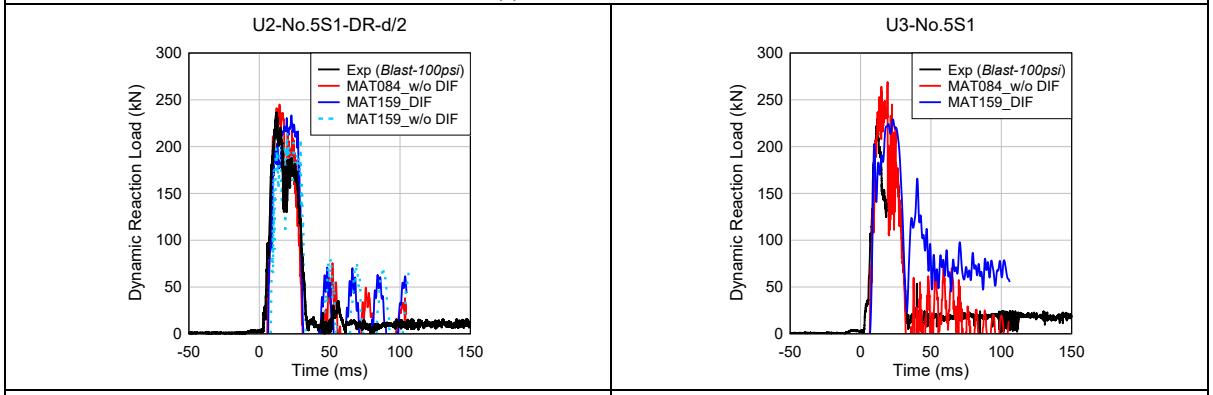

(b) U2-No.5S1-DR-d/2 (c) U3-No.5S1

Figure 9.23 Predicted load response (Series 3: UHPC-SS)

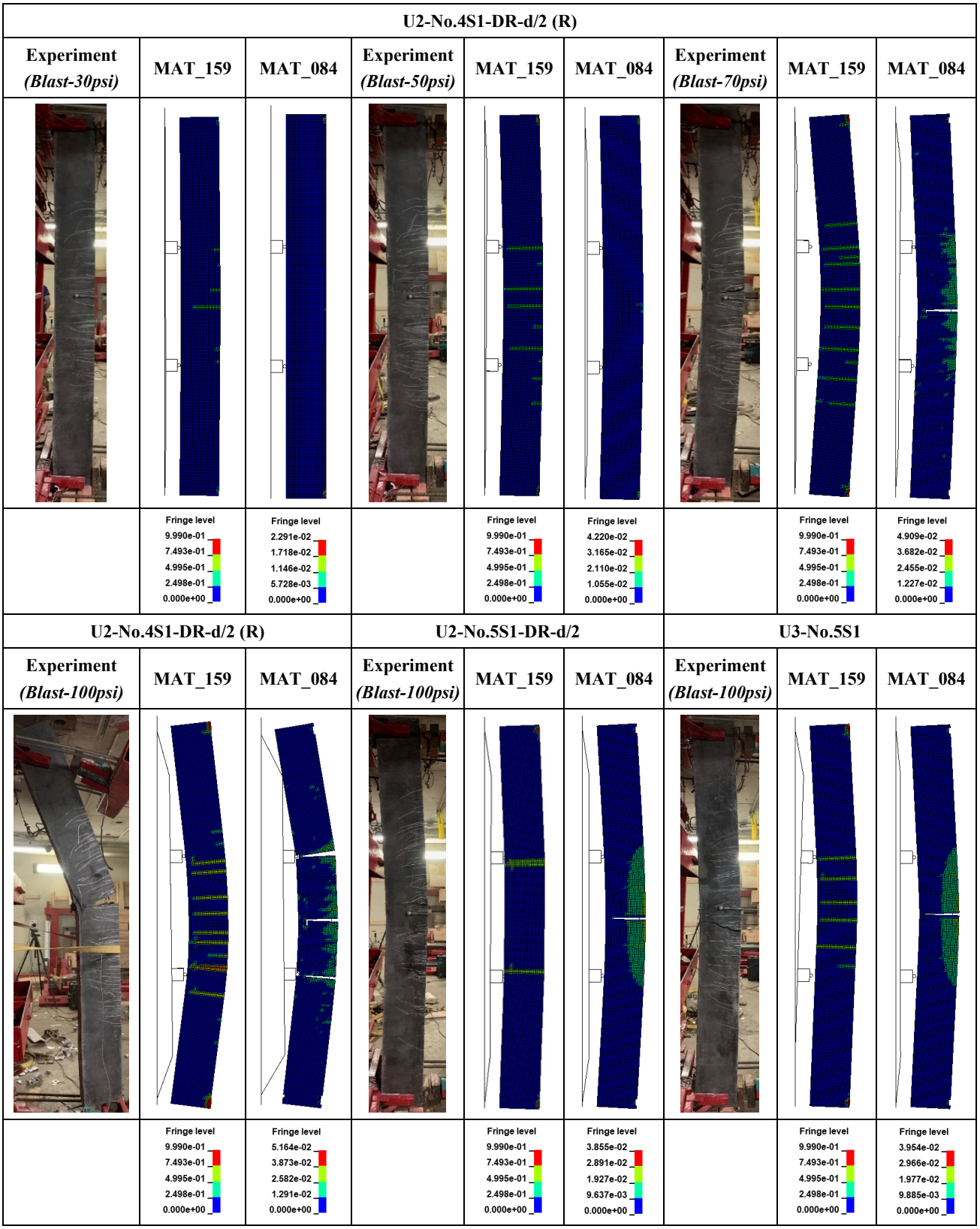

Figure 9.24 Damage mode of specimens (Series 3: UHPC-SS)

9.3 Conclusions

This chapter presented a numerical research program to predict the static and dynamic responses of the test beams in this PhD program using finite element (FE) modelling. The 2D nonlinear finite element software VecTor2 was used to predict the static and dynamic behaviour of the high-strength concrete (HSC) beams tested in Series 1 and 2. While the 3D finite-element (FE) software LS-DYNA was used to predict the blast response of UHPC beams tested in Series 3. The following conclusions can be drawn from this study:

1. 2D finite element modelling using software VecTor2, with appropriate material models, can well predict the static load-deflection response of HSC and HSFRC beams with varying steel types and detailing. Importantly, the FE models can well predict failure modes such as bar rupture, concrete crushing and shear failure.
2. The 2D FE models developed in software VecTor2 can also predict the maximum displacements, dynamic load reaction curves, and failure modes of HSC and HSFRC beams from Series 1 and 2 under blast loading. Although, the blast displacements were less accurately predicted during subsequent cycles, with the results sensitive to the choice of damping coefficients.
3. The 3D finite element blast analysis using software LS-DYNA, with appropriate selection of material models for the UHPC and steel reinforcement, allowed for reasonable predictions of the overall blast behaviour of UHPC beams with varying steel types and detailing, in terms of experimental dynamic displacements, load-time histories, and damage modes.
4. In general, both the Winfrith_Concrete model (MAT_084) and the CSCM model MAT_159) with calibrated values can well simulate the blast response of UHPC materials. However the calibrated CSCM model had a lower UHPC tensile strength, which resulted in U2-No.4HS-DR-d/2 having earlier bar rupture failure when compared to the experiment.

9.4 References (Chapter 9)

Amin, A., Foster, S. J., & Muttoni, A. (2015). Derivation of the σ-wrelationship for SFRC from prism bending tests. *Structural Concrete, 16*(1), 93-105. doi:https://doi.org/10.1002/suco.201400018

ASTM C1609 / C1609M-19 (2019). Standard Test Method for Flexural Performance of Fiber-Reinforced Concrete (Using Beam With Third-Point Loading). ASTM International, West Conshohocken, PA, pp. 9.

Barbachyn, S. M., Devine, R. D., Thrall, A. P., & Kurama, Y. C. (2017). Effect of High-Strength Materials on Lateral Strength of Stocky Reinforced Concrete Walls. *ACI Structural Journal, 114*(4), 923-936. doi:https://doi.org/10.14359/51689722

Bernard, E. S., Amin, A., & Gilbert, R. I. (2020). Assessment of MC2010 and AS3600 models for estimating instantaneous flexural crack widths in fibre reinforced concrete members. *Engineering Structures, 208*, 110271. doi:https://doi.org/10.1016/j.engstruct.2020.110271

Cao, Y. Y. Y., Yu, Q., Tang, W. H., & Brouwers, H. J. H. (2020). Numerical investigation on ballistic performance of coarse-aggregated layered UHPFRC. *Construction and Building Materials, 250*, 118867. doi:https://doi.org/10.1016/j.conbuildmat.2020.118867

Chan, T., & Mackie, K. R. (2018, June 18-21, 2018). *Substructure Connection in High Seismic Zones Utilizing Ultra-high Performance Concrete.* Paper presented at the 16th European Conference on Earthquake Engineering, Thessal.

Chen, L., Hu, Y., Ren, H., Xiang, H., Zhai, C., & Fang, Q. (2019). Performances of the RC column under close-in explosion induced by the double-end-initiation explosive cylinder. *International Journal of Impact Engineering, 132*, 103326. doi:https://doi.org/10.1016/j.ijimpeng.2019.103326

Cortés-Puentes, W. L., & Palermo, D. (2012). Modeling of RC Shear Walls Retrofitted with Steel Plates or FRP Sheets. *Journal of Structural Engineering, 138*(5), 602-612. doi:https://doi.org/10.1061/(asce)st.1943-541x.0000466

Deluce, J. R., Lee, S.-C., & Vecchio, F. J. (2014). Crack model for steel fiber-reinforced concrete members containing conventional reinforcement. *ACI Structural Journal, 111*(1), 93-102. doi:https://doi.org/10.14359/51686433

Fan, W., Guo, W., Sun, Y., Chen, B., & Shao, X. (2018a). Experimental and numerical investigations of a novel steel-UHPFRC composite fender for bridge protection in vessel collisions. *Ocean Engineering, 165*, 1-21. doi:https://doi.org/10.1016/j.oceaneng.2018.07.028

Fan, W., Shen, D., Huang, X., & Sun, Y. (2020a). Reinforced concrete bridge structures under barge impacts: FE modeling, dynamic behaviors, and UHPFRC-based strengthening. *Ocean Engineering, 216*, 108116. doi:https://doi.org/10.1016/j.oceaneng.2020.108116

Fan, W., Shen, D., Yang, T., & Shao, X. (2019). Experimental and numerical study on low-velocity lateral impact behaviors of RC, UHPFRC and UHPFRC-strengthened columns. *Engineering Structures, 191*, 509-525. doi:https://doi.org/10.1016/j.engstruct.2019.04.086

Fan, W., Shen, D., Zhang, Z., Huang, X., & Shao, X. (2020b). A novel UHPFRC-based protective structure for bridge columns against vehicle collisions: Experiment, simulation, and optimization. *Engineering Structures, 207*, 110247. doi:https://doi.org/10.1016/j.engstruct.2020.110247

Fan, W., Xu, X., Zhang, Z., & Shao, X. (2018b). Performance and sensitivity analysis of UHPFRC-strengthened bridge columns subjected to vehicle collisions. *Engineering Structures, 173*, 251-268. doi:https://doi.org/10.1016/j.engstruct.2018.06.113

Federation Internationale du Beton (2013). fib Model Code for Concrete Structures 2010. Berlin: Ernst & Sohn Publishing House, pp. 434.

Fujikake, K., Senga, T., Ueda, N., Ohno, T., & Katagiri, M. (2006). Study on Impact Response of Reactive Powder Concrete Beam and Its Analytical Model. *Journal of Advanced Concrete Technology, 4*(1), 99-108. doi:https://doi.org/10.3151/jact.4.99

Gholipour, G., & Billah, A. H. M. M. (2022a). Dynamic behavior of bridge columns reinforced with shape memory alloy rebar and UHPFRC under lateral impact loads. *International Journal of Impact Engineering, 168*, 104297. doi:https://doi.org/10.1016/j.ijimpeng.2022.104297

Gholipour, G., & Billah, A. H. M. M. (2022b). Nonlinear Analysis of Shear-Deficient Beams Strengthened Using UHPFRC under Combined Impact and Blast Loads. *Journal of Structural Engineering, 148*(6), 04022056. doi:https://doi.org/10.1061/(asce)st.1943-541x.0003368

Graybeal, B. A. (2006). Material property characterization of ultra-high performance concrete. *No. FHWA-HRT-06-103*: Federal Highway Administration, Office of Infrastructure pp. 186

Guo, W., Fan, W., Shao, X., Shen, D., & Chen, B. (2018). Constitutive model of ultra-high-performance fiber-reinforced concrete for low-velocity impact simulations. *Composite Structures, 185*, 307-326. doi:https://doi.org/10.1016/j.compstruct.2017.11.022

Hallquist, J. O. (2007). LS-DYNA keyword user's manual. *Livermore Software Technology Corporation*, pp. 2937

Hoang, A. L., & Fehling, E. (2017). Influence of steel fiber content and aspect ratio on the uniaxial tensile and compressive behavior of ultra high performance concrete. *Construction and Building Materials, 153*, 790-806. doi:https://doi.org/10.1016/j.conbuildmat.2017.07.130

Hrynyk, T. D., & Vecchio, F. J. (2016). Modeling of Reinforced and Fiber-Reinforced Concrete Slabs under Impact Loads. *ACI Special Publication, 321*, 8.1-8.20.

Isojeh, B., El-Zeghayar, M., & Vecchio, F. J. (2019). Numerical Analysis of Reinforced Concrete and Steel-Fiber Concrete Elements under Fatigue Loading. *Journal of Structural Engineering, 145*(11), 04019126. doi:https://doi.org/10.1061/(asce)st.1943-541x.0002349

Jia, P. C., Wu, H., Wang, R., & Fang, Q. (2021). Dynamic responses of reinforced ultra-high performance concrete members under low-velocity lateral impact. *International Journal of Impact Engineering, 150*, 103818. doi:https://doi.org/10.1016/j.ijimpeng.2021.103818

Lai, J., Guo, X., & Zhu, Y. (2015). Repeated penetration and different depth explosion of ultra-high performance concrete. *International Journal of Impact Engineering, 84*, 1-12. doi:https://doi.org/10.1016/j.ijimpeng.2015.05.006

Lai, J., Yang, H., Wang, H., Zheng, X., & Wang, Q. (2018). Properties and modeling of ultra-high-performance concrete subjected to multiple bullet impacts. *Journal of Materials in Civil Engineering, 30*(10), 04018256. doi:https://doi.org/10.1061/(ASCE)MT.1943-5533.0002462

Lee, J.-Y., Aoude, H., Yoon, Y.-S., & Mitchell, D. (2020). Impact and blast behavior of seismically-detailed RC and UHPFRC-Strengthened columns. *International Journal of Impact Engineering, 143*, 103628. doi:https://doi.org/10.1016/j.ijimpeng.2020.103628

Lee, S.-C., Cho, J.-Y., & Vecchio, F. J. (2011a). Diverse embedment model for steel fiber-reinforced concrete in tension: model development. *ACI Materials Journal, 108*(5), 516-525. doi:https://doi.org/10.14359/51683261

Lee, S.-C., Cho, J.-Y., & Vecchio, F. J. (2011b). Diverse embedment model for steel fiber-reinforced concrete in tension: Model verification. *ACI Materials Journal, 108*(5), 526-535. doi:https://doi.org/10.14359/51683262

Lee, S.-C., Cho, J.-Y., & Vecchio, F. J. (2013). Tension-Stiffening Model for Steel Fiber-Reinforced Concrete Containing Conventional Reinforcement. *ACI Structural Journal, 110*(4), 639-648. doi:https://doi.org/10.14359/51685749

Lee, S.-C., Cho, J.-Y., & Vecchio, F. J. (2016). Analysis of steel fiber-reinforced concrete elements subjected to shear. *ACI Structural Journal, 113*(2), 275-285. doi:https://doi.org/10.14359/51688474

Lee, S.-C., Oh, J. H., & Cho, J. Y. (2015). Compressive Behavior of Fiber-Reinforced Concrete with End-Hooked Steel Fibers. *Materials, 8*(4), 1442-1458. doi:https://doi.org/10.3390/ma8041442

Li, J., & Wu, C. (2018). Damage evaluation of ultra-high performance concrete columns after blast loads. *International Journal of Protective Structures, 9*(1), 44-64. doi:https://doi.org/10.1177/2041419617743986

Li, R. W., Zhou, D. Y., & Wu, H. (2020). Experimental and numerical study on impact resistance of RC bridge piers under lateral impact loading. *Engineering Failure Analysis, 109*, 104319. doi:https://doi.org/10.1016/j.engfailanal.2019.104319

Liao, Q., Xie, X., & Yu, J. (2022). Numerical investigation on dynamic performance of reinforced ultra‐high ductile concrete‐ultra‐high performance concrete panel under explosion. *Structural Concrete*, 1-15. doi:https://doi.org/10.1002/suco.202100919

Liu, J., Li, J., Fang, J., Liu, K., Su, Y., & Wu, C. (2022). Investigation of ultra-high performance concrete slabs under contact explosions with a calibrated K&C model. *Engineering Structures, 255*, 113958. doi:https://doi.org/10.1016/j.engstruct.2022.113958

Liu, J., Wu, C., & Chen, X. (2017a). Numerical study of ultra-high performance concrete under non-deformable projectile penetration. *Construction and Building Materials, 135*, 447-458. doi:https://doi.org/10.1016/j.conbuildmat.2016.12.216

Liu, J., Wu, C., Li, J., Su, Y., & Chen, X. (2018a). Numerical investigation of reactive powder concrete reinforced with steel wire mesh against high-velocity projectile penetration. *Construction and Building Materials, 166*, 855-872. doi:https://doi.org/10.1016/j.conbuildmat.2018.02.001

Liu, J., Wu, C., Li, J., Su, Y., Shao, R., Liu, Z., & Chen, G. (2017b). Experimental and numerical study of reactive powder concrete reinforced with steel wire mesh against projectile penetration. *International Journal of Impact Engineering, 109*, 131-149. doi:https://doi.org/10.1016/j.ijimpeng.2017.06.006

Liu, J., Wu, C., Su, Y., Li, J., Shao, R., Chen, G., & Liu, Z. (2018b). Experimental and numerical studies of ultra-high performance concrete targets against high-velocity projectile impacts. *Engineering Structures, 173*, 166-179. doi:https://doi.org/10.1016/j.engstruct.2018.06.098

Lulec, A. (2017). *Simplified Analytical Tools for Impact and Impulsive Loading Analysis of Reinforced Concrete Structures.* (PhD thesis). University of Toronto, Toronro, ON, Canada.

Naval Facilities Engineering Service Center Port hueneme CA (1998). *Dynamic increase factors for concrete*.

Mander, J. B., Priestley, M. J. N., & Park, R. (1988). Theoretical Stress-Strain Model for Confined Concrete. *Journal of Structural Engineering, 114*(8), 1804-1826. doi:https://doi.org/10.1061/(Asce)0733-9445(1988)114:8(1804)

Mao, L., Barnett, S., Begg, D., Schleyer, G., & Wight, G. (2014). Numerical simulation of ultra high performance fibre reinforced concrete panel subjected to blast loading. *International Journal of Impact Engineering, 64*, 91-100. doi:https://doi.org/10.1016/j.ijimpeng.2013.10.003

Mao, L., & Barnett, S. J. (2017). Investigation of toughness of ultra high performance fibre reinforced concrete (UHPFRC) beam under impact loading. *International Journal of Impact Engineering, 99*, 26-38. doi:https://doi.org/10.1016/j.ijimpeng.2016.09.014

Oppong, K., Saini, D., & Shafei, B. (2021). Ultra high-Performance Concrete for Improving Impact Resistance of Bridge Superstructures to Overheight Collision. *Journal of Bridge Engineering, 26*(9), 04021060. doi:https://doi.org/10.1061/(asce)be.1943-5592.0001736

Palermo, D., & Vecchio, F. J. (2007). Simulation of Cyclically Loaded Concrete Structures Based on the Finite-Element Method. *Journal of Structural Engineering, 133*(5), 728-738. doi:https://doi.org/10.1061/(asce)0733-9445(2007)133:5(728)

Popovics, S. (1973). A numerical approach to the complete stress-strain curve of concrete. *Cement and Concrete Research, 3*(5), 583-599. doi:https://doi.org/10.1016/0008-8846(73)90096-3

Ren, G. M., Wu, H., Fang, Q., Liu, J. Z., & Gong, Z. M. (2016). Triaxial compressive behavior of UHPCC and applications in the projectile impact analyses. *Construction and Building Materials, 113*, 1-14. doi:https://doi.org/10.1016/j.conbuildmat.2016.02.227

Ren, L., Yu, X., Zheng, M., Xue, Z., Wu, B., & He, Y. (2022). Evaluation of typical dynamic damage models used for UHPC based on SHPB technology. *Engineering Fracture Mechanics, 269*, 108562. doi:https://doi.org/10.1016/j.engfracmech.2022.108562

United States, Federal Highway Administration, Office of Infrastructure Research and Development (2013). *Ultra-high performance concrete: A state-of-the-art report for the bridge community*.

Saatci, S. (2007). *Behaviour and modelling of reinforced concrete structures subjected to impact loads.* (PhD thesis). University of Toronto, Toronro, ON, Canada.

Saatci, S., & Vecchio, F. J. (2009). Nonlinear Finite Element Modeling of Reinforced Concrete Structures under Impact Loads. *ACI Structural Journal, 106*(5), 717-725. doi:https://doi.org/10.14359/51663112

Sagals, G., Orbovic, N., & Blahoianu, A. (2011). Sensitivity studies of reinforced concrete slabs under impact loading. *Transactions of the 21st SMiRT*.

Saini, D., Oppong, K., & Shafei, B. (2021). Investigation of Concrete Constitutive Models for Ultra-High Performance Fiber-Reinforced Concrete under Low-Velocity Impact. *International Journal of Impact Engineering, 157*, 103969. doi:https://doi.org/10.1016/j.ijimpeng.2021.103969

Schwer, L. (2010). An introduction to the Winfrith concrete model. *Schwer Engineering & Consulting Services*.

Schwer, L. (2011). *The Winfrith concrete model: Beauty or beast? Insights into the Winfrith concrete model.* Paper presented at the 8th European LS-DYNA users conference.

Seckin, M. (1981). *Hysteretic behaviour of cast-in-place exterior beam-column-slab subassemblies.* (PhD thesis). University of Toronto, Toronro, ON, Canada.

Sturt, R. (2019). MAT_WINFRITH - RATE=2 Ottosen yield surface. . Retrieved from https://ftp.lstc.com/anonymous/outgoing/support/FAQ_kw/concrete/mat84_winfrith

Su, Q., Wu, H., & Fang, Q. (2022). Calibration of KCC model for UHPC under impact and blast loadings. *Cement and Concrete Composites, 127*, 104401. doi:https://doi.org/10.1016/j.cemconcomp.2021.104401

Susetyo, J., Gauvreau, P., & Vecchio, F. J. (2013). Steel Fiber-Reinforced Concrete Panels in Shear: Analysis and Modeling. *ACI Structural Journal, 110*(2), 285-296. doi:https://doi.org/10.14359/51684408

Tai, Y. S. (2009). Flat ended projectile penetrating ultra-high strength concrete plate target. *Theoretical and Applied Fracture Mechanics, 51*(2), 117-128. doi:https://doi.org/10.1016/j.tafmec.2009.04.005

Thai, D. K., & Kim, S. E. (2015). Failure analysis of UHPFRC panels subjected to aircraft engine model impact. *Engineering Failure Analysis, 57*, 88-104. doi:https://doi.org/10.1016/j.engfailanal.2015.07.005

Thiagarajan, G., Kadambi, A. V., Robert, S., & Johnson, C. F. (2015). Experimental and finite element analysis of doubly reinforced concrete slabs subjected to blast loads. *International Journal of Impact Engineering, 75*, 162-173. doi:https://doi.org/10.1016/j.ijimpeng.2014.07.018

Trommels, H. (2013). *Towards Simplified Tools for Analysis of Reinforced Concrete Structures Subjected to Impact and Impulsive Loading: A Preliminary Investigation.* (MASc thesis). University of Toronto, Toronro, ON, Canada.

Vecchio, F. J. (1992). Finite Element Modeling of Concrete Expansion and Confinement. *Journal of Structural Engineering, 118*(9), 2390-2406. doi:https://doi.org/10.1061/(asce)0733-9445(1992)118:9(2390)

Vecchio, F. J. (2000). Disturbed Stress Field Model for Reinforced Concrete: Formulation. *Journal of Structural Engineering, 126*(9), 1070-1077. doi:https://doi.org/10.1061/(asce)0733-9445(2000)126:9(1070)

Vecchio, F. J. (2001). Disturbed Stress Field Model for Reinforced Concrete: Implementation. *Journal of Structural Engineering, 127*(1), 12-20. doi:https://doi.org/10.1061/(asce)0733-9445(2001)127:1(12)

Vecchio, F. J., & Collins, M. P. (1986). The modified compression-field theory for reinforced concrete elements subjected to shear. *ACI Structural Journal, 83*(2), 219-231. doi:https://doi.org/10.14359/10416

Vecchio, F. J., & Shim, W. (2004). Experimental and Analytical Reexamination of Classic Concrete Beam Tests. *Journal of Structural Engineering, 130*(3), 460-469. doi:https://doi.org/10.1061/(asce)0733-9445(2004)130:3(460)

Wan, W., Yang, J., Xu, G., & Liu, Y. (2021). Determination and evaluation of Holmquist-Johnson-Cook constitutive model parameters for ultra-high-performance concrete with steel fibers. *International Journal of Impact Engineering, 156*, 103966. doi:https://doi.org/10.1016/j.ijimpeng.2021.103966

Wang, W., Wu, C., Li, J., Liu, Z., & Lv, Y. (2019a). Behavior of ultra-high performance fiber-reinforced concrete (UHPFRC) filled steel tubular members under lateral impact loading. *International Journal of Impact Engineering, 132*, 103314. doi:https://doi.org/10.1016/j.ijimpeng.2019.103314

Wang, W., Wu, C., Li, J., Liu, Z., & Zhi, X. (2019b). Lateral impact behavior of double-skin steel tubular (DST) members with ultra-high performance fiber-reinforced concrete (UHPFRC). *Thin-Walled Structures, 144*, 106351. doi:https://doi.org/10.1016/j.tws.2019.106351

Wei, J., Li, J., & Wu, C. (2019). An experimental and numerical study of reinforced conventional concrete and ultra-high performance concrete columns under lateral impact loads. *Engineering Structures, 201*, 109822. doi:https://doi.org/10.1016/j.engstruct.2019.109822

Wei, J., Li, J., Wu, C., Liu, Z.-x., & Fang, J. (2021). Impact resistance of ultra-high performance concrete strengthened reinforced concrete beams. *International Journal of Impact Engineering, 158*, 104023. doi:https://doi.org/10.1016/j.ijimpeng.2021.104023

Wong, P., Vecchio, F., & Trommels, H. (2013). VecTor2 & Formworks user's manual (Second Edition). *University of Toronto, Canada*, pp. 347

Wu, H., Ren, G. M., Fang, Q., & Liu, J. Z. (2019). Response of ultra-high performance cementitious composites filled steel tube (UHPCC-FST) subjected to low-velocity impact. *Thin-Walled Structures, 144*, 106341. doi:https://doi.org/10.1016/j.tws.2019.106341

Wu, Y., Crawford, J. E., & Magallanes, J. M. (2012). *Performance of LS-DYNA concrete constitutive models.* Paper presented at the 12th International LS-DYNA users conference.

Xu, S., Wu, P., Liu, Z., & Wu, C. (2021). Calibration of CSCM model for numerical modeling of UHPCFTWST columns against monotonic lateral loading. *Engineering Structures, 240*, 112396. doi:https://doi.org/10.1016/j.engstruct.2021.112396

Xu, S., Wu, P., & Wu, C. (2020). Calibration of KCC concrete model for UHPC against low-velocity impact. *International Journal of Impact Engineering, 144*, 103648. doi:https://doi.org/10.1016/j.ijimpeng.2020.103648

Yan, J., Liu, Y., Bai, F., Ni, X., Xu, Y., Yan, Z., & Huang, F. (2022). Dynamic response of GFRP-reinforced UHPC beams under close-in blast loading. *Materials & Design*, 111140. doi:https://doi.org/10.1016/j.matdes.2022.111140

Yang, T., Wang, W., Liu, Z., Wu, C., Xu, S., & Yang, Y. (2021). Behavior of CFRP-UHPFRC-steel double skin tubular columns against low-velocity impact. *Composite Structures, 261*, 113284. doi:https://doi.org/10.1016/j.compstruct.2020.113284

Yin, H., Shirai, K., & Teo, W. (2019a). Finite element modelling to predict the flexural behaviour of ultra-high performance concrete members. *Engineering Structures, 183*, 741-755. doi:https://doi.org/10.1016/j.engstruct.2019.01.046

Yin, H., Shirai, K., & Teo, W. (2019b). Numerical model for predicting the structural response of composite UHPC–concrete members considering the bond strength at the interface. *Composite Structures, 215*, 185-197. doi:https://doi.org/10.1016/j.compstruct.2019.02.040

Yoo, D.-Y., Banthia, N., Kim, S.-W., & Yoon, Y.-S. (2015). Response of ultra-high-performance fiber-reinforced concrete beams with continuous steel reinforcement subjected to low-velocity impact loading. *Composite Structures, 126*, 233-245. doi:https://doi.org/10.1016/j.compstruct.2015.02.058

Zhang, F., Shedbale, A. S., Zhong, R., Poh, L. H., & Zhang, M.-H. (2021). Ultra-high performance concrete subjected to high-velocity projectile impact: implementation of K&C model with consideration of failure surfaces and dynamic increase factors. *International Journal of Impact Engineering, 155*. doi:https://doi.org/10.1016/j.ijimpeng.2021.103907

Zhang, T., Wu, H., Fang, Q., Huang, T., Gong, Z. M., & Peng, Y. (2017a). UHP-SFRC panels subjected to aircraft engine impact: Experiment and numerical simulation. *International Journal of Impact Engineering, 109*, 276-292. doi:https://doi.org/10.1016/j.ijimpeng.2017.07.012

Zhang, T., Wu, H., Zhang, F. J., Fang, Q., & Huang, T. (2017b). Ballistic limit of aircraft engine missile impact on ultra-high-performance steel-fiber-reinforced concrete panels. *International Journal of Protective Structures, 8*(4), 503-523. doi:https://doi.org/10.1177/2041419617716498

Chapter 10 Conclusions

10.1 Conclusions

This thesis has presented the experimental and analytical results of a study that investigated the static and blast behavior of RC beams designed with high-strength (HSS) and stainless steel (SS) reinforcement. As a part of the experimental study, forty-four beams, subdivided into three series, were tested under either quasi-static bending or simulated blast loads using the University of Ottawa shock-tube. The variables that were included in the tests from Series 1 (HSC-HSS) and Series 2 included: the influence of detailing, the effects of steel grade/type, steel ratio and steel fibers. In addition, the variables that were included in the tests from Series 3 (UHPC-NSS, UHPC-HSS and UHPC-SS) included: the effect of steel grade/type, concrete type, steel ratio and detailing & fiber content.

The following conclusions are drawn from the experimental results of the beams from Series 1 and 2:

1 The use of stainless steel increased the load-carrying capacity of the plain and fiber-reinforced HSC beams built with stirrups under static loading. The use of stainless bars also improved blast performance by reducing displacements and increasing blast capacity. In general, the use of moderate stainless steel ratio (ρ =1.5%) combined with high-strength concrete allowed for relatively ductile response under static and blast loads;

2 The use of steel fibers further improved the blast response of the beams with stainless bars. In the beams with stirrups, the use of 1% fibers reduced displacements at equivalent blasts, and increased blast capacity. Importantly, the provision of fibers enhanced damage tolerance, and reduced the amount of spalling and secondary blast fragments;

3 In the beams without stirrups, the use of 1% steel fibers increased shear capacity allowing for a near-doubling in failure impulse. However, the use of fibers was insufficient to prevent shear failure and fully replace stirrups owing to the increased shear demands imposed by the higher-strength and strain-hardening stainless steel bars. Thus, fibers should be combined with transverse reinforcement to prevent shear failures in stainless steel reinforced beams;

4 Replacing ordinary steel bars with near equal-strength amounts of stainless steel bars (i.e., similar ρf_y ratios) allowed for similar beam responses under static and blast loading. The coupled use of reduced amounts of stainless bars and fibers was particularly effective under blast loading. The differences in terms of displacement control and damage tolerance were still more significant when comparing beams CF100-No.5S1-S (ρ = 1.5%, and fibers) and C100-20M-S (ρ = 2.4%, no fibers), confirming the benefits of combining fibers and stainless steel reinforcement.

5 The use of blast detailing significantly enhanced the response of the beams reinforced with high-strength or stainless steel under both static and blast loads. Under static loading, the use of top continuity (compression) bars and closely-spaced ties increased load-carrying capacity, stiffness and ductility due to the ability of the improved detailing to enhance the toughness of the concrete compression zone. Likewise, blast detailing significantly enhanced blast response by reducing displacements, increasing blast capacity and allowing for significant post-blast residual resistance;

6 The use of moderate amounts of steel fibers (as low as 0.75%) can be used to relax blast detailing in beams reinforced with high-strength or stainless steel bars by increasing tie spacing from d/4 to d/2. In this research program, fibers and intermediate detailing allowed for significantly high static, blast and post-blast resistance, with better control of damage when compared to the companion HSC beams designed with blast detailing;

7 The results show that substitution of normal-strength bars with high-strength bars or stainless steel bars increased the capacity of the beams under both static and blast loads. Similarly, fibers and reduced amounts of high-strength or stainless bars allowed for similar performance when compared to beams with larger amounts of normal-strength reinforcement. On the other hand, it is important to consider the possibility of bar fracture when designing well-detailed HSS-RC beams, especially when using low steel ratios and/or fibers. The use of stainless steel was effective in preventing bar fracture failures even in the case of SS-RC beams with low steel ratios and/or fibers;

8 Under static loading, the use of duplex 2304 stainless steel reinforcement (S2) resulted in increased beam strength, with the same ability to sustain loads up to the end of testing, despite its reduced ultimate strain capacity when compared to austenitic XM-28 reinforcement (S1). The influence of stainless steel type was more limited under blast loads, however the S2 reinforcement led to an increase in post-blast residual capacity when compared to the S1 bars.

9 All beams with blast detailing showed significant residual post-blast capacity which closely matched the responses and failure modes of the undamaged beams tested under static loads only. All beams showed high RRI (low damage), high RSI (low stiffness degradation) and significant TEI (high residual energy absorption capacity) due to the positive influence of the blast detailing. In addition, the TEI index was able to indicate the change in failure mode in the beams tested under repeated blast loads.

The following conclusions are drawn from the experimental results of the beams from Series 3:

1. In Group 1, the use of UHPC with 3% fibers prevented shear failure and significantly enhanced all aspects of flexural response when compared to companion HSC beams with nominal detailing under static loading. Likewise, under blast loading, the use of UHPC prevented shear failure and showed higher blast capacity when compared to companion HSC beams with nominal detailing. The higher compressive strength and toughness of UHPC prevented damage in compression, but its's high bond capacity resulted in bar fracture failures in the beams with ordinary or high-strength steel bars.
2. In Group 2, the UHPC beams with intermediate detailing showed increased strength and stiffness when compared to the companion HSC beams with blast detailing under static loading. As a result, the UHPC beams showed better ability to control displacements at equivalent (or larger) blasts under blast loading. However, the ductility of the UHPC beams (under both static and blast loads) was reduced due to the bar fracture failures.
3. Increasing the tension steel ratio in the UHPC beams had a significant effect on performance, regardless of the steel type. Under static loading, increasing the tension steel ratio effectively increased the failure displacement and ductility of the UHPC beams. Under blast loading, increasing the steel ratio resulted in better control of displacements under equivalent blast loading and delayed or prevented bar fracture. In addition, the ductility in the post-blast residual test was significantly improved.
4. When comparing companion UHPC beams with equal amounts of high-strength and normal-strength bars under static loading, the HS reinforcement significantly increased load carrying capacity, with a less prominent effect on failure displacement. The use of higher-strength steel prevented bar rupture in the Group 1 beam under blast loading,

and allowed for significant post-blast capacity. In addition, under static loading, UHPC beams with similar ρf_y ratios (but lower amounts of high-strength bars) showed similar peak strengths, and similar or improved control of blast displacements (when compared to beams with greater amounts of normal-strength bars).

5. Substitution of normal-strength bars with stainless steel (SS) bars in the UHPC beams did not increase beam capacity but resulted in remarkable enhancements in performance, with increases in failure displacement, ductility and overall toughness under static loads. The SS bars were able to better utilize the high compressive capacity of the UHPC, with failure occurring due to crushing of concrete rather than fracture of the tension steel reinforcement. Likewise, under blast loads, the use of stainless steel improved blast load resistance and control of displacements, and prevented bar rupture. The significant ductility without bar rupture was also observed in the post-blast tests.
6. Detailing & fiber content had limited effects on the performance of the UHPC beams under static or blasts. Under static loads, UHPC beams with nominal and intermediate detailing showed similar load-deflection responses and failure modes. Increasing fiber content (from 3% to 2%) resulted in a moderate increase in peak load (in the NS and SS sets) and a slight delay in failure displacement (in the NS and HS sets). After crack localization and loss of fiber bridging capacity, the U3 and U2 beams showed a near-perfect match in load-displacement response indicating that the response was governed by the steel reinforcement in this later stage of loading. As a result, the U3 and U2 beams showed comparable displacement responses and damage mode in the blast tests and similar residual load-displacement curves in the post-blast tests.

As a part of the numerical study, the behaviour of the high-strength concrete (HSC) beams tested in Series 1 and 2 were predicted using the 2D nonlinear finite element software VecTor2. The dynamic responses of the UHPC beams from Series 3 were predicted using the 3D finite-element (FE) software LS-DYNA.

The following conclusions are drawn from the numerical results:

1. 2D finite element modelling using software VecTor2, with appropriate material models, can well predict the static load-deflection response of HSC and HSFRC beams with

varying steel types and detailing. Importantly, the FE models can well predict failure modes such as bar rupture, concrete crushing and shear failure.

2. The 2D FE models developed in software VecTor2 can also predict the maximum displacements, dynamic load reaction curves, and failure modes of HSC and HSFRC beams from Series 1 and 2 under blast loading. Although, the blast displacements were less accurately predicted during subsequent cycles, with the results sensitive to the choice of damping coefficients.
3. The 3D finite element blast analysis using software LS-DYNA, with appropriate selection of material models for the UHPC and steel reinforcement, allowed for reasonable predictions of the overall blast behaviour of UHPC beams with varying steel types and detailing, in terms of experimental dynamic displacements, load-time histories, and damage modes.
4. In general, both the Winfrith_Concrete model (MAT_084) and the CSCM model MAT_159) with calibrated values can well simulate the blast response of UHPC materials. However the calibrated CSCM model had a lower UHPC tensile strength, which resulted in U2-No.4HS-DR-d/2 having earlier bar rupture failure when compared to the experiment.

10.2 Recommendations for future work

The following recommendations for future studies are suggested:

- Study the effects of detailing in HSC and UHPC columns and walls built with varying steel types under combined axial and blast loads.
- Further study the effects of varying fiber contents (from 1% to 4%), fiber types (with varying lengths, aspect ratios, etc.) on ductility and bar fracture failures in UHPC beams with varying steel types under static and blast loads. Likewise, the effects of varied and higher reinforcement ratios ($>0.5\rho_b$) on ductility and failure mode are also recommended.
- The majority of the tests in this research considered one type of SS reinforcement (XM-28). Further research on the influence of different types of stainless steel (2304, 2205, 316LN, 304, 2101) on the structural performance and HSC and UHPC beams under static and blast loads is recommended.

- The beams in this study were tested using a shock-tube which simulates far-field type blast loading. Experimental and numerical studies are recommended to study the behaviour of HSC and UHPC structural components built with varying steel types under close-in or contact explosions. Likewise research on the impact behaviour of such structures is also recommended.
- For the 2D FE modelling, develop tension stiffening models for the ASTM A1035 high-strength steel and ASTM A955 stainless steel, since tension stiffening response of the concrete might be affected by reinforcement type. The development of appropriate tension models (tension softening and tension stiffening) for the behaviour of UHPC is also recommended.
- For the 3D FE modelling: Further calibrate the CSCM models to better predict the responses of UHPC structures in software LS-DYNA.
- Comparing the benefits of implementing different steel types (carbon steel, stainless steel and high strength steel) in flexural members in terms of their life cycle costs.

References (all chapters)

Aaleti, S., Petersen, B., & Sritharan, S. (2013). Design Guide for Precast UHPC Waffle Deck Panel System, including Connections. *No. FHWA-HIF-13-032*: U.S. Federal Highway Administration, pp. 125

ACI Committee 544 (1988). Design considerations for steel-fiber reinforced concrete. ACI 544.4R-188, American Concrete Institution, Detroit, Mich., pp. 18.

ACI Committee 544 (2002). Report on Fiber Reinforced Concrete. 544.1R-96, American Concrete Institute, Farmington Hills, pp. 66.

Adhikary, S. D., Li, B., & Fujikake, K. (2014). Residual resistance of impact-damaged reinforced concrete beams. *Magazine of Concrete Research, 67*(7), 364-378. doi:https://doi.org/10.1680/macr.14.00312

AFGC (2013). Ultra high performance fibre-reinforced concretes. AFGC & SETRA Working Group Paris, France, pp. 175.

Aghdasi, P., & Ostertag, C. P. (2020). Tensile fracture characteristics of Green Ultra-High Performance Fiber-Reinforced Concrete (G-UHP-FRC) with longitudinal steel reinforcement. *Cement and Concrete Composites, 114*, 103749. doi:https://doi.org/10.1016/j.cemconcomp.2020.103749

Al-Ta'an, S., & Al-Feel, J. (1990). Evaluation of shear strength of fibre-reinforced concrete beams. *Cement and Concrete Composites, 12*(2), 87-94. doi:https://doi.org/10.1016/0958-9465(90)90045-Y

Algassem, O., Li, Y., & Aoude, H. (2019). Ability of steel fibers to enhance the shear and flexural behavior of high-strength concrete beams subjected to blast loads. *Engineering Structures, 199*, 109611. doi:https://doi.org/10.1016/j.engstruct.2019.109611

Amin, A., Foster, S. J., & Muttoni, A. (2015). Derivation of the σ-wrelationship for SFRC from prism bending tests. *Structural Concrete, 16*(1), 93-105. doi:https://doi.org/10.1002/suco.201400018

Aoude, H., Belghiti, M., Cook, W. D., & Mitchell, D. (2012). Response of Steel Fiber-Reinforced Concrete Beams with and without Stirrups. *ACI Structural Journal, 109*(3), 359-367. doi:https://doi.org/10.14359/51683749

Aoude, H., Dagenais, F. P., Burrell, R. P., & Saatcioglu, M. (2015). Behavior of ultra-high performance fiber reinforced concrete columns under blast loading. *International Journal of Impact Engineering, 80*, 185-202. doi:https://doi.org/10.1016/j.ijimpeng.2015.02.006

Ashour, S. A., & Wafa, F. F. (1993). Flexural behavior of high-strength fiber reinforced concrete beams. *ACI Structural Journal, 90*(3), 279-287. doi:https://doi.org/10.14359/4186

ASTM A1035/A1035M-11 (2011). Standard Specification for Deformed and Plain, Low-Carbon, Chromium, Steel Bars for Concrete Reinforcement. ASTM International, West Conshohocken, PA, pp. 5.

ASTM C1856/C1856M-17 (2017). Standard Practice for Fabricating and Testing Specimens of Ultra-High Performance Concrete. ASTM International, West Conshohocken, PA, pp. 4.

ASTM C39 / C39M-18 (2018). Standard Test Method for Compressive Strength of Cylindrical Concrete Specimens. ASTM International, West Conshohocken, PA, pp. 8.

ASTM C1609 / C1609M-19 (2019). Standard Test Method for Flexural Performance of Fiber-Reinforced Concrete (Using Beam With Third-Point Loading). ASTM International, West Conshohocken, PA, pp. 9.

ASTM A955/A955M − 20c (2020a). Standard Specification for Deformed and Plain Stainless Steel Bars for Concrete Reinforcement. ASTM International, West Conshohocken, PA, pp. 16.

A1035/A1035M − 20 (2020b). Standard Specification for Deformed and Plain, Low-Carbon, Chromium, Steel Bars for Concrete Reinforcement. ASTM International, West Conshohocken, PA, pp. 7.

Bandelt, M. J., & Billington, S. L. (2016). Impact of Reinforcement Ratio and Loading Type on the Deformation Capacity of High-Performance Fiber-Reinforced Cementitious Composites Reinforced with Mild Steel. *Journal of Structural Engineering, 142*(10), 04016084. doi:https://doi.org/10.1061/(asce)st.1943-541x.0001562

Barbachyn, S. M., Devine, R. D., Thrall, A. P., & Kurama, Y. C. (2017). Effect of High-Strength Materials on Lateral Strength of Stocky Reinforced Concrete Walls. *ACI Structural Journal, 114*(4), 923-936. doi:https://doi.org/10.14359/51689722

Bernard, E. S., Amin, A., & Gilbert, R. I. (2020). Assessment of MC2010 and AS3600 models for estimating instantaneous flexural crack widths in fibre reinforced concrete members. *Engineering Structures, 208*, 110271. doi:https://doi.org/10.1016/j.engstruct.2020.110271

Burrell, R. P., Aoude, H., & Saatcioglu, M. (2013). Blast Behaviour of Ultra High Strength CRC Columns. *ACI Special Publication, 293*, 1-18.

Cao, Y. Y. Y., Yu, Q., Tang, W. H., & Brouwers, H. J. H. (2020). Numerical investigation on ballistic performance of coarse-aggregated layered UHPFRC. *Construction and Building Materials, 250*, 118867. doi:https://doi.org/10.1016/j.conbuildmat.2020.118867

Cavill, B., Rebentrost, M., & Perry, V. (2006). *Ductal®-An ultra-high performance material for resistance to blasts and impacts.* Paper presented at the 1st Specialty Conference on Disaster Mitigation, Calgary, Alberta, Canada.

CEB-FIP (1991). Model Code 1990. Comite Euro-International Du Beton, Paris, pp. 87-109.

Cernica, J., & Charignon, M. (1963). Ultimate static and impulse loading of reinforced concrete beams. *ACI Journal Proceedings, 60*(9), 1219-1298.

Chan, T., & Mackie, K. R. (2018, June 18-21, 2018). *Substructure Connection in High Seismic Zones Utilizing Ultra-high Performance Concrete.* Paper presented at the 16th European Conference on Earthquake Engineering, Thessal.

Charles, C. J. (2019). *Effect of detailing and fibers on the static and blast behaviour of high-strength concrete beams.* (MASc. thesis). University of Ottawa, Ottawa, ON, Canada.

Chen, L., Hu, Y., Ren, H., Xiang, H., Zhai, C., & Fang, Q. (2019). Performances of the RC column under close-in explosion induced by the double-end-initiation explosive cylinder. *International Journal of Impact Engineering, 132*, 103326. doi:https://doi.org/10.1016/j.ijimpeng.2019.103326

Cheng, M. Y., & Giduquio, M. B. (2014). Cyclic behavior of reinforced concrete flexural members using high-strength flexural reinforcement. *ACI Structural Journal, 111*(4), 893-902. doi:https://doi.org/10.14359/51686632

Cortés-Puentes, W. L., & Palermo, D. (2012). Modeling of RC Shear Walls Retrofitted with Steel Plates or FRP Sheets. *Journal of Structural Engineering, 138*(5), 602-612. doi:https://doi.org/10.1061/(asce)st.1943-541x.0000466

Concrete Reinforcing Steel Institute (2001). *Evaluation of reinforcing bars in old reinforced concrete structures*. Engineering Data Rep. 48.

Canadian Standards Association (CSA) (2012). Design and assessment of buildings subjected to blast loads. CSA S850-12, Mississauga, ON, Canada, pp. 126.

Canadian Standards Association (CSA) (2014). Design of concrete structures. CAN/CSA A23.3-14, Mississauga, ON, pp. 295.

Concrete Reinforcing Steel Institute (2017). *FAQs About Low-Carbon, Chromium ASTM A1035 Types CS, CM and CL Steel Reinforcing Bar (ETN-M-11-17)*. http://resources.crsi.org/index.cfm/_api/render/file/?method=inline&fileID=119C15CA-A667-FBFE-FC13E2CE25B8DD93.

Dancygier, A. N., & Karinski, Y. S. (2019). Effect of cracking localization on the structural ductility of normal strength and high strength reinforced concrete beams with steel fibers. *International Journal of Protective Structures, 10*(4), 457–469. doi:https://doi.org/10.1177/2041419618824609

De Carufel, S., & Aoude, H. (2020). Combined use of UHPC and High-Performance Steel to Improve the Blast Performance of Columns with Square Cross-section. *ACI Symposium Publication, 341*, 27-47.

Deluce, J. R., Lee, S.-C., & Vecchio, F. J. (2014). Crack model for steel fiber-reinforced concrete members containing conventional reinforcement. *ACI Structural Journal, 111*(1), 93-102. doi:https://doi.org/10.14359/51686433

Fan, W., Guo, W., Sun, Y., Chen, B., & Shao, X. (2018a). Experimental and numerical investigations of a novel steel-UHPFRC composite fender for bridge protection in vessel collisions. *Ocean Engineering, 165*, 1-21. doi:https://doi.org/10.1016/j.oceaneng.2018.07.028

Fan, W., Shen, D., Huang, X., & Sun, Y. (2020a). Reinforced concrete bridge structures under barge impacts: FE modeling, dynamic behaviors, and UHPFRC-based strengthening. *Ocean Engineering, 216*, 108116. doi:https://doi.org/10.1016/j.oceaneng.2020.108116

Fan, W., Shen, D., Yang, T., & Shao, X. (2019). Experimental and numerical study on low-velocity lateral impact behaviors of RC, UHPFRC and UHPFRC-strengthened columns. *Engineering Structures, 191*, 509-525. doi:https://doi.org/10.1016/j.engstruct.2019.04.086

Fan, W., Shen, D., Zhang, Z., Huang, X., & Shao, X. (2020b). A novel UHPFRC-based protective structure for bridge columns against vehicle collisions: Experiment, simulation, and optimization. *Engineering Structures, 207*, 110247. doi:https://doi.org/10.1016/j.engstruct.2020.110247

Fan, W., Xu, X., Zhang, Z., & Shao, X. (2018b). Performance and sensitivity analysis of UHPFRC-strengthened bridge columns subjected to vehicle collisions. *Engineering Structures, 173*, 251-268. doi:https://doi.org/10.1016/j.engstruct.2018.06.113

Feng, Z., Li, C., Yoo, D.-Y., Pan, R., He, J., & Ke, L. (2021). Flexural and cracking behaviors of reinforced UHPC beams with various reinforcement ratios and fiber contents. *Engineering Structures, 248*, 113266. doi:https://doi.org/10.1016/j.engstruct.2021.113266

Federation Internationale du Beton (2013). fib Model Code for Concrete Structures 2010. Berlin: Ernst & Sohn Publishing House, pp. 434.

Foglar, M., Hajek, R., Fladr, J., Pachman, J., & Stoller, J. (2017). Full-scale experimental testing of the blast resistance of HPFRC and UHPFRC bridge decks. *Construction and Building Materials, 145*, 588-601. doi:https://doi.org/10.1016/j.conbuildmat.2017.04.054

Fujikake, K. (2014). Impact performance of ultra-high performance fiber reinforced concrete beam and its analytical evaluation. *International Journal of Protective Structures, 5*(2), 167-186. doi:https://doi.org/10.1260/2041-4196.5.2.167

Fujikake, K., Senga, T., Ueda, N., Ohno, T., & Katagiri, M. (2006a). Effects of Strain Rate on Tensile Behavior of Reactive Powder Concrete. *Journal of Advanced Concrete Technology, 4*(1), 79-84. doi:https://doi.org/10.3151/jact.4.79

Fujikake, K., Senga, T., Ueda, N., Ohno, T., & Katagiri, M. (2006b). Study on Impact Response of Reactive Powder Concrete Beam and Its Analytical Model. *Journal of Advanced Concrete Technology, 4*(1), 99-108. doi:https://doi.org/10.3151/jact.4.99

Gholipour, G., & Billah, A. H. M. M. (2022a). Dynamic behavior of bridge columns reinforced with shape memory alloy rebar and UHPFRC under lateral impact loads. *International Journal of Impact Engineering, 168*, 104297. doi:https://doi.org/10.1016/j.ijimpeng.2022.104297

Gholipour, G., & Billah, A. H. M. M. (2022b). Nonlinear Analysis of Shear-Deficient Beams Strengthened Using UHPFRC under Combined Impact and Blast Loads. *Journal of Structural Engineering, 148*(6), 04022056. doi:https://doi.org/10.1061/(asce)st.1943-541x.0003368

Giduquio, M. B., Cheng, M.-Y., & Wibowo, L. S. (2015). High-Strength Flexural Reinforcement in Reinforced Concrete Flexural Members under Monotonic Loading. *ACI Structural Journal, 112*(6), 793-803. doi:https://doi.org/10.14359/51688057

Graybeal, B. A. (2006). Material property characterization of ultra-high performance concrete. *No. FHWA-HRT-06-103*: Federal Highway Administration, Office of Infrastructure pp. 186

Graybeal, B. A., & Baby, F. (2013). Development of Direct Tension Test Method for Ultra-High-Performance Fiber-Reinforced Concrete. *ACI Materials Journal, 110*(2), 177-186. doi:https://doi.org/10.14359/51685532

Graybeal, B. A., & Baby, F. (2019). Tension Testing of Ultra-High Performance Concrete. *No. FHWA-HRT-17-053*: U.S. Federal Highway Administration, pp. 206

Guertin-Normoyle, C. (2017). *Blast Performance of Ultra-High Performance Concrete Beams Tested Under Shock-Tube Induced Loads.* (MASc. thesis). University of Ottawa, Ottawa, ON, Canada.

Guo, W., Fan, W., Shao, X., Shen, D., & Chen, B. (2018). Constitutive model of ultra-high-performance fiber-reinforced concrete for low-velocity impact simulations. *Composite Structures, 185*, 307-326. doi:https://doi.org/10.1016/j.compstruct.2017.11.022

Hallquist, J. O. (2007). LS-DYNA keyword user's manual. *Livermore Software Technology Corporation*, pp. 2937

Hasgul, U., Turker, K., Birol, T., & Yavas, A. (2018). Flexural behavior of ultra‐high‐performance fiber reinforced concrete beams with low and high reinforcement ratios. *Structural Concrete, 19*(6), 1577-1590. doi:https://doi.org/10.1002/suco.201700089

Hoang, A. L., & Fehling, E. (2017). Influence of steel fiber content and aspect ratio on the uniaxial tensile and compressive behavior of ultra high performance concrete. *Construction and Building Materials, 153*, 790-806. doi:https://doi.org/10.1016/j.conbuildmat.2017.07.130

Hrynyk, T. D., & Vecchio, F. J. (2016). Modeling of Reinforced and Fiber-Reinforced Concrete Slabs under Impact Loads. *ACI Special Publication, 321*, 8.1-8.20.

Huynh, L., Foster, S., Valipour, H., & Randall, R. (2015). High strength and reactive powder concrete columns subjected to impact: experimental investigation. *Construction and Building Materials, 78*, 153-171. doi:https://doi.org/10.1016/j.conbuildmat.2015.01.026

Imam, M., Vandewalle, L., & Mortelmans, F. (1995). Shear–moment analysis of reinforced high strength concrete beams containing steel fibres. *Canadian Journal of Civil Engineering, 22*(3), 462-470. doi:https://doi.org/10.1139/l95-054

Isojeh, B., El-Zeghayar, M., & Vecchio, F. J. (2019). Numerical Analysis of Reinforced Concrete and Steel-Fiber Concrete Elements under Fatigue Loading. *Journal of Structural Engineering, 145*(11), 04019126. doi:https://doi.org/10.1061/(asce)st.1943-541x.0002349

Jia, P. C., Wu, H., Wang, R., & Fang, Q. (2021). Dynamic responses of reinforced ultra-high performance concrete members under low-velocity lateral impact. *International Journal of Impact Engineering, 150*, 103818. doi:https://doi.org/10.1016/j.ijimpeng.2021.103818

Japan Society of Civil Engineers (1993). Impact behavior and design of structures. Structural Engineering Series 6 (in Japanese). Japan Society of Civil Engineers, Tokyo, pp.

Kahanji, C., Ali, F., & Nadjai, A. (2017). Structural performance of ultra-high-performance fiber-reinforced concrete beams. *Structural Concrete, 18*(2), 249-258. doi:https://doi.org/10.1002/suco.201600006

Keenan, W. A. (1963). Blast Loading of Concrete Beams Reinforced with High-Strength Deformed Bars. *Technical Report R226*: U.S. Naval Civil Engineering Laboratory,

Khaksefidi, S., Ghalehnovi, M., & de Brito, J. (2021). Bond behaviour of high-strength steel rebars in normal (NSC) and ultra-high performance concrete (UHPC). *Journal of Building Engineering, 33*, 101592. doi:https://doi.org/10.1016/j.jobe.2020.101592

Khalil, W. I., & Tayfur, Y. (2013). Flexural strength of fibrous ultra high performance reinforced concrete beams. *ARPN Journal of Engineering and Applied Sciences, 8*(3), 200-214.

Kishi, N., & Mikami, H. (2012). Empirical formulas for designing reinforced concrete beams under impact loading. *ACI Structural Journal, 109*(4), 509-519. doi:https://doi.org/10.14359/51683870

Lai, J., Guo, X., & Zhu, Y. (2015). Repeated penetration and different depth explosion of ultra-high performance concrete. *International Journal of Impact Engineering, 84*, 1-12. doi:https://doi.org/10.1016/j.ijimpeng.2015.05.006

Lai, J., Yang, H., Wang, H., Zheng, X., & Wang, Q. (2018). Properties and modeling of ultra-high-performance concrete subjected to multiple bullet impacts. *Journal of Materials in Civil Engineering, 30*(10), 04018256. doi:https://doi.org/10.1061/(ASCE)MT.1943-5533.0002462

Lee, J.-Y., Aoude, H., Yoon, Y.-S., & Mitchell, D. (2020). Impact and blast behavior of seismically-detailed RC and UHPFRC-Strengthened columns. *International Journal of Impact Engineering, 143*, 103628. doi:https://doi.org/10.1016/j.ijimpeng.2020.103628

Lee, S.-C., Cho, J.-Y., & Vecchio, F. J. (2011a). Diverse embedment model for steel fiber-reinforced concrete in tension: model development. *ACI Materials Journal, 108*(5), 516-525. doi:https://doi.org/10.14359/51683261

Lee, S.-C., Cho, J.-Y., & Vecchio, F. J. (2011b). Diverse embedment model for steel fiber-reinforced concrete in tension: Model verification. *ACI Materials Journal, 108*(5), 526-535. doi:https://doi.org/10.14359/51683262

Lee, S.-C., Cho, J.-Y., & Vecchio, F. J. (2013). Tension-Stiffening Model for Steel Fiber-Reinforced Concrete Containing Conventional Reinforcement. *ACI Structural Journal, 110*(4), 639-648. doi:https://doi.org/10.14359/51685749

Lee, S.-C., Cho, J.-Y., & Vecchio, F. J. (2016). Analysis of steel fiber-reinforced concrete elements subjected to shear. *ACI Structural Journal, 113*(2), 275-285. doi:https://doi.org/10.14359/51688474

Lee, S.-C., Oh, J. H., & Cho, J. Y. (2015). Compressive Behavior of Fiber-Reinforced Concrete with End-Hooked Steel Fibers. *Materials, 8*(4), 1442-1458. doi:https://doi.org/10.3390/ma8041442

Lepage, A., Tavallali, H., Pujol, S., & Rautenberg, J. M. (2012). High-performance steel bars and fibers as concrete reinforcement for seismic-resistant frames. *Advances in Civil Engineering, 2012*, 450981. doi:https://doi.org/10.1155/2012/450981

Li, J., & Wu, C. (2018). Damage evaluation of ultra-high performance concrete columns after blast loads. *International Journal of Protective Structures, 9*(1), 44-64. doi:https://doi.org/10.1177/2041419617743986

Li, J., Wu, C., & Hao, H. (2015a). An experimental and numerical study of reinforced ultra-high performance concrete slabs under blast loads. *Materials and Design, 82*, 64-76. doi:https://doi.org/10.1016/j.matdes.2015.05.045

Li, J., Wu, C., & Hao, H. (2015b). Investigation of ultra-high performance concrete slab and normal strength concrete slab under contact explosion. *Engineering Structures, 102*, 395-408. doi:https://doi.org/10.1016/j.engstruct.2015.08.032

Li, J., Wu, C., Hao, H., & Su, Y. (2015c). Investigation of ultra-high performance concrete under static and blast loads. *International Journal of Protective Structures, 6*(2), 217-235. doi:https://doi.org/10.1260/2041-4196.6.2.217

Li, J., Wu, C., Hao, H., Wang, Z., & Su, Y. (2016). Experimental investigation of ultra-high performance concrete slabs under contact explosions. *International Journal of Impact Engineering, 93*, 62-75. doi:https://doi.org/10.1016/j.ijimpeng.2016.02.007

Li, R. W., Zhou, D. Y., & Wu, H. (2020). Experimental and numerical study on impact resistance of RC bridge piers under lateral impact loading. *Engineering Failure Analysis, 109*, 104319. doi:https://doi.org/10.1016/j.engfailanal.2019.104319

Li, Y., Algassem, O., & Aoude, H. (2018). Response of high-strength reinforced concrete beams under shock-tube induced blast loading. *Construction and Building Materials, 189*, 420-437. doi:https://doi.org/10.1016/j.conbuildmat.2018.09.005

Li, Y., & Aoude, H. (2019). Blast response of beams built with high-strength concrete and high-strength ASTM A1035 bars. *International Journal of Impact Engineering, 130*, 41-67. doi:https://doi.org/10.1016/j.ijimpeng.2019.02.007

Li, Y., & Aoude, H. (2020). Influence of steel fibers on the static and blast response of beams built with high-strength concrete and high-strength reinforcement. *Engineering Structures, 221*, 111031. doi:https://doi.org/10.1016/j.engstruct.2020.111031

Liao, Q., Xie, X., & Yu, J. (2022). Numerical investigation on dynamic performance of reinforced ultra‐high ductile concrete‐ultra‐high performance concrete panel under explosion. *Structural Concrete*, 1-15. doi:https://doi.org/10.1002/suco.202100919

Liao, Z., Tang, D., Li, Z., Xue, Y., & Shao, L. (2019). Study on explosion resistance performance experiment and damage assessment model of high-strength reinforcement concrete beams. *International Journal of Impact Engineering, 133*, 103362. doi:https://doi.org/10.1016/j.ijimpeng.2019.103362

Liu, J., Li, J., Fang, J., Liu, K., Su, Y., & Wu, C. (2022a). Investigation of ultra-high performance concrete slabs under contact explosions with a calibrated K&C model. *Engineering Structures, 255*, 113958. doi:https://doi.org/10.1016/j.engstruct.2022.113958

Liu, J., Li, J., Fang, J., Su, Y., & Wu, C. (2022b). Ultra-high performance concrete targets against high velocity projectile impact – a-state-of-the-art review. *International Journal of Impact Engineering, 160*. doi:10.1016/j.ijimpeng.2021.104080

Liu, J., Wu, C., & Chen, X. (2017a). Numerical study of ultra-high performance concrete under non-deformable projectile penetration. *Construction and Building Materials, 135*, 447-458. doi:https://doi.org/10.1016/j.conbuildmat.2016.12.216

Liu, J., Wu, C., Li, J., Su, Y., & Chen, X. (2018a). Numerical investigation of reactive powder concrete reinforced with steel wire mesh against high-velocity projectile penetration. *Construction and Building Materials, 166*, 855-872. doi:https://doi.org/10.1016/j.conbuildmat.2018.02.001

Liu, J., Wu, C., Li, J., Su, Y., Shao, R., Liu, Z., & Chen, G. (2017b). Experimental and numerical study of reactive powder concrete reinforced with steel wire mesh against projectile penetration. *International Journal of Impact Engineering, 109*, 131-149. doi:https://doi.org/10.1016/j.ijimpeng.2017.06.006

Liu, J., Wu, C., Su, Y., Li, J., Shao, R., Chen, G., & Liu, Z. (2018b). Experimental and numerical studies of ultra-high performance concrete targets against high-velocity projectile impacts. *Engineering Structures, 173*, 166-179. doi:https://doi.org/10.1016/j.engstruct.2018.06.098

Luccioni, B., Isla, F., Codina, R., Ambrosini, D., Zerbino, R., Giaccio, G., & Torrijos, M. C. (2017). Effect of steel fibers on static and blast response of high strength concrete. *International Journal of Impact Engineering, 107*, 23-37. doi:https://doi.org/10.1016/j.ijimpeng.2017.04.027

Lulec, A. (2017). *Simplified Analytical Tools for Impact and Impulsive Loading Analysis of Reinforced Concrete Structures.* (PhD thesis). University of Toronto, Toronro, ON, Canada.

Magnusson, J., Hallgren, M., & Ansell, A. (2010). Air-blast-loaded, high-strength concrete beams. Part I: Experimental investigation. *Magazine of Concrete Research, 62*(2), 127-136. doi:https://doi.org/10.1680/macr.2008.62.2.127

Naval Facilities Engineering Service Center Port hueneme CA (1998). *Dynamic increase factors for concrete*.

Mander, J. B., Priestley, M. J. N., & Park, R. (1988). Theoretical Stress-Strain Model for Confined Concrete. *Journal of Structural Engineering, 114*(8), 1804-1826. doi:https://doi.org/10.1061/(Asce)0733-9445(1988)114:8(1804)

Mansur, M. A., Chin, M. S., & Wee, T. H. (1997). Flexural behavior of high-strength concrete beams. *ACI Structural Journal, 94*(6), 663-674. doi:https://doi.org/10.14359/9726

Mao, L., Barnett, S., Begg, D., Schleyer, G., & Wight, G. (2014). Numerical simulation of ultra high performance fibre reinforced concrete panel subjected to blast loading. *International Journal of Impact Engineering, 64*, 91-100. doi:https://doi.org/10.1016/j.ijimpeng.2013.10.003

Mao, L., & Barnett, S. J. (2017). Investigation of toughness of ultra high performance fibre reinforced concrete (UHPFRC) beam under impact loading. *International Journal of Impact Engineering, 99*, 26-38. doi:https://doi.org/10.1016/j.ijimpeng.2016.09.014

Mavis, F., & Greaves, M. (1957). Destructive impulse loading of reinforced concrete beams. *ACI Journal Proceedings, 54*(9), 233-252.

Mavis, F., & Richards, F. (1955). Impulse testing of concrete beams. *ACI Journal Proceedings, 52*(9), 93-102.

Mavis, F., & Stewart, J. (1959). Further tests of dynamically loaded beams. *ACI Journal Proceedings, 55*(5), 1215-1223.

Miyamoto, A., King, M. W., & Fujii, M. (1989). Non-linear dynamic analysis and design concepts for RC beams under impulsive loads. *Bulletin of the New Zealand national society for earthquake engineering, 22*(2), 98-111.

Mylrea, T. (1940). Effect of impact on reinforced concrete beams. *ACI Journal Proceedings, 36*(6), 581-594.

NEHRP Consultants Joint Venture (2014). *Use of High-Strength Reinforcement in Earthquake-Resistant Concrete Structures*. Washington, DC.

Oppong, K., Saini, D., & Shafei, B. (2021). Ultra high-Performance Concrete for Improving Impact Resistance of Bridge Superstructures to Overheight Collision. *Journal of Bridge Engineering, 26*(9), 04021060. doi:https://doi.org/10.1061/(asce)be.1943-5592.0001736

Othman, H., & Marzouk, H. (2016). Impact response of ultra-high-performance reinforced concrete plates. *ACI Structural Journal, 113*(6), 1325-1334. doi:https://doi.org/10.14359/51689157

Ousalem, H., Takatsu, H., Ishikawa, Y., & Kimura, H. (2009). Use of high-strength bars for the seismic performance of high-strength concrete columns. *Journal of Advanced Concrete Technology, 7*(1), 123-134. doi:https://doi.org/10.3151/jact.7.123

Palermo, D., & Vecchio, F. J. (2007). Simulation of Cyclically Loaded Concrete Structures Based on the Finite-Element Method. *Journal of Structural Engineering, 133*(5), 728-738. doi:https://doi.org/10.1061/(asce)0733-9445(2007)133:5(728)

Pam, H., Kwan, A., & Islam, M. (2001). Flexural strength and ductility of reinforced normal-and high-strength concrete beams. *Proceedings of the Institution of Civil Engineers: Structures and Buildings, 146*(4), 381-389. doi:https://doi.org/10.1680/stbu.146.4.381.45454

Park, R. (1989). Evaluation of ductility of structures and structural assemblages from laboratory testing. *Bulletin of the New Zealand national society for earthquake engineering, 22*(3), 155-166.

Park, R., & Paulay, T. (1975). *Reinforced concrete structures*. New York: John Wiley & Sons.

Pokhrel, M., & Bandelt, M. J. (2019). Material properties and structural characteristics influencing deformation capacity and plasticity in reinforced ductile cement-based composite structural components. *Composite Structures, 224*, 111013. doi:https://doi.org/10.1016/j.compstruct.2019.111013

Popovics, S. (1973). A numerical approach to the complete stress-strain curve of concrete. *Cement and Concrete Research, 3*(5), 583-599. doi:https://doi.org/10.1016/0008-8846(73)90096-3

Qi, J., Wang, J., & Ma, Z. J. (2017). Flexural response of high-strength steel-ultra-high-performance fiber reinforced concrete beams based on a mesoscale constitutive model: Experiment and theory. *Structural Concrete, 19*(3), 719-734. doi:https://doi.org/10.1002/suco.201700043

Rabi, M., Shamass, R., & Cashell, K. A. (2022). Structural performance of stainless steel reinforced concrete members: A review. *Construction and Building Materials, 325*, 126673. doi:https://doi.org/10.1016/j.conbuildmat.2022.126673

Rashid, M., & Mansur, M. (2005). Reinforced high-strength concrete beams in flexure. *ACI Structural Journal, 102*(3), 462-471. doi:https://doi.org/10.14359/14418

Rautenberg, J. M., Pujol, S., Tavallali, H., & Lepage, A. (2013). Drift capacity of concrete columns reinforced with high-strength steel. *ACI Structural Journal, 110*(2), 307-317. doi:https://doi.org/10.14359/51684410

Ren, G. M., Wu, H., Fang, Q., Liu, J. Z., & Gong, Z. M. (2016). Triaxial compressive behavior of UHPCC and applications in the projectile impact analyses. *Construction and Building Materials, 113*, 1-14. doi:https://doi.org/10.1016/j.conbuildmat.2016.02.227

Ren, L., Yu, X., Zheng, M., Xue, Z., Wu, B., & He, Y. (2022). Evaluation of typical dynamic damage models used for UHPC based on SHPB technology. *Engineering Fracture Mechanics, 269*, 108562. doi:https://doi.org/10.1016/j.engfracmech.2022.108562

Roller, C., Mayrhofer, C., Riedel, W., & Thoma, K. (2013). Residual load capacity of exposed and hardened concrete columns under explosion loads. *Engineering Structures, 55*, 66-72. doi:https://doi.org/10.1016/j.engstruct.2011.12.004

United States, Federal Highway Administration, Office of Infrastructure Research and Development (2013). *Ultra-high performance concrete: A state-of-the-art report for the bridge community*.

Saatci, S. (2007). *Behaviour and modelling of reinforced concrete structures subjected to impact loads.* (PhD thesis). University of Toronto, Toronro, ON, Canada.

Saatci, S., & Vecchio, F. J. (2009). Nonlinear Finite Element Modeling of Reinforced Concrete Structures under Impact Loads. *ACI Structural Journal, 106*(5), 717-725. doi:https://doi.org/10.14359/51663112

Sagals, G., Orbovic, N., & Blahoianu, A. (2011). Sensitivity studies of reinforced concrete slabs under impact loading. *Transactions of the 21st SMiRT*.

Saini, D., Oppong, K., & Shafei, B. (2021). Investigation of Concrete Constitutive Models for Ultra-High Performance Fiber-Reinforced Concrete under Low-Velocity Impact. *International Journal of Impact Engineering, 157*, 103969. doi:https://doi.org/10.1016/j.ijimpeng.2021.103969

Schwer, L. (2010). An introduction to the Winfrith concrete model. *Schwer Engineering & Consulting Services*.

Schwer, L. (2011). *The Winfrith concrete model: Beauty or beast? Insights into the Winfrith concrete model.* Paper presented at the 8th European LS-DYNA users conference.

Seckin, M. (1981). *Hysteretic behaviour of cast-in-place exterior beam-column-slab subassemblies.* (PhD thesis). University of Toronto, Toronro, ON, Canada.

Shao, Y., & Billington, S. L. (2019). Predicting the two predominant flexural failure paths of longitudinally reinforced high-performance fiber-reinforced cementitious composite structural members. *Engineering Structures, 199*, 109581. doi:https://doi.org/10.1016/j.engstruct.2019.109581

Shao, Y., & Billington, S. L. (2021). Impact of cyclic loading on longitudinally-reinforced UHPC flexural members with different fiber volumes and reinforcing ratios. *Engineering Structures, 241*, 112454. doi:https://doi.org/10.1016/j.engstruct.2021.112454

Simms, L. (1945). Actual and estimated impact resistance of some reinforced-concrete units failing in bending. *Journal of the Institution of Civil Engineers, 23*(4), 163-179.

Stolz, A., Fischer, K., Roller, C., & Hauser, S. (2014). Dynamic bearing capacity of ductile concrete plates under blast loading. *International Journal of Impact Engineering, 69*, 25-38. doi:https://doi.org/10.1016/j.ijimpeng.2014.02.008

Sturt, R. (2019). MAT_WINFRITH - RATE=2 Ottosen yield surface. . Retrieved from https://ftp.lstc.com/anonymous/outgoing/support/FAQ_kw/concrete/mat84_winfrith

Su, J., Wang, J., Li, Z., & Liang, X. (2019). Effect of reinforcement grade and concrete strength on seismic performance of reinforced concrete bridge piers. *Engineering Structures, 198*, 109512. doi:https://doi.org/10.1016/j.engstruct.2019.109512

Su, Q., Wu, H., & Fang, Q. (2022). Calibration of KCC model for UHPC under impact and blast loadings. *Cement and Concrete Composites, 127*, 104401. doi:https://doi.org/10.1016/j.cemconcomp.2021.104401

Susetyo, J., Gauvreau, P., & Vecchio, F. J. (2013). Steel Fiber-Reinforced Concrete Panels in Shear: Analysis and Modeling. *ACI Structural Journal, 110*(2), 285-296. doi:https://doi.org/10.14359/51684408

Tai, Y. S. (2009). Flat ended projectile penetrating ultra-high strength concrete plate target. *Theoretical and Applied Fracture Mechanics, 51*(2), 117-128. doi:https://doi.org/10.1016/j.tafmec.2009.04.005

Thai, D. K., & Kim, S. E. (2015). Failure analysis of UHPFRC panels subjected to aircraft engine model impact. *Engineering Failure Analysis, 57*, 88-104. doi:https://doi.org/10.1016/j.engfailanal.2015.07.005

Thiagarajan, G., Kadambi, A. V., Robert, S., & Johnson, C. F. (2015). Experimental and finite element analysis of doubly reinforced concrete slabs subjected to blast loads. *International Journal of Impact Engineering, 75*, 162-173. doi:https://doi.org/10.1016/j.ijimpeng.2014.07.018

Trejo, D., Link, T. B., & Barbosa, A. R. (2016). Effect of Reinforcement Grade and Ratio on Seismic Performance of Reinforced Concrete Columns. *ACI Structural Journal, 113*(5), 907-916. doi:https://doi.org/10.14359/51689015

Trommels, H. (2013). *Towards Simplified Tools for Analysis of Reinforced Concrete Structures Subjected to Impact and Impulsive Loading: A Preliminary Investigation.* (MASc thesis). University of Toronto, Toronro, ON, Canada.

Vecchio, F. J. (1992). Finite Element Modeling of Concrete Expansion and Confinement. *Journal of Structural Engineering, 118*(9), 2390-2406. doi:https://doi.org/10.1061/(asce)0733-9445(1992)118:9(2390)

Vecchio, F. J. (2000). Disturbed Stress Field Model for Reinforced Concrete: Formulation. *Journal of Structural Engineering, 126*(9), 1070-1077. doi:https://doi.org/10.1061/(asce)0733-9445(2000)126:9(1070)

Vecchio, F. J. (2001). Disturbed Stress Field Model for Reinforced Concrete: Implementation. *Journal of Structural Engineering, 127*(1), 12-20. doi:https://doi.org/10.1061/(asce)0733-9445(2001)127:1(12)

Vecchio, F. J., & Collins, M. P. (1986). The modified compression-field theory for reinforced concrete elements subjected to shear. *ACI Structural Journal, 83*(2), 219-231. doi:https://doi.org/10.14359/10416

Vecchio, F. J., & Shim, W. (2004). Experimental and Analytical Reexamination of Classic Concrete Beam Tests. *Journal of Structural Engineering, 130*(3), 460-469. doi:https://doi.org/10.1061/(asce)0733-9445(2004)130:3(460)

Voo, Y. L., Poon, W. K., & Foster, S. J. (2010). Shear Strength of Steel Fiber-Reinforced Ultrahigh-Performance Concrete Beams without Stirrups. *Journal of Structural Engineering, 136*(11), 1393-1400. doi:https://doi.org/10.1061/(asce)st.1943-541x.0000234

Wan, W., Yang, J., Xu, G., & Liu, Y. (2021). Determination and evaluation of Holmquist-Johnson-Cook constitutive model parameters for ultra-high-performance concrete with steel fibers. *International Journal of Impact Engineering, 156*, 103966. doi:https://doi.org/10.1016/j.ijimpeng.2021.103966

Wang, W., Wu, C., Li, J., Liu, Z., & Lv, Y. (2019a). Behavior of ultra-high performance fiber-reinforced concrete (UHPFRC) filled steel tubular members under lateral impact loading. *International Journal of Impact Engineering, 132*, 103314. doi:https://doi.org/10.1016/j.ijimpeng.2019.103314

Wang, W., Wu, C., Li, J., Liu, Z., & Zhi, X. (2019b). Lateral impact behavior of double-skin steel tubular (DST) members with ultra-high performance fiber-reinforced concrete (UHPFRC). *Thin-Walled Structures, 144*, 106351. doi:https://doi.org/10.1016/j.tws.2019.106351

Wei, J., Li, J., & Wu, C. (2019). An experimental and numerical study of reinforced conventional concrete and ultra-high performance concrete columns under lateral impact loads. *Engineering Structures, 201*, 109822. doi:https://doi.org/10.1016/j.engstruct.2019.109822

Wei, J., Li, J., Wu, C., Liu, Z.-x., & Fang, J. (2021). Impact resistance of ultra-high performance concrete strengthened reinforced concrete beams. *International Journal of Impact Engineering, 158*, 104023. doi:https://doi.org/10.1016/j.ijimpeng.2021.104023

Wong, P., Vecchio, F., & Trommels, H. (2013). VecTor2 & Formworks user's manual (Second Edition). *University of Toronto, Canada*, pp. 347

Wu, B., & Xu, S. (2020). Experimental study on damage evaluation of stainless steel–reinforced concrete piers under lateral impact. *Advances in Mechanical Engineering, 12*(5), 168781402092488. doi:https://doi.org/10.1177/1687814020924886

Wu, B., Xu, S., & Zhang, G. (2019a). Study on Cumulative Damage Law of Stainless Steel-Reinforced Concrete Columns under Step Impact Loading. *Advances in Materials Science and Engineering, 2019*, 1-8. doi:https://doi.org/10.1155/2019/4076145

Wu, C., Oehlers, D. J., Rebentrost, M., Leach, J., & Whittaker, A. S. (2009). Blast testing of ultra-high performance fibre and FRP-retrofitted concrete slabs. *Engineering Structures, 31*(9), 2060-2069. doi:https://doi.org/10.1016/j.engstruct.2009.03.020

Wu, H., Ren, G. M., Fang, Q., & Liu, J. Z. (2019b). Response of ultra-high performance cementitious composites filled steel tube (UHPCC-FST) subjected to low-velocity impact. *Thin-Walled Structures, 144*, 106341. doi:https://doi.org/10.1016/j.tws.2019.106341

Wu, Y., Crawford, J. E., & Magallanes, J. M. (2012). *Performance of LS-DYNA concrete constitutive models.* Paper presented at the 12th International LS-DYNA users conference.

Xu, J., Wu, C., Xiang, H., Su, Y., Li, Z.-X., Fang, Q., . . . Li, J. (2016). Behaviour of ultra high performance fibre reinforced concrete columns subjected to blast loading. *Engineering Structures, 118*, 97-107. doi:https://doi.org/10.1016/j.engstruct.2016.03.048

Xu, S., Wu, P., Liu, Z., & Wu, C. (2021). Calibration of CSCM model for numerical modeling of UHPCFTWST columns against monotonic lateral loading. *Engineering Structures, 240*, 112396. doi:https://doi.org/10.1016/j.engstruct.2021.112396

Xu, S., Wu, P., & Wu, C. (2020). Calibration of KCC concrete model for UHPC against low-velocity impact. *International Journal of Impact Engineering, 144*, 103648. doi:https://doi.org/10.1016/j.ijimpeng.2020.103648

Yan, J., Liu, Y., Bai, F., Ni, X., Xu, Y., Yan, Z., & Huang, F. (2022). Dynamic response of GFRP-reinforced UHPC beams under close-in blast loading. *Materials & Design*, 111140. doi:https://doi.org/10.1016/j.matdes.2022.111140

Yang, I. H., Park, J., Bui, T. Q., Kim, K. C., Joh, C., & Lee, H. (2020). An Experimental Study on the Ductility and Flexural Toughness of Ultrahigh-Performance Concrete Beams Subjected to Bending. *Materials, 13*(10), 2225. doi:https://doi.org/10.3390/ma13102225

Yang, T., Wang, W., Liu, Z., Wu, C., Xu, S., & Yang, Y. (2021). Behavior of CFRP-UHPFRC-steel double skin tubular columns against low-velocity impact. *Composite Structures, 261*, 113284. doi:https://doi.org/10.1016/j.compstruct.2020.113284

Yi, N.-H., Kim, J.-H. J., Han, T.-S., Cho, Y.-G., & Lee, J. H. (2012). Blast-resistant characteristics of ultra-high strength concrete and reactive powder concrete. *Construction and Building Materials, 28*(1), 694-707. doi:https://doi.org/10.1016/j.conbuildmat.2011.09.014

Yin, H., Shirai, K., & Teo, W. (2019a). Finite element modelling to predict the flexural behaviour of ultra-high performance concrete members. *Engineering Structures, 183*, 741-755. doi:https://doi.org/10.1016/j.engstruct.2019.01.046

Yin, H., Shirai, K., & Teo, W. (2019b). Numerical model for predicting the structural response of composite UHPC–concrete members considering the bond strength at the interface. *Composite Structures, 215*, 185-197. doi:https://doi.org/10.1016/j.compstruct.2019.02.040

Yoo, D.-Y., Banthia, N., Kim, S.-W., & Yoon, Y.-S. (2015). Response of ultra-high-performance fiber-reinforced concrete beams with continuous steel reinforcement subjected to low-velocity impact loading. *Composite Structures, 126*, 233-245. doi:https://doi.org/10.1016/j.compstruct.2015.02.058

Yoo, D.-Y., Banthia, N., & Yoon, Y.-S. (2016). Experimental and numerical study on flexural behavior of ultra-high-performance fiber-reinforced concrete beams with low reinforcement ratios. *Canadian Journal of Civil Engineering, 44*(1), 18-28. doi:https://doi.org/10.1139/cjce-2015-0384

Yoo, D.-Y., Banthia, N., & Yoon, Y.-S. (2017a). Impact Resistance of Reinforced Ultra-High-Performance Concrete Beams with Different Steel Fibers. *ACI Structural Journal, 114*(1), 113-124. doi:https://doi.org/10.14359/51689430

Yoo, D.-Y., Yuan, T., Yang, J.-M., & Yoon, Y.-S. (2017b). Feasibility of replacing minimum shear reinforcement with steel fibers for sustainable high-strength concrete beams. *Engineering Structures, 147*, 207-222. doi:https://doi.org/10.1016/j.engstruct.2017.06.004

Zanuy, C., & Ulzurrun, G. S. D. (2018). Residual behavior of reinforced steel fiber‐reinforced concrete beams damaged by impact. *Structural Concrete, 20*(2), 597-613. doi:https://doi.org/10.1002/suco.201800253

Zhang, F., Shedbale, A. S., Zhong, R., Poh, L. H., & Zhang, M.-H. (2021). Ultra-high performance concrete subjected to high-velocity projectile impact: implementation of K&C model with consideration of failure surfaces and dynamic increase factors. *International Journal of Impact Engineering, 155*. doi:https://doi.org/10.1016/j.ijimpeng.2021.103907

Zhang, G., Xu, S., Xie, H., Zhou, X., & Wang, Y. (2017a). Behavior of stainless steel–reinforced concrete piers under lateral impact loading. *Advances in Mechanical Engineering, 9*(5), 168781401770993. doi:https://doi.org/10.1177/1687814017709936

Zhang, T., Wu, H., Fang, Q., Huang, T., Gong, Z. M., & Peng, Y. (2017b). UHP-SFRC panels subjected to aircraft engine impact: Experiment and numerical simulation. *International Journal of Impact Engineering, 109*, 276-292. doi:https://doi.org/10.1016/j.ijimpeng.2017.07.012

Zhang, T., Wu, H., Zhang, F. J., Fang, Q., & Huang, T. (2017c). Ballistic limit of aircraft engine missile impact on ultra-high-performance steel-fiber-reinforced concrete panels. *International Journal of Protective Structures, 8*(4), 503-523. doi:https://doi.org/10.1177/2041419617716498

Zhou, X., Zhang, H., Zhang, W., & Zhang, G. (2020). Study on the Influence of Closed-Cell Aluminum Foam on the Impact Performance of Concrete Pier after Equal Replacement with Stainless Steel Reinforcement. *Advances in Materials Science and Engineering, 2020*, 1-17. doi:https://doi.org/10.1155/2020/8356319

Zhou, X., Zhang, W., Gao, Y., Zhang, G., & Xiong, R. (2019). A Comparative Test Study of the Impact Performances of Stainless-Steel Rebar Equal-Strength Replacement Piers. *International Journal of Steel Structures, 20*(1), 67-79. doi:https://doi.org/10.1007/s13296-019-00269-5

Appendix

Appendix A Detailed experimental results

A.1 Chapter overview

This appendix chapter presents the individual experimental results for the beams in this PhD program. **Section A1.2** presents the detailed static results from Series 1, 2 and 3, while the detailed blast test results are presented in **Section A1.3**.

A.2 Static test results

This section presents the static test results of the beams in **Series 1** (HSC-HSS), **Series 2** (HSC-SS) and **Series 3** (UHPC-NSS, UHPC-HSS and UHPC-SS). The key data extracted from the load-deflection curves includes: the yield load (P_y) and maximum load (P_{max}), yield displacement (Δ_y) and maximum displacement (Δ_{max}), secant stiffness (k_s), ductility (Δ_{max}/Δ_y), toughness (area under the load-deflection curve until Δ_{max}) and the failure mechanism. The beams with high-strength steel reinforcement do not show well-defined yield points, therefore the "yield" displacement was approximated using the procedure shown in **Figure A.1a** (Pam et al., 2001; Park, 1989). The definitions of the variables extracted from the load vs. mid-span deflection curve are shown in **Figure A.1b** and summarized as follows:

A: Load corresponding to yielding of specimen;
B: Maximum load resisted by the specimen;
C: Displacement at yield;
D: Displacement at failure;
E: A_{OABD}: toughness or area under the curve (shaded in grey).

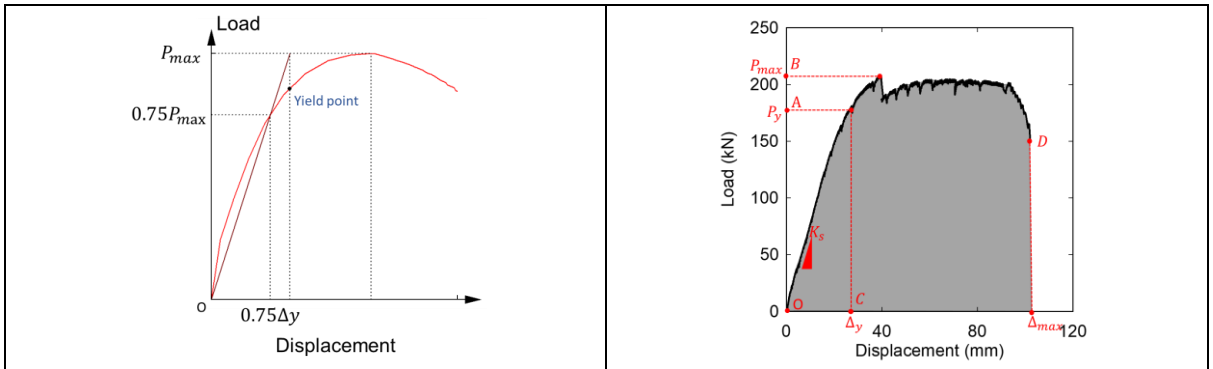

(a) Method to determine yield point | (b) Defination of variables

Figure A.1 Illustration of the variables in static test

A.2.1.Static test results in Series 1 (HSC-HSS)

A.2.1.1. C100-No.4HS-DR-d/4

Beam C100-No.4HS-DR-d/4 was designed with high-strength concrete and 2-No.4 high-strength steel bars in tension. The beam design met the blast detailing requirements in the CSA S850 standard with provision of top continuity bars (2 - No.3 HS bars) and closed ties spaced at d/4 (s = 50 mm) throughout the span. **Table A.1** summarizes key parameters from the static test. **Figure A.2** shows the load-deflection curve, and strain data are presented in **Figure A.3. Figure A.4** shows photos of major events during testing.

The first hairline cracks were observed in the flexural zone at a load of 20 kN. Yielding of the beam occurred at 25.2 mm with a tension longitudinal reinforcement strain of 7.2 mm/m. As the applied load was increased, the beam reached a peak load of 160.5 kN at a displacement of 36 mm. After reaching peak capacity, the concrete cover in the compression zone began to crush resulting in a 40 kN drop in capacity, after which the beam continued to carry load. Failure occurred at a displacement of 80 mm due to rupture of the high-strength bars in tension. The beam showed a high ductility of Δ_{max}/Δ_y = 3.2, with a total toughness A_u = 9.7 kJ.

Table A.1 Static test results of C100-No.4HS-DR-d/4

Beam	Load		Displacement		Secant Stiffness k_s (N/mm)	Ductility Δ_{max}/Δ_y	Toughness A_u (J)
	Yield P_y (kN)	Peak P_{max} (kN)	Yield Δ_y (mm)	Failure Δ_{max} (mm)			
C100-No.4HS-DR-d/4	140.6	160.5	25.2	79.9	7079	3.2	9673

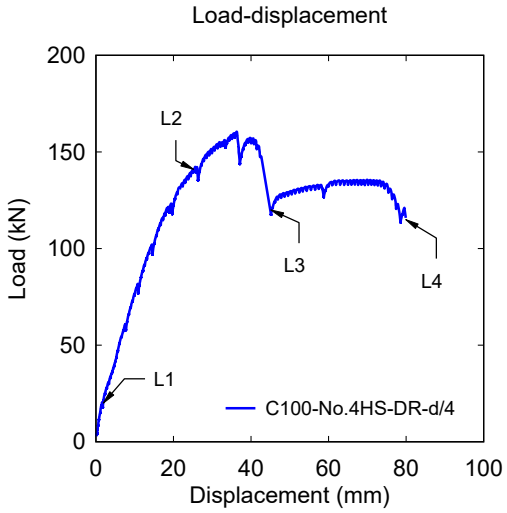

Figure A.2 Load-displacement response for beam C100-No.4HS-DR-d/4

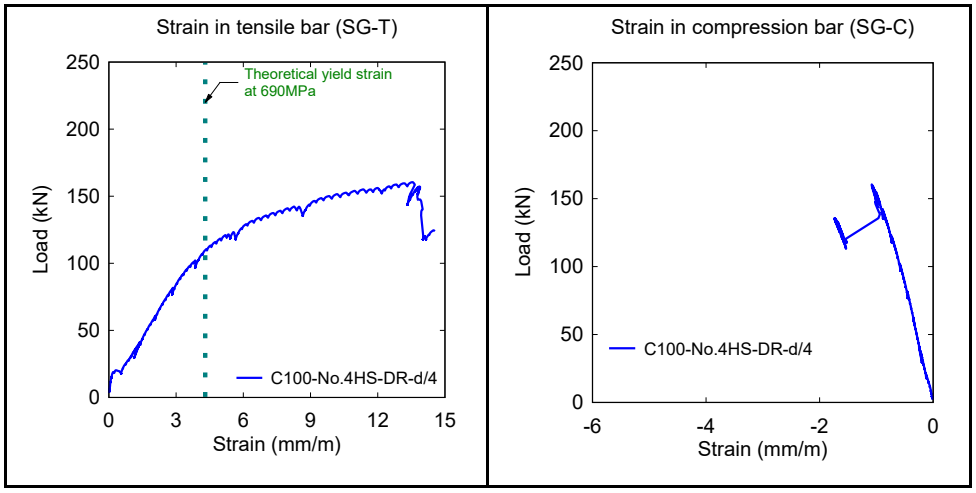

Figure A.3 Load-strain data for beam C100-No.4HS-DR-d/4

Load stage	Load	20 kN	Δ_{mid}	1.9 mm	Max. Crack width	HL
L1: First crack						
	Load	141 kN	Δ_{mid}	25.2 mm	Max. Crack width	0.6 mm
L2: Yield	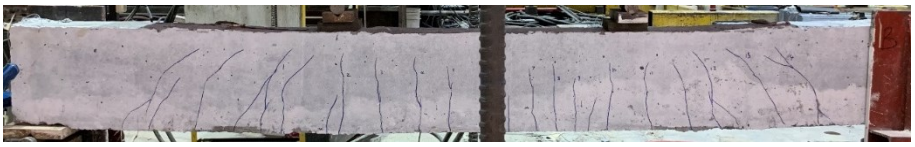					
	Load	120 kN	Δ_{mid}	45.1 mm	Max. Crack width	1.25 mm
L3: Concrete crushing						
	Load	/	Δ_{mid}	79.9 mm	Max. Crack width	-
L4: Bar rupture						

Figure A.4 Major events for beam C100-No.4HS-DR-d/4

A.2.1.2. C100-No.5HS-DR-d/4

Beam C100-No.5HS-DR-d/4 was designed with high-strength concrete, high-strength reinforcement and blast detailing, but had an increased tension steel ratio when compared to the previous specimen. Longitudinal reinforcement in tension/compression consisted of 2-No.5/2-No.4 high-strength bars, with closed ties at d/4 spacing (s= 50 mm). **Table A.2** summarizes the static test results. **Figure A.5** shows the load-deflection curve, and strain data are presented in **Figure A.6. Figure A.7** shows photos of major events during testing.

The beam behaviour was similar to the previous specimen. The first hairline cracks were found in the flexural zone at a load of 20 kN. Yielding of the beam occurred at a displacement of 28.4 mm with a corresponding tension reinforcement strain of 6.6 mm/m. As the applied load was increased, the beam reached its peak capacity of 207.9 kN at a displacement of 40 mm. The load capacity suddenly dropped (by ~ 25 kN) at a displacement of 50 mm due to top concrete cover crushing. The strain data shows that the high-strength compression bars underwent high strains prior to failure. The beam failed in bar rupture at a displacement of 96 mm. The beam showed high ductility of Δ_{max}/Δ_y = 3.4, with a total toughness A_u = 18 kJ.

Table A.2 Static test results of C100-No.5HS-DR-d/4

Beam	Load		Displacement		Secant Stiffness k_s (N/mm)	Ductility Δ_{max}/Δ_y	Toughness A_u (J)
	Yield P_y (kN)	Peak P_{max} (kN)	Yield Δ_y (mm)	Failure Δ_{max} (mm)			
C100-No.5HS-DR-d/4	184.1	207.9	28.4	96.3	7960	3.4	18028

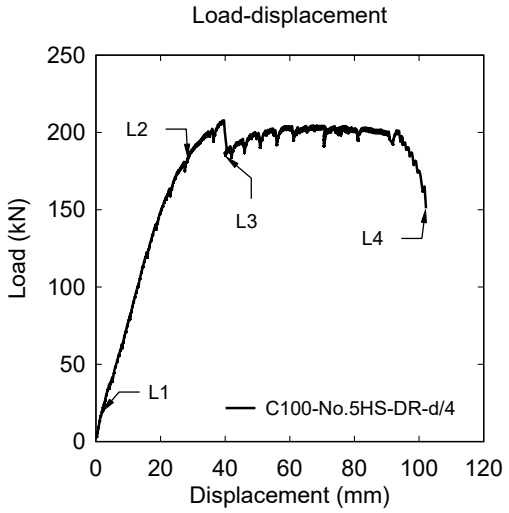

Figure A.5 Load-displacement response for beam C100-No.5HS-DR-d/4

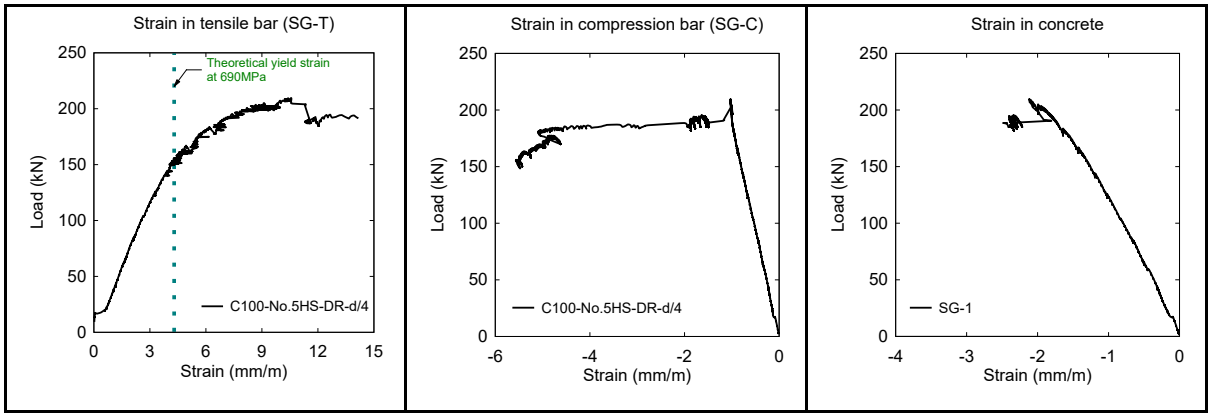

Figure A.6 Load-strain data for beam C100-No.5HS-DR-d/4

Load stage	Load	20 kN	Δ_{mid}	2.2 mm	Max. Crack width	HL
L1: First crack						
	Load	184.1 kN	Δ_{mid}	28.4 mm	Max. Crack width	0.8 mm
L2: Yield						
	Load	184 kN	Δ_{mid}	40 mm	Max. Crack width	1.25 mm
L3: Concrete crushing						
	Load	-	Δ_{mid}	96.3 mm	Max. Crack width	-
L4: Bar rupture						

Figure A.7 Major events for beam C100-No.5HS-DR-d/4

A.2.1.3. CF100-No.5-DR-d/2

Beam CF100-No.4HS-DR-d/2 was designed with high-strength concrete but contained 0.75% of steel fibers. Longitudinal reinforcement in tension/compression consisted of 2-No.5/2-No.4 high-strength bars, with an intermediate tie spacing of d/2 (s = 100 mm). **Table A.3** summarized the static test result for the beam. **Figure A.8** shows the load-deflection and load-strain response of the concrete in the compression zone (no steel strain data is available). **Figure A.9** shows photos of major events during testing.

The first hairline cracks were observed in the flexural zone at an applied load of 45 kN which is delayed when compared to the plain HSC beam. Yielding of the longitudinal reinforcement occurred at 26.1 mm of displacement. The beam reached its peak load of 244.5 kN at a displacement of 55 mm. After reaching its peak capacity, the load began to decrease due to the increase in cracked widths in the tension zone. The top concrete cover showed signs of crushing at a displacement of 70 mm. Eventually, the beam failed in bar rupture at a displacement of 116 mm. The beam showed high ductility of Δ_{max}/Δ_y = 4.4, and a high toughness of A_u = 23.7 kJ.

Table A.3 Static test results of CF100-No.5HS-DR-d/2

Beam	Load		Displacement		Secant Stiffness k_s (N/mm)	Ductility Δ_{max}/Δ_y	Toughness A_u (J)
	Yield P_y (kN)	Peak P_{max} (kN)	Yield Δ_y (mm)	Failure Δ_{max} (mm)			
CF100-No.5HS-DR-d/2	213.5	244.5	26.1	116.0	10049	4.4	23658

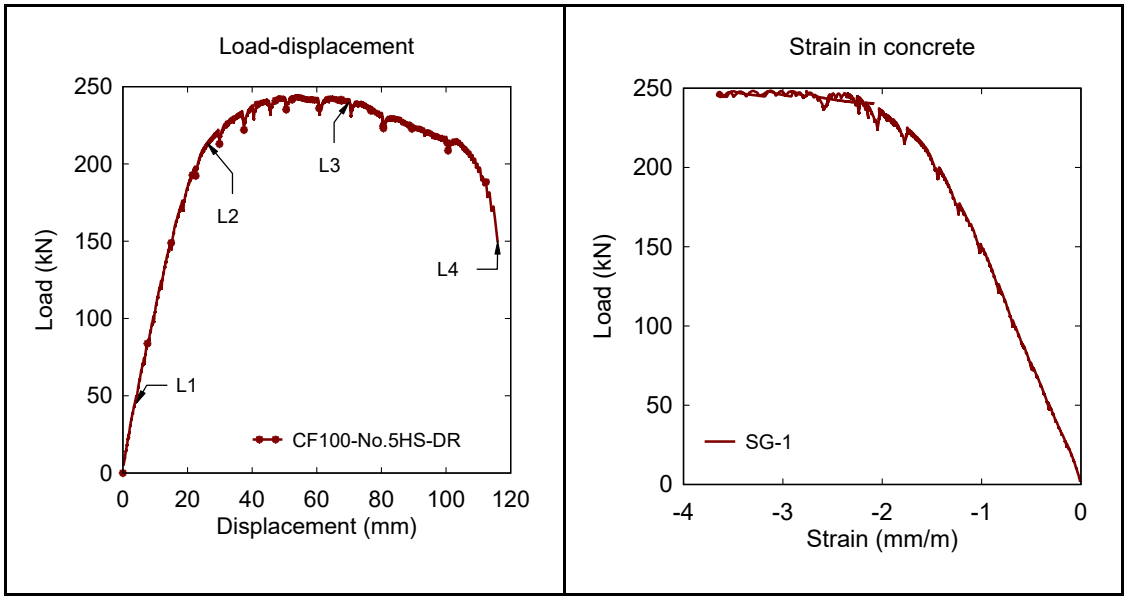

Figure A.8 Load-displacement and strain data for beam CF100-No.5HS-DR-d/2

Load stage	Load	45.2 kN	Δ_{mid}	4.2 mm	Max. Crack width	HL
L1: First crack						
	Load	213.5 kN	Δ_{mid}	26.1 mm	Max. Crack width	0.6 mm
L2: Yield						
	Load	240 kN	Δ_{mid}	70 mm	Max. Crack width	3 mm
L3: Concrete crushing						
	Load	-	Δ_{mid}	116 mm	Max. Crack width	-
L3: Bar rupture						

Figure A.9 Major events for beam CF100-No.5HS-DR-d/2

A.2.2. Static test results in Series 2 (HSC-SS)

A.2.2.1. C100-No.5S1-S

Beam C100-No.5S1-S was designed with high-strength concrete and stainless steel reinforcement. The beam was singly-reinforced with 2-No.5 XM-28 stainless steel bars, with U-shaped stirrups spaced at d/2 (s=100 mm) in the shear spans only. **Table A.4** summarizes the static test result of the beam. **Figure A.10** shows the load-deflection curve and strain data. **Figure A.11** shows photos of major events during testing.

The first hairline cracks were observed in the flexural zone at a load of 20 kN. Yielding of the beam occurred when the load reached 105.2 kN (Δ_y = 12.3 mm). Due to the nature of the stainless steel stress-strain curve, the load capacity kept increasing after yielding. Upon reaching its maximum capacity of 121.6 kN, the beam failed suddenly due to concrete crushing in the compressive zone at a displacement of 42.6 mm. The overall ductility was Δ_{max}/Δ_y = 2.7 with a toughness A_u = 4.1 kJ.

Table A.4 Static test results of C100-No.5S1-S

Beam	Load		Displacement		Secant Stiffness k_s (N/mm)	Ductility Δ_{max}/Δ_y	Toughness A_u (J)
	Yield P_y (kN)	Peak P_{max} (kN)	Yield Δ_y (mm)	Failure Δ_{max} (mm)			
C100-No.5S1-S	105.2	121.6	15.6	42.6	6744	2.73	4061

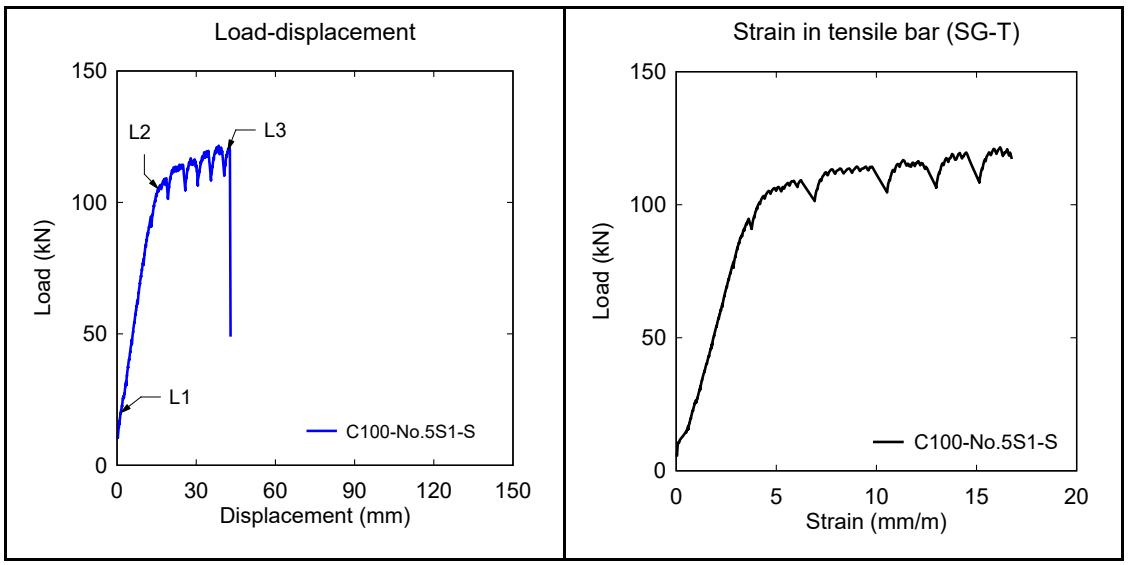

Figure A.10 Load-displacement and strain data for beam C100-No.5S1-S

	Load	20	Δ_{mid}	1.4	Max. Crack width	HL
L1: First crack	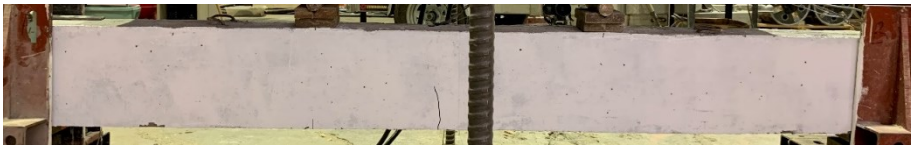					
	Load	105.2	Δ_{mid}	15.6	Max. Crack width	0.25
L2: Yield	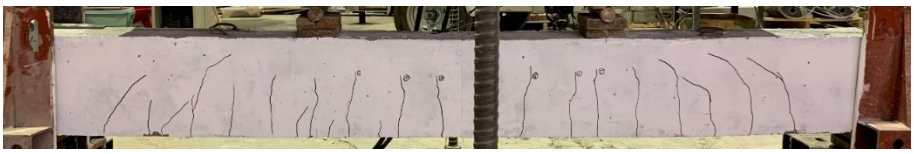					
	Load	-	Δ_{mid}	41	Max. Crack width	-
L3: Concrete crushing	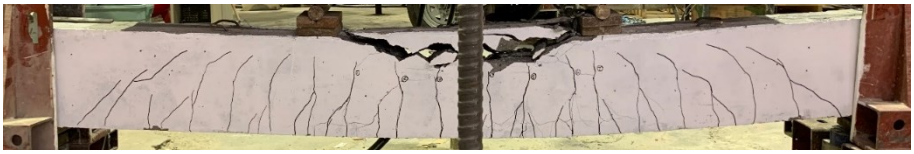					

Figure A.11 Major events for beam C100-No.5S1-S

A.2.2.2. CF100-No.5S1

Beam CF100-No.5S1 was designed with high-strength concrete, 1% of 30mm hooked end steel fibers, and was singly-reinforced with 2-No.5 XM-28 stainless bars in tension, without stirrups in the shear span. The objective of this test was to study the effect of steel fibers on shear capacity and the ability of fibers to replace stirrups in beams with stainless steel reinforcement. **Table A.5** summarizes the static test results. **Figure A.12** shows the load-deflection curve and strain data. **Figure A.13** shows photos of major events during testing.

The first hairline cracks were observed in the flexural zone at an applied load of 40 kN. As the applied load was increased, the specimen experienced a sudden shear failure, with the fibers pulling out at the critical shear crack. The maximum load was 139.3 kN with a corresponding displacement of 15.8 mm. It is noted that the shear capacity is increased when compared to the expected capacity of the plain concrete beam without stirrups (89.3 kN – see **Figure A.14**), however the fibers were not able to fully replace the stirrups due to the high shear demands imposed by the stainless steel reinforcing bars.

Table A.5 Static test results of CF100-No.5S1

Beam	Load		Displacement		Secant Stiffness k_s (N/mm)	Ductility Δ_{max}/Δ_y	Toughness A_u (J)
	Yield P_y (kN)	Peak P_{max} (kN)	Yield Δ_y (mm)	Failure Δ_{max} (mm)			
CF100-No.5S1	-	139.3	-	15.8	8807	-	1333

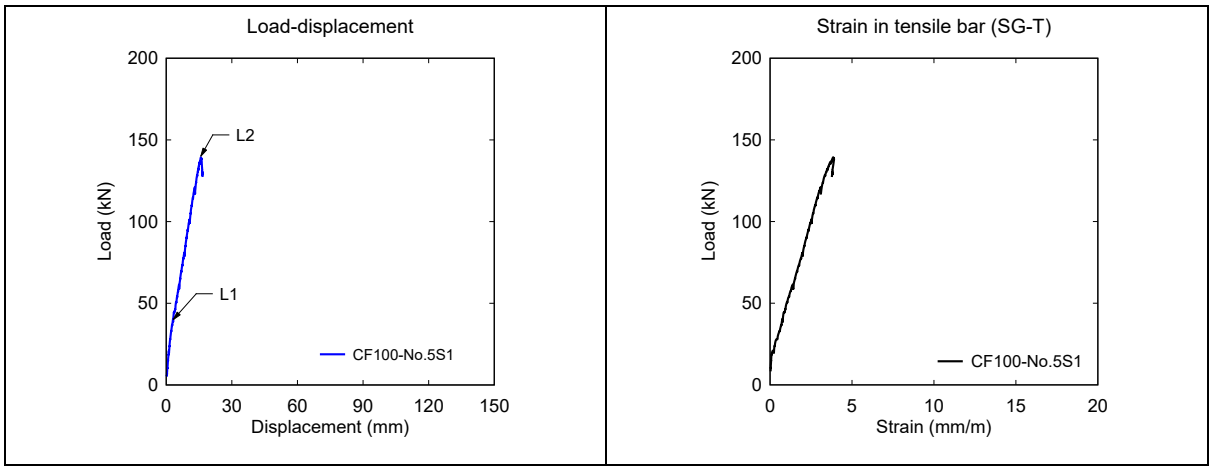

Figure A.12 Load-displacement and strain data for beam CF100-No.5S1

	Load	40 kN	Δ_{mid}	3.2 mm	Max. Crack width	HL
L1: First crack	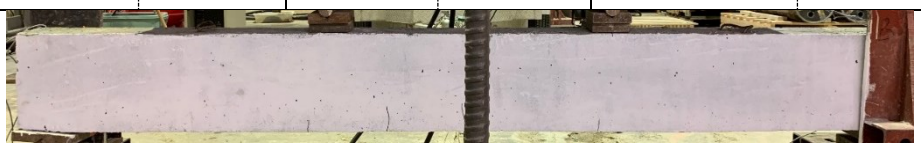					
	Load	139.3 kN	Δ_{mid}	15.8 mm	Max. Crack width	/
L2: Shear failure	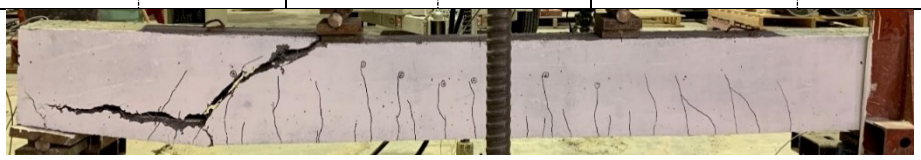					

Figure A.13 Major events for beam CF100-No.5S1

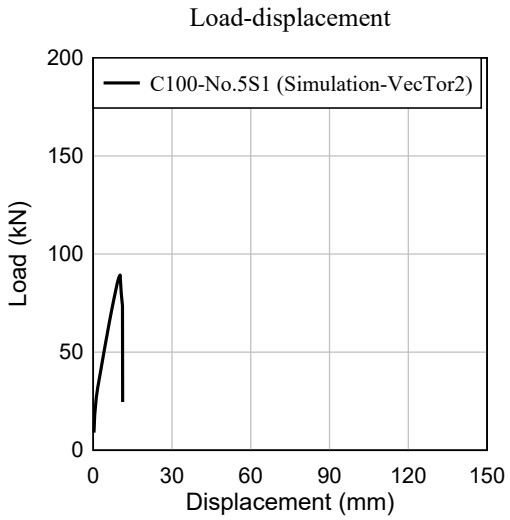

Figure A.14 Load-displacement curve for C100-No.5S1 simulated using VecTor2

A.2.2.3. CF100-No.5S1-S

Beam CF100-No.5S1-S was designed with high-strength concrete, 1% of 30mm hooked end steel fibers and stainless steel reinforcement. The beam was singly-reinforced with 2-No.5 XM-28 stainless steel bars, with U-shaped stirrups spaced at d/2 (s=100 mm) in the shear spans only. **Table A.6** summarizes the static test result of the beam. **Figure A.15** shows the load-deflection curve and strain data. **Figure A.16** shows photos of major events during testing.

The first hairline cracks were observed in the flexural zone at a load of 40 kN. Yielding of the beam occurred when the load reached 146.9 kN (Δ_y = 17.1 mm). Due to the nature of the stainless steel stress-strain curve, the load capacity kept increasing after yielding. Upon reaching its maximum capacity of 157.8 kN, the load showed a sudden drop at a displacement of 50 mm due to concrete crushing and fiber pullout. However, the beam continued to carry load up to a displacement of 115 mm. The overall ductility was Δ_{max}/Δ_y = 6.75 with a toughness A_u = 12.9 kJ.

Table A.6 Static test results of CF100-No.5S1-S

Beam	Load		Displacement		Secant Stiffness k_s (N/mm)	Ductility Δ_{max}/Δ_y	Toughness A_u (J)
	Yield P_y (kN)	Peak P_{max} (kN)	Yield Δ_y (mm)	Failure Δ_{max} (mm)			
CF100-No.5S1-S	146.9	157.8	17.1	115.5	8591	6.75	12886

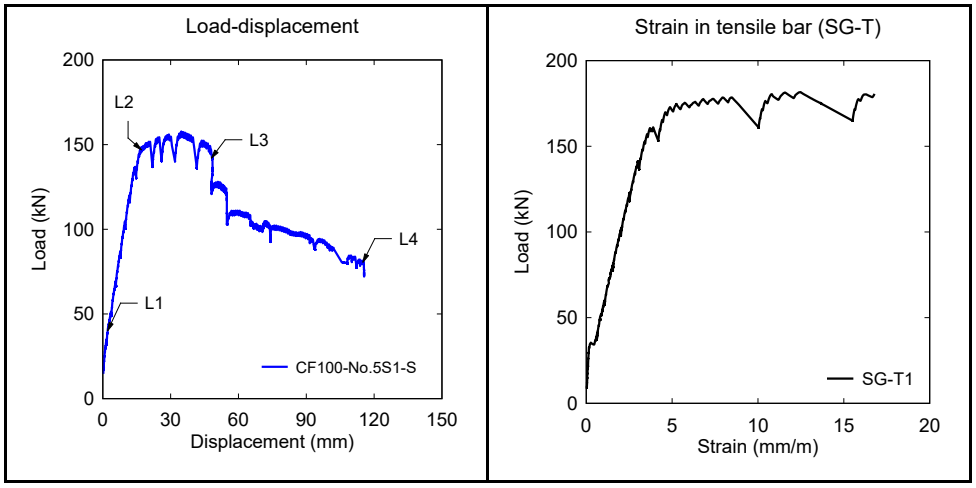

Figure A.15 Load-displacement and strain data for beam CF100-No.5S1-S

	Load	40 kN	Δ_{mid}	2.1 mm	Max. Crack width	HL
L1: First crack	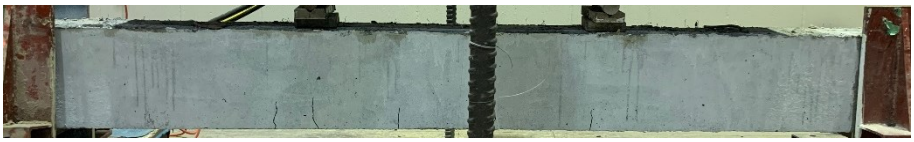					
	Load	146.9 kN	Δ_{mid}	17.1 mm	Max. Crack width	0.2 mm
L2: Yield	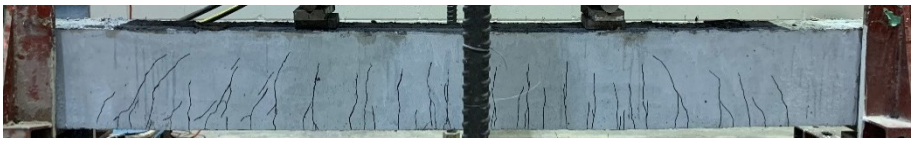					
	Load	142 kN	Δ_{mid}	50 mm	Max. Crack width	1.3 mm
L3: Concrete crushing						
	Load	80.5 kN	Δ_{mid}	115 mm	Max. Crack width	-
L4: End of testing						

Figure A.16 Major events for beam CF100-No.5S1-S

A.2.2.4. C100-No.4S1-DR-d/4

Beam C100-No.4S1-DR-d/4 was designed with high-strength concrete, stainless steel reinforcement and the more stringent blast detailing provisions in the CSA S850 standard. Longitudinal steel in tension/compression consisted of 2-No.4/2-No.3 XM-28 stainless steel bars with closed ties spaced at d/4 (s = 50 mm) throughout the beam span. **Table A.7** summarizes the static test result. **Figure A.17** shows the load-deflection curve and strain data. **Figure A.18** shows photos of major events during testing.

The first hairline cracks were observed in the flexural zone at a load of 20 kN. Yielding of the beam occurred at a displacement of 24.3 mm with a corresponding applied load of 91.1 kN. As the applied load was increased, the beam reached its peak load of 108.5 kN at a displacement of 70 mm. After reaching its peak capacity, the concrete cover in the beam's midspan compression zone experienced crushing resulting in a moderate drop in capacity (74 kN). The use of blast detailing prevented complete crushing failure allowing the beam to sustain pronounced post-peak deflections until the end of testing (deflection of 150 mm) without bar rupture. The overall ductility was Δ_{max}/Δ_y = 6.2 with a toughness A_u = 13.4 kJ.

Table A.7 Static test results of C100-No.4S1-DR-d/4

Beam	Load		Displacement		Secant Stiffness k_s (N/mm)	Ductility Δ_{max}/Δ_y	Toughness A_u (J)
	Yield P_y (kN)	Peak P_{max} (kN)	Yield Δ_y (mm)	Failure Δ_{max} (mm)			
C100-No.4S1-DR-d/4	91.1	108.5	24.3	150	5303	6.17	13439

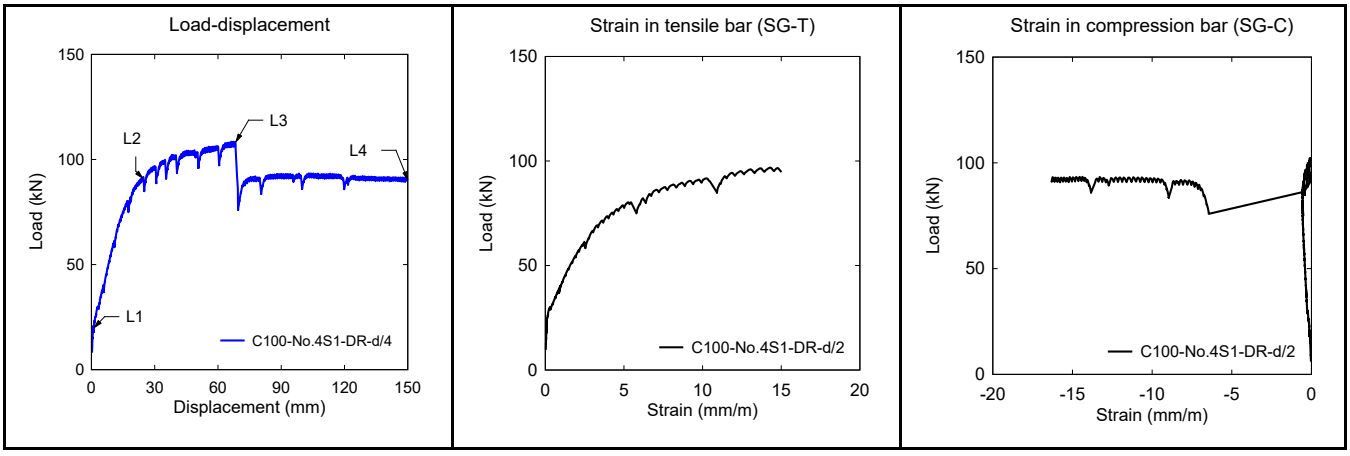

Figure A.17 Load-displacement and strain data for beam C100-No.4S1-DR-d/4

<table>
<tr><td></td><td>Load</td><td>20 kN</td><td>Δ_{mid}</td><td>1.3 mm</td><td>Max. Crack width</td><td>HL</td></tr>
<tr><td>L1:
First crack</td><td colspan="6"> 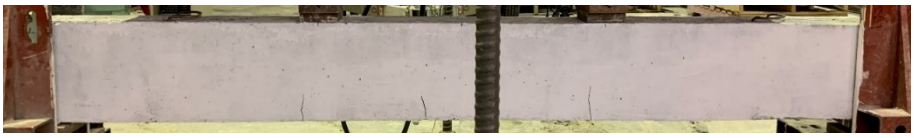 </td></tr>
<tr><td></td><td>Load</td><td>91.1 kN</td><td>Δ_{mid}</td><td>24.3 mm</td><td>Max. Crack width</td><td>0.55 mm</td></tr>
<tr><td>L2:
Yield</td><td colspan="6"> 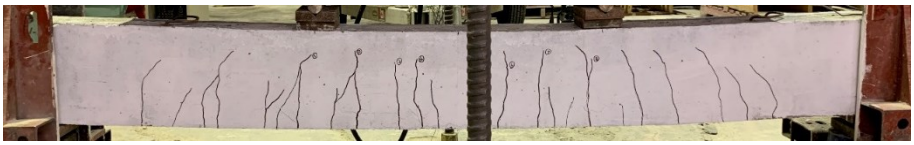 </td></tr>
<tr><td></td><td>Load</td><td>108.4 kN</td><td>Δ_{mid}</td><td>70 mm</td><td>Max. Crack width</td><td>2 mm</td></tr>
<tr><td>L3:
Peak load
&
Concrete crushing</td><td colspan="6"> 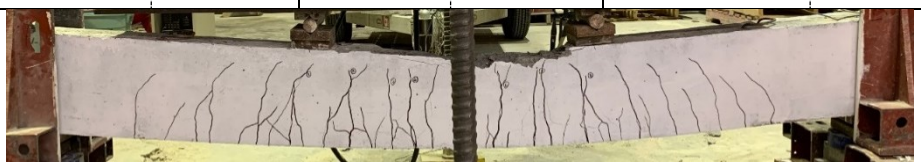
 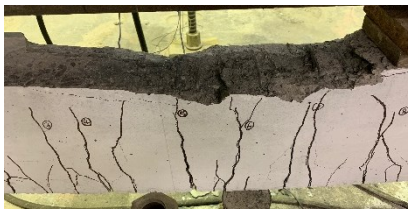 </td></tr>
<tr><td></td><td>Load</td><td>90.4 kN</td><td>Δ_{mid}</td><td>150 mm</td><td>Max. Crack width</td><td>-</td></tr>
<tr><td>L4:
End of testing</td><td colspan="6"> 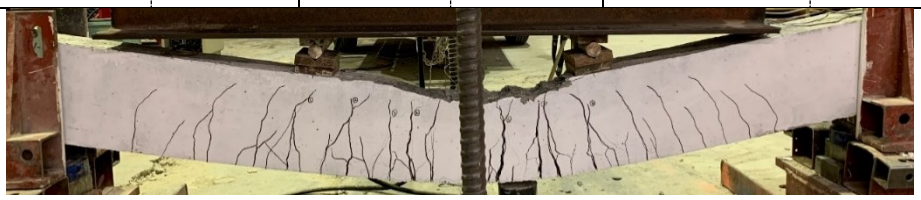
  </td></tr>
</table>

Figure A.18 Major events for beam C100-No.4S1-DR-d/4

A.2.2.5. C100-No.5S1-DR-d/4

Beam C100-No.5S1-DR-d/4 was designed with high-strength concrete, 2-No.5/2-No.4 XM-28 stainless steel longitudinal bars in tension/compression, and closed ties spaced at d/4 (s=50 mm) throughout the beam span. Therefore, the design was similar to the previous specimen with the exception of the increased longitudinal steel ratio. **Table A.8** summarizes the static test result. **Figure A.19** shows the load-deflection curve and strain data. **Figure A.20** shows photos of major events during testing.

The first hairline cracks were observed in the flexural zone at a load of 20 kN. Yielding of the beam occurred at a displacement of 17.5 mm with a corresponding applied load of 116 kN. The beam reached its peak load capacity of 135.7 kN at a displacement of 46.7 mm. Thereafter, the concrete cover in the compression zone crushed resulted in a moderate drop in capacity (113 kN). However, the beam was able to sustain its residual load capacity until a displacement of 150 mm due to the improved detailing. Buckling of the top compression bars was eventually observed in the midspan zone, resulting in a further drop in capacity near the end of testing. The ductility was Δ_{max}/Δ_y = 8.6 with a toughness A_u = 17 kJ.

Table A.8 Static test results of C100-No.5S1-DR-d/4

Beam	Load		Displacement		Secant Stiffness k_s (N/mm)	Ductility Δ_{max}/Δ_y	Toughness A_u (J)
	Yield P_y (kN)	Peak P_{max} (kN)	Yield Δ_y (mm)	Failure Δ_{max} (mm)			
C100-No.5S1-DR-d/4	116.0	135.7	17.5	147	7769	8.57	17033

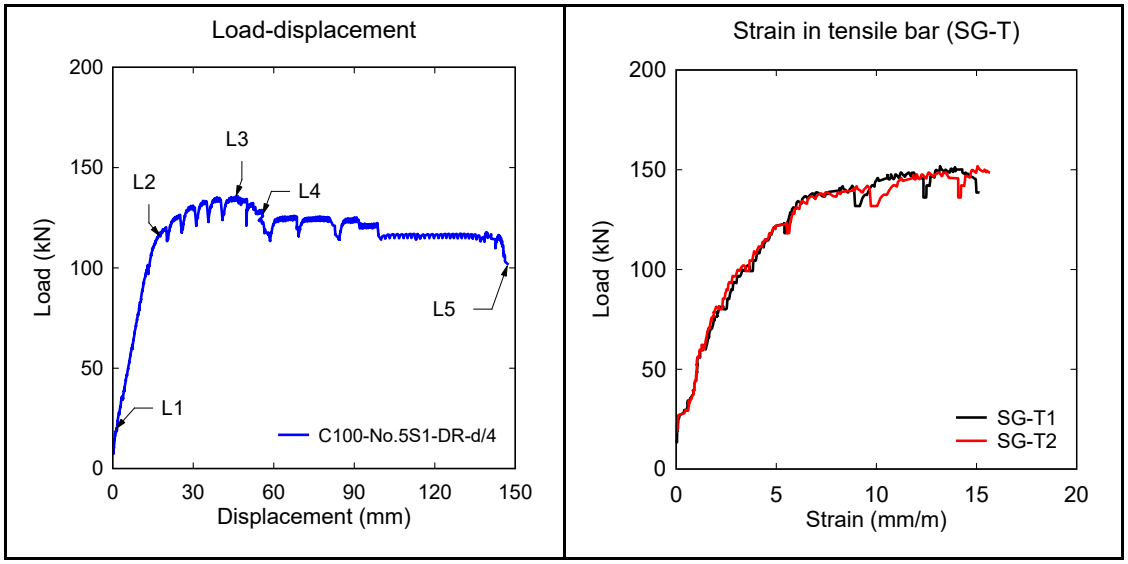

Figure A.19 Load-displacement and strain data for beam C100-No.5S1-DR-d/4

<table>
<tr><td></td><td>Load</td><td>20 kN</td><td>Δ_{mid}</td><td>1.3 mm</td><td>Max. Crack width</td><td>HL</td></tr>
<tr><td>L1:
First crack</td><td colspan="6"> 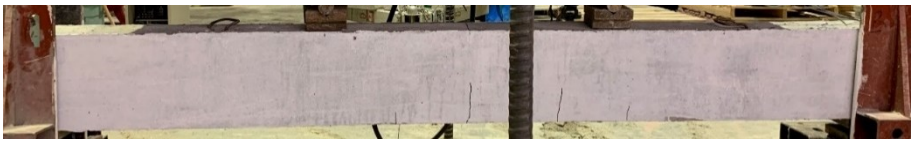 </td></tr>
<tr><td></td><td>Load</td><td>116 kN</td><td>Δ_{mid}</td><td>17.5 mm</td><td>Max. Crack width</td><td>0.3 mm</td></tr>
<tr><td>L2:
Yield</td><td colspan="6"> 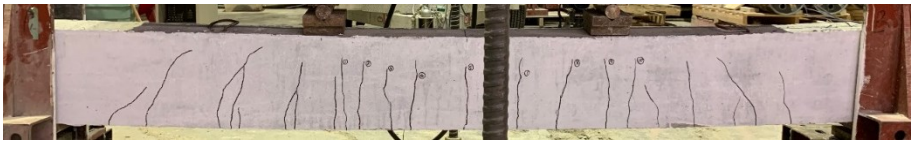 </td></tr>
<tr><td rowspan="2">L3:
Peak Load</td><td>Load</td><td>135.7 kN</td><td>Δ_{mid}</td><td>46 mm</td><td>Max. Crack width</td><td>1.2 mm</td></tr>
<tr><td colspan="6"> 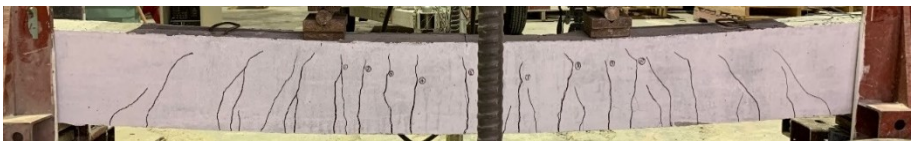 </td></tr>
<tr><td></td><td>Load</td><td>127 kN</td><td>Δ_{mid}</td><td>56 mm</td><td>Max. Crack width</td><td>2 mm</td></tr>
<tr><td>L4:
Concrete crushing</td><td colspan="6"> 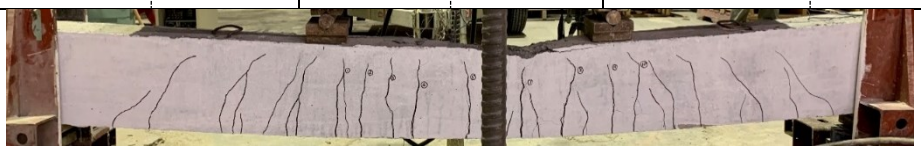
 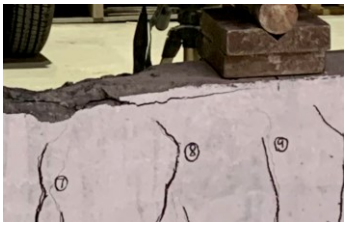 </td></tr>
<tr><td></td><td>Load</td><td>101 kN</td><td>Δ_{mid}</td><td>147 mm</td><td>Max. Crack width</td><td>-</td></tr>
<tr><td>L5:
End testing:
buckling</td><td colspan="6"> 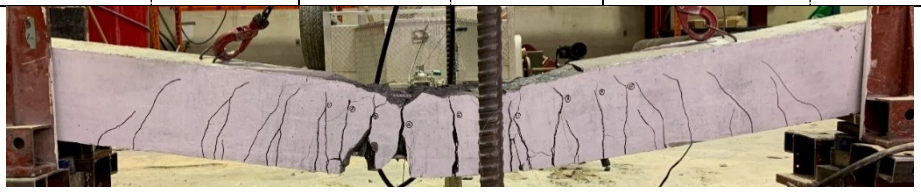
  </td></tr>
</table>

Figure A.20 Major events for beam C100-No.5S1-DR-d/4

A.2.2.6. CF100-No.5S1-DR-d/2

Beam CF100-No.5S1-DR-d/4 was designed with high-strength concrete and 0.75% of steel fibers. To match the design of the HSC-NSS beam tested by Charles (2019), the fibers consisted of a hybrid mix of 30 mm hooked-end fibers & 13 mm smooth steel fibers (0.5% and 0.25%). Longitudinal reinforcement in tension/compression consisted of 2-No.5/2-No.4 XM-28 stainless steel bars and intermediate ties spaced at d/2 (s = 100 mm). **Table A.9** summarizes static test result of the beam. **Figure A.21** shows the load-deflection curve and strain data. **Figure A.22** shows photos of major events during testing.

The first hairline cracks were observed in the flexural zone at a load of 40 kN. Yielding occurred at a displacement of 17.8 mm with a corresponding applied load of 134.2 kN. The beam reached its peak capacity of 153.3 kN at a displacement of 44.2 mm. Thereafter, the load capacity began to gradually decrease due to fiber pullout in the midspan tension zone. Pullout of the smooth steel fibers was observed at a displacement of 60 mm with a corresponding maximum crack width of 3 mm. Pullout of the longer hooked-end steel fibers occurred at a displacement of 80 mm with a corresponding maximum crack width of 5 mm. The test was terminated at a displacement of 150 mm. The use of top bars, fibers and intermediate ties allowed the beam to reach a high ductility of Δ_{max}/Δ_y = 8.4 and toughness A_u = 19.3 kJ. No bar rupture occurred during the test.

Table A.9 Static test results of CF100-No.5S1-DR-d/2

Beam	Load		Displacement		Secant Stiffness k_s (N/mm)	Ductility Δ_{max}/Δ_y	Toughness A_u (J)
	Yield P_y (kN)	Peak P_{max} (kN)	Yield Δ_y (mm)	Failure Δ_{max} (mm)			
CF100-No.5S1-DR-d/2	134.2	153.3	17.8	150	8608	8.43	19250

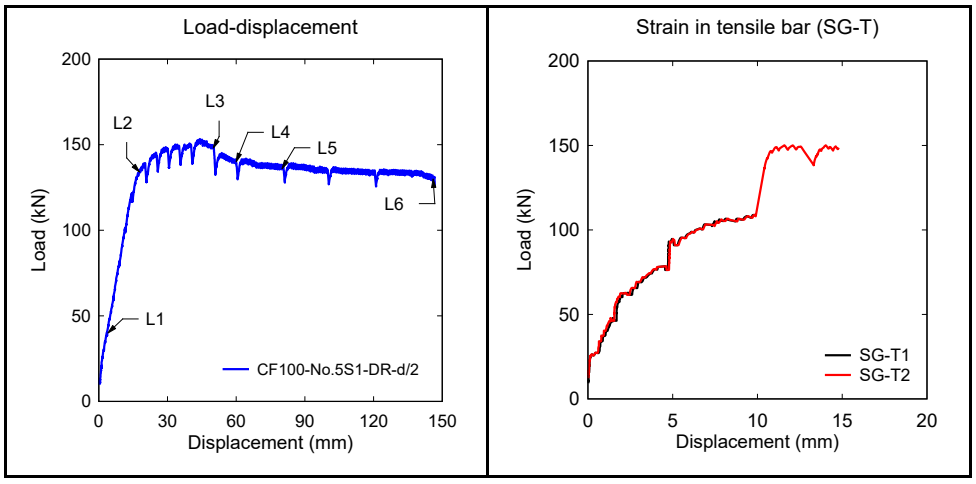

Figure A.21 Load-displacement and strain data for beam CF100-No.5S1-DR-d/2

<table>
<tr><td></td><td>Load</td><td>40 kN</td><td>Δ_{mid}</td><td>4 mm</td><td>Max. Crack width</td><td>HL</td></tr>
<tr><td>L1:
First crack</td><td colspan="6"> 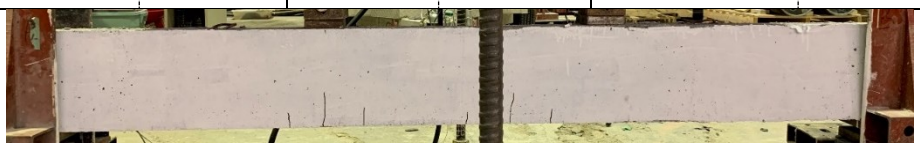 </td></tr>
<tr><td></td><td>Load</td><td>134 kN</td><td>Δ_{mid}</td><td>17.8 mm</td><td>Max. Crack width</td><td>0.15 mm</td></tr>
<tr><td>L2:
Yield</td><td colspan="6"> 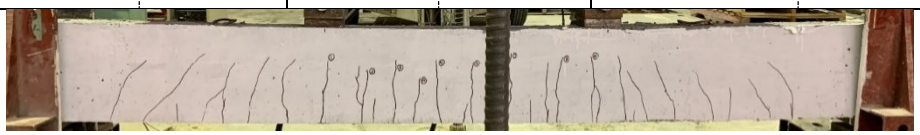 </td></tr>
<tr><td></td><td>Load</td><td>148 kN</td><td>Δ_{mid}</td><td>50 mm</td><td>Max. Crack width</td><td>0.8 mm</td></tr>
<tr><td>L3:
Concrete
crushing</td><td colspan="6"> 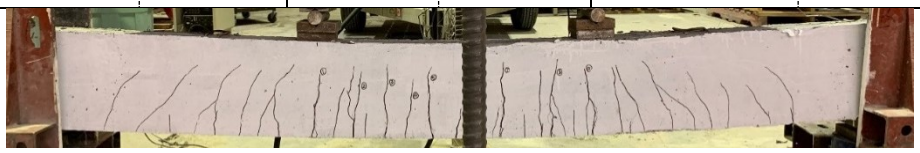 </td></tr>
<tr><td></td><td>Load</td><td>140 kN</td><td>Δ_{mid}</td><td>60 mm</td><td>Max. Crack width</td><td>3 mm</td></tr>
<tr><td>L4:
Short fiber
pullout</td><td colspan="6"> 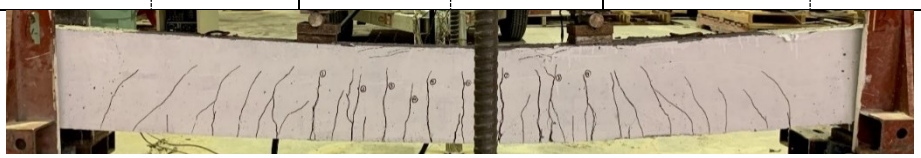
  </td></tr>
<tr><td></td><td>Load</td><td>136 kN</td><td>Δ_{mid}</td><td>80 mm</td><td>Max. Crack width</td><td>5 mm</td></tr>
<tr><td>L5:
Long fiber
pullout</td><td colspan="6"> 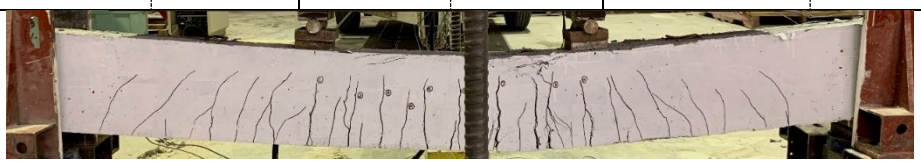
 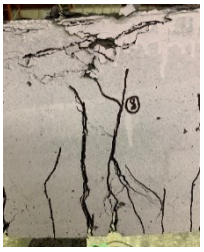 </td></tr>
<tr><td></td><td>Load</td><td>130 kN</td><td>Δ_{mid}</td><td>150 mm</td><td>Max. Crack width</td><td>-</td></tr>
<tr><td>L6:
End testing</td><td colspan="6"> 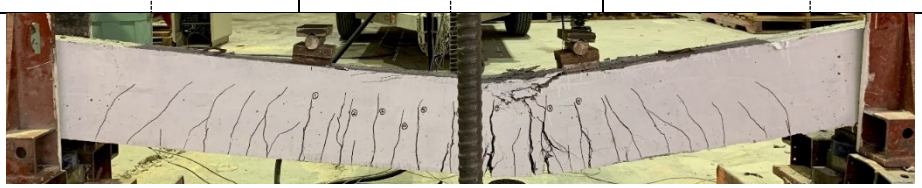 </td></tr>
</table>

Figure A.22 Major events for beam CF100-No.5S1-DR-d/2

A.2.2.7. C100-No.5S2-DR-d/4

Beam C100-No.5S2-DR-d/4 was designed with high-strength concrete, No.5/No.4 2304 stainless steel bars in tension/compression, and closed ties spaced at d/4 (s=50 mm) throughout the beam span. Therefore, its design was identical to C100-No.5S1-DR-d/4 with the exception of type S2 (duplex – 2304) stainless bars. **Table A.10** summarizes the static test result. The load-deflection curve and strain data are presented in **Figure A.23**. **Figure A.24** shows photos of major events during testing.

The first hairline cracks were observed in the flexural zone at a load of 20 kN. Yielding of the beam occurred at a displacement of 23.7 mm with a corresponding applied load of 149.1 kN. The beam reached peak load capacity of 169.8 kN at a displacement of 43.3 mm. After reaching peak capacity, the concrete cover in the compression zone began to crush resulting in a moderate drop in capacity. However, the use of blast detailing prevented failure allowing the beam to sustain pronounced post-peak deflections until the end of testing at a large deflection of 150 mm, with a ductility of Δ_{max}/Δ_y = 6.3 and toughness A_u = 19.8 kJ. It is noted that these values are slightly lower and higher (respectively) when compared to the companion beam with S1 stainless bars.

Table A.10 Static test results of C100-No.5S2-DR-d/4

Beam	Load		Displacement		Secant Stiffness k_s (N/mm)	Ductility Δ_{max}/Δ_y	Toughness A_u (J)
	Yield P_y (kN)	Peak P_{max} (kN)	Yield Δ_y (mm)	Failure Δ_{max} (mm)			
C100-No.5S2-DR-d/4	149.1	169.8	23.7	150	7821	6.30	19769

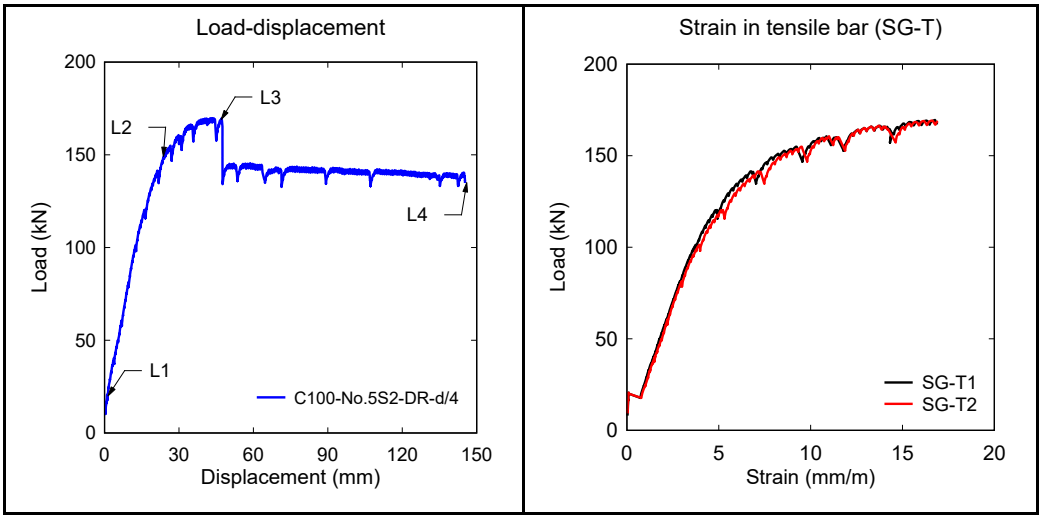

Figure A.23 Load-displacement and strain data for beam C100-No.5S2-DR-d/4

<table>
<tr><td></td><td>Load</td><td>20 kN</td><td>Δ_{mid}</td><td>1.4 mm</td><td>Max. Crack width</td><td>HL</td></tr>
<tr><td>L1:
First crack</td><td colspan="6"> 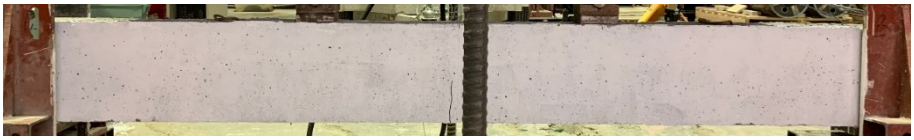 </td></tr>
<tr><td></td><td>Load</td><td>149.1 kN</td><td>Δ_{mid}</td><td>23.7 mm</td><td>Max. Crack width</td><td>0.4 mm</td></tr>
<tr><td>L2:
Yield</td><td colspan="6"> 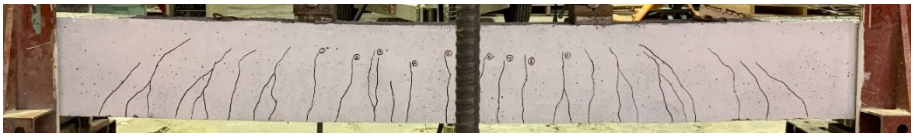 </td></tr>
<tr><td></td><td>Load</td><td>169 kN</td><td>Δ_{mid}</td><td>47 mm</td><td>Max. Crack width</td><td>1.2 mm</td></tr>
<tr><td>L3:
Concrete crushing</td><td colspan="6"> 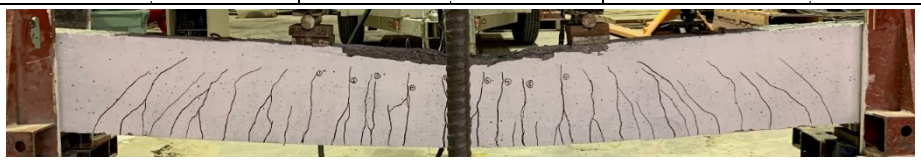 </td></tr>
<tr><td></td><td>Load</td><td>135 kN</td><td>Δ_{mid}</td><td>150 mm</td><td>Max. Crack width</td><td>-</td></tr>
<tr><td>L4:
End testing:
buckling</td><td colspan="6"> 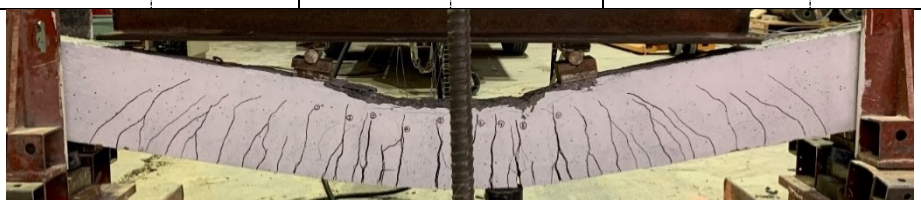
 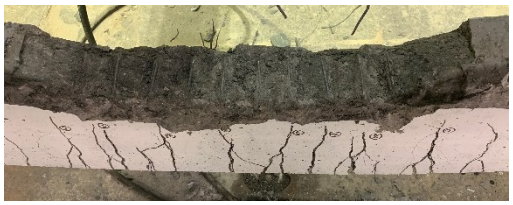 </td></tr>
</table>

Figure A.24 Major events for beam C100-No.5S2-DR-d/4

A.2.3. Static test results in Series 3 (UHPC)

A.2.3.1.U2-15M-DR-d/2

Beam U2-15M-DR-d/2 was designed with ultra-high performance concrete, 2% steel fibers, and was doubly-reinforced with 2-15M/2-10M normal-strength tension/compression bars and intermediate ties at s = d/2 (100 mm) throughout its span. **Table A.11** summarized the static test results. **Figure A.25** shows the load-deflection curve, and strain data are presented in **Figure A.26. Figure A.27** shows photos of major events during testing.

The first hairline cracks were observed in the flexural zone at a load of 40 kN. As the steel started to yield, the maximum load of 181.2 kN was reached at a corresponding displacement of 12.8 mm. As the beam went into the post-yield range, the fibers at the major crack began to pull-out, resulting in a drop in load capacity. The beam ultimately failed due to bar rupture at a displacement of 49.1 mm. Despite the sudden failure, the beam showed a relatively high ductility of Δ_{max}/Δ_y = 3.8 and a toughness A_u = 6.7 kJ. No concrete crushing was observed with many closely spaced secondary cracks throughout the span.

Table A.11 Static test results of U2-15M-DR-d/2

Beam	Load		Displacement		Secant Stiffness k_s (N/mm)	Ductility Δ_{max}/Δ_y	Toughness A_u (J)
	Yield P_y (kN)	Peak P_{max} (kN)	Yield Δ_y (mm)	Failure Δ_{max} (mm)			
U2-15M-DR-d/2	181.2	181.2	12.8	49.1	14156	3.84	6733

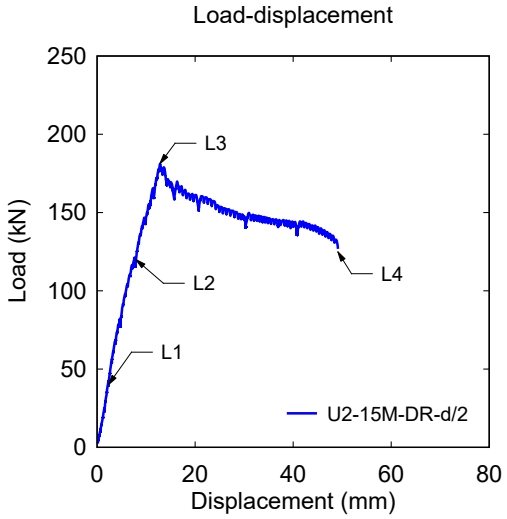

Figure A.25 Load-displacement response for beam U2-15M-DR-d/2

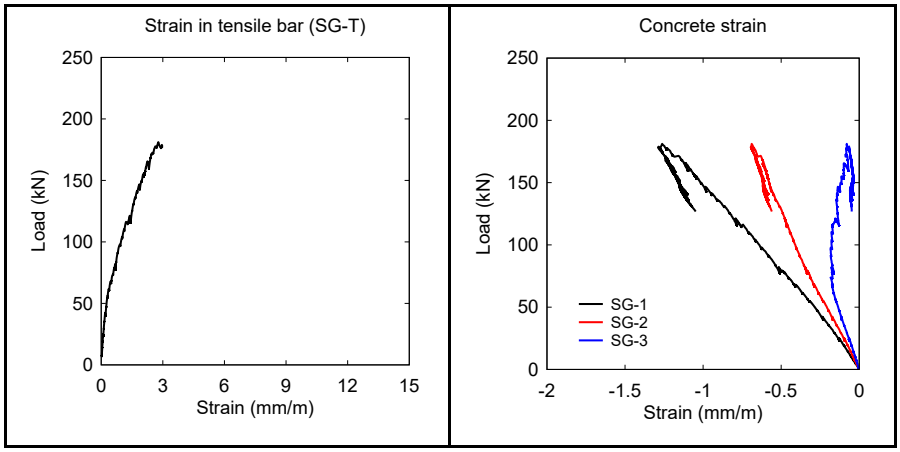

Figure A.26 Load-strain data for beam U2-15M-DR-d/2

	Load	40 kN	Δ_{mid}	2.3 mm	Max. Crack width	HL
L1: First crack						
	Load	120 kN	Δ_{mid}	7.9 mm	Max. Crack width	HL
L2: Service load ($0.6 f_y$)						
	Load	181.2 kN	Δ_{mid}	12.8 mm	Max. Crack width	1.0 mm
L3: Yield						
	Load	-	Δ_{mid}	49.1 mm	Max. Crack width	-
L4 Bar rupture						

Figure A.27 Major events for beam U2-15M-DR-d/2

A.2.3.2. U2-20M-DR-d/2

Beam U2-20M-DR-d/2 was designed with ultra-high performance concrete, 2% steel fiber, 2-20M/2-10M normal-strength tension/compression bars and intermediate ties spaced at d/2 (s = 100 mm) throughout the span. This beam had an increased tension steel ratio when compared to the previous specimen. **Table A.12** summarizes the static test results. **Figure A.28** shows the load-deflection curve, and strain data are presented in **Figure A.29. Figure A.30** shows photos of major events during testing.

The first hairline cracks were found in the flexural zone at a load of 40 kN. The yield of the beam occurred at a displacement of 14.2 mm with a corresponding applied load of 201.8 kN. The beam reached a peak load capacity of 207 kN at a displacement of 27.1 mm. Thereafter the fibers began to pullout at the major crack resulting in a gradual drop in load capacity. Eventually, the beam failed in bar rupture at a displacement of 81.7 mm. Similar to the previous beam no crushing was observed with a distinct distributed crack pattern. The increased steel ratio delayed bar fracture and allowed the UHPC beam to reach a higher ductility of Δ_{max}/Δ_y = 5.8 and toughness A_u = 14.5 kJ when compared to the previous beam.

Table A.12 Static test results of U2-20M-DR-d/2

Beam	Load		Displacement		Secant Stiffness k_s (N/mm)	Ductility Δ_{max}/Δ_y	Toughness A_u (J)
	Yield P_y (kN)	Peak P_{max} (kN)	Yield Δ_y (mm)	Failure Δ_{max} (mm)			
U2-20M-DR-d/2	201.8	207.0	14.2	81.7	14211	5.75	14470

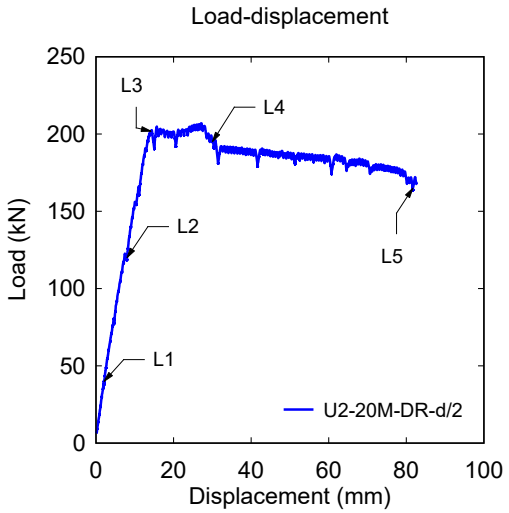

Figure A.28 Load-displacement response for beam U2-20M-DR-d/2

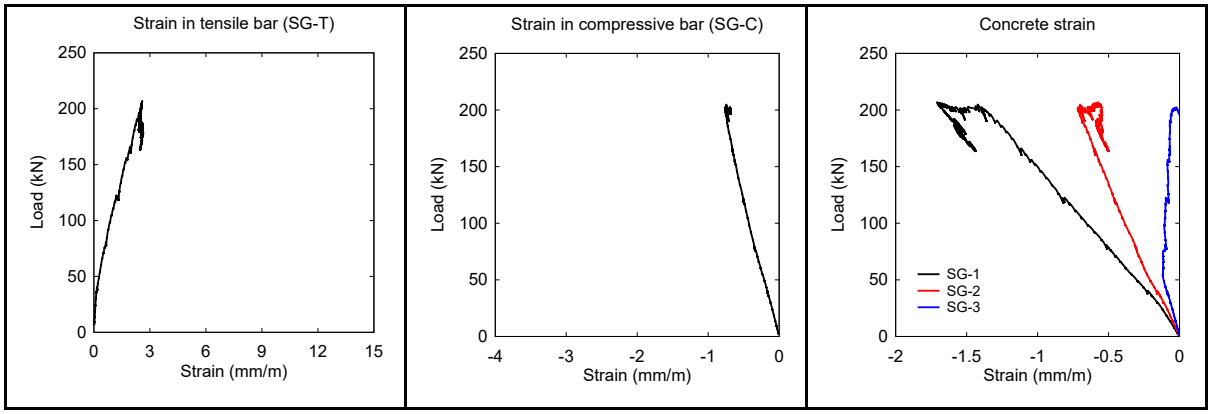

Figure A.29 Load-strain data for beam U2-20M-DR-d/2

	Load	40 kN	Δ_{mid}	2.1 mm	Max. Crack width	HL
L1: First crack						
	Load	120 kN	Δ_{mid}	8.0 mm	Max. Crack width	HL
L2: Service load ($0.6 f_y$)						
	Load	201.8 kN	Δ_{mid}	14.2 mm	Max. Crack width	1.0 mm
L3: Yield						
	Load	195 kN	Δ_{mid}	30 mm	Max. Crack width	9 mm
L4: Crack localiztion						
	Load	-	Δ_{mid}	81.7 mm	Max. Crack width	-
L5: Bar rupture						

Figure A.30 Major events for beam U2-20M-DR-d/2

A.2.3.3. U3-15M

Beam U3-15M was designed with ultra-high performance concrete, 3% steel fiber, 2-15M normal-strength tension bars without stirrups in the shear span. **Table A.13** summarizes the static test results, and **Figure A.31** shows the load-deflection curve**. Figure A.32** shows photos of major events during testing.

The first hairline cracks were found in the flexural zone at a load of 40 kN. The yield of the beam occurred at a displacement of 11.6 mm with a corresponding applied load of 190.7 kN. Thereafter the fibers began to pullout at the major crack resulting in a gradual drop in load capacity. At a displacement of 20 mm, the load experienced a sudden drop due to complete fiber pullout. Eventually, the beam failed in bar rupture at a displacement of 55.7 mm. The beam showed a relatively high ductility of Δ_{max}/Δ_y = 4.8 and a toughness A_u = 8.0 kJ. No concrete crushing was observed with many closely spaced cracks throughout the span.

Table A.13 Static test results of U3-15M

Beam	Load		Displacement		Secant Stiffness k_s (N/mm)	Ductility Δ_{max}/Δ_y	Toughness A_u (J)
	Yield P_y (kN)	Peak P_{max} (kN)	Yield Δ_y (mm)	Failure Δ_{max} (mm)			
U3-15M	190.7	190.7	11.6	55.7	16437	4.8	7971

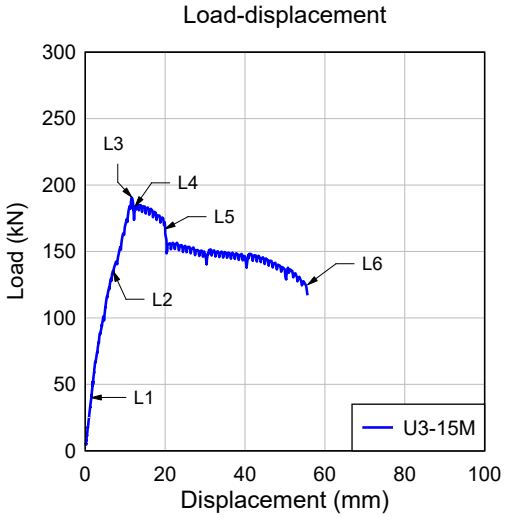

Figure A.31 Load-displacement response for beam U3-15M

	Load	40 kN	Δ_{mid}	1.5 mm	Max. Crack width	HL
L1: First crack						
	Load	135 kN	Δ_{mid}	7 mm	Max. Crack width	HL
L2: Service load ($0.6\,f_y$)						
	Load	191 kN	Δ_{mid}	11.6 mm	Max. Crack width	HL
L3: Yield						
	Load	184 kN	Δ_{mid}	12.5 mm	Max. Crack width	5 mm
L4: Crack localiztion						
	Load	167 kN	Δ_{mid}	20 mm	Max. Crack width	10 mm
L5: Fiber pullout						
	Load	-	Δ_{mid}	55.7 mm	Max. Crack width	-
L6: Bar rupture						

Figure A.32 Major events for beam U3-15M

A.2.3.4. U2-No.4HS-DR-d/2

Beam U2-No.4HS-DR-d/2 was designed with ultra-high performance concrete, 2% steel fibers, 2-No.4/2-No.3 high-strength tension/compression bars and intermediate ties spaced at d/2 (s=100 mm). **Table A.14** summarizes the static test result of the beam. **Figure A.33** shows the load-deflection curve, and strain data are presented in **Figure A.34**. **Figure A.35** shows photos of major events during testing.

The first hairline cracks were observed in the flexural zone at a load of 40 kN. Yielding of the beam is occurred at a displacement of 14.1 mm with a corresponding applied load of 151.2 kN. The beam reached peak load capacity of 178.4 kN at a displacement of 39.5 mm. Crack localization was observed shortly after reaching the peak capacity. The beam failed due to rupture of the ASTM A1035 tension bars at a displacement of 39.5 mm. The beam showed a ductility of 2.8 and overall toughness of 5.2 kJ. No crushing was observed prior to failure, with the formation of many closely spaced fine cracks throughout the beam span.

Table A.14 Static test results of U2-No.4HS-DR-d/2

Beam	Load		Displacement		Secant Stiffness k_s (N/mm)	Ductility Δ_{max}/Δ_y	Toughness A_u (J)
	Yield P_y (kN)	Peak P_{max} (kN)	Yield Δ_y (mm)	Failure Δ_{max} (mm)			
U2-No.4HS-DR-d/2	151.2	178.4	14.1	39.5	10723	2.8	5174

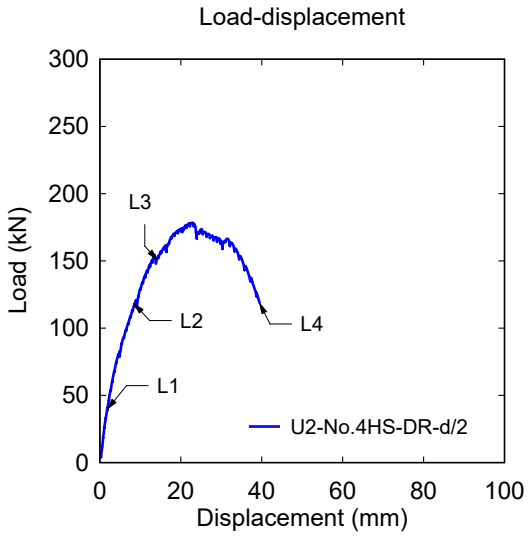

Figure A.33 Load-displacement response for beam U2-No.4HS-DR-d/2

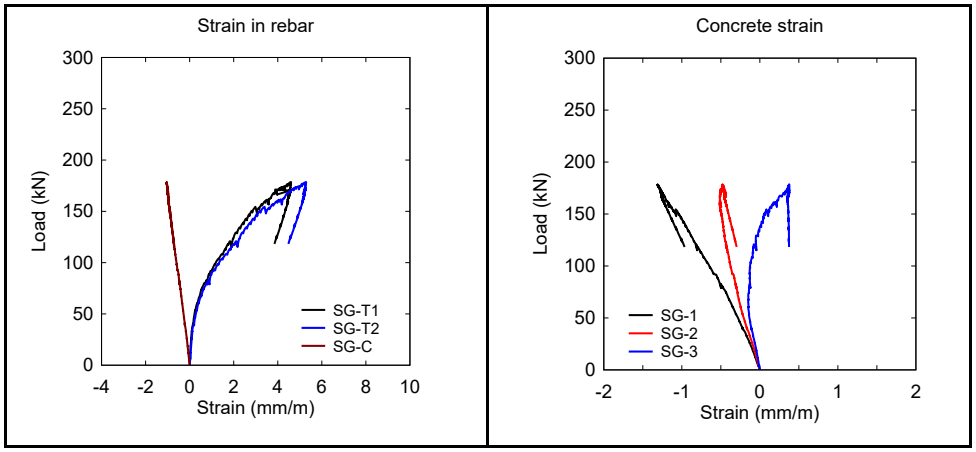

Figure A.34 Load-strain data for beam U2-No.4HS-DR-d/2

	Load	40 kN	Δ_{mid}	1.9 mm	Max. Crack width	HL
L1: First crack						
	Load	118 kN	Δ_{mid}	8.5 mm	Max. Crack width	HL
L2: Service load ($0.6 f_y$)						
	Load	151.2 kN	Δ_{mid}	14.1 mm	Max. Crack width	
L3: Yield						
	Load	-	Δ_{mid}	39.5 mm	Max. Crack width	-
L4: Bar rupture						

Figure A.35 Major events for beam U2-No.4HS-DR-d/2

A.2.3.5. U2-No.5HS-DR-d/2

Beam U2-No.5HS-DR-d/2 was designed with ultra-high performance concrete, 2% steel fibers, 2-No.5/2-No.4 high-strength tension/compression bars and intermediate ties spaced at d/2 (s=100 mm). **Table A.15** summarizes the static test result of the beam. **Figure A.36** shows the load-deflection curve, and strain data are presented in **Figure A.37**. **Figure A.38** shows photos of major events during testing.

The first hairline cracks were observed in the flexural zone at a load of 40 kN. Yielding of the beam is occurred at a displacement of 24.1 mm with a corresponding applied load of 249.5 kN. The beam reached peak load capacity of 286.6 kN at a displacement of 44.8 mm. Crack localization was observed shortly after reaching the peak capacity. The beam failed due to rupture of the ASTM A1035 tension bars at a displacement of 55.1 mm with concrete crushing at compression zone and the formation of many closely spaced fine cracks throughout the beam span. The beam showed a ductility of 2.4 and overall toughness of 11.8 kJ.

Table A.15 Static test results of U2-No.5HS-DR-d/2

Beam	Load		Displacement		Secant Stiffness k_s (N/mm)	Ductility Δ_{max}/Δ_y	Toughness A_u (J)
	Yield P_y (kN)	Peak P_{max} (kN)	Yield Δ_y (mm)	Failure Δ_{max} (mm)			
U2-No.5HS-DR-d/2	249.5	286.6	23.2	55.1	12573	2.38	11828

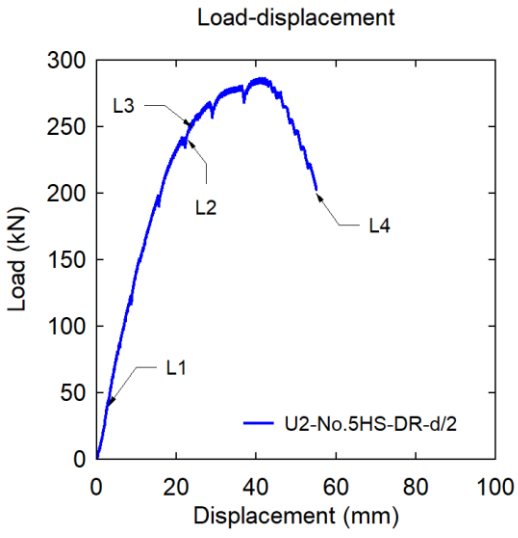

Figure A.36 Load-displacement response for beam U2-No.5HS-DR-d/2

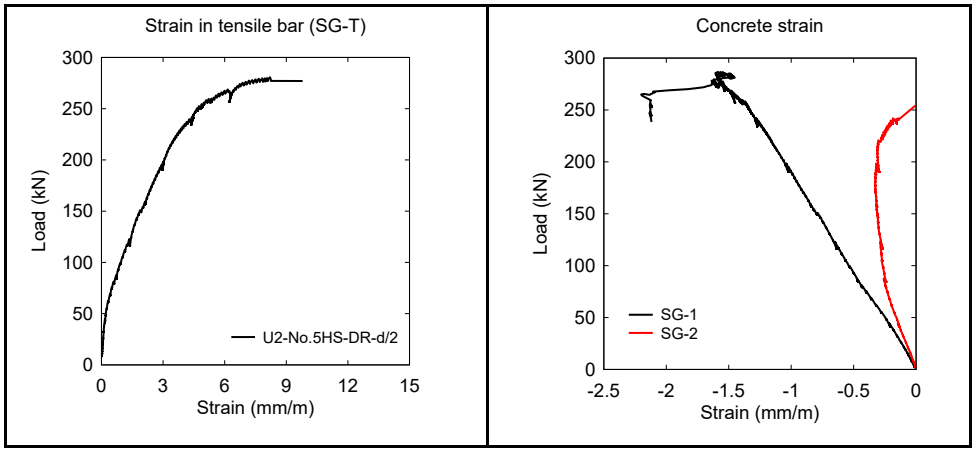

Figure A.37 Load-strain data for beam U2-No.5HS-DR-d/2

	Load	40 kN	Δ_{mid}	2.9 mm	Max. Crack width	HL
L1: First crack						
	Load	240 kN	Δ_{mid}	23.0 mm	Max. Crack width	0.6 mm
L2: Service load ($0.6 f_y$)						
	Load	249.5 kN	Δ_{mid}	23.2 mm	Max. Crack width	3.0 mm
L3: Yield						
	Load	-	Δ_{mid}	55.1 mm	Max. Crack width	-
L4: Bar rupture	 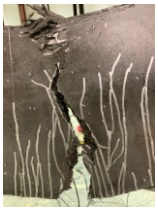					

Figure A.38 Major events for beam U2-No.5HS-DR-d/2

A.2.3.6. U3-No.5HS

Beam U3-No.5HS was designed with ultra-high performance concrete having a higher fiber content of 3%, 2-No.5 high-strength bars in tension, without top (compression) reinforcement or stirrups. **Table A.16** summarizes the static test result of the beam. **Figure A.39** shows the load-deflection curve, and strain data are presented in **Figure A.40**. **Figure A.41** shows photos of major events during testing.

The first hairline cracks were observed in the flexural zone at an applied load of 40 kN. The beam reached yield strength of 247.1kN at a displacement of 20.3 mm. The maximum load resisted by the beam was 280.5 kN. Eventually the beam failed in bar rupture at a displacement of 56.5 mm. Owing to the lack of compression reinforcement, the beam completely broke into two parts at failure. Nonetheless the use of 3% steel fibers prevented shear failure and allowed the beam to reach its full flexural capacity. The ductility ratio and toughness were found to be 2.8 and 12 kJ, respectively.

Table A.16 Static test results of U3-No.5HS

Beam	Load		Displacement		Secant Stiffness k_s (N/mm)	Ductility Δ_{max}/Δ_y	Toughness A_u (J)
	Yield P_y (kN)	Peak P_{max} (kN)	Yield Δ_y (mm)	Failure Δ_{max} (mm)			
U3-No.5HS	247.1	280.5	20.3	56.5	15217	2.78	11973

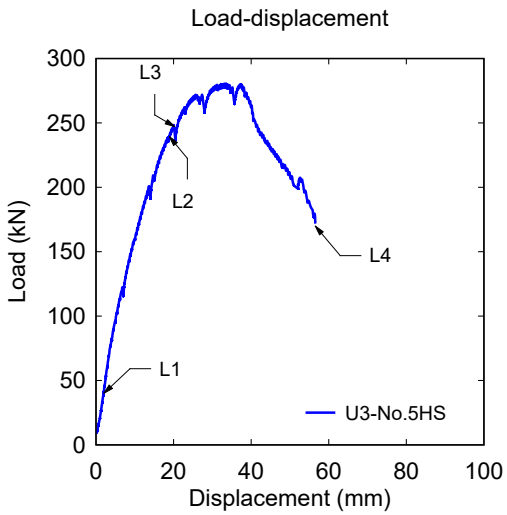

Figure A.39 Load-displacement response for beam U3-No.5HS

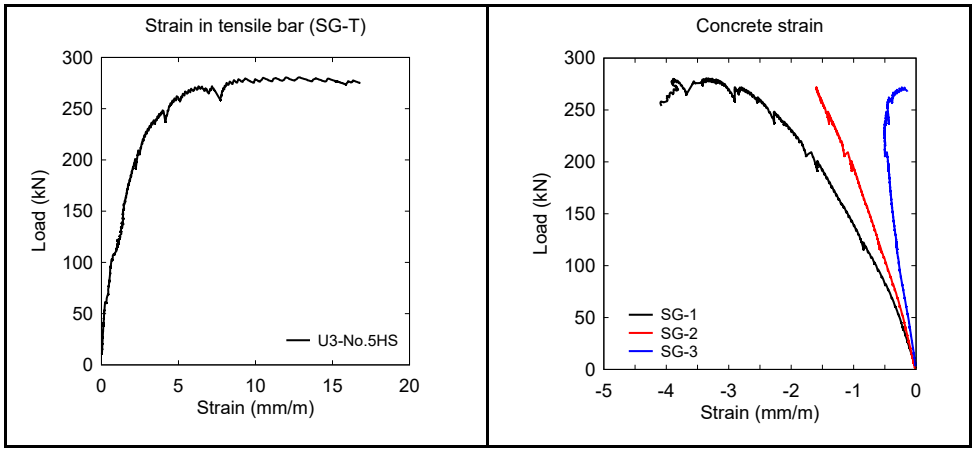

Figure A.40 Load-strain data for beam U3-No.5HS

	Load	40 kN	Δ_{mid}	2.0 mm	Max. Crack width	HL
L1: First crack	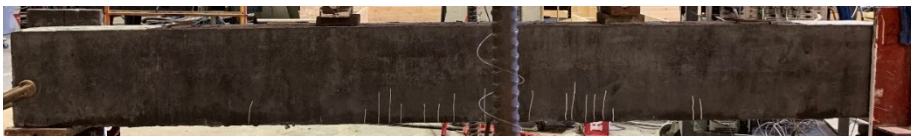					
	Load	239.4 kN	Δ_{mid}	18.9 mm	Max. Crack width	0.3 mm
L2: Service load ($0.6 f_y$)						
	Load	247.1 kN	Δ_{mid}	20.3 mm	Max. Crack width	3.0 mm
L3: Yield						
	Load	-	Δ_{mid}	56.5 mm	Max. Crack width	-
L4: Bar rupture						

Figure A.41 Major events for beam U3-No.5HS

A.2.3.7. U2-No.4S1-DR-d/2

Beam U2-No.4S1-DR-d/2 was designed with ultra-high performance concrete, 2% steel fibers, 2-No.4/2-No.3 XM-28 stainless steel tension/compression bars and intermediate ties spaced at d/2 (s=100 mm). **Table A.17** summarizes the static test result of the beam. **Figure A.42** shows the load-deflection curve, and strain data are presented in **Figure A.43**. **Figure A.44** shows photos of major events during testing.

The first hairline cracks were observed in the flexural zone at an applied load of 40 kN. The beam reached yield strength of 107.9 kN at a displacement of 10.3 mm. The maximum load resisted by the beam was 126.2 kN. Crack localization was observed shortly after reaching the peak capacity. The beam failed due to rupture of the stainless steel tension bars at a displacement of 92.8 mm. The beam showed a ductility of 12 and overall toughness of 10.3 kJ. No crushing was observed prior to failure.

Table A.17 Static test results of U2-No.4S1-DR-d/2

Beam	Load		Displacement		Secant Stiffness k_s (N/mm)	Ductility Δ_{max}/Δ_y	Toughness A_u (J)
	Yield P_y (kN)	Peak P_{max} (kN)	Yield Δ_y (mm)	Failure Δ_{max} (mm)			
U2-No.4S1-DR-d/2	107.9	126.2	10.3	92.8	10476	12.0	10295

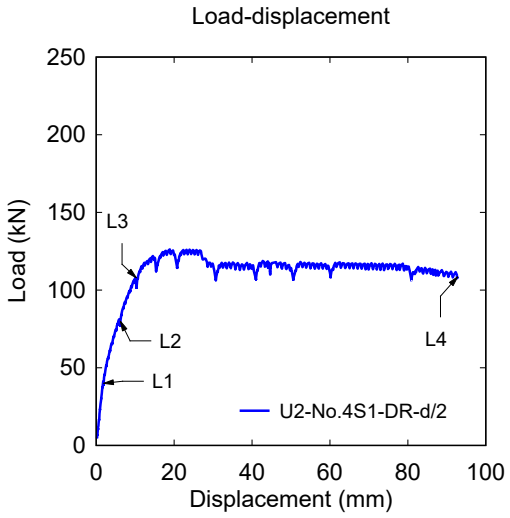

Figure A.42 Load-displacement response for beam U2-No.4S1-DR-d/2

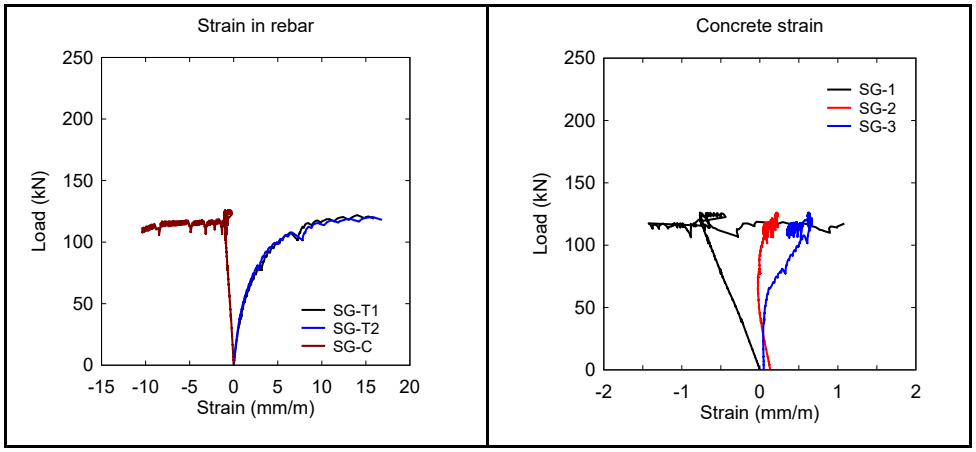

Figure A.43 Load-strain data for beam U2-No.4S1-DR-d/2

	Load	40 kN	Δ_{mid}	2.0 mm	Max. Crack width	HL
L1: First crack						
	Load	80 kN	Δ_{mid}	6.2 mm	Max. Crack width	HL
L2: Service load ($0.6 f_y$)						
	Load	107.9 kN	Δ_{mid}	10.3 mm	Max. Crack width	
L3: Yield						
	Load	-	Δ_{mid}	92.8 mm	Max. Crack width	-
L4: Bar rupture						

Figure A.44 Major events for beam U2-No.4S1-DR-d/2

A.2.3.8. U2-No.5S1-DR-d/2

Beam U2-No.5S1-DR-d/2 was designed with ultra-high performance concrete, 2% steel fibers, 2-No.5/2-No.4 XM-28 stainless steel tension/compression bars and intermediate ties spaced at d/2 (s=100 mm). **Table A.18** summarizes the static test result of the beam. **Figure A.45** shows the load-deflection curve, and strain data are presented in **Figure A.46**. **Figure A.47** shows photos of major events during testing.

The first hairline cracks were observed in the flexural zone at an applied load of 40 kN. The beam reached yield strength of 153.1 kN at a displacement of 12.1 mm. The maximum load resisted by the beam was 172.4 kN. Crack localization is delayed in the beam with stainless steel bars, which allows the plasticity in the steel reinforcement to spread over a longer length, and prevents bar fracture. Crushing of UHPC is clearly visible at the end of testing (Δ = 150 mm) which indicates that the SS bars allowed for a better utilization of UHPC's high compression capacity. The ductility ratio and toughness were found to be 10.8 and 21.5 kJ, respectively.

Table A.18 Static test results of U2-No.5S1-DR-d/2

Beam	Load		Displacement		Secant Stiffness k_s (N/mm)	Ductility Δ_{max}/Δ_y	Toughness A_u (J)
	Yield P_y (kN)	Peak P_{max} (kN)	Yield Δ_y (mm)	Failure Δ_{max} (mm)			
U2-No.5S1-DR-d/2	153.1	172.4	12.1	150	12653	10.8	21491

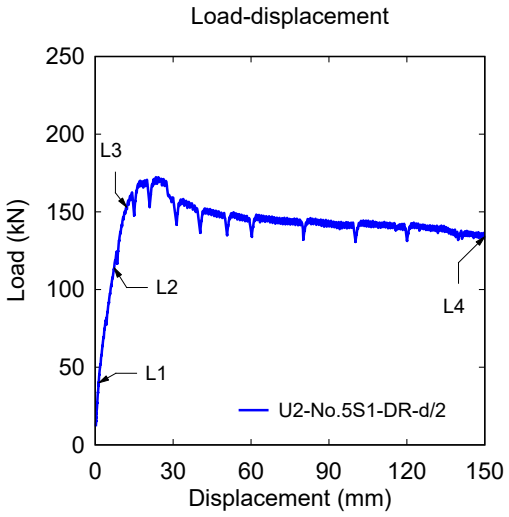

Figure A.45 Load-displacement response for beam U2-No.5S1-DR-d/2

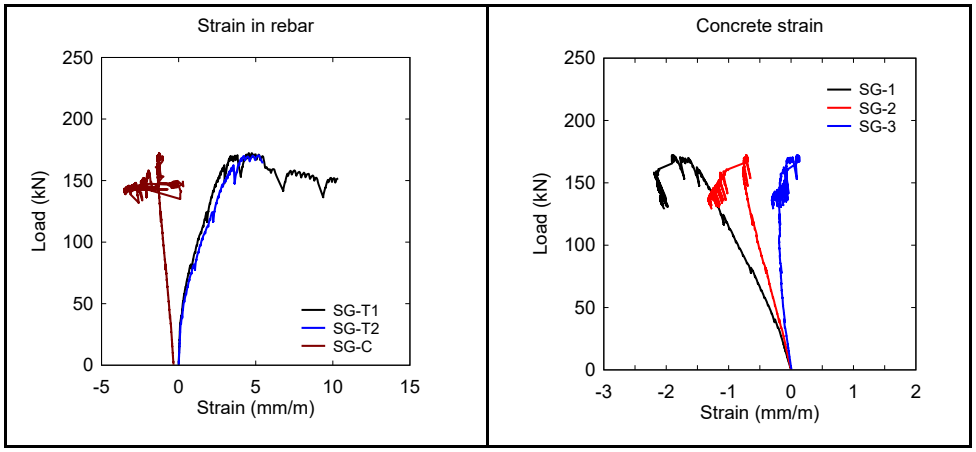

Figure A.46 Load-strain data for beam U2-No.5S1-DR-d/2

	Load	40 kN	Δ_{mid}	1.4 mm	Max. Crack width	HL
L1: First crack						
	Load	114 kN	Δ_{mid}	7.3 mm	Max. Crack width	HL
L2: Service load ($0.6 f_y$)						
	Load	153 kN	Δ_{mid}	12.1 mm	Max. Crack width	HL
L3: Yield						
	Load	134 kN	Δ_{mid}	150 mm	Max. Crack width	-
L4: Concrete crushing						

Figure A.47 Major events for beam U2-No.5S1-DR-d/2

A.2.3.9. U3-No.5S1

Beam U3-No.5S1 was designed with ultra-high performance concrete, 3% steel fiber, 2-No.5 XM-28 stainless steel tension bars without stirrups in the shear span. **Table A.19** summarizes the static test result of the beam. **Figure A.48** shows the load-deflection curve, and strain data are presented in **Figure A.49**. **Figure A.50** shows photos of major events during testing.

The first hairline cracks were observed in the flexural zone at an applied load of 40 kN. The beam reached yield strength of 207.8 kN at a displacement of 14.8 mm. The maximum load resisted by the beam was 207.8 kN. Crack localization was observed shortly after reaching the peak capacity. The test was terminated at a displacement of 124 mm due to loading transfer beam hitting the test specimen, however the use of stainless bars prevented bar rupture. The ductility ratio and toughness were found to be 8.38 and 18.6 kJ, respectively.

Table A.19 Static test results of U3-No.5S1

Beam	Load		Displacement		Secant Stiffness k_s (N/mm)	Ductility Δ_{max}/Δ_y	Toughness A_u (J)
	Yield P_y (kN)	Peak P_{max} (kN)	Yield Δ_y (mm)	Failure Δ_{max} (mm)			
U3-No.5S1	207.8	207.8	14.8	124	14040	8.38	18561

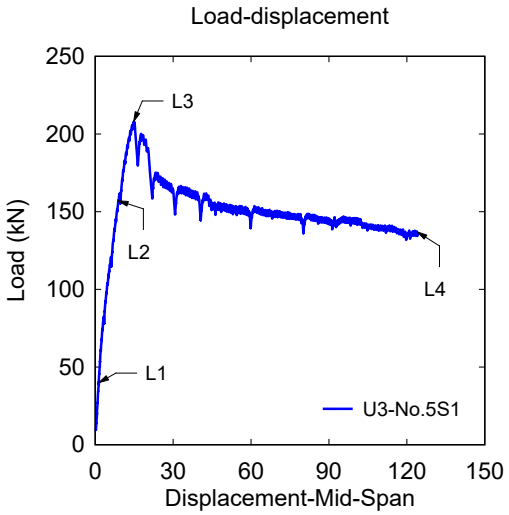

Figure A.48 Load-displacement response for beam U3-No.5S1

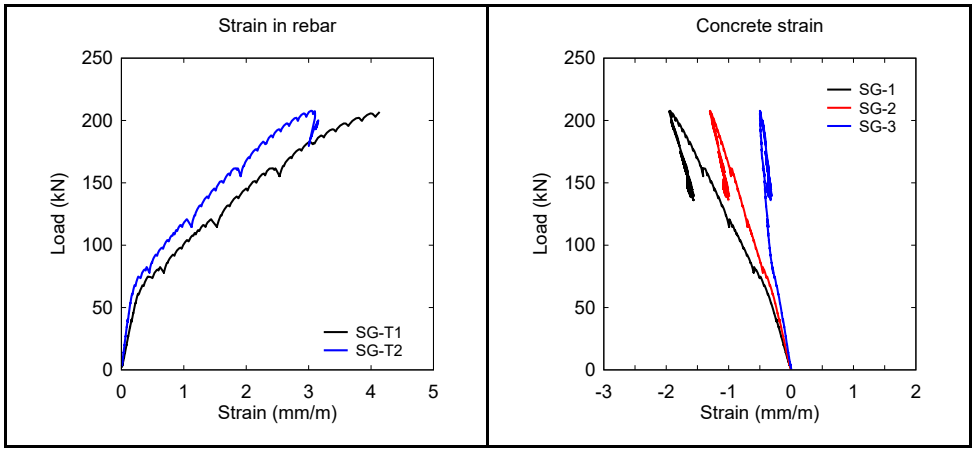

Figure A.49 Load-strain data for beam U3-No.5S1

	Load	40 kN	Δ_{mid}	1.4 mm	Max. Crack width	HL
L1: First crack						
	Load	157 kN	Δ_{mid}	8.9 mm	Max. Crack width	HL
L2: Service load ($0.6 f_y$)						
	Load	208 kN	Δ_{mid}	14.8 mm	Max. Crack width	HL
L3: Yield						
	Load	137 kN	Δ_{mid}	124 mm	Max. Crack width	-
L4: Testing terminated						

Figure A.50 Major events for beam U3-No.5S1

A.3 Blast and post-blast test results

This section presents the blast and post-blast static test results for the beams in **Series 1** (HSC-HSS), **Series 2** (HSC-SS) and **Series 3** (UHPC-NSS, UHPC-HSS and UHPC-SS). The pressure, impulse, displacement and load time-histories curves, as well as damage photos, are presented for each beam. Key data for each beam is summarized in a Table which reports the shockwave data (P_r, I_r and t_d = peak reflected pressure, positive impulse, and positive phase duration) as well as specimen response after each test (D_{max}, D_{res} and θ_{max} = maximum displacement, residual displacement and support rotation). The table also compares the results with the response limits in the CSA S850 blast standard (CSA, 2012). As shown in **Table A.20**, these response limits (B1-B4) correspond to specific values of support rotation (θ_{max}) or ductility ratio (μ_{max}). In the case of singly-reinforced, B1, B2, B3 and B4 correspond to $\mu_{max} = 1$, $\theta_{max} = 1°$ and 2°, $\theta_{max} = 2°$ and 5°, and $\theta_{max} = 10°$, respectively. While B1, B2, B3 and B4 correspond to $\mu_{max} = 1$, $\theta_{max} = 1°$ and 4°, $\theta_{max} = 4°$ and 6°, and $\theta_{max} = 10°$ for doubly-reinforced beams. These limits in turn define component damage levels: "Blowout" (greater than B4), "Hazardous failure" (between B4 and B3); "Heavy" (between B3 and B2); "Moderate" (between B2 and B1) and "Superficial" (less than B1). The definitions of the different variables extracted from the blast tests are shown in **Figure A.51a** are summarized as follows:

P_r: maximum reflected pressure;

t_d: positive phase duration (time taken for the maximum pressure to decay to zero);

I_r: reflected impulse (area under the positive phase of the pressure-time history curve);

d_{max}: maximum displacement;

d_{res}: residual displacement.

Many of the beams tested in this study had significant residual capacity after blast testing. These blast-damaged beams were subsequently tested under static four-point bending to assess their post-blast residual capacity. The results of these tests include: maximum residual capacity (P_{max}^R), residual secant stiffness (k_s^R) and maximum cumulative residual displacement (Δ_{max}^R), along with the static results from the original undamaged (i.e. companion static) beams. Photos of the beams before and after residual static testing are also presented. The definitions of the different variables extracted from the post-blast residual tests are shown in **Figure A.51b** and are summarized as follows:

P_{max}^R: maximum load resisted by the specimen in post-blast residual test;

Δ_{test}^{R}: displacement at failure in post-blast residual test;

Δ_{max}^{R}: maximum cumulative residual displacement during the post-blast test, taken as the sum of the residual displacements during blast testing (d_{res}) and the maximum displacement sustained during the post-blast static test (Δ_{test}^{R}).

The definitions of the variable index to evaluate post-blast residual test are summarized as follows:

RRI: residual resistance index ($RRI = \frac{P_{max}^{R}}{P_{max}}$)

RSI: ratio of secant stiffness of impact-damaged to undamaged specimens ($RSI = \frac{k_s^R}{k_s}$)

RDI: residual displacement index ($RDI = \frac{\Delta_{max}^{R}}{\Delta_{max}}$)

IEI: impact energy index ($\text{IEI} = \frac{A}{A+B}$)

REI: residual energy index ($\text{REI} = \frac{C}{A+B}$)

TEI: total energy index ($\text{TEI} = \text{IEI} + \text{REI}$)

Table A.20 Response limits for reinforced concrete (adopted from CSA-S850)

Element type		B1		B2		B3		B4	
		μ_{max}	θ_{max}	μ_{max}	θ_{max}	μ_{max}	θ_{max}	μ_{max}	θ_{max}
Flexure	Single-reinforced slab or beam	1	-	-	2°	-	5°	-	10°
	Double-reinforced slab or beam without shear reinforcement	1	-	-	2°	-	5°	-	10°
	Double-reinforced slab or beam with shear reinforcement	1	-	-	4°	-	6°	-	10°
	With tension membrane	1	-	-	6°	-	12°	-	20°

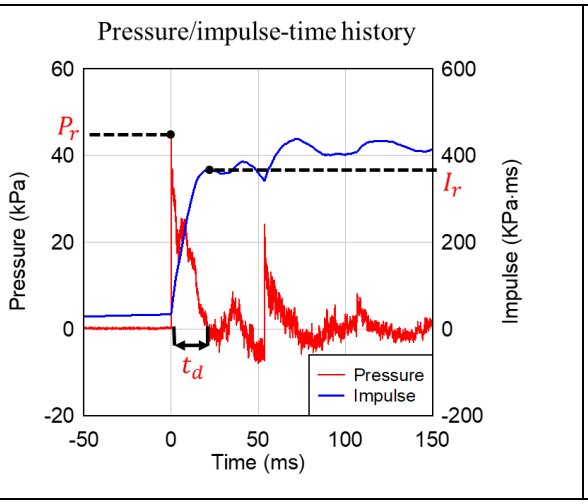

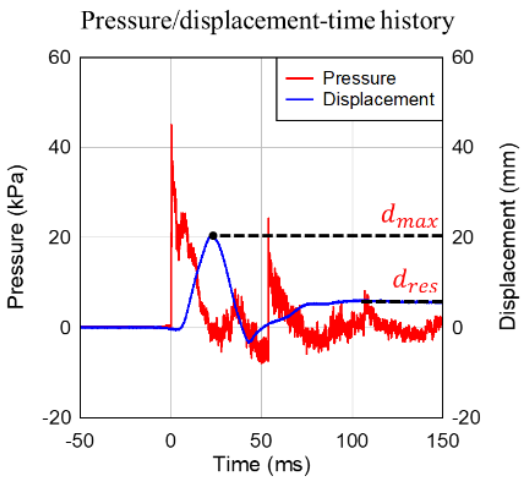

(a) Definition of the variables in the blast test

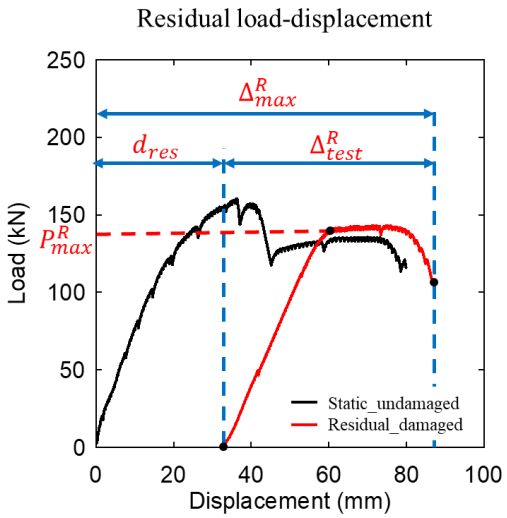

(b) Definition of the variables in the post-blast test

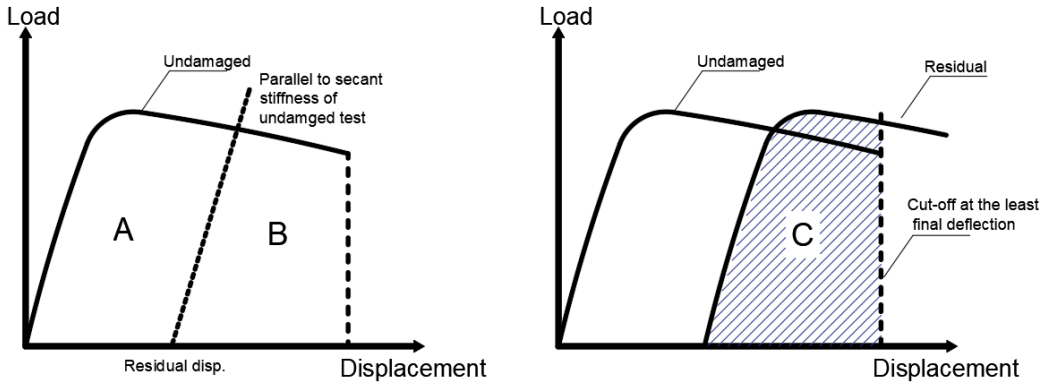

(c) Definition of the index in the post-blast residual test

Figure A.51 Illustration of the variables in the blast and post-blast tests

A.3.1. Blast and post-blast test results in Series 1 (HSC-HSS)

A.3.1.1. C100-No.4HS-DR-d/4

Beam C100-No.4HS-DR-d/4 was designed with high-strength concrete and 2-No.4 high-strength steel bars in tension. The beam design met the blast detailing requirements in the CSA S850 standard with provision of top continuity bars (2 - No.3 HS bars) and closed ties spaced at d/4 (s = 50 mm) throughout the span. The beam was tested under repeat blast loads at driver pressures (P_d) of 30 psi, 50psi and 70 psi. **Table A.21** summarizes the blast test results and **Figure A.53** shows the pressure, impulse, displacement and dynamic reaction – time histories. The damage patterns after each blast test are presented in **Figure A.52**.

Blast-30psi was meant to test the beam within the elastic range and caused the formation of hairline cracks along the beam span. Support rotations (θ_{max}) remained below 1° (superficial damage) with maximum (D_{max}) and residual (D_{res}) displacements of 20.4 mm and 5.4 mm. *Blast-50psi* resulted in the formation of a major crack having a width of 0.5 mm in the midspan flexural zone, with further extension of existing cracks. The beam sustained displacements of $D_{max} = 35.6\,mm$, $D_{res} = 9.2\,mm$, with a maximum support rotation of $\theta_{max} = 1.8°$ (B1-B2: moderate damage). During the last shot (*Blast-70psi*), the beam reached a maximum displacement of D_{max}=52.6 mm, with a residual deformation of d_{res}=24.7 mm and maximum support rotation of $\theta_{max} = 2.7°$ (B1-B2: moderate damage). Damage was limited to top cover concrete crushing, while the closely spaced ties ensured integrity of core concrete and prevented bar buckling. During the test the principal crack increased to 3.0 mm.

After dynamic testing, the beam was tested under static four-point bending to assess its post-blast residual capacity. The results from the residual test are summarized in **Table A.22**. The residual load-deflection response is compared to the undamaged beam response in **Figure A.54**, while **Figure A.55** shows a photo of the beam after residual testing. The beam showed a maximum capacity (P^R_{max} = 143.2 kN) which is similar to the post-peak response in the undamaged beam. The beam failed in bar rupture at a maximum residual displacement (Δ^R_{test}) of 53.9 mm with a maximum cumulative residual displacement (Δ^R_{max}) of 85.7 mm.

Table A.21 Dynamic test result of C100-No.4HS-DR-d/4

Beam	Blast ID (Psi)	Shockwave Properties			Specimen Response					CSA S850 Response limits and Component damage	
		P_r (kPa)	I_r (kPa·ms)	t_d (ms)	D_{max} (mm)	D_{res} (mm)	θ_{max} (°)	$d_{\sum res}$ (mm)	Observed Damage [Max. Crack width]	Response limit	Expected Damage level
C100-No.4HS-DR-d/4	30	45.0	367.2	20.9	20.4	5.4	1.0	5.4	Minor F cracking [HL]	B1	Superficial
	50	57.5	531.5	20.8	35.6	9.2	1.8	14.6	Moderate F cracking [0.5]	B1-B2	Moderate
	70	80.5	722.5	20.9	52.6	24.7	2.7	39.3	Cover crushing & Moderate F cracking [3.0]	B1-B2	Moderate

Figure A.52 Blast damage for beam C100-No.4HS-DR-d/4

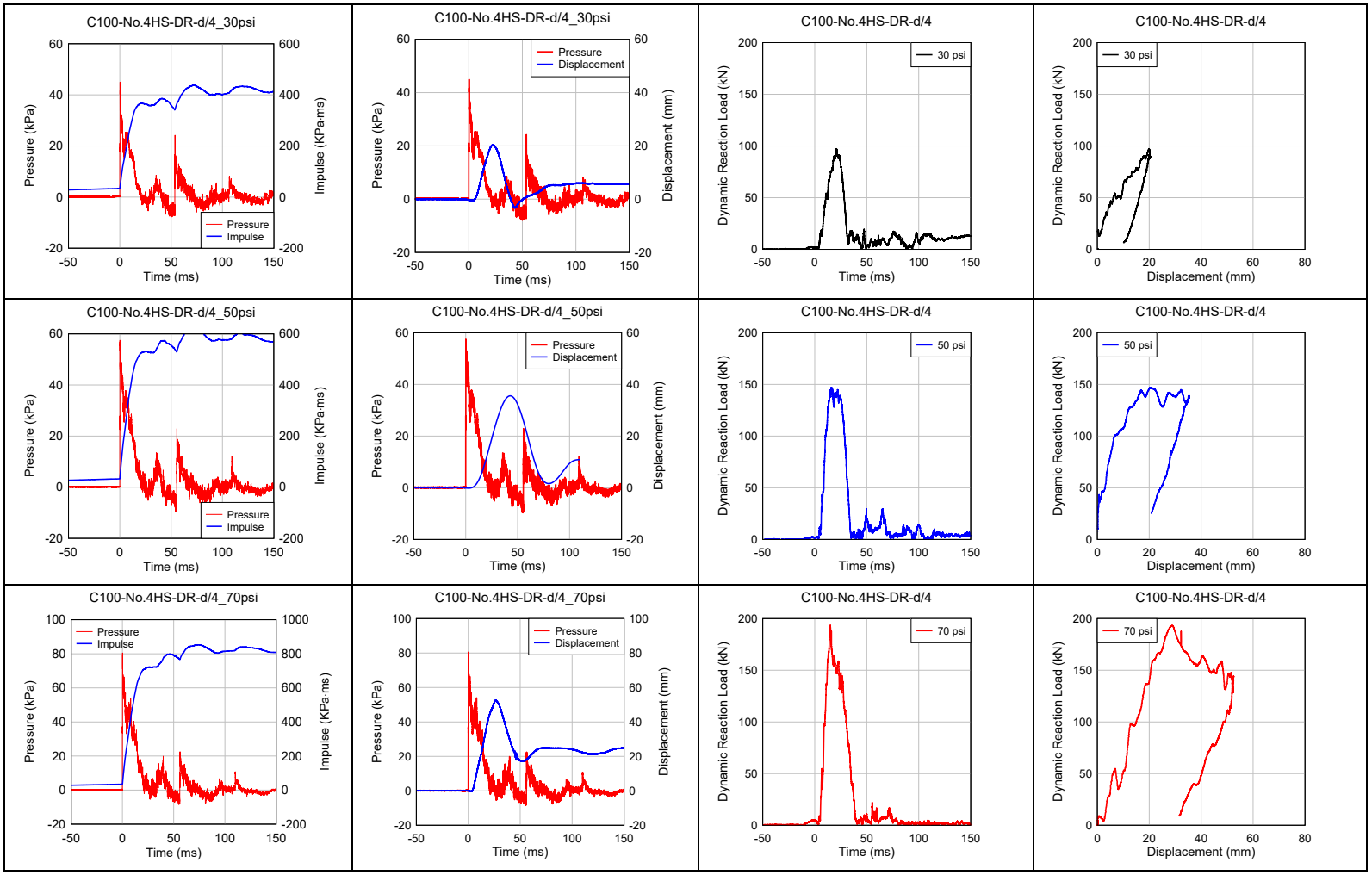

Figure A.53 Blast results for beam C100-No.4HS-DR-d/4.

(pressure/impulse-time, displacement-time, dynamic reaction-time histories and dynamic reaction-displacement response)

Table A.22 Residual static test result of C100-No.4HS-DR-d/4

Beam	Dynamic loading type	Load		Stiffness		Displacement			Energy-absorption		
		P_{max}^{R} (kN)	RRI	k_s^R (N/mm)	RSI	Δ_{test}^{R} (mm)	Δ_{max}^{R} (mm)	RDI	IEI	REI	TEI
C100-No.4HS-DR-d/4	Repeated blast testing	143.2	89%	5529	78%	53.9	85.7	107%	0.477	0.498	0.975

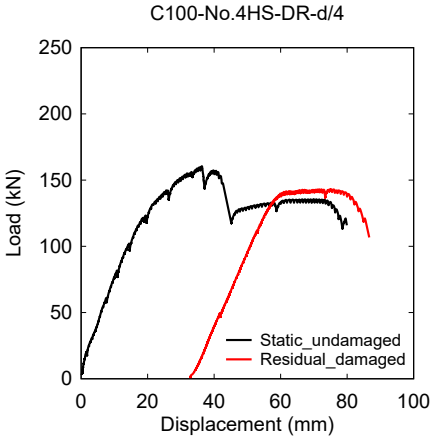

Figure A.54 Post-blast residual results for beam C100-No.4HS-DR-d/4

Figure A.55 Beam C100-No.4HS-DR-d/4 after the post-blast residual static test

A.3.1.2. C100-No.4HS-DR-d/4 (x1)

Beam C100-No.4HS-DR-d/4 [x1] had identical properties to the previous specimen but was tested under a single blast load at a driver pressure of 70 psi. **Table A.23** summarizes the blast test results and **Figure A.56** shows the pressure, impulse, mid-span displacement and dynamic reaction load – time histories. Damage after testing is shown in **Figure A.57**.

This beam only experienced some moderate flexural cracks (2 mm) after testing without concrete crushing or spalling. The maximum and residual displacements were 53.9 mm and 26.7 mm, respectively, with a corresponding maximum support rotation (θ_{max}) of 2.8° (B1-B2: moderate damage). It is noted that while the damage is slightly less pronounced, the displacements and maximum rotation are similar to that of the companion beam tested under repeated blasts.

After the dynamic blast test, the beam was tested under static loading to assess its post-blast residual capacity. The results from the residual test are summarized in **Table A.24**. The residual load-deflection response is compared to the undamaged beam response in **Figure A.58**, while **Figure A.59** shows a photo of the beam after testing. The blast-damaged beam had a similar capacity (P^R_{max} = 161.5 kN) when compared to the companion beam which was tested under static loads only. Similar to the "undamaged" beam, the loss of the top cover concrete resulted in a drop in load capacity, however the beam continued to carry loads, eventually failing due to bar rupture. The maximum residual displacement (Δ^R_{test}) was 57.4 mm, with a maximum cumulative displacement (Δ^R_{max}) of 84.1 mm.

Table A.23 Dynamic test result of C100-No.4HS-DR-d/4 (x1)

Beams	Blast ID (Psi)	Shockwave Properties			Specimen Response					CSA S850 Response limits and Component damage	
		P_r (kPa)	I_r (kPa·ms)	t_d (ms)	D_{max} (mm)	D_{res} (mm)	θ_{max} (°)	$d_{\Sigma res}$ (mm)	Observed Damage [Max. Crack width]	Response limit	Expected Damage level
C100-No.4HS-DR-d/4 (x1)	70	80.6	723.8	21.3	53.9	26.7	2.8	26.7	Moderate F cracking [2.0]	B1-B2	Moderate

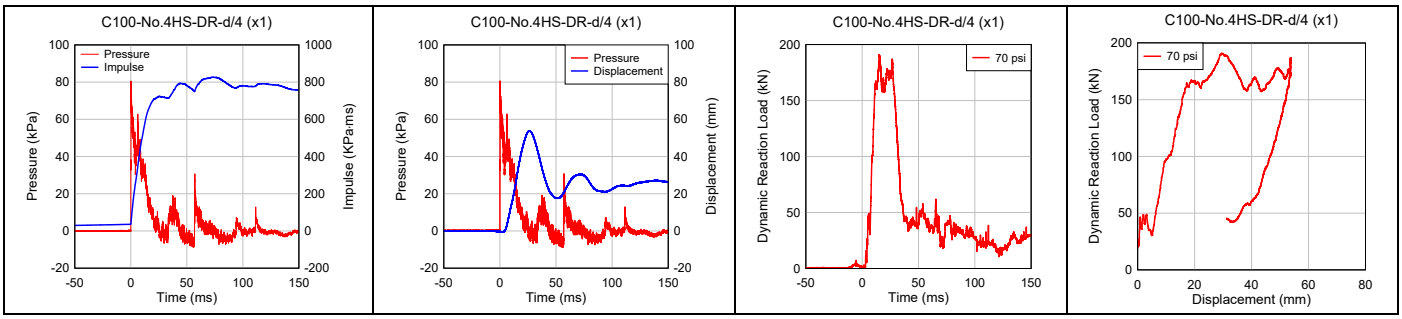

Figure A.56 Blast results for beam C100-No.4HS-DR-d/4 [x1].

(pressure/impulse-time, displacement-time, dynamic reaction-time histories and dynamic reaction-displacement response)

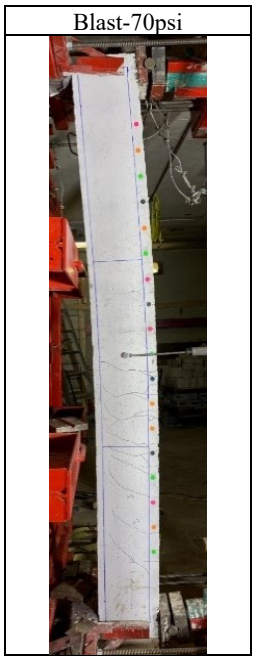

Figure A.57 Blast damage for beam C100-No.4HS-DR-d/4 (x1)

Table A.24 Residual test result of C100-No.4HS-DR-d/4 (x1)

Beam	Dynamic loading type	Load		Stiffness		Displacement			Energy-absorption		
		P_{max}^{R} (kN)	RRI	k_s^R (N/mm)	RSI	Δ_{test}^{R} (mm)	Δ_{max}^{R} (mm)	RDI	IEI	REI	TEI
C100-No.4HS-DR-d/4 [x1]	Single	161.5	101%	6629	94%	57.4	84.1	105%	0.411	0.631	1.042

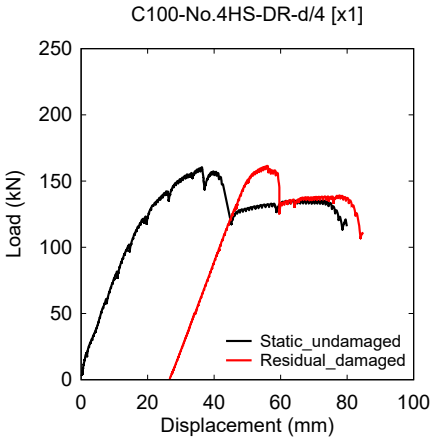

Figure A.58 Post-blast residual results for beam C100-No.4HS-DR-d/4 [x1]

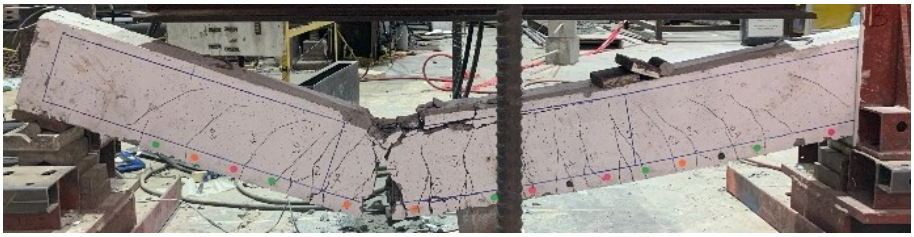

Figure A.59 Beam C100-No.4HS-DR-d/4 (x1) after post-blast residual static test

A.3.1.3. C100-No.5HS-DR-d/4

Beam C100-No.5HS-DR-d/4 was similar in the design to the previous two specimens but had an increased tension steel ratio. Longitudinal reinforcement consisted of No.5/No.4 bars in tension/compression, with closed ties spaced at d/4 (s=50 mm). This beam was tested under repeat blasts at P_d = 30 psi, 50 psi, 70 psi and 90 psi. **Table A.25** summarizes the blast test results for this beam. **Figure A.60** shows pressure, impulse, displacement and dynamic reaction – time histories at each blast, while photos of damage are shown in **Figure A.61**.

Blast-30psi tested the beam within the elastic range, and resulted in the formation of hairline cracks in the flexural zone with displacements of D_{max} = 15.2 mm and D_{res} = 1.3 mm. The maximum Support rotations remained below 1° (<B1: superficial). *Blast-50psi* inflicted moderate damages with a major crack width of 0.3 mm, with displacements D_{max} = 26.8 mm and D_{res} = 4.3 mm, and a support rotation, θ_{max} = 1.4° (B1-B2: moderate). *Blast-70psi* led to further cracks with the formation of a 1.0 mm major flexural crack just below the upper loading point, with displacements of D_{max} = 41.4 mm ($\theta_{max} = 2.1°$) and D_{res} = 8.8 mm. The last shot (*Blast-90psi*) resulted in top cover concrete crushing and moderate flexural cracks (2.5mm in width) in the midspan zone. The maximum and residual displacement were 56.4 mm and 17.8 mm, with corresponding maximum support rotation θ_{max} of 2.7°. As predicted by the CSA S850 standard, the damage was limited to 'moderate' levels.

After the dynamic blast test, the beam was tested under static four-point bending to assess its post-blast residual capacity. **Table A.26** summarizes the results from the residual test. The residual load-deflection response is compared to the undamaged beam response in **Figure A.62,** while **Figure A.63** shows photos of the beam after residual testing.

The beam shows a peak residual capacity (P_{max}^R) which matched the expected post-peak strength observed in the undamaged beam, while the residual stiffness (k_s^R) was approximately 80% of that of the undamaged specimen. The beam eventually failed due to buckling of the compression bars near the midspan at a maximum residual displacement (Δ_{test}^R) of 48.6 mm, and cumulative displacement (Δ_{max}^R) of 88.6 mm. No bar rupture was observed in the residual static test, although failure occurred earlier when compared to the undamaged beam.

Table A.25 Dynamic test result of C100-No.5HS-DR-d/4

Beams	Blast ID (Psi)	Shockwave Properties			Specimen Response					CSA S850 Response limits and Component damage	
		P_r (kPa)	I_r (kPa·ms)	t_d (ms)	D_{max} (mm)	D_{res} (mm)	θ_{max} (°)	$d_{\Sigma res}$ (mm)	Observed Damage [Max. Crack width]	Response limit	Expected Damage level
C100-No.5HS-DR-d/4	30	44.2	362.9	20.1	15.2	1.3	0.8	1.3	Minor F cracking [HL]	<B1	Superficial
	50	63.4	574.1	20.7	26.8	4.3	1.4	5.6	Minor F cracking [0.3]	B1-B2	Moderate
	70	85.7	739.6	21.3	41.4	8.8	2.1	14.4	Moderate F cracking [1.0]	B1-B2	Moderate
	90	90.4	876.5	21.6	56.4	17.8	2.9	32.2	Cover crushing & Moderate F cracking [2.5]	B1-B2	Moderate

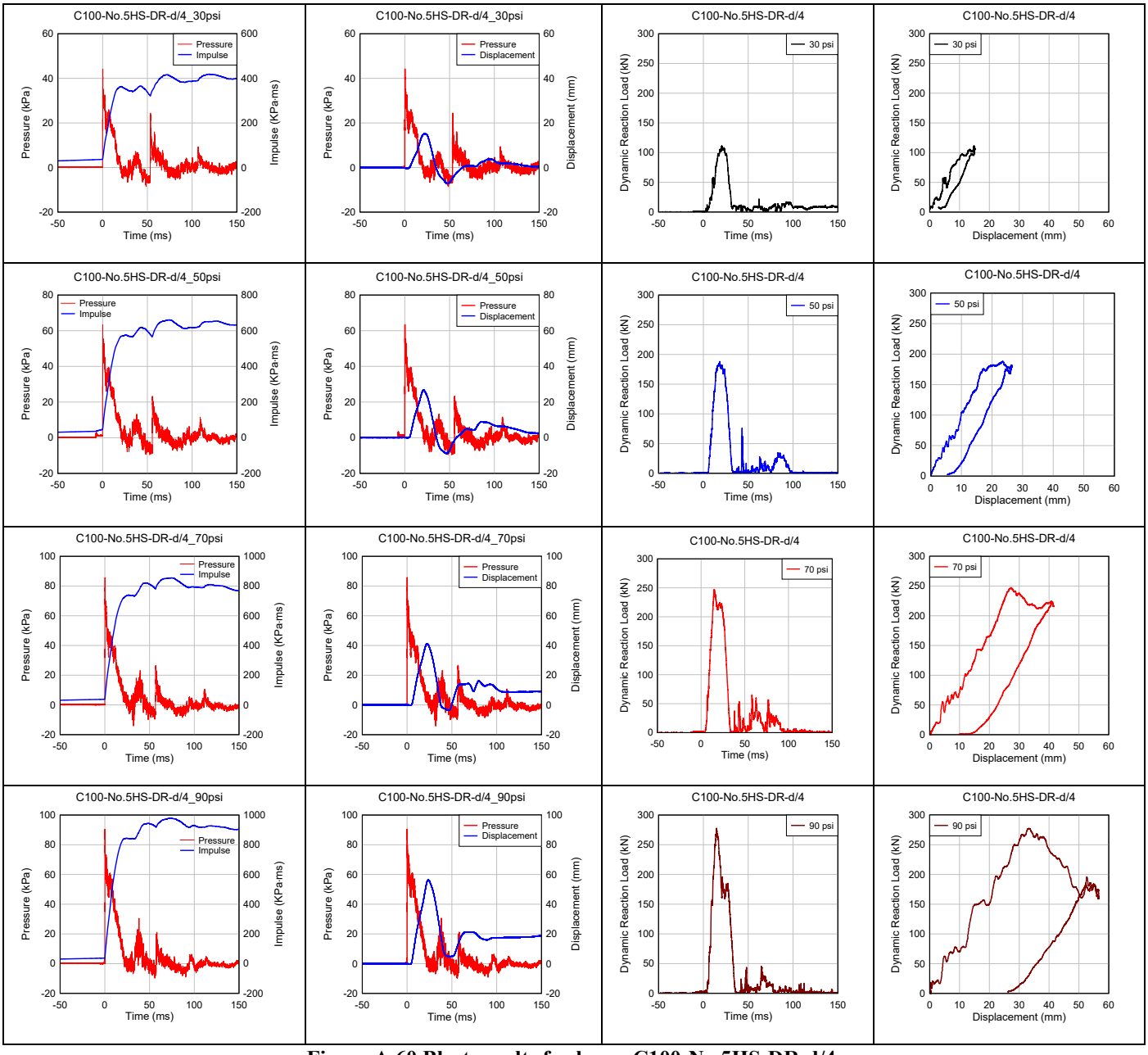

Figure A.60 Blast results for beam C100-No.5HS-DR-d/4.

(pressure/impulse-time, displacement-time, dynamic reaction-time histories and dynamic reaction-displacement response)

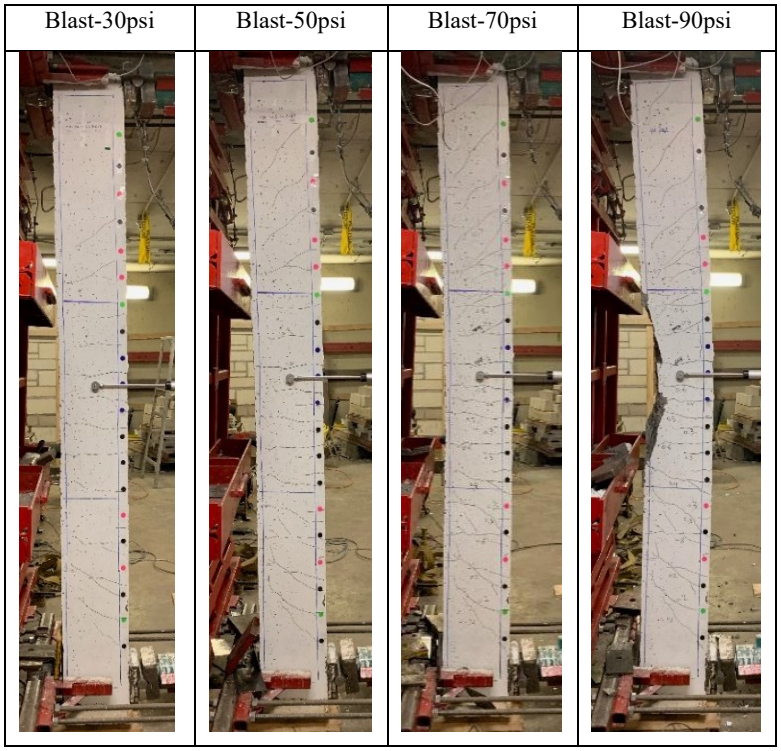

Figure A.61 Blast damage for beam C100-No.5HS-DR-d/4

Table A.26 Residual test result of C100-No.5HS-DR-d/4

Beam	Dynamic loading type	Load		Stiffness		Displacement			Energy-absorption		
		P_{max}^{R} (kN)	RRI	k_s^R (N/mm)	RSI	Δ_{test}^{R} (mm)	Δ_{max}^{R} (mm)	RDI	IEI	REI	TEI
C100-No.5HS-DR-d/4	Repeated	205.4	99%	6401	80%	48.6	88.6	92%	0.372	0.385	0.757

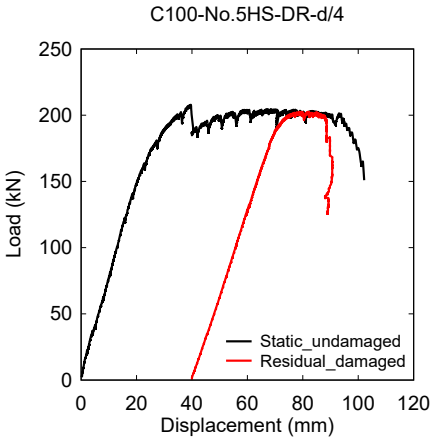

Figure A.62 Post-blast residual results for beam C100-No.5HS-DR-d/4

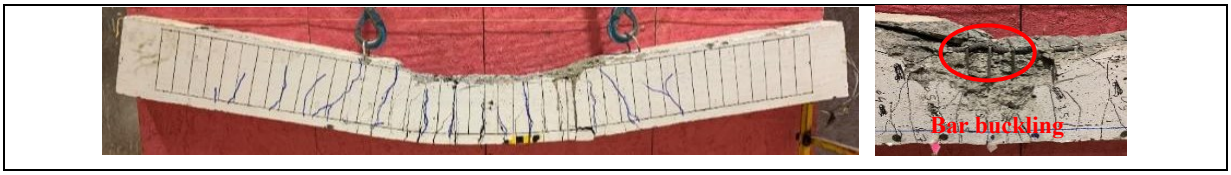

Figure A.63 Beam C100-No.5HS-DR-d/4 after the post-blast residual static test

A.3.1.4. C100-No.5HS-DR-d/4 (x1)

Beam C100-No.5HS-DR-d/4 [x1] had identical properties to the previous specimen but was tested under single blast load at a driver pressure of 90 psi. **Table A.27** summarizes the blast test results and **Figure A.64** shows the pressure, impulse, displacement and dynamic reaction – time histories. The damage pattern after blast testing is shown in **Figure A.65**.

The beam sustained some moderate flexural cracks (1.5 mm in width) and top cover concrete crushing after the single application of *Blast-90psi*. The maximum and residual displacement were recorded as 51.7 mm and 21.0 mm, respectively, with $\theta_{max} = 2.7°$ (B1-B2: Moderate). The results are similar to the companion beam tested under repeated blasts.

After the dynamic blast test, the beam was tested under static loading to assess its post-blast residual capacity. **Table A.28** summarizes the residual test results. The residual load-deflection response is compared to the undamaged beam response in **Figure A.66** while **Figure A.67** shows photos of the beam after testing. The beam had similar peak residual capacity (P^R_{max} = 209.3 kN) and residual secant stiffness (k^R_s) when compared to the expected capacity observed in the undamaged beam. Failure occurred at maximum residual displacement (Δ^R_{max}) of 90.8 mm due to combined compression bar buckling and tension bar rupture.

Table A.27 Dynamic test result of C100-No.5HS-DR-d/4 (x1)

Beams	Blast ID (Psi)	Shockwave Properties			Specimen Response					CSA S850 Response limits and Component damage	
		P_r (kPa)	I_r (kPa·ms)	t_d (ms)	D_{max} (mm)	D_{res} (mm)	θ_{max} (°)	$d_{\sum res}$ (mm)	Observed Damage [Max. Crack width]	Response limit	Expected Damage level
C100-No.5HS-DR-d/4 (x1)	90	82.7	824.4	21.7	51.7	21.0	2.7	21	Cover crushing & Moderate F cracking [1.5]	B1-B2	Moderate

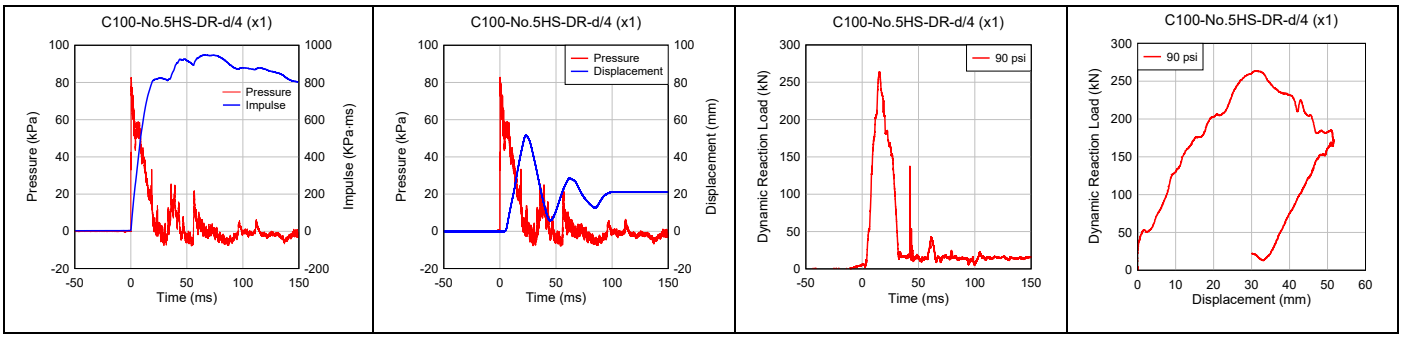

Figure A.64 Blast results for beam C100-No.5HS-DR-d/4[x1].

(pressure/impulse-time, displacement-time, dynamic reaction-time histories and dynamic reaction-displacement response)

Figure A.65 Blast damage for beam C100-No.5HS-DR-d/4 (x1)

Table A.28 Residual test result of C100-No.5HS-DR-d/4 (x1)

Beam	Dynamic loading type	Load		Stiffness		Displacement			Energy-absorption		
		P_{max}^{R} (kN)	RRI	k_s^R (N/mm)	RSI	Δ_{test}^{R} (mm)	Δ_{max}^{R} (mm)	RDI	IEI	REI	TEI
C100-No.5HS-DR-d/4 (x1)	Single	209.3	101%	7918	99%	90.8	111.8	116%	0.275	0.771	1.046

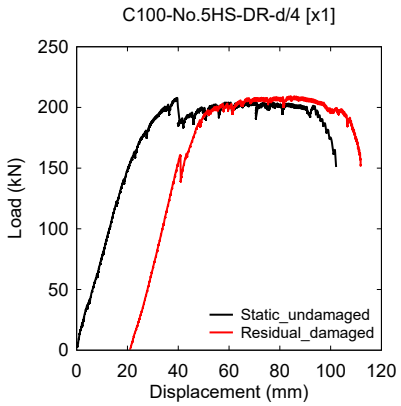

Figure A.66 Post-blast residual results for beam C100-No.5HS-DR-d/4 (x1)

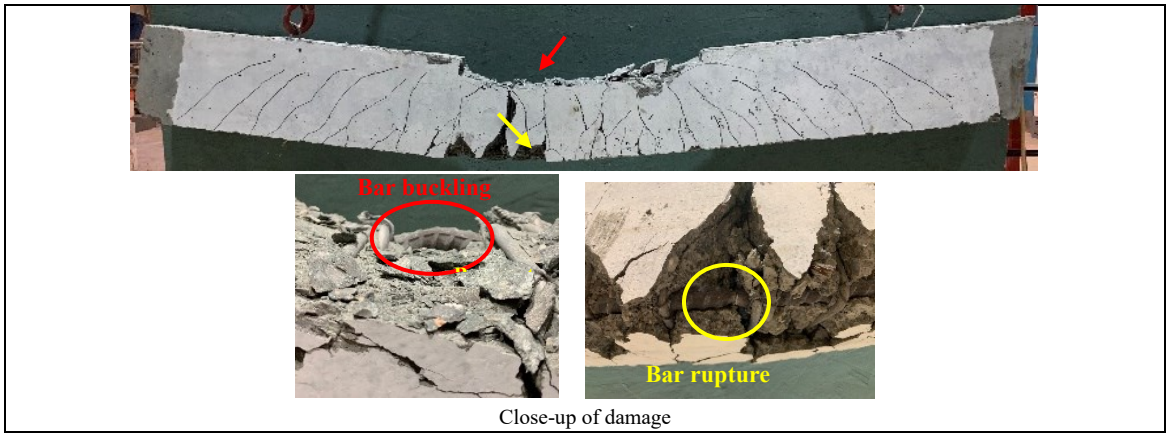

Figure A.67 Beam C100-No.5HS-DR-d/4 (x1) after the post-blast residual static test

A.3.1.5. CF100-No.5HS-DR-d/2

Beam CF100-No.4HS-DR-d/2 was designed with 100 MPa high-strength concrete, 0.75% steel fibers, No.5/No.4 high-strength longitudinal tension/compression bar and intermediate (d/2) tie spacing (s=100 mm). This beam was tested under repeat blasts at P_d = 30 psi, 50 psi, 70 psi and 90 psi. **Table A.29** summarizes the blast test results and **Figure A.68** shows the pressure, impulse, displacement and dynamic reaction – time history curves. The damage patterns after each blast test are presented in **Figure A.69**.

Blast-30psi and *Blast-50psi* tested the beam within the elastic range and caused the formation of hairline flexural cracks along the beam. These tests results in maximum displacements (support rotations) of D_{max} = 15.6 mm (θ_{max} = 0.8°) and D_{max} = 25 mm (θ_{max} = 1.3°), corresponding to "superficial" and "moderate" damage. As shown in **Figure A.69**, damage was more prominent after *Blast-70psi*, with the major crack expanding to a width of 0.4 mm. The maximum and residual displacement were 56.4 mm and 17.8 mm, with corresponding maximum support rotation (θ_{max}) of 1.7°, which is still in the "moderate" range. Even after the last shot (*Blast-90psi*), damage remained well controlled in the fiber-reinforced concrete beam, with no crushing, spalling or secondary fragments. The maximum and residual displacement were recorded as 40.9 mm (θ_{max} = 2.1°) and 15.6 mm, respectively.

After the dynamic blast test, the beam was tested under static four-point bending to assess its post-blast residual capacity. **Table A.30** summarizes the residual test results. The residual load-deflection response is compared to the undamaged beam response in **Figure A.70**, while **Figure A.**71 shows photos of the beam after residual testing. The peak residual capacity (P_{max}^R = 244.3 kN) of the beam was similar to the peak capacity observed in the undamaged beam response. However, the stiffness (k_s^R) was ~ 87% of that of the undamaged beam. The blast-damaged beam failed in bar rupture mode at a maximum residual displacement (Δ_{test}^R) of 74.0 mm, which is somewhat earlier when compared to the undamaged beam response.

Table A.29 Dynamic test result of CF100-No.5HS-DR-d/2

Beams	Blast ID (Psi)	Shockwave Properties			Specimen Response					CSA S850 Response limits and Component damage	
		P_r (kPa)	I_r (kPa·ms)	t_d (ms)	D_{max} (mm)	D_{res} (mm)	θ_{max} (°)	$d_{\sum res}$ (mm)	Observed Damage [Max. Crack width]	Response limit	Expected Damage level
CF100-No.5HS-DR-d/2	30	44.1	350.6	20.3	15.6	2.3	0.8	2.3	Minor F cracking [HL]	<B1	Superficial
	50	62.9	530.0	20.6	25.0	0.9	1.3	3.2	Minor F cracking [HL]	B1-B2	Moderate
	70	78.3	725.9	21.6	32.6	7.7	1.7	10.9	Minor F cracking [0.4]	B1-B2	Moderate
	90	94.4	920.8	22.2	40.9	15.6	2.1	26.5	Moderate F cracking [1.25]	B1-B2	Moderate

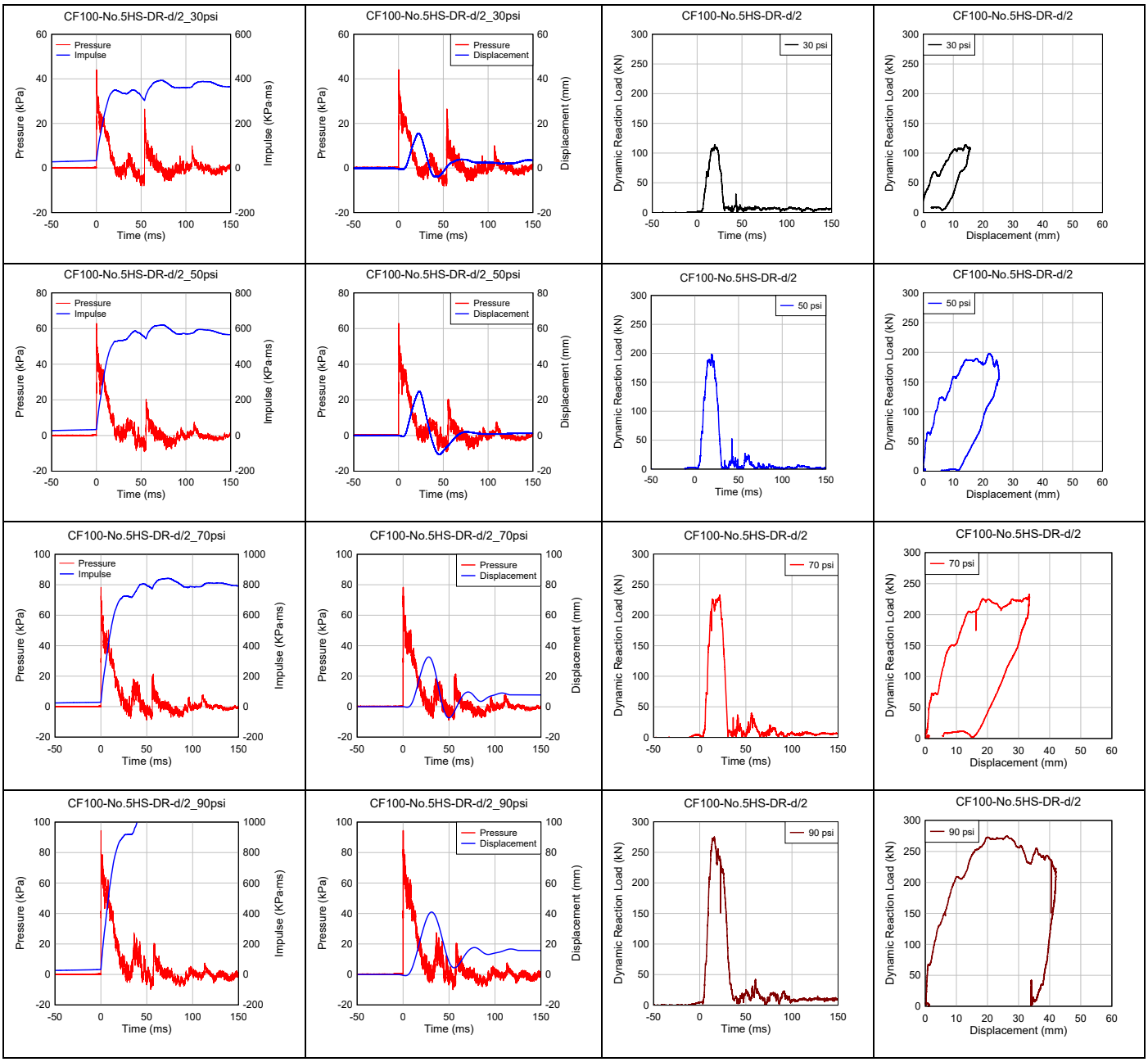

Figure A.68 Blast results for beam CF100-No.5HS-DR-d/2

(pressure/impulse-time; displacement-time; dynamic reaction-time history; dynamic reaction-displacement response)

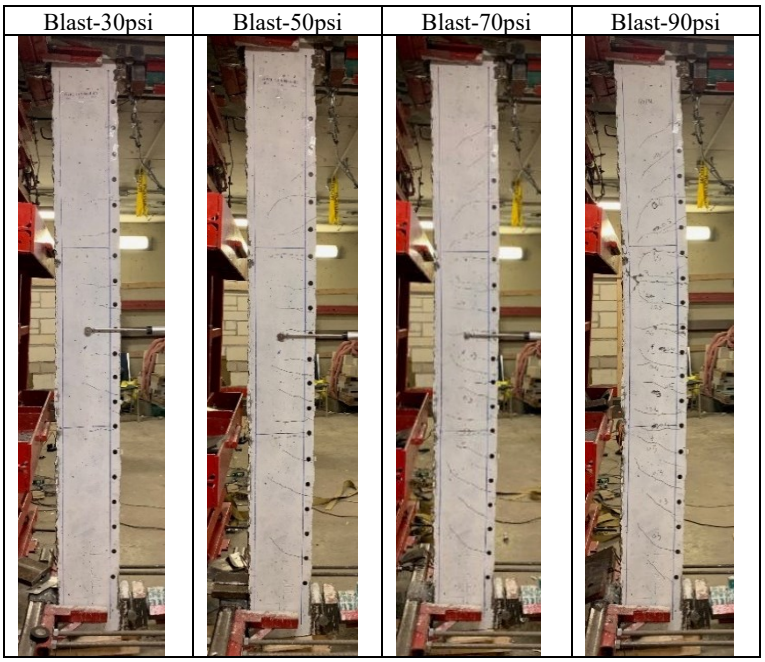

Figure A.69 Blast damage for beam CF100-No.5HS-DR-d/2

Table A.30 Residual test result of CF100-No.4HS-DR-d/4 (x1)

Beam	Dynamic loading type	Load		Stiffness		Displacement			Energy-absorption		
		P_{max}^{R} (kN)	RRI	k_s^R (N/mm)	RSI	Δ_{test}^{R} (mm)	Δ_{max}^{R} (mm)	RDI	IEI	REI	TEI
CF100-No.5HS-DR-d/2	Repeated	244.3	100%	8749	87%	74.0	100.5	87%	0.333	0.548	0.880

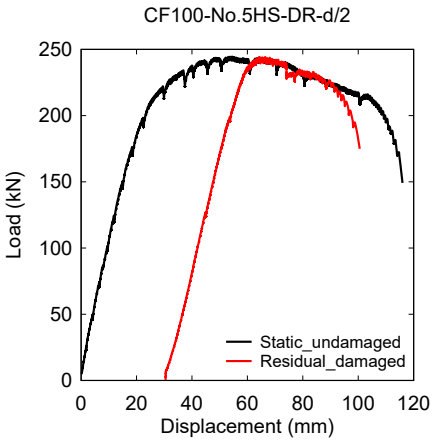

Figure A.70 Post-blast residual results for beam CF100-No.5HS-DR-d/2

Figure A.71 Beam CF100-No.5HS-DR-d/2 after the post-blast residual static test

A.3.2.Blast and post-blast test results in Series 2 (HSC-SS)

A.3.2.1. C100-No.5S1-S

Beam C100-No.5S1-S was designed with 100 MPa high-strength concrete and stainless steel reinforcement. The beam was singly-reinforced with 2-No.5 XM-28 stainless steel bars, with U-shaped stirrups spaced at d/2 (s=100 mm) in the shear spans only. The beam was tested under repeat blast loads at driver pressures (P_d) of 30 psi, 50psi and 70 psi. **Table A.31** summarizes the blast test results and **Figure A.72** shows the pressure, impulse, displacement and dynamic reaction – time histories. The damage patterns after each blast test are presented in **Figure A.73**.

Blast-30psi was meant to test the beam within the elastic range and caused the formation of hairline cracks along the beam span. Support rotations (θ_{max}) remained below 1° (superficial damage) with maximum (D_{max}) and residual (D_{res}) displacements of 16.6 mm and 2.0 mm. *Blast-50psi* resulted in the formation of a major crack having a width of 3.0 mm in the midspan flexural zone, with further extension of existing cracks. The beam sustained displacements of $D_{max} = 30.5\,mm$, $D_{res} = 5.6\,mm$, with a maximum support rotation of $\theta_{max} = 1.6°$ (B1-B2: moderate damage). During the last shot (*Blast-70psi*), the beam reached a maximum displacement of d_{max}= 134 mm, with a residual deformation of d_{res}= 87 mm and maximum support rotation of $\theta_{max} = 6.9°$ (B3-B4: hazardous damage). Damage was associated with top cover compression concrete crushing and tension concrete spalling.

No post-blast residual test was performed.

Table A.31 Dynamic test result of C100-No.5S1-S

Beam	Blast ID (Psi)	Shockwave Properties			Specimen Response					CSA S850 Response limits and Component damage	
		P_r (kPa)	I_r (kPa·ms)	t_d (ms)	D_{max} (mm)	D_{res} (mm)	θ_{max} (°)	$D_{\Sigma res}$ (mm)	Observed Damage [Max. Crack width]	Response limit	Expected Damage level
C100-No.5S1-S	30	46.7	371.6	21.5	16.6	2.0	0.9	2	Minor cracking [0.25]	<B1	Superficial
	50	57.6	539.0	23.1	30.5	5.6	1.6	7.6	Moderate cracking [3.0]	B1-B2	Moderate
	70	76.1	707.3	24.4	134	87	6.9	94.6	Severe concrete crushing & spalling	B3-B4	Hazardous

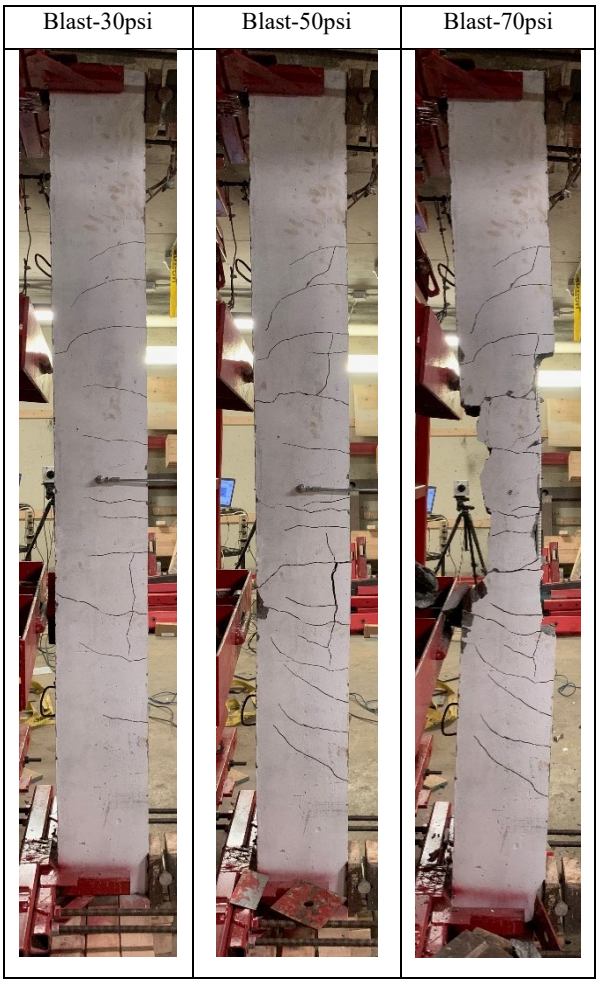

Figure A.72 Blast damage for beam C100-No.5S1-S

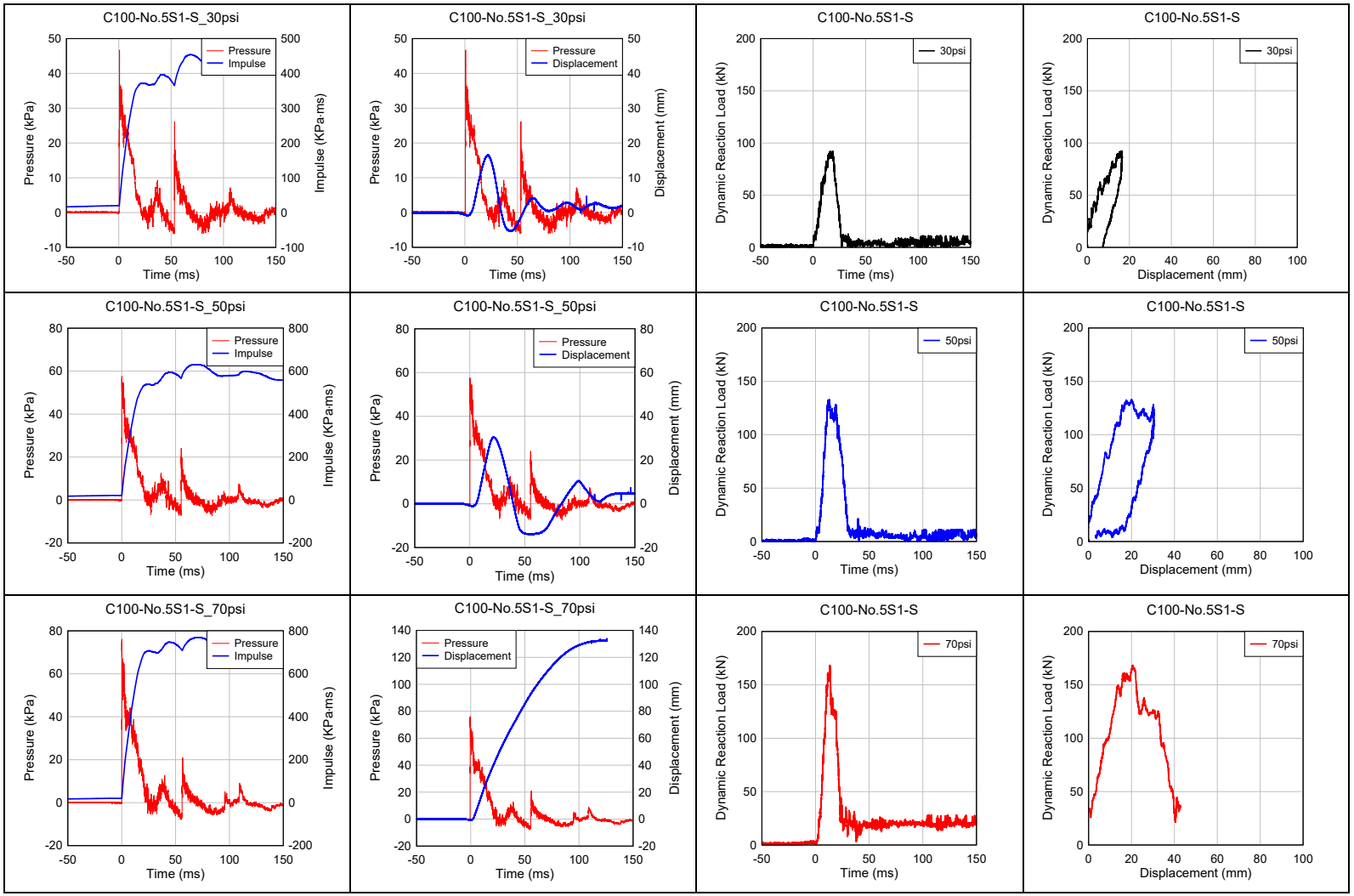

Figure A.73 Blast results for beam C100-No.5S1-S.

(pressure/impulse-time, displacement-time, dynamic reaction-time histories and dynamic reaction-displacement response)

A.3.2.2. CF100-No.5S1-S

Beam CF100-No.5S1-S was designed with 100 MPa high-strength concrete, 1% of 30mm hooked end steel fibers and stainless steel reinforcement. The beam was singly-reinforced with 2-No.5 XM-28 stainless steel bars, with U-shaped stirrups spaced at d/2 (s=100 mm) in the shear spans only. This beam was tested under repeat blasts at P_d = 30 psi, 50 psi, 70 psi and 90 psi. **Table A.32** summarizes the blast test results for this beam. **Figure A.74** shows pressure, impulse, displacement and dynamic reaction – time histories at each blast, while photos of damage are shown in **Figure A.75**.

Blast-30psi tested the beam within the elastic range, and resulted in the formation of hairline cracks in the flexural zone with displacements of D_{max} = 14.5 mm and D_{res} = 0 mm. The maximum Support rotations remained below 1° (<B1: superficial). *Blast-50psi* inflicted moderate damages with a major crack width of 0.55 mm, with displacements D_{max} = 21.8 mm and D_{res} = 0.5 mm, and a support rotation, θ_{max} = 1.1° (B1-B2: moderate). *Blast-70psi* led to further cracks with the formation of a 5 mm major flexural crack just below the upper loading point, with displacements of D_{max} = 50.2 mm ($\theta_{max} = 2.6°$) and D_{res} = 15.7 mm. The last shot (*Blast-90psi*) resulted in complete fiber pullout (15mm in width) in the midspan zone. The maximum and residual displacement were 93.8 mm and 43.6 mm, with corresponding maximum support rotation θ_{max} of 4.8° (B2-B3: heavy).

No post-blast residual test was performed.

Table A.32 Dynamic test result of CF100-No.5S1-S

Beams	Blast ID (Psi)	Shockwave Properties			Specimen Response					CSA S850 Response limits and Component damage	
		P_r (kPa)	I_r (kPa·ms)	t_d (ms)	D_{max} (mm)	D_{res} (mm)	θ_{max} (°)	$D_{\sum res}$ (mm)	Observed Damage [Max. Crack width]	Response limit	Expected Damage level
CF100-No.5S1-S	30	43.0	376.7	21.9	14.5	0	0.7	0	Minor cracking [HL]	<B1	Superficial
	50	56.8	481.8	22.9	21.8	0.5	1.1	0.5	Moderate cracking [0.55]	B1-B2	Moderate
	70	75.3	764.6	24.4	50.2	15.7	2.6	16.2	Moderate cracking [5]	B2-B3	Heavy
	90	89.4	841.5	24.7	93.8	43.6	4.8	59.8	Fiber pullout [15]	B2-B3	Heavy

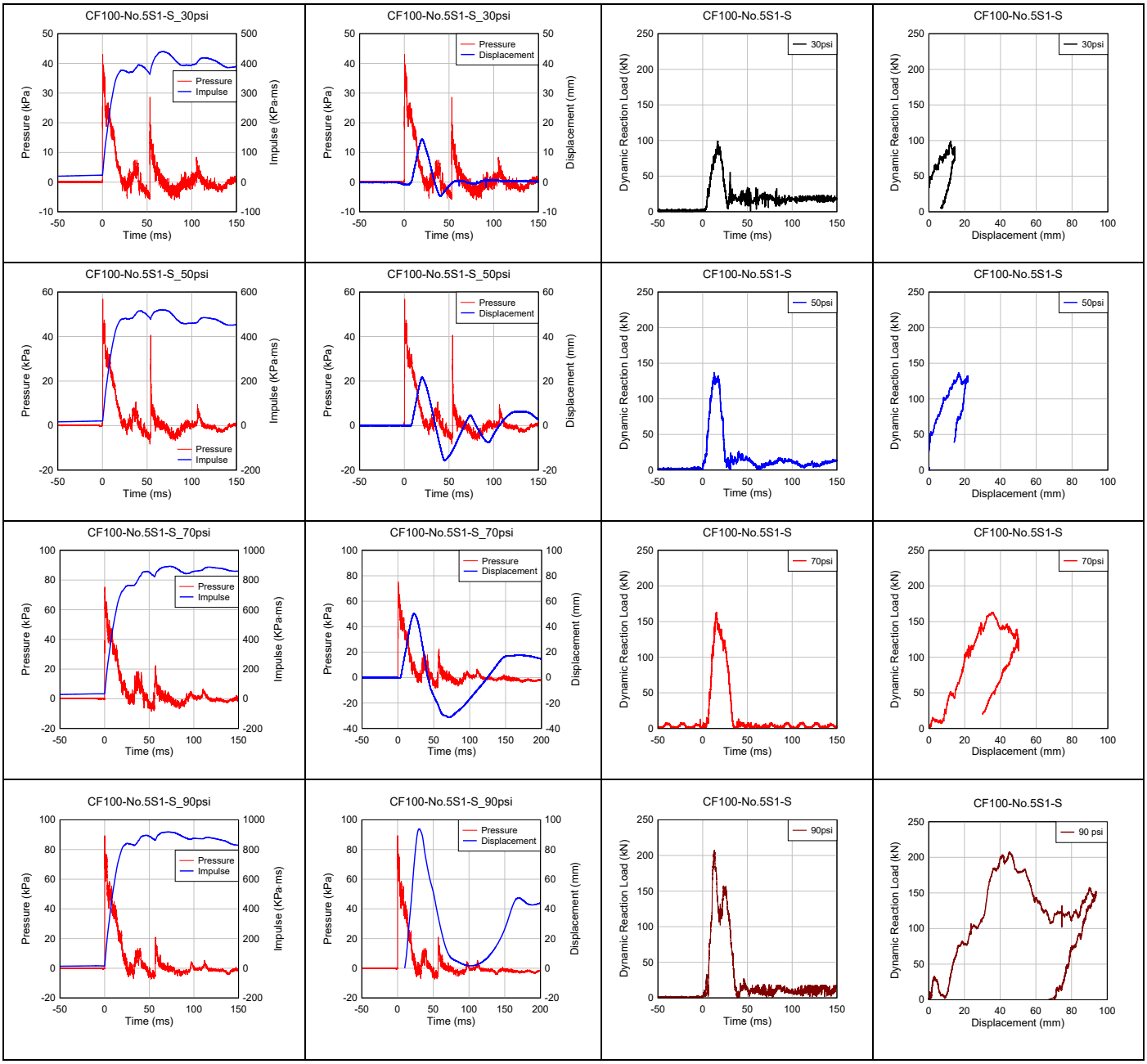

Figure A.74 Blast results for beam CF100-No.5S1-S

(pressure/impulse-time, displacement-time, dynamic reaction-time histories and dynamic reaction-displacement response)

Blast-30psi	Blast-50psi	Blast-70psi	Blast-90psi
			

Figure A.75 Blast damage for beam CF100-No.5S1-S

A.3.2.3. C100-No.5S1

Beam C100-No.5S1 was designed with 100 MPa high-strength concrete and stainless steel reinforcement. The beam was singly-reinforced with 2-No.5 XM-28 stainless steel bars, without stirrups in the shear spans. The beam was tested under a single blast load at a driver pressure of 30 psi. **Table A.33** summarizes the blast test results and **Figure A.76** shows the pressure, impulse, mid-span displacement and dynamic reaction load – time histories. Damage after testing is shown in **Figure A.77**.

Due to lack of stirrup in the shear span, the beam failed in shear. The maximum and residual displacements were 18.9 mm and 2.4 mm, respectively, with a corresponding maximum support rotation (θ_{max}) of 1.0° (B1: superficial).

No post-blast residual test was performed.

Table A.33 Dynamic test result of C100-No.5S1

Beams	Blast ID (Psi)	Shockwave Properties			Specimen Response					CSA S850 Response limits and Component damage	
		P_r (kPa)	I_r (kPa·ms)	t_d (ms)	D_{max} (mm)	D_{res} (mm)	θ_{max} (°)	$D_{\Sigma res}$ (mm)	Observed Damage [Max. Crack width]	Response limit	Expected Damage level
C100-No.5S1	30	39.1	365.6	20.7	18.9	2.4	1.0	2.4	Shear failure	-	-

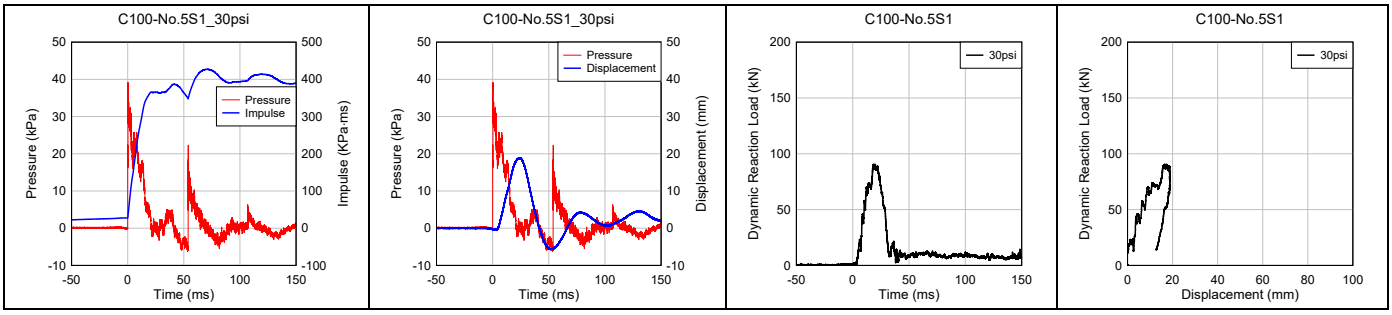

Figure A.76 Blast results for beam C100-No.5S1.

(pressure/impulse-time, displacement-time, dynamic reaction-time histories and dynamic reaction-displacement response)

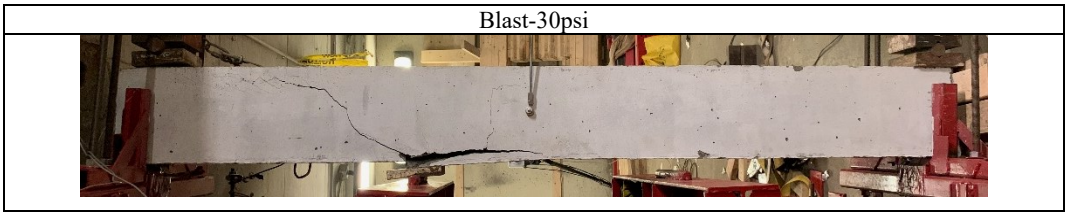

Figure A.77 Blast damage for beam C100-No.5S1

A.3.2.4. CF100-No.5S1

Beam CF100-No.5S1 was designed with 100 MPa high-strength concrete, 1% of 30mm hooked end steel fibers and stainless steel reinforcement. The beam was singly-reinforced with 2-No.5 XM-28 stainless steel bars, without stirrups in the shear spans only. The beam was tested under repeat blast loads at driver pressures (P_d) of 30 psi, 50psi and 70 psi. **Table A.34** summarizes the blast test results and **Figure A.78** shows the pressure, impulse, displacement and dynamic reaction – time histories. The damage patterns after each blast test are presented in **Figure A.79**.

Blast-30psi was meant to test the beam within the elastic range and caused the formation of hairline cracks along the beam span. Support rotations (θ_{max}) remained below 1° (superficial damage) with maximum (D_{max}) and residual (D_{res}) displacements of 13.8 mm and 2.7 mm. *Blast-50psi* resulted in the formation of a major crack having a width of 0.5 mm in the midspan flexural zone, with further extension of existing cracks. The shear crack was observed after this shot. The beam sustained displacements of $D_{max} = 24\ mm$, $D_{res} = 2.5\ mm$, with a maximum support rotation of $\theta_{max} = 1.2°$ (B1-B2: moderate damage). After the last shot (*Blast-70psi*), the beam eventually failed in shear with a maximum displacement of D_{max}= 117.8 mm, a residual deformation of D_{res}= 81.1 mm and maximum support rotation of $\theta_{max} =$ 6.1° (B2-B3: heavy damage).

No post-blast residual test was performed.

Table A.34 Dynamic test result of CF100-No.5S1

Beam	Blast ID (Psi)	Shockwave Properties			Specimen Response					CSA S850 Response limits and Component damage	
		P_r (kPa)	I_r (kPa·ms)	t_d (ms)	D_{max} (mm)	D_{res} (mm)	θ_{max} (°)	$D_{\Sigma res}$ (mm)	Observed Damage [Max. Crack width]	Response limit	Expected Damage level
CF100-No.5S1	30	41.9	350.3	21.1	13.8	2.7	0.7	2.7	Minor cracking [HL]	<B1	Superficial
	50	57.6	551.6	21.3	24.0	2.5	1.2	5.2	Moderate cracking [0.5]	B1-B2	Moderate
	70	80.8	713.0	22.8	117.8	81.1	6.1	86.3	Shear failure	-	-

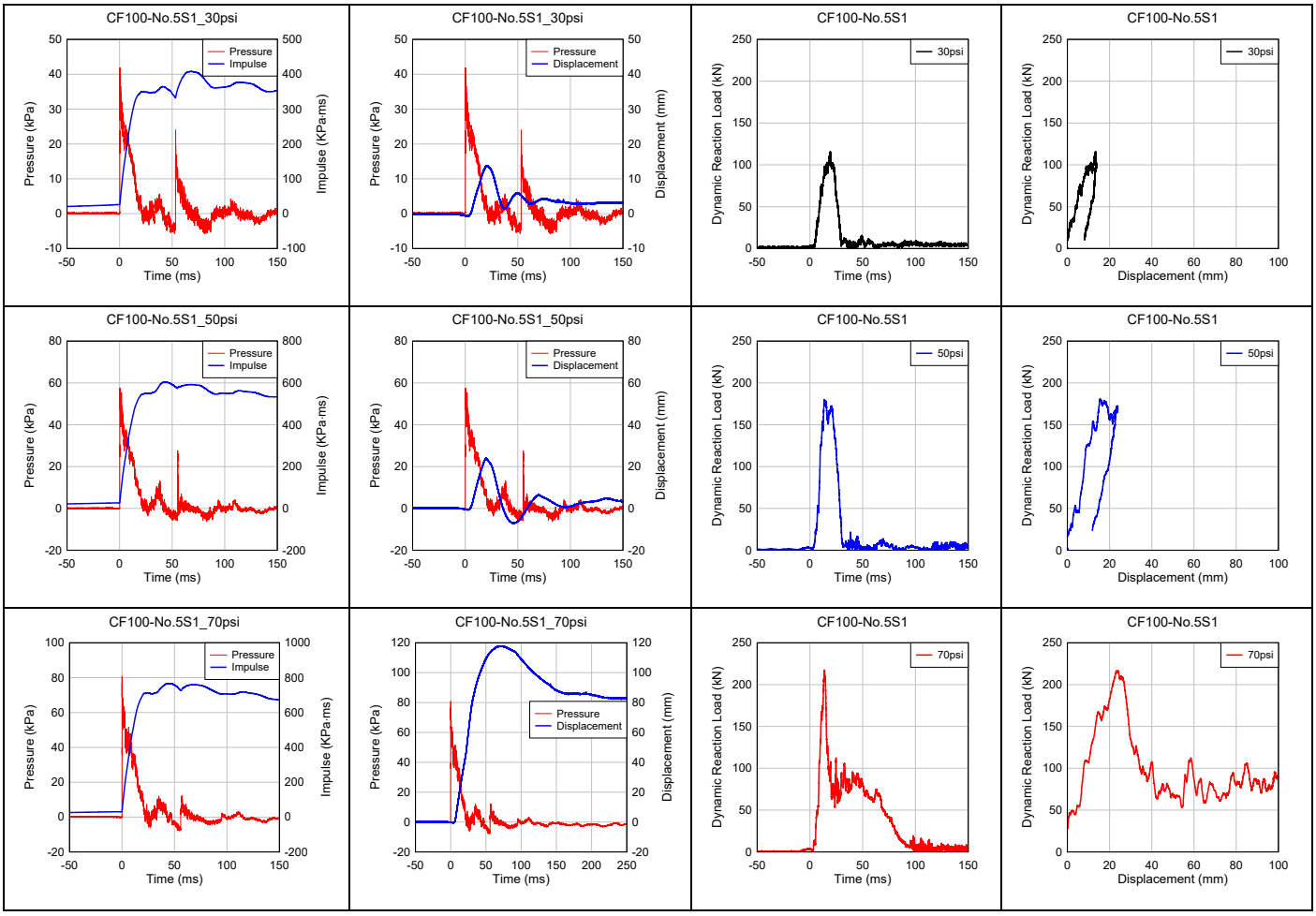

Figure A.78 Blast results for beam CF100-No.5S1

(pressure/impulse-time, displacement-time, dynamic reaction-time histories and dynamic reaction-displacement response)

Blast-30psi	Blast-50psi	Blast-70psi
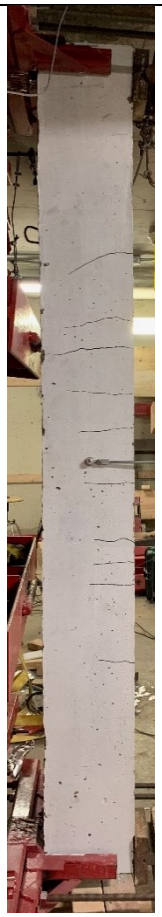		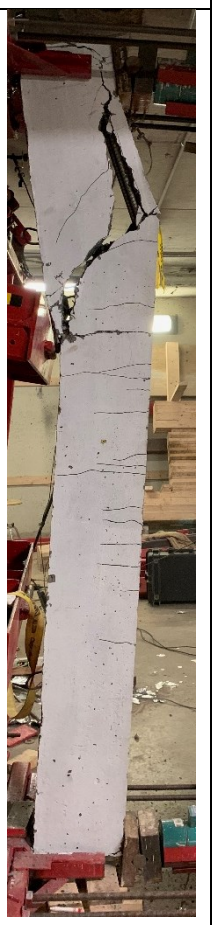

Figure A.79 Blast damage for beam CF100-No.5S1

A.3.2.5. C100-No.4S1-DR-d/4

Beam C100-No.4S1-DR-d/4 was designed with 100 MPa high-strength concrete and 2-No.4 XM-28 stainless steel bars in tension. The beam design met the blast detailing requirements in the CSA S850 standard with provision of top continuity bars (2 - No.3 S1 bars) and closed ties spaced at d/4 (s = 50 mm) throughout the span. The beam was tested under repeat blast loads at driver pressures (P_d) of 30 psi, 50psi, 70 and 90 psi. **Table A.35** summarizes the test results and **Figure A.80** shows the pressure, impulse, displacement and dynamic reaction – time histories. The damage after each test is shown in **Figure A.81**.

Blast-30psi was meant to test the beam within the elastic range and caused the formation of hairline cracks along the beam span. Support rotations (θ_{max}) remained below 1° (superficial damage) with maximum (D_{max}) and residual (D_{res}) displacements of 19.8 mm and 3.5 mm. *Blast-50psi* resulted in the formation of a major crack having a width of 0.45 mm in the midspan flexural zone, with further extension of existing cracks. The beam sustained displacements of $D_{max} = 36.3\ mm$, $D_{res} = 12\ mm$, with a maximum support rotation of $\theta_{max} = 1.9°$ (B1-B2: moderate damage). *Blast-70psi* led to further cracks with the formation of a 1.5 mm major flexural crack just below the upper loading point, with displacements of D_{max} = 61.4 mm ($\theta_{max} = 3.2°$) and D_{res} = 32.1 mm. The last shot (*Blast-90psi*) resulted in top cover concrete crushing and moderate flexural cracks in the midspan zone. The maximum and residual displacement were 108.9 mm and 68.4 mm, with corresponding maximum support rotation θ_{max} of 5.6° (B2-B3: heavy damage).

After dynamic testing, the beam was tested under static four-point bending to assess its post-blast residual capacity. The results from the residual test are summarized in **Table A.36**. The residual load-deflection response is compared to the undamaged beam response in **Figure A.82**, while **Figure A.83** shows a photo of the beam after residual testing. The beam showed a maximum capacity (P_{max}^R = 91.2 kN) which is similar to the post-peak response in the undamaged beam. The test was terminated at a residual displacement (Δ_{test}^R) of 90 mm without bar rupture. The maximum cumulative residual displacement (Δ_{max}^R) was 206 mm.

Table A.35 Dynamic test result of C100-No.4S1-DR-d/4

Beams	Blast ID (Psi)	Shockwave Properties			Specimen Response					CSA S850 Response limits and Component damage	
		P_r (kPa)	I_r (kPa·ms)	t_d (ms)	D_{max} (mm)	D_{res} (mm)	θ_{max} (°)	$D_{\sum res}$ (mm)	Observed Damage [Max. Crack width]	Response limit	Expected Damage level
C100-No.4S1-DR-d/4	30	45.4	369.4	20.6	19.8	3.5	1.0	3.5	Minor F cracking	<B1	Superficial
	50	56.1	503.7	21.2	36.3	12.0	1.9	15.5	Moderate F cracking [0.45]	B1-B2	Moderate
	70	84.1	697.9	22.0	61.4	32.1	3.2	47.6	Moderate F cracking [1.5]	B1-B2	Moderate
	90	94.2	870.8	24.3	108.9	68.4	5.6	116	Cover crushing & Moderate F cracking	B2-B3	Heavy

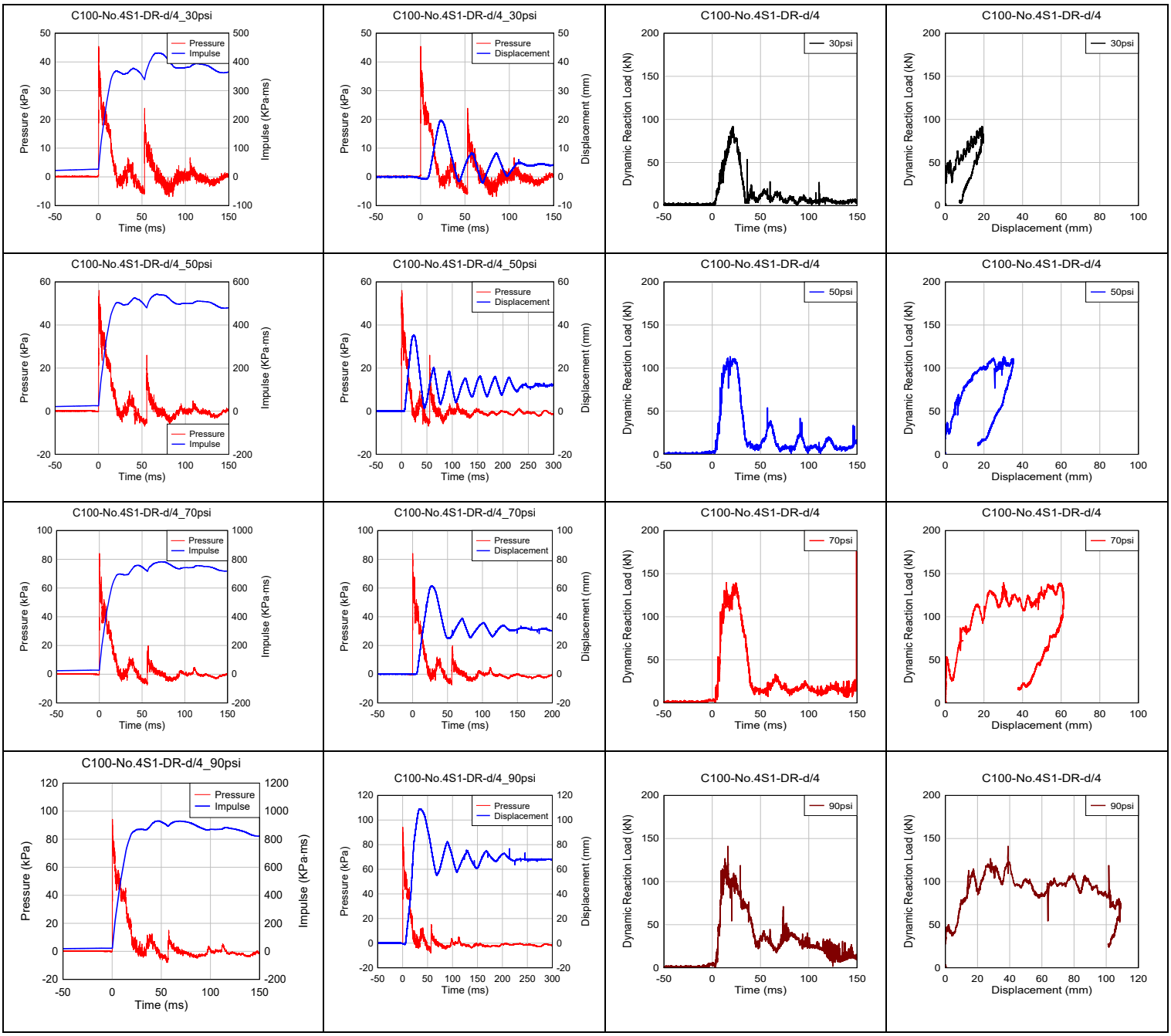

Figure A.80 Blast results for beam C100-No.4S1-DR-d/4.

(pressure/impulse-time, displacement-time, dynamic reaction-time histories and dynamic reaction-displacement response)

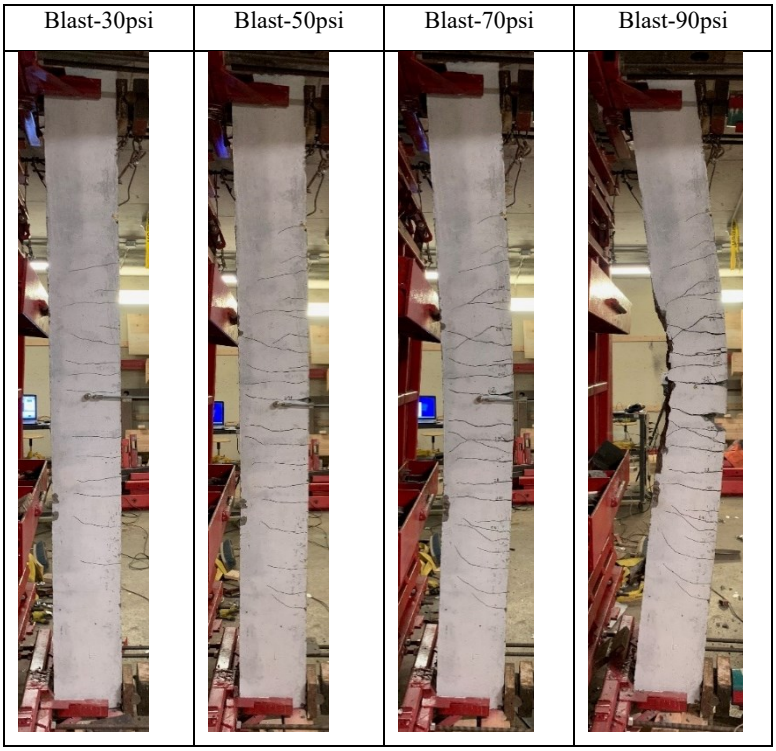

Figure A.81 Blast damage for beam C100-No.4S1-DR-d/4

Table A.36 Residual test result of C100-No.4S1-DR-d/4

Beam	Dynamic loading type	Load		Stiffness		Displacement			Energy-absorption		
		P_{max}^{R} (kN)	RRI	k_s^R (N/mm)	RSI	Δ_{test}^{R} (mm)	Δ_{max}^{R} (mm)	RDI	IEI	REI	TEI
C100-No.4S1-DR-d/4	Repeated	91.2	0.841	3264	0.616	90	206	1.373	0.88	0.13	1.01

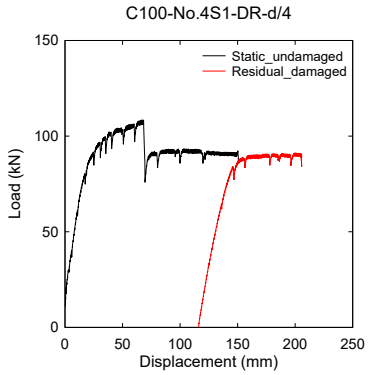

Figure A.82 Post-blast residual results for beam C100-No.4S1-DR-d/4

Figure A.83 Beam C100-No.4S1-DR-d/4 after the post-blast residual static test

A.3.2.6. C100-No.5S1-DR-d/4

Beam C100-No.5S1-DR-d/4 was similar in the design to the previous two specimens but had an increased tension steel ratio. Longitudinal reinforcement consisted of No.5/No.4 XM-28 stainless steel bars in tension/compression, with closed ties spaced at d/4 (s=50 mm). This beam was tested under repeat blasts at P_d = 30 psi, 50 psi, 70 psi and 90 psi. **Table A.37** summarizes the blast test results and **Figure A.84** shows the pressure, impulse, displacement and dynamic reaction – time histories. The damage patterns after each blast test are presented in **Figure A.85**.

Blast-30psi was meant to test the beam within the elastic range and caused the formation of hairline cracks along the beam span. Support rotations (θ_{max}) remained below 1° (superficial damage) with maximum (D_{max}) and residual (D_{res}) displacements of 18.9 mm and 3.5 mm. *Blast-50psi* resulted in the formation of a major crack having a width of 0.25 mm in the midspan flexural zone, with further extension of existing cracks. The beam sustained displacements of $D_{max} = 27.6\,mm$, $D_{res} = 3.8\,mm$, with a maximum support rotation of $\theta_{max} = 1.4°$ (B1-B2: moderate damage). *Blast-70psi* led to further cracks with the formation of a 0.7 mm major flexural crack just below the upper loading point, with displacements of D_{max} = 49.1 mm ($\theta_{max} = 2.5°$) and D_{res} = 27.7 mm. The last shot (*Blast-90psi*) resulted in top cover concrete crushing and moderate flexural cracks in the midspan zone. The maximum and residual displacement were 108.9 mm and 68.4 mm, with corresponding maximum support rotation θ_{max} of 3.8° (B1-B2: moderate damage).

After dynamic testing, the beam was tested under static four-point bending to assess its post-blast residual capacity. The results from the residual test are summarized in **Table A.38**. The residual load-deflection response is compared to the undamaged beam response in **Figure A.86**, while **Figure A.55** shows a photo of the beam after residual testing. The beam showed a maximum capacity (P_{max}^R = 126.9 kN) which is similar to the post-peak response in the undamaged beam. The beam reached a maximum residual displacement (Δ_{test}^R) of 150 mm without bar rupture. The maximum cumulative residual displacement (Δ_{max}^R) was 225.9 mm.

Table A.37 Dynamic test result of C100-No.5S1-DR-d/4

Beams	Blast ID (Psi)	Shockwave Properties			Specimen Response					CSA S850 Response limits and Component damage	
		P_r (kPa)	I_r (kPa·ms)	t_d (ms)	d_{max} (mm)	d_{res} (mm)	θ_{max} (°)	$d_{\sum res}$ (mm)	Observed Damage [Max. Crack width]	Response limit	Expected Damage level
C100-No.5S1-DR-d/4	30	45.4	359.2	20.7	18.9	3.5	1.0	3.5	Minor F cracking	<B1	Superficial
	50	62.6	524.9	22.0	27.6	3.8	1.4	7.3	Minor F cracking [0.25]	B1-B2	Moderate
	70	84.3	723.5	24.5	49.1	27.7	2.5	35	Moderate F cracking [0.7]	B1-B2	Moderate
	90	92.3	900.4	24.9	74.7	40.9	3.8	75.9	Cover crushing & Moderate F cracking	B1-B2	Moderate

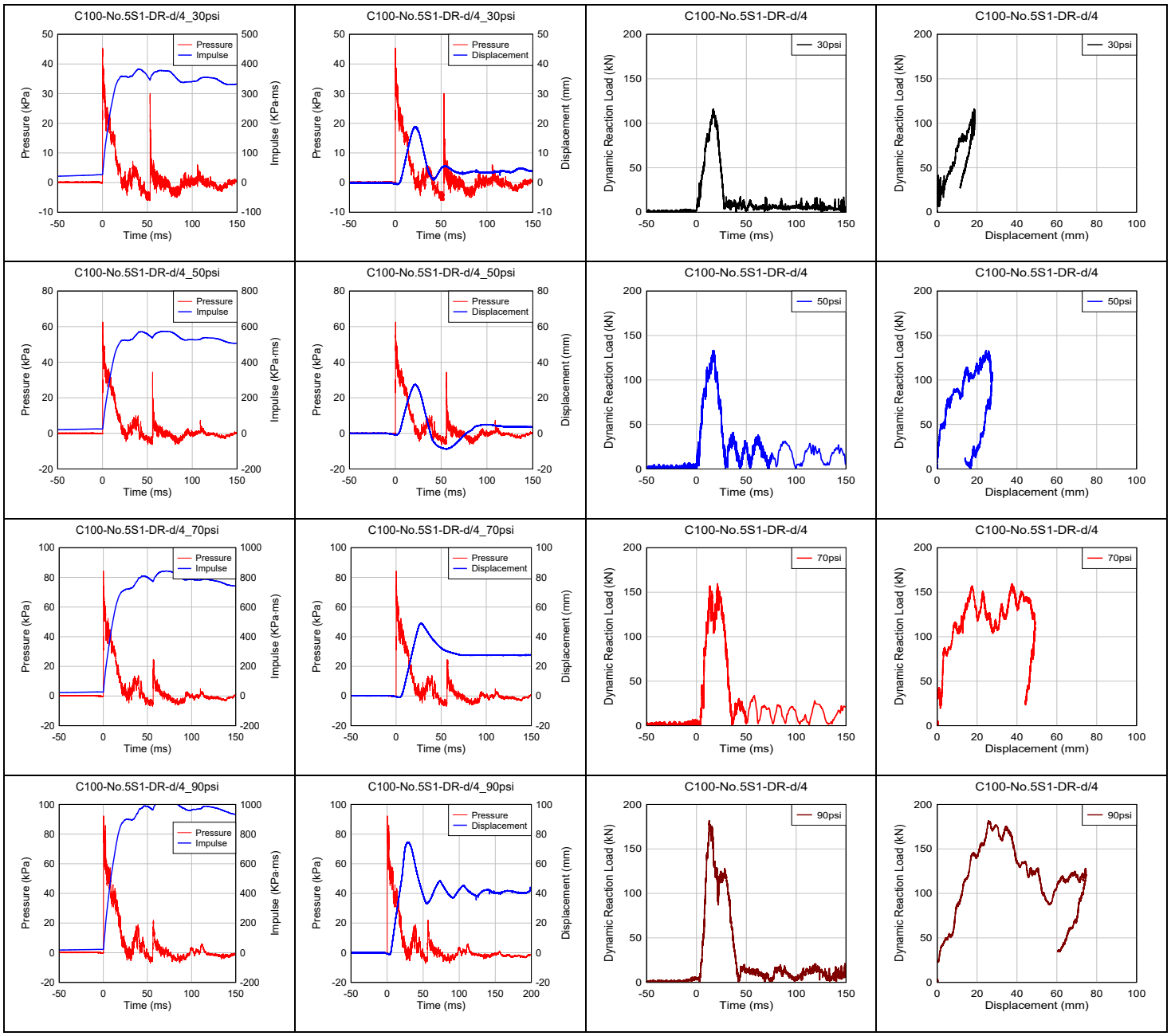

Figure A.84 Blast results for beam C100-No.5S1-DR-d/4.

(pressure/impulse-time, displacement-time, dynamic reaction-time histories and dynamic reaction-displacement response)

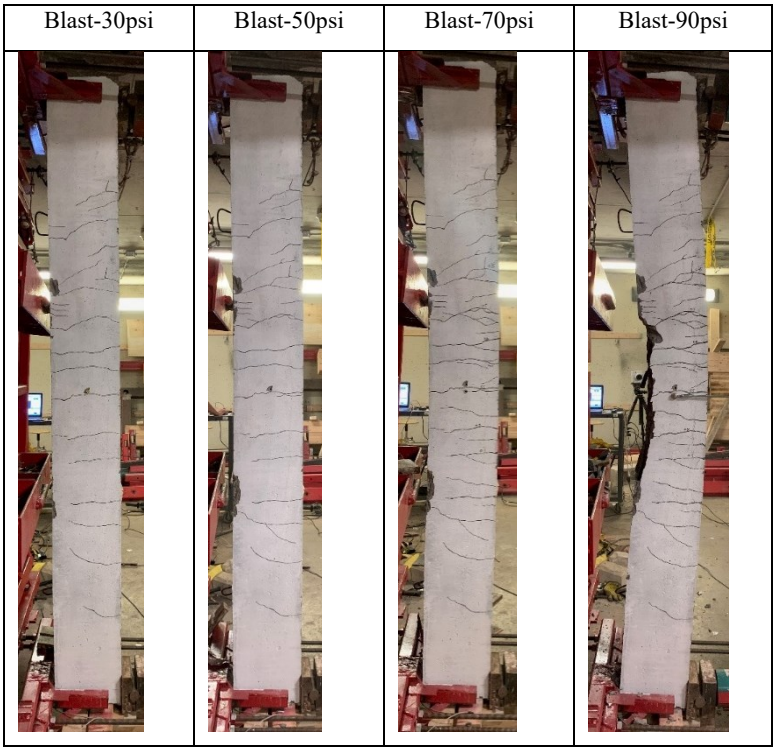

Figure A.85 Blast damage for beam C100-No.5S1-DR-d/4

Table A.38 Residual test result of C100-No.5S1-DR-d/4

Beam	Dynamic loading type	Load		Stiffness		Displacement			Energy-absorption		
		P_{max}^{R} (kN)	RRI	k_s^R (N/mm)	RSI	Δ_{test}^{R} (mm)	Δ_{max}^{R} (mm)	RDI	IEI	REI	TEI
C100-No.5S1-DR-d/4	Repeated	126.9	0.935	5434	0.699	150	225.9	1.506	0.54	0.53	1.07

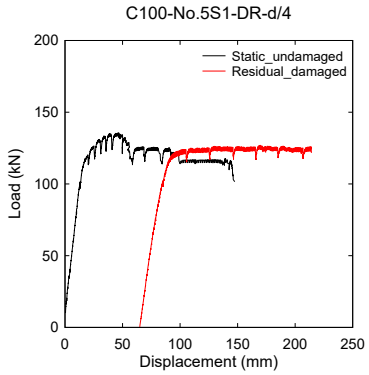

Figure A.86 Post-blast residual results for beam C100-No.5S1-DR-d/4

Figure A.87 Beam C100-No.5S1-DR-d/4 after the post-blast residual static test

A.3.2.7. C100-No.5S1-DR-d/4 [x1]

Beam C100-No.5S1-DR-d/4 [x1] had identical properties to the previous specimen but was tested under single blast load at a driver pressure of 90 psi. **Table A.39** summarizes the blast test results and **Figure A.88** shows the pressure, impulse, displacement and dynamic reaction – time histories. The damage pattern after blast testing is shown in **Figure A.89**.

The beam sustained some moderate flexural cracks (0.95 mm in width) and top cover concrete crushing after the single application of *Blast-90psi*. The maximum and residual displacement were recorded as 62.6 mm and 33.8 mm, respectively, with $\theta_{max} = 3.4°$ (B1-B2: Moderate). The results are similar to the companion beam tested under repeated blasts.

After the dynamic blast test, the beam was tested under static four-point bending to assess its post-blast residual capacity. **Table A.40** summarizes the residual test results. The residual load-deflection response is compared to the undamaged beam response in **Figure A.90** while **Figure A.91** shows photos of the beam after testing. The beam had similar peak residual capacity (P^R_{max} = 140.7 kN) but reduced residual secant stiffness (k^R_s) when compared to the response in the undamaged beam. The test was terminated at a residual displacement (Δ^R_{test}) of 137 mm without bar rupture. The maximum cumulative residual displacement (Δ^R_{max}) was 170.8 mm.

Table A.39 Dynamic test result of C100-No.5S1-DR-d/4 (x1)

Beams	Blast ID (Psi)	Shockwave Properties			Specimen Response					CSA S850 Response limits and Component damage	
		P_r (kPa)	I_r (kPa·ms)	t_d (ms)	D_{max} (mm)	D_{res} (mm)	θ_{max} (°)	$D_{\sum res}$ (mm)	Observed Damage [Max. Crack width]	Response limit	Expected Damage level
C100-No.5S1-DR-d/4 (x1)	90	84.6	851.6	24.6	65.6	33.8	3.4	33.8	Moderate F cracking [0.95]	B1-B2	Moderate

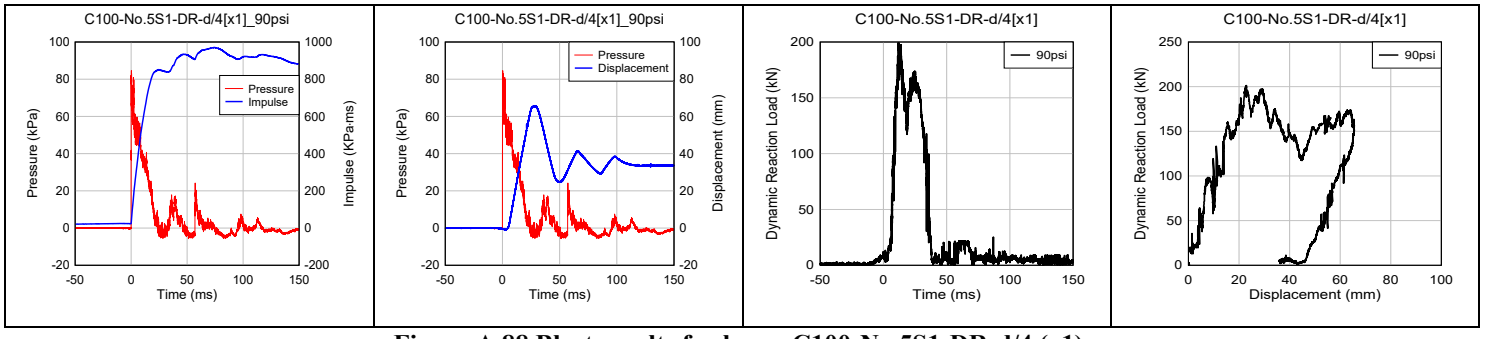

Figure A.88 Blast results for beam C100-No.5S1-DR-d/4 (x1).

(pressure/impulse-time, displacement-time, dynamic reaction-time histories and dynamic reaction-displacement response)

Figure A.89 Blast damage for beam C100-No.5S1-DR-d/4 (x1)

Table A.40 Residual test result of C100-No.5S1-DR-d/4 (x1)

Beam	Dynamic loading type	Load		Stiffness		Displacement			Energy-absorption		
		P_{max}^{R} (kN)	RRI	k_s^R (N/mm)	RSI	Δ_{test}^{R} (mm)	Δ_{max}^{R} (mm)	RDI	IEI	REI	TEI
C100-No.5S1-DR-d/4 (x1)	Single	140.7	1.037	6999	0.901	137	170.8	1.139	0.32	0.77	1.09

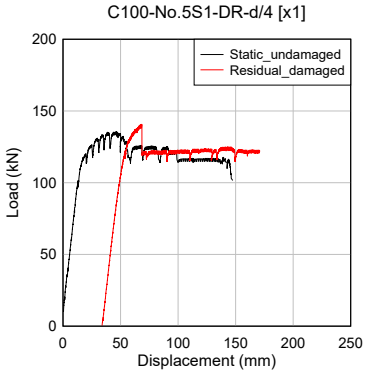

Figure A.90 Post-blast residual results for beam C100-No.5S1-DR-d/4 (x1)

Figure A.91 Beam C100-No.5S1-DR-d/4 (x1) after the post-blast residual static test

A.3.2.8. CF100-No.5S1-DR-d/2

Beam CF100-No.4HS-DR-d/2 was designed with 100 MPa high-strength concrete, 0.75% steel fibers, No.5/No.4 XM-28 stainless steel longitudinal tension/compression bar and intermediate (d/2) tie spacing (s=100 mm). This beam was tested under repeat blasts at P_d = 30 psi, 50 psi, 70 psi and 90 psi. The beam was tested under repeat blast loads at driver pressures (P_d) of 30 psi, 50psi, 70 and 90 psi. **Table A.41** summarizes the blast test results and **Figure A.92** shows the pressure, impulse, displacement and dynamic reaction – time histories. The damage patterns after each blast test are presented in **Figure A.93**.

Blast-30psi was meant to test the beam within the elastic range and caused the formation of hairline cracks along the beam span. Support rotations (θ_{max}) remained below 1° (superficial damage) with maximum (D_{max}) and residual (D_{res}) displacements of 17.1 mm and 3.3 mm. *Blast-50psi* resulted in the formation of a major crack having a width of 0.35 mm in the midspan flexural zone, with further extension of existing cracks. The beam sustained displacements of $D_{max} = 23.8\,mm$, $D_{res} = 4.8\,mm$, with a maximum support rotation of $\theta_{max} = 1.2°$ (B1-B2: moderate damage). *Blast-70psi* led to further cracks with the formation of a 1.5 mm major flexural crack just below the upper loading point, with displacements of D_{max} = 39.2 mm ($\theta_{max} = 2.0°$) and D_{res} = 14.5 mm. The last shot (*Blast-90psi*) resulted in minor concrete crushing and complete fiber pullout with a maximum crack width of 8.0 mm in the midspan zone. The maximum and residual displacement were 59.3 mm and 31.3 mm, with corresponding maximum support rotation θ_{max} of 3.8° (B1-B2: moderate damage).

After dynamic testing, the beam was tested under static four-point bending to assess its post-blast residual capacity. The results from the residual test are summarized in **Table A.42**. The residual load-deflection response is compared to the undamaged beam response in **Figure A.94**, while **Figure A.55** shows a photo of the beam after residual testing. The beam showed a maximum capacity (P_{max}^R = 136.2 kN) which is similar to the post-peak response in the undamaged beam. The beam reached a maximum residual displacement (Δ_{test}^R) of 100 mm without bar rupture. The maximum cumulative residual displacement (Δ_{max}^R) was 153.9 mm.

Table A.41 Dynamic test result of CF100-No.5S1-DR-d/2

Beams	Blast ID (Psi)	Shockwave Properties			Specimen Response					CSA S850 Response limits and Component damage	
		P_r (kPa)	I_r (kPa·ms)	t_d (ms)	D_{max} (mm)	D_{res} (mm)	θ_{max} (°)	$D_{\sum res}$ (mm)	Observed Damage [Max. Crack width]	Response limit	Expected Damage level
CF100-No.5S1-DR-d/2	30	39.8	379.9	21.1	17.1	3.3	0.9	3.3	Minor F cracking	<B1	Superficial
	50	64.7	534.0	21.8	23.8	4.8	1.2	8.2	Minor F cracking [0.35]	B1-B2	Moderate
	70	78.4	713.4	22.1	39.2	14.5	2.0	22.7	Moderate F cracking [1.5]	B1-B2	Moderate
	90	87.2	854.3	23.4	59.3	31.3	3.0	54	Moderate F cracking [8.0]	B1-B2	Moderate

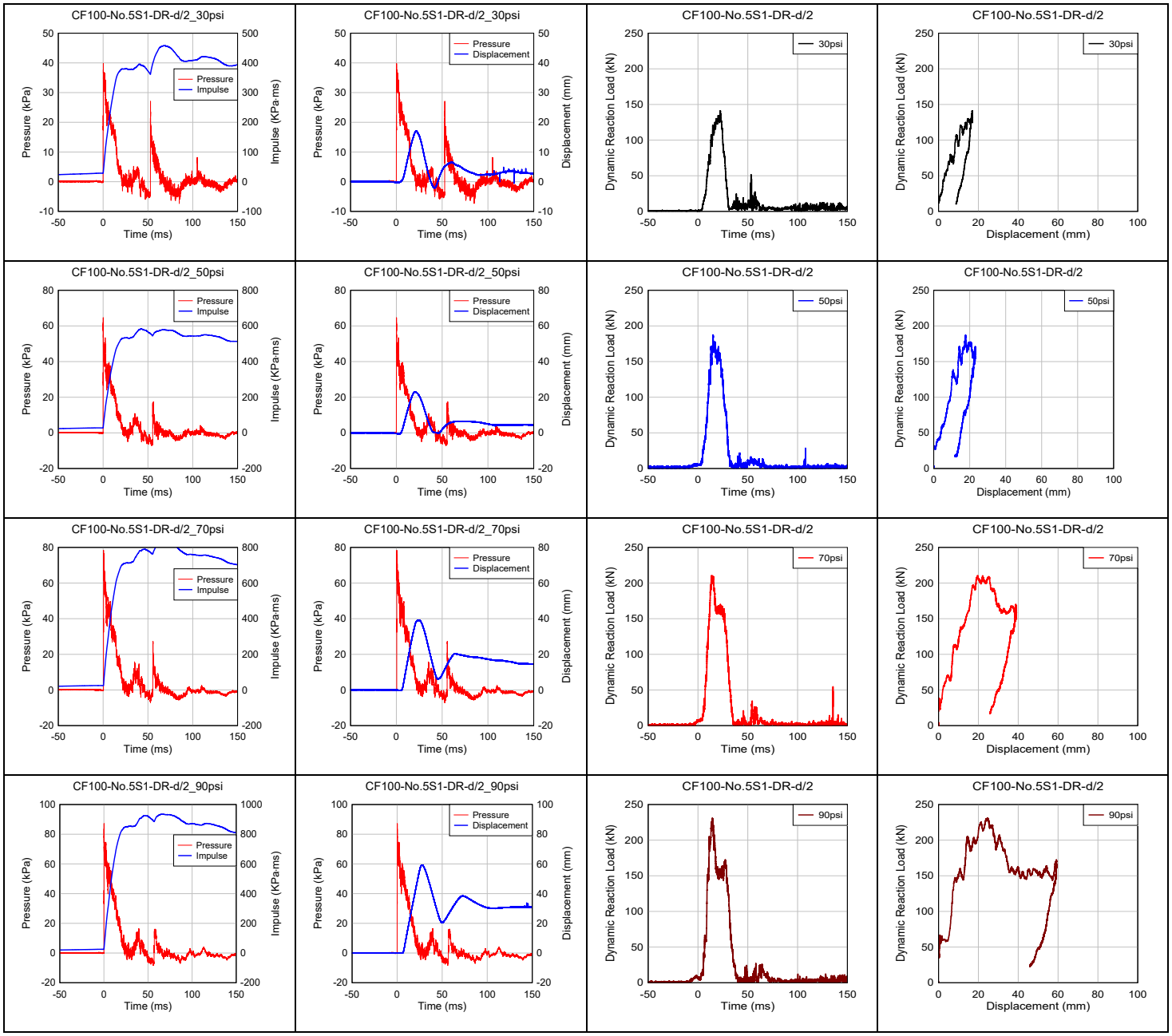

Figure A.92 Blast results for beam CF100-No.5S1-DR-d/2.

(pressure/impulse-time, displacement-time, dynamic reaction-time histories and dynamic reaction-displacement response)

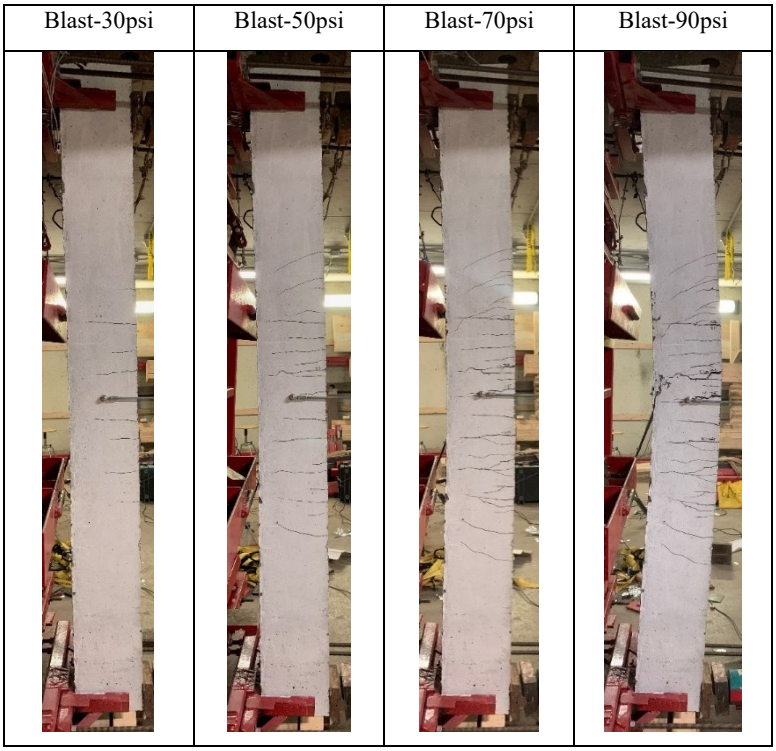

Figure A.93 Blast damage for beam CF100-No.5S1-DR-d/2

Table A.42 Residual test result of CF100-No.5S1-DR-d/2

Beam	Dynamic loading type	Load		Stiffness		Displacement			Energy-absorption		
		P_{max}^{R} (kN)	RRI	k_s^R (N/mm)	RSI	Δ_{test}^{R} (mm)	Δ_{max}^{R} (mm)	RDI	IEI	REI	TEI
CF100-No.5S1-DR-d/2	Repeated	136.2	0.802	7623	0.886	100	153.9	1.026	0.46	0.60	1.05

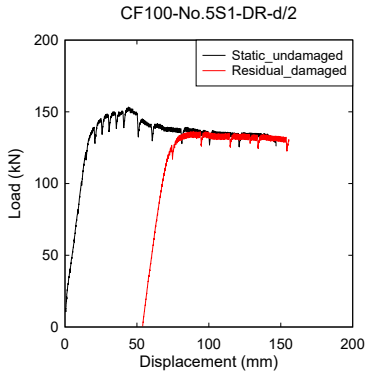

Figure A.94 Post-blast residual results for beam CF100-No.5S1-DR-d/2

Figure A.95 Beam CF100-No.5S1-DR-d/2 after the post-blast residual static test

A.3.2.9. C100-No.5S2-DR-d/4

Beam C100-No.5S1-DR-d/4 was similar in the design to the previous two specimens but had an increased tension steel ratio. Longitudinal reinforcement consisted of No.5/No.4 XM-28 stainless steel bars in tension/compression, with closed ties spaced at d/4 (s=50 mm). This beam was tested under repeat blasts at P_d = 30 psi, 50 psi, 70 psi and 90 psi. **Table A.43** summarizes the blast test results and **Figure A.96** shows the pressure, impulse, displacement and dynamic reaction – time histories. The damage patterns after each blast test are presented in **Figure A.97**.

Blast-30psi was meant to test the beam within the elastic range and caused the formation of hairline cracks along the beam span. Support rotations (θ_{max}) remained below 1° (superficial damage) with maximum (D_{max}) and residual (D_{res}) displacements of 16.9 mm and 4.4 mm. *Blast-50psi* resulted further extension of existing cracks in the midspan. The beam sustained displacements of $D_{max} = 27\ mm$, $D_{res} = 3.6\ mm$, with a maximum support rotation of $\theta_{max} = 1.4°$ (B1-B2: moderate damage). *Blast-70psi* led to further cracks with the formation of a 0.45 mm major flexural crack just below the upper loading point, with displacements of D_{max} = 45.0 mm ($\theta_{max} = 2.3°$) and D_{res} = 13.5 mm. The last shot (*Blast-90psi*) resulted in top cover concrete crushing and moderate flexural cracks in the midspan zone. The maximum and residual displacement were 74.3 mm and 40.1 mm, with corresponding maximum support rotation θ_{max} of 3.8° (B1-B2: moderate damage).

After dynamic testing, the beam was tested under static four-point bending to assess its post-blast residual capacity. The results from the residual test are summarized in **Table A.44**. The residual load-deflection response is compared to the undamaged beam response in **Figure A.98**, while **Figure A.99** shows a photo of the beam after residual testing. The beam showed a maximum capacity (P_{max}^R = 141.5 kN) which is similar to the post-peak response in the undamaged beam. The beam reached a maximum residual displacement (Δ_{test}^R) of 145 mm without bar rupture. The maximum cumulative residual displacement (Δ_{max}^R) was 207.5 mm.

Table A.43 Dynamic test result of C100-No.5S2-DR-d/4

Beams	Blast ID (Psi)	Shockwave Properties			Specimen Response					CSA S850 Response limits and Component damage	
		P_r (kPa)	I_r (kPa·ms)	t_d (ms)	D_{max} (mm)	D_{res} (mm)	θ_{max} (°)	$D_{\sum res}$ (mm)	Observed Damage [Max. Crack width]	Response limit	Expected Damage level
C100-No.5S2-DR-d/4	30	46.2	341.1	20.2	16.9	4.4	0.9	4.4	Minor F cracking [HL]	<B1	Superficial
	50	64.6	523.3	21.2	27.0	3.6	1.4	8	Minor F cracking [HL]	B1-B2	Moderate
	70	74.8	691.8	21.8	45.0	13.5	2.3	21.5	Moderate F cracking [0.45]	B1-B2	Moderate
	90	84.3	897.9	24.0	74.3	40.1	3.8	61.6	Cover crushing & Moderate F cracking	B1-B2	Moderate

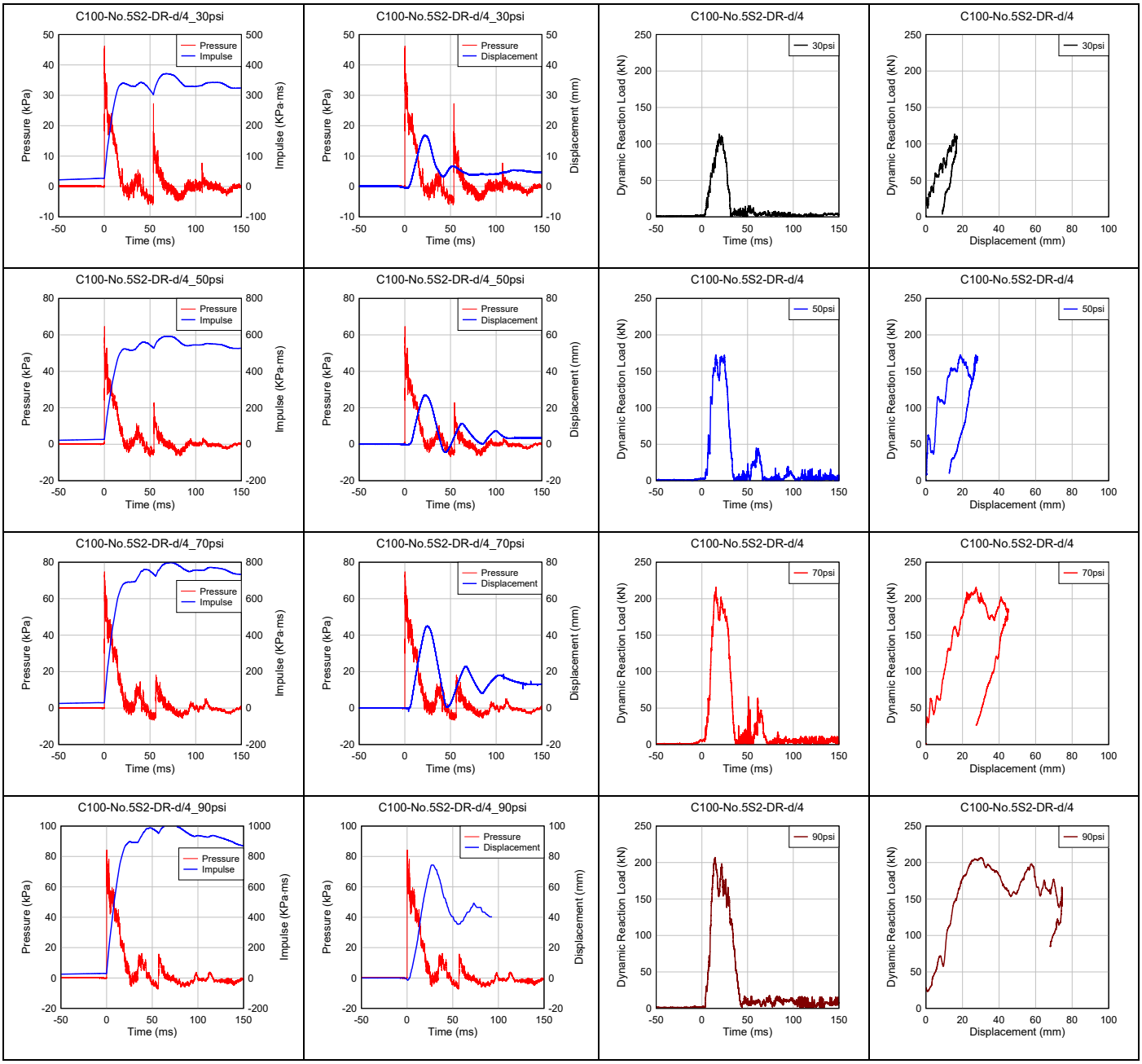

Figure A.96 Blast results for beam C100-No.5S2-DR-d/4.

(pressure/impulse-time, displacement-time, dynamic reaction-time histories and dynamic reaction-displacement response)

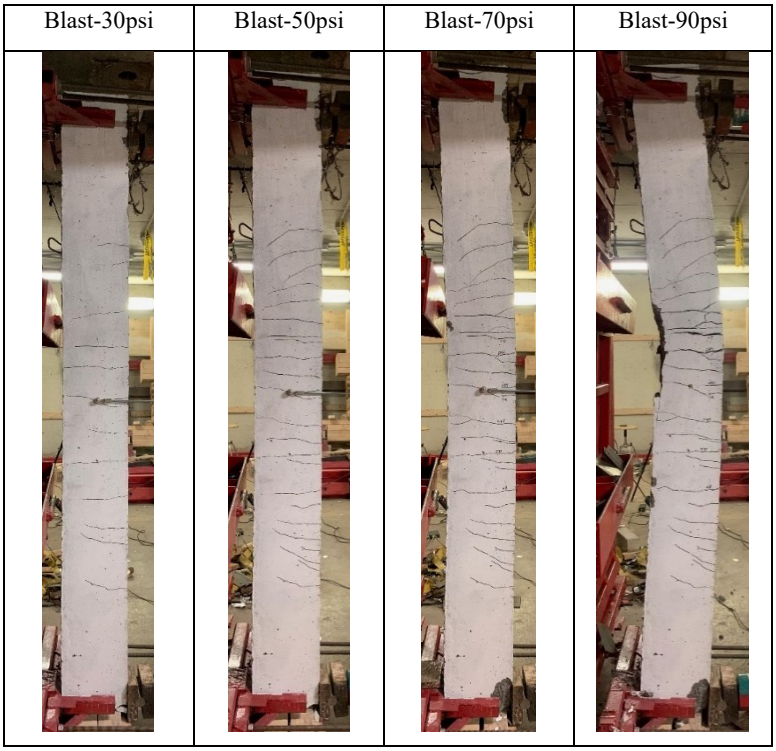

Figure A.97 Blast damage for beam C100-No.5S2-DR-d/4

Table A.44 Residual test result of C100-No.5S2-DR-d/4

Beam	Dynamic loading type	Load		Stiffness		Displacement			Energy-absorption		
		P_{max}^{R} (kN)	RRI	k_s^R (N/mm)	RSI	Δ_{test}^{R} (mm)	Δ_{max}^{R} (mm)	RDI	IEI	REI	TEI
C100-No.5S2-DR-d/4	Repeated	141.5	0.923	4755	0.608	145	207.5	1.383	0.55	0.52	1.07

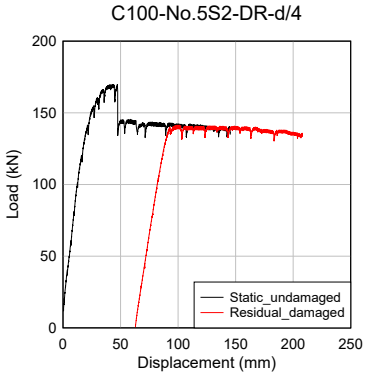

Figure A.98 Post-blast residual results for beam C100-No.5S2-DR-d/4

Figure A.99 Beam C100-No.5S2-DR-d/4 after the post-blast residual static test

A.3.3.Blast and post-blast test results in Series 3 (UHPC)

A.3.3.1. U2-15M-DR-d/2

Beam U2-15M-DR-d/2 was designed with ultra-high performance concrete, 2% steel fiber, 15M/10M normal-strength bars in tension/compression bar, with intermediate ties spaced at d/2 (100 mm). The beam was tested under single blast loads at P_d = 100 psi. **Table A.45** and **Table A.46** summarize the blast and post-blast test results, while **Figure A.100** shows complete reflected pressure, reflected impulse, mid-span displacement and dynamic reaction histories. The damage after blast testing is shown in **Figure A.101.** The results of the residual static test, along with those of the undamaged beam are shown in **Figure A.102** while **Figure A.103** shows photos of the beam after residual static testing.

The beam reached maximum/residual displacements of 64.1/52.5 mm and a maximum rotation (θ_{max}) of 2.8°. According to the CSA S80 standard the damage in the beam is expected to reach moderate levels. The actual damage consisted of two full-depth flexural cracks having widths of 6 mm and 13 mm near the point load locations, with crack localization and fiber pullout. During the post-blast static test, the beam experienced bar rupture during reloading, which indicates that the tension steel was near its rupture strain capacity after the blast test.

Table A.45 Dynamic test result of U2-15M-DR-d/2

Beams	Blast ID (Psi)	Shockwave Properties			Specimen Response					CSA S850 Response limits and Component damage	
		P_r (kPa)	I_r (kPa·ms)	t_d (ms)	D_{max} (mm)	D_{res} (mm)	θ_{max} (°)	$D_{\Sigma res}$ (mm)	Observed Damage [Max. Crack width]	Response limit	Expected Damage level
U2-15M-DR-d/2	100	104.0	978.5	23.1	64.1	52.5	3.3	52.5	Fiber pullout [13 mm]	B1-B2	Moderate

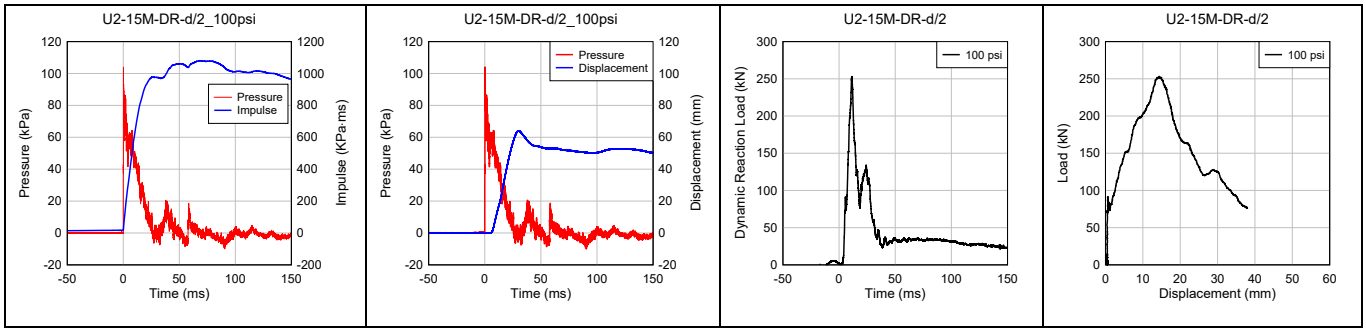

Figure A.100 Blast results for beam U2-15M-DR-d/2

(pressure/impulse-time; displacement-time; dynamic reaction-time history; dynamic reaction-displacement response)

Blast-100psi	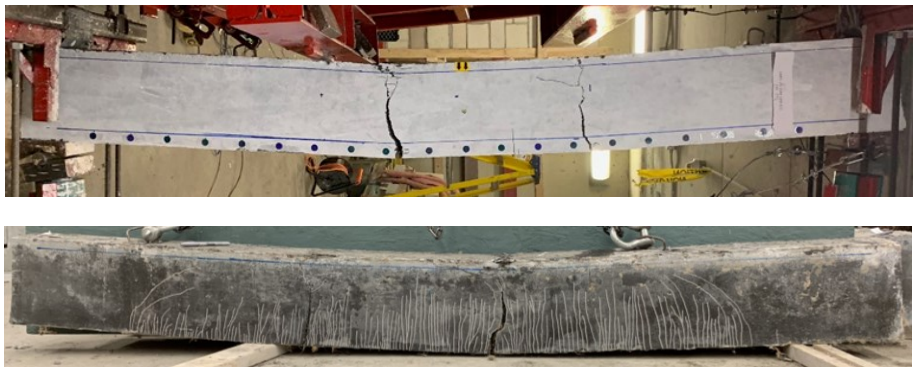

Figure A.101 Blast damage for beam U2-15M-DR-d/2

Table A.46 Residual test result of U2-15M-DR-d/2

Beam	Dynamic loading type	Load		Stiffness		Displacement			Energy-absorption		
		P_{max}^{R} (kN)	RRI	k_s^R (N/mm)	RSI	Δ_{test}^{R} (mm)	Δ_{max}^{R} (mm)	RDI	IEI	REI	TEI
U2-15M-DR-d/2	Single	125.9	69%	13597	96%	9.3	61.8	-	-	-	-

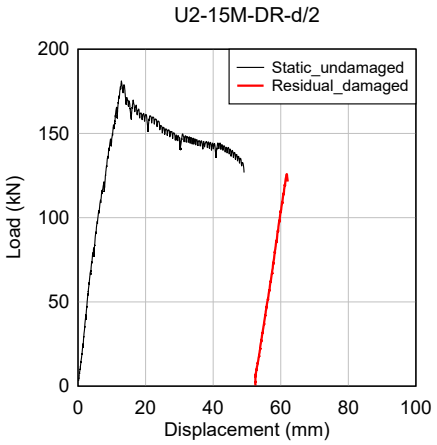

Figure A.102 Post-blast residual results for beam U2-15M-DR-d/2

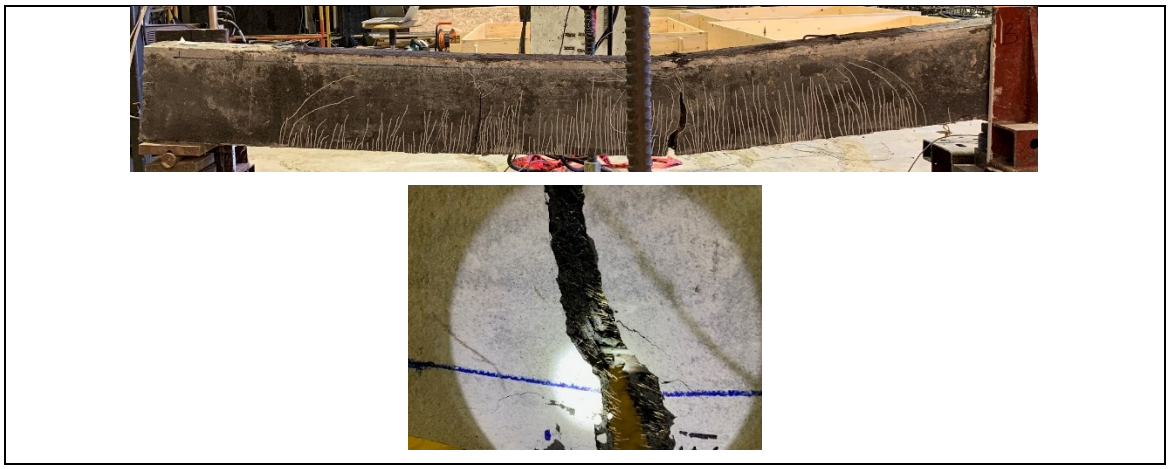

Figure A.103 Failure mode after the post-blast residual static test

A.3.3.2. U2-20M-DR-d/2

Beam U2-20M-DR-d/2 was designed with ultra-high performance concrete, 2% steel fibers, 20M/10M normal-strength bars in tension/compression and intermediate ties spaced at d/2 (100 mm). Thus the beam had an increased tension steel ratio when compared to the previous specimen. The beam was tested under single blast load at P_d =100 psi. **Table A.47** and **Table A.48** summarize the blast and post-blast test results and **Figure A.104** shows the pressure, impulse, displacement and dynamic reaction histories. The damage after the blast test is shown in **Figure A.105**. The results of the residual static test are shown in **Figure A.106** and **Figure A.107**.

The single application of *blast-100 psi* resulted in maximum and residual displacements were 48.3 mm and 26.8 mm, with a maximum support rotation (θ_{max}) of 2.5°. According to the CSA S80 standard the damage in the beam is expected to reach "moderate" levels. The actual damage consisted of crack localization near the point load location with a full depth crack having a width of 15 mm. Fiber pullout was observed at this location while all remaining cracks remained well controlled.

The beam still had significant post-blast residual capacity during the post-blast test. The beam had a peak residual strength (P^R_{max}) of 205.9 kN and secant stiffness of 14190 N/mm, which are similar to the results from the undamaged beam test (RRI = 99% and RSI = 100%). The beam failed in bar rupture at a residual displacement (Δ^R_{test}) of 86.7 mm.

Table A.47 Dynamic test result of U2-20M-DR-d/2

Beams	Blast ID (Psi)	Shockwave Properties			Specimen Response					CSA S850 Response limits and Component damage	
		P_r (kPa)	I_r (kPa·ms)	t_d (ms)	D_{max} (mm)	D_{res} (mm)	θ_{max} (°)	$D_{\Sigma res}$ (mm)	Observed Damage [Max. Crack width]	Response limit	Expected Damage level
U2-20M-DR-d/2	100	94.3	994.5	22.4	48.3	26.8	2.5	26.8	Fiber pullout [15 mm]	B1-B2	Moderate

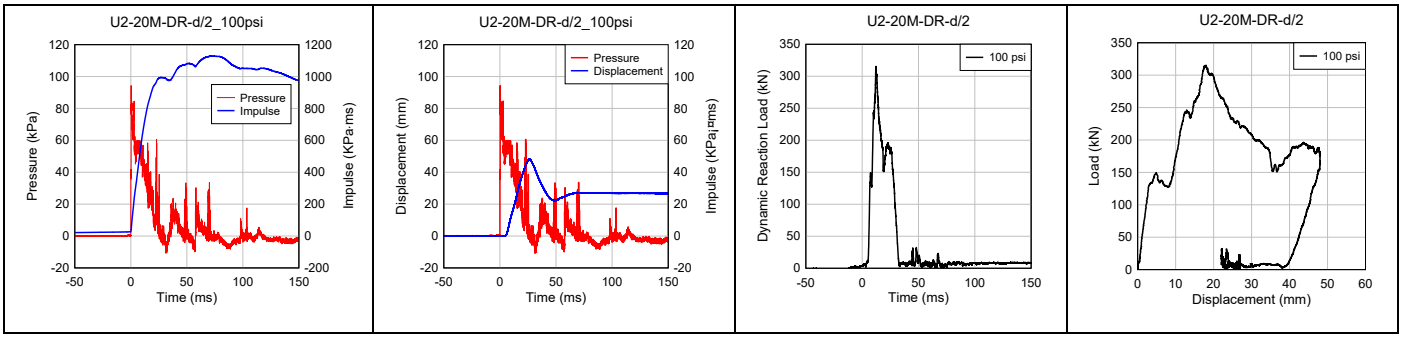

Figure A.104 Blast results for beam U2-20M-DR-d/2

(pressure/impulse-time; displacement-time; dynamic reaction-time history; dynamic reaction-displacement response)

Blast-100psi	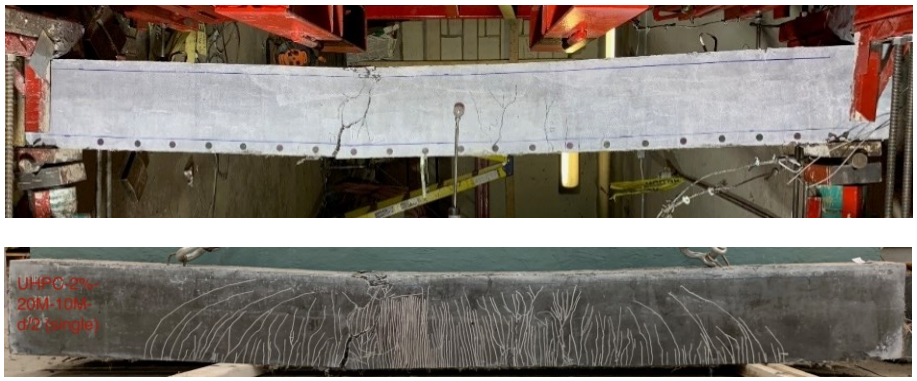

Figure A.105 Blast damage for beam U2-20M-DR-d/2

Table A.48 Residual test result of U2-20M-DR-d/2

Beam	Dynamic loading type	Load		Stiffness		Displacement			Energy-absorption		
		P_{max}^{R} (kN)	RRI	k_s^R (N/mm)	RSI	Δ_{test}^{R} (mm)	Δ_{max}^{R} (mm)	RDI	IEI	REI	TEI
U2-20M-DR-d/2	Single	205.9	99%	14190	100%	86.7	113.5	139%	0.395	0.627	1.023

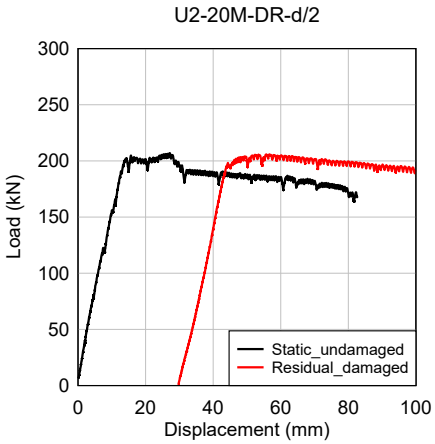

Figure A.106 Post-blast residual results for beam U2-20M-DR-d/2

Figure A.107 Failure mode after the post-blast residual static test

A.3.3.3. U2-20M-DR-d/2 (R)

Beam U2-20M-DR-d/2 (R) was identical to the previous beam but was tested under repeated blasts at P_d = 30 psi, 70 psi and 100 psi. **Table A.49** and **Table A.50** summarize the blast and post-blast test results, while **Figure A.108** shows complete pressure, impulse, displacement and dynamic reaction histories. The damage after blast testing is shown in **Figure A.109.** The results of the residual static test are shown in **Figure A.110** and **Figure A.111**.

Blast-30psi resulted in the formation of hairline cracks in the flexural zone with displacements of D_{max} = 8.4 mm and D_{res} = 0.6 mm. *Blast-70psi* resulted in further hairline cracks, with maximum and residual displacements of 21.5 mm and 1.2 mm. The maximum support rotations remained below 1° during both shots. The last shot (*Blast-90psi*) resulted in crack localization with one major crack in the mid-span having a width of 11 mm. The maximum and residual displacements were 46.3 mm and 26.8 mm, with corresponding maximum support rotation (θ_{max}) of 2.4°.

During the post-blast residual static test, the maximum capacity ($P_{max}^{R} = 187.2\ kN$) of the blast-damaged beam was 90% when compared to post-peak strength of the undamaged beam, while the residual stiffness (k_s^R) was similar to that of the undamaged beam (RSI = 97%). Eventually, the beam failed in bar rupture at a maximum residual displacement (Δ_{test}^{R}) of 61.9 mm with a cumulative displacement (Δ_{max}^{R}) of 90.5 mm.

Table A.49 Dynamic test result of U2-20M-DR-d/2 (R)

Beams	Blast ID (Psi)	Shockwave Properties			Specimen Response					CSA S850 Response limits and Component damage	
		P_r (kPa)	I_r (kPa·ms)	t_d (ms)	D_{max} (mm)	D_{res} (mm)	θ_{max} (°)	$D_{\sum res}$ (mm)	Observed Damage [Max. Crack width]	Response limit	Expected Damage level
U2-20M-DR-d/2 (R)	30	42.4	346.1	20.2	8.4	0.6	0.4	0.6	Minor F cracking [HL]	<B1	Superficial
	70	83.4	708.9	21.8	21.5	1.2	1.0	1.8	Minor F cracking [HL]	<B1	Superficial
	100	104	996.1	24.4	46.3	26.8	2.4	28.6	Crack localization & fiber pullout [11 mm]	B1-B2	Moderate

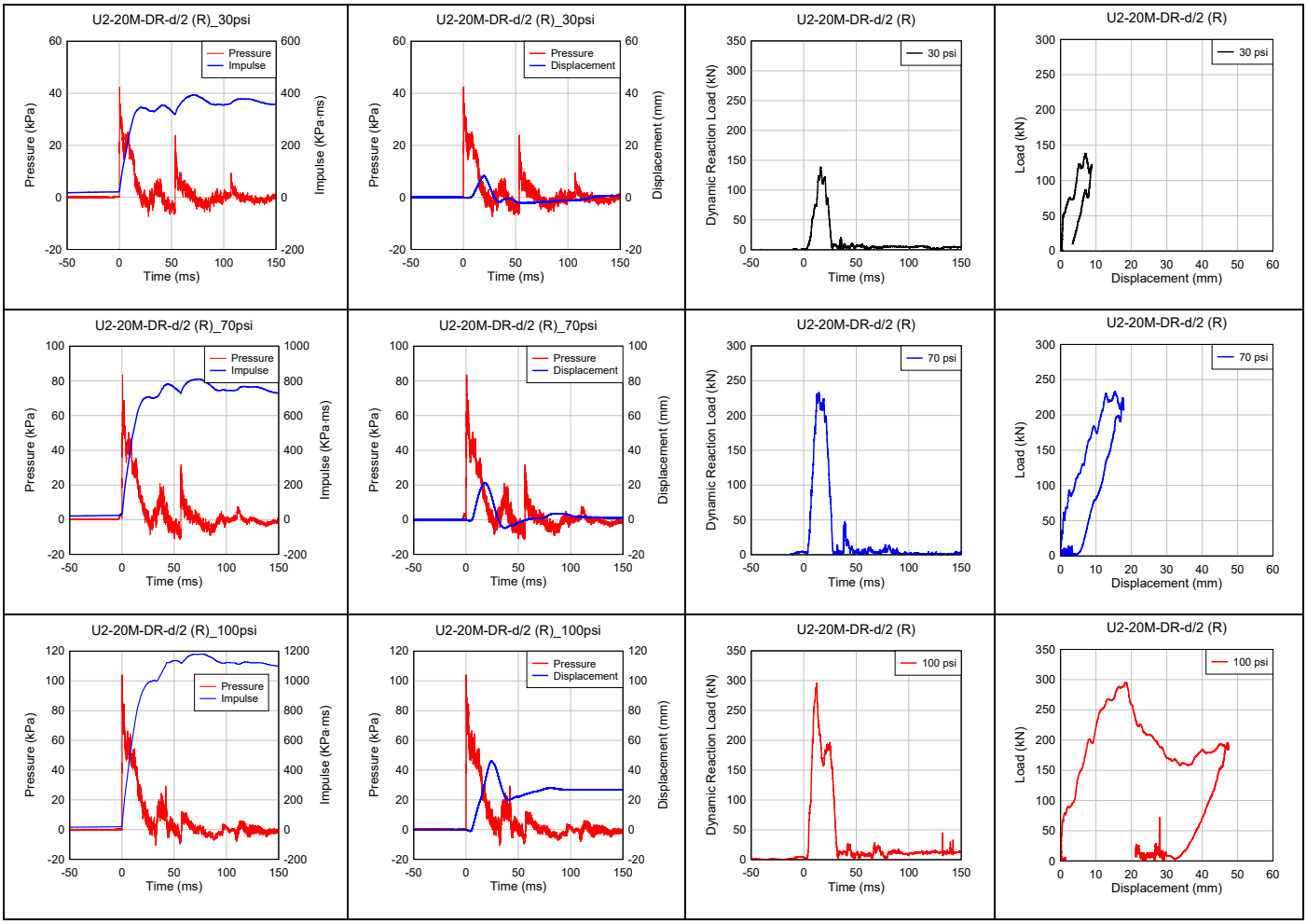

Figure A.108 Blast results for beam U2-20M-DR-d/2(R)

(pressure/impulse-time; displacement-time; dynamic reaction-time history; dynamic reaction-displacement response)

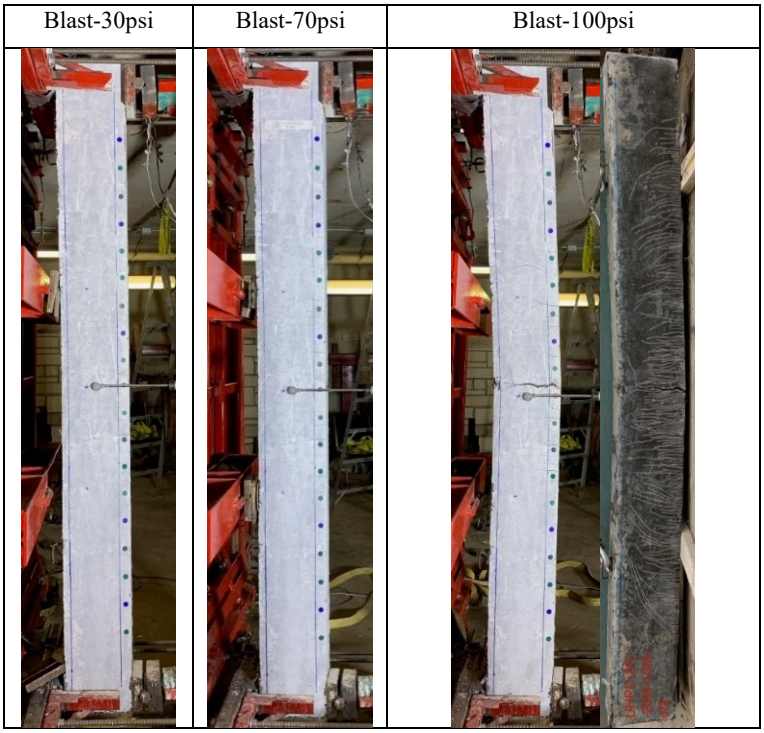

Figure A.109 Blast damage for beam U2-20M-DR-d/2(R)

Table A.50 Residual test result of U2-20M-DR-d/2 (R)

Beam	Dynamic loading type	Load		Stiffness		Displacement			Energy-absorption		
		P_{max}^{R} (kN)	RRI	k_s^R (N/mm)	RSI	Δ_{test}^{R} (mm)	Δ_{max}^{R} (mm)	RDI	IEI	REI	TEI
U2-20M-DR-d/2 (R)	Repeated	187.2	90%	13785	97%	61.9	90.5	117%	0.409	0.604	1.013

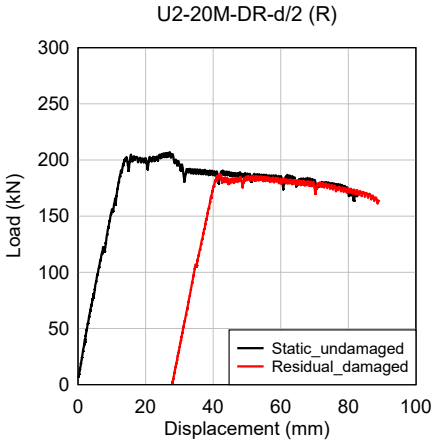

Figure A.110 Post-blast residual results for beam U2-20M-DR-d/2(R)

Figure A.111 Failure mode after the post-blast residual static test

A.3.3.4. U3-15M

Beam U3-15M was designed with ultra-high performance concrete, 3% steel fibers, 2-15M normal-strength steel bars in tension, but did not have any top (compression) bars or stirrups. **Table A.51** summarizes the blast test results and **Figure A.112** shows the reflected pressure, reflected impulse, mid-span displacement and dynamic reaction histories at P_d = 100 psi. The damage patterns after the blast test are presented in **Figure A.113**.

Blast-100psi resulted in bar rupture failure. Owing to the lack of compression reinforcement, the beam completely broke into two parts. The beam damage was hazardous, which corresponds to the damage state predicted by the CSA S850 standard.

No post-blast residual test was performed.

Table A.51 Dynamic test result of U3-15M

Beams	Blast ID (Psi)	Shockwave Properties			Specimen Response					CSA S850 Response limits and Component damage	
		P_r (kPa)	I_r (kPa·ms)	t_d (ms)	D_{max} (mm)	D_{res} (mm)	θ_{max} (°)	$D_{\Sigma res}$ (mm)	Observed Damage [Max. Crack width]	Response limit	Expected Damage level
U3-15M	100	107.7	1001.4	23.8	-	-	-	-	Bar rupture	> B4	Hazardous

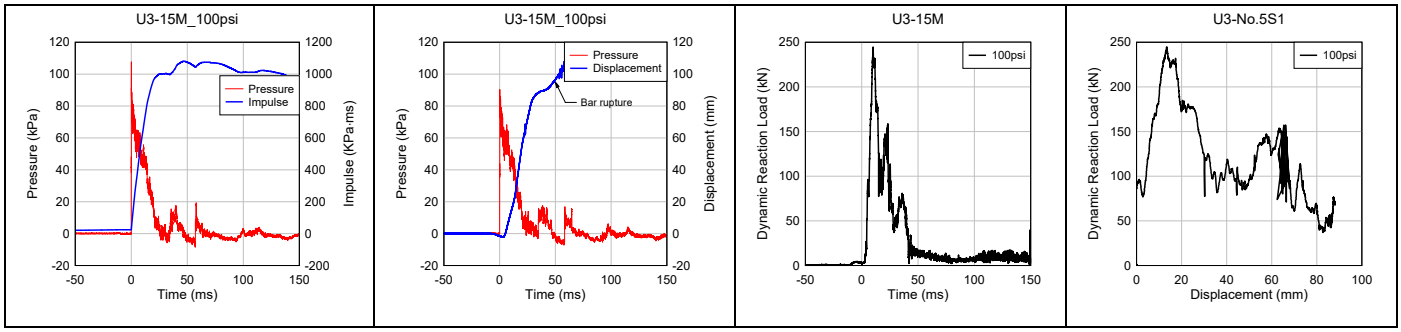

Figure A.112 Blast results for beam U3-15M

(pressure/impulse-time; displacement-time; dynamic reaction-time history; dynamic reaction-displacement response)

Blast-100psi

Figure A.113 Blast damage for beam U3-15M

A.3.3.5. U1-No.5HS-DR-d/4

Beam U1-No.5HS-DR-d/4 was designed with ultra-high performance concrete, 1% steel fibers, No.5/No.4 high-strength longitudinal tension/compression bar and closed ties spaced at d/4 (50 mm), which matches the stringent requirement in the CSA S850 standard. **Table A.52** and **Table A.53** summarize the blast and post-blast test results and **Figure A.114** shows complete pressure, impulse, displacement and dynamic reaction histories from the blast test (single shot at 100 psi). The damage after the blast is shown in **Figure A.115**. The results from the residual static test are shown in **Figure A.116** and **Figure A.117**.

Blast-100psi (which corresponds to the maximum available driver pressure) only resulted in maximum and residual displacements of 38.1 mm and 10.9 mm, with a maximum rotation (θ_{max}) of 2.0°. The CSA S850 standard predicts moderate damage, however the actual damage was minor with a maximum crack width of 0.8 mm.

The post-blast residual test demonstrates that the beam still had significant residual capacity even after the intense blast. The beam had a peak residual capacity (P_{max}^{R}) of 276.7 kN and secant stiffness of 10677 N/mm. The beam finally failed in bar rupture at a maximum residual displacement (Δ_{test}^{R}) of 60 mm with a cumulative displacement (Δ_{max}^{R}) of 70.9 mm.

Table A.52 Dynamic test result of U1-No.5HS-DR-d/4

Beams	Blast ID (Psi)	Shockwave Properties			Specimen Response					CSA S850 Response limits and Component damage	
		P_r (kPa)	I_r (kPa·ms)	t_d (ms)	D_{max} (mm)	D_{res} (mm)	θ_{max} (°)	$D_{\Sigma res}$ (mm)	Observed Damage [Max. Crack width]	Response limit	Expected Damage level
U1-No.5HS-DR-d/4	100	96	941.0	22.1	38.1	10.9	2.0	10.9	Moderate F cracking [0.8 mm]	B1-B2	Moderate

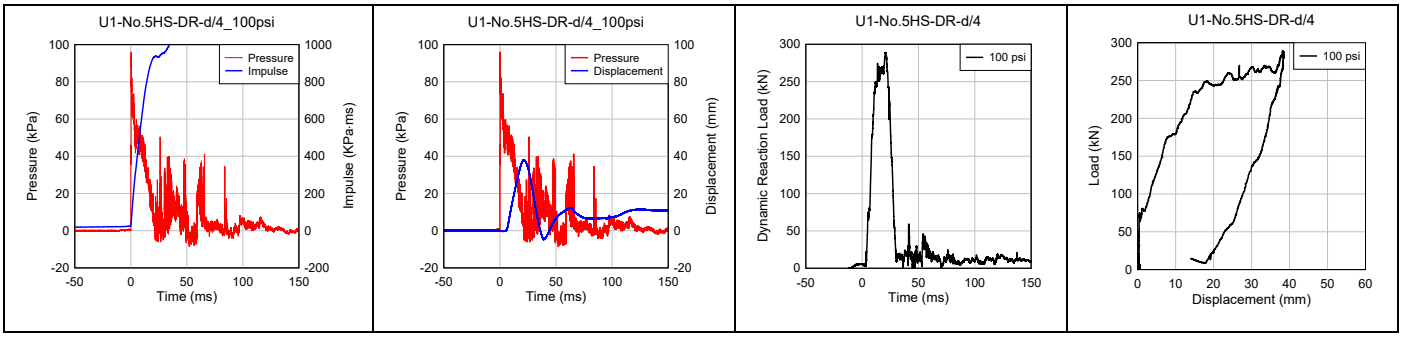

Figure A.114 Blast results for beam U1-No.5HS-DR-d/4

(pressure/impulse-time; displacement-time; dynamic reaction-time history; dynamic reaction-displacement response)

Blast-100psi	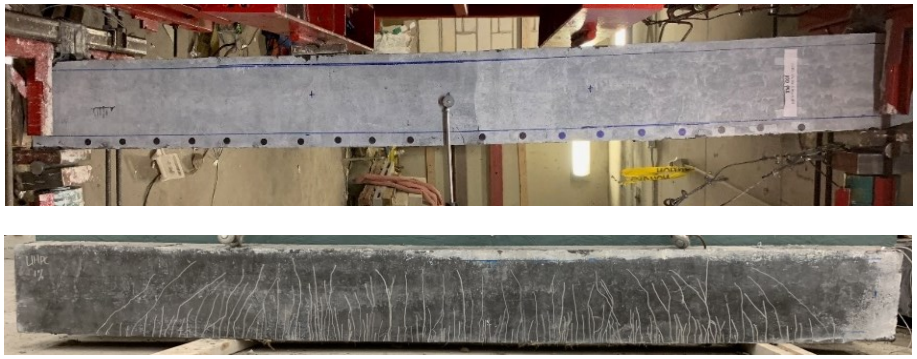

Figure A.115 Blast damage for beam U1-No.5HS-DR-d/4

Table A.53 Residual test result of U1-No.5HS-DR-d/4

Beam	Dynamic loading type	Load		Stiffness		Displacement			Energy-absorption		
		P_{max}^{R} (kN)	RRI	k_s^R (N/mm)	RSI	Δ_{test}^{R} (mm)	Δ_{max}^{R} (mm)	RDI	IEI	REI	TEI
U1-No.5HS-DR-d/4	Single	276.7	-	10677	-	60	70.9	-	-	-	-

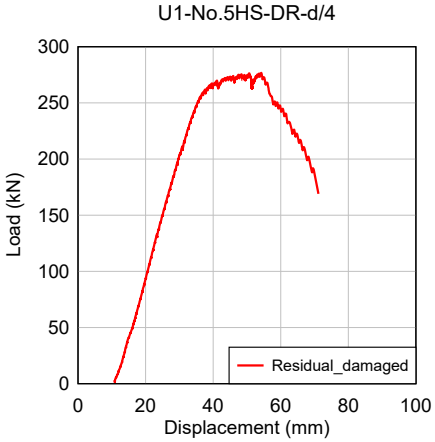

Figure A.116 Post-blast residual results for beam U1-No.5HS-DR-d/4

Figure A.117 Failure mode after the post-blast residual static test

A.3.3.6. U2-No.4HS-DR-d/2 (R)

Beam U2-No.4HS-DR-d/2 was designed with ultra-high performance concrete, 2% steel fibers, No.4/No.3 high-strength tension/compression bars and intermediate ties spaced at d/2 (100 mm). The beam was tested under repeat blast loads at driver pressures (P_d) of 30 psi, 50 psi, 70 psi and 100 psi. **Table A.54** summarizes the blast test results and **Figure A.118** shows the pressure, impulse, displacement and dynamic reaction – time histories. The damage patterns after each blast test are presented in **Figure A.119**.

Blast-30psi was meant to test the beam within the elastic range and caused the formation of hairline cracks along the beam span. Support rotations (θ_{max}) remained below 1° with maximum (D_{max}) and residual (D_{res}) displacements of 11.3 mm and 3.0 mm. *Blast-50psi* caused further hairline cracks in the mid-span zone, with displacements D_{max} = 19.8 mm and D_{res} = 2.5 mm, and a support rotation, θ_{max} = 1.0°. *Blast-70psi* resulted in the formation of a major crack having a width of 0.8 mm in the midspan flexural zone, with further extension of existing cracks. The beam sustained displacements of $D_{max} = 31.2\ mm$, $D_{res} = 9.0\ mm$, with a maximum support rotation of $\theta_{max} = 1.6°$. During the last shot (*Blast-100psi*), the beam failed by rupture of the high-strength bars.

Table A.54 Dynamic test result of U2-No.4HS-DR-d/2 (R)

Beams	Blast ID (Psi)	Shockwave Properties			Specimen Response					CSA S850 Response limits and Component damage	
		P_r (kPa)	I_r (kPa·ms)	t_d (ms)	d_{max} (mm)	d_{res} (mm)	θ_{max} (°)	$d_{\Sigma res}$ (mm)	Observed Damage [Max. Crack width]	Response limit	Expected Damage level
U2-No.4HS-DR-d/2 (R)	30	50.2	393.3	20.6	11.3	3.0	0.6	3.0	Minor F cracking [HL]	<B1	Superficial
	50	62.3	557.9	22.0	19.8	2.5	1.0	5.5	Minor F cracking [HL]	<B1	Superficial
	70	87.4	728.4	22.5	31.2	9.0	1.6	14.5	Crack Localization [0.8]	B1-B2	Moderate
	100	98.6	970.2	24.3	42.8	-	-	-	Bar rupture	> B4	Hazardous

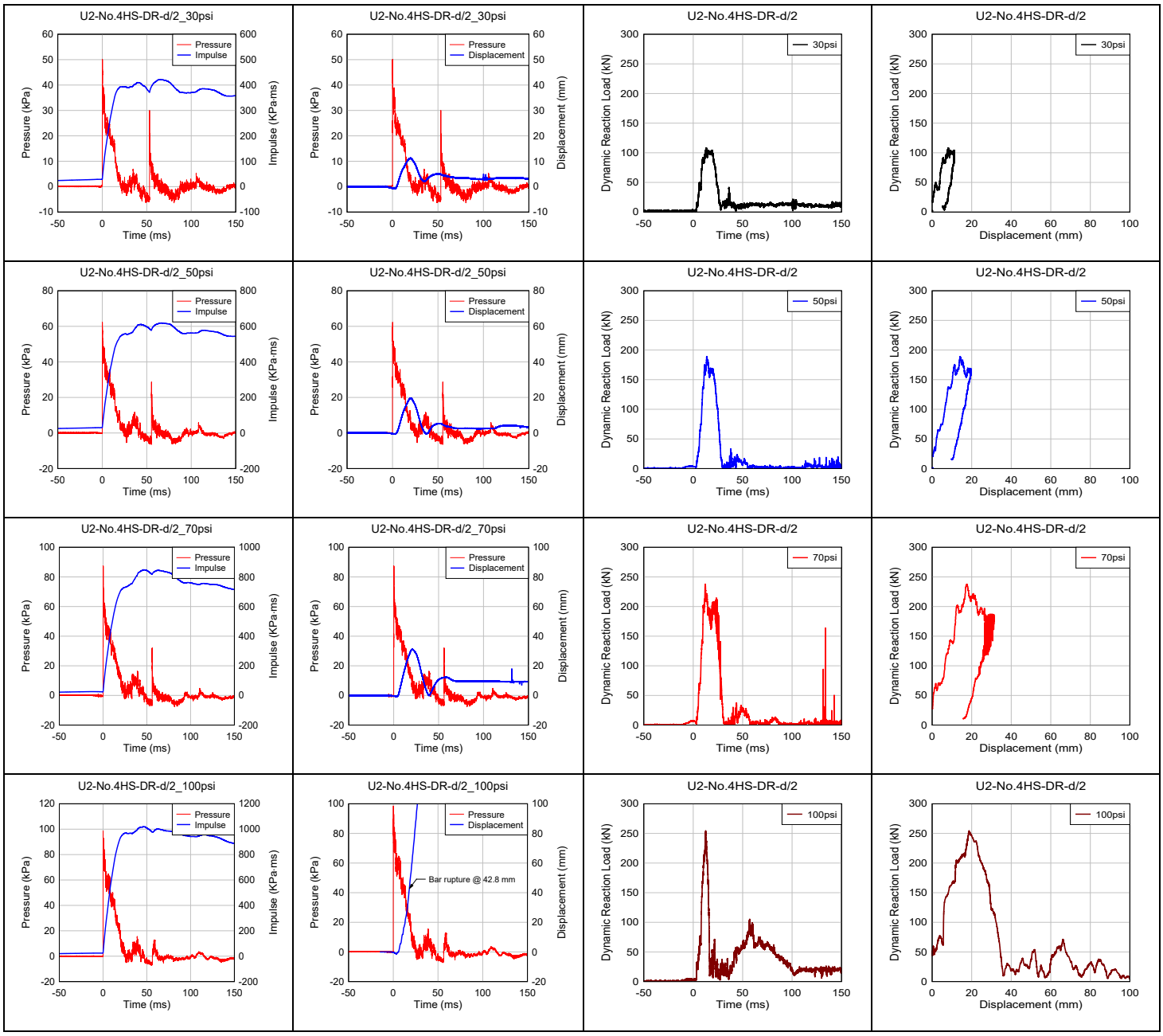

Figure A.118 Blast results for beam U2-No.4HS-DR-d/2 (R).

(pressure/impulse-time; displacement-time; dynamic reaction-time history; dynamic reaction-displacement response)

Blast-30psi	Blast-50psi	Blast-70psi	Blast-100psi
		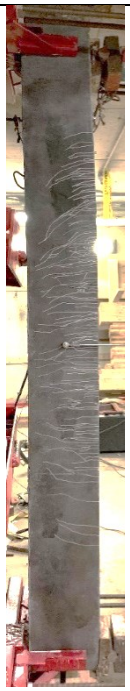	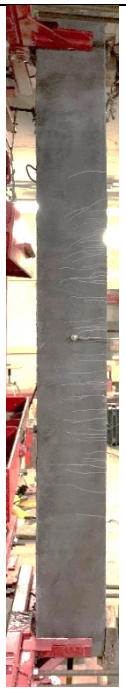

Figure A.119 Blast damage for beam U2-No.4HS-DR-d/2 (R)

A.3.3.7. U2-No.5HS-DR-d/2

Beam U2-No.5HS-DR-d/2 was designed with ultra-high performance concrete, 2% steel fibers, No.5/No.4 high-strength tension/compression bars and intermediate ties spaced at d/2 (100 mm). **Table A.55** and **Table A.56** summarize the blast and post-blast test results and **Figure A.120** shows complete reflected pressure, reflected impulse, mid-span displacement and dynamic reaction histories after the 100 psi shot. The damage patterns after the blast test are shown in **Figure A.121**. The results from the residual static test, along with those of the original undamaged beam are shown in **Figure A.122**, while **Figure A.123** shows photos of the beam after residual testing.

Blast-100psi resulted in the formation of a major crack width of 1.5 mm at the beam mid-span, with maximum and residual displacements of 35.9 mm and 11.1 mm, and a maximum support rotation (θ_{max}) of 1.8°. Beam damage was moderate, which matches the damage level predicted by the CSA S850 standard.

The post-blast residual test shows that the beam still had significant residual capacity after blast testing. The beam had a peak residual capacity (P_{max}^{R}) of 293.5 kN and stiffness (k_s^R) of 12483 N/mm, which are similar to those of the undamaged beam (RRI = 102% and RSI = 99%). The beam finally failed in bar rupture at a maximum residual displacement (Δ_{test}^{R}) of 52.8 mm with a cumulative displacement (Δ_{max}^{R}) of 63.9 mm

Table A.55 Dynamic test result of U2-No.5HS-DR-d/2

Beams	Blast ID (Psi)	Shockwave Properties			Specimen Response					CSA S850 Response limits and Component damage	
		P_r (kPa)	I_r (kPa·ms)	t_d (ms)	D_{max} (mm)	D_{res} (mm)	θ_{max} (°)	$D_{\Sigma res}$ (mm)	Observed Damage [Max. Crack width]	Response limit	Expected Damage level
U2-No.5HS-DR-d/2	100	106	981.0	22.5	35.9	11.1	1.8	11.1	Moderate F cracking [1.5 mm]	B1-B2	Moderate

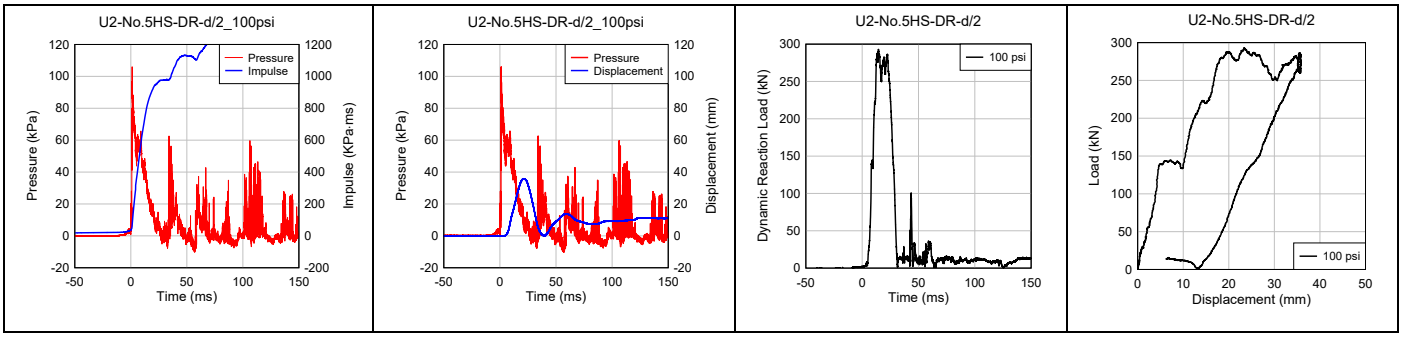

Figure A.120 Blast results for beam U2-No.5HS-DR-d/2

(pressure/impulse-time; displacement-time; dynamic reaction-time history; dynamic reaction-displacement response)

Blast-100psi	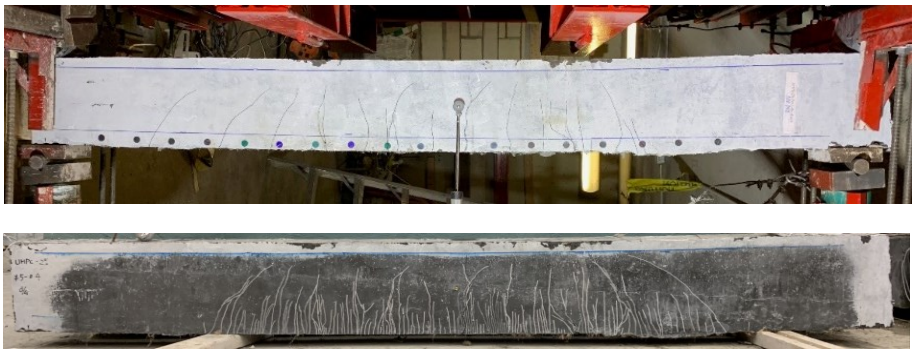

Figure A.121 Blast damage for beam U2-No.5HS-DR-d/2

Table A.56 Residual test result of U2-No.5HS-DR-d/2

Beam	Dynamic loading type	Load		Stiffness		Displacement			Energy-absorption		
		P_{max}^{R} (kN)	RRI	k_s^R (N/mm)	RSI	Δ_{test}^{R} (mm)	Δ_{max}^{R} (mm)	RDI	IEI	REI	TEI
U2-No.5HS-DR-d/2	Single	293.5	102%	12483	99%	52.8	63.9	116%	0.247	0.762	1.008

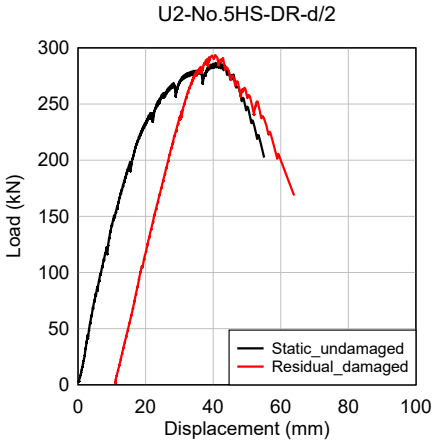

Figure A.122 Post-blast residual results for beam U2-No.5HS-DR-d/2

Figure A.123 Failure mode after the post-blast residual static test

A.3.3.8. U3-No.5HS

Beam U3-No.5HS was designed with ultra-high performance concrete, 3% steel fibers, 2-No.5 high-strength bars in tension, but did not have any top (compression) bars or stirrups. **Table A.57** and **Table A.58** summarize the blast and post-blast test results and **Figure A.124** shows the pressure, impulse, displacement and dynamic reaction histories at P_d = 100 psi. The damage patterns after the blast test are presented in **Figure A.125**. The results from the residual static test are shown in **Figure A.126** and **Figure A.127**.

Similar to the previous beam, *Blast-100psi* only resulted in minor damage with the formation of one major crack with a width of 2 mm. The maximum and residual displacements were 34.9 mm and 7.0 mm, with a maximum rotation (θ_{max}) of 1.8°. The beam damage was moderate, which corresponds to the damage state predicted by the CSA S850 standard.

The post-blast residual static test shows that the beam still had significant post-blast residual capacity. The beam had a peak residual capacity (P_{max}^R) of 291.2 kN and stiffness (k_s^R) of 14271 N/mm, which are similar to those of the undamaged beam (RRI = 104% and RSI = 94%). The beam finally failed in bar rupture at a maximum residual displacement (Δ_{test}^R) of 48.4 mm with a cumulative displacement (Δ_{max}^R) of 55.4 mm. Due to the lack of top bars the beam completely collapsed at failure.

Table A.57 Dynamic test result of U3-No.5HS

Beams	Blast ID (Psi)	Shockwave Properties			Specimen Response					CSA S850 Response limits and Component damage	
		P_r (kPa)	I_r (kPa·ms)	t_d (ms)	D_{max} (mm)	D_{res} (mm)	θ_{max} (°)	$D_{\Sigma res}$ (mm)	Observed Damage [Max. Crack width]	Response limit	Expected Damage level
U3-No.5HS	100	93.8	968.1	22.2	34.9	7.0	1.8	7.0	Moderate F cracking [0.8 mm]	B1-B2	Moderate

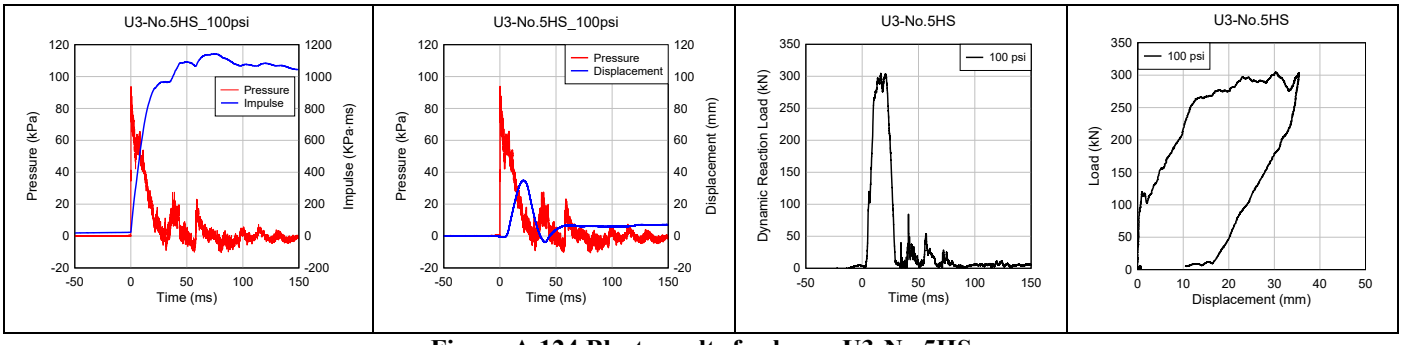

Figure A.124 Blast results for beam U3-No.5HS

(pressure/impulse-time; displacement-time; dynamic reaction-time history; dynamic reaction-displacement response)

Blast-100psi	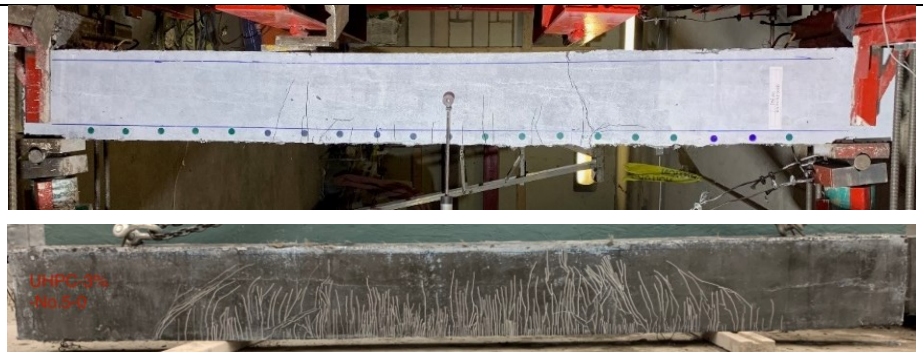

Figure A.125 Blast damage for beam U2-20M-DR-d/2

Table A.58 Residual test result of U3-No.5HS

Beam	Dynamic loading type	Load		Stiffness		Displacement			Energy-absorption		
		P_{max}^{R} (kN)	RRI	k_s^R (N/mm)	RSI	Δ_{test}^{R} (mm)	Δ_{max}^{R} (mm)	RDI	IEI	REI	TEI
U3-No.5HS	Single	291.2	104%	14271	94%	48.4	55.4	89%	0.164	0.745	0.909

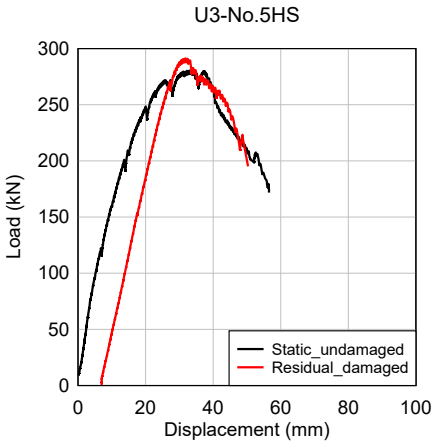

Figure A.126 Post-blast residual results for beam U3-No.5HS

Figure A.127 Failure modes after the post-blast residual static tests

A.3.3.9. U2-No.4S1-DR-d/2 (R)

Beam U2-No.4S1-DR-d/2 (R) was designed with ultra-high performance concrete, 2% steel fibers, No.4/No.3 XM-28 stainless steel tension/compression bars and intermediate ties spaced at d/2 (100 mm). The beam was tested under repeat blast loads at driver pressures (P_d) of 30 psi, 50 psi, 70 psi and 100 psi. **Table A.59** summarizes the blast test results and **Figure A.128** shows the pressure, impulse, displacement and dynamic reaction – time histories. The damage patterns after each blast test are presented in **Figure A.129**.

Blast-30psi was meant to test the beam within the elastic range and caused the formation of hairline cracks along the beam span. Support rotations (θ_{max}) remained below 1° with maximum (D_{max}) and residual (D_{res}) displacements of 12.3 mm and 2.8 mm. *Blast-50psi* caused a major crack having a width of 2.5 mm in the mid-span, with displacements D_{max} = 28.6 mm and D_{res} = 11.6 mm, and a support rotation, θ_{max} = 1.5°. *Blast-70psi* resulted in the further extension of the localized crack which expanded to 13 mm in the midspan flexural zone. The beam sustained displacements of $D_{max} = 53.9\ mm$, $D_{res} = 32.5\ mm$, with a maximum support rotation of $\theta_{max} = 2.8°$ (moderate damage). During the last shot (*Blast-100psi*), the beam failed by bar fracture.

Table A.59 Dynamic test result of U2-No.4S1-DR-d/2 (R)

Beams	Blast ID (Psi)	Shockwave Properties			Specimen Response					CSA S850 Response limits and Component damage	
		P_r (kPa)	I_r (kPa·ms)	t_d (ms)	D_{max} (mm)	D_{res} (mm)	θ_{max} (°)	$D_{\sum res}$ (mm)	Observed Damage [Max. Crack width]	Response limit	Expected Damage level
U2-No.4S1-DR-d/2 (R)	30	43.3	363.1	20.5	12.3	2.8	0.6	2.8	Minor F cracking [HL]	<B1	Superficial
	50	58.3	557.6	21.3	28.6	11.6	1.5	14.4	Moderate F cracking [2.5]	B1-B2	Moderate
	70	75.2	733.4	22.7	53.9	32.5	2.8	46.9	Crack localization & fiber pullout [13]	B1-B2	Moderate
	100	88.7	955.4	24.1	96.5	-	-	-	Bar rupture	> B4	Hazardous

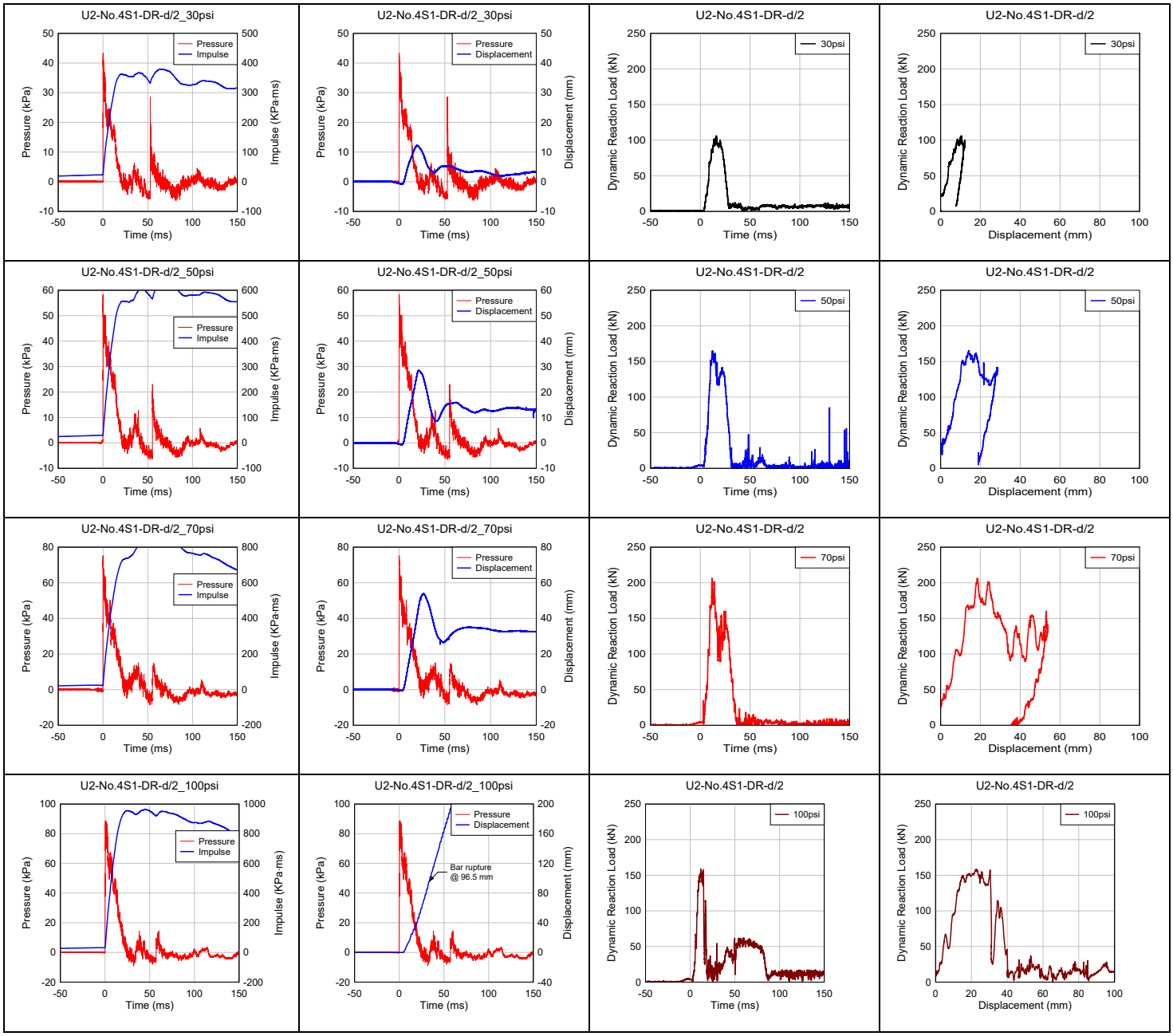

Figure A.128 Blast results for beam U2-No.4S1-DR-d/2 (R).

(pressure/impulse-time; displacement-time; dynamic reaction-time history; dynamic reaction-displacement response)

Blast-30psi	Blast-50psi	Blast-70psi	Blast-100psi
			

Figure A.129 Blast damage for beam U2-No.4S1-DR-d/2 (R)

A.3.3.10. U2-No.5S1-DR-d/2

Beam U2-No.5HS-DR-d/2 was designed with ultra-high performance concrete, 2% steel fibers, No.5/No.4 high-strength tension/compression bars and intermediate ties spaced at d/2 (100 mm). **Table A.60** and **Table A.61** summarize the blast and post-blast test results and **Figure A.130** shows the pressure, impulse, displacement and dynamic reaction histories after the 100 psi shot. The damage after the blast test is shown in **Figure A.131**. The results from the residual static test are shown in **Figure A.132** and **Figure A.133**.

Blast-100psi resulted in the formation of a major crack width of 10 mm at the beam mid-span, with maximum and residual displacements of 57.5 mm and 36.5 mm, and a maximum support rotation (θ_{max}) of 3.0°. Beam damage was moderate, which matches the damage level predicted by the CSA S850 standard. The post-blast residual test shows that the beam still had significant residual capacity after blast testing. The beam had a peak residual capacity (P_{max}^{R}) of 160.7 kN and stiffness (k_s^R) of 11714 N/mm, which are slightly lower than those of the undamaged beam (RRI = 93% and RSI = 93%). The beam reached a maximum residual displacement (Δ_{test}^{R}) of 150 mm without bar rupture. The maximum cumulative residual displacement (Δ_{max}^{R}) was 186.5 mm.

Table A.60 Dynamic test result of U2-No.5S1-DR-d/2

Beams	Blast ID (Psi)	Shockwave Properties			Specimen Response					CSA S850 Response limits and Component damage	
		P_r (kPa)	I_r (kPa·ms)	t_d (ms)	D_{max} (mm)	D_{res} (mm)	θ_{max} (°)	$D_{\sum res}$ (mm)	Observed Damage [Max. Crack width]	Response limit	Expected Damage level
U2-No.5S1-DR-d/2	100	96.3	966.5	24.2	57.5	36.5	3.0	36.5	Crack localization & fiber pullout [10]	B1-B2	Moderate

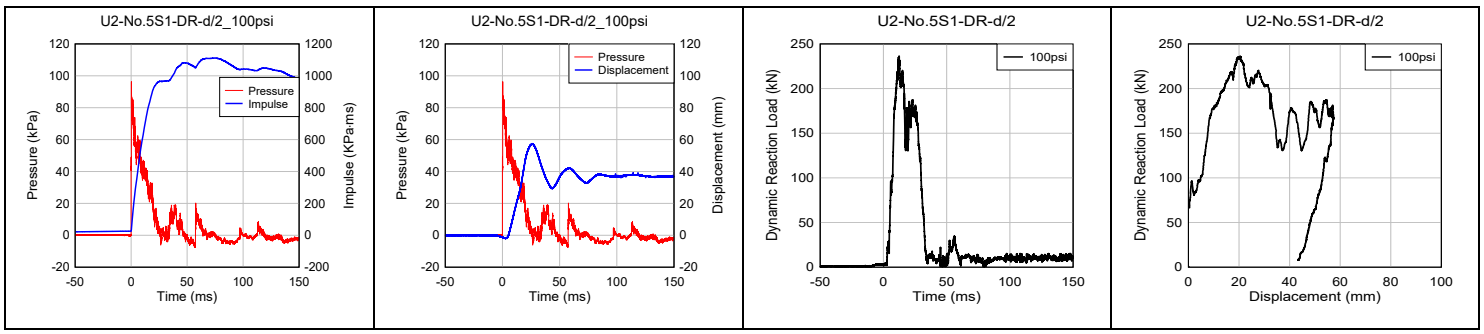

Figure A.130 Blast results for beam U2-No.5S1-DR-d/2

(pressure/impulse-time; displacement-time; dynamic reaction-time history; dynamic reaction-displacement response)

Blast-100psi	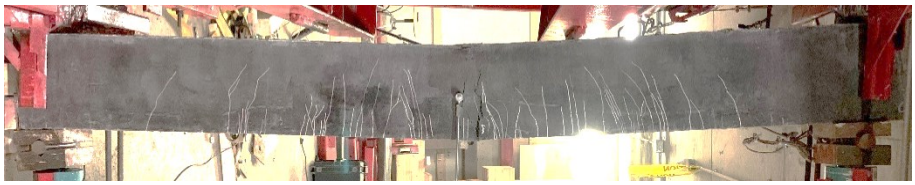

Figure A.131 Blast damage for beam U2-No.5S1-DR-d/2

Table A.61 Residual test result of U2-No.5S1-DR-d/2

Beam	Dynamic loading type	Load		Stiffness		Displacement			Energy-absorption		
		P_{max}^{R} (kN)	RRI	k_s^R (N/mm)	RSI	Δ_{test}^{R} (mm)	Δ_{max}^{R} (mm)	RDI	IEI	REI	TEI
U2-No.5S1-DR-d/2	Single	160.7	93%	11714	93%	150	186.5	124%	0.34	0.78	1.12

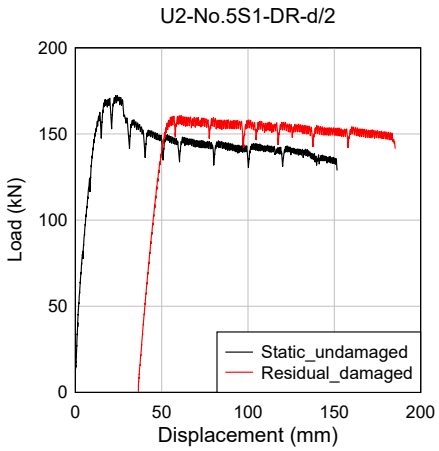

Figure A.132 Post-blast residual results for beam U2-No.5S1-DR-d/2

Figure A.133 Failure mode after the post-blast residual static test

A.3.3.11. U3-No.5S1

Beam U3-No.5S1 was designed with ultra-high performance concrete, 3% steel fiber, 2-No.5 XM-28 stainless steel tension bars without stirrups in the shear span. **Table A.62** and **Table A.63** summarize the blast and post-blast test results and **Figure A.134** shows complete pressure, impulse, displacement and dynamic reaction histories after the 100 psi shot. The damage after the blast test is shown in **Figure A.135**. The results from the residual static test are shown in **Figure A.136** and **Figure A.137**.

Blast-100psi resulted in the formation of a major crack width of 12 mm at the beam mid-span, with maximum and residual displacements of 54.2 mm and 31.5 mm, and a maximum support rotation (θ_{max}) of 2.8°. Beam damage was moderate, which matches the damage level predicted by the CSA S850 standard. The post-blast residual test shows that the beam still had significant residual capacity after blast testing. The beam had a peak residual capacity (P_{max}^{R}) of 164.2 kN and stiffness (k_s^R) of 11260 N/mm, which are less than those of the undamaged beam (RRI = 79% and RSI = 80%). The beam reached a maximum residual displacement (Δ_{test}^{R}) of 130 mm without bar rupture. The maximum cumulative residual displacement (Δ_{max}^{R}) was 161.5 mm.

Table A.62 Dynamic test result of U3-No.5S1

Beams	Blast ID (Psi)	Shockwave Properties			Specimen Response					CSA S850 Response limits and Component damage	
		P_r (kPa)	I_r (kPa·ms)	t_d (ms)	D_{max} (mm)	D_{res} (mm)	θ_{max} (°)	$D_{\sum res}$ (mm)	Observed Damage [Max. Crack width]	Response limit	Expected Damage level
U3-No.5S1	100	90.3	923.5	24.0	54.2	31.5	2.8	31.5	Crack localization & fiber pullout [12]	B1-B2	Moderate

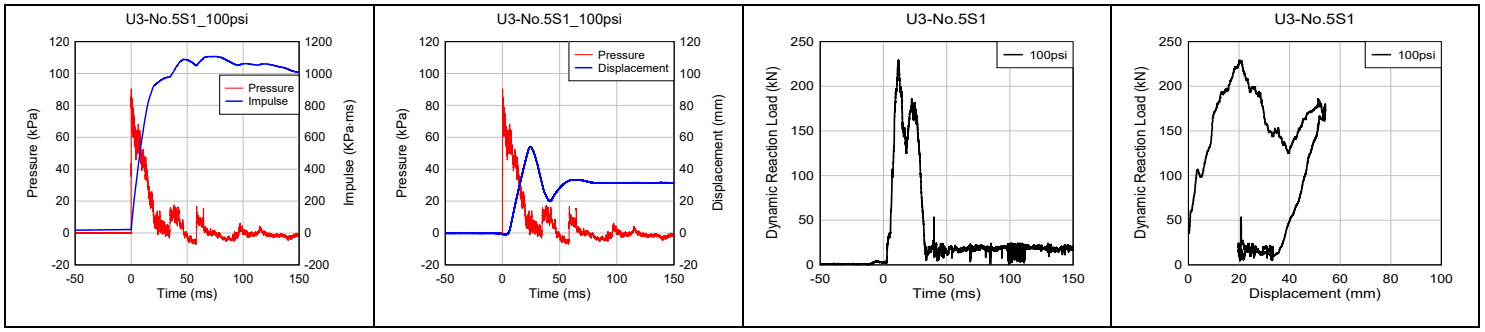

Figure A.134 Blast results for beam U3-No.5S1

(pressure/impulse-time; displacement-time; dynamic reaction-time history; dynamic reaction-displacement response)

Blast-100psi	

Figure A.135 Blast damage for beam U3-No.5S1

Table A.63 Residual test result of U3-No.5S1

Beam	Dynamic loading type	Load		Stiffness		Displacement			Energy-absorption		
		P_{max}^{R} (kN)	RRI	k_s^R (N/mm)	RSI	Δ_{test}^{R} (mm)	Δ_{max}^{R} (mm)	RDI	IEI	REI	TEI
U3-No.5S1	Single	164.2	79%	11260	80%	130	161.5	130%	0.39	0.74	1.13

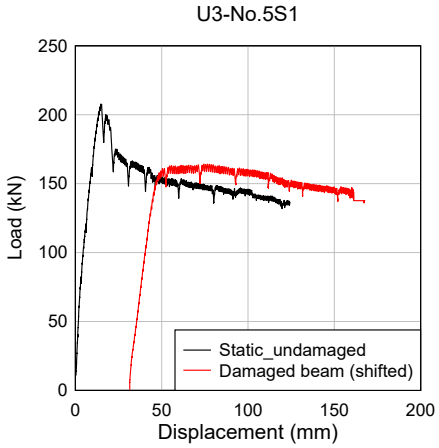

Figure A.136 Post-blast residual results for beam U3-No.5S1

Figure A.137 Failure mode after the post-blast residual static test